

<b>REPORT DOCUMENTATION PAGE</b>			Form Approved OMB NO. 0704-0188	
<p>The public reporting burden for this collection of information is estimated to average 1 hour per response, including the time for reviewing instructions, searching existing data sources, gathering and maintaining the data needed, and completing and reviewing the collection of information. Send comments regarding this burden estimate or any other aspect of this collection of information, including suggestions for reducing this burden, to Washington Headquarters Services, Directorate for Information Operations and Reports, 1215 Jefferson Davis Highway, Suite 1204, Arlington VA, 22202-4302. Respondents should be aware that notwithstanding any other provision of law, no person shall be subject to any penalty for failing to comply with a collection of information if it does not display a currently valid OMB control number.</p> <p>PLEASE DO NOT RETURN YOUR FORM TO THE ABOVE ADDRESS.</p>				
1. REPORT DATE (DD-MM-YYYY) 08-06-2009		2. REPORT TYPE Final Report		3. DATES COVERED (From - To) 1-Oct-2003 - 30-Jun-2007
4. TITLE AND SUBTITLE Meshless Local Petrov-Galerkin Method for Solving Contact, Impact and Penetration Problems			5a. CONTRACT NUMBER DAAD19-03-I-0336	
			5b. GRANT NUMBER	
			5c. PROGRAM ELEMENT NUMBER 611102	
6. AUTHORS Satya N Atluri			5d. PROJECT NUMBER 611102	
			5e. TASK NUMBER	
			5f. WORK UNIT NUMBER	
7. PERFORMING ORGANIZATION NAMES AND ADDRESSES University of California - Irvine Office of Research Administration The Regents of the University of California Irvine, CA 92697 -7600			8. PERFORMING ORGANIZATION REPORT NUMBER	
9. SPONSORING/MONITORING AGENCY NAME(S) AND ADDRESS(ES) U.S. Army Research Office P.O. Box 12211 Research Triangle Park, NC 27709-2211			10. SPONSOR/MONITOR'S ACRONYM(S) ARO	
			11. SPONSOR/MONITOR'S REPORT NUMBER(S) 45475-EG.1	
12. DISTRIBUTION AVAILABILITY STATEMENT Approved for public release; Distribution Unlimited				
13. SUPPLEMENTARY NOTES The views, opinions and/or findings contained in this report are those of the author(s) and should not be construed as an official Department of the Army position, policy or decision, unless so designated by other documentation.				
14. ABSTRACT This research presents the development of a three-dimensional theoretical and computational procedures, for contact, impact, and penetration mechanics, based on the Meshless Local Petrov-Galerkin (MLPG) approach. In the current implementation, both velocities and velocity-gradients are interpolated independently, and their compatibility is enforced only at nodal points. As a result, the time consuming differentiations of the shape functions at all integration points is avoided, and therefore, the numerical process becomes more stable and				
15. SUBJECT TERMS Impact Penetration Advanced Computational Methods				
16. SECURITY CLASSIFICATION OF:			17. LIMITATION OF ABSTRACT SAR	15. NUMBER OF PAGES
a. REPORT U	b. ABSTRACT U	c. THIS PAGE U		
			19a. NAME OF RESPONSIBLE PERSON Satya Atluri	
			19b. TELEPHONE NUMBER 949-824-9946	

**Final Report on**  
**The research project:**

**Meshless Local Petrov-Galerkin Method for Solving Contact, Impact and Penetration Problems**

**Award Number: DAAD19-03-1-0336**

**: Army Research Office (Durham NC)**

**Period of Performance: 09/30/02 to 11/30/06**

**Prepared by**

**By Satya N. Atluri**

**Principal Investigator**

**Department of Aerospace Engineering,  
University of California , Irvine  
Irvine, CA 92612, USA  
Tel: 949.824.9946/9966;  
Fax: 949.824.9967**

## List of Publications

This list contains the archival papers published in open literature, based on research performed under this project. These papers are appended to this report.

No.	Author	Title and Source
001	Atluri SN	Applications of DTALE: Damage Tolerance Analysis & Life Enhancement[3-D Non-planar Crack Growth] <i>SID:Structural Integrity &amp; Durability, 1(1), 1-21, April 2005</i>
002	Atluri SN, and Kobayashi AS	Analytical Mechanics of Solids <i>Chapter 1, in Handbook of Experimental Mechanics( W.N. Sharpe, Ed), Springer Verlag, 2008</i>
003	Atluri SN, Shen SP	Simulation of a 4(th) order ODE: Illustration of various primal & mixed MLPG methods <i>CMES:Computer Modeling in Engineering &amp; Sciences 7 (3): 241-268 MAR 2005</i>
004	Atluri SN, Shen SP	The Basis of meshless domain discretization: the meshless local Petrov-Galerkin (MLPG) method <i>Advances in Computational Mathematics 23 (1-2): 73-93 JUL 2005</i>
005	Han ZD, Atluri SN	Truly Meshless Local Petrov-Galerkin (MLPG) solutions of traction & displacement BIEs <i>CMES:Computer Modeling in Engineering &amp; Sciences 4 (6): 665-678 DEC 2003</i>
006	Han ZD, Liu HT, Rajendran AM, Atluri SN	The Applications of Meshless Local Petrov-Galerkin (MLPG) Approaches in High-Speed Impact, Penetration and Perforation Problems <i>CMES: Computer Modeling in Engineering &amp; Sciences, 14(2) 119-128 ,2006</i>
007	Han ZD, Rajendran AM, Atluri SN	Meshless Local Petrov-Galerkin (MLPG) approaches for solving nonlinear problems with large deformations and rotations <i>CMES:Computer Modeling in Engineering &amp; Sciences 10 (1): 1-12 OCT 2005</i>

No.	Author	Title and Source
008	Li S, Atluri SN	The MLPG mixed collocation method for material orientation and topology optimization of anisotropic solids and structures <i>CMES-COMPUTER MODELING IN ENGINEERING &amp; SCIENCES</i> Volume: 30 Issue: 1 Pages: 37-56, 2008
009	Li,S; and Atluri,SN	Topology-optimization of Structures Based on the MLPG Mixed Collocation Method <i>CMES: Computer Modeling in Engineering &amp; Sciences, Vol. 26, No. 1, pp. 61-74, 2008</i>
010	Liu CS, Atluri SN	A novel time integration method for solving a large system of non-linear algebraic equations <i>CMES-COMPUTER MODELING IN ENGINEERING &amp; SCIENCES</i> Volume: 31 Issue: 2 Pages: 71-83, 2008.
011	Liu HT, Han ZD, Rajendran, AM, Atluri SN	Computational Modeling of Impact Response with the RG Damage Model and the Meshless Local Petrov-Galerkin (MLPG) Approaches <i>CMC-Computers, Materials &amp; Continua, 4(1) 43-54,2006</i>
012	Nie YF, Atluri SN, Zuo CW	The optimal radius of the support of radial weights used in moving least squares approximation <i>CMES:Computer Modeling in Engineering &amp; Sciences 12 (2): 137-147 APR 2006</i>
013	Han ZD, Atluri SN	Meshless Local Petrov-Galerkin (MLPG)Mixed Methods for Solid Mechanics <i>Advances in Computational &amp; Experimental Engineering and Science, 2007, pp.1748-</i>
014	Shen SP, Atluri SN	Atomic-level stress calculation and continuum-molecular system equivalence <i>CMES:Computer Modeling in Engineering &amp; Sciences 6 (1): 91-104 2004</i>
015	Shen SP, Atluri SN	Computational nano-mechanics and multi-scale simulation <i>CMC-Computers, Materials &amp; Continua 1 (1): 59-90 MAR 2004</i>
016	Shen SP, Atluri SN	Multiscale simulation based on the meshless local Petrov-Galerkin (MLPG) method <i>CMES:Computer Modeling in Engineering &amp; Sciences 5 (3): 235-255 MAR 2004</i>

No.	Author	Title and Source
017	Sladek J.; Sladek V.; Solek P.; Atluri SN	Modeling of Piezoelectric and Piezomagnetic Solids by the MLPG Method <i>in Advances in the MLPG Method ( Eds. SN Atluri, J Sladek, and J Soric), Tech Science Press, GA, 2008.</i>
018	Young DL, Fan CM, Hu SP, and Atluri SN	The Eulerian-Lagrangian Method of Fundamental Solutions for Two- dimensional Unsteady Burgers' Equations <i>Engineering Analysis with Boundary Element Methods, Volume: 32 Issue: 5 Pages: 395-412, 2008</i>
019	Z. D. Han, A. M. Rajendran and S. N. Atluri	Meshless Local Petrov-Galerkin (MLPG) Approaches for Solving Nonlinear Problems with Large Deformation and Rotation <i>Advances in Computational &amp; Experimental Engineering and Science, 2005, INDIA, pp. 1059-</i>
020	Z. D Han and S. N. Atluri	SGBEM for Damage Tolerance Analysis and Safe Life Estimation <i>Advances in Computational &amp; Experimental Engineering and Science, 2008, pp.1389-</i>
021	J.S. Eom, S. N. Atluri	A Comparison of Efficient Meshless Methods with Accelerated Differentiation Algorithms <i>Advances in Computational &amp; Experimental Engineering and Science, 2008, pp.859-</i>

## **Applications of DTALE: Damage Tolerance Analysis & Life Enhancement[3-D Non-planar Crack Growth]**

*Atluri SN*

**Abstract:** The solution of three-dimensional cracks (arbitrary surfaces of discontinuity) in solids and structures is considered. The BEM, developed based on the symmetric Galerkin BIEs, is used for obtaining the fracture solutions at the arbitrary crack-front. The finite element method is used to model the uncracked global (built-up) structure for obtaining the stresses in an otherwise uncracked body. The solution for the cracked structural component is obtained in an iteration procedure, which alternates between FEM solution for the uncracked body, and the SGBEM solution for the crack in the local finite-sized subdomain. In addition, some crack growth models are used to advance the crack front in fatigue and other stable-crack-growth situations. The crack-surface mesh is also changed correspondingly in the BEM model, while the FEM model for the uncracked structure is kept unchanged. The automatic crack growth analysis is achieved by repeating the fracture analysis, and the life of the structural components is estimated. Furthermore, the initial crack size and shape in a structure, as emanating from a microscopic defect, can be determined by utilizing the automatic crack-growth feature. Some state-of-the-art numerical solutions are also presented to indicate the type of problems that can now be solved using currently available techniques. All these methodologies are embedded in a user-friendly software, DTALE (Damage Tolerance Analysis and Life Enhancement), which is available for commercial use, in the safety evaluation and life-estimation of a variety of structures. Life enhancement methodologies with deliberate introduction of residual stress-fields, is also a feature of DTALE.

*Source: SID:Structural Integrity & Durability, 1(1), 1-21, April 2005*

## **Simulation of a 4(th) order ODE: Illustration of various primal & mixed MLPG methods**

*Atluri SN, Shen SP*

**Abstract:** Various MLPG methods, with the MLS approximation for the trial function, in the solution of a  $4^{\text{th}}$  order ordinary differential equation are illustrated. Both the primal MLPG methods and the mixed MLPG methods are used. All the possible local weak forms for a  $4^{\text{th}}$  order ordinary differential equation are presented. In the first kind of mixed MLPG methods, both the displacement and its second derivative are interpolated independently through the MLS interpolation scheme. In the second kind of mixed MLPG methods, the displacement, its first derivative, second derivative and third derivative are interpolated independently through the MLS interpolation scheme. The nodal values of the independently interpolated derivatives are expressed in terms of nodal values of the independently interpolated displacements, by simply enforcing the strain-displacement relationships directly by collocation at the nodal points. The mixed MLPG methods avoid the need for a direct evaluation of high order derivatives of the primary variables in the local weak forms, and thus reduce the continuity-requirement on the trial function. Numerical results are presented to illustrate the effectiveness of the primal, as well as two kind of mixed MLPG methods. It is concluded that the mixed MLPG methods are very cost-effective.

*Source: CMES:Computer Modeling in Engineering & Sciences 7 (3): 241-268 MAR 2005*

Paper 004:

## **The Basis of meshless domain discretization: the meshless local Petrov-Galerkin (MLPG) method**

*Atluri SN, Shen SP*

**Abstract:** The MLPG method is the general basis for several variations of meshless methods presented in recent literature. The interrelation of the various meshless approaches is presented in this paper. Several variations of the meshless interpolation schemes are reviewed also. Recent developments and applications of the MLPG methods are surveyed.

*Source: Advances in Computational Mathematics 23 (1-2): 73-93 JUL 2005*

## **Truly Meshless Local Petrov-Galerkin (MLPG) solutions of traction & displacement BIEs**

*Han ZD, Atluri SN*

**Abstract:** The numerical implementation of the truly Meshless Local Petrov-Galerkin (MLPG) type weak-forms of the displacement and traction boundary integral equations is presented, for solids undergoing small deformations. In the accompanying part I of this paper, the general MLPG/BIE weak-forms were presented [Atluri, Han and Shen (2003)]. The MLPG weak forms provide the most general basis for the numerical solution of the non-hyper-singular displacement and traction BIEs [given in Han, and Atluri (2003)], which are simply derived by using the gradients of the displacements of the fundamental solutions [Okada, Rajiyah, and Atluri (1989a,b)]. By employing the various types of test functions, in the MLPG-type weak-forms of the non-hyper-singular dBIE and tBIE over the local sub-boundary surfaces, several types of MLPG/BIEs are formulated, while also using several types of non-element meshless interpolations for trial functions over the surface of the solid. Specifically, three types of MLPG/BIEs are formulated in that paper, i.e. MLPG/BIE1, MLPG/BIE2, and MLPG/BIE6, as per the consistent categorizations of the MLPG domain methods [Atluri and Shen (2002a)]. As the accompanying part II, this paper is devoted to MLPG/BIE6. In particular, the moving least squares (MLS) method has been extended for the approximation on three dimensional surfaces, which makes it possible for the MLPG/BIE methods to be truly meshless. Numerical examples, including crack problems, are presented to demonstrate that the present methods are very promising, especially for solving the elastic problems in which the singularities in displacements, strains, and stresses, are of primary concern.

This paper is based on research performed under the support of ARO. The authors gratefully acknowledge this support.

*Source: CMES:Computer Modeling in Engineering & Sciences 4 (6): 665-678 DEC 2003*

Paper 006:

## **The Applications of Meshless Local Petrov-Galerkin (MLPG) Approaches in High-Speed Impact, Penetration and Perforation Problems**

*Han ZD, Liu HT, Rajendran AM, Atluri SN*

**Abstract:** This paper presents the implementation of a three-dimensional dynamic code, for contact, impact, and penetration mechanics, based on the Meshless Local Petrov-Galerkin (MLPG) approach. In the current implementation, both velocities and velocity-gradients are interpolated independently, and their compatibility is enforced only at nodal points. As a result, the time consuming differentiations of the shape functions at all integration points is avoided, and therefore, the numerical process becomes more stable and efficient. The ability of the MLPG code for solving high-speed contact, impact and penetration problems with large deformations and rotations is demonstrated through several computational simulations, including the Taylor impact problem, and some ballistic impact and perforation problems. The computational times for the above simulations are recorded, and are compared with those of the popular finite element code (Dyna3D), to demonstrate the efficiency of the present MLPG approach.

*Source: CMES: Computer Modeling in Engineering & Sciences, 14(2) 119-128, 2006*

## **Meshless Local Petrov-Galerkin (MLPG) approaches for solving nonlinear problems with large deformations and rotations**

*Han ZD, Rajendran AM, Atluri SN*

**Abstract:** A nonlinear formulation of the Meshless Local Petrov-Galerkin (MLPG) finite-volume mixed method is developed for the large deformation analysis of static and dynamic problems. In the present MLPG large deformation formulation, the velocity gradients are interpolated independently, to avoid the time consuming differentiations of the shape functions at all integration points. The nodal values of velocity gradients are expressed in terms of the independently interpolated nodal values of displacements (or velocities), by enforcing the compatibility conditions directly at the nodal points. For validating the present large deformation MLPG formulation, two example problems are considered: 1) large deformations and rotations of a hyper-elastic cantilever beam, and 2) impact of an elastic-plastic solid rod (cylinder) on a rigid surface (often called as the Taylor impact test). The MLPG result for the cantilever beam problem was successfully compared with results from both analytical modeling and a commercial finite element code simulation. The final shapes of the plastically deformed rod obtained from a well-known finite element code, and the present MLPG code were also successfully compared. The direct comparison of computer run times between the finite element method (FEM) and the large deformation mixed MLPG method showed that the MLPG method was relatively more efficient than the FEM, at least for the two example problems considered in the present study.

*Source: CMES:Computer Modeling in Engineering & Sciences 10 (1): 1-12 OCT 2005*

Paper 008:

## **The MLPG mixed collocation method for material orientation and topology optimization of anisotropic solids and structures**

*Li S, Atluri SN*

**Abstract:** In this paper, a method based on a combination of an optimization of directions of orthotropy, along with topology optimization, is applied to continuum orthotropic solids with the objective of minimizing their compliance. The spatial discretization algorithm is the so called Meshless Local Petrov-Galerkin (MLPG) ``mixed collocation" method for the design domain, and the material-orthotropy orientation angles and the nodal volume fractions are used as the design variables in material optimization and topology optimization, respectively. Filtering after each iteration diminishes the checkerboard effect in the topology optimization problem. The example results are provided to illustrate the effects of the orthotropic material characteristics in structural topology-optimization.

*Source: CMES-COMPUTER MODELING IN ENGINEERING & SCIENCES Volume: 30 Issue: 1 Pages: 37-56, 2008*

Paper 009:

## **Topology-optimization of Structures Based on the MLPG Mixed Collocation Method**

*Li,S; and Atluri,SN*

**Abstract:** The Meshless Local Petrov-Galerkin (MLPG) ``mixed collocation" method is applied to the problem of topology-optimization of elastic structures. In this paper, the topic of compliance minimization of elastic structures is pursued, and nodal design variables which represent nodal volume fractions at discretized nodes are adopted. A so-called nodal sensitivity filter is employed, to prevent the phenomenon of checkerboarding in numerical solutions to the topology-optimization problems. The example results presented in the paper demonstrate the suitability and versatility of the MLPG ``mixed collocation" method, in implementing structural topology-optimization.

*Source: CMES: Computer Modeling in Engineering & Sciences, Vol. 26, No. 1, pp. 61-74, 2008*

## A novel time integration method for solving a large system of non-linear algebraic equations

*Liu CS, Atluri SN*

**Abstract:** Iterative algorithms for solving a nonlinear system of algebraic equations of the type:  $F_i(x_j)=0, \{i,j=1,\dots,n\}$  date back to the seminal work of Issac Newton. Nowadays a Newton-like algorithm is still the most popular one due to its easy numerical implementation. However, this type of algorithm is sensitive to the initial guess of the solution and is expensive in the computations of the Jacobian matrix  $\partial F_i / \partial x_j$  and its inverse at each iterative step. In a time-integration of a system of nonlinear Ordinary Differential Equations (ODEs) of the type  $\dot{B}_{ij}x_j + F_i = 0$  where  $B_{ij}$  are nonlinear functions of  $x_j$ , the methods which involve an inverse of the Jacobian matrix  $B_{ij} = \partial F_i / \partial x_j$  are called "Implicit", while those that do not involve an inverse of  $\partial F_i / \partial x_j$  are called "Explicit". In this paper a natural system of explicit ODEs is derived from the given system of nonlinear algebraic equations (NAEs), by introducing a fictitious time, such that it is a mathematically equivalent system in the  $n+1$ -dimensional space as the original algebraic equations system is in the  $n$ -dimensional space. The iterative equations are obtained by applying numerical integrations on the resultant ODEs, which do not need the information of  $\partial F_i / \partial x_j$  and its inverse. The computational cost is thus greatly reduced. Numerical examples given confirm that this fictitious time integration method (FTIM) is highly efficient to find the true solutions with residual errors being much smaller. Also, the FTIM is used to study the attracting sets of fixed points, when multiple roots exist.

*Source: CMES-COMPUTER MODELING IN ENGINEERING & SCIENCES Volume: 31 Issue: 2 Pages: 71-83, 2008.*

Paper 011:

## **Computational Modeling of Impact Response with the RG Damage Model and the Meshless Local Petrov-Galerkin (MLPG) Approaches**

*Liu HT, Han ZD, Rajendran, AM, Atluri SN*

**Abstract:** The Rajendran-Grove (RG) ceramic damage model is a three-dimensional internal variable based constitutive model for ceramic materials, with the considerations of micro-crack extension and void collapse. In the present paper, the RG ceramic model is implemented into the newly developed computational framework based on the Meshless Local Petrov-Galerkin (MLPG) method, for solving high-speed impact and penetration problems. The ability of the RG model to describe the internal damage evolution and the effective material response is investigated. Several numerical examples are presented, including the rod-on-rod impact, plate-on-plate impact, and ballistic penetration. The computational results are compared with available experiments, as well as those obtained by the popular finite element code (Dyna3D).

*Source: CMC-Computers, Materials & Continua, 4(1) 43-54, 2006*

Paper 012:

## **The optimal radius of the support of radial weights used in moving least squares approximation**

*Nie YF, Atluri SN, Zuo CW*

**Abstract:** Owing to the meshless and local characteristics, moving least squares (MLS) methods have been used extensively to approximate the unknown function of partial differential equation initial boundary value problem. In this paper, based on matrix analysis, a sufficient and necessary condition for the existence of inverse of coefficient matrix used in MLS methods is developed firstly. Then in the light of approximate theory, a practical mathematics model is posed to obtain the optimal radius of support of radial weights used in MLS methods. As an example, while uniform distributed particles and the 4<sup>th</sup> order spline weight function are adopted in MLS method in two dimension domain and two kinds of norms are used to measure error, optimal results for linear and quadratic basis are gained. Finally, the test data verify that the optimal values are correct. The research idea can be used in 3-dimension problems too.

*Source: CMES:Computer Modeling in Engineering & Sciences 12 (2): 137-147 APR 2006*

Paper 013:

## **Meshless Local Petrov-Galerkin (MLPG) Mixed Methods for Solid Mechanics**

*Han ZD, Atluri SN*

**Abstract:** Various methods have been developed within the framework of the Meshless Local Petrov-Galerkin (MLPG) approach, for solving solid mechanics problems. A "mixed" interpolation scheme is adopted in the present implementation: the displacements, displacement gradients, and stresses are interpolated independently using identical interpolation. The system of algebraic equations for the problem is obtained by enforcing the momentum balance laws at the nodal points. Numerical examples show that the MLPG mixed methods are accurate and efficient, and stable.

*Source: Advances in Computational & Experimental Engineering and Science, 2007, pp.1748-*

## **Atomic-level stress calculation and continuum-molecular system equivalence**

*Shen SP, Atluri SN*

**Abstract:** An atomistic level stress tensor is defined with physical clarity, based on the SPH method. This stress tensor rigorously satisfies the conservation of linear momentum, and is appropriate for both homogeneous and inhomogeneous deformations. The formulation is easier to implement than other stress tensors that have been widely used in atomistic analysis, and is validated by numerical examples. The present formulation is very robust and accurate, and will play an important role in the multiscale simulation, and in molecular dynamics. An equivalent continuum is also defined for the molecular dynamics system, based on the developed definition of atomistic stress and in conjunction with the SPH technique. The process is simple and easy to implement, and the fields are with high-order continuity. This equivalent continuum maintains the physical attributes of the atomistic system. This development provides a systematic approach to the continuum analysis of the discrete atomic systems.

*Source: CMES:Computer Modeling in Engineering & Sciences 6 (1): 91-104 2004*

Paper 015:

## **Computational nano-mechanics and multi-scale simulation**

*Shen SP, Atluri SN*

**Abstract:** This article provides a review of the computational nanomechanics, from the methods to classical molecular dynamics simulations, and multi- temporal and spatial scale simulations. The recent improvements and developments are briefly discussed. Their applications in nanomechanics and nanotubes are also summarized.

*Source: CMC-Computers, Materials & Continua 1 (1): 59-90 MAR 2004*

## **Multiscale simulation based on the meshless local Petrov-Galerkin (MLPG) method**

*Shen SP, Atluri SN*

**Abstract:** A multiscale simulation technique based on the MLPG methods, and finite deformation mechanics, is developed, implemented, and tested. Several alternate time-dependent interfacial conditions, between the atomistic and continuum regions, are systematically studied, for the seamless multiscale simulation, by decomposing the displacement of atoms in the equivalent-continuum region into long and short wave-length components. All of these methods for enforcing the interface conditions can ensure the passage of information accurately between the atomistic and continuum regions, while they lead to different performances at short wavelengths. The presently proposed Solution Method 2 reduces the phonon reflections at the interface, without increasing the computational burden. Multiple length scale, multiple time step, and meshless local Petrov-Galerkin (MLPG) methods are used in the numerical examples.

*Source: CMES:Computer Modeling in Engineering & Sciences 5 (3): 235-255 MAR 2004*

## Modeling of Piezoelectric and Piezomagnetic Solids by the MLPG Method

*Sladek J.; Sladek V.; Sulek P.; Atluri SN*

**Abstract:** A meshless method based on the local Petrov-Galerkin approach is proposed to solve 2-D and 3-D axisymmetric boundary value problems in piezoelectric and magneto-electric-elastic solids with continuously varying material properties. Axial symmetry of geometry and boundary conditions reduces the original 3-D boundary value problem into a 2-D problem in the axial cross section. Stationary and transient dynamic problems are considered in this paper. The mechanical fields are described by the equations of motion with an inertial term. To eliminate the time-dependence in the governing partial differential equations the Laplace-transform technique is applied to the governing equations, which are satisfied in the Laplace-transformed domain in a weak-form on small subdomains. Nodal points are spread on the analyzed domain and each node is surrounded by a small circle for simplicity. The spatial variation of the displacements and the electric potential are approximated by the Moving Least-Squares (MLS) scheme. After performing the spatial integrations, one obtains a system of linear algebraic equations for unknown nodal values. The boundary conditions on the global boundary are satisfied by the collocation of the MLS-approximation expressions for the displacements and the electric potential at the boundary nodal points. The Stehfest's inversion method is applied to obtain the final time-dependent solutions.

*Source: in Advances in the MLPG Method ( Eds. SN Atluri, J Sladek, and J Soric), Tech Science Press, GA, 2008.*

## **The Eulerian-Lagrangian Method of Fundamental Solutions for Two-dimensional Unsteady Burgers' Equations**

*Young DL, Fan CM, Hu SP, and Atluri SN*

**Abstract:** The Eulerian–Lagrangian method of fundamental solutions is proposed to solve the two-dimensional unsteady Burgers' equations. Through the Eulerian–Lagrangian technique, the quasi-linear Burgers' equations can be converted to the characteristic diffusion equations. The method of fundamental solutions is then adopted to solve the diffusion equation through the diffusion fundamental solution; in the meantime the convective term in the Burgers' equations is retrieved by the back-tracking scheme along the characteristics. The proposed numerical scheme is free from mesh generation and numerical integration and is a truly meshless method. Two-dimensional Burgers' equations of one and two unknown variables with and without considering the disturbance of noisy data are analyzed. The numerical results are compared very well with the analytical solutions as well as the results by other numerical schemes. By observing these comparisons, the proposed meshless numerical scheme is convinced to be an accurate, stable and simple method for the solutions of the Burgers' equations with irregular domain even using very coarse collocating points.

*Source: Engineering Analysis with Boundary Element Methods, Volume: 32 Issue: 5 Pages: 395-412, 2008*

## **Meshless Local Petrov-Galerkin (MLPG) Approaches for Solving Nonlinear Problems with Large Deformation and Rotation**

*Z. D. Han, A. M. Rajendran and S. N. Atluri*

**Abstract:** A nonlinear formulation of the Meshless Local Petrov-Galerkin (MLPG) finite-volume mixed method is developed for the large deformation analysis of static and dynamic problems. In the present MLPG large deformation formulation, the velocity gradients are interpolated independently, to avoid the time consuming differentiations of the shape functions at all integration points. The nodal values of velocity gradients are expressed in terms of the independently interpolated nodal values of displacements (or velocities), by enforcing the compatibility conditions directly at the nodal points. For validating the present large deformation MLPG formulation, two example problems are considered: 1) large deformations and rotations of a hyper-elastic cantilever beam, and 2) impact of an elastic-plastic solid rod (cylinder) on a rigid surface (often called as the Taylor impact test). The MLPG result for the cantilever beam problem was successfully compared with results from both analytical modeling and a commercial finite element code simulation. The final shapes of the plastically deformed rod obtained from a well-known finite element code, and the present MLPG code were also successfully compared. The direct comparison of computer run times between the finite element method (FEM) and the large deformation mixed MLPG method showed that the MLPG method was relatively more efficient than the FEM, at least for the two example problems considered in the present study.

This paper is based on research performed under the support of ARO. The authors gratefully acknowledge this support.

*Source: Advances in Computational & Experimental Engineering and Science, 2005, INDIA, pp. 1059-*

## **SGBEM for Damage Tolerance Analysis and Safe Life Estimation**

*Z. D Han and S. N. Atluri*

**Abstract:** The solution of 3-D arbitrary cracks is obtained by using the alternating method between the Symmetric Galerkin Boundary Element Method (SGBEM) and the finite element method (FEM). It is based on an iteration procedure, which alternates between FEM solution for the uncracked body, and the SGBEM solution for the crack in the local finite-sized subdomain. In addition, some crack growth models are used to advance the crack front in fatigue and other stable-crack-growth situations. The crack-surface mesh is also changed correspondingly in the BEM model, while the FEM model for the uncracked structure is kept unchanged. The automatic crack growth analysis is achieved by repeating the fracture analysis, and the life of the structural components is estimated. Furthermore, the initial crack size and shape in a structure, as emanating from a microscopic defect, can be determined by utilizing the automatic crack-growth feature. Some state-of-the-art numerical solutions are also presented to indicate the type of problems that can now be solved using currently available techniques.

*Source: Advances in Computational & Experimental Engineering and Science, 2008, pp.1389-*

## **A Comparison of Efficient Meshless Methods with Accelerated Differentiation Algorithms**

*J.S. Eom, S. N. Atluri*

**Abstract:** A series of efficient meshless methods with their own differentiation algorithm are compared in this paper. The computational cost for complicated derivative of the interpolation functions in the meshless analysis is more expensive than traditional element-based method. Several promising meshless methods with simplified and accelerated algorithm are recently proposed in order to reduce or avoid the direct differentiation of meshless interpolation function. In the framework of Meshless Local Petrov-Galerkin (MLPG) method, a mixed approach allows to use the independent interpolation scheme for the displacements and its gradients and stresses. It also reduces the support size and lowers requirements for trial function. In MLPG mixed Finite Difference Method, the divergence of the stress tensor is more efficiently obtained through the generalized finite difference method. Differential quadrature (DQ) method can be adopted for computing derivatives of a meshless interpolation from a weighted linear sum of the function value at neighboring nodes. For aforementioned methods, the accuracy, the efficiency, and applicability of the methods are numerically tested to linear static elasticity problems. Their advantages and disadvantages are compared and discussed based on numerical observation.

This paper is based on research performed under the support of ARO. The authors gratefully acknowledge this support.

*Source: Advances in Computational & Experimental Engineering and Science, 2008, pp.859-*

# Applications of DTALE: Damage Tolerance Analysis and Life Enhancement [3-D Non-planar Fatigue Crack Growth]

S. N. Atluri<sup>1</sup>

**Abstract:** The solution of three-dimensional cracks (arbitrary surfaces of discontinuity) in solids and structures is considered. The BEM, developed based on the symmetric Galerkin BIEs, is used for obtaining the fracture solutions at the arbitrary crack-front. The finite element method is used to model the uncracked global (built-up) structure for obtaining the stresses in an otherwise uncracked body. The solution for the cracked structural component is obtained in an iteration procedure, which alternates between FEM solution for the uncracked body, and the SGBEM solution for the crack in the local finite-sized subdomain. In addition, some crack growth models are used to advance the crack front in fatigue and other stable-crack-growth situations. The crack-surface mesh is also changed correspondingly in the BEM model, while the FEM model for the uncracked structure is kept unchanged. The automatic crack growth analysis is achieved by repeating the fracture analysis, and the life of the structural components is estimated. Furthermore, the initial crack size and shape in a structure, as emanating from a microscopic defect, can be determined by utilizing the automatic crack-growth feature. Some state-of-the-art numerical solutions are also presented to indicate the type of problems that can now be solved using currently available techniques. All these methodologies are embedded in a user-friendly software, DTALE (Damage Tolerance Analysis and Life Enhancement), which is available for commercial use, in the safety evaluation and life-estimation of a variety of structures. Life enhancement methodologies with deliberate introduction of residual stress-fields, is also a feature of DTALE.

**keyword:** damage tolerance analysis, life enhancement, arbitrary 3D surface crack, finite element method, symmetric Galerkin boundary element method, the alter-

nating method.

## 1 Introduction

The calculation of fracture mechanics parameters (such as the stress intensity factors of Modes I, II and III), for arbitrary non-planar three-dimensional surface and internal cracks, remains an important task in the structural integrity assessment and damage tolerance analysis [Atluri (1997)]. The three-dimensional stress analyses of crack configurations have received a lot of attention in the last two decades. Various methods have been investigated to obtain the stress-intensity factors for surface cracks: the finite element method (FEM), the boundary element method (BEM), the coupled FEM-BEM method and the FEM-BEM alternating method, as summarized in [Atluri (1986)]. They were used successfully for this purpose.

The finite element method is generally regarded as the most powerful numerical method since it can handle complicated geometries and loading conditions. The fracture mechanics problems are solved by using singularity elements [Tan, Newman and Bigelow (1996); Raju and Newman (1979)] or displacement hybrid elements [Atluri and Kathiresan (1975)], or by using certain path-independent and domain-independent integrals based on conservative laws of continuum mechanics [Nikishkov and Atluri (1987); Shivakumar and Raju (1992)]. Unfortunately, these methods require an explicit finite-element modeling of cracks, such as in HKS/ABAQUS. They encounter a serious difficulty in the mesh generation when they are applied to three-dimensional problems, with the extremely high human labor cost for creating appropriate meshes for cracks in structural components of arbitrary geometry. In addition, it is almost impossible to keep creating the meshes with high quality, during crack propagation.

It is well known that boundary element methods (BEM) have distinct advantages over domain approaches in solving of linear elastic fracture mechanics problems. In

---

<sup>1</sup> Center for Aerospace Research & Education, University of California, Irvine, 5251 California Avenue, Suite 140 Irvine, CA, 92612, USA

BEM, the mesh should be generated only for the boundary of the structure, and for the crack surface. Consequently, it is simpler to create a boundary element mesh, in comparison to a finite element mesh for a body with a crack. The traditional (collocation) boundary element method has certain features, which make it suitable for the solution of crack problems. Recent publications on the dual boundary element method [Cisilino and Aliabadi (1999)] can serve as an example of application of traditional BEM to linear and non-linear fracture mechanics problems. The symmetric Galerkin boundary element method (SGBEM) [Han and Atluri (2002, 2003a)] has been recently developed, based on a weakly singular weak-form of integral equations. The system matrix shows symmetry and sign-definiteness. The SGBEM overcomes some drawbacks of the traditional boundary element methods, including the nonsymmetrical matrix of the equation system, and the hypersingular kernels. Another advantage of the SGBEM is that, after a special transformation to remove the singularity from kernels, the system matrices can be integrated with the use of usual Gaussian quadrature rule [Andra (1998); Erichsen and Sauter (1998)]. But from the numerical point of view, the SGBEM, like all BEM approaches, entails fully populated coefficient matrices, which hinders their application to large-scale problems with complex geometry.

The coupled FEM-BEM approaches are also proposed for fracture analyses by limiting the employment of the BEM to the fractured region [Keat, Annigeri and Cleary (1988); Frangi and Novati (2002)]. The SGBEM shows its special advantage in such a coupled approach, with its symmetric system matrices and sign-definiteness. An obvious disadvantage of this approach is that, both the mesh of fractured region for BEM and the mesh for the remaining part for FEM should be modified when it is necessary to analyze cracks of different sizes and locations, including crack-growth.

The alternating method, generally known as the Schwartz-Neumann alternating method, obtains the solution on a domain that is the intersection of two other overlapping domains [Kantorovich and Krylov (1964)]. The procedure has been applied to fracture mechanical analyses. Normally the two domains are defined to be: one, a finite body without the crack; and the second, an infinite body with cracks. The solution is obtained by iterating between the solution for the uncracked finite body (usually using FEM), and the cracks in an infinite region ob-

tained with collocation BEM or SGBEM. Each solution can be solved by various methods [Atluri (1997); Nishiooka and Atluri (1983); Vijaykumar and Atluri (1981); Wang and Atluri (1996)]. For a complex geometry with the arbitrary cracks, the alternating procedure has been implemented by iterating between the FEM and the SGBEM [Nikishkov, Park and Atluri (2001); Han and Atluri (2002)]. In [Nikishkov, Park and Atluri (2001)], two solutions are employed iteratively: 1. The FEM solution for stresses in the uncracked global structure; 2. The SGBEM solution for the crack in an infinite body – thus only the crack surfaces are modeled in the SGBEM. This approach has been applied to the embedded cracks with high accuracy. It also demonstrated the flexibility in choosing the overlapping domains for different crack configurations. From a computational point of view, it also shows its efficiency in saving both computational and human labor time, by leveraging the existing FE models. This work has been extended in [Han and Atluri (2002)], in which the solution is obtained by alternating between two finite domains: the global uncracked structure is solved by using the FEM, and a local cracked subdomain is solved by using the SGBEM. It eliminates the need for evaluating the singular integral of tractions at the free surface, during the alternating procedure when surface crack problems are considered. At the same time, it limits the employment of the SGBEM only for the local cracked subdomain, and reduces the computational cost and memory requirements, since the SGBEM entails the fully populated system matrix. In addition, the alternating method may be also extended for the crack problems by using the truly meshless methods, through the meshless local Petrov-Galerkin approach (MLPG), pioneered by Atluri and his colleagues [Atluri(2004); Atluri, Han and Shen(2003); Han and Atluri (2003b, 2004a, 2004b)]. The present work discusses the recent development of the alternating method based on FEM and SGBEM, embedded in a commercial-quality software, DTALE: “Damage Tolerance Analysis and Life Enhancement”. With DTALE, the BEM is applied only for the local crack subdomain, and reduces the computational cost and memory requirements. With the use of the built-in FEM solver, DTALE can handle much more complex structural components than pure BEM solvers. In addition, DTALE provides an interface to commercial FEM codes (such as NASTRAN, ABAQUS and MARC) to retrieve the FEM solutions of uncracked structures. From the modeling

point of view, this approach makes the full use of the existing FE models to avoid any model regeneration, which is extremely high in human labor cost. The presently proposed procedure is demonstrated by solving both the embedded and surface cracks problems. The stress intensity factors are calculated and compared with the earlier published solutions. The good agreements show that the FEM-SGBEM alternating method between two finite domains is very efficient and highly accurate for 3D arbitrary crack problems. DTALE is also used to solve the problem of mixed-mode fatigue-growth of an initially-semi-circular surface flaw which is inclined to the direction of tensile loading in a thick plate. In addition, the automatic determination of the initial crack is also demonstrated by using the DTALE.

## 2 Formulation of the non-hyper-singular symmetric Galerkin boundary element method

The non-hypersingular displacement and traction BIEs for a linear elastic, homogeneous, isotropic solid, are summarized in this section. Consider a linear elastic, homogeneous, isotropic body in a domain  $\Omega$ , with a boundary  $\partial\Omega$ . The Lamé constants of the linear elastic isotropic body are  $\lambda$  and  $\mu$ ; and the corresponding Young's modulus and Poisson's ratio are  $E$  and  $\nu$ , respectively. We use Cartesian coordinates  $\xi_i$ , and the attendant base vectors  $\mathbf{e}_i$ , to describe the geometry in  $\Omega$ . The solid is assumed to undergo infinitesimal deformations. The equations of balance of linear and angular momentum can be written as:

$$\nabla \cdot \boldsymbol{\sigma} + \mathbf{f} = \mathbf{0}; \quad \boldsymbol{\sigma} = \boldsymbol{\sigma}^t; \quad \nabla = \mathbf{e}_i \frac{\partial}{\partial \xi_i} \quad (1)$$

The constitutive relations of an isotropic linear elastic homogeneous solid are:

$$\boldsymbol{\sigma} = \lambda \mathbf{I} (\nabla \cdot \mathbf{u}) + 2\mu \boldsymbol{\epsilon} \quad (2)$$

It is well known that the displacement vector, which is a continuous function of  $\boldsymbol{\xi}$ , can be derived, in general, from the Galerkin-vector-potential  $\boldsymbol{\phi}$  such that:

$$\mathbf{u} = \nabla^2 \boldsymbol{\phi} - \frac{1}{2(1-\nu)} \nabla (\nabla \cdot \boldsymbol{\phi}) \quad (3)$$

Consider a point unit load applied in an arbitrary direction  $\mathbf{e}^p$  at a generic location  $\mathbf{x}$  in a linear elastic isotropic homogeneous infinite medium. It is well-known that the

displacement solution is given by the Galerkin-vector-displacement-potential:

$$\boldsymbol{\phi}^{*p} = (1-\nu) F^* \mathbf{e}^p \quad (4)$$

in which  $F^*$  is a scalar function, as

$$F^* = \frac{r}{8\pi\mu(1-\nu)} \quad \text{for 3D problems} \quad (5)$$

and

$$F^* = \frac{-r^2 \ln r}{8\pi\mu(1-\nu)} \quad \text{for 2D problems} \quad (6)$$

where  $r = \|\boldsymbol{\xi} - \mathbf{x}\|$

The corresponding displacements are derived, by using Eq. (3), as:

$$u_i^{*p}(\mathbf{x}, \boldsymbol{\xi}) = (1-\nu) \delta_{pi} F_{,kk}^* - \frac{1}{2} F_{,pi}^* \quad (7)$$

and the gradients of the displacements in (7) are:

$$u_{i,j}^{*p}(\mathbf{x}, \boldsymbol{\xi}) = (1-\nu) \delta_{pi} F_{,kkj}^* - \frac{1}{2} F_{,pij}^* \quad (8)$$

By taking the fundamental solution  $u_i^{*p}(\mathbf{x}, \boldsymbol{\xi})$  in Eq. (7) as the test functions, one may write the weak-form of the equilibrium Eq. (1). The traditional displacement BIE can be written as,

$$u_p(\mathbf{x}) = \int_{\partial\Omega} t_j(\boldsymbol{\xi}) u_j^{*p}(\mathbf{x}, \boldsymbol{\xi}) dS - \int_{\partial\Omega} n_i(\boldsymbol{\xi}) u_j(\boldsymbol{\xi}) \sigma_{ij}^{*p}(\mathbf{x}, \boldsymbol{\xi}) dS \quad (9)$$

Where  $\sigma_{ij}^{*p}$  is the stress field of the fundamental solution, as

$$\begin{aligned} \sigma_{ij}^{*p}(\mathbf{x}, \boldsymbol{\xi}) &\equiv E_{ijkl} u_{k,l}^{*p} \\ &= \mu [(1-\nu) \delta_{pi} F_{,kkj}^* + \nu \delta_{ij} F_{,pkk}^* - F_{,pij}^*] \\ &\quad + \mu (1-\nu) \delta_{pj} F_{,kki}^* \end{aligned} \quad (10)$$

Instead of the *scalar* weak form of Eq. (1), as used for the displacement BIE, we may also write a *vector* weak form of Eq. (1), by using the tensor test functions  $u_{i,j}^{*p}(\mathbf{x}, \boldsymbol{\xi})$  in Eq. (8) [as originally proposed in Okada, Rajiyah, and Atluri (1989), Okada and Atluri(1994)], and derive

a non-hypersingular integral equation for tractions in a linear elastic solid [Han and Atluri (2003)],

$$-t_b(\mathbf{x}) = \int_{\partial\Omega} t_q(\boldsymbol{\xi}) n_a(\mathbf{x}) \sigma_{ab}^{*q}(\mathbf{x}, \boldsymbol{\xi}) dS + \int_{\partial\Omega} D_p u_q(\boldsymbol{\xi}) n_a(\mathbf{x}) \Sigma_{abpq}^*(\mathbf{x}, \boldsymbol{\xi}) dS \quad (11)$$

where  $\Sigma_{abpq}^*$  is another derived kernel function, which were first given by Han and Atluri [2]

$$\begin{aligned} \Sigma_{ijpq}^*(\mathbf{x}, \boldsymbol{\xi}) &= E_{ijkl} e_{nlp} \sigma_{nq}^{*k}(\mathbf{x}, \boldsymbol{\xi}) \\ &= \mu^2 [(e_{inp} F_{jqn} - e_{inp} \delta_{jq} F_{bbn} \\ &\quad + e_{int} e_{tqk} e_{jpm} F_{kmn}) \\ &\quad + \nu (e_{inq} \delta_{jp} F_{bbn} + e_{jqn} \delta_{ip} F_{bbn})] \end{aligned} \quad (12)$$

and the surface tangential operator  $D_t$  is defined as,

$$D_t = n_r e_{rst} \frac{\partial}{\partial \xi_s} \quad (13)$$

The singularity of  $u_i^{*p}$  is  $O(1/r)$ , as the second derivatives of  $F^*$  are included. The singularities are  $O(1/r^2)$  for  $\sigma_{ij}^{*p}$  and  $\Sigma_{abpq}^*$  because of the third derivatives of  $F^*$ . Thereafter, the displacement and traction BIEs in Eqs. (9) and (11) have the non-hyper-singularities only. It should be noted that these two integral equations for  $u_p(\mathbf{x})$  and  $t_b(\mathbf{x})$  are derived independently of each other. On the other hand, if we derive the integral equation for the displacement-gradients, by directly differentiating  $u_p(\mathbf{x})$  in Eq. (9), a hyper-singularity is clearly introduced due to the forth derivatives.

Furthermore, Eqs. (9) and (11) may be satisfied in weak-forms over the boundary surface  $\partial\Omega$ , by using a Galerkin scheme. One may obtain the symmetric Galerkin displacement and traction BIEs after applying Stokes' theorem, as

$$\begin{aligned} \frac{1}{2} \int_{\partial\Omega} \hat{t}_p(\mathbf{x}) u_p(\mathbf{x}) dS_x &= \int_{\partial\Omega} \hat{t}_p(\mathbf{x}) dS_x \int_{\partial\Omega} t_j(\boldsymbol{\xi}) u_j^{*p}(\mathbf{x}, \boldsymbol{\xi}) dS_\xi \\ &\quad + \int_{\partial\Omega} \hat{t}_p(\mathbf{x}) dS_x \int_{\partial\Omega} D_i(\boldsymbol{\xi}) u_j(\boldsymbol{\xi}) G_{ij}^{*p}(\mathbf{x}, \boldsymbol{\xi}) dS_\xi \\ &\quad + \int_{\partial\Omega} \hat{t}_p(\mathbf{x}) dS_x \int_{\partial\Omega}^{CPV} n_i(\boldsymbol{\xi}) u_j(\boldsymbol{\xi}) \phi_{ij}^{*p}(\mathbf{x}, \boldsymbol{\xi}) dS_\xi \end{aligned} \quad (14)$$

$$\begin{aligned} & - \frac{1}{2} \int_{\partial\Omega} t_b(\mathbf{x}) \hat{u}_b(\mathbf{x}) dS_x \\ &= \int_{\partial\Omega} D_a \hat{u}_b(\mathbf{x}) dS_x \int_{\partial\Omega} t_q(\boldsymbol{\xi}) G_{ab}^{*q}(\mathbf{x}, \boldsymbol{\xi}) dS_\xi \\ &\quad - \int_{\partial\Omega} t_q(\boldsymbol{\xi}) dS_\xi \int_{\partial\Omega}^{CPV} n_a(\mathbf{x}) \hat{u}_b(\mathbf{x}) \phi_{ab}^{*q}(\mathbf{x}, \boldsymbol{\xi}) dS_x \\ &\quad + \int_{\partial\Omega} D_a \hat{u}_b(\mathbf{x}) dS_x \int_{\partial\Omega} D_p u_q(\boldsymbol{\xi}) H_{abpq}^*(\mathbf{x}, \boldsymbol{\xi}) dS_\xi \end{aligned} \quad (15)$$

where  $G_{ij}^{*p}$ ,  $\phi_{ij}^{*p}$  and  $H_{ijpq}^*$  are kernel functions and given as [Han and Atluri (2003)],

For 3D problems,

$$G_{ij}^{*p}(\mathbf{x}, \boldsymbol{\xi}) = \frac{1}{8\pi(1-\nu)r} [(1-2\nu)e_{ipj} + e_{ikj}r_{,k}r_{,p}] \quad (16a)$$

$$\phi_{ij}^{*p}(\mathbf{x}, \boldsymbol{\xi}) = \frac{1}{4\pi r^2} \delta_{pj} r_{,i} \quad (16b)$$

$$\begin{aligned} H_{ijpq}^*(\mathbf{x}, \boldsymbol{\xi}) &= \frac{\mu}{8\pi(1-\nu)r} [4\nu\delta_{iq}\delta_{jp} - \delta_{ip}\delta_{jq} \\ &\quad - 2\nu\delta_{ij}\delta_{pq} + \delta_{ij}r_{,p}r_{,q} + \delta_{pq}r_{,i}r_{,j} \\ &\quad - 2\delta_{ip}r_{,j}r_{,q} - \delta_{jq}r_{,i}r_{,p}] \end{aligned} \quad (16c)$$

For 2D problems,

$$G_{ij}^{*p}(\mathbf{x}, \boldsymbol{\xi}) = \frac{1}{4\pi(1-\nu)} [-(1-2\nu)\ln r e_{ipj} + e_{ikj}r_{,k}r_{,p}] \quad (17a)$$

$$\phi_{ij}^{*p}(\mathbf{x}, \boldsymbol{\xi}) = \frac{1}{2\pi r} \delta_{pj} r_{,i} \quad (17b)$$

$$\begin{aligned} H_{ijpq}^*(\mathbf{x}, \boldsymbol{\xi}) &= \frac{\mu}{4\pi(1-\nu)} [-4\nu\ln r \delta_{iq}\delta_{jp} \\ &\quad + \ln r \delta_{ip}\delta_{jq} + 2\nu\ln r \delta_{ij}\delta_{pq} \\ &\quad + \delta_{ij}r_{,p}r_{,q} + \delta_{pq}r_{,i}r_{,j} \\ &\quad - 2\delta_{ip}r_{,j}r_{,q} - \delta_{jq}r_{,i}r_{,p}] \end{aligned} \quad (17c)$$

For a crack problem shown in Fig. 1, the boundary surface  $\partial\Omega$  includes the prescribed displacement surface  $S_u$ , the prescribed traction surface  $S_t$ , and the crack surface  $S_c$ . We apply the weak-form displacement integral equation on the prescribed displacement boundary surfaces  $S_u$  and obtain the formulation as:

$$\begin{aligned} \frac{1}{2} \int_{S_u} \hat{t}_p(\mathbf{x}) u_p(\mathbf{x}) dS_x &= \int_{S_u} \hat{t}_p(\mathbf{x}) dS_x \int_{\partial\Omega} t_j(\boldsymbol{\xi}) u_j^{*p}(\mathbf{x}, \boldsymbol{\xi}) dS_\xi \\ &\quad + \int_{S_u} \hat{t}_p(\mathbf{x}) dS_x \int_{\partial\Omega} D_i(\boldsymbol{\xi}) u_j(\boldsymbol{\xi}) G_{ij}^{*p}(\mathbf{x}, \boldsymbol{\xi}) dS_\xi \\ &\quad + \int_{S_u} \hat{t}_p(\mathbf{x}) dS_x \int_{\partial\Omega}^{CPV} n_i(\boldsymbol{\xi}) u_j(\boldsymbol{\xi}) \phi_{ij}^{*p}(\mathbf{x}, \boldsymbol{\xi}) dS_\xi \end{aligned} \quad (18)$$

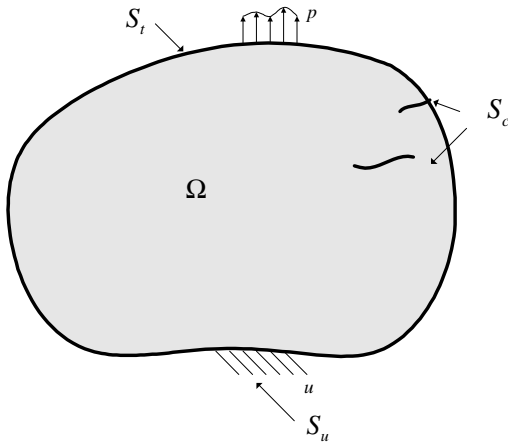


**Figure 1** : A linear elastic isotropic domain containing cracks (Original problem)

We apply the weak-form traction integral equation on the prescribed traction boundary surfaces  $S_t$  and obtain the similar formulation as:

$$\begin{aligned}
 & -\frac{1}{2} \int_{S_t} t_b(\mathbf{x}) \hat{u}_b(\mathbf{x}) dS_x \\
 & = \int_{S_t} D_a \hat{u}_b(\mathbf{x}) dS_x \int_{S_t+S_u} t_q(\xi) G_{ab}^{*q}(\mathbf{x}, \xi) dS_\xi \\
 & - \int_{S_t+S_u} t_q(\xi) dS_\xi \int_{S_t}^{CPV} n_a(\mathbf{x}) \hat{u}_b(\mathbf{x}) \phi_{ab}^{*q}(\mathbf{x}, \xi) dS_x \\
 & + \int_{S_t} D_a \hat{u}_b(\mathbf{x}) dS_x \int_{\partial\Omega} D_p u_q(\xi) H_{abpq}^*(\mathbf{x}, \xi) dS_\xi
 \end{aligned} \quad (19)$$

We also apply the weak-form traction integral equation on the crack  $S_c$ , which are conceived as a set of prescribed traction boundary surfaces. We have

$$\begin{aligned}
 & -\frac{1}{2} \int_{S_c} t_b(\mathbf{x}) \hat{u}_b(\mathbf{x}) dS_x \\
 & = \int_{S_c} D_a \hat{u}_b(\mathbf{x}) dS_x \int_{S_t+S_u} t_q(\xi) G_{ab}^{*q}(\mathbf{x}, \xi) dS_\xi \\
 & - \int_{S_t+S_u} t_q(\xi) dS_\xi \int_{S_c}^{CPV} n_a(\mathbf{x}) \hat{u}_b(\mathbf{x}) \phi_{ab}^{*q}(\mathbf{x}, \xi) dS_x \\
 & + \int_{S_c} D_a \hat{u}_b(\mathbf{x}) dS_x \int_{\partial\Omega} D_p u_q(\xi) H_{abpq}^*(\mathbf{x}, \xi) dS_\xi
 \end{aligned} \quad (20)$$

The SGBEM requires the  $C_0$  continuous trial and testing functions over the boundary surface  $\partial\Omega = S_u \cup S_t \cup S_c$ . This can be satisfied after discretization. Special attention should be paid to the crack surfaces. The displacement discontinuities,  $u(x) = u^+(x^+) - u^-(x^-)$ , must be zero around the crack fronts where  $u^+(x^+) = u^-(x^-)$ . A

special treatment is also required to enforce the  $C_0$  continuities for the surface cracks that intersect the normal boundary surface  $S_u \cup S_t$ . In the present work, quarter-point singular elements are adopted and the displacement discontinuities are set to zero explicitly for the crack front. In addition, the weak-form can be also written for the local sub boundary, by using the generate MLPG approach. It has been presented in [Alturi, Han and Shen (2003)].

### 3 Schwartz-Neumann Alternating Method

The Schwartz-Neumann alternating method is based on the superposition principle. The solution on a given domain is the sum of the solutions on two other overlapping domains. The alternating method converges unconditionally when there are only traction boundary conditions specified on the body. In the present work, the overlapping domains are the given finite domain, but without the cracks; a local portion of the original given domain as described below. The local subdomain can be selected to include only the traction boundary conditions so that the alternating procedure converges unconditionally. To take advantages of both the FEM and SGEM, the FEM, which is a robust method for large-scale elastic problems, is used to solve the whole uncracked global structure. The SGBEM, which is most suitable the crack analyses, is used for modeling a local finite-sized subdomain containing embedded or surface cracks. The size of SGBEM domain is also limited in order to improve the computational efficiency, by avoiding an overly-large fully populated system matrix.

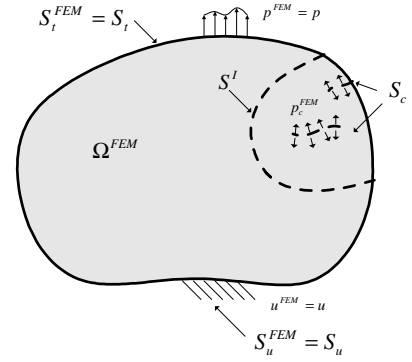
We consider a structure containing cracks, as shown in Fig. 1. The crack surfaces are denoted collectively as  $S_c$ . The alternating method uses the following two problems to solver the original one. Let us define that the domain for the FEM, denoted as  $\Omega^{FEM}$  in Fig. 2(a), is the same as the original domain  $\Omega$  but no cracks are included. All the prescribed tractions  $p$  are applied to the FEM domain on  $S_t^{FEM}$ , as well as all the prescribed displacement  $u$  on  $S_u^{FEM}$ . Another domain  $\Omega^{SGBEM}$  is defined for the SGBEM as shown in Fig. 2(b), which is a local finite-sized subdomain containing all the cracks. It is clear that the same crack surfaces are inherited from the original ones, as  $S_c^{SGBEM}$ . We define the boundary conditions in a way that the shared overall boundary between these two domains is defined as the traction free surface of the SGBEM domain, denoted as  $S_t^{SGBEM}$  with

$p^{SGBEM} = 0$ . The intersection surface  $S^I$  is treated as the boundary of the SGBEM domain with the prescribed displacements, denoted as  $S_u^{SGBEM}$ . We can also restrict all prescribed displacements,  $u^{SGBEM}$ , to be zero on  $S_u^{SGBEM}$ . One obvious advantage of this approach is that two overlapping domains are limited to the local portion containing the cracks, without any restriction to the remaining portion. This distinguishing feature makes it possible that all other structure elements can be used in the FEM domain, which are widely used in industry. It also allows the present alternating approach to be implemented within any commercial FEM solver without any restriction. Another advantage is that the independence of the crack model and finite element model of the body allows one to easily change the crack model in order to simulate crack growth or perform the parametric study.

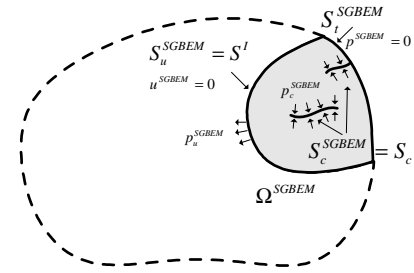
To solve the original problem, the superposition of the two alternate problems, FEM and SGBEM, yields the original solution for the prescribed displacements  $u$  and tractions  $p$  with cracks. The detailed procedures are described as follows.

1. Using FEM, solve the problem on domain  $\Omega^{FEM}$  with all externally prescribed displacements and tractions, but without the cracks. The tractions on crack surfaces  $S_c^{SGBEM}$  can be obtained as  $p_c^{SGBEM} \equiv -p_c^{FEM}$ .
2. Using SGBEM, solve the local problem on domain  $\Omega^{SGBEM}$  only with the tractions on the crack surface. The prescribed displacements  $u^{SGBEM}$  on  $S_u^{SGBEM}$  are set to zero as well as the zero prescribed tractions  $p^{SGBEM}$  on  $S_t^{SGBEM}$ . The only loads are the non-zero tractions on the crack surfaces, i.e.,  $p_c^{SGBEM}$  on  $S_c^{SGBEM}$ . Then the tractions on the intersection surface  $S^I$  are obtained as a part of the SGBEM solution explicitly, denoted as  $p_u^{SGBEM}$  on  $S_u^{SGBEM}$ .
3. Applying the tractions on the intersection surface as the residual forces to the FEM domain, denoted as  $p^{FEM} \equiv -p_u^{SGBEM}$  on  $S^I$  in Fig. 2(c), re-solve the FEM problem and obtain the traction  $p_c^{SGBEM}$  on crack surfaces  $S_c^{SGBEM}$ .
4. Repeat steps 2 and 3 until the residual load  $p^{FEM}$  is small enough.
5. By adding the SGBEM solution to the FEM one, the original one is obtained.

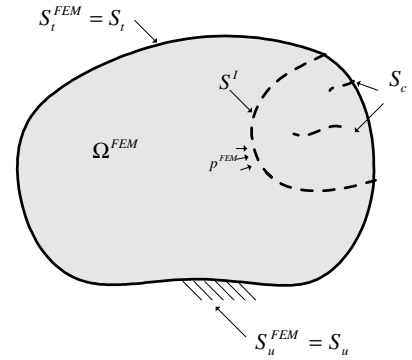
We now examine the solution with the given boundary and loading conditions for the original problem (denoted by superscript Org):



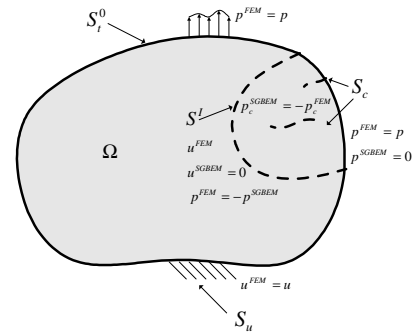
(a) the uncracked body for FEM



(b) the local SGBEM domain containing cracks



(c) FEM model subjected to residual loads



(d) alternating solution for the original problem

**Figure 2 :** Superposition principle for FEM-SGBEM alternating method

i) for the given traction on  $S_t$ , we have  $p^{FEM} = p$  and  $p^{SGBEM} = 0$  and get

$$p^{Org} = p^{FEM} + p^{SGBEM} = p \quad \text{on } S_t \quad (21)$$

ii) for the given displacement on  $S_u$ , the SGBEM domain does not contain any portion of  $S_u$  and thus, we obtain

$$u^{Org} = u^{FEM} = u \quad \text{on } S_t \quad (22)$$

iii) for the crack surface  $S_c$ , we define that tractions for SGBEM model  $p_c^{SGBEM}$  equal to  $-p_c^{FEM}$  from the FEM solution, and thus the tractions on crack surfaces are zero as in the original problem, i.e.,

$$p_c^{Org} = p_c^{FEM} + p_c^{SGBEM} = 0 \quad \text{on } S_c \quad (23)$$

iv) for the intersection surface  $S^I$ , we define that the residual tractions on FEM model  $p^{FEM}$  equals to  $-p^{SGBEM}$  from the SGBEM solution, and obtain

$$p_c^{Org} = p_c^{FEM} + p_c^{SGBEM} = 0 \quad \text{on } S^I \quad (24)$$

We also specify that the zero displacements for the SGBEM model, i.e.  $u^{SGBEM} = 0$  on  $S^I$ , and thus, there no displacement discontinuities along the intersection surface,

$$u^{Org} = u^{FEM} \quad \text{on } S^I \quad (25)$$

As shown in Fig. 2 (d), the solution obtained here satisfies all the boundary and loading conditions for the original problem. From the uniqueness of the elastic linear problem, we obtain the solution for the original problem

From a computational point of view, the present approach is very efficient in saving the CPU time. This results from two reasons. The first reason is that some terms for SGBEM equations are ignored, and Eqs. (18), (19) and 3 can be simplified as follows

For weak-form displacement integral on  $S_u^{SGBEM}$

$$\begin{aligned} 0 &= \int_{S_u} \hat{t}_p(\mathbf{x}) dS_x \int_{S_u} t_j(\xi) u_j^{*p}(\mathbf{x}, \xi) dS_\xi \\ &+ \int_{S_u} \hat{t}_p(\mathbf{x}) dS_x \int_{S_t+S_c} D_i(\xi) u_j(\xi) G_{ij}^{*p}(\mathbf{x}, \xi) dS_\xi \\ &+ \int_{S_u} \hat{t}_p(\mathbf{x}) dS_x \int_{S_t+S_c}^{CPV} n_i(\xi) u_j(\xi) \phi_{ij}^{*p}(\mathbf{x}, \xi) dS_\xi \end{aligned} \quad (26)$$

For weak-form traction integral on  $S_t^{SGBEM}$

$$\begin{aligned} 0 &= \int_{S_t} D_a \hat{u}_b(\mathbf{x}) dS_x \int_{S_u} t_q(\xi) G_{ab}^{*q}(\mathbf{x}, \xi) dS_\xi \\ &- \int_{S_u} t_q(\xi) dS_\xi \int_{S_t}^{CPV} n_a(\mathbf{x}) \hat{u}_b(\mathbf{x}) \phi_{ab}^{*q}(\mathbf{x}, \xi) dS_x \\ &+ \int_{S_t} D_a \hat{u}_b(\mathbf{x}) dS_x \int_{S_t+S_c} D_p u_q(\xi) H_{abpq}^*(\mathbf{x}, \xi) dS_\xi \end{aligned} \quad (27)$$

For weak-form traction integral on  $S_c^{SGBEM}$

$$\begin{aligned} &-\frac{1}{2} \int_{S_c} t_b(\mathbf{x}) \hat{u}_b(\mathbf{x}) dS_x \\ &= \int_{S_c} D_a \hat{u}_b(\mathbf{x}) dS_x \int_{S_u} t_q(\xi) G_{ab}^{*q}(\mathbf{x}, \xi) dS_\xi \\ &- \int_{S_u} t_q(\xi) dS_\xi \int_{S_c}^{CPV} n_a(\mathbf{x}) \hat{u}_b(\mathbf{x}) \phi_{ab}^{*q}(\mathbf{x}, \xi) dS_x \\ &+ \int_{S_c} D_a \hat{u}_b(\mathbf{x}) dS_x \int_{S_t+S_c} D_p u_q(\xi) H_{abpq}^*(\mathbf{x}, \xi) dS_\xi \end{aligned} \quad (28)$$

$$K_{eq} = \sqrt[4]{K_I^4 + 6K_I^2 K_{II}^2 + K_{II}^4 + \frac{K_{III}^4}{(1-\nu)^2}} \quad (29)$$

The second reason is that the residual forces applied to the FEM problem are obtained as a part the SGBEM solution explicitly. There is no extra computer time to determine the forces, which is normally needed when the alternating procedure is performed between the solutions for the uncracked finite body and the infinite body containing cracks. The singular residual forces may be encountered when the surface cracks are included the later cases, which introduces the numerical errors during the alternating procedures. Therefore the surface crack solutions near the free surface are not accurate, which is well known as the boundary-layer effect. In some researches, the fictitious extended cracks are used with imaginary tractions to reduce such errors [Nishioka and Atluri (1983)]. Unfortunately, the fictitious extended portion and the imaginary tractions are hard to be defined when the arbitrary non-planar surface cracks are considered. In the present work, the original solution is obtained accurately by using the non-singular alternating method with the weak singular SGBEM.

#### 4 Automatic crack growth

The crack growth analysis plays an important role in the damage tolerance analysis for determining the life of the

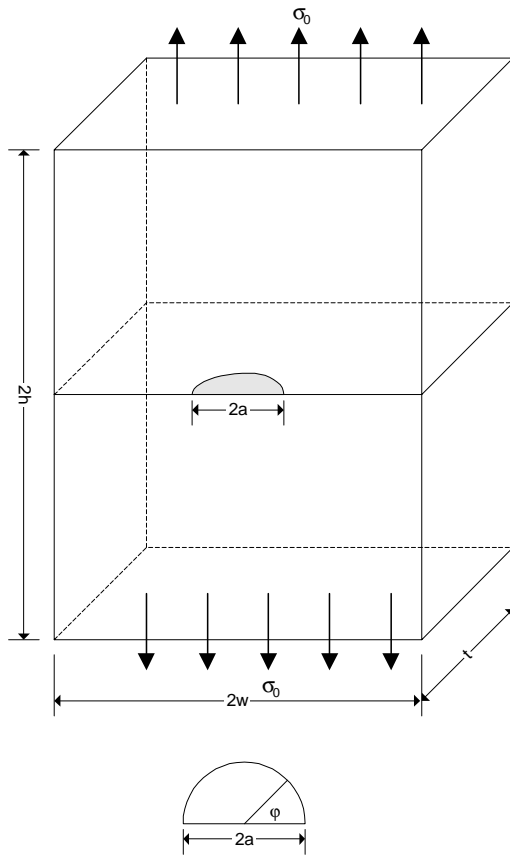


**Figure 3** : a semi-circular crack in a plate under tension

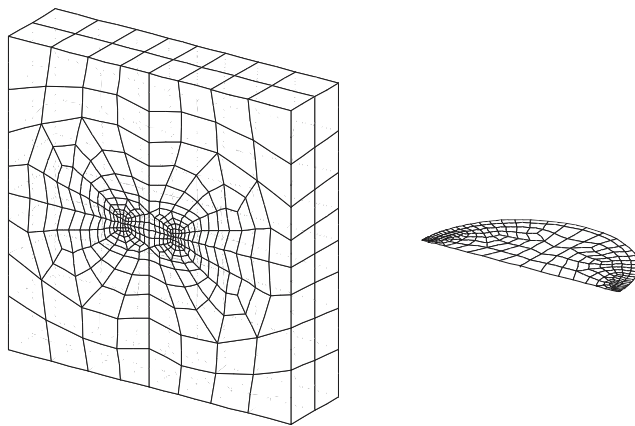
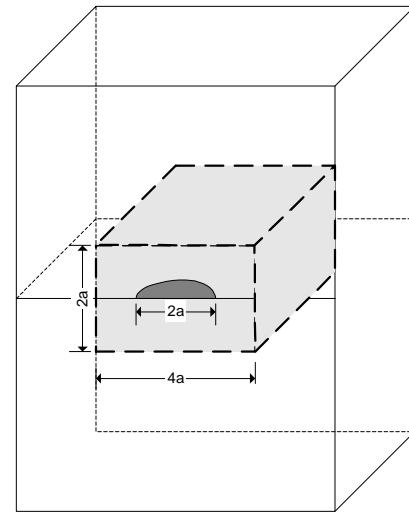
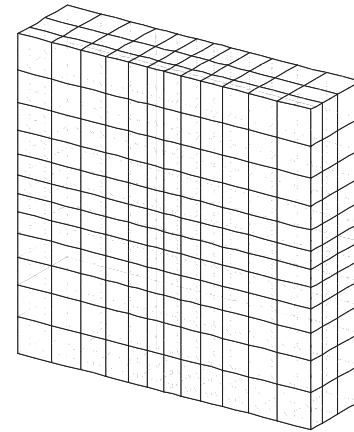


**Figure 4** : Mesh of a semi-circular crack in a plate for the SGBEM

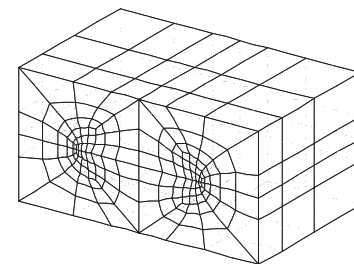
structure. Several models can be used to predict the direction and extension of cracks. The models for crack extension use in the equivalent K factors for the mixed mode and the stress ratio, such as the Paris, Walker and Forman fatigue models. In the current implementation,



(a)



(b)



(c)

**Figure 5** : Models of a semi-circular crack in a plate for FEM-SGBEM alternating method: (a) local finite body defined in the plate, (b) the FEM model without the crack and (c) the local SGBEM model with the crack

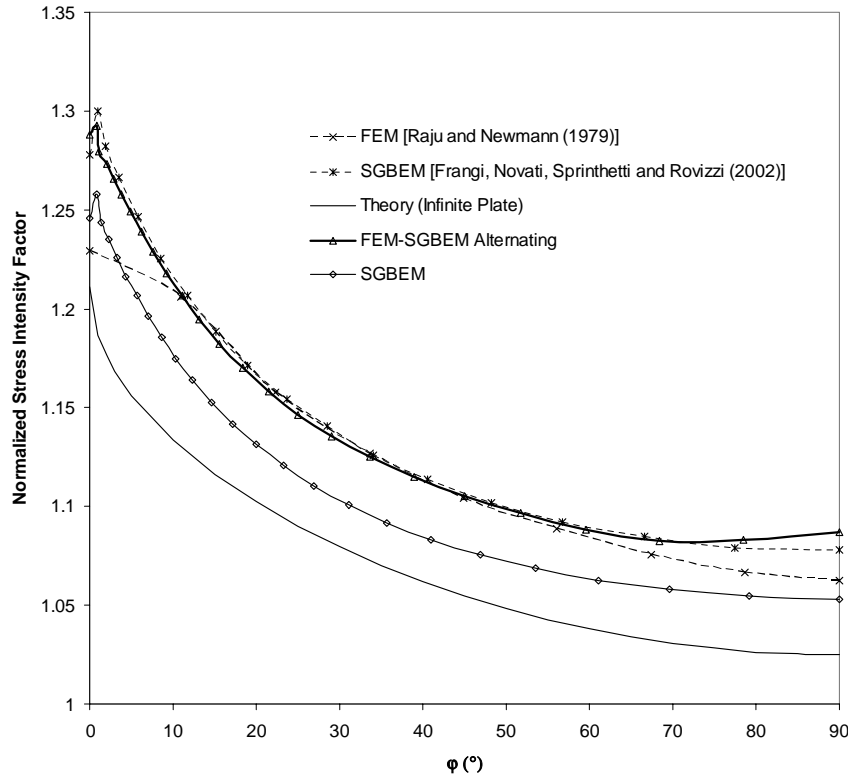


**Figure 6** : Normalized stress intensity factors ( $K_I/\sqrt{\pi a}$ ) for a semi-circular crack in a plate

the equivalent K factor is calculated as

Thereafter, the rate of crack extension is governed by the corresponding models as

$$\frac{da}{dN} = f(K_{eq}, R, \dots) \quad (30)$$

The maximum circumferential stress theory is used for the direction, as

$$K_I \sin \alpha + K_{II} (3 \cos \alpha - 1) = 0 \quad (31)$$

Once the crack extension and direction are obtained, the crack can be advanced by adding another layer of the elements around the crack front to grow the crack. As one of the most important feature of the alternating method, the FEM model keeps unchanged and is solved only once during the crack growth because the models for the FEM and BEM are fully decoupled. It makes that the alternating method is very efficient for crack-growth problems. In addition, the mesh generation is robust because only the 3D surface mesh is required for the advanced crack surface, instead of embedding the new crack surface into a finite body.

## 5 Numerical Examples

### 5.1 Semi-circular surface cracks

In order to verify the accuracy of the present alternating method for treating surface cracks in finite bodies, we first consider a semi-circular surface crack in a plate as shown in Fig. 3. Uniform tensile stresses  $\sigma_0$  are applied at two opposite faces of the plate in the direction perpendicular to the cracks.  $a$  is the radius of the semi circular crack. The plate configuration considered is characterized by the geometric ratios  $\frac{h}{a} = 5$ ,  $\frac{w}{a} = 5$  and  $\frac{t}{a} = 2.5$ . The poisson ratio  $\nu = 0.3$  is chosen.

We first use the SGBEM method to simulate the entire problem with the mesh shown in Fig. 4. Then we solve the problem with the alternating method. The FEM model is created for the uncracked body, shown in Fig. 5(b), with the uniform tensile stresses being applied at the top and bottom surfaces. The local SGBEM model is also created in the plate, shown in Fig. 5(a). It is similar to the model in Fig. 4 for pure SGBEM solution, so that we create the mesh for this local finite body with similar meshes for the boundary and crack surfaces. The front and back surfaces are free and others are the prescribed

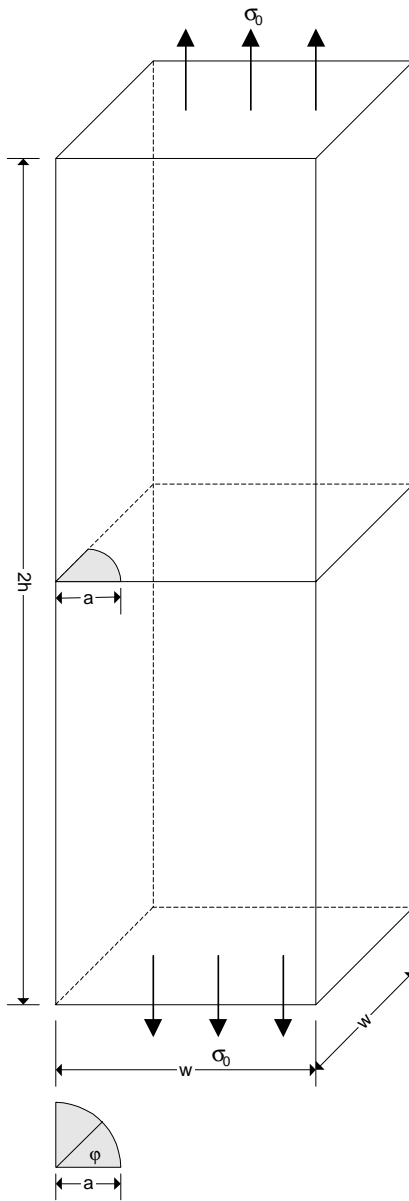


**Figure 7** : a quarter-circular crack in a square bar under tension

displacement ones.

This problem is a pure mode-I problem and has been solved by using the FEM [Raju and Newman (1979)] and the SGBEM [Frangi, Novati, Sprinthetti and Rovizzi (2002)]. The analytical solution is available for the infinite plate. The ratios chosen for this problem are large enough to represent a crack in the infinite plate. As shown in Fig. 6, a comparison of the normalized stress intensity factors by using the SGBEM-FEM alternating method with the referenced solutions shows a good

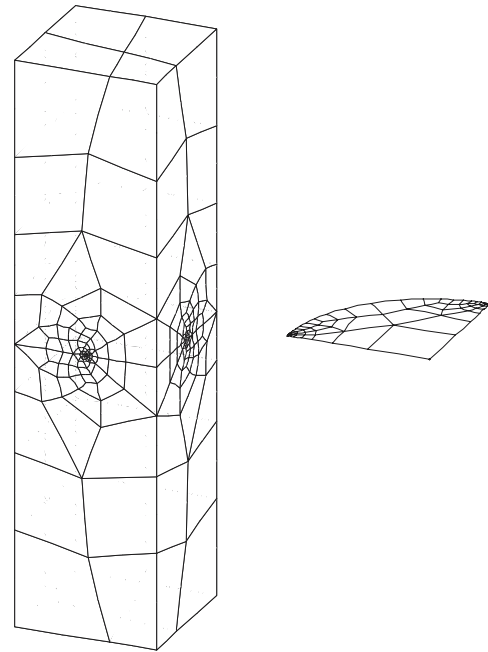


**Figure 8** : Mesh of a quarter-circular crack in a square bar for the SGBEM

agreement for all crack-front locations. It is well known that the stress intensity factors tend to zero in a boundary layer where the crack front approaches free surface of the body, when a surface crack breaks the outer surface at a right angle. This effect is also confirmed by using alternating method.

## 5.2 A quarter-circular crack in a square bar

The second example for the surface crack is a square bar which contains a quarter-circular crack, as shown in Fig. 7. Uniform tensile stresses  $\sigma_0$  are applied at the two ends. Let  $a$  denote the radius of the quarter-circular crack, and the other dimensions are defined as  $\frac{w}{a} = 5$  and  $\frac{h}{a} = 4$ . The Poisson ratio  $\nu = 0.3$  is chosen here. The dimensions are chosen to be the same as those used in Li, Mear and Xiao (1998) for comparison purpose.

Again, we use both the SGBEM for the entire domain; and the FEM-SGBEM alternating method to solve this problem with the meshes in Figs. 8 and 9, respectively. The local SGBEM domain is created by truncating the square bar as shown in Fig. 9(a). Then the top and bottom surfaces are subjected to the zero prescribed displacements and others are free.

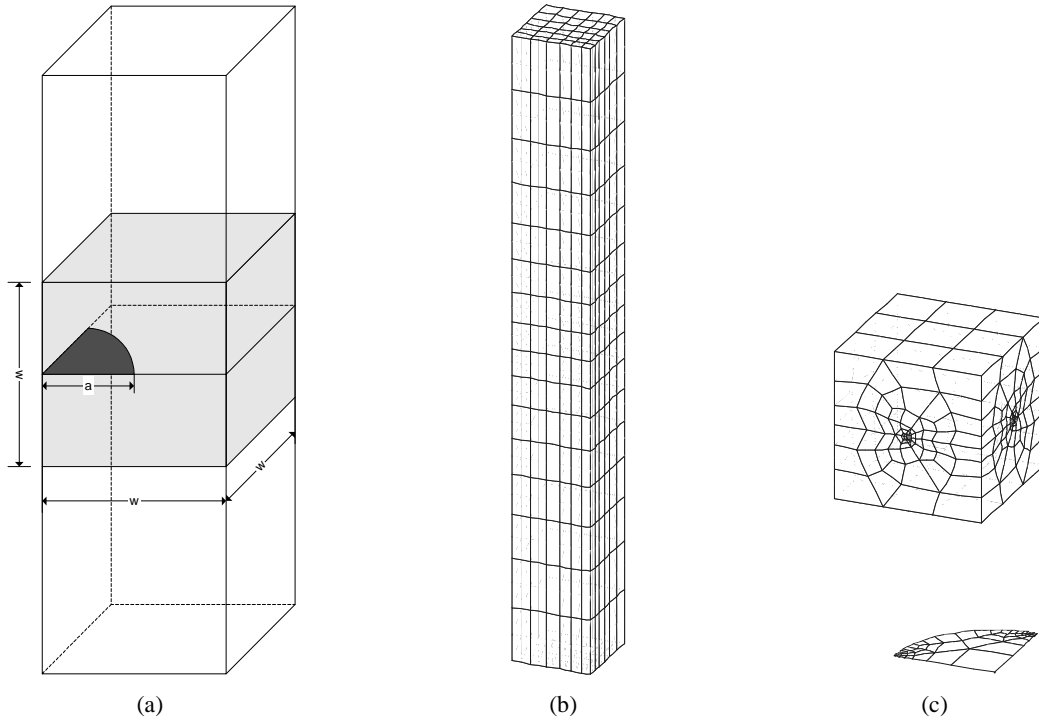


**Figure 9** : Models of a quarter-circular crack in a square bar for FEM-SGBEM alternating method: (a) local finite body defined in the plate, (b) the FEM model without the crack and (c) the local SGBEM model with the crack

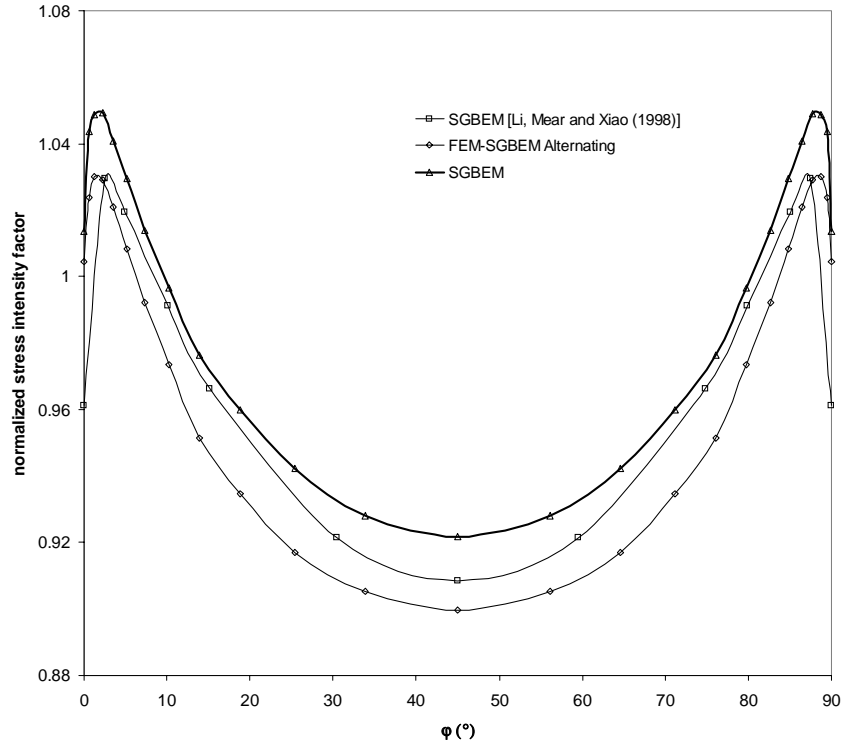


**Figure 10** : Normalized stress intensity factors ( $K_I / (\sigma_0 \sqrt{\pi a})$ ) for a quarter-circular crack in a square bar

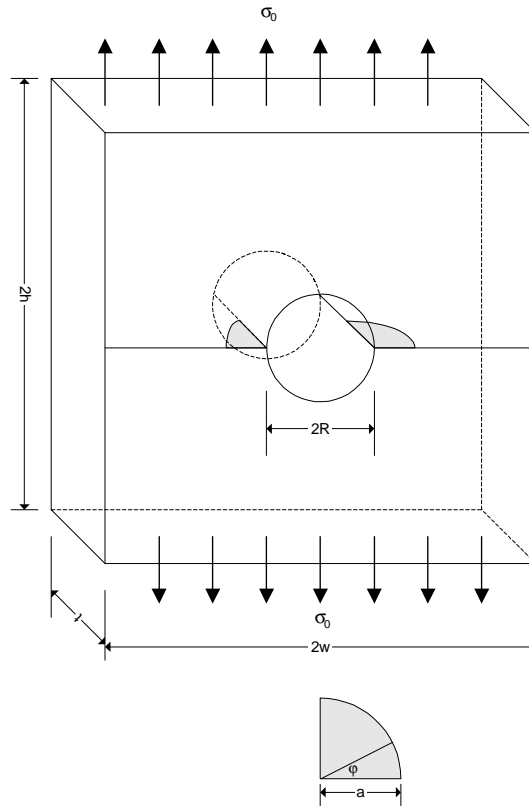


**Figure 11** : a corner crack at a circular hole in a finite-thickness plate under tension

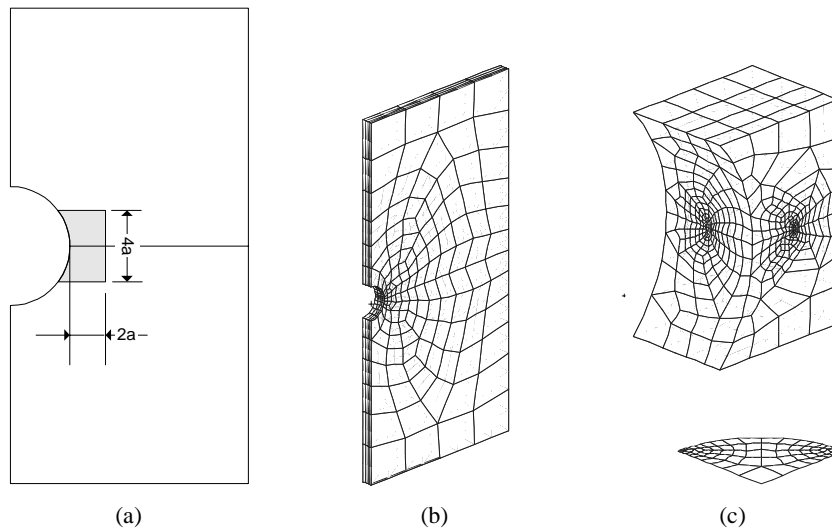


**Figure 12** : Models of a corner crack at a circular hole in a finite-thickness plate for FEM-SGBEM alternating method: (a) local finite body defined in the plate, (b) the FEM model without the crack and (c) the local SGBEM model with the crack

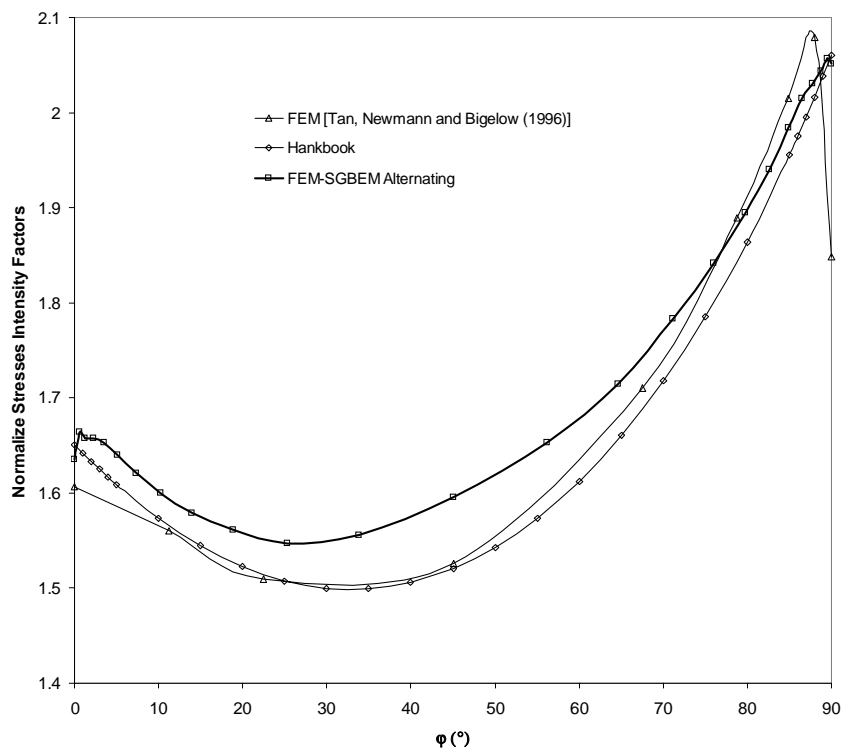


**Figure 13** : Normalized stress intensity factors ( $K_I / (\sigma_0 \sqrt{\pi a})$ ) for a corner circular crack at a hole in a finite-thickness plate

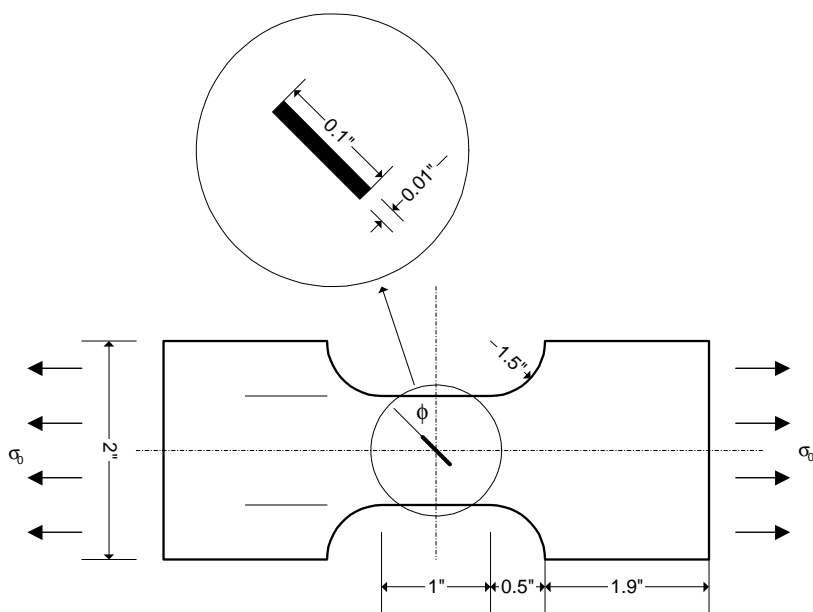


**Figure 14** : Inclined semi-circular surface crack specimen

Numerical results are displayed in Fig. 10 in terms of the normalized stress intensity factor contribution along the crack front. A good agreement is observed, as well as those points near the free surface. Again the boundary effect is also evidenced by the alternating method.

### 5.3 Corner crack at a circular hole in a finite-thickness plate

As the third example, the corner crack at a circular hole in a plate is considered and shown in Fig. 11. This example has been considered by many investigators for three dimensional fracture analyses with various methods. The geometry is characterized by the ratios:  $\frac{h}{t} = \frac{w}{t} = 8$ ,  $\frac{R}{t} = 1.5$  and  $\frac{a}{t} = 0.5$ . The passion ratio is taken as  $\nu = 0.3$ .

This problem is analyzed by using the alternating method only. The meshes adopted are depicted in Fig. 12(b)-(c), in which only half of the specimen was analyzed due to symmetry. The FEM model has about 3300 degrees of freedom (DOFs). In the contrast, the FEM models used in Tan, Newman and Bigelow (1996) had more than 16000 DOFs in conjunction with special singularity elements for the crack front. The local SGBEM model is cut by three planar surfaces around the crack with zero prescribed displacements, as shown in Fig. 12 (a). All boundary and crack surfaces are discretized with about 500 quadrilateral elements, and with 24 elements along the crack front.

The normalized stress intensity factors along the crack front are plotted in Fig. 13. The results are compared to the available published solutions [Tan, Newman and Bigelow (1996)]. The boundary effects are obtained for two ends of the crack front near to the free surface, and the boundary layer at the lateral free surface is thinner than the FEM solution.

### 5.4 Nonplanar fatigue growth of an inclined semi-circular surface crack in a plate

Fatigue-growth of an inclined surface crack in a plate is considered. As shown in Fig. 14, the modified ASTM E740 specimen has been tested for the mixed-mode fatigue growth [Forth, Keat and Favrow (2002)]. The specimens were taken from actual parts made from 7075-T73 aluminum. The crack orientation  $\phi = 30^\circ$  is used. Maximum tensile stresses  $\sigma_0 = 15.88 \text{ ksi}$  are applied with a load ratio  $R = 0.7$ . The Forman equation is chosen to advance the crack and front and determine the fatigue

cycles:

$$\frac{da}{dN} = C \left( \frac{1-f}{1-R} \Delta K \right)^n \frac{(1 - \Delta K_{th}/\Delta K)^p}{(1 - K_{\max}/K_{crit})^q} \quad (32)$$

where the growth rate  $\frac{da}{dN}$  is based on empirical material constants  $C$ ,  $n$ ,  $p$  and  $q$ ;  $f$  depends on the ratio  $R$ ;  $\Delta K_{th}$  is the threshold value of  $\Delta K$ ;  $K_{crit}$  is the critical stress intensity factor. This model is details in the reference manual of NASGRO 3.0 [NASA, NASGRO (2001)]. The material constants are taken as  $C = 1.49 \times 10^{-8}$ ,  $n = 3.321$ ,  $p = 0.5$ ,  $q = 1.0$ ,  $K_{Ie} = 50 \text{ ksi}\sqrt{\text{in}}$ ,  $K_{IC} = 28 \text{ ksi}\sqrt{\text{in}}$ ,  $\Delta K_{th} = 3.0 \text{ ksi}\sqrt{\text{in}}$ ,  $C_{th}^+ = 2.0$ ,  $C_{th}^- = 1.0$ ,  $R_{cl} = 0.7$ ,  $\alpha = 1.9$ ,  $A_k = 1.0$ ,  $B_k = 1.0$ ,  $S_{\max}/\sigma_0 = 0.3$ ,  $\sigma_{YS} = 60 \text{ ksi}$  and  $\sigma_{UTS} = 74 \text{ ksi}$ .

We model the uncracked specimen with the mesh as in Fig. 15b for FEM. The local SGBEM model is located in the central portion that contains the inclined surface crack, as illustrated in Fig. 15a with the attendant mesh being shown in Fig. 15c. The top and bottom surfaces are cutting surfaces and subjected to the zero prescribed displacements while others are free.

First, the initial crack is analyzed and stress intensity factors are normalized by  $K_0 = \sigma_0 \sqrt{\pi a}$  and shown in Fig. 16. Good agreements are obtained in comparison with other results [Shivakumar and Raju (1992); He and Hutchinsen (2000); Nikishkov, Park and Atluri (2001)].

The crack growth is simulated by adding one layer of elements along the crack front, in each increment. The newly added points are determined through the K solutions. 15 advancements are performed. The fatigue load cycles are calculated and compared with the experimental data [Forth, Keat and Favrow (2002)], shown in Fig. 17. The normalized stress intensity factors during the crack growing are given in Fig. 18, which are also normalized by  $K_0 = \sigma_0 \sqrt{\pi a}$ . KI keeps increasing while KII and KIII are decreasing during the crack growth. It confirms that this mixed-mode crack becomes the mode-I dominated one while growing. The shape of the final crack is very similar to the experimental photograph in Fig. 19. It is clear that while the crack, in its initial configuration, starts out as a mixed-mode crack, after a substantial growth, the crack configuration is such that it is in a pure mode-I state.

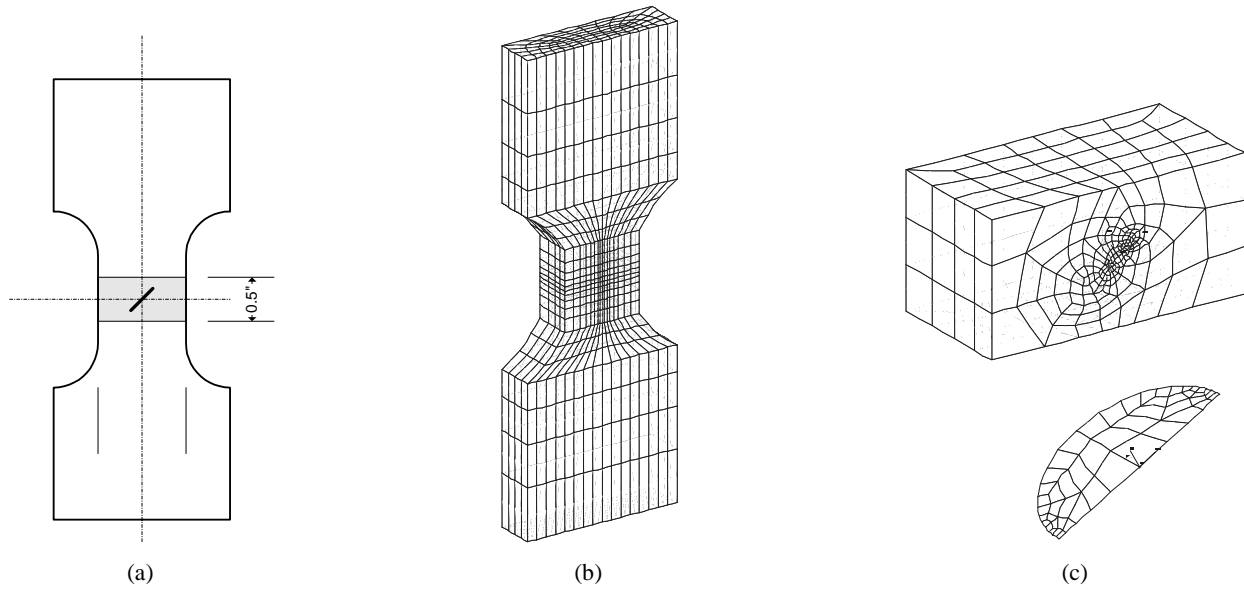


**Figure 15 :** Models of an inclined surface crack in a tensile plate for FEM-SGBEM alternating method: (a) local finite body defined in the specimen, (b) the FEM model for the specimen without the crack and (c) the local SGBEM model with the crack

### 5.5 Automatic detection of an initial nozzle corner flaw

As the final example, the initial crack at a nozzle corner is detected by using the program DTALE, which employs the present alternating method. The geometries of the nozzle and of the flaw in a longitudinal plane are shown in Fig. 20. Two types of initial flaws, as shown in Fig. 21, one a quarter-circular flaw (MATH) of depth  $a = 9.5\text{cm}$  and a similar “natural” flaw (EXPR) obtained in a photoelastic test [Smith, Jolles and Peters (1976)] were assumed in the damage tolerance analysis. In most analyses, the experimental results are not available. The shape, size and orientation of the initial flaw need to be assumed based on the users’ experience, which is not easy. An alternative way is to do the parametric study by creating many initial flaws based on the combination of the parameters of the shape, size, and orientation. From the computational point of view, it is not efficient, if other parameters are also considered including load cases and boundary conditions.

In the present study, one may determine the initial flaw by utilizing the automatic crack-growth function in DTALE. At the beginning, a smaller initial crack is introduced as the crack seed, and the program grows the crack seed with the same loading and boundary conditions. The present study, the Walker’s fatigue model is used to grow

the crack seed, without the threshold value of the stress intensity factor. After several advancements of the crack seed, the larger crack flaw can be obtained with the proper shape and orientation. As shown in Fig. 21, an initial crack seed is given as the black portion. The automatically detected portion of the initial flaw is shown in gray, which agrees with the experimental results. The fatigue model for the small crack can be used here for more accurate initial crack detection, because it fits the development of the initial crack well.

## 6 Conclusions

In this paper the Schwartz-Neumaan alternating method has been extended to analyze surface cracks. It is shown that the singular traction integral is avoided during the alternating procedure between the FEM and SGBEM, when both solutions are based on finite bodies. This approach shows a strong computational competitiveness, in comparison to the normal alternating methods, by avoiding the stress calculation on the boundary surfaces of FEM models. Indeed, the alternating procedure converges unconditionally by imposing the proposed prescribed displacements and tractions in the present approach. The accuracy and efficiency of the proposed approach have been verified on some 3D problems with published solutions by using other methods. The soft-

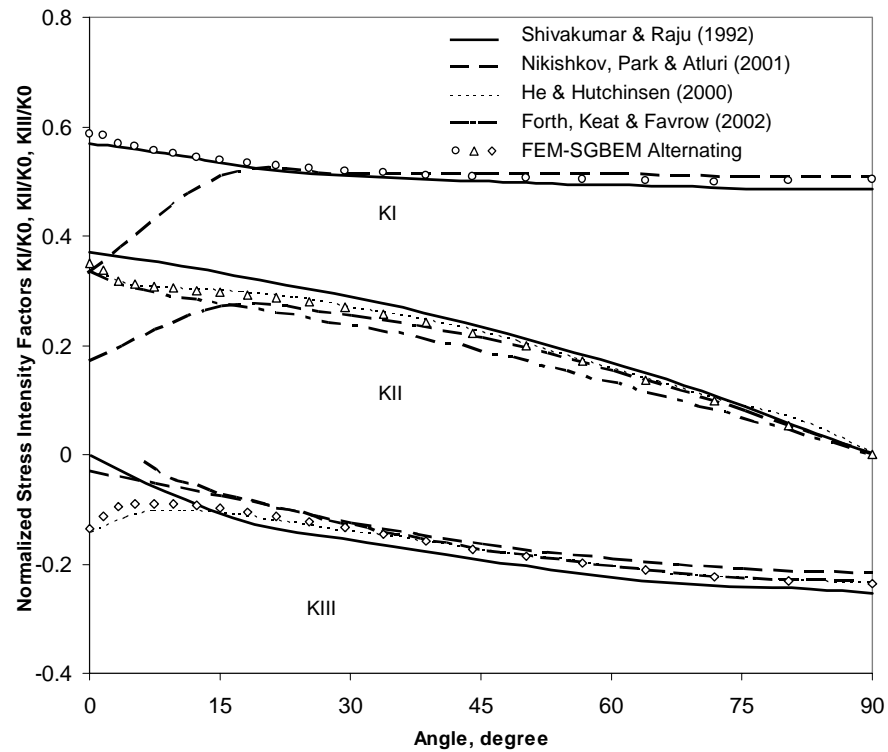


**Figure 16 :** Normalized stress intensity factors KI, KII and KIII for an inclined semi-circular surface crack in a tensile plate

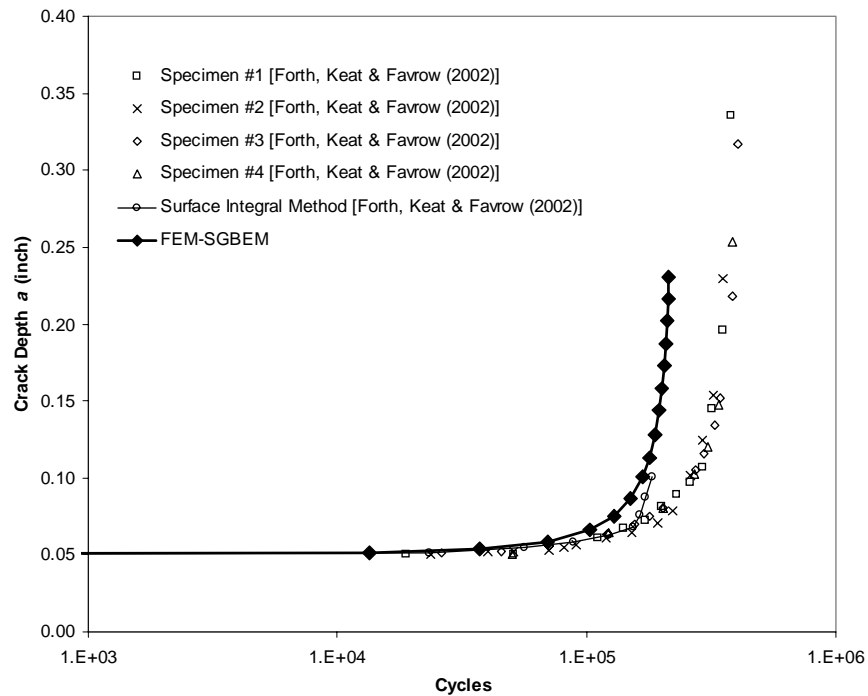


**Figure 17 :** Fatigue load cycles of an inclined semi-circular surface crack in a tensile plate

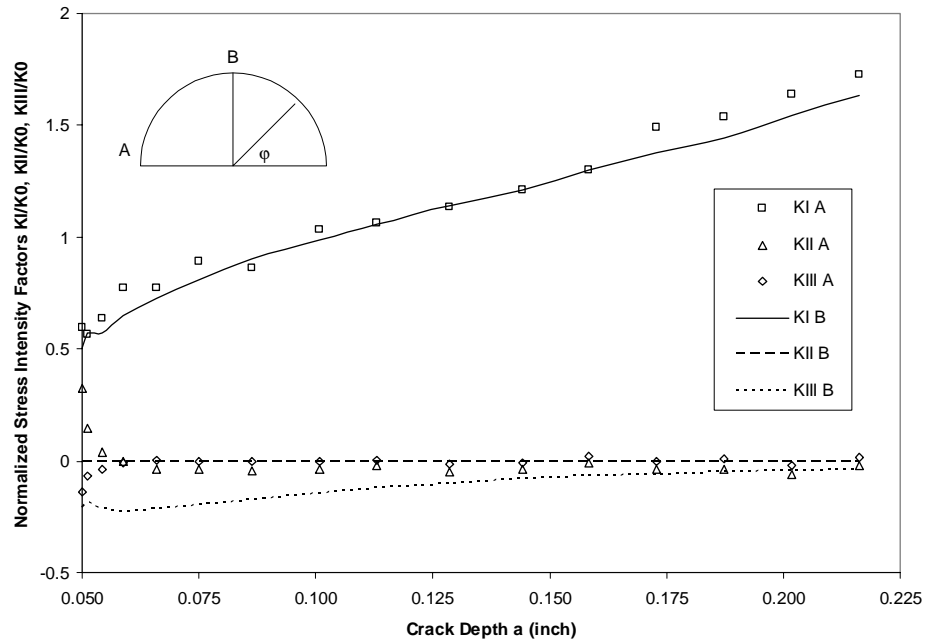


**Figure 18 :** Normalized stress intensity factors KI, KII and KIII for the mixed-mode fatigue growth of an inclined semi-circular surface crack in a tensile plate

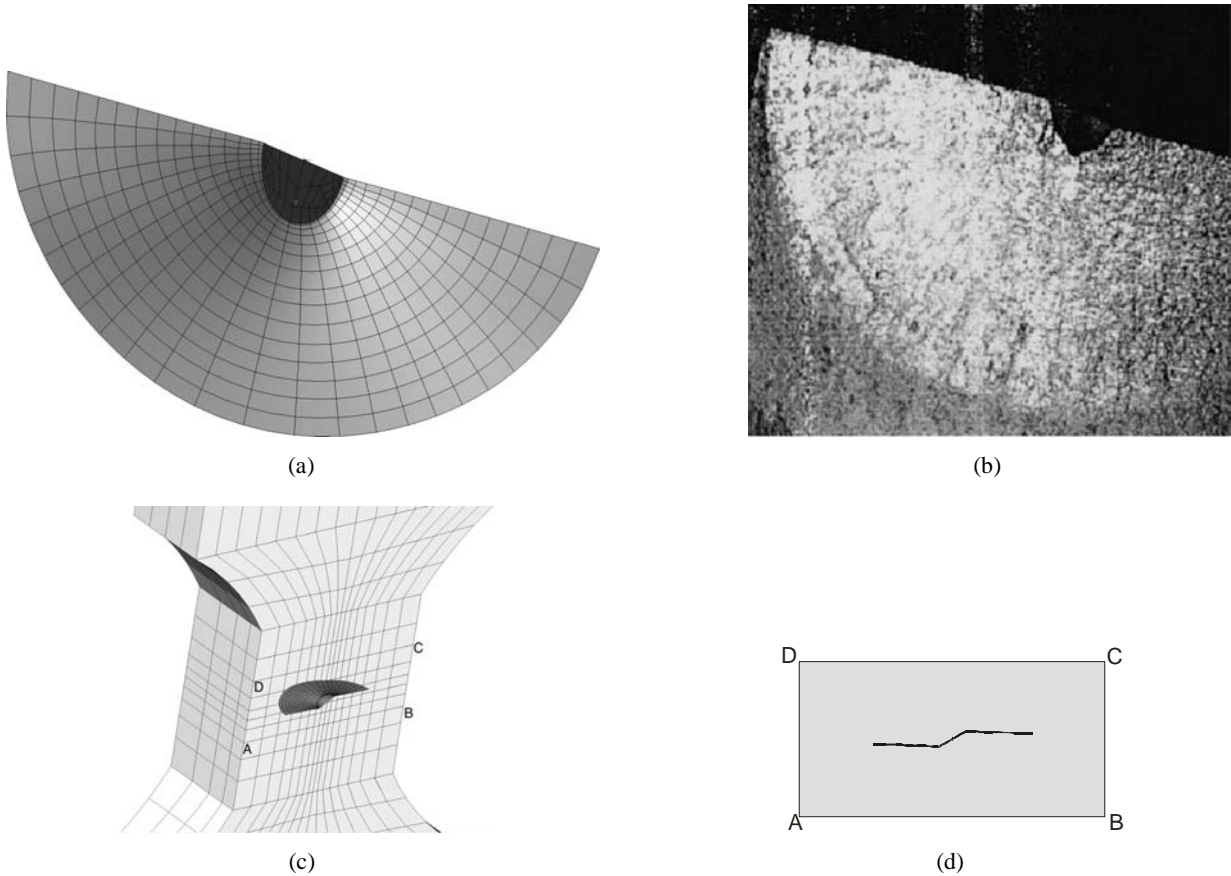


**Figure 19 :** Final crack of an inclined surface crack in a tensile plate: (a) the final crack after 15 increments by using FEM-SGBEM alternating method, (b) the photograph of the final crack taken from the specimen, (c) the final crack in the uncracked body, (d) the intersection path of the final crack with the free surface of the specimen, ABCD

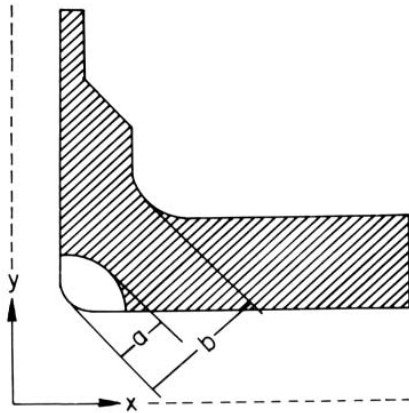
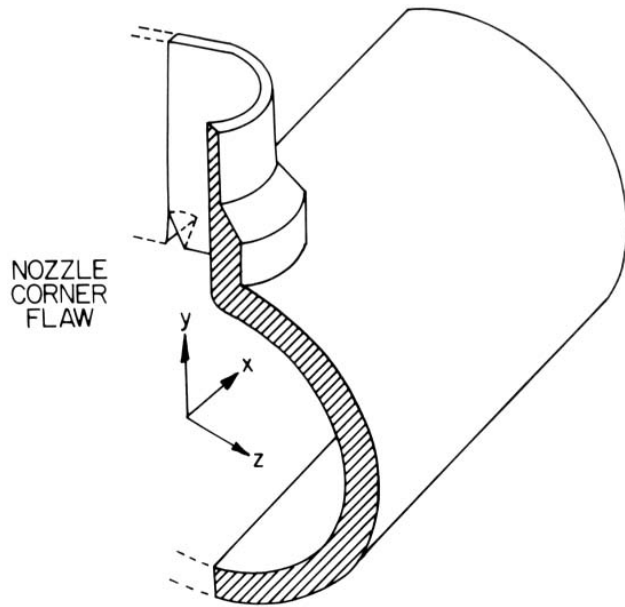


**Figure 20** : Surface-flaw near a pressure-vessel-nozzle junction

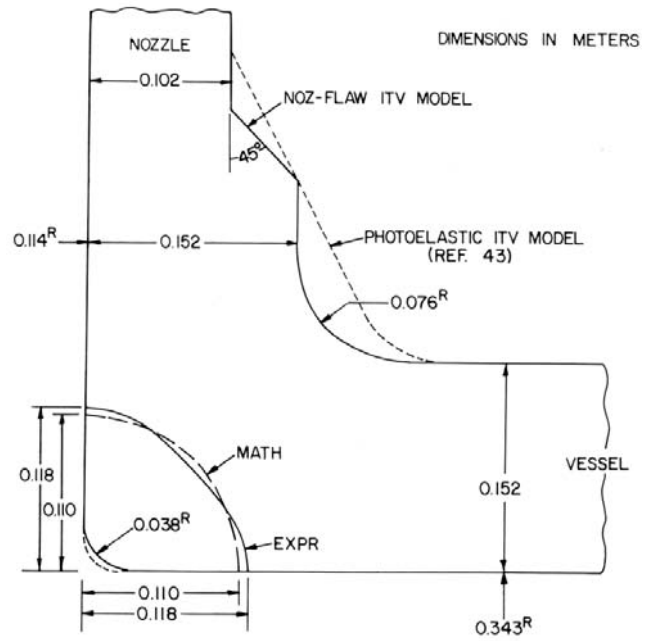


**Figure 21** : Geometry of an intermediate-test-vessel nozzle configuration

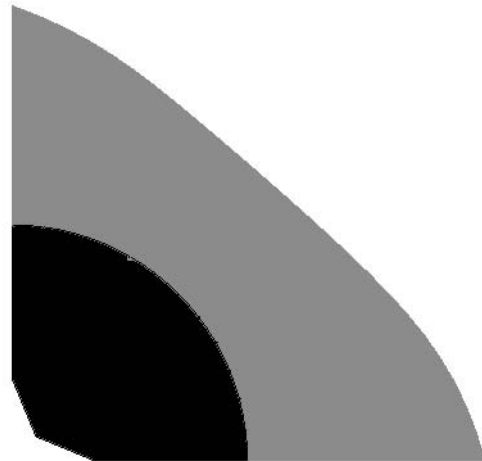


**Figure 22** : Automatic initial crack detection

ware package, DTALE, has been developed based on the present method. DTALE can be seen to have a wide industrial application, in estimating the life of a variety of safety-critical structures. With DTALE, the effect of residual stresses in a structure, due to processes such as welding, cold-working, shot-peening, etc., on the life of the structure, including a possible life-enhancement, can also be assessed.

## References

- Andra, H.** (1998): Integration of singular integrals for the Galerkin-type boundary element method in 3D elasticity. *Comp. Methods Appl. Mech. Engng*, vol. 157, pp. 239-249.
- Atluri, S.N** (2004): *The Meshless Local Petrov-Galerkin (MLPG) Method for Domain & Boundary Discretizations*, Tech Science Press, 680 pages.
- Atluri, S. N.** (1997): *Structural Integrity and Durability*, Tech Science Press, Forsyth.
- Atluri, S. N.** (1986): *Computational Methods in the mechanics of fracture* (North Holland, Amsterdam) also translated into Russian, Mir Publishers, Moscow.
- Atluri, S. N.; Han, Z. D.; Shen, S.** (2003): Meshless Local Petrov-Galerkin (MLPG) approaches for weakly-singular traction & displacement boundary integral equations, *CMES: Computer Modeling in Engineering & Sciences*, vol. 4, no. 5, pp. 507-517.
- Atluri, S. N.; Kathiresan, K.** (1975): An assumed displacement hybrid finite element model for three-dimensional linear elastic fracture mechanics analysis. Presented at the 12<sup>th</sup> Annual Meeting of the Society of Engineering Science, University of Texas, Austin.
- Cisilino, A.P.; Aliabadi, M.H.** (1999): Threedimensional boundary element analysis of fatigue crack growth in linear and non-linear fracture problems. *Eng. Fract. Mech.*, vol. 63, pp. 713-733.
- Forth, S. C.; Keat W. D.; Favrow L. H.** (2002): Experimental and computational investigation of three-dimensional mixed-mode fatigue, *Fatigue Fract. Engng. Mater. Struct.*, vol. 25, pp 3-15.
- Erichsen, S.; Sauter, S.A.** (1998): Efficient automatic quadrature in 3-d Galerkin BEM. *Com. Methods Appl. Mech. Engng*, vol. 157, pp. 215-224.
- Frangi, A.; Novati, G.** (2002): Fracture mechanics in 3D by a coupled FE-BE approach, IABEM 2002, International Association for Boundary Element Methods, UT Austin, Texas, May 28-30.
- Frangi, A; Novati, G.; Sprinthetti, R.; Rovizzi, M.** (2002): 3D fracture analysis by the symmetric Galerkin BEM, *Computational Mechanics*, vol. 28, pp. 220-232.
- Han. Z. D.; Atluri, S. N.** (2002): SGBEM (for Cracked Local Subdomain) - FEM (for uncracked global Structure) Alternating Method for Analyzing 3D Surface Cracks and Their Fatigue-Growth, *CMES: Computer Modeling in Engineering & Sciences*, vol. 3 no. 6, pp. 699-716.
- Han. Z. D.; Atluri, S. N.** (2003a): On Simple Formulations of Weakly-Singular Traction & Displacement BIE, and Their Solutions through Petrov-Galerkin Approaches, *CMES: Computer Modeling in Engineering & Sciences*, vol. 4 no. 1, pp. 5-20.
- Han. Z. D.; Atluri, S. N.** (2003b): Truly Meshless Local Petrov-Galerkin (MLPG) Solutions of Traction & Displacement BIEs, *CMES: Computer Modeling in Engineering & Sciences*, vol. 4 no. 6, pp. 665-678.
- Han. Z. D.; Atluri, S. N.** (2004a): Meshless Local Petrov-Galerkin (MLPG) approaches for solving 3D Problems in elasto-statics, *CMES: Computer Modeling in Engineering & Sciences*, vol. 6 no. 2, pp. 169-188.
- Han. Z. D.; Atluri, S. N.** (2004b): A Meshless Local Petrov-Galerkin (MLPG) Approach for 3-Dimensional Elasto-dynamics, *CMC: Computers, Materials & Continua*, vol. 1 no. 2, pp. 129-140.
- He, M. Y.; Hutchinson, J. W.** (2000): Surface crack subject to mixed mode loading. *Engng. Fract. Mech.* 65, 1-14.
- Kantorovich, L. V.; Krylov, V. I.** (1964): *Approximate methods of higher analysis* (translated by Curtis D. Bester) (John Wiley & Sons, Inc., New York & London).
- Keat, W.D.; Annigeri, B.S.; Cleary, M.P.** (1988): Surface integral and finite element hybrid method for two and three-dimensional fracture mechanics analysis. *Int. J. Fracture*, vol. 36, pp. 35-53.
- Murakami, Y.** (1987): *Stress Intensity Factors Handbook*, Pergamon Press.
- NASA** (2001), The reference manual of fatigue crack growth computer program "NASGRO" version 3.0, JSC-22267B, Nov. 2001.
- Nikishkov, G.P.; Atluri, S.N.** (1987): Calculation of fracture mechanics parameters for an arbitrary three-dimensional crack.

- imensional crack by the “equivalent domain integral” method. *Int. J. Numer. Meth. Engng*, vol. 24, pp. 851-867.
- Nikishkov, G.P.; Park, J.H.; Atluri, S. N.** (2001): SGBEM-FEM alternating method for analyzing 3D non-planar cracks and their growth in structural components, *CMES: Computer Modeling in Engineering & Sciences*, vol.2, no.3, pp.401-422.
- Nishioka, T.; Atluri, S.N.** (1983): Analytical solution for embedded elliptical cracks and finite element alternating method for elliptical surface cracks, subjected to arbitrary loadings. *Eng. Fract. Mech.*, vol. 17, pp. 247-268.
- Okada, H.; Atluri, S. N.** (1994): Recent developments in the field-boundary element method for finite/small strain elastoplasticity, *Int. J. Solids Struct.* vol. 31 n. 12-13, pp. 1737-1775.
- Okada, H.; Rajiyah, H.; Atluri, S. N.** (1989)a: A Novel Displacement Gradient Boundary Element Method for Elastic Stress Analysis with High Accuracy, *J. Applied Mech.*, April 1989, pp. 1-9.
- Okada, H.; Rajiyah, H.; Atluri, S. N.** (1989)b: Non-hyper-singular integral representations for velocity (displacement) gradients in elastic/plastic solids (small or finite deformations), *Comp. Mech.*, vol. 4, pp. 165-175.
- Okada, H.; Rajiyah, H.; Atluri, S. N.** (1990): A full tangent stiffness field-boundary-element formulation for geometric and material non-linear problems of solid mechanics, *Int. J. Numer. Meth. Eng.*, vol. 29, no. 1, pp. 15-35.
- Raju, I. S.; Newman, J. C. Jr** (1979): Stress-intensity factors for a wide range of semi-elliptical surface cracks in finite-thickness plates, *Engineering Fracture Mechanics*, vol. 11, pp. 817-829.
- Shivakumar, K.N.; Raju, I.S.** (1992): An equivalent domain integral method for three-dimensional mixed-mode fracture problems. *Eng. Fract. Mech.*, vol. 42, pp. 935-959.
- Smith, C. W.; Jolles, M.; and Peters, W. H.** (1976): Stress intensities of nozzle cracks in reactor vessels, VPI-E-76-25, ORNL/SUB-7015/1 (Virginia Polytechnic and State Univ.)
- Tan, P. W.; Newman, J. C. Jr.; Bigelow, C. A.** (1996): Three-dimensional finite-element analyses of corner cracks at stress concentrations, *Engineering Fracture Mechanics*, vol. 55, no. 3, pp. 505-512.
- Vijaykumar, K.; Atluri, S.N.** (1981): An embedded elliptical crack, in an infinite solid, subject to arbitrary crack-face tractions, *J. Appl. Mech.*, vol. 103(1), pp. 88-96.
- Wang, L.; Atluri, S.N.** (1996): Recent Advances in the alternating methods for elastic and inelastic fracture analyses, *Computer methods in Applied Mechanics and Engineering*, vol. 137, pp. 1-57.

# Simulation of a 4<sup>th</sup> Order ODE: Illustration of Various Primal & Mixed MLPG Methods

S. N. Atluri<sup>1</sup> and Shengping Shen<sup>1</sup>

**Abstract:** Various MLPG methods, with the MLS approximation for the trial function, in the solution of a 4<sup>th</sup> order ordinary differential equation are illustrated. Both the primal MLPG methods and the mixed MLPG methods are used. All the possible local weak forms for a 4<sup>th</sup> order ordinary differential equation are presented. In the first kind of mixed MLPG methods, both the displacement and its second derivative are interpolated independently through the MLS interpolation scheme. In the second kind of mixed MLPG methods, the displacement, its first derivative, second derivative and third derivative are interpolated independently through the MLS interpolation scheme. The nodal values of the independently interpolated derivatives are expressed in terms of nodal values of the independently interpolated displacements, by simply enforcing the strain-displacement relationships directly by collocation at the nodal points. The mixed MLPG methods avoid the need for a direct evaluation of high order derivatives of the primary variables in the local weak forms, and thus reduce the continuity-requirement on the trial function. Numerical results are presented to illustrate the effectiveness of the primal, as well as two kind of mixed MLPG methods. It is concluded that the mixed MLPG methods are very cost-effective.

**keyword:** MLPG, Mixed Methods, Moving Least Squares, Local Weak Forms.

## 1 Introduction

Most problems in mechanics are characterized by partial differential equations, in space and time. The development of approximate methods for the solution of these PDEs has attracted the attention of engineers, physicists

and mathematicians for several decades. In the beginning, the finite difference methods were extensively developed to solve these equations. As being derived from the variational principles, or their equivalent weak-forms, the finite element methods have emerged as the most successful methods to solve these partial differential equations, over the past three decades. Recently, the so-called meshless methods of discretization have become very attractive, as they are efficient for solving PDEs by avoiding the tedium of mesh-generation, especially for those problems having complicated geometries, as well as those involving large strains. As a systematic framework for developing various truly-meshless methods, the Meshless Local Petrov-Galerkin (MLPG) approach has been proposed as a fundamentally new concept [Atluri and Zhu (1998); Atluri and Shen (2002a, b); Atluri (2004)]. The generality of the MLPG approach, based on the symmetric or unsymmetric weak-forms of the PDEs, and using a variety of interpolation methods (trial functions), test functions, and integration schemes without background cells, has been widely investigated [Atluri and Shen (2002a, b); Atluri(2004)].

Remarkable successes of the MLPG method have been reported in solving the convection-diffusion problems [Lin and Atluri (2000)]; fracture mechanics [Batra and Ching (2002)]; Navier-Stokes flows [Lin and Atluri (2001)]; and plate bending problems [Long and Atluri (2002)]. Recently, the MLPG method has made some strides, and it is applied successfully in studying strain gradient materials [Tang, Shen and Atluri, (2003)], three dimensional elasticity problems [Li, Shen, Han and Atluri (2003), Han and Atluri (2004a)], elastodynamics [Han and Atluri (2004b)], and multiscale structure and nanomechanics [Shen and Atluri (2004, 2005)]. These research successes demonstrate that the MLPG method is one of the most promising alternative methods for computational mechanics. The interrelation of the various meshless approaches, and the recent developments and

---

<sup>1</sup> Center for Aerospace Research & Education  
University of California at Irvine  
5251 California Avenue, #140  
Irvine, CA 92617, USA

applications of the MLPG methods can be founded in Atluri (2004).

Very recently, Atluri, Han and Rajendran (2004) developed a mixed MLPG method for the 2<sup>nd</sup> order partial differential equation system of elasticity, in which both strains and displacements were independently interpolated through meshless interpolation schemes. The nodal values of strains were expressed in terms of the independently interpolated nodal values of displacements, by simply enforcing the strain-displacement relationships directly by collocation at the nodal points. The mixed MLPG method avoids the direct differentiation of the trial function (and the evaluation of these directly derived derivatives at each Gauss point in the integration of the weak form), and reduces the continuity-requirement on the trial function by one-order. A smaller interpolation domain can be used in the meshless approximation with a lower-order polynomial basis. The mixed MLPG method improves very much the efficiency of the primal MLPG method. In this paper, we will employ this idea to solve the 4<sup>th</sup> order ordinary differential equation.

The 4<sup>th</sup> order ordinary differential equation is more complicated. For the 4<sup>th</sup> order ordinary differential equation, in the conventional displacement-based approaches in FEM, the interpolation of displacement requires  $C^1$  continuity (in order to ensure convergence of the finite element procedure for 4<sup>th</sup> order theories), which inevitably involves very complicated shape functions. These shape functions involve large numbers of degrees of freedom in every element, including nodal displacements, nodal rotations (i.e. first order gradients of displacement), and even higher order derivatives.  $C^1$  continuous methods are mostly feasible only for one-dimensional problems. The standard approach for solving Bernoulli-Euler beam problems is by employing  $C^1$  continuous Hermite cubic shape functions, interpolating both displacements and rotations (i.e., slopes, the 1<sup>st</sup> derivative). For two dimensional problems, such as involving plate and shell analysis,  $C^1$  continuous methods are very complicated, and formulations for three-dimensional problems become more or less intractable. The high computational cost and large number of degrees of freedom soon place such formulations beyond the realm of practicality. Atluri, Cho and Kim (1999) presented an analysis of thin beam problems using the MLPG method with a generalized moving least squares (GMLS) approximation. Then, Cho & Atluri (2001) extended it to the shear flexi-

ble beams based on a locking-free formulation. Raju and Phillips (2003) applied MLPG with the GMLS approximation to a continuous beam problem to evaluate their effectiveness, and discussed the effects of various parameters on the numerical results clearly and systematically. Long & Atluri (2002) analyzed the bending problem of a thin plate by means of MLPG with the MLS approximation.

In this paper, we will illustrate various MLPG methods with the MLS approximation for the simulation of the 4<sup>th</sup> order ordinary differential equation (of a beam on an elastic foundation), including both the primal MLPG methods and the mixed MLPG methods. All the possible local weak forms for a 4<sup>th</sup> order ordinary differential equation are given in this paper.

The outline of the paper is as follows. In Section 2, the meshless interpolation-the moving least square method is described briefly for the sake of completeness. The local weak forms and the corresponding primal MLPG methods are discussed in Section 3, and their numerical results are also presented. In Section 4, the first kind of mixed MLPG methods and their numerical results are given. In the first kind of mixed MLPG methods, both the displacement and its second derivative are interpolated independently through meshless interpolation schemes. The second kind of mixed MLPG methods and their numerical results are presented in Section 5. In the second kind of mixed MLPG methods, the displacement, its first derivative, second derivative and third derivative are all interpolated independently through meshless interpolation schemes. The conclusions and discussions are given in Section 6.

## 2 Meshless Interpolation: the Moving Least Square Method

In general, meshless methods use a local interpolation, or an approximation, to represent the trial function, using the values (or the fictitious values) of the unknown variable at some randomly located nodes in the local vicinity. A variety of local interpolation schemes that interpolate the data at randomly scattered points (without the need for a mesh) are currently available [Atluri and Shen (2002a, b), Atluri (2004)].

The moving least-square method is generally considered to be one of the best schemes to interpolate data with a reasonable accuracy. Basically the MLS interpolation

does not pass through the nodal data. Consider a domain in question with control points for boundaries (i.e. nodes on boundaries) and some scattered nodes inside, where every node has its undetermined nodal coefficient (fictitious nodal value) and an influence radius (radius for local weight function). Now for the distribution of trial function at any point  $x$  and its neighborhood  $\Omega_x$  located in the problem domain  $\Omega$ ,  $u^h(x)$  may be defined by

$$u^h(x) = \mathbf{p}^T(x) \mathbf{a}(x) \quad \forall x \in \Omega_x \quad (1)$$

where  $\mathbf{p}^T(x) = [p_1(x), p_2(x), \dots, p_m(x)]$  is a complete monomial basis of order  $m$ , and  $\mathbf{a}(x)$  is a vector containing coefficients  $a_j(x)$ ,  $j=1, 2, \dots, m$  which are functions of the space co-ordinates  $x$ . The commonly used bases in 1-D are the linear basis ( $m=2$ ), due to their simplicity. In the present 4th order problem, we will also employ the quadratic basis ( $m=3$ )

$$\mathbf{p}^T(x) = [1 \quad x \quad x^2] \quad (2)$$

and the cubic basis ( $m=4$ )

$$\mathbf{p}^T(x) = [1 \quad x \quad x^2 \quad x^3] \quad (3)$$

The coefficient vector  $\mathbf{a}(x)$  is determined by minimizing a weighted discrete  $L_2$  norm, which can be defined as

$$J(x) = \sum_{I=1}^N w_I(x) [\mathbf{p}^T(x_I) \mathbf{a}(x) - \hat{u}^I]^2 \quad (4)$$

where  $w_I(x)$ , is a weight function associated with the node  $I$ , with  $w_I(x) > 0$  for all  $x$  in the support of  $w_I(x)$ ,  $x_I$  denotes the value of  $x$  at node  $I$ ,  $N$  is the number of nodes in  $\Omega_x$  for which the weight functions  $w_I(x) > 0$ . Here it should be noted that  $\hat{u}^I$ ,  $I=1, 2, \dots, N$ , in equation (4), are the fictitious nodal values (undetermined nodal coefficients), and not the exact nodal values of the unknown trial function  $u^h(\mathbf{x})$ , in general.

Solving for  $\mathbf{a}(x)$  by minimizing  $J$  in equation (4), and substituting it into equation (1), give a relation which may be written in the form of an interpolation function similar to that used in the FEM, as

$$u^h(x) = \sum_{I=1}^N \phi^I(x) \hat{u}^I, \quad u^h(x_I) \equiv u^I \neq \hat{u}^I, \quad x \in \Omega_x \quad (5)$$

where

$$\phi^I(x) = \sum_{j=1}^m p_j(x) [\mathbf{A}^{-1}(x) \mathbf{B}(x)]_{jI} \quad (6)$$

with the matrix  $\mathbf{A}(x)$  and  $\mathbf{B}(x)$  being defined by:

$$\mathbf{A}(x) = \sum_{I=1}^N w_I(x) \mathbf{p}(x_I) \mathbf{p}^T(x_I) \quad (7)$$

$$\mathbf{B}(x) = [w_1(x) \mathbf{p}(x_1), w_2(x) \mathbf{p}(x_2), \dots, w_N(x) \mathbf{p}(x_N)] \quad (8)$$

Equation (6) can be rewritten as

$$\Phi(x) = \alpha^T(x) \mathbf{B}(x) \quad (9)$$

with

$$\mathbf{A}\alpha = \mathbf{p} \quad (10)$$

The partial derivatives of  $\alpha$  are obtained through the relations:

$$\mathbf{A}\alpha_{,x} = \mathbf{p}_{,x} - \mathbf{A}_{,x}\alpha \quad (11)$$

$$\mathbf{A}\alpha_{,xx} = \mathbf{p}_{,xx} - \mathbf{A}_{,xx}\alpha - 2\mathbf{A}_{,x}\alpha_{,x} \quad (12)$$

$$\alpha_{,xxx} = \mathbf{p}_{,xxx} - \mathbf{A}_{,xxx}\alpha - 3\mathbf{A}_{,xx}\alpha_{,x} - 3\mathbf{A}_{,x}\alpha_{,xx} \quad (13)$$

Now, the partial derivatives of  $\phi^I(\mathbf{x})$  are obtained as

$$\phi_{,x}^I = \alpha_{,x}^T \mathbf{B}_I + \alpha^T \mathbf{B}_{I,x} \quad (14)$$

$$\phi_{,xx}^I = \alpha_{,xx}^T \mathbf{B}_I + 2\alpha_{,x}^T \mathbf{B}_{I,x} + \alpha^T \mathbf{B}_{I,xx} \quad (15)$$

$$\phi_{,xxx}^I = \alpha_{,xxx}^T \mathbf{B}_I + 3\alpha_{,xx}^T \mathbf{B}_{I,x} + 3\alpha_{,x}^T \mathbf{B}_{I,xx} + \alpha^T \mathbf{B}_{I,xxx} \quad (16)$$

in which  $\mathbf{B}_I$  is the  $I$ th column of matrix  $\mathbf{B}$ . Thus, the derivatives of  $\phi^I(\mathbf{x})$  become rather complicated.

The nodal shape function is complete up to the order of the basis. The smoothness of the nodal shape function  $\phi^I(x)$  is determined by that of the basis and of the weight function. The choice of the weight function is more or less arbitrary as long as the weight function is positive and continuous. The following weight function is considered in the present work:

$$w_I(x) = \begin{cases} 1 - \sum_{k=1}^p a_k \left(\frac{d_I}{r_I}\right)^k & 0 \leq d_I \leq r_I = \rho_I h_I \\ 0 & d_I > r_I = \rho_I h_I \end{cases} \quad (17)$$

where  $d_I = |x - x_I|$  is the distance from node  $x_I$  to point  $x$ ,  $h_I$  is the nodal distance,  $\rho_I$  is the scaling parameter for the size of the sub-domain  $\Omega_{Ir}^I$ , and  $p$  is the order of spline function. The coefficients  $a_k$  are obtained by taking the following boundary conditions:

$$\begin{cases} w_I(d_I/r_I = 0) = 1, & m_0 = 0 \\ \frac{\partial^{m_0} w_I(d_I/r_I = 0)}{\partial x^{m_0}} = 0, & m_0 \geq 1 \end{cases} \quad (18)$$

and

$$\begin{cases} w_I(d_I/r_I = 1) = 0, & m_1 = 0 \\ \frac{\partial^{m_1} w_I(d_I/r_I = 1)}{\partial x^{m_1}} = 0, & m_1 \geq 1 \end{cases}$$

where  $p = m_0 + m_1 + 1$ . The form of the weight functions may be changed by the geometry of the sub-domain  $\Omega_{Ir}^I$  over which the weight function is non-zero. Since the weight function is a type of a polynomial, the “nodal shape function” given in equation (6) has the characteristics of a rational function. One can easily obtain a global  $C^l$  continuity up to a desired order  $l$  if the order of spline is changed. Therefore, the  $C^l$  continuity depends upon value of  $m_0$  and  $m_1$  in equations (18) and (19), i.e.  $\phi(\mathbf{x}) \in C^{\min(m_0, m_1)}$  if  $m_0$  is even;  $\phi(\mathbf{x}) \in C^{\min(m_0+1, m_1)}$  if  $m_0$  is odd. It is very important to preserve the smoothness of the derivatives of shape functions, because discontinuities and vertices in the derivatives of the shape functions make numerical integration difficult. In this paper, we choose a 4<sup>th</sup> order spline function ( $C^2$ )

$$w_I(x) = \begin{cases} 1 - 6\left(\frac{d_I}{r_I}\right)^2 + 8\left(\frac{d_I}{r_I}\right)^3 - 3\left(\frac{d_I}{r_I}\right)^4, & 0 \leq d_I \leq r_I \\ 0, & d_I \geq r_I \end{cases} \quad (20)$$

as well as a 7<sup>th</sup> order spline function ( $C^3$ ),

$$w_I(x) = 1 - 35\left(\frac{d_I}{r_I}\right)^4 + 84\left(\frac{d_I}{r_I}\right)^5 - 70\left(\frac{d_I}{r_I}\right)^6 + 20\left(\frac{d_I}{r_I}\right)^7 \quad (21)$$

for  $0 \leq d_I \leq r_I$ , as weight functions.

Now, in order to depict its performance, we will employ the MLS to simulate the following function, which is the

known exact solution of the 4<sup>th</sup> order differential equation

$$\begin{aligned} \frac{d^4 u}{dx^4} + u - 1 &= 0, \quad 0 < x < 1 \\ u = u'' &= 0, \quad x = 0, \text{ and } 1 \end{aligned} \quad (22)$$

i.e.,

$$\begin{aligned} (19) \quad u_{exact} &= 1 + \left( \frac{-e^{-\frac{1}{\sqrt{2}}} \left( \cos \frac{1}{\sqrt{2}} + e^{-\frac{1}{\sqrt{2}}} \right)}{2e^{-\frac{1}{\sqrt{2}}} \cos \frac{1}{\sqrt{2}} + e^{-\frac{2}{\sqrt{2}}} + 1} \right) e^{\frac{x}{\sqrt{2}}} \cos \frac{x}{\sqrt{2}} \\ &+ \left( \frac{-e^{-\frac{1}{\sqrt{2}}} \sin \frac{1}{\sqrt{2}}}{2e^{-\frac{1}{\sqrt{2}}} \cos \frac{1}{\sqrt{2}} + e^{-\frac{2}{\sqrt{2}}} + 1} \right) e^{\frac{x}{\sqrt{2}}} \sin \frac{x}{\sqrt{2}} \\ &+ \left( \frac{-\left( e^{-\frac{1}{\sqrt{2}}} \cos \frac{1}{\sqrt{2}} + 1 \right)}{2e^{-\frac{1}{\sqrt{2}}} \cos \frac{1}{\sqrt{2}} + e^{-\frac{2}{\sqrt{2}}} + 1} \right) e^{-\frac{x}{\sqrt{2}}} \cos \frac{x}{\sqrt{2}} \\ &+ \left( \frac{-e^{-\frac{1}{\sqrt{2}}} \sin \frac{1}{\sqrt{2}}}{2e^{-\frac{1}{\sqrt{2}}} \cos \frac{1}{\sqrt{2}} + e^{-\frac{2}{\sqrt{2}}} + 1} \right) e^{-\frac{x}{\sqrt{2}}} \sin \frac{x}{\sqrt{2}} \end{aligned} \quad (23)$$

In this simulation, the linear basis, and the 7<sup>th</sup> order spline function (21) are employed; 20 nodes are distributed evenly from 0 to 1, the radius of the support domain of the trial function is taken to be  $5.5h_I$ . Thus, setting:

$$u_{exact}(x_J) = \sum_{I=1}^{20} \phi^I(x_J) \hat{u}^I; \quad J = 1, \dots, 20 \quad (24)$$

and using (6), we obtain the values of  $\hat{u}^I$ . Then we obtain the interpolation  $u^h(x)$  for  $u_{exact}$ , as:

$$u^h(x) = \sum_{I=1}^{20} \phi^I(x) \hat{u}^I \quad (25)$$

Fig. 1 shows the distinction between the exact nodal values  $u^I$  of the trial function  $u^h(x)$ , and the fictitious nodal values  $\hat{u}^I$ . Figs. 2-5 compare the values of the function  $u^h(x)$  and its 1<sup>st</sup>-3<sup>rd</sup> order derivatives calculated from the MLS interpolation with the corresponding exact values obtained from (23). From these figures, we can see that the MLS can interpolate the function  $u_{exact}$  and its first

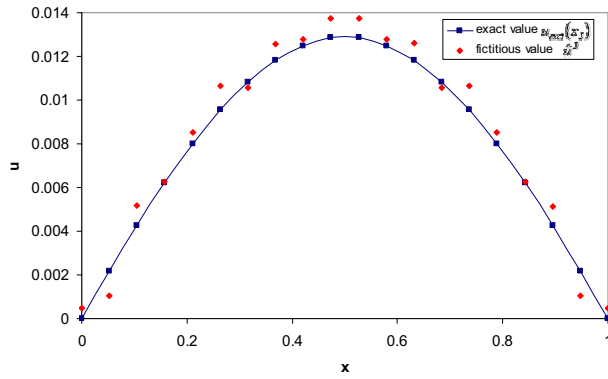


**Figure 1 :** The distinction between the exact nodal values  $u^l$  of the trial function  $u^h(x)$ , and the fictitious nodal values  $\hat{u}^l$ .

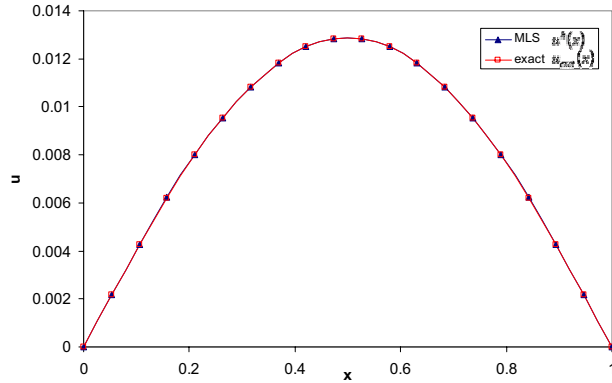


**Figure 2 :** The function  $u$ .

derivative very well, but it has poor accuracy to interpolate the higher order derivatives. Hence, in the weak forms, we should avoid the appearance of the higher order derivatives of  $u^h(x)$ .

### 3 Local Weak Forms and Primal MLPG Methods

Consider a 4<sup>th</sup> order ODE

$$\frac{d^4 u}{dx^4} + u - 1 = 0 \quad (26)$$

in domain  $\Omega$  ( $0 \leq x \leq 1$ ). Equation (26) is actually the governing equation for a thin beam on an elastic foundation undergoing small deformations, in which  $u$  is the normalized transverse displacement. The boundary conditions at  $x=0$  and  $x=1$  can have several combinations.

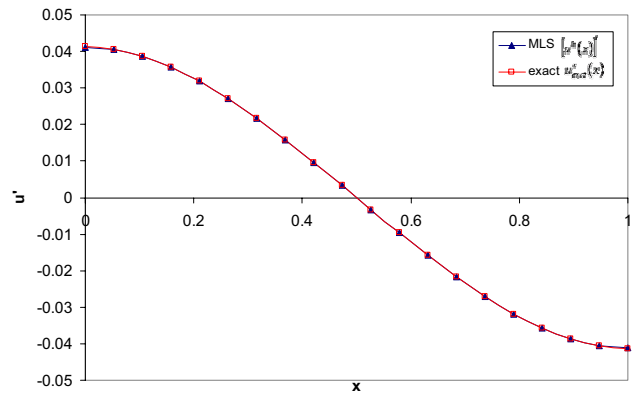


**Figure 3 :** The first derivative of the function  $u$ .

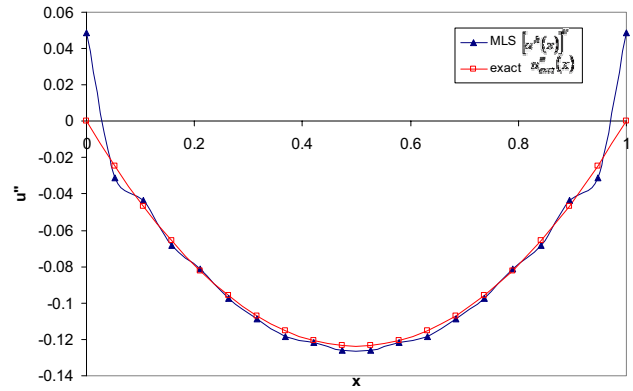


**Figure 4 :** The second derivative of the function  $u$ .

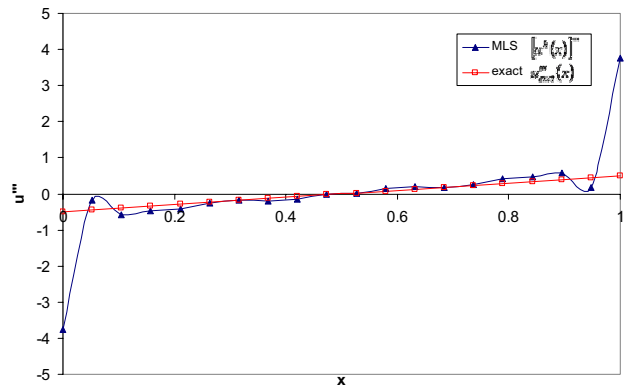


**Figure 5 :** The third derivative of the function  $u$ .

The essential boundary conditions are of the form

$$u = \bar{u} \text{ on } \Gamma_u \quad (27)$$

$$u' = \bar{u}' \text{ on } \Gamma_u' \quad (28)$$

and the natural boundary conditions are of the form

$$u''' = \bar{u}''' \text{ on } \Gamma_u''' \quad (29)$$

$$u'' = \bar{u}'' \text{ on } \Gamma_u'' \quad (30)$$

where  $\Gamma_u$ ,  $\Gamma_u'$ ,  $\Gamma_u''$ , and  $\Gamma_u'''$  denote the boundary points where  $u$  (deflection),  $u'$  (slope),  $u'''$  (shear), and  $u''$  (moment) are prescribed, respectively. Note that the prescriptions of  $\bar{u}$  &  $\bar{u}'''$ , and  $\bar{u}'$  &  $\bar{u}''$  are mutually disjoint, i.e., when  $u = \bar{u}$  is prescribed,  $u'''$  becomes the corresponding reaction, and when  $u' = \bar{u}'$  is prescribed,  $u''$  becomes the corresponding reaction.

Now, we will give all the local weak forms for equation (26), which are the basis of the MLPG methods. A generalized local weak form (LWF) of the 4<sup>th</sup> order differential equation (26) over a local subdomain  $\Omega_s$ , can be written as:

$$\int_{\Omega_s} \left( \frac{d^4 u}{dx^4} + u - 1 \right) v dx = 0 \quad (31)$$

The local weak form (31) includes the fourth derivative of the trial function. If the test function  $v$  is taken to be the Delta function, the collocation method will be derived from equation (31). In section 2, it is shown that it is too difficult to obtain the accurate higher order derivatives of the trial function; moreover, they are not very accurate. Hence, this weak form is not appropriate for the numerical implementation. In fact, we did implement the collocation in our numerical experiments; However, we could not obtain any meaningful results, as was expected (these numerical results are omitted in this paper).

To obtain an accurate and efficient meshless method, one should decrease the order of the derivatives of the trial function in the local weak forms. There are two ways to reach this goal. One is by means of integrating by parts, through which the differentiation can be transferred from the trial function,  $u$ , to the test function,  $v$ . Then, the higher order derivatives in the domain integration will disappear. However, the higher order derivatives of the trial function still appear in the local boundary integral (local boundary for 1D problem). This is the primal MLPG method. Another promising approach is the use of the “mixed” MLPG approach [Atluri, Han, Rajendran (2004)], wherein, independent meshless interpolations are also used for the derivatives, as well as the function

per se. The mixed methods are described in detail in the next section. In this section, we limit ourselves to the primal MLPG methods.

### 3.1 Unsymmetric local weak form 1

By integrating (31) by part once, one obtain:

$$n_x [u''' v]_{\Gamma_s} - \int_{\Omega_s} u''' v' dx + \int_{\Omega_s} (u - 1) v dx = 0 \quad (32)$$

where  $n_x [\cdot]_{\Gamma_s}$  denotes the boundary term and  $n_x$  is the outward normal. For one-dimensional problems, the local boundary  $\Gamma_s$  has two points, and  $n_x$  has the values of  $\pm 1$ . Equation (32) is an unsymmetric weak form, and the trial function should be  $C^2$  continuous. There is a third derivative of function  $u$  in LWF (32). Imposing the boundary conditions (29), one obtains

$$n_x [\bar{u}''' v]_{\Gamma_{su}'''} + n_x [u''' v]_{\Gamma_{su}} + n_x [u''' v]_{L_s} - \int_{\Omega_s} u''' v' dx + \int_{\Omega_s} (u - 1) v dx = 0 \quad (33)$$

where  $\Gamma_{su}'''$  is the boundary where  $u'''$  is prescribed on the local boundary ( $\Gamma_s \cap \Gamma_u'''$ ). In general, when a local boundary,  $\Gamma_s$ , intersects a global boundary,  $\Gamma$ , four boundary condition possibilities exist. These possibilities are  $\Gamma_s \cap \Gamma_u$ ,  $\Gamma_s \cap \Gamma_u'$ ,  $\Gamma_s \cap \Gamma_u''$ , and  $\Gamma_s \cap \Gamma_u'''$ , and are denoted as  $\Gamma_{su}$ ,  $\Gamma_{su}'$ ,  $\Gamma_{su}''$ , and  $\Gamma_{su}'''$ , respectively; and  $L_s$  is the other part of the local boundary which is inside the solution domain. Since the boundary  $\Gamma_u$  and  $\Gamma_u'''$  are mutually disjoint, and are related by  $\Gamma = \Gamma_u \cup \Gamma_u'''$ , the local boundary  $\Gamma_s$  can be decomposed into disjoint subsets of  $L_s$ ,  $\Gamma_{su}$  and  $\Gamma_{su}'''$ . By the same reason, it can also be decomposed into disjoint subsets  $L_s$ ,  $\Gamma_{su}'$  and  $\Gamma_{su}''$ . By using these decompositions, along with the boundary conditions (27)-(30), equation (33) is obtained.

In order to simplify the above equation, we can select a test function  $v$  such that it vanishes over  $L_s$ , then equation (33) can be rewritten as

$$\begin{aligned} & \int_{\Omega_s} u v dx - \int_{\Omega_s} u''' v' dx + n_x [u''' v]_{\Gamma_{su}} \\ &= \int_{\Omega_s} v dx - n_x [\bar{u}''' v]_{\Gamma_{su}'''} \end{aligned} \quad (34)$$

With equation (5), one may discretize the local unsymmetric weak form (34) as

$$\sum_{I=1}^N \int_{\Omega_s} \left[ \phi^I(x) v - \frac{d^3 \phi^I(x)}{dx^3} v' \right] dx \hat{u}_I + \sum_{I=1}^N n_x \left[ \frac{d^3 \phi^I(x)}{dx^3} v \right]_{\Gamma_{su}} \hat{u}_I = \int_{\Omega_s} v dx - n_x [\bar{u}''' v]_{\Gamma_{su}'''} \quad (35)$$

As discussed in Atluri (2004), one may choose the Heaviside function as the test function, and obtains

$$n_x [u''' v]_{\Gamma_{su}} + n_x [u''' v]_{L_s} + \int_{\Omega_s} u v dx = \int_{\Omega_s} v dx - n_x [\bar{u}''' v]_{\Gamma_{su}'''} \quad (36)$$

Equation (36) can be discretized as

$$\sum_{I=1}^N n_x \left[ \frac{d^3 \phi^I(x)}{dx^3} v \right]_{\Gamma_{su}} \hat{u}_I + \sum_{I=1}^N n_x \left[ \frac{d^3 \phi^I(x)}{dx^3} v \right]_{L_s} \hat{u}_I + \sum_{I=1}^N \int_{\Omega_s} \phi^I(x) v dx \hat{u}_I = \int_{\Omega_s} v dx - n_x [\bar{u}''' v]_{\Gamma_{su}'''} \quad (37)$$

In this study, the collocation method is used to impose the boundary conditions. For boundary node  $x_I$ , one has

$$\beta_1 u(x_I) + \beta_2 u'(x_I) + \beta_3 u''(x_I) = \beta_1 \bar{u} + \beta_2 \bar{u}' + \beta_3 \bar{u}'' \quad (38)$$

It is noted that actually there exist only 1 or 2 terms in both sides of equation (38), depending on the combination of the boundary conditions.

However, as discussed in Section 2, we know that the MLS interpolation is hardly capable of approximating the third derivative of function  $u$ . Our numerical experiments based on LWF (33), cannot obtain any stable and convergent results (using some special parameter-combinations, one may happen to obtain some good results), using either weight function (20) or Heaviside function as test function. Hence, the unsymmetric local weak form (33) is not appropriate for the numerical implementation either. However, the mixed MLPG method based on this LWF (33) can still generate stable and convergent results, as will be described in next section.

### 3.2 Symmetric local weak form

Integrating (31) by parts twice yields the following symmetric local weak form,

$$n_x [u''' v]_{\Gamma_s} - n_x [u'' v']_{\Gamma_s} + \int_{\Omega_s} u'' v'' dx + \int_{\Omega_s} (u-1) v dx = 0 \quad (39)$$

This is a symmetric local weak form, and both the trial and test function should be  $C^1$  continuous. Imposing the boundary conditions (29) and (30), one obtains

$$n_x [\bar{u}''' v]_{\Gamma_{su}'''} + n_x [u''' v]_{\Gamma_{su}} + n_x [u''' v]_{L_s} - n_x [\bar{u}'' v']_{\Gamma_{su}''} - n_x [u'' v']_{\Gamma_{su}'} - n_x [u'' v']_{L_s} + \int_{\Omega_s} u'' v'' dx + \int_{\Omega_s} (u-1) v dx = 0 \quad (40)$$

In order to simplify the above equation, one can select a test function  $v$  such that it, and its derivative, vanish over  $L_s$ , then equation (40) can be rewritten as

$$n_x [u''' v]_{\Gamma_{su}} - n_x [u'' v']_{\Gamma_{su}'} + \int_{\Omega_s} u'' v'' dx + \int_{\Omega_s} u v dx = \int_{\Omega_s} v dx - n_x [\bar{u}''' v]_{\Gamma_{su}'''} + n_x [\bar{u}'' v']_{\Gamma_{su}''} \quad (41)$$

By means of the MLS interpolation (5), the local symmetric weak form (41) can be discretized as

$$\sum_{I=1}^N n_x \left[ \frac{d^3 \phi^I(x)}{dx^3} v \right]_{\Gamma_{su}} \hat{u}_I - \sum_{I=1}^N n_x \left[ \frac{d^2 \phi^I(x)}{dx^2} v' \right]_{\Gamma_{su}'} \hat{u}_I + \sum_{I=1}^N \int_{\Omega_s} \left[ \phi^I(x) v + \frac{d^2 \phi^I(x)}{dx^2} v'' \right] dx \hat{u}_I = \int_{\Omega_s} v dx - n_x [\bar{u}''' v]_{\Gamma_{su}'''} + n_x [\bar{u}'' v']_{\Gamma_{su}''} \quad (42)$$

The collocation method is used to impose the boundary conditions. For boundary node  $x_I$ , one has

$$\beta_1 u(x_I) + \beta_2 u'(x_I) = \beta_1 \bar{u} + \beta_2 \bar{u}' \quad (43)$$

It is noted that actually there may exist 0 to 2 terms in each sides of equation (43), depending on the combination of the boundary conditions.

To illustrate their effectiveness, the MLPG methods based on the LWF (41) are used to solve equation (26) with boundary conditions:

$$u = u'' = 0 \text{ at } x = 0, 1 \quad (44)$$

The exact solution is equation (22).

For the purpose of error estimation and convergence studies, the following norm is used:

$$\|u\| = \left( \int_{\Omega} u^2 dx \right)^{\frac{1}{2}} \quad (45)$$

The relative errors for every order derivative are defined as

$$e_k = \frac{\left\| \left( \frac{d^{(k)}u}{dx^k} \right)^{\text{num}} - \left( \frac{d^{(k)}u}{dx^k} \right)^{\text{exact}} \right\|}{\left\| \left( \frac{d^{(k)}u}{dx^k} \right)^{\text{exact}} \right\|}, \quad k = 0, 1, 2, 3 \quad (46)$$

For the present problem of a beam on elastic foundation, the normalized elastic energy stored in the system, at equilibrium, may be written as

$$W = \frac{1}{2} \int_0^1 (u'' + u^2) dx$$

The relative error for the energy is defined as

$$e_p = \frac{|W^{\text{num}} - W^{\text{exact}}|}{|W^{\text{exact}}|} \quad (47)$$

At first, we use the cubic basis, i.e.  $m=4$ . Both the weight function in the MLS interpolation and the test function are taken to be equation (20). 41 nodes are used ( $h=0.025$ , with  $h$  being the distance between nodes). Fig. 6 shows the influence of the radius of the test domain on the relative errors  $e_0$  and  $e_1$ , where the radius of the trial function domain is taken to be  $4.5h$ . From this figure, it can be found that the relative errors of the function  $u$  and its first derivative are less than 1% when the trial function domain is big enough ( $> 2.5h$ ). It is noticed that the accuracy is not sensitive to the radius of the test domain

from  $3.5h$ . Fig. 7 shows the influence of the radius of the trial domain on the errors  $e_0$  and  $e_1$ , where the radius of the test domain is taken to be  $3.5h$ . The results for the function  $u$  and its first derivative are highly accurate. The relative errors  $e_0$  and  $e_1$  are not sensitive to the radius of the trial function domain from  $3.5h$  to  $5.5h$ , and less than 1%. For the linear ( $m=2$ ) basis, the same trends can be observed. However, for  $m=2$ , a larger radius of the trial function domain should be chosen to obtain an accurate and stable result. In fact, in MLS, to increase the radius of the trial function domain is equivalent to increase  $m$  of the basis function.

The convergence rate is investigated with three nodal configurations: 11, 21, and 41 nodes. We also consider the effects of the basis functions: linear ( $m=2$ ) and cubic ( $m=4$ ) bases are used in this investigation. For cubic ( $m=4$ ) basis, the radius of the test domain is taken to be  $3.5h$ , and the radius of the trial domain is taken to be  $4.5h$ . For linear ( $m=2$ ) basis, the radius of the test domain is taken to be  $3.5h$ , and the radius of the trial domain is taken to be  $8h$ . The relative errors  $e_0$  and  $e_1$  and the convergence rates  $R$  of the displacement and first derivative are depicted in Fig. 8, for both  $m=4$  and  $m=2$ . The convergence rates  $R$  of the relative errors  $e_2$ ,  $e_3$  and  $e_p$  for the second, third derivatives and the energy, are plotted in Fig. 9 only for  $m=4$ . It can be seen that the present MLPG method has high rates of convergence for norms  $e_0$ ,  $e_1$ ,  $e_2$ , and  $e_p$ , and gives very accurate results for the unknown variable, its first and second derivatives, and the energy. The results from the cubic ( $m=4$ ) basis are more accurate, and of higher convergent rate than those from the linear ( $m=2$ ) basis. However, the results for the third derivative are not very accurate, and the convergence rate for the relative error  $e_3$  is not high.

### 3.3 Unsymmetric local weak form 2

Integrating (31) by parts three times yields the following local unsymmetric weak form,

$$\begin{aligned} & n_x [u'''v]_{\Gamma_s} - n_x [u''v']_{\Gamma_s} + n_x [u'v'']_{\Gamma_s} \\ & - \int_{\Omega_s} u'v''' dx + \int_{\Omega_s} (u-1)v dx = 0 \end{aligned} \quad (48)$$

This is an unsymmetric weak form, and the trial function can be  $C^0$  continuous. Imposing the boundary conditions (29) and (30), one obtains

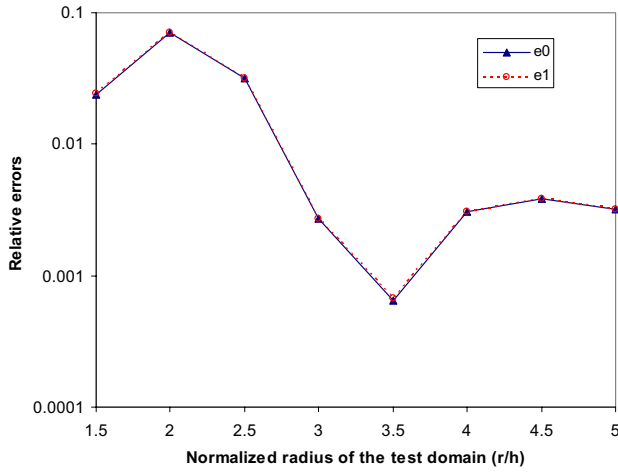


**Figure 6 :** The influence of the test domain size (41 nodes).

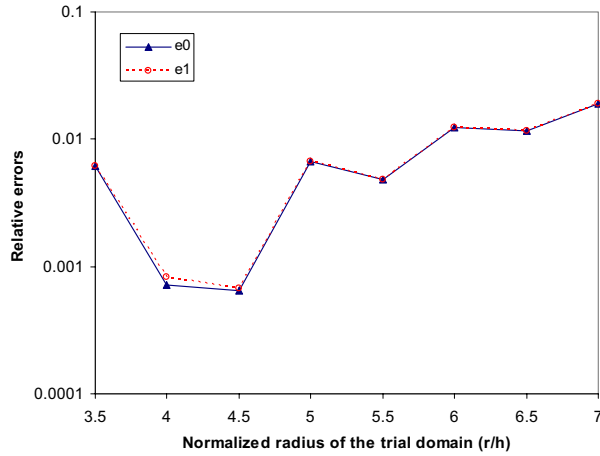


**Figure 7 :** The influence of the trial domain size (41 nodes).

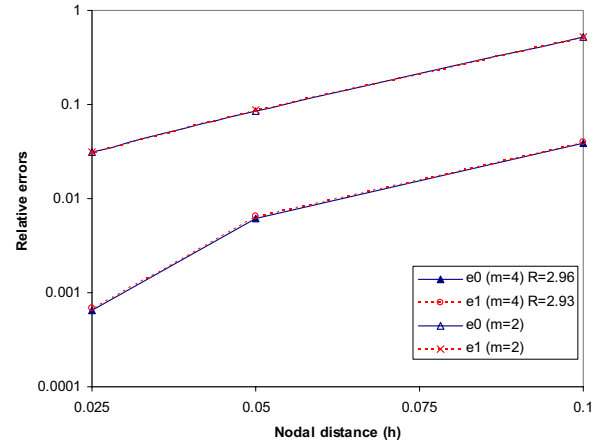


**Figure 8 :** Convergence rate in relative errors  $e_0$  and  $e_1$ .

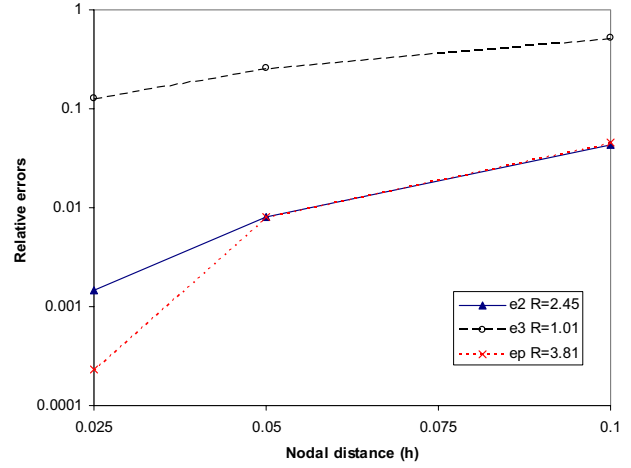


**Figure 9 :** Convergence rate in relative errors  $e_2$ ,  $e_3$ , and  $e_p$ .

function is given in (20) and (21). Then equation (49) can be simplified as

$$\begin{aligned}
 & n_x [\bar{u}''' v]_{\Gamma_{su''}} + n_x [u''' v]_{\Gamma_{su}} + n_x [u''' v]_{L_s} \\
 & - n_x [\bar{u}'' v']_{\Gamma_{su''}} - n_x [u'' v']_{\Gamma_{su'}} - n_x [u'' v']_{L_s} \\
 & + n_x [\bar{u}' v'']_{\Gamma_{su'}} + n_x [u' v'']_{\Gamma_{su''}} + n_x [u' v'']_{L_s} \\
 & - \int_{\Omega_s} u' v''' dx + \int_{\Omega_s} (u-1) v dx = 0
 \end{aligned}$$

$$\begin{aligned}
 & n_x [u''' v]_{\Gamma_{su}} - n_x [u'' v']_{\Gamma_{su'}} + n_x [u' v'']_{\Gamma_{su''}} \\
 & + \int_{\Omega_s} u v dx - \int_{\Omega_s} u' v''' dx \\
 & = \int_{\Omega_s} v dx - n_x [\bar{u}''' v]_{\Gamma_{su''}} \\
 & + n_x [\bar{u}'' v']_{\Gamma_{su''}} - n_x [\bar{u}' v'']_{\Gamma_{su'}}
 \end{aligned} \tag{49}$$

One can select a test function  $v$  such that itself, and its first and second derivatives vanish over  $L_s$ . Such a test

With equation (5), one may discretize the local symmet-

ric weak form (50) as

$$\begin{aligned}
 & \sum_{I=1}^N n_x \left[ \frac{d^3 \phi^I(x)}{dx^3} v \right]_{\Gamma_{su}} \hat{u}_I - \sum_{I=1}^N n_x \left[ \frac{d^2 \phi^I(x)}{dx^2} v' \right]_{\Gamma_{su'}} \hat{u}_I + \\
 & \sum_{I=1}^N n_x \left[ \frac{d \phi^I(x)}{dx} v'' \right]_{\Gamma_{su''}} \hat{u}_I \\
 & + \sum_{I=1}^N \int_{\Omega_s} \left[ \phi^I(x) v - \frac{d \phi^I(x)}{dx} v''' \right] dx \hat{u}_I \\
 & = \int_{\Omega_s} v dx - n_x [\bar{u}''' v]_{\Gamma_{su'''}} + n_x [\bar{u}'' v']_{\Gamma_{su''}} \\
 & - n_x [\bar{u}' v'']_{\Gamma_{su'}}
 \end{aligned} \quad (51)$$

The collocation method is used to impose the only boundary condition, which does not appear in the left side of equation (51). For boundary node  $x_I$ , one has

$$\beta_1 u(x_I) = \beta_1 \bar{u} \quad (52)$$

In the numerical example, we also use the cubic basis, i.e.  $m=4$ . The weight function in MLS is taken to be as in equation (20), while the test function in LWF (49) is chosen to be as in equation (21). 41 nodes are used ( $h=0.025$ ) to consider the influences of the radius of both test and trial domains. Fig. 10 shows the influence of the radius of the test domain on the errors  $e_0$  and  $e_1$ , where the radius of the trial function domain is taken to be  $4.5h$ . From this figure, it can be found that the accuracy of the function,  $u$  as well as its first derivative, is high, when the trial function domain is big enough ( $> 2.5h$ ). Similarly, it is noticed that the accuracy is not sensitive to the radius of the test domain from  $3.5h$ . Fig. 11 shows the influence of the radius of the trial domain on the errors  $e_0$  and  $e_1$ , where the radius of the test domain is taken to be  $3.5h$ . The results for the function  $u$ , as well as its first derivative, are of high accuracy. The relative errors  $e_0$  and  $e_1$  are less than 1%, and are not sensitive to the radius of the trial function domain as the radius of the trial domain is greater than  $4h$ . For the linear ( $m=2$ ) basis, the same trends can be observed. Again, for  $m=2$ , a larger radius of the trial function domain should be chosen to obtain an accurate and stable result.

Similarly, the convergence rate is investigated with three nodal configurations: 11, 21, and 41 nodes. The effects of the basis functions: linear ( $m=2$ ) and cubic ( $m=4$ ) bases are investigated. For cubic ( $m=4$ ) basis, the radius

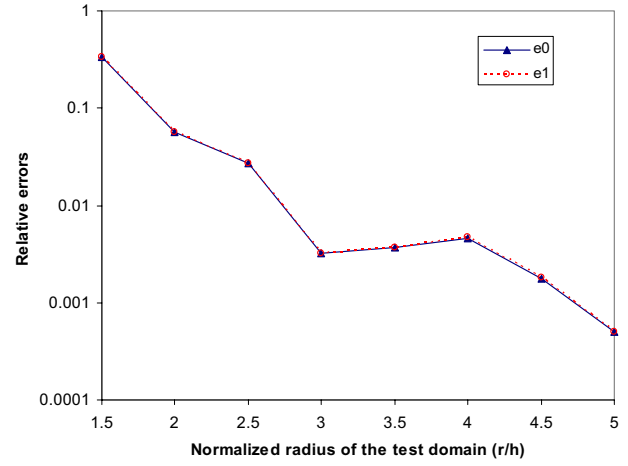


**Figure 10** : The influence of the test domain size (41 nodes).

of the test domain is taken to be  $3.5h$ , and the radius of the trial domain is taken to be  $4.5h$ . For linear ( $m=2$ ) basis, the radius of the test domain is taken to be  $3h$ , and the radius of the trial domain is taken to be  $6.5h$ . The relative errors  $e_0$  and  $e_1$  and the convergence rates  $R$  of the displacement and first derivative are depicted in Fig. 12, for both  $m=4$  and  $m=2$ . The convergence rates  $R$  of the relative errors  $e_2$ ,  $e_3$  and  $e_p$  for the second, third derivatives and the energy, are plotted in Fig. 13 only for  $m=4$ . It can be seen that the present MLPG method has stable convergence rates for norms  $e_0$ ,  $e_1$ ,  $e_2$ , and  $e_p$ , and gives reasonably accurate results for the unknown variable, its first and second derivatives, and the energy. The results from the cubic ( $m=4$ ) basis are more accurate, and are of a higher convergent rate than those from the linear ( $m=2$ ) basis. However, the results for the third derivative are not very accurate, and the convergence rate for the relative error  $e_3$  is not high.

### 3.4 Unsymmetric local weak form 3

Integrating (31) by parts four times yields the following unsymmetric local weak form,

$$\begin{aligned}
 & n_x [u''' v]_{\Gamma_s} - n_x [u'' v']_{\Gamma_s} + n_x [u' v'']_{\Gamma_s} \\
 & - n_x [u v''']_{\Gamma_s} + \int_{\Omega_s} u \frac{d^4 v}{dx^4} dx + \int_{\Omega_s} (u-1) v dx = 0 \quad (53)
 \end{aligned}$$

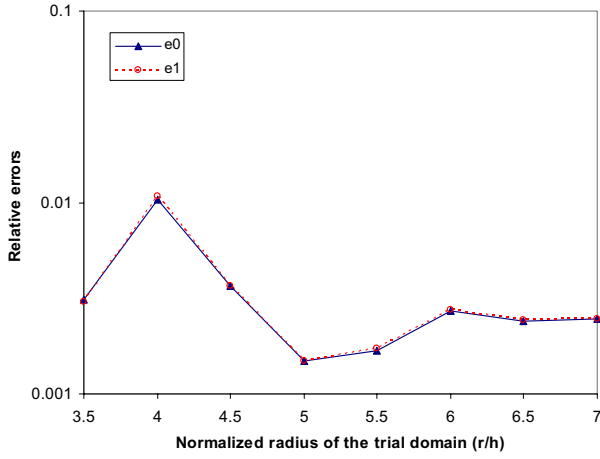


**Figure 11 :** The influence of the trial domain size (41 nodes).

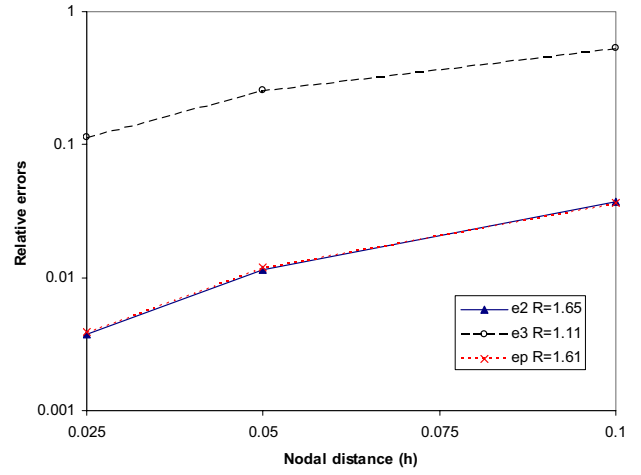


**Figure 13 :** Convergence rate in relative errors  $e_2$ ,  $e_3$ , and  $e_p$ .

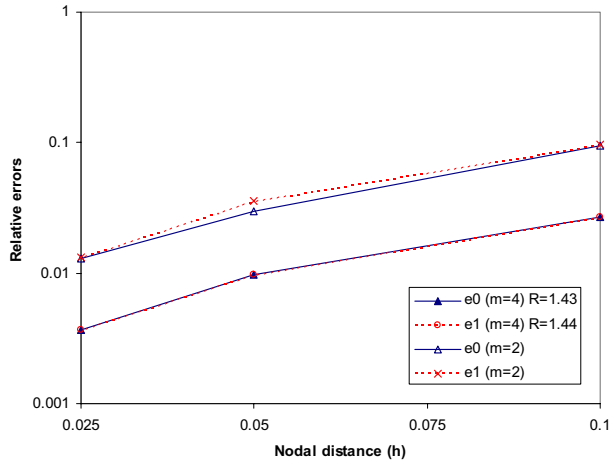


**Figure 12 :** Convergence rate in relative errors  $e_0$  and  $e_1$ .

In this weak form, no derivatives of the trial function appear in the domain integration. Moreover, all the boundary conditions become “natural” boundary conditions. Then, there is no difficulty in the implementation of the boundary conditions.

Imposing the boundary conditions (29) and (30), one obtains

$$\begin{aligned}
 & n_x [\bar{u}''' v]_{\Gamma_{su}'''} + n_x [u''' v]_{\Gamma_{su}} + n_x [u''' v]_{L_s} \\
 & - n_x [\bar{u}'' v']_{\Gamma_{su}''} - n_x [u'' v']_{\Gamma_{su}'} - n_x [u'' v']_{L_s} \\
 & + n_x [\bar{u}' v'']_{\Gamma_{su}'} + n_x [u' v'']_{\Gamma_{su}''} + n_x [u' v'']_{L_s} \\
 & - n_x [\bar{u} v''']_{\Gamma_{su}} - n_x [u v''']_{\Gamma_{su}''} - n_x [u v''']_{L_s} \\
 & + \int_{\Omega_s} u \frac{d^4 v}{dx^4} dx + \int_{\Omega_s} (u-1) v dx = 0
 \end{aligned} \quad (54)$$

In order to simplify the above equation, we can select a test function  $v$ , such that itself and its first, second and third derivatives vanish over  $L_s$ . Such a test function is given in (21). Then equation (54) can be rewritten as

$$\begin{aligned}
 & n_x [u''' v]_{\Gamma_{su}} - n_x [u'' v']_{\Gamma_{su}'} + n_x [u' v'']_{\Gamma_{su}''} \\
 & - n_x [u v''']_{\Gamma_{su}'''} + \int_{\Omega_s} u \frac{d^4 v}{dx^4} dx + \int_{\Omega_s} u v dx \\
 & = \int_{\Omega_s} v dx - n_x [\bar{u}''' v]_{\Gamma_{su}'''} + n_x [\bar{u}'' v']_{\Gamma_{su}''} \\
 & - n_x [\bar{u}' v'']_{\Gamma_{su}'} + n_x [\bar{u} v''']_{\Gamma_{su}}
 \end{aligned} \quad (55)$$

With equation (5), one may discretize the local unsymmetric weak form (55) as

$$\begin{aligned}
& \sum_{I=1}^N n_x \left[ \frac{d^3 \phi^I(x)}{dx^3} v \right]_{\Gamma_{su}} \hat{u}_I - \sum_{I=1}^N n_x \left[ \frac{d^2 \phi^I(x)}{dx^2} v' \right]_{\Gamma_{su'}} \hat{u}_I + \\
& \sum_{I=1}^N n_x \left[ \frac{d \phi^I(x)}{dx} v'' \right]_{\Gamma_{su''}} \hat{u}_I - \sum_{I=1}^N n_x [\phi^I(x) v''']_{\Gamma_{su''}} \hat{u}_I \\
& + \sum_{I=1}^N \int_{\Omega_s} \phi^I(x) \left[ v + \frac{d^4 v}{dx^4} \right] dx \hat{u}_I \\
& = \int_{\Omega_s} v dx - n_x [\bar{u}''' v]_{\Gamma_{su''}} + n_x [\bar{u}'' v']_{\Gamma_{su''}} \\
& - n_x [\bar{u}' v'']_{\Gamma_{su'}} + n_x [\bar{u} v''']_{\Gamma_{su}} \quad (56)
\end{aligned}$$

To illustrate the effectiveness of the MLPG method base on the local weak form (54). The same problem as that in the Subsection 3.2 is solved here. We also start with the cubic basis, i.e.  $m=4$ , in the MLS interpolation. The weight function in MLS is taken to be equation (20), while the test function in LWF (55) is chosen to be equation (21), because of the  $C^3$  continuity-requirement for the test function. 41 nodes are used ( $h=0.025$ ). Fig. 14 shows the influence of the radius of the test domain on the errors  $e_0$  and  $e_1$ , where the radius of the trial function domain is taken to be  $4.5h$ . From this figure, it can be found that the accuracy of the function  $u$ , and its first derivative, is very high when the trial function domain is big enough ( $> 2.5h$ ). Similarly, it is noticed that the accuracy is not sensitive to the radius of the test domain from  $3-6h$ , the relative errors  $e_0$  and  $e_1$  are less than 1%. Fig. 15 shows the influence of the radius of the trial domain on the errors  $e_0$  and  $e_1$ , where the radius of the test domain is taken to be  $4h$ . The results for the function  $u$  and its first derivative are of high accuracy. The relative errors  $e_0$  and  $e_1$  are not sensitive to the radius of the trial function domain. For the linear ( $m=2$ ) basis, the same trends can be observed. Again, for  $m=2$ , a larger radius of the trial function domain should be chosen to obtain an accurate and stable result. It can be found that the results in this subsection are more accurate than those in the previous subsections, since no derivative of the trial function appears in the domain integration in the local weak form.

Similarly, the convergence rate is investigated with three nodal configurations: 11, 21, and 41 nodes. We also consider the effects of the basis functions, and linear ( $m=2$ ) and cubic ( $m=4$ ) bases are used in this investigation. For cubic ( $m=4$ ) basis, the radius of the test domain is taken

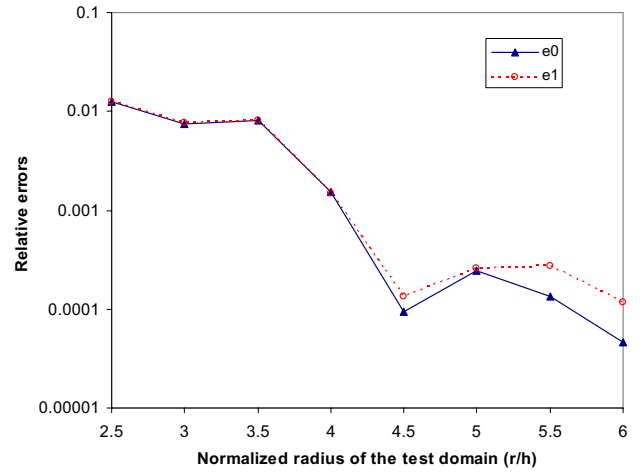


**Figure 14 :** The influence of the test domain size (41 nodes).

to be  $4h$ , and the radius of the trial domain is taken to be  $5h$ . For linear ( $m=2$ ) basis, the radius of the test domain is taken to be  $4h$ , and the radius of the trial domain is taken to be  $6.5h$ . The results clearly illustrate stable convergence rates for both  $e_0$  and  $e_1$  for the present MLPG methods. Obviously, the results from the cubic ( $m=4$ ) basis are more accurate than those from the linear ( $m=2$ ) basis. The relative errors  $e_0$  and  $e_1$  and the convergence rates  $R$  of the displacement and first derivative are depicted in Fig. 16, for both  $m=4$  and  $m=2$ . The convergence rates  $R$  of the relative errors  $e_2$ ,  $e_3$  and  $e_p$  for the second, third derivatives and the energy, are plotted in Fig. 17 only for  $m=4$ . It can be seen that the present MLPG method has high convergence rates for norms  $e_0$ ,  $e_1$ ,  $e_2$ , and  $e_p$ , and gives very accurate results for the unknown variable, as well as its first and second derivatives, and the energy. The results from the cubic ( $m=4$ ) basis are more accurate and of higher convergent rate than those from the linear ( $m=2$ ) basis. However, the results for the third derivative are not very accurate, and the convergent rate for the relative error  $e_3$  is low.

#### 4 The First Kind of Mixed MLPG Methods

For a  $4^{th}$  order ODE, there are two approaches to develop the MLPG mixed methods. In this section, the first kind of mixed MLPG methods will be developed to solve the  $4^{th}$  order ODE. In the first kind of mixed MLPG methods, both the displacement as well as its second derivative are

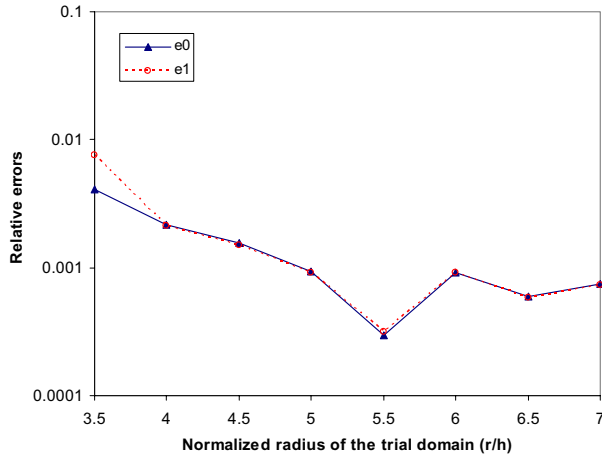


**Figure 15 :** The influence of the trial domain size (41 nodes).

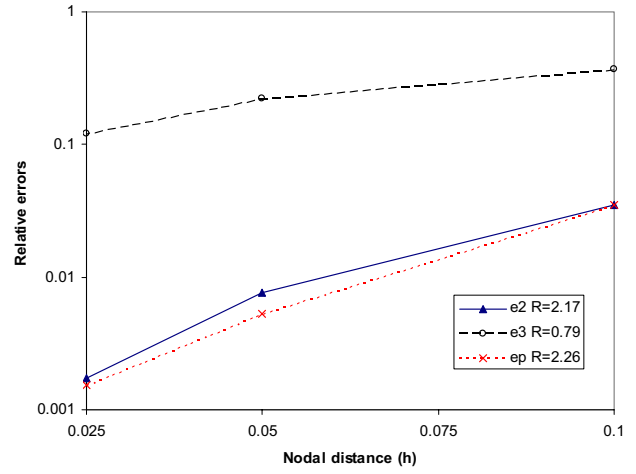


**Figure 17 :** Convergence rate in relative errors  $e_2$ ,  $e_3$ , and  $e_p$ .

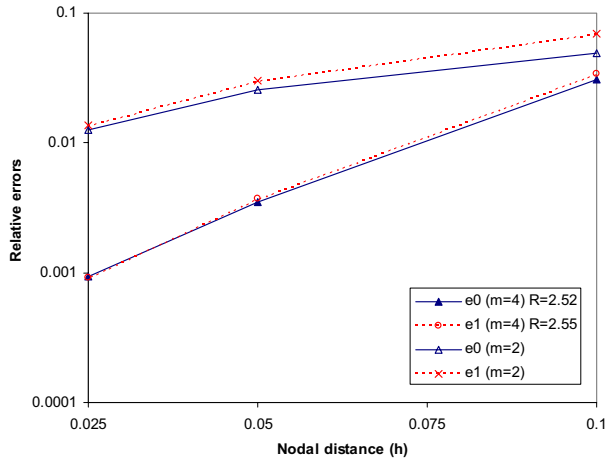


**Figure 16 :** Convergence rate in relative errors  $e_0$  and  $e_1$ .

interpolated independently through meshless interpolation schemes, in order to eliminate the direct differentiation of the trial function to obtain its second and higher order derivatives of the shape function in the local weak forms.

First, we introduce a function  $z$  as

$$u'' = z \quad (57)$$

Then, equation (26) becomes

$$z'' + u - 1 = 0$$

With the use of the MLS approximation, the function  $z$  can be independently interpolated as

$$z^h(x) = \sum_{l=1}^N \phi^l(x) \hat{z}^l, \quad z^h(x_l) \equiv \hat{z}^l \neq z^l, \quad x \in \Omega_x \quad (59)$$

#### 4.1 Local weak form I

Analogously, a local weak form can be derived as

$$n_x [z'v]_{\Gamma_s} - \int_{\Omega_s} z'v'dx + \int_{\Omega_s} (u-1)vdx = 0 \quad (60)$$

This weak form corresponds to the local unsymmetric weak form (32), but, now there exist only the first derivatives of  $z$  and  $v$  in the local weak form, and the requirement of the continuity for the trial function  $z$  is only  $C^0$ . As discussed in Section 2, the direct differentiation of  $u$  is not efficient in calculating its higher order derivatives everywhere. Thus, compared to the primal MLPG method based on LWF (32), the present mixed MLPG method should be more efficient.

In order to simplify the above equation, a test function  $v$  can be selected such that it vanishes over  $L_s$ , then equation (60) can be rewritten as

$$\begin{aligned} n_x [z'v]_{\Gamma_{su}} + \int_{\Omega_s} uvdx - \int_{\Omega_s} z'v'dx \\ = \int_{\Omega_s} vdx - n_x [\bar{z}'v]_{\Gamma_{su}'''} \end{aligned} \quad (58) \quad (61)$$

With the interpolations (5) and (59), one may discretize the local weak form (61) as

$$\begin{aligned} & \sum_{I=1}^N n_x \left[ \frac{d\phi^I(x)}{dx} v \right]_{\Gamma_{su}} \hat{z}_I + \\ & \sum_{I=1}^N \int_{\Omega_s} \left[ \phi^I(x) v \hat{u}_I - \frac{d\phi^I(x)}{dx} v' \hat{z}_I \right] dx \\ & = \int_{\Omega_s} v dx - n_x [\bar{z}' v]_{\Gamma_{su}'''} \end{aligned} \quad (62)$$

One may choose the Heaviside function as the test function, and obtains

$$\begin{aligned} & n_x [z' v]_{\Gamma_{su}} + n_x [z' v]_{L_s} + \int_{\Omega_s} u v dx \\ & = \int_{\Omega_s} v dx - n_x [\bar{z}' v]_{\Gamma_{su}'''} \end{aligned} \quad (63)$$

Equation (63) can be discretized as

$$\begin{aligned} & \sum_{I=1}^N n_x \left[ \frac{d\phi^I(x)}{dx} v \right]_{\Gamma_{su}} \hat{z}_I + \sum_{I=1}^N n_x \left[ \frac{d\phi^I(x)}{dx} v \right]_{L_s} \hat{z}_I \\ & + \sum_{I=1}^N \int_{\Omega_s} \phi^I(x) v dx \hat{u}_I = \int_{\Omega_s} v dx - n_x [\bar{z}' v]_{\Gamma_{su}'''} \end{aligned} \quad (64)$$

In equation (62) or (64), there are  $2N$  independent unknowns ( $N$  second derivative variables  $\hat{z}_I$  and  $N$  displacement variables  $\hat{u}_I$ ), but the number of the equation is only  $N$ . However, one can reduce the number of the variables by relating  $z$  to  $u''$  via the collocation methods, without any changes to equation (62) or (64). The collocation method is employed to enforce equation (57) only at each node  $x_I$ , instead of the entire solution domain. Thus, the function  $z$  at node  $x_I$  is expressed in terms of the function  $u$  at node  $x_I$ , as

$$z(x_I) = u''(x_I) \quad (65)$$

With the interpolations (5) and (59), the two sets of nodal variables can be transformed through a linear algebraic matrix,

$$\hat{z}_I = H_{IJ} \hat{u}_J \quad (66)$$

where the transformation matrix  $\mathbf{H}$  is banded. Substituting equation (66) into equation (62) or (64), one can obtain a linear algebraic equation system of  $\hat{u}_I$ .

The collocation method is used to impose the boundary conditions. For boundary node  $x_I$ , one has

$$\beta_1 u(x_I) + \beta_2 u'(x_I) + \beta_3 z(x_I) = \beta_1 \bar{u} + \beta_2 \bar{u}' + \beta_3 \bar{z} \quad (67)$$

It is noted that actually there exist only 1 or 2 terms on both the sides of equation (67), depending on the combination of the boundary conditions.

To demonstrate the effectiveness of this method, the same numerical example as in Section 3 is considered in this section.

In this subsection, only the linear basis, i.e.  $m=2$ , is employed in the MLS interpolation, and the weight function in MLS is taken to be equation (20).

#### 4.1.1 The test function is taken to be the weight function

At first, we take equation (20) as the test function, i.e. use the discretized equation (62). 41 nodes are used ( $h=0.025$ ). Fig. 18 shows the influence of the radius of the test domain on the errors  $e_0$  and  $e_1$ , where the radius of the trial function domain is taken to be  $5.1h$ . It is noticed that the relative errors  $e_0$  and  $e_1$  (around 2%) are almost independent of the radius of the test domain from  $1-3.5h$ . Fig. 19 shows the influence of the radius of the trial domain on the errors  $e_0$  and  $e_1$ , where the radius of the test domain is taken to be  $2.5h$ . The results for the function  $u$  and its first derivative are acceptable (less than 10%). The relative errors  $e_0$  and  $e_1$  are not very sensitive to the radius of the trial function domain from  $2.5-5.5h$ . The convergence rate is investigated with three nodal configurations: 11, 21, and 41 nodes for linear ( $m=2$ ) basis. The radius of the test domain is taken to be  $2.5h$ , and the radius of the trial domain is taken to be  $2.5h$ . The results clearly demonstrate stable convergence rates for both  $e_0$  and  $e_1$  for the present mixed MLPG methods. The relative errors  $e_0$  and  $e_1$  and the convergence rates  $R$  of the displacement and first derivative are depicted in Fig. 20. The convergence rates  $R$  of the relative errors  $e_2$ ,  $e_3$  and  $e_p$  for the second, third derivatives and the energy, are plotted in Fig. 21. It can be seen that the present mixed MLPG method has stable convergence rate for norms  $e_0$ ,  $e_1$ ,  $e_2$ , and  $e_p$ , and gives reasonably accurate results for the unknown variable, its first and second derivatives, and the energy. However,

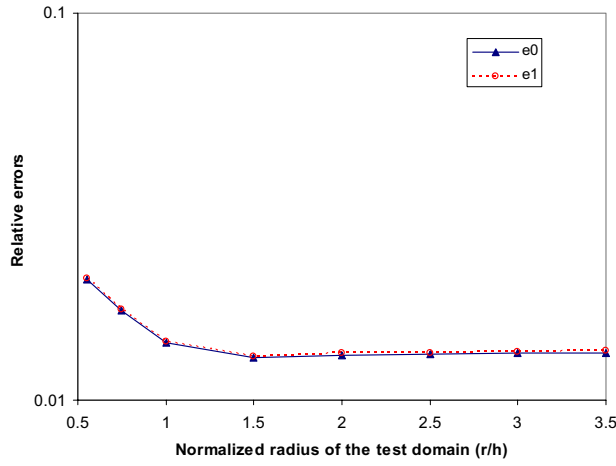


**Figure 18 :** The influence of the test domain size (41 nodes).

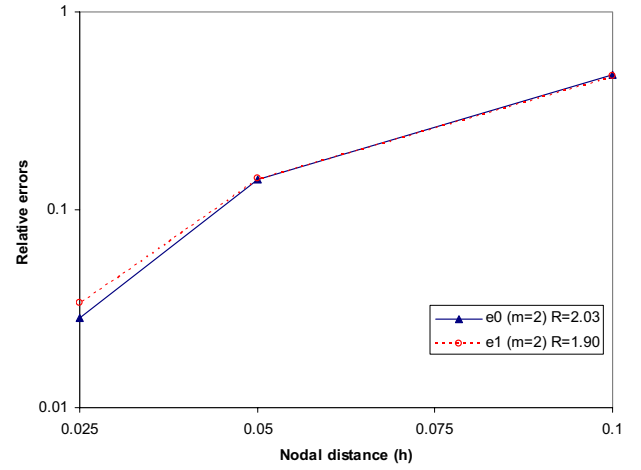


**Figure 20 :** Convergence rate in relative errors  $e_0$  and  $e_1$ .

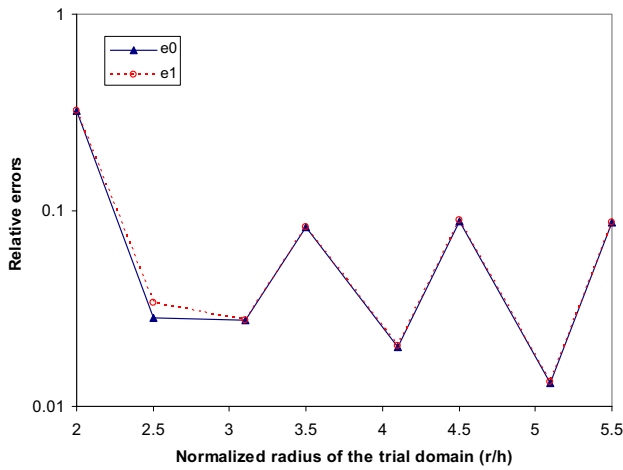


**Figure 19 :** The influence of the trial domain size (41 nodes).

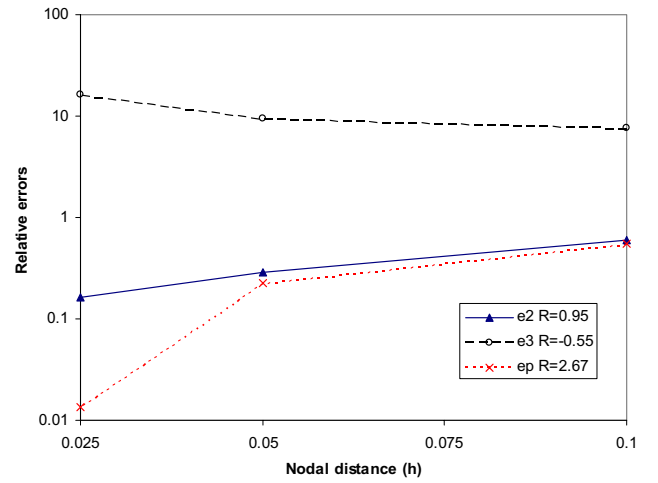


**Figure 21 :** Convergence rate in relative errors  $e_2$ ,  $e_3$ , and  $e_p$ .

the results for the third derivative are not accurate, and the convergence rate for the relative error  $e_3$  is not stable. These figures show that, based on the same LWF (32), the mixed MLPG method can obtain stable results, although the accuracy of the results is not very high, while the primal MLPG method cannot work.

#### 4.1.2 The test function is taken to be Heaviside function

Now, we choose Heaviside function as the test function, i.e. use the discretized equation (64). 41 nodes are used ( $h=0.025$ ). Fig. 22 shows the influence of the radius of

the test domain on the errors  $e_0$  and  $e_1$ , where the radius of the trial function domain is taken to be  $5.1h$ . It is noticed that the relative errors  $e_0$  and  $e_1$  (around 1%) are almost independent of the radius of the test domain from  $0.5$ - $2.5h$ . Fig. 23 shows the influence of the radius of the trial domain on the errors  $e_0$  and  $e_1$ , where the radius of the test domain is taken to be  $2.5h$ . The results for the function  $u$  and its first derivative are acceptable. The relative errors  $e_0$  and  $e_1$  are not very sensitive to the radius of the trial function domain from  $2.5$ - $5.5h$ . The convergence rate is investigated with three nodal configurations: 11, 21, and 41 nodes for linear ( $m=2$ ) basis. The radius of

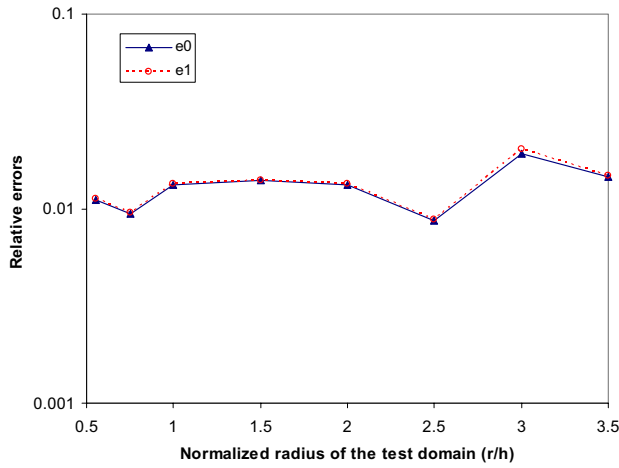


**Figure 22 :** The influence of the test domain size (41 nodes).

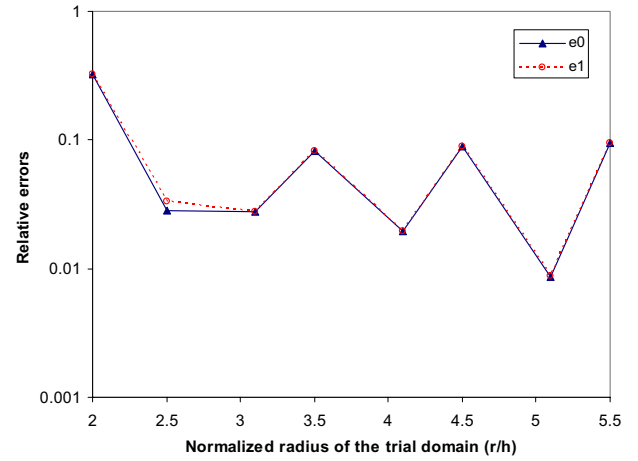


**Figure 23 :** The influence of the trial domain size (41 nodes).

the trial domain is taken to be  $5.1h$ , and the radius of the test domain is taken to be  $2.5h$ . The relative errors  $e_0$  and  $e_1$  and the convergence rates  $R$  of the displacement and first derivative are depicted in Fig. 24. The convergence rates  $R$  of the relative errors  $e_2$ ,  $e_3$  and  $e_p$  for the second, third derivatives and the energy, are plotted in Fig. 25. It can be seen that the present mixed MLPG method has stable convergence rates for norms  $e_0$ ,  $e_1$ ,  $e_2$ , and  $e_p$ , and gives reasonably accurate results for the unknown variable, its first and second derivatives, and the energy. However, the results for the third derivative are not accurate, and the convergence rate for the relative error  $e_3$  is not stable. The mixed MLPG method with the Heaviside function being the test function is more accurate than the mixed MLPG method with equation (20) being the test function.

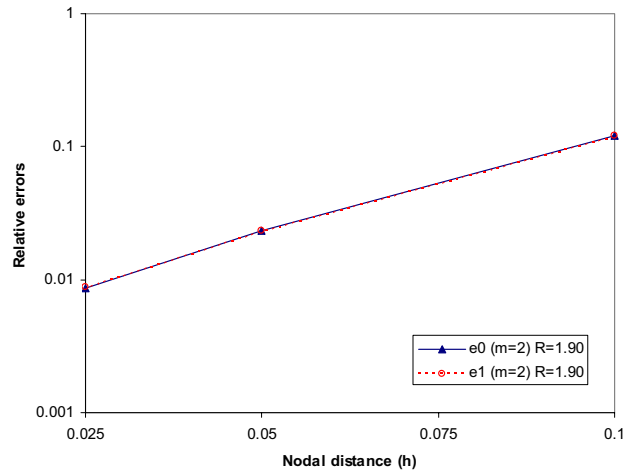


**Figure 24 :** Convergence rate in relative errors  $e_0$  and  $e_1$ .

#### 4.2 Local weak form 2

In LWF (60), there still exists the first derivative of  $z$  in the domain integration, which can be eliminated by integrating (60) by part once. Thus, another local weak form can be obtained as

$$n_x [z'v]_{\Gamma_s} - n_x [zv']_{\Gamma_s} + \int_{\Omega_s} zv'' dx + \int_{\Omega_s} (u-1)v dx = 0 \quad (68)$$

which corresponds to the local symmetric weak form (39), but no derivatives of either  $z$  or  $u$  appear in the do-

main integration. In LWF (39), there the second derivative of  $u$  occurs in the domain integration.

In order to simplify the above equation, we can select a test function  $v$  such that, itself and its first derivative, vanish over  $L_s$ , then equation (68) can be rewritten as

$$n_x [z'v]_{\Gamma_{su}} - n_x [zv']_{\Gamma_{su'}} + \int_{\Omega_s} uv dx + \int_{\Omega_s} zv'' dx = \int_{\Omega_s} v dx - n_x [\bar{z}'v]_{\Gamma_{su''}} + n_x [\bar{z}v']_{\Gamma_{su''}} \quad (69)$$

With equations (5) and (59), one may discretize the local

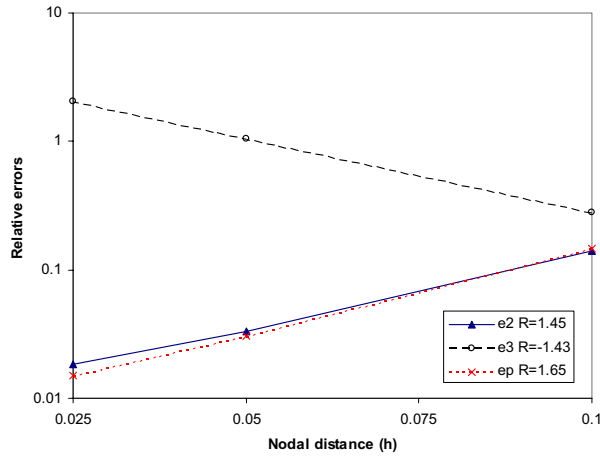


**Figure 25 :** Convergence rate in relative errors  $e_2$ ,  $e_3$ , and  $e_p$ .

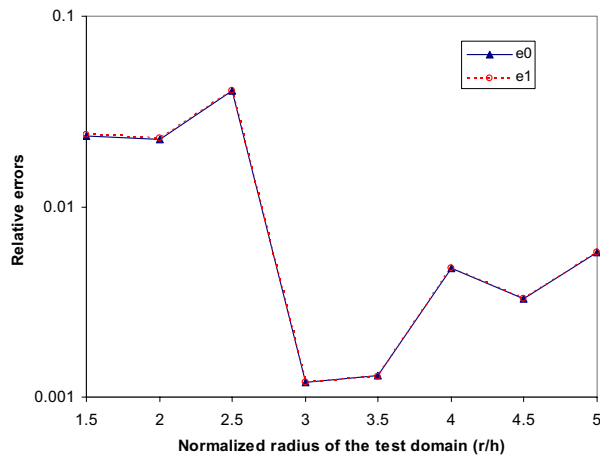


**Figure 26 :** The influence of the test domain size (41 nodes).

weak form (69) as

$$\begin{aligned}
 & \sum_{I=1}^N n_x \left[ \frac{d\phi^I(x)}{dx} v \right]_{\Gamma_{su}} \hat{z}_I - \sum_{I=1}^N n_x [\phi^I(x) v']_{\Gamma_{su'}} \hat{z}_I \\
 & + \sum_{I=1}^N \int_{\Omega_s} [\phi^I(x) v \hat{u}_I - \phi^I(x) v'' \hat{z}_I] dx \\
 & = \int_{\Omega_s} v dx - n_x [\bar{z} v]_{\Gamma_{su''}} + n_x [\bar{z} v']_{\Gamma_{su''}} \quad (70)
 \end{aligned}$$

Substituting equation (66) into equation (70), one can ob-

tain a linear algebraic equation system of  $\hat{u}_I$ .

The collocation method is employed to impose the boundary conditions, as in equation (43).

To illustrate the effectiveness of this method, the same numerical example as in the previous section is considered here again. At first, the cubic basis ( $m=4$ ) is used in the MLS interpolation. Both the weight function in MLS and the test function are taken to be equation (20). 41 nodes are used ( $h=0.025$ ). Fig. 26 shows the influence of the radius of the test domain on the relative errors  $e_0$  and  $e_1$ , where the radius of the trial function domain is taken to be  $4.5h$ . From this figure, it can be found that the accuracy of the function  $u$  and its first derivative is high when the test function domain is big enough ( $> 2.5h$ ). It is noticed that the relative errors  $e_0$  and  $e_1$  are not sensitive to the radius of the test domain from  $3-5h$  (less than 1%). Fig. 27 shows the influence of the radius of the trial domain on the errors  $e_0$  and  $e_1$ , where the radius of the test domain is taken to be  $3.5h$ . The results for the function  $u$  and its first derivative are accurate. The relative errors  $e_0$  and  $e_1$  are not sensitive to the radius of the trial function domain from  $3.5-7h$ . For the linear ( $m=2$ ) basis, the same trends can be observed. However, for  $m=2$ , a larger radius of the trial function domain should be chosen to obtain an accurate and stable result.

The convergence rate is investigated with three nodal configurations: 11, 21, and 41 nodes. We also consider the effects of the basis functions: linear ( $m=2$ ) and cubic ( $m=4$ ) bases are used in this investigation. For cubic ( $m=4$ ) basis, the radius of the test domain is taken to be  $4h$ , and the radius of the trial domain is taken to be  $4.5h$ . For linear ( $m=2$ ) basis, the radius of the test domain is taken to be  $3.5h$ , and the radius of the trial domain is taken to be  $8h$ . The relative errors  $e_0$  and  $e_1$  and the convergence rates  $R$  of the displacement and first derivative are depicted in Fig. 28, for both  $m=4$  and  $m=2$ . The convergence rates  $R$  of the relative errors  $e_2$ ,  $e_3$  and  $e_p$  for the second, third derivatives and the energy, are plotted in Fig. 29 only for  $m=4$ . It can be seen that the present mixed MLPG method has high rates of convergence for norms  $e_0$ ,  $e_1$ ,  $e_2$ , and  $e_p$ , and gives reasonably accurate results for the unknown variable, its first and second derivatives, and the energy. The results from the cubic ( $m=4$ ) basis are more accurate and of higher convergent rate than those from the linear ( $m=2$ ) basis. However, the results for the third derivative are not very accurate, while the convergence rate for the relative error

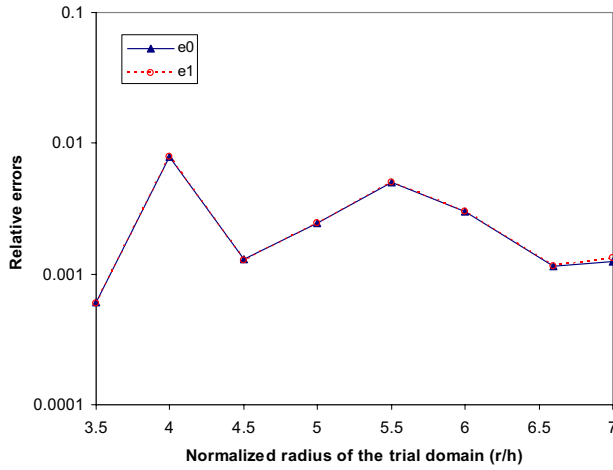


**Figure 27 :** The influence of the trial domain size (41 nodes).

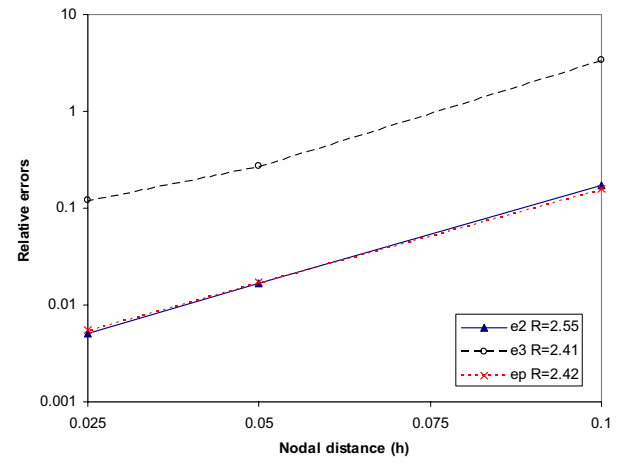


**Figure 29 :** Convergence rate in relative errors  $e_2$ ,  $e_3$ , and  $e_p$ .

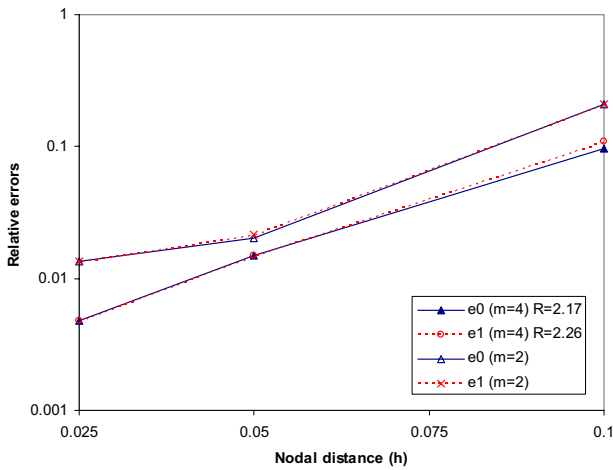


**Figure 28 :** Convergence rate in relative errors  $e_0$  and  $e_1$ .

$e_3$  is high.

Compared to the corresponding primal MLPG method based on the local weak form (39), this mixed MLPG method requires less Gaussian points, and is more stable and accurate. The mixed MLPG method is cheaper and faster.

### 4.3 Local weak form 3

By means of the idea of the mixed MLPG method, the local weak form (53) can be rewritten as,

$$n_x [z'v]_{\Gamma_s} - n_x [zv']_{\Gamma_s} + n_x [u'v'']_{\Gamma_s} - n_x [uv''']_{\Gamma_s} + \int_{\Omega_s} u \frac{d^4 v}{dx^4} dx + \int_{\Omega_s} (u-1)v dx = 0 \quad (71)$$

Compared to the LWF (53), the LWF (71) does not have higher derivatives in the local boundary.

Imposing the boundary conditions (29) and (30), one obtains

$$n_x [\bar{z}'v]_{\Gamma_{su''}} + n_x [z'v]_{\Gamma_{su}} + n_x [z'v]_{L_s} - n_x [\bar{z}v']_{\Gamma_{su''}} - n_x [zv']_{\Gamma_{su'}} - n_x [zv']_{L_s} + n_x [\bar{u}'v'']_{\Gamma_{su'}} + n_x [u'v'']_{\Gamma_{su''}} + n_x [u'v'']_{L_s} - n_x [\bar{u}v''']_{\Gamma_{su}} - n_x [uv''']_{\Gamma_{su''}} - n_x [uv''']_{L_s} + \int_{\Omega_s} u \frac{d^4 v}{dx^4} dx + \int_{\Omega_s} (u-1)v dx = 0 \quad (72)$$

In order to simplify the above equation, we can select a test function  $v$  such that, itself and its first, second and third derivatives vanish over  $L_s$ . Such a test function is given in (21). Then equation (72) can be rewritten as

$$\begin{aligned}
& n_x [z'v]_{\Gamma_{su}} - n_x [zv']_{\Gamma_{su'}} + n_x [u'v'']_{\Gamma_{su''}} \\
& - n_x [uv''']_{\Gamma_{su''}} + \int_{\Omega_s} u \frac{d^4 v}{dx^4} dx + \int_{\Omega_s} uv dx \\
& = \int_{\Omega_s} v dx - n_x [\bar{z}'v]_{\Gamma_{su''}} + n_x [\bar{z}v']_{\Gamma_{su''}} \\
& - n_x [\bar{u}'v'']_{\Gamma_{su'}} + n_x [\bar{u}v''']_{\Gamma_{su}} \quad (73)
\end{aligned}$$

With the interpolations (5) and (59), one may discretize the local symmetric weak form (73) as

$$\begin{aligned}
& \sum_{I=1}^N n_x \left[ \frac{d\phi^I(x)}{dx} v \right]_{\Gamma_{su}} \hat{z}_I - \sum_{I=1}^N n_x [\phi^I(x) v']_{\Gamma_{su'}} \hat{z}_I + \\
& \sum_{I=1}^N n_x \left[ \frac{d\phi^I(x)}{dx} v'' \right]_{\Gamma_{su''}} \hat{u}_I - \sum_{I=1}^N n_x [\phi^I(x) v''']_{\Gamma_{su''}} \hat{u}_I \\
& + \sum_{I=1}^N \int_{\Omega_s} \phi^I(x) \left[ v + \frac{d^4 v}{dx^4} \right] dx \hat{u}_I \\
& = \int_{\Omega_s} v dx - n_x [\bar{z}'v]_{\Gamma_{su''}} + n_x [\bar{z}v']_{\Gamma_{su''}} \\
& - n_x [\bar{u}'v'']_{\Gamma_{su'}} + n_x [\bar{u}v''']_{\Gamma_{su}} \quad (74)
\end{aligned}$$

Substituting equation (66) into equation (74), one can obtain a linear algebraic equation system of  $\hat{u}_I$ .

The numerical results still start with the cubic basis, i.e.  $m=4$ , in the MLS approximation. The weight function in MLS is taken to be equation (20), while the test function in LWF (73) is chosen to be equation (21). 41 nodes are used ( $h=0.025$ ). Fig. 30 shows the influence of the radius of the test domain on the errors  $e_0$  and  $e_1$ , where the radius of the trial function domain is taken to be  $4.5h$ . From this figure, it can be found that the accuracy of the function  $u$  and its first derivative is very high when the trial function domain is big enough ( $> 2.5h$ ). Similarly, it is noticed that the accuracy is not sensitive to the radius of the test domain from  $3-6h$ . Fig. 31 shows the influence of the radius of the trial domain on the errors  $e_0$  and  $e_1$ , where the radius of the test domain is taken to be  $4h$ . The results for the function  $u$ , as well as its first derivative, are of high accuracy. The relative errors  $e_0$  and  $e_1$  are less than 1% for the radius of the trial function domain between  $3.5-7h$ . For the linear ( $m=2$ ) basis, the same trends can be observed. However, in this mixed

MLPG method, for  $m=2$ , a larger radius of the trial function domain is needed, in order to obtain an accurate and stable result.

Similarly, the convergence rate is investigated with three nodal configurations: 11, 21, and 41 nodes. We also consider the effects of the basis functions: linear ( $m=2$ ) and cubic ( $m=4$ ) bases are used in this investigation. For cubic ( $m=4$ ) basis, the radius of the test domain is taken to be  $4h$ , and the radius of the trial domain is taken to be  $4.5h$ . For linear ( $m=2$ ) basis, the radius of the test domain is taken to be  $4h$ , and the radius of the trial domain is taken to be  $6.5h$ . The relative errors  $e_0$  and  $e_1$  and the convergence rates  $R$  of the displacement and first derivative are depicted in Fig. 32, for both  $m=4$  and  $m=2$ . The convergence rates  $R$  of the relative errors  $e_2$ ,  $e_3$  and  $e_p$  for the second, third derivatives and the energy, are plotted in Fig. 33 only for  $m=4$ . It can be seen that the present MLPG method has high rates of convergence for norms  $e_0$ ,  $e_1$ ,  $e_2$ , and  $e_p$ , and gives very accurate results for the unknown variable, its first and second derivatives, and the energy. This mixed MLPG method can obtain the almost the same accurate results for both  $m=2$  and  $m=4$ . However, the results for the third derivative are not very accurate, and the convergence rate for the relative error  $e_3$  is low.

Compared to the corresponding primal MLPG method based on the local weak form (53), this mixed MLPG method requires less Gaussian points, and is more stable and accurate, especially for  $m=2$ . The mixed MLPG method is cheaper and faster.

## 5 The Second Kind of Mixed MLPG Methods

In the first kind of mixed MLPG methods, there still exists the first derivative of  $z$  or  $u$  in the local weak forms. To avoid fully the appearance of any derivatives in the local weak forms, in this section, the second kind of the mixed MLPG methods are introduced. In the second kind of mixed MLPG methods, the displacement, its first derivative, second derivative, as well as the third derivative are all interpolated independently through meshless interpolation schemes. The second kind of mixed MLPG method is developed by introducing the following 3 functions

$$\begin{aligned}
u' &= g \\
g' &= z \\
z' &= q \quad (75)
\end{aligned}$$

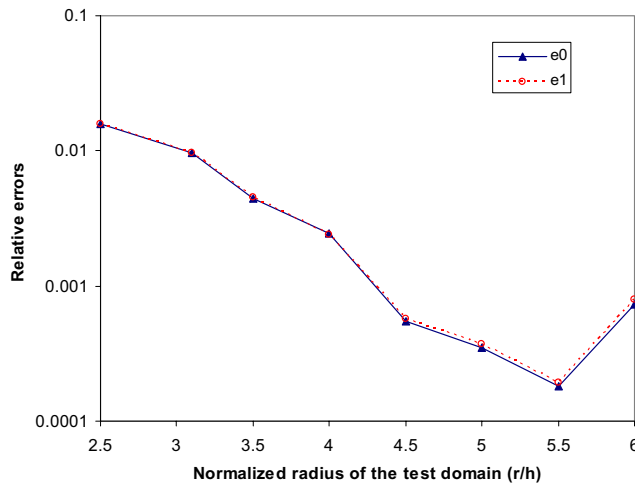


**Figure 30** : The influence of the test domain size (41 nodes).

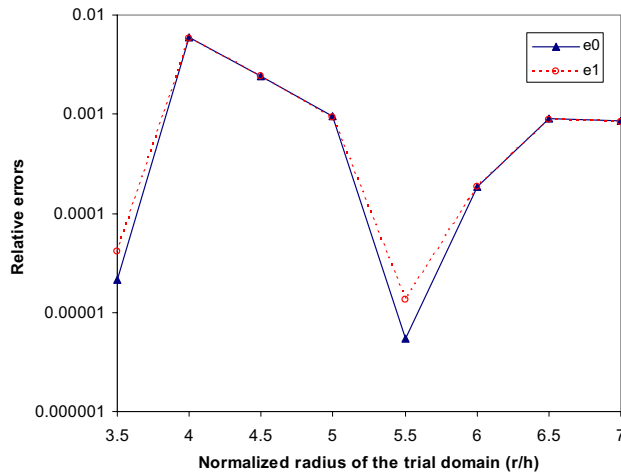


**Figure 31** : The influence of the trial domain size (41 nodes).

Then, equation (26) becomes

$$q' + u - 1 = 0 \quad (76)$$

With the use of the MLS approximation, the functions  $g$ ,  $z$ , and  $q$  can be independently interpolated as

$$g^h(x) = \sum_{l=1}^N \phi^l(x) \hat{g}^l, g^h(x_l) \equiv g^l \neq \hat{g}^l, x \in \Omega_x \quad (77)$$

$$z^h(x) = \sum_{l=1}^N \phi^l(x) \hat{z}^l, z^h(x_l) \equiv z^l \neq \hat{z}^l, x \in \Omega_x \quad (78)$$

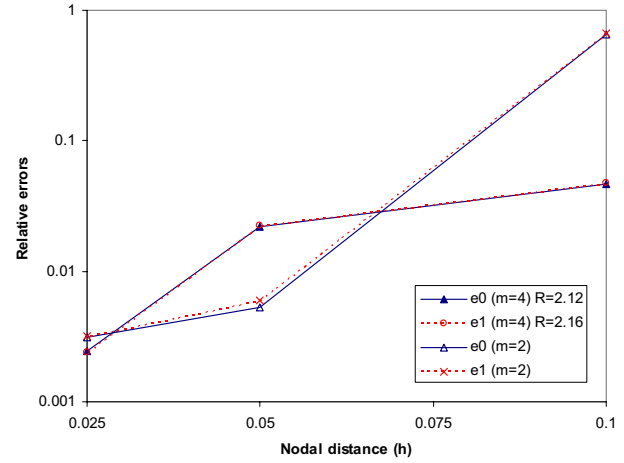


**Figure 32** : Convergence rate in relative errors  $e_0$  and  $e_1$ .

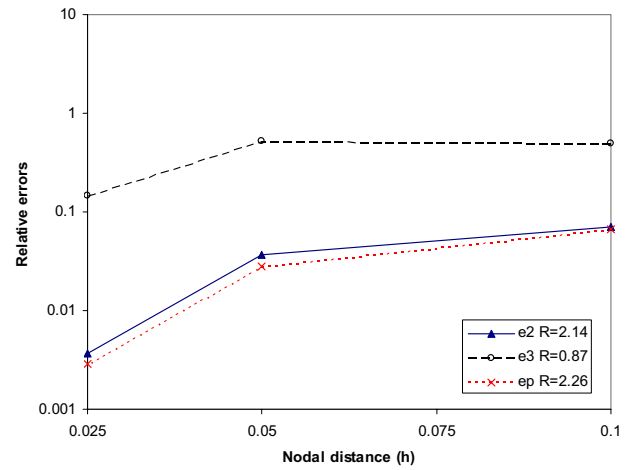


**Figure 33** : Convergence rate in relative errors  $e_2$ ,  $e_3$ , and  $e_p$ .

$$q^h(x) = \sum_{l=1}^N \phi^l(x) \hat{q}^l, q^h(x_l) \equiv q^l \neq \hat{q}^l, x \in \Omega_x \quad (79)$$

### 5.1 The local weak form 1

Analogously, the following local weak forms can be derived, as

$$n_x[qv]_{\Gamma_s} - \int_{\Omega_s} qv'dx + \int_{\Omega_s} (u-1)vdv = 0 \quad (80)$$

This weak form corresponds to the unsymmetric weak form (32) or (60). However, no derivative of the trial functions appear in this local weak form.

In order to simplify the above equation, one can select a test function  $v$  such that it vanishes over  $L_s$ ; then equation (80) can be rewritten as

$$n_x [qv]_{\Gamma_{su}} + \int_{\Omega_s} uvdx - \int_{\Omega_s} qv'dx = \int_{\Omega_s} vdx - n_x [\bar{q}v]_{\Gamma_{su''}} \quad (81)$$

With equations (5) and (79), one may discretize the local weak form (81) as

$$\begin{aligned} & \sum_{I=1}^N n_x [\phi^I(x) v]_{\Gamma_{su}} \hat{q}_I + \sum_{I=1}^N \int_{\Omega_s} \phi^I(x) [v\hat{u}_I - v'\hat{q}_I] dx \\ & = \int_{\Omega_s} vdx - n_x [\bar{q}v]_{\Gamma_{su''}} \end{aligned} \quad (82)$$

In equation (82), there are  $2N$  independent unknowns ( $N$  second derivative variables  $\hat{q}_I$  and  $N$  displacement variables  $\hat{u}_I$ ), but the number of the equation is only  $N$ . However, one can reduce the number of the variables by transforming the variables  $g$ ,  $z$ , and  $q$  back to the displacement variable via the collocation methods, without any changes to equation (82). The collocation method is employed to enforce equation (75) only at each node  $x_I$ , instead of the entire solution domain. Thus, the functions  $g$ ,  $z$ , and  $q$  at node  $x_I$  are expressed in terms of the derivatives of the related function at node  $x_I$ , as

$$\begin{aligned} g(x_I) &= u'(x_I) \\ z(x_I) &= g'(x_I) \\ q(x_I) &= z'(x_I) \end{aligned} \quad (83)$$

With the interpolations (5) and (77)-(79), the two related sets of nodal variables can be transformed through a linear algebraic matrix,

$$\begin{aligned} \hat{g}_I &= G_{IJ} \hat{u}_J \\ \hat{z}_I &= G_{IJ} \hat{g}_J \\ \hat{q}_I &= G_{IJ} \hat{z}_J \end{aligned} \quad (84)$$

where the transformation matrix  $\mathbf{G}$  is banded. Through (84), the nodal variables of the function  $g$ ,  $z$ , and  $q$  can be related to the nodal variable of function  $u$ , as

$$\begin{aligned} \hat{g}_I &= G_{IJ} \hat{u}_J \\ \hat{z}_I &= R_{IJ} \hat{u}_J \\ \hat{q}_I &= T_{IJ} \hat{u}_J \end{aligned} \quad (85)$$

where  $\mathbf{R} = \mathbf{G}^2$ , and  $\mathbf{T} = \mathbf{G}^3$ .

Substituting equation (85) into equation (82), one can obtain a linear algebraic equation system of  $\hat{u}_I$ .

However, our numerical experiments based on LWF (80), cannot obtain any stable and convergent results (using some special parameter-combinations, one may happen to obtain some good results), using either weight function (20) or Heaviside function as test function. Hence, this local weak form is not appropriate for the numerical implementation either. This may be since the errors introduced by the collocation method are enlarged by  $\mathbf{T} = \mathbf{G}^3$ .

## 5.2 The local weak form 2

By using the auxiliary functions (75), the local weak form (39) can be rewritten as

$$n_x [qv]_{\Gamma_s} - n_x [zv']_{\Gamma_s} + \int_{\Omega_s} zv''dx + \int_{\Omega_s} (u-1)vdx = 0 \quad (86)$$

Compared to the local symmetric weak form (39), the LWF (86) has no derivative of the trial function in either domain integration or local boundary integration.

In order to simplify the above equation, we can select a test function  $v$  such that, itself and its first derivative, vanishes over  $L_s$ . then equation (86) can be rewritten as

$$\begin{aligned} & n_x [qv]_{\Gamma_{su}} - n_x [\bar{z}v']_{\Gamma_{su'}} + \int_{\Omega_s} uvdx + \int_{\Omega_s} zv''dx \\ & = \int_{\Omega_s} vdx - n_x [\bar{q}v]_{\Gamma_{su''}} + n_x [\bar{z}v']_{\Gamma_{su''}} \end{aligned} \quad (87)$$

With the interpolations (5) and (78), one may discretize the local weak form (87) as

$$\begin{aligned} & \sum_{I=1}^N n_x [\phi^I(x) v]_{\Gamma_{su}} \hat{q}_I - \sum_{I=1}^N n_x [\phi^I(x) v']_{\Gamma_{su'}} \hat{z}_I \\ & + \sum_{I=1}^N \int_{\Omega_s} [\phi^I(x) v\hat{u}_I - \phi^I(x) v'\hat{z}_I] dx \\ & = \int_{\Omega_s} vdx - n_x [\bar{q}v]_{\Gamma_{su''}} + n_x [\bar{z}v']_{\Gamma_{su''}} \end{aligned} \quad (88)$$

Substituting equation (85) into equation (88), one can obtain a linear algebraic equation system of  $\hat{u}_I$ .

The collocation method is employed to impose the boundary conditions, as in equation (43).

To illustrate the effectiveness of this method, we consider the same numerical example as in previous section again. At first, we use the cubic basis, i.e.  $m=4$  in the MLS interpolation. Both the weight function in MLS, and the test function, are taken to be as in equation (20). 41 nodes are used ( $h=0.025$ ). Fig. 34 shows the influence of the radius of the test domain on the errors  $e_0$  and  $e_1$ , where the radius of the trial function domain is taken to be  $4.5h$ . From this figure, it can be found that the accuracies of the function  $u$  and its first derivative are very high, when the test function domain is big enough ( $> h$ ). The relative errors  $e_0$  and  $e_1$  are less than 0.01%. It is noticed that the accuracy is almost independent of the radius of the test domain from  $1.5-5h$ . Fig. 35 shows the influence of the radius of the trial domain on the errors  $e_0$  and  $e_1$ , where the radius of the test domain is taken to be  $3.5h$ . The results for the function  $u$  and its first derivative are highly accurate. The relative errors  $e_0$  and  $e_1$  are not sensitive to the radius of the trial function domain from  $3.5-7h$ . For the linear ( $m=2$ ) basis, the same trends can be observed. In this method, for  $m=2$ , the requirement of a larger radius of the trial function domain is not needed.

The convergence rate is investigated with three nodal configurations: 11, 21, and 41 nodes. We also consider the effects of the basis functions: linear ( $m=2$ ) and cubic ( $m=4$ ) bases are used in this investigation. For cubic ( $m=4$ ) basis, the radius of the test domain is taken to be  $4h$ , and the radius of the trial domain is taken to be  $5h$ . For linear ( $m=2$ ) basis, the radius of the test domain is taken to be  $3.5h$ , and the radius of the trial domain is taken to be  $4.5h$ . The relative errors  $e_0$  and  $e_1$  and the convergence rates  $R$  of the displacement and first derivative are depicted in Fig. 36, for both  $m=4$  and  $m=2$ . The convergence rates  $R$  of the relative errors  $e_2$ ,  $e_3$  and  $e_p$  for the second, third derivatives and the energy, are plotted in Fig. 37 only for  $m=4$ . It can be seen that the present mixed MLPG method has very high rates of convergence for norms  $e_0$ ,  $e_1$ ,  $e_2$ , and  $e_p$ , and gives very accurate results for the unknown variable, its first and second derivatives, and the energy. The results from the cubic ( $m=4$ ) basis are more accurate, and are of higher convergent rate than those from the linear ( $m=2$ ) basis. However, the results for the third derivative are not very accurate, while the convergence rate for the relative error  $e_3$  is very high. Compared to the corresponding primal MLPG method

based on the local weak form (39), this mixed MLPG method requires less Gaussian points, is more stable, and the results is of two-orders higher accuracy. This mixed MLPG method is also more accurate than the corresponding first kind of mixed MLPG method.

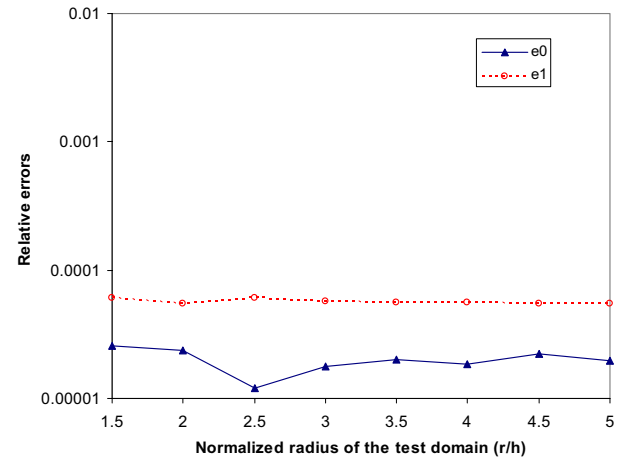


**Figure 34 :** The influence of the test domain size (41 nodes).

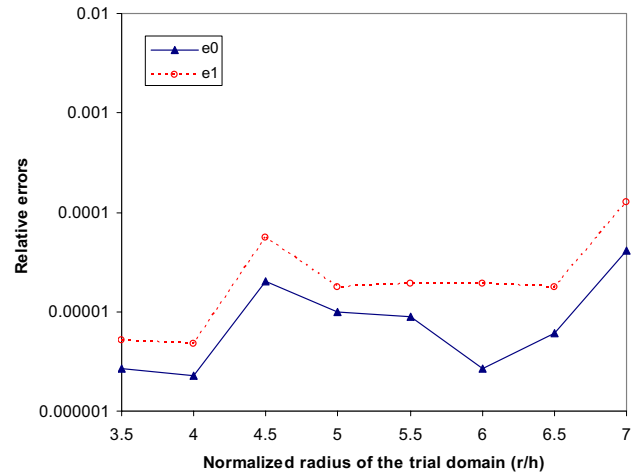


**Figure 35 :** The influence of the trial domain size (41 nodes).

### 5.3 The local weak form 3

By using the auxiliary functions (75), the local weak form (48) can be rewritten as

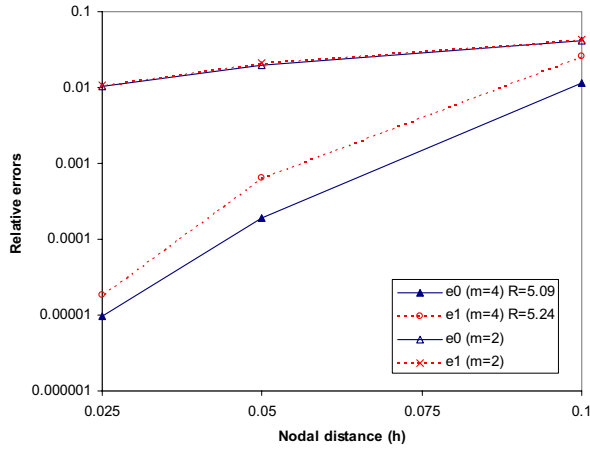


**Figure 36 :** Convergence rate in relative errors  $e_0$  and  $e_1$ .

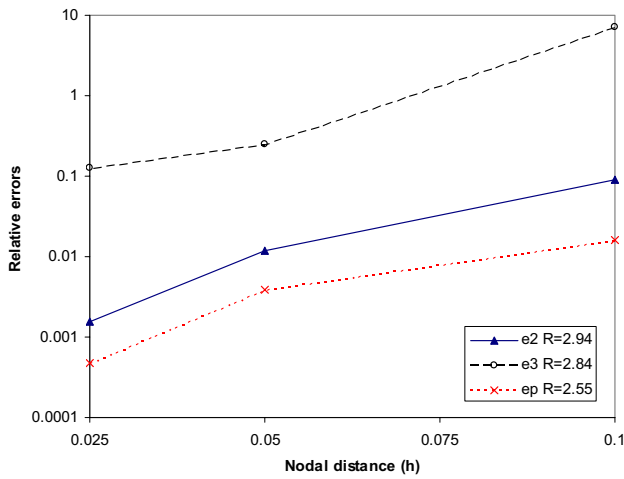


**Figure 37 :** Convergence rate in relative errors  $e_2$ ,  $e_3$ , and  $e_p$ .

$$n_x [qv]_{\Gamma_s} - n_x [zv']_{\Gamma_s} + n_x [gv'']_{\Gamma_s} - \int_{\Omega_s} gv''' dx + \int_{\Omega_s} (u-1)v dx = 0 \quad (89)$$

Compared to the local symmetric weak form (48), the LWF (89) has no derivatives of the trial function in either domain integration or local boundary integration.

Imposing the boundary conditions (29) and (30), one obtains

$$\begin{aligned} & n_x [\bar{q}v]_{\Gamma_{su}'''} + n_x [qv]_{\Gamma_{su}} + n_x [qv]_{L_s} \\ & - n_x [\bar{z}v']_{\Gamma_{su}''} - n_x [zv']_{\Gamma_{su}'} - n_x [zv']_{L_s} \\ & + n_x [\bar{g}v'']_{\Gamma_{su}'} + n_x [gv'']_{\Gamma_{su}''} + n_x [gv'']_{L_s} \\ & - \int_{\Omega_s} gv''' dx + \int_{\Omega_s} (u-1)v dx = 0 \end{aligned} \quad (90)$$

In order to simplify the above equation, one can select a test function  $v$  such that, itself and its first and second derivatives, vanish over  $L_s$ . Such test functions are given in (20) and (21). Then equation (90) can be rewritten as

$$\begin{aligned} & n_x [qv]_{\Gamma_{su}} - n_x [zv']_{\Gamma_{su}'} + n_x [gv'']_{\Gamma_{su}''} \\ & + \int_{\Omega_s} uv dx - \int_{\Omega_s} gv''' dx \\ & = \int_{\Omega_s} v dx - n_x [\bar{q}v]_{\Gamma_{su}'''} + n_x [\bar{z}v']_{\Gamma_{su}''} - n_x [\bar{g}v'']_{\Gamma_{su}'} \end{aligned} \quad (91)$$

With the interpolations (5) and (78), one may discretize the local weak form (91) as

$$\begin{aligned} & \sum_{l=1}^N n_x [\phi^l(x)v]_{\Gamma_{su}} \hat{q}_l - \sum_{l=1}^N n_x [\phi^l(x)v']_{\Gamma_{su}'} \\ & + \sum_{l=1}^N n_x [\phi^l(x)v'']_{\Gamma_{su}''} \hat{g}_l \\ & + \sum_{l=1}^N \int_{\Omega_s} \phi^l(x) [\hat{u}_l v - \hat{g}_l v'''] dx \\ & = \int_{\Omega_s} v dx - n_x [\bar{q}v]_{\Gamma_{su}'''} + n_x [\bar{z}v']_{\Gamma_{su}''} - n_x [\bar{g}v'']_{\Gamma_{su}'} \end{aligned} \quad (92)$$

The collocation method is used to impose the boundary condition as in equation (52). Substituting equation (85) into equation (92), one can obtain a linear algebraic equation system of  $\hat{u}_l$ .

The collocation method is used to impose the boundary conditions, as in equation (43).

To illustrate the effectiveness of this method, we consider the same numerical example again. Similarly, we start with the cubic basis, i.e.  $m=4$ , in the MLS interpolation. The weight function in MLS is taken to be equation (20),

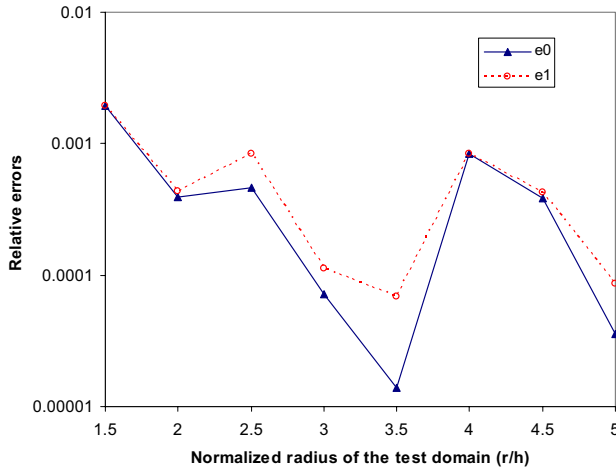


**Figure 38** : The influence of the test domain size (41 nodes).

while the test function in LWF (49) is chosen to be equation (21). 41 nodes are used ( $h=0.025$ ). Fig. 38 shows the influence of the radius of the test domain on the errors  $e_0$  and  $e_1$ , where the radius of the trial function domain is taken to be  $4.5h$ . From this figure, it can be found that the accuracy of the function  $u$ , as well as its first derivative, is very high when the test function domain is big enough ( $> h$ ). The relative errors  $e_0$  and  $e_1$  are less than 0.1%, when the radius of the test domain is greater than  $1.5h$ . It is noticed that the accuracy is not sensitive to the radius of the test domain from  $1.5-5h$ . Fig. 39 shows the influence of the radius of the trial domain on the errors  $e_0$  and  $e_1$ , where the radius of the test domain is taken to be  $3.5h$ . The results for the function  $u$  and its first derivative are high accurate. The relative errors  $e_0$  and  $e_1$  are not sensitive to the radius of the trial function domain from  $3.5-7h$ . For the linear ( $m=2$ ) basis, the same trends can be observed. In this method, for  $m=2$ , the requirement of a larger radius of the trial function domain is not needed either.

The convergence rate is investigated with three nodal configurations: 11, 21, and 41 nodes. We also consider the effects of the basis functions: linear ( $m=2$ ) and cubic ( $m=4$ ) bases are used in this investigation. For cubic ( $m=4$ ) basis, the radius of the test domain is taken to be  $4h$ , and the radius of the trial domain is taken to be  $5h$ . For linear ( $m=2$ ) basis, the radius of the test domain is taken to be  $3.5h$ , and the radius of the trial domain is

taken to be  $4.5h$ . The relative errors  $e_0$  and  $e_1$  and the convergence rates  $R$  of the displacement and first derivative are depicted in Fig. 40, for both  $m=4$  and  $m=2$ . The convergence rates  $R$  of the relative errors  $e_2$ ,  $e_3$  and  $e_p$  for the second, third derivatives and the energy, are plotted in Fig. 41 only for  $m=4$ . It can be seen that the present mixed MLPG method has very high rates of convergence for norms  $e_0$ ,  $e_1$ ,  $e_2$ , and  $e_p$ , and gives very accurate results for the unknown variable, its first and second derivatives, and the energy. The results from the cubic ( $m=4$ ) basis are more accurate, and are of higher convergent rate than those from the linear ( $m=2$ ) basis, although in this method the results from  $m=2$  are already very accurate. However, the results for the third derivative are not very accurate, while the convergence rate for the relative error  $e_3$  is very high.

Compared to the corresponding primal MLPG method based on the local weak form (48), this mixed MLPG method requires less Gaussian points, is more stable, and the results is of two-orders higher accuracy. This mixed MLPG method is more accurate, cheaper and faster.

#### 5.4 The local weak form 4

By using the auxiliary functions (75), the local weak form (53) can be rewritten as

$$n_x [qv]_{\Gamma_s} - n_x [zv']_{\Gamma_s} + n_x [gv'']_{\Gamma_s} - n_x [uv''']_{\Gamma_s} + \int_{\Omega_s} u \frac{d^4 v}{dx^4} dx + \int_{\Omega_s} (u-1)v dx = 0 \quad (93)$$

Compared to the local symmetric weak form (53), the LWF (93) has no derivative of the trial function in either domain integration or local boundary integration.

Imposing the boundary conditions (29) and (30), one obtains

$$n_x [\bar{q}v]_{\Gamma_{su}'''} + n_x [qv]_{\Gamma_{su}} + n_x [qv]_{L_s} - n_x [\bar{z}v']_{\Gamma_{su}'''} - n_x [zv']_{\Gamma_{su}'''} - n_x [zv']_{L_s} + n_x [\bar{g}v'']_{\Gamma_{su}'''} + n_x [gv'']_{\Gamma_{su}'''} + n_x [gv'']_{L_s} - n_x [\bar{u}v''']_{\Gamma_{su}'''} - n_x [uv''']_{\Gamma_{su}'''} - n_x [uv''']_{L_s} + \int_{\Omega_s} u \frac{d^4 v}{dx^4} dx + \int_{\Omega_s} (u-1)v dx = 0 \quad (94)$$

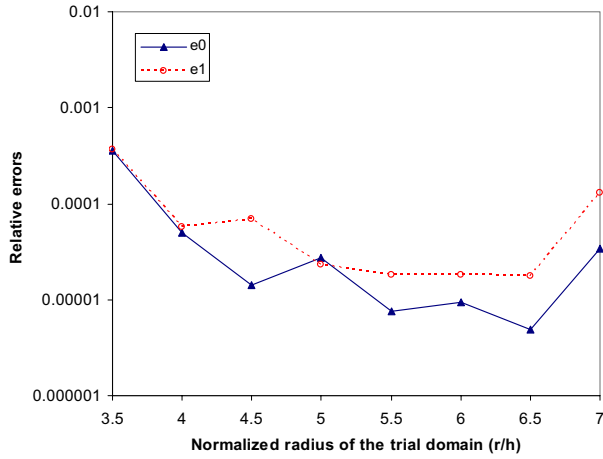


**Figure 39** : The influence of the trial domain size (41 nodes).

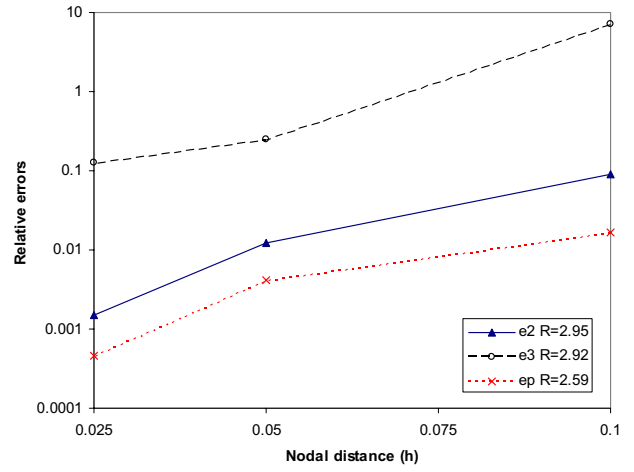


**Figure 41** : Convergence rate in relative errors  $e_2$ ,  $e_3$ , and  $e_p$ .

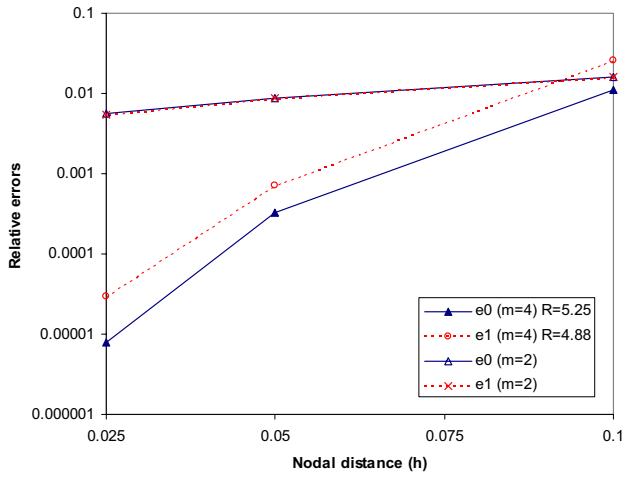


**Figure 40** : Convergence rate in relative errors  $e_0$  and  $e_1$ .

$$\begin{aligned}
 & n_x [qv]_{\Gamma_{su}} - n_x [zv']_{\Gamma_{su'}} + n_x [gv'']_{\Gamma_{su''}} \\
 & - n_x [uv''']_{\Gamma_{su'''}} + \int_{\Omega_s} u \frac{d^4 v}{dx^4} dx + \int_{\Omega_s} uv dx \\
 & = \int_{\Omega_s} v dx - n_x [\bar{q}v]_{\Gamma_{su'''}} + n_x [\bar{z}v']_{\Gamma_{su''}} \\
 & - n_x [\bar{g}v'']_{\Gamma_{su'}} + n_x [\bar{u}v''']_{\Gamma_{su}}
 \end{aligned} \tag{95}$$

With the interpolations (5) and (78), one may discretize the local symmetric weak form (95) as

$$\begin{aligned}
 & \sum_{I=1}^N n_x [\phi^I(x) v]_{\Gamma_{su}} \hat{q}_I - \sum_{I=1}^N n_x [\phi^I(x) v']_{\Gamma_{su'}} \hat{z}_I + \\
 & \sum_{I=1}^N n_x [\phi^I(x) v'']_{\Gamma_{su''}} \hat{g}_I - \sum_{I=1}^N n_x [\phi^I(x) v''']_{\Gamma_{su'''}} \hat{u}_I \\
 & + \sum_{I=1}^N \int_{\Omega_s} \phi^I(x) \left[ v + \frac{d^4 v}{dx^4} \right] dx \hat{u}_I \\
 & = \int_{\Omega_s} v dx - n_x [\bar{q}v]_{\Gamma_{su'''}} + n_x [\bar{z}v']_{\Gamma_{su''}} \\
 & - n_x [\bar{g}v'']_{\Gamma_{su'}} + n_x [\bar{u}v''']_{\Gamma_{su}}
 \end{aligned} \tag{96}$$

In order to simplify the above equation, we can select a test function  $v$  such that it and its first, second and third derivatives vanish over  $L_s$ . Such a test function is given in (21). Then, equation (94) can be rewritten as

Substituting equation (85) into equation (96), one can obtain a linear algebraic equation system of  $\hat{u}_I$ .

Again, the same numerical example is considered to illustrate the effectiveness of this method. We also start

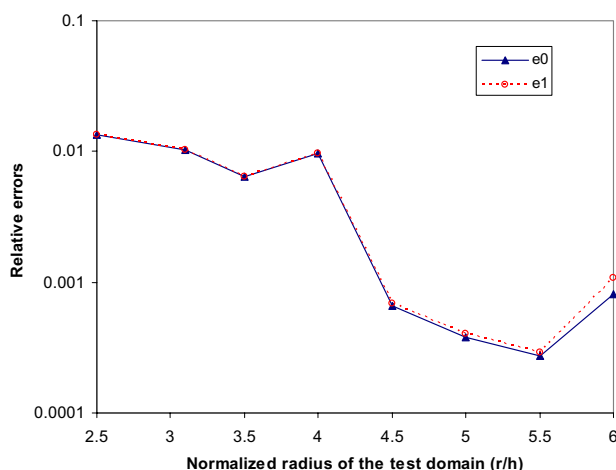


**Figure 42 :** The influence of the test domain size (41 nodes).

with the cubic basis, i.e.  $m=4$ , in the MLS interpolation. The weight function in MLS is taken to be equation (20), while the test function in LWF (95) is chosen to be equation (21). 41 nodes are used ( $h=0.025$ ). Fig. 42 shows the influence of the radius of the test domain on the errors  $e_0$  and  $e_1$ , where the radius of the trial function domain is taken to be  $4.5h$ . From this figure, it can be found that the accuracy of the function  $u$  and its first derivative is high when the trial function domain is big enough ( $\geq 2.5h$ ). Similarly, it is noticed that the accuracy is not sensitive to the radius of the test domain from  $3-6h$ , and the relative errors  $e_0$  and  $e_1$  are less than 1%. Fig. 43 shows the influence of the radius of the trial domain on the errors  $e_0$  and  $e_1$ , where the radius of the test domain is taken to be  $4h$ . The results for the function  $u$  and its first derivative are of high accuracy. The relative errors  $e_0$  and  $e_1$  are not sensitive to the radius of the trial function domain. For the linear ( $m=2$ ) basis, the same trends can be observed. In this method, for  $m=2$ , the requirement of a larger radius of the trial function domain is no longer needed.

Similarly, the convergence rate is investigated with three nodal configurations: 11, 21, and 41 nodes. We also consider the effects of the basis functions: linear ( $m=2$ ) and cubic ( $m=4$ ) bases are used in this investigation. For cubic ( $m=4$ ) basis, the radius of the test domain is taken to be  $4h$ , and the radius of the trial domain is taken to be  $5h$ . For linear ( $m=2$ ) basis, the radius of the test domain is taken to be  $4h$ , and the radius of the trial domain is taken to be  $6.5h$ . The relative errors  $e_0$  and  $e_1$  and the conver-

gence rates  $R$  of the displacement and first derivative are depicted in Fig. 44, for both  $m=4$  and  $m=2$ . The convergence rates  $R$  of the relative errors  $e_2$ ,  $e_3$  and  $e_p$  for the second, third derivatives and the energy, are plotted in Fig. 45 only for  $m=4$ . It can be seen that the present mixed MLPG method has very high rates of convergence for norms  $e_0$ ,  $e_1$ ,  $e_2$ , and  $e_p$ , and gives very accurate results for the unknown variable, its first and second derivatives, and the energy. However, the results for the third derivative are not very accurate, while the convergence rate for the relative error  $e_3$  is very high. In this method the results from  $m=2$  are also very accurate.

Compared to the corresponding primal MLPG method based on the local weak form (39), this mixed MLPG method requires less Gaussian points, is more stable and accurate. This mixed MLPG method is also more accurate than the corresponding first kind of mixed MLPG method. This mixed MLPG method possesses very high convergence rates for the displacement and its first to third derivatives.

## 6 Conclusions

Both the primal and mixed MLPG methods are presented for the 4<sup>th</sup> order ordinary differential equations. Various local weak forms are developed. In the first kind of mixed MLPG methods, both the displacement and its second derivative are interpolated independently through the moving least squares interpolation scheme. In the second kind of mixed MLPG methods, the displacement, its first derivative, the second derivative and the third derivative are all interpolated independently through the moving least squares interpolation scheme. The mixed MLPG methods avoid the occurrence of high order derivatives of the primary trial function, in the local weak forms, and thus reduce the continuity-requirement on the trial function. The mixed MLPG methods are far more efficient than the primal MLPG methods. The numerical examples demonstrate that both the primal and mixed MLPG methods obtain accurate results and possess excellent rate of convergence for the displacement, its first and second derivatives, and the energy. However, among them, the second kind of mixed MLPG methods give more stable and accurate results, and possess very high convergence rates, even for the third derivative.

**Acknowledgement:** This work was supported by the U. S. Army Research Office, and the U. S. Army Re-

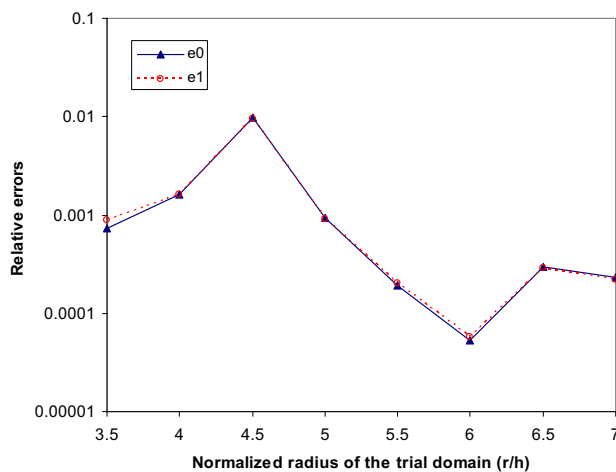


**Figure 43 :** The influence of the trial domain size (41 nodes).

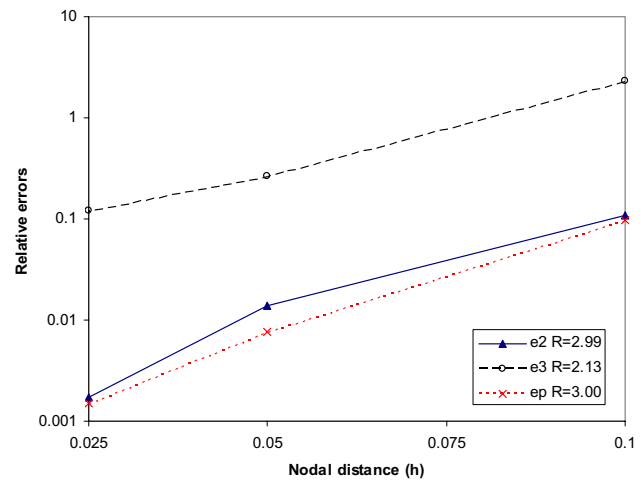


**Figure 45 :** Convergence rate in relative errors  $e_2$ ,  $e_3$ , and  $e_p$ .

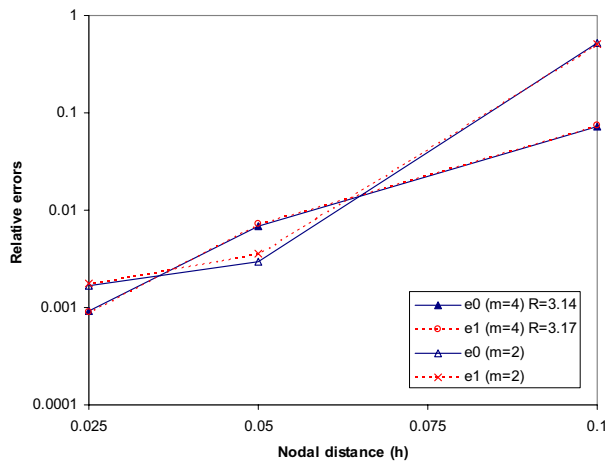


**Figure 44 :** Convergence rate in relative errors  $e_0$  and  $e_1$ .

search Laboratory, under a cooperative research agreement with the University of California at Irvine. The Cognizant Program Official at the U. S. Army Research Labs is Dr. R. Namburu. Partial support for this work was also provided by the Office of Naval Research, in the program directed by Dr. Y.D.S. Rajapakse.

## References

**Atluri, S. N.** (2004): *The meshless method (MLPG) for domain & bie discretizations*. Tech Science Press, USA, 680 pages.

**Atluri, S. N.; Cho, J. Y.; Kim, H. G.** (1999): Analysis of the beams, using the meshless local Petrov-Galerkin method, with generalized moving least squares interpolations. *Comput. Mech.* 24: 334-347.

**Atluri, S. N.; Han, Z. D.; Rajendran, A. M.** (2004): A new implementation of the meshless finite volume method, through the MLPG “mixed” approach. *CMES: Computer Modeling in Engineering & Sciences* 6(6): 491-513.

**Atluri, S. N.; Shen, S.** (2002a): *The meshless local Petrov-Galerkin (MLPG) method*. Tech Science Press, USA, 440 pages.

**Atluri, S. N.; Shen, S.** (2002b): The meshless local Petrov-Galerkin (MLPG) method: A simple & less-costly alternative to the finite element and boundary element method. *CMES: Computer Modeling in Engineering & Sciences* 3 (1): 11-52.

**Atluri, S. N.; Zhu, T.** (1998): A new meshless local Petrov-Galerkin (MLPG) approach in computational mechanics. *Comput. Mech.* 22: 117-127.

**Batra, R. C.; Ching, H. K.** (2002): Analysis of elastodynamic deformations near a crack/notch tip by the meshless local Petrov-Galerkin (MLPG) method. *CMES: Computer Modeling in Engineering & Sciences* 3 (6): 717-730.

**Cho, J. Y.; Atluri, S. N.** (2001): Analysis of shear flexible beams, using the meshless local Petrov-Galerkin

method, based on a locking-free formulation. *Eng. Comput.* 18 (1-2): 215-240.

**Han, Z. D.; Atluri, S. N.** (2004a): Meshless local Petrov-Galerkin (MLPG) approaches for solving 3D problems in elasto-statics. *CMES: Computer Modeling in Engineering & Sciences* 6 (2): 169-188.

**Han, Z. D.; Atluri, S. N.** (2004b): A meshless local Petrov-Galerkin (MLPG) approaches for solving 3-Dimesnsional elasto-dynamics. *CMC: Computer, Materials & Continua* 1 (2): 129-140.

**Li, Q.; Shen, S.; Han, Z. D.; Atluri, S. N.** (2003): Application of Meshless Local Petrov-Galerkin (MLPG) to Problems with Singularities, and Material Discontinuities, in 3-D Elasticity. *CMES: Computer Modeling in Engineering & Sciences* 4(5): 567-581.

**Lin, H.; Atluri, S. N.** (2000): Meshless local Petrov-Galerkin (MPLG) method for convection-diffusion problems. *CMES: Computer Modeling in Engineering & Sciences* 1 (2): 45-60

**Lin, H.; Atluri, S. N.** (2001): The meshless local Petrov-Galerkin (MPLG) method for solving incompressible Navier-stokes equations. *CMES: Computer Modeling in Engineering & Sciences* 2 (2): 117-142

**Long, S. Y.; Atluri, S. N.** (2002): A meshless local Petrov-Galerkin method for solving the bending problem of a thin plate. *CMES: Computer Modeling in Engineering & Sciences* 3 (1): 53-63.

**Raju, I. S.; Phillips, D. R.** (2003): Further Developments in the MLPG Method for Beam Problems. *CMES: Computer Modeling in Engineering & Sciences* 4 (1): 141-160.

**Shen, S.; Atluri, S. N.** (2004): Multiscale simulation based on the meshless local Petrov-Galerkin (MLPG) method. *CMES: Computer Modeling in Engineering & Sciences* 5(3): 235-255.

**Shen, S.; Atluri, S. N.** (2005): A tangent stiffness MLPG method for atom/continuum multiscale simulation. *CMES: Computer Modeling in Engineering & Sciences* 7(1): 49-67.

## The basis of meshless domain discretization: the meshless local Petrov–Galerkin (MLPG) method

Satya N. Atluri and Shengping Shen

*Center for Aerospace Research & Education, University of California at Irvine, Irvine, CA 92697-3975, USA*

E-mail: satluri@uci.edu

Received 6 March 2003; accepted 8 December 2003

Communicated by Z. Wu and B.Y.C. Hon

The MLPG method is the general basis for several variations of meshless methods presented in recent literature. The interrelation of the various meshless approaches is presented in this paper. Several variations of the meshless interpolation schemes are reviewed also. Recent developments and applications of the MLPG methods are surveyed.

**Keywords:** MLPG, local weak form, meshless method

**AMS subject classification:** 65N30

### 1. Introduction

Meshless methods, as alternative numerical approaches to eliminate the well-known drawbacks in the finite element and boundary element methods, have attracted much attention in recent decades, due to their flexibility, and due to their potential in negating the need for the human-labor intensive process of constructing geometric meshes in a domain. Such meshless methods are especially useful in those problems with discontinuities or moving boundaries. The main objective of the meshless methods is to get rid of, or at least alleviate the difficulty of, meshing and remeshing the entire structure; by only adding or deleting nodes in the entire structure, instead. Meshless methods may also alleviate some other problems associated with the finite element method, such as locking, element distortion, and others.

Sometimes, in numerical simulations, a mesh may result in an inherent bias. For example, the simulation of the strain localization problem is very sensitive to the mesh alignment [38]. This is one of the reasons why the meshless method is so attractive. Moreover, in the finite element method, the construction of even a  $C^1$  trial function approximation is difficult, and has been unsatisfactory so far. However, the trial functions commonly employed in the MLPG method, can achieve high-order continuous approximations (even  $C^\infty$  approximations) in a very straightforward manner. Hence, the MLPG

method will clearly excel the finite element method, for materials with strain gradient effects, and in thin-shell analysis.

The objective of this paper is to present an interrelation of the various meshless approaches, and review the recent developments and applications of the MLPG methods. These approaches are associated with weak forms. Some meshless methods are based on global weak forms. The major dilemma in the class of meshless methods, which are based on the global weak forms, revolves around how to evaluate the integrals in the weak form. In many methods, such as the element-free Galerkin method, the background cells are used for this integration. As a matter of fact, the background cell integration does not lead to a truly meshless method. Hence, in order to develop a truly meshless method, the local weak forms must be used, so as to avoid the background mesh, besides employing the meshless interpolations for trial and test functions. The truly meshless method should be based on local weak forms, which is the main point of the departure of the MLPG methods. The MLPG concept provides a rational basis for constructing a variety of meshless methods. MLPG method is the general basis for several recent published variations of meshless methods, such as the finite point method, the finite cloud method, SPH, the finite sphere method, and the local point interpolation method, etc., as shown in this paper. Moreover, the MLPG methods, based on local weak formulations, can also include all the other meshless methods based on global formulation, as special cases.

## 2. Basis of truly meshless methods: the local weak forms

In the MLPG method, a local weak form over a local subdomain  $\Omega_s$ , which is located entirely inside the global domain  $\Omega$ , is used. This is the most distinguishing feature of the MLPG. Even though a particular approximation of the local weak form gives the same resulting discretized equations, as from the Galerkin approximation of the global weak form, the local weak form provides a clear concept for a local meshless integration of the weak-form, which does not need any background integration cells over the entire domain. Also, it leads to a natural way to construct the global stiffness matrix: not through the integration over a contiguous mesh, and by assembly of the stiffness matrices of the elements in the mesh, but through the integration over local subdomains. These local subdomains may overlap each other. In contrast to the conventional Galerkin finite element method, which is based on the global weak form, the MLPG method [7,8] stems from a weak form over a subdomain  $\Omega_s$  as shown in figure 1, where the domain of support of the test function  $\Omega_{te}^I$  is synonymous with the subdomain  $\Omega_s$ .

Consider a linear Poisson's equation (in a global domain  $\Omega$ , bounded by  $\Gamma$ ):

$$\nabla^2 u(\mathbf{x}) = p(\mathbf{x}), \quad \mathbf{x} \in \Omega, \quad (1)$$

where  $p$  is a given source function, with boundary conditions

$$u = \bar{u} \quad \text{on } \Gamma_u; \quad \frac{\partial u}{\partial n} \equiv q = \bar{q} \quad \text{on } \Gamma_q, \quad (2)$$

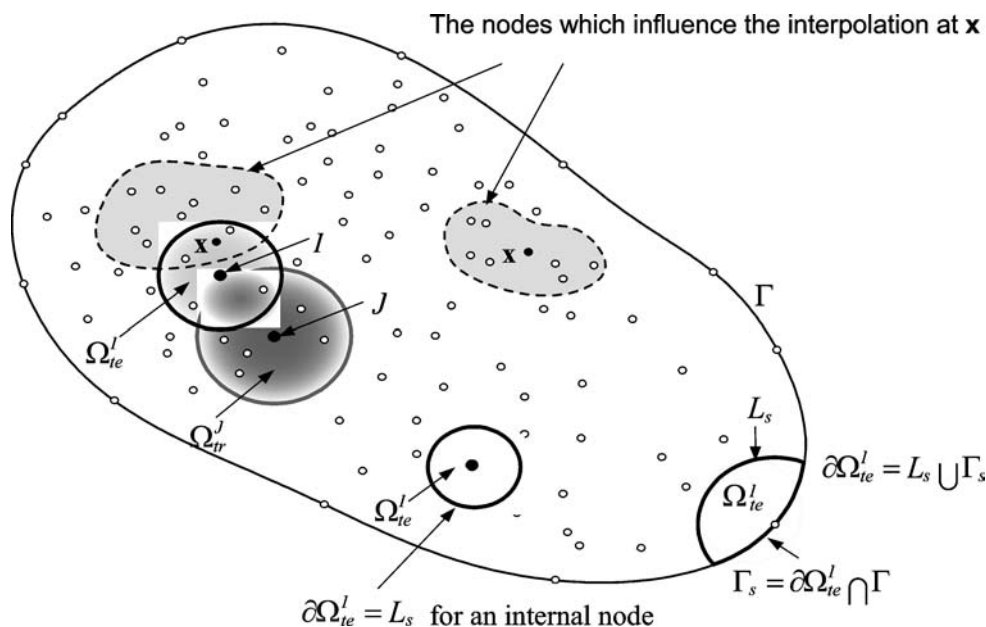


Figure 1. Schematics of the MLPG method.

A local unsymmetric weak formulation (LUSWF1) of the problem (1) is written as

$$\int_{\Omega_\infty} (\nabla^2 u - p)v \, d\Omega = 0, \quad (3)$$

Using the divergence theorem, the local symmetric weak formulation (LSWF) is defined

$$\int_{L_s} qv \, d\Gamma + \int_{\Gamma_{su}} qv \, d\Gamma + \int_{\Gamma_{sa}} \bar{q}v \, d\Gamma - \int_{\Omega_s} (u_{,i}v_{,i} + pv) \, d\Omega - \alpha \int_{\Gamma_u} (u - \bar{u})v \, d\Gamma = 0 \quad (4a)$$

in which,  $\Gamma_{sq}$  is a part of  $\partial\Omega_s$ , over which the natural boundary condition is specified. The LSWF requires that both  $u$  and  $v$  be  $C^0$  continuous.

We can select a test function  $v$  such that it vanishes over  $L_s$ . Therefore the first integral in equation (4a) vanishes. Then, we obtain the following local weak form (LSWF),

$$\int_{\Omega_s} u_{,i} v_{,i} d\Omega - \int_{\Gamma_{su}} q v d\Gamma + \alpha \int_{\Gamma_u} u v d\Gamma = \int_{\Gamma_{sq}} \bar{q} v d\Gamma - \int_{\Omega_s} p v d\Omega + \alpha \int_{\Gamma_u} \bar{u} v d\Gamma. \quad (4b)$$

Using the divergence theorem twice yields another “local unsymmetric weak formulation” (LUSWF2),

$$\begin{aligned} & \int_{L_s} q v d\Gamma - \int_{L_s} u v_{,i} n_i d\Gamma + \int_{\Gamma_{sq}} \bar{q} v d\Gamma + \int_{\Gamma_{su}} q v d\Gamma - \int_{\Gamma_{sq}} u v_{,i} n_i d\Gamma \\ & - \int_{\Gamma_{su}} \bar{u} v_{,i} n_i d\Gamma + \int_{\Omega_s} u \nabla^2 v d\Omega - \int_{\Omega_s} p v d\Omega = 0. \end{aligned} \quad (5a)$$

This LUSWF requires that  $v$  be at least  $C^1$  continuous, while  $u$  may be discontinuous. Also, by selecting a test function  $v$  which vanishes over  $L_s$ , we obtain

$$\begin{aligned} & \int_{\Gamma_{su}} q v d\Gamma - \int_{L_s} u v_{,i} n_i d\Gamma - \int_{\Gamma_{sq}} u v_{,i} n_i d\Gamma + \int_{\Omega_s} u \nabla^2 v d\Omega \\ & = \int_{\Omega_s} p v d\Omega - \int_{\Gamma_{sq}} \bar{q} v d\Gamma + \int_{\Gamma_{su}} \bar{u} v_{,i} n_i d\Gamma. \end{aligned} \quad (5b)$$

It should be noted that these local weak forms (3)–(5) hold, irrespective of the size and shape of  $\partial\Omega_s$ . With the local weak form for any point  $\mathbf{x}$ , the problem (1) becomes one as if we are dealing with a localized boundary value problem over an sphere  $\Omega_s$ . The equilibrium equation and the boundary conditions are satisfied, a posteriori, in all local subdomains and on their  $\Gamma_s$ , respectively. Theoretically, as long as the union of all local domains covers the global domain, the equilibrium equation and the boundary conditions will be satisfied, a posteriori, in the global domain and on the boundary  $\Gamma$ , respectively.

In MLPG, the Petrov–Galerkin method is used in each local subdomain, which uses the trial function and test function from different spaces. If the local domain  $\Omega_s$  is taken to be the entire domain  $\Omega$ , we can get three corresponding ‘global’ weak formulations of the differential equation (1). Many of the so-called meshless methods, such as the EFG (element-free Galerkin) method, are based on the global weak form over the entire domain  $\Omega$ . In finite volume, boundary element, the Galerkin finite element, and element free Galerkin [16] methods, which are based on the global Galerkin formulation, one uses the global weak form over the entire domain  $\Omega$  (or boundary), to solve the problem numerically.

MLPG provides a rational basis for constructing meshless methods with a greater degree of flexibility. The MLPG method is a very general concept whose underlying concept serves as a basis for a large number of variously named minor variations, such as: finite points method [39], finite spheres method [21], finite clouds method [1], boundary node method [17], boundary clouds method [28], regular boundary node method [65], SPH [36], etc.

### 3. Meshless approximation of trial functions

In this section, various available methods of approximating a trial function over an arbitrary domain without using a mesh, are discussed. In general, meshless interpolations are constructed among a set of scattered nodes that have no particular topological connection among them. An appropriate meshless interpolation scheme should satisfy the following requirements:

1. Locality;
2. Continuity;
3. Consistency (or completeness).

Moreover, the sensitivity of any meshless interpolation scheme to a variable number of nodes in each interpolation domain must be low enough to preserve the freedom of adding, moving or removing nodes. The first requirement is crucial to the meshless method, for it makes the method efficient. Otherwise, the interpolation will produce a full width stiffness matrix. The second arises from the local weak forms, which ensure that the weak forms are integrable. The third depends on the order of the partial differential equations to be solved. The continuity and consistency conditions are related to the convergence of the interpolant-based weak-form methods. A variety of typical local interpolation schemes is summarized in this section.

The moving least-square method is generally considered to be one of the best schemes to interpolate data with a reasonable accuracy. Here is given a brief summary of the MLS, for its details, see [4,16].

Consider a subdomain  $\Omega_{\mathbf{x}}$ , which is defined as the neighborhood of a point  $\mathbf{x}$  and denoted as the domain of definition of the MLS approximation for the trial function at  $\mathbf{x}$ . To approximate the distribution of the function  $u$  in  $\Omega_{\mathbf{x}}$ , over  $N$  randomly located nodes  $\{\mathbf{x}_I\}$ , the moving least squares approximant  $u^h(\mathbf{x})$  of  $u$ ,  $\forall \mathbf{x} \in \Omega_{\mathbf{x}}$ , can be defined by

$$u^h(\mathbf{x}) = \mathbf{p}^T(\mathbf{x})\mathbf{a}(\mathbf{x}) \quad \forall \mathbf{x} \in \Omega_{\mathbf{x}}, \quad (6)$$

where  $\mathbf{p}^T(\mathbf{x}) = [p_1(\mathbf{x}), p_2(\mathbf{x}), \dots, p_m(\mathbf{x})]$  is a complete monomial basis,  $m$  is the number of terms in the basis; we denote by  $t$  the highest-order polynomial which is completely included in the basis; and  $\mathbf{a}(\mathbf{x})$  is an  $m$ -length vector which are functions of the space coordinates  $\mathbf{x}$ . MLS interpolation possesses  $t$ -order completeness. The linear basis assures that the MLS approximation has the linear completeness. Thus, it can reproduce any smooth function and its first derivative with arbitrary accuracy, as the approximation is refined. The vector  $\mathbf{a}(\mathbf{x})$  is determined by minimizing a weighted discrete  $L_2$  norm:

$$J(\mathbf{x}) = \sum_{I=1}^N w_I(\mathbf{x}) [\mathbf{p}^T(\mathbf{x}_I)\mathbf{a}(\mathbf{x}) - \hat{u}^I]^2, \quad (7)$$

where  $w_I(\mathbf{x})$  is a weight function associated with the node  $I$ , with  $w_I(\mathbf{x}) > 0$  for all  $\mathbf{x}$  in the support of  $w_I(\mathbf{x})$ . It should be noted that  $\hat{u}^I$  are the fictitious nodal values, and not the actual nodal values of the trial function  $u^h(\mathbf{x})$ , in general. Then, a relation is given as

$$u^h(\mathbf{x}) = \sum_{I=1}^N \phi^I(\mathbf{x}) \hat{u}^I, \quad u^h(\mathbf{x}_I) \equiv u^I \neq \hat{u}^I, \quad \mathbf{x} \in \Omega_{\mathbf{x}}. \quad (8)$$

The expression of  $\phi^I(\mathbf{x})$ , the shape function of the MLS approximation, can be found in [5]. The fact that  $\phi^I(\mathbf{x})$  vanishes, for  $\mathbf{x}$  not in the support of nodal point  $\mathbf{x}_I$ , preserves the local character of the moving least squares approximation. The nodal shape function is complete up to the order of the basis. The smoothness of the nodal shape function is determined by that of the basis, and of the weight function.

The choice of the weight function is more or less arbitrary, as long as the weight function is positive and continuous. It is noted that the basis functions can be other function than monomial. *The smoothness of the shape functions  $\phi^I(\mathbf{x})$  is determined by that of the basis function  $\mathbf{P}(\mathbf{x})$  and of the weight functions  $w_I(\mathbf{x})$ .* Let  $w_I(\mathbf{x}) \in C^k(\Omega)$  and  $p_j(\mathbf{x}) \in C^l(\Omega)$ , the shape functions  $\phi^I(\mathbf{x}) \in C^r(\Omega)$  with  $r = \min(k, l)$ . Usually, the order of the continuity for the basis function  $\mathbf{P}(\mathbf{x})$  is higher than that for the weight functions  $w_I(\mathbf{x})$ , thus  $r = k$ . For example, for the monomial basis function,  $p_j(\mathbf{x}) \in C^\infty(\Omega)$ , in this case, the order of the continuity for the shape functions only depends on the weight functions  $w_I(\mathbf{x})$ . Hence, it is easy for the MLS approximation to yield a higher order of continuity for the shape functions, simply by increasing  $k$ . A simple practical way is to use high-order spline functions. The following weight function is recommended:

$$w_I(\mathbf{x}) = \begin{cases} 1 - \sum_{k=1}^p a_k \left( \frac{d_I}{r_I} \right)^k, & 0 \leq d_I \leq r_I = \rho_I h_I, \\ 0, & d_I > r_I = \rho_I h_I, \end{cases} \quad (9)$$

where  $d_I = |\mathbf{x} - \mathbf{x}_I|$ ,  $h_I$  in the nodal distance,  $\rho_I$  is the scaling parameter for the size of the subdomain  $\Omega_{\text{tr}}^I$ , and  $p$  is the order of spline function. The coefficients  $a_k$  are obtained by taking the following boundary conditions:

$$\begin{cases} w_I \left( \frac{d_I}{r_I} = 0 \right) = 1, & m_0 = 0, \\ \frac{\partial^{m_0} w_I(d_I/r_I = 0)}{\partial x^{m_0}} = 0, & m_0 \geq 1, \end{cases} \quad \text{and} \quad \begin{cases} w_I \left( \frac{d_I}{r_I} = 1 \right) = 0, & m_1 = 0, \\ \frac{\partial^{m_1} w_I(d_I/r_I = 1)}{\partial x^{m_1}} = 0, & m_1 \geq 1, \end{cases} \quad (10)$$

where  $p = m_0 + m_1 + 1$ . The form of the weight functions may be changed by the geometry of the subdomain  $\Omega_{\text{tr}}^I$ . Since the weight function is a type of a polynomial, the “nodal shape function” has the characteristics of a rational function.  $m_0$  controls the interior continuity in the local subdomain, while  $m_1$  controls the boundary continuity of the local subdomain. One can easily obtain a global  $C^l$  continuity up to a desired order  $l$  if the order of spline is changed. Therefore, the  $C^l$  continuity depends upon value of

$m_0$  and  $m_1$  in equation (10), i.e.  $\phi(\mathbf{x}) \in C^{\min(m_0, m_1)}$ . It is very important to preserve the smoothness of the derivatives of shape functions, because discontinuities and vertices in the derivatives of the shape functions make numerical integration difficult.

The size of support,  $r_I$ , of the weight function  $w_I$  associated with node  $I$  should be chosen such that  $r_I$  should be large enough to have sufficient number of nodes covered in the domain of definition of every sample point ( $N \geq m$ ), in order to ensure the regularity of  $\mathbf{A}$ . A very small  $r_I$  may result in a relatively large numerical error, while using the Gauss numerical quadrature to calculate the entities in the system stiffness matrix. On the other hand,  $r_I$  should also be small enough to maintain the local character of the MLS approximation. If  $N = m$ , no effect of the weight functions is presented and the FEM type interpolation is recovered, then  $u^h(\mathbf{x}_I) = \hat{u}^I$ .

The locality of the shape functions  $\phi^I(\mathbf{x})$  is determined by the basis function  $\mathbf{P}(\mathbf{x})$  and the weight functions  $w_I(\mathbf{x})$ . *For the monomial basis functions which are global, the local weight functions  $w_I(\mathbf{x})$  enable the shape functions  $\phi^I(\mathbf{x})$  to be local.*

A generalization of the MLS interpolation scheme using the data for the derivative of a function, in addition to the value of the function itself, at a finite number of nodes, can be found in [2].

Actually, MLS can be the general basis for several variations of meshless interpolations, such as:

1. Shepard functions [47];
2. Least squares [39];
3. Local point interpolation [33];
4. Local radial point interpolation [33];
5. Compact support radial basis functions [59,63]; and so on.

If the MLS nodal shape functions only represent a globally constant function, i.e.  $m = 1$ , we obtain the so-called Shepard function [47]. The Shepard functions satisfy the zeroth order completeness. The Shepard shape functions have a simpler structure than the higher order MLS shape functions, but they are still in a rational form. The application of the Shepard function in MLPG can be found in [5].

*If the weight function in the MLS is taken to be the Heaviside function, then we can get the local (truncated) least square (LSQ) scheme from the MLS.* The computational cost for calculating the local LSQ shape functions and their derivative is, of course, less than that of MLS. However, the locality is coerced by the Heaviside function, which lowers the performance (including global continuity) of the shape functions. For Heaviside function,  $m_0 = \infty$ ,  $m_1 = -1$ , which leads to a global  $C^{-1}$  continuity shape function. As shown by Onate et al. [39], the use of a Gaussian or spline weight function in MLS improves considerably the results with respect to the least-square (LSQ) approach. As noted in the beginning of this section, to add or delete nodes freely, the sensitivity of the meshless interpolation scheme to a variable number of nodes in each interpolation domain  $\Omega_{\text{tr}}^I$  must be low enough. However, the local LSQ approximation is very sensitive

to the neighbors of the evaluated node due to the truncated locality, while this sensitivity is quite low in MLS methods [39]. Moreover, in MLS, a high-order continuous approximation throughout the whole domain can be constructed for high-order differential equations easily, simply by adjusting value of  $m_0$  and  $m_1$  of the weight function, without increasing the bandwidth. Those indicate some advantage of the MLS method for practical applications.

If, in addition, we take  $N = m$  in local LSQ method, then one can get the so-called local point interpolation [33]. Obviously, this method inherits all the shortcomings of local LSQ scheme due to the same truncated locality, listed in the proceeding paragraph. In [33], the basis functions are taken to be monomial; and thus, as a matter of fact, it is not a new method: it is just a FEM type interpolation. Here, we list the procedure. The unknown function  $u(\mathbf{x})$  can be interpolated from the neighboring nodes of a point  $\mathbf{x}$  using the polynomials basis functions as

$$u^h(\mathbf{x}) = \sum_{I=1}^N p_I(\mathbf{x})a_I = \mathbf{p}^T(\mathbf{x})\mathbf{a}. \quad (11)$$

The coefficients  $a_I$  are determined by enforcing the above equation at the  $N$  nodes surrounding point  $\mathbf{x}$ , as  $\mathbf{u} = \mathbf{P}\mathbf{a}$ , where  $\mathbf{u}^T = [u^1, u^2, \dots, u^N]$ ,  $\mathbf{P}^T = [\mathbf{p}_1(\mathbf{x}_1), \mathbf{p}_2(\mathbf{x}_2), \dots, \mathbf{p}_N(\mathbf{x}_N)]$ . Hence, it can be obtained that  $\mathbf{a} = \mathbf{P}^{-1}\mathbf{u}$ . So, we have

$$u^h(\mathbf{x}) = \mathbf{p}^T \mathbf{P}^{-1} \mathbf{u}. \quad (12)$$

For the monomial basis function  $p_I(\mathbf{x})$ , this procedure is totally same as that in the FEM.

In LPIM, to ensure  $N = m$ , where  $m$  is fixed for certain order completeness, it means that the number of nodes in the local domain is constrained by the number of the monomial basis functions; and thus, it reduces the flexibility of the meshless interpolation. Moreover, for an arbitrarily chosen set of scattered nodes, special techniques should be used to assure a successful computation of shape functions (to avoid the matrix  $\mathbf{P}$  to be singular). If the basis functions are taken to be globally supported radial basis functions, then one can get the so-called Local Radial Point Interpolation (LRPIM) [33]. This method is stable and flexible compared to LPIM. It is noted that the LRPIM method suffers from a lack of consistency. Hence, to remedy this, a sum of polynomials up to degree  $t$  with additional constraints is attached to the interpolation function [33,44]. The details related to the radial basis functions can be founded in the review paper [44].

Compact support, positive definite Radial Basis Functions have been suggested only recently [59,63]. If  $N = m$  is taken in MLS method, and the basis functions are taken to be compact support radial basis functions, we get yet another new local interpolation: Compact Support Radial Basis Functions (CSRBF). In this scheme,  $u^h(\mathbf{x}_I) = \hat{u}^I$ . In this case, the basis function is local because it is compact supported. Therefore, the weight function can be taken to be 1, which belongs to  $C^\infty(\Omega)$ . The resulting shape function is not truncated local. It is not sensitive to the neighbors of the evaluated node. A high-order continuous approximation throughout the whole domain can be constructed easily for high-order differential equations, simply by choosing higher-order continuous

compact support radial basis function, without increasing the band-width. However, this interpolation suffers from a lack of completeness. Atluri and Shen [5] employed this interpolation in MLPG method. Zhang et al. [66] employed both global and compact support radial basis function in the collocation method. The Hermite–Birkhoff-type interpolation of scattered multidimensional data, through radial basis functions, can be found in [62]; and this type of interpolation is desirable when the derivative is also used as a degree of freedom at each node.

Meshless methods can also be based on partitions of unity [11]. PU method is not a good choice for the MLPG method, since the test function needs  $m$  unknowns per node, or indirectly,  $m$  test functions are needed; otherwise there are insufficient equations to determine the unknowns. In addition, it is more time-consuming to form and solve the resulting algebraic equations, since the dimension of the stiffness matrix will be  $m$  times of that in the case when MLS are used [5].

The reproducing kernel particle method (RKPM) is developed in [32]. Here, the shape function was derived from the reproducing conditions. The equivalence between MLS and RKPM is discussed in [26].

There also exist some other meshless interpolations, such as smoothed particle hydrodynamics (SPH) [36], finite cloud method [1], etc.

It is noted that the nodal shape functions (trial functions) from the MLS, Shepard function, partition of unity, RKPM, and CS-RBF interpolations possess a high-order of continuity. This high-order of continuity provides solutions with smooth derivatives, and is very different to the FEM. Thus, these methods have the advantage of providing better (smooth) approximation of stresses. Consequently, the postprocessing in MLPG is relatively straightforward, and no additional stress smoothing is required. On the other hand, the LPIM [33] and LRPIM [33] suffer from a lower continuity due to the truncated locality; further more, the LPIM leads more or less to an FEM-type interpolation.

The approximations with  $N = m$  (LPIM, LRPIM, CSRBF), are interpolation type, and possess Delta function property. The approximations with  $N \neq m$ , are fit type and do not possess Delta property. The latter are optimal methods, and hence, achieve a high-order continuous approximation over the entire domain; this is one of the reasons why a meshless method is beyond the FEM, as compared to LPIM, LRPIM, etc. Although the interpolation type can result in simple shape functions, when compared to the fit type, it still cannot remedy the integration difficulties in the meshless method. That the Gaussian integration is not so good in a meshless method as in the FEM, is mainly because the domain of the interpolation is different to the domain of the integration. With the Delta property, in meshless method, the essential boundary conditions can be directly implemented same as in FEM.

In trial-function interpolation schemes without the Kronecker delta properties, it is not easy to implement the essential boundary conditions. However, the enforcement of essential boundary conditions is not the problem now, some convenient treatments have been proposed. In many researches, a Lagrange multiplier technique has been used to impose the essential boundary conditions. However, this technique produces a non-banded and a nonpositive definite stiffness matrix. One of the promising methods to

enforce the essential boundary conditions in meshless methods is the penalty parameter technique as developed by Zhu and Atluri [67], which is efficient and does not need any other additional unknown variables. A collocation method is also a very important technique to enforce the essential boundary conditions in the meshless method [67] due to its simplicity. Our numerical results show that both the penalty parameter and collocation techniques are effective and convenient [4,5]. Another technique to exactly impose the essential boundary conditions in meshless methods is a transformation method developed by Atluri et al. [3].

#### 4. The basis of meshless domain discretization: the meshless local Petrov–Galerkin (MLPG) approach

In general, in MLPG, the nodal trial and test functions can be different, the nodal trial function may correspond to any one of the interpolant schemes listed in section 3; and the test function may be totally different. Furthermore, the size of the subdomains over which the nodal trial and test functions are, respectively, nonzero, may be different.

Soon after the debut of the concept of MLPG [7], variants of the MLPG method appeared in literature, by using different trial-function interpolant schemes, or different test functions, or different shapes of the support domain of the trial function, or different shapes of the support domain of the test function, or even different shapes of the local domain  $\Omega_s$ . Actually, if there are  $N$  different trial-function interpolating schemes,  $M$  different test functions,  $L$  different shapes of the support domain of the trial function,  $I$  different shapes of the support domain of the test function, and  $J$  different shapes of the local domain  $\Omega_s$ , then  $(N \times M \times L \times I \times J)$  number of MLPG methods can be developed!

Based on the concept of the MLPG, the test functions over each local  $\Omega_s$  can be chosen through a variety of ways:

- (1) the weight function in the MLS approximation;
- (2) the collocation Dirac's Delta function;
- (3) the error function in the differential equation, using discrete least squares;
- (4) the modified fundamental solution to the differential equation;
- (5) constant for second order PDE (or linear function for 4th order PDE);
- (6) identical to the trial function;
- (7) any other convenient functions.

We label these methods as MLPG1, MLPG2, MLPG3, MLPG4, MLPG5, and MLPG6 corresponding to the first six terms, respectively [4,5].

As a known test function is used in the local weak form (LWF), the use of the LWF for one point (and here for one domain  $\Omega_s$ ) will yield only one algebraic equation. One can obtain as many equations as the number of nodes. Hence, as many local domains

$\Omega_s$  as the number of nodes are needed in the global domain, in order to obtain as many equations as the number of unknowns.

#### 4.1. MLPG1, MLPG5, and MLPG6 based on the LSWF

MLPG1 is developed by employing the MLS weight function (9) (or some other compact continuous functions) as the test function in each  $\Omega_s$ . Substitution of any meshless interpolations listed in section 3 into the LSWF (4b) for all the nodes, leads to the following discretized system of linear equations:

$$\mathbf{K} \cdot \hat{\mathbf{u}} = \mathbf{f}, \quad (13)$$

where the entries of the global ‘stiffness’ matrix  $\mathbf{K}$  and the global ‘load’ vector  $\mathbf{f}$ , respectively, are defined as:

$$K_{IJ} = \int_{\Omega_s} \phi_{,k}^J(\mathbf{x}) v_{,k}(\mathbf{x}, \mathbf{x}_I) d\Omega - \int_{\Gamma_{Su}} \frac{\partial \phi^J(\mathbf{x})}{\partial n} v(\mathbf{x}, \mathbf{x}_I) d\Gamma + \alpha \int_{\Gamma_{Su}} \phi^J(\mathbf{x}) v(\mathbf{x}, \mathbf{x}_I) d\Gamma, \quad (14)$$

$$f_I = \int_{\Gamma_{Su}} \bar{q}(\mathbf{x}) v(\mathbf{x}, \mathbf{x}_I) d\Gamma - \int_{\Omega_s} p(\mathbf{x}) v(\mathbf{x}, \mathbf{x}_I) d\Omega + \alpha \int_{\Gamma_{Su}} \bar{u}(\mathbf{x}) v(\mathbf{x}, \mathbf{x}_I) d\Gamma. \quad (15)$$

The details of MLPG1 using the MLS, Shepard function and CSRBF to approximate the trial functions can be found in [5,7]. By employing LPIM and LRPIM to construct the shape functions instead of MLS, Liu and Gu [33] repeated this procedure, and get an MLPG1 method; however, they labeled it the “meshfree local point interpolation method (LPIM)”.

MLPG5 is derived from the LSWF (4a); while any meshless interpolations can be used to approximate the trial function. A constant function for second order PDE (or linear function for 4th order PDE) is taken to be the test function in each  $\Omega_s$ . The reason to choose such a test function is to try to avoid the domain integration in the LSWF. The entries of the global ‘stiffness’ matrix  $\mathbf{K}$  and the global ‘load’ vector  $\mathbf{f}$  are defined by

$$K_{IJ} = - \int_{L_s} \phi_{,k}^J(\mathbf{x}) n_k d\Gamma - \int_{\Gamma_{Su}} \phi_{,k}^J(\mathbf{x}) n_k d\Gamma + \alpha \int_{\Gamma_{Su}} \phi^J(\mathbf{x}) d\Gamma, \quad (16)$$

$$f_I = \int_{\Gamma_{Su}} \bar{q}(\mathbf{x}) d\Gamma - \int_{\Omega_s} p(\mathbf{x}) d\Omega + \alpha \int_{\Gamma_{Su}} \bar{u}(\mathbf{x}) d\Gamma. \quad (17)$$

The numerical integration plays an important role in the convergence of numerical solutions of meshless methods. It may be difficult to perform the domain integration for the stiffness matrix in meshless methods, due to the fact that the domain of the interpolation is different to the domain of the integration. From equation (16), it can be seen that the domain integral over  $\Omega_s$  is altogether avoided, which greatly improves the effectiveness of this method. Hence, this method is an attractive meshless method. The

details of MLPG5 using the MLS, Shepard function and CSRBF to construct the shape functions can be found in [4,5].

In MLPG6, the trial and test functions come from the same space. To obtain the discrete equations from the LSWF (4b), any meshless interpolations can be used to approximate the trial function. The entries of the global ‘stiffness’ matrix  $\mathbf{K}$  and the global ‘load’ vector  $\mathbf{f}$  can be found in [5].

Atluri et al. [3] studied MLPG6 in great detail by using the MLS, Shepard function and partitions of unity. Their results showed that the partition method for numerical integration must be used to get a convergent result. Based on their research and the results in [5], it can be concluded that the Galerkin method is not a good option for the MLPG method, from the viewpoint of calculation and application. By employing partition of unity to construct the shape functions, and taking the shape of the local domain to be sphere, De and Bathe [21] repeated this procedure, and get an MLPG6 method; however, they called it the “method of finite sphere (MFS)”.

The test function can also be chosen to be any other function. Based on LSWF, Barry and Thulasi [12] introduced Wachspress polynomials as test functions with the subdomain to  $N$ -sided polygons (Wachspress cells), and use MLS to construct the trial functions. They named it Wachspress MLPG method (WMLPG). However, in this method, to form the Wachspress cells is the same as to generate meshes in FEM.

#### 4.2. MLPG2 and MLPG3 based on LUSWF1

MLPG2 and MLPG3 are based on the local unsymmetric weak formulation (LUSWF1) (3). MLPG2 employs the collocation Dirac’s Delta function as the test function in each  $\Omega_s$ . Any interpolations listed in section 3 can be used into the LUSWF1 (3) for the internal nodes. The detail of MLPG2 can be found in [5]. MLPG2 does not involve any numerical integration to generate the global stiffness matrix, so it is the simplest form of the meshless method.

Thus, the collocation method can be treated simply as a special case of the MLPG approach. Smoothed Particle Hydrodynamics (SPH) [36] is one of the earliest meshless methods in computational mechanics. SPH can also be regarded as an MLPG2, by using SPH to approximate the trial functions. Finite point method (FPM) [39] is a point collocation method by employing the weighted least squares as the trial functions. If we use the weighted least squares to approximate the trial functions in MLPG2, we can get FPM. Using the finite cloud method to approximate the trial functions in MLPG2, one can get finite cloud method (FCM) [1]. The details of MLPG2 using the MLS, Shepard function and CSRBF to approximate the trial functions can be found in [5].

MLPG3 employs the error function as the test function in each  $\Omega_s$ . In this method, the test function can also be assumed as in the discrete least square method. The test function and the trial function come from the same space in MLPG3. Any interpolations listed in section 3 can be used as the trial function. The entries of the ‘stiffness’ matrix  $\mathbf{K}$  and ‘load’ vector  $\mathbf{f}$  are derived in [5].

The details of MLPG3 using the MLS, Shepard function and CSRBF to approximate the trial functions can be found in [5]. In MLPG3, letting the local domain to be the entire domain, in conjugation with MLS, leads to so-called least-squares meshfree method (LSMFM) [43].

#### 4.3. The LBIE based on LUSWF2

Based on the local unsymmetric weak formulation (LUSWF2) (5b), MLPG4 (the LBIE) is developed by employing the modified fundamental solution  $u^*$  (which vanishes at  $\partial\Omega_s$  as long as  $\partial\Omega_s$  does not intersect with  $\Gamma$ ), as the test function. Any meshless interpolations discussed in section 3 can be used to approximate the trial function.

The details of this method, using the MLS, Shepard function and CSRBF to construct the shape functions, can be found in [5,68]. It is noted that no derivatives of the shape functions are needed, in constructing the stiffness matrix for the interior nodes, as well as for those boundary nodes with no essential boundary condition prescribed sections on their local boundaries. However, singular integrals appear in the local boundary integral equation (defined only over a sphere centered at each point in question), to which special attention should be paid [50].

#### 4.4. Summary

A summary of the meshless approximations is given in table 1, where  $t$  denotes the highest-order of the polynomial which is completely included in the basis. A summary of the variety of MLPG methods is given in table 2. In this table, for convenience, we denote the support of the trial function as  $\Omega_{tr}$ , and the support of the test function as  $\Omega_{te}$ . The interrelationships of these developments can also be illustrated as in figure 2. Underlying all these meshless methods is the general concept of the meshless local Petrov–Galerkin method; thus, MLPG provides a rational basis for constructing meshless methods with a greater degree of flexibility.

In [5], a comprehensive study to these six MLPG methods is conducted. Among them, MLPG5 yields somewhat of a better result than the others, while all the methods

Table 1  
Selected meshless approximation of the trial function.

Interpolation ( $u$ )	Continuity	Completeness	Delta function property
MLS ( $u_1$ )	Highorder	$t$	No
Shepard function ( $u_2$ )	High order	0	No
Partitions of unity ( $u_3$ )	High order	$t$	No
RKPM ( $u_4$ )	High order	$t$	No
LPIM ( $u_5$ )	$\leq C^0$	$t$	Yes
LRPIM ( $u_6$ )	$\leq C^0$	$t$	Yes
CS-RBF ( $u_7$ )	High order	none	Yes
Finite cloud ( $u_8$ )	High order	$t$	No
SPH ( $u_9$ )	High order	0	No

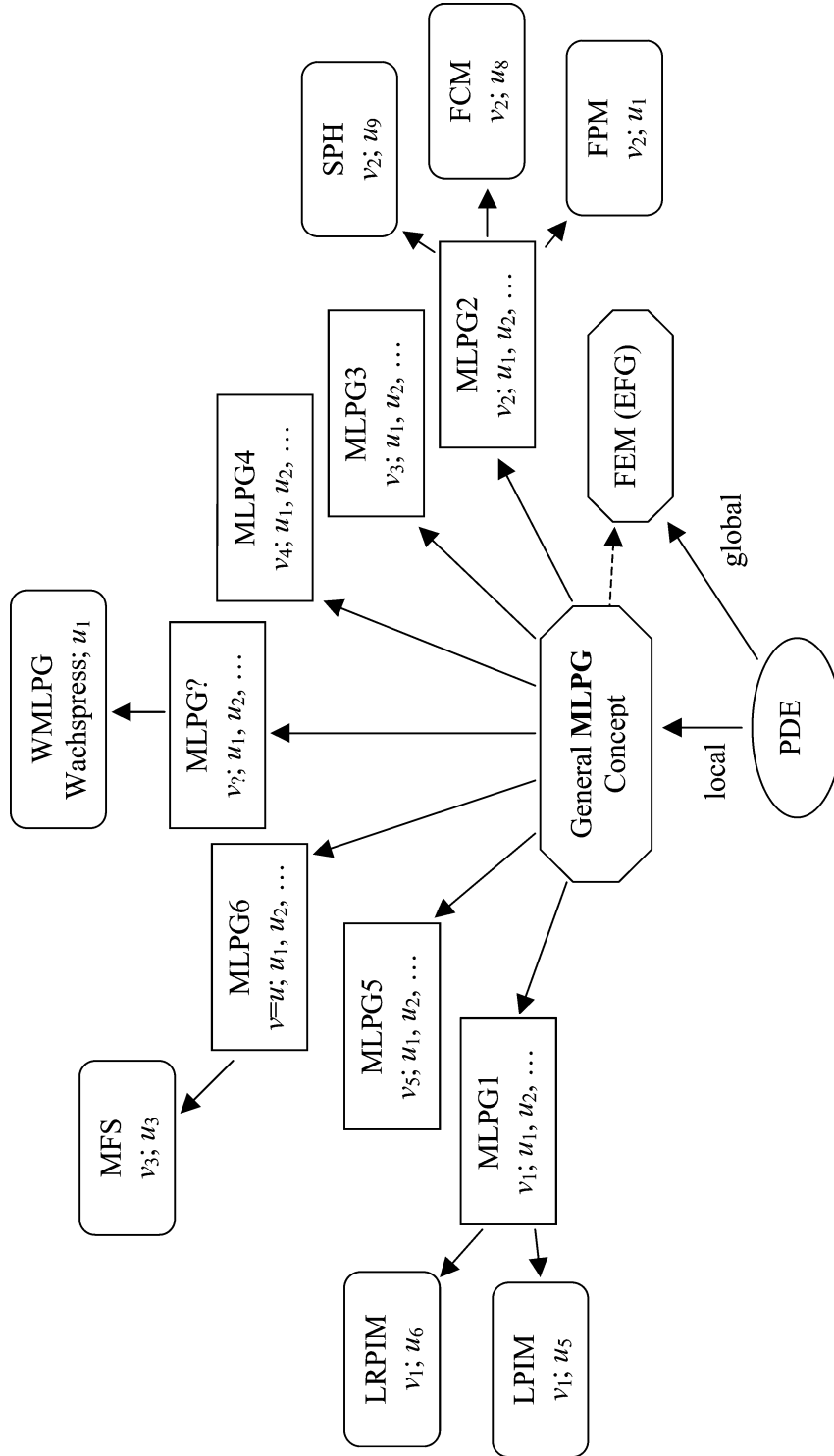


Figure 2. Variation of the MLPG approaches.

Table 2  
Meshless local Petrov–Galerkin (MLPG) methods.

Methods	Test function ( $v$ ) in $\Omega_{te}$	Local weak form over each $\Omega_s$	Relation between $\Omega_{te}$ and $\Omega_{tr}$	Integral to evaluate the weak-form
MLPG1	MLS weight function ( $v_1$ )	LSWF	$\Omega_{te} < \Omega_{tr}$	Domain integral
MLPG2	Kronecker delta ( $v_2$ )	LUSWF1	$\Omega_{te}$ can be arbitrary	None
MLPG3	Least square $\phi_{,ii}^I(\mathbf{x})$ ( $v_3$ )	LUSWF1	$\Omega_{te} = \Omega_{tr}$	Domain integral
MLPG4	Fundamental solution $u^*$ ( $v_4$ )	LUSWF2	$\Omega_{te} < \Omega_{tr}$	Singular boundary integral
MLPG5	Constant ( $v_5$ )	LSWF	$\Omega_{te} < \Omega_{tr}$	Regular boundary integral
MLPG6	Same as the trial function ( $v = u$ )	LSWF	$\Omega_{te} = \Omega_{tr}$	Domain integral

possess high accuracy. For the trial-function interpolations, it seems that the MLS yields somewhat of a better result than the Shepard function or the CSRBF. The rates of convergence in all the MLPG methods, especially using the MLS and Shepard functions as the trial function, are higher than that in the FEM.

MLPG has little or no preprocessing and postprocessing costs, thus the human-labor cost in MLPG5 is negligible compared to that in FEM; for the same accuracy, the computational cost in MLPG5 is also lower than that in FEM. Thus, we are certain that MLPG5 may prove to be a simple and efficient alternative to the currently popular finite element and boundary element methods.

## 5. Applications of the MLPG approach

Due to the distinct advantages, the MLPG methods are widely adopted as some of the efficient computational techniques to solve applied mechanics problems.

Atluri and Zhu [9] solved some elasto-static problems by using MLPG1. Kim and Atluri [27] solved some elasto-static problems by using MLPG6 with polygonal local-domains, and a method which uses primary and secondary nodes in the domain and on the global boundary is introduced. This method is very useful in an adaptive calculation. Batra and his coworkers employed MLPG1 method to analyze static [19], and transient [13] deformations near a crack/notch tip in a linear elastic plate. The row-sum technique was used to obtain the lumped mass matrices. The Newmark family of methods was taken as the time integration scheme. The numerical results showed that the MLPG method is an appreciate tool to treat the elastic problem.

MLPG4 has been successfully applied to potential problems, elastostatics, elastodynamics, thermoelasticity, and plate bending problems [6,48,49,51,53–55,68,69]. A summary of recent developments in the applications of MLPG4 can be found in [52].

Using MLPG6 with generalized MLS to construct the shape functions, Atluri et al. [2] studied the deformation of thin beams. Then, Cho and Atluri [20] extended it to the shear flexible beams based on a locking-free formulation. Raju and Phillips [46] applied MLPG1 and MLPG5 to a continuous beam problem to evaluate their effective-

ness, and discussed the effects of various parameters on the numerical results clearly and systematically. Their numerical results show that both MLPG1 and MLPG5 methods are effective. Gu and Liu [24] analyzed the static and free vibration of thin plate by means of MLPG1. Xiao and McCarthy [64] investigated the unilateral contact problem of beam by using MLPG1. Long and Atluri [34] applied MLPG1 to solve thin (Kirchhoff) plates. The quintic spline weight function is used in the MLS approximation, which leads to  $C^2$  approximations. Their numerical results show that the MLPG method possesses an excellent rate of convergence for the deflection and strain energy. Qian et al. [45] used MLPG1 and MLPG5 to analyze the deformation fields in a thick plate with a higher-order shear and normal deformable plate theory, and presented extensive studies on various parameters of the MLPG method for plate problems. Their numerical results showed that both MLPG1 and MLPG5 methods are effective to treat the elastostatic problem of a plate.

Tang et al. [57] developed a true rotation-free numerical approach based on the MLPG1 method for materials within the Toupin–Mindlin framework of strain gradient type constitutive theory. The remarkable accuracy in these numerical simulations shows promising characteristics of MLPG for solving general problems of material inelasticity, where strain-gradient effects may be important.

Recently, the MLPG method is extended to the three dimension problem. Li et al. [29] applied it to the 3-D problem problems with singularities, and material discontinuities. The high-order nature of MLPG provided accurate stress simulation when dealing with singular problem like Boussinesq problem which is very difficulty for FEM. Their numerical results also verified this viewpoint. With the combination of MLPG5 (interior) and MLPG2 (boundary), the truly meshless method can be applied efficiently to any 3-D solid with complicated geometry.

MLPG method is also promising in fluid mechanics. In fact, the MLPG method is much more flexible for introducing the upwinding concept, with very clear physical meaning. Several upwinding schemes for the MLPG method have been developed and applied to simulate the convective–diffusive transport [30] and the incompressible Navier–Stokes equations [31].

## 6. Other meshless methods

The research into meshless methods has become very active, only after the publication of the diffuse element method by Nayroles et al. [37]. Several so-called meshless methods (Element Free Galerkin (EFG)) by Belytschko et al. [16]; Reproducing Kernel Particle Method (RKPM) by Liu et al. [32]; the Partition of Unity Finite Element Method (PUFEM) by Babuska and Melenk [11]; hp-cloud method by Duarte and Oden [22]; Natural Element Method (NEM) by Sukumar et al. [56]; Meshless Galerkin methods using Radial Basis Functions (RBF) by Wendland [61]; have also been reported in literature since then. *The major differences in these meshless methods come only from the techniques used for interpolating the trial functions. All those method is based on the global symmetric weak forms.* Even though no mesh is required in these methods for the in-

terpolation of the trial and test functions for the solution variables, the use of shadow elements is inevitable in these methods, for the integration of the weak-form, or of the ‘energy’. Therefore, these methods are not truly meshless. If we take the local domain to be the entire domain in the local symmetric weak forms, and use the Galerkin method, the meshless methods based on global symmetric weak forms can be derived from the MLPG6 method. In general, MLPG method, based on local weak formulations, can include all the other meshless methods based on global formulation, as special cases. Besides in MLPG1, Liu and his coworkers [58] also used LPIM and LRPIM to construct the shape functions in the global Galerkin method.

To avoid the background mesh in the methods based on the global weak forms, Beissel and Belytschko [14] replaced the Gaussian quadrature with nodal integration. However, the nodal integration leads to a numerical instability [14]. In order to avoid the instability, a so-called stabilized conforming nodal integration was proposed by Chen et al. [18]. A Voronoi diagram is employed to obtain representative nodal domain and the associated weights for the stabilized conforming nodal integration. Hao et al. [25] proposed the moving particle finite element method (MPFEM), which is a combination of the finite element method and element-free Galerkin method. The nodal integration, instead of Gaussian quadrature, is employed to integrate the global weak form. At each node, the shape functions are constructed by enforcing certain reproducing conditions, by means of neighboring nodes that form element-like configurations. To determine the neighboring nodes, a searching algorithm was utilized. Then, the Delauney triangulation is used to compute the integration weight for this node. This procedure is similar to that of constructing elements.

Luan et al. [35] proposed a finite-cover element-free method (FCEFM). This method is mathematically based on the finite cover of manifold. Based on the global weak form, the system is discretized by virtue of the multiple weighted moving least square approximation. To integral the global weak form, a so-called “moving window procedure” is used: a rectangle or square window scans from one end of the domain to another step by step. It is noted that the domain is scanned with the window with no overlapping. As a matter of fact, this procedure is almost same as the use of background mesh.

Pardo [40–42] developed a very interesting meshless method based on a path integral formulation of linear elasticity. The well-known Feynman path integral formulation of quantum mechanics is equivalent to the Schrödinger equation. The differential equation governing the continuum system can be replaced by a fictitious Feynman path integral formulation by finding adequate infinitesimal Feynman propagators. Since the Feynman path integral formulation is a global form, to avoid the background mesh, the “local” concept must be introduced: a set of compact supported infinitesimal propagators are used. This method is a truly meshless method. However, it is not easy to derive the Feynman propagators from functional integrations, especially the compact supported infinitesimal Feynman propagators.

## 7. Conclusion

This paper summarizes the recent developments in the meshless methods. It is stated that MLPG is the general basis of truly meshless domain discretizations. Based on the general concept of the meshless local Petrov–Galerkin (MLPG) method, different types of meshless trial functions and different types of meshless test functions can be used, leading to a large variety of MLPG methods. Due to the locality, absolutely no meshes are needed in MLPG either for interpolation of the trial and test functions, or for the integration of the weak forms, while in other meshless methods (such as the EFG) require background cells. MLPG5 shows the potential to be a simple and efficient alternative to the currently popular finite element and boundary element methods. Although the MLPG method has made some strides, there are still many challenges remaining, such as an adequate numerical integration scheme, and its applications in the Nanotechnology, etc. A fast, accurate, cheap, and robust MLPG method is still on the way.

## Acknowledgements

The authors are pleased to acknowledge the support of the U.S. Army, NASA, and ONR (and the respective program officials Drs. R. Namburu, A.M. Rajendran, I.S. Raju, and Y.D.S. Rajapakse), of their research efforts.

## References

- [1] N.R. Aluru and G. Li, Finite cloud method: a true meshless technique based on a fixed reproducing kernel approximation, *Internat. J. Numer. Methods Engrg.* 50(10) (2001) 2373–2410.
- [2] S.N. Atluri, J.Y. Cho and H.G. Kim, Analysis of the beams, using the meshless local Petrov–Galerkin method, with generalized moving least squares interpolations, *Comput. Mech.* 24 (1999) 334–347.
- [3] S.N. Atluri, H.G. Kim and J.Y. Cho, A critical assessment of the truly meshless local Petrov–Galerkin (MLPG) and local boundary integral equation (LBIE) methods, *Comput. Mech.* 24 (1999) 348–372.
- [4] S.N. Atluri and S. Shen, *The Meshless Local Petrov–Galerkin (MLPG) Method* (Tech Science Press, Los Angeles, CA, 2002).
- [5] S.N. Atluri and S. Shen, The meshless local Petrov–Galerkin (MLPG) method: A simple and less-costly alternative to the finite element and boundary element methods, *CMES: Comput. Modeling Engrg. Sci.* 3(1) (2002) 11–52.
- [6] S.N. Atluri, J. Sladek, V. Sladek and T. Zhu, The local boundary integral equation (LBIE) and its meshless implementation for linear elasticity, *Comput. Mech.* 25 (2000) 180–198.
- [7] S.N. Atluri and T. Zhu, A new meshless local Petrov–Galerkin (MLPG) approach to nonlinear problems in computational modeling and simulation, *Comput. Modeling Simulation Engrg.* 3 (1998) 187–196.
- [8] S.N. Atluri and T. Zhu, A new meshless local Petrov–Galerkin (MLPG) approach in computational mechanics, *Comput. Mech.* 22 (1998) 117–127.
- [9] S.N. Atluri and T. Zhu, The meshless local Petrov–Galerkin (MLPG) approach for solving problems in elastostatics, *Comput. Mech.* 25 (2000) 169–179.
- [10] S.N. Atluri and T. Zhu, New concepts in meshless methods, *Internat. J. Numer. Mech. Engrg.* 47 (2000) 537–556.
- [11] I. Babuska and J.M. Melenk, The partition of unity method, *Internat. J. Numer. Methods Engrg.* 40 (1997) 727–758.

- [12] W. Barry and V. Thulasi, A wachspress meshless local Petrov–Galerkin method, [www.sce.ait.ac.th/people/faculty/wjbarry/](http://www.sce.ait.ac.th/people/faculty/wjbarry/) (2002).
- [13] R.C. Batra and H.K. Ching, Analysis of elastodynamic deformations near a crack/notch tip by the meshless local Petrov–Galerkin (MLPG) method, *CMES: Comput. Modeling Engrg. Sci.* 3(6) (2002) 717–730.
- [14] S. Beissel and T. Belytschko, Nodal integration of element-free Galerkin method, *Comput. Methods Appl. Mech. Engrg.* 139 (1996) 49–74.
- [15] T. Belytschko, Y. Krongauz, D. Organ, M. Fleming and P. Krysl, Meshless methods: An overview and recent developments, *Comput. Methods Appl. Mech. Engrg.* 139 (1996) 3–47.
- [16] T. Belytschko, Y.Y. Lu and L. Gu, Element-free Galerkin methods, *Internat. J. Numer. Methods Engrg.* 37 (1994) 229–256.
- [17] M.K. Chati and S. Mukherjee, The boundary node method for three-dimensional problems in potential theory, *Internat. J. Numer. Methods Engrg.* 47(9) (2000) 1523–1547.
- [18] J.S. Chen, C.T. Wu, S. Yoon and Y. You, A stabilized conforming nodal integration for Galerkin mesh-free methods, *Internat. J. Numer. Methods Engrg.* 50 (2001) 435–466.
- [19] H.K. Ching and R.C. Batra, Determination of crack tip fields in linear elastostatics by the meshless local Petrov–Galerkin (MLPG) method, *CMES: Comput. Modeling Engrg. Sci.* 2(2) (2001) 273–290.
- [20] J.Y. Cho and S.N. Atluri, Analysis of shear flexible beams, using the meshless local Petrov–Galerkin method, based on a locking-free formulation, *Engrg. Comput.* 18(1/2) (2001) 215–240.
- [21] S. De and K.J. Bathe, The method of finite spheres, *Comput. Mech.* 25(4) (2000) 329–345.
- [22] C. Duarte and J.T. Oden, Hp-cloud – a meshless method to solve boundary-value problems, *Comput. Methods Appl. Mech. Engrg.* 139 (1996) 237–262.
- [23] R.A. Gingold and J.J. Monaghan, Smoothed particle hydrodynamics: Theory and application to non-spherical stars, *Mon. Not. Roy. Astronom. Soc.* 181 (1977) 375–389.
- [24] Y.T. Gu and G.R. Liu, A meshless local Petrov–Galerkin (MLPG) formulation for static and free vibration analysis of thin plates, *CMES: Comput. Modeling Engrg. Sci.* 2(4) (2001) 463–476.
- [25] S. Hao, H.S. Park and W.K. Liu, Moving particle finite element method, *Internat. J. Numer. Methods Engrg.* 53(8) (2002) 1937–1958.
- [26] X. Jin, G. Li and N.R. Aluru, On the equivalence between least-squares and kernel approximations in meshless methods, *CMES: Comput. Modeling Engrg. Sci.* 2(4) (2001) 463–476.
- [27] H.G. Kim and S.N. Atluri, Arbitrary placement of secondary nodes and error control in the meshless local Petrov–Galerkin (MPLG) method, *CMES: Comput. Modeling Engrg. Sci.* 1(3) (2000) 11–32.
- [28] G. Li and N.R. Aluru, Boundary cloud method: A combined scattered point/boundary integral approach for boundary-only analysis, *Comput. Methods Appl. Math.* 191(21/22) (2002) 2337–2370.
- [29] Q. Li, S. Shen, Z.D. Han and S.N. Atluri, Application of meshless local Petrov–Galerkin (MLPG) to problems with singularities and material discontinuities in 3-D elasticity, *CMES: Comput. Modeling Engrg. Sci.* 4(5) (2003) 567–581.
- [30] H. Lin and S.N. Atluri, Meshless local Petrov–Galerkin (MPLG) method for convection–diffusion problems, *CMES: Comput. Modeling Engrg. Sci.* 1(2) (2000) 45–60.
- [31] H. Lin and S.N. Atluri, The meshless local Petrov–Galerkin (MPLG) method for solving incompressible Navier–Stokes equations, *CMES: Comput. Modeling Engrg. Sci.* 2(2) (2001) 117–142.
- [32] W.K. Liu, Y. Chen, R.A. Uras and C.T. Chang, Generalized multiple scale reproducing kernel particle methods, *Comput. Methods Appl. Mech. Engrg.* 139 (1996) 91–157.
- [33] G.R. Liu and Y.T. Gu, Comparisons of two meshfree local point interpolation methods for structural analyses, *CMES: Comput. Mech.* 29(2) (2002) 107–121.
- [34] S.Y. Long and S.N. Atluri, A meshless local Petrov–Galerkin method for solving the bending problem of a thin plate, *CMES: Comput. Modeling Engrg. Sci.* 3(1) (2002) 53–63.
- [35] M. Luan, R. Tian and Q. Yang, A new numerical method – finite-cover based element-free method, in: *Proc. of the 10th Internat. Conf. on Computer Methods and Advances in Geomechanics*, University of Arizona, Tucson, AZ, USA, 2001.

- [36] J.J. Monaghan, Particle methods for hydrodynamics, *Comput. Phys. Rep.* 3 (1985) 71–124.
- [37] B. Nayroles, G. Touzot and P. Villon, Generalizing the finite element method: Diffuse approximation and diffuse elements, *Comput. Mech.* 10 (1992) 307–318.
- [38] A. Needleman, Material rate dependent and mesh sensitivity in localization problems, *Comput. Methods Appl. Mech. Engrg.* 67 (1988) 68–85.
- [39] E. Onate, S. Idelsohn, O.C. Zienkiewicz and R.L. Taylor, A finite point method in computational mechanics. Applications to convective transport and fluid flow, *Internat. J. Numer. Methods Engrg.* 39 (1996) 3839–3866.
- [40] E. Pardo, Meshless method for linear elastostatics based on a path integral formulation, *Internat. J. Numer. Methods Engrg.* 47(8) (2000) 1463–1480.
- [41] E. Pardo, Convergence and accuracy of the path integral approach for elastostatics, *Comput. Methods Appl. Mech.* 191(19/20) (2002) 2191–2219.
- [42] E. Pardo, Blurred derivatives and meshless methods, *Internat. J. Numer. Methods Engrg.* 56(2) (2003) 295–324.
- [43] S.H. Park and S.K. Young, The least-squares meshfree method, *Internat. J. Numer. Methods Engrg.* 52 (2001) 997–1012.
- [44] M.J.D. Powell, The theory of radial basis function approximation in 1990, in: *Advances in Numerical Analysis*, Vol. 2, ed. W. Light (Clarendon Press, Oxford, 1992) pp. 105–210.
- [45] L.F. Qian, R.C. Batra and L.M. Chen, Elastostatic deformations of a thick plate by using a higher-order shear and normal deformable plate theory and two meshless local Petrov–Galerkin (MLPG) method, *CMES: Comput. Modeling Engrg. Sci.* 4(1) (2003) 161–176.
- [46] I.S. Raju and D.R. Phillips, Further developments in the MLPG method for beam problems, *CMES: Comput. Modeling Engrg. Sci.* 4(1) (2003) 141–160.
- [47] D. Shepard, A two-dimensional function for irregularly spaced points, in: *Proc. of ACM National Conf.*, 1968, pp. 517–524.
- [48] J. Sladek and V. Sladek, A Trefftz function approximation in local boundary integral equations, *Comput. Mech.* 28(3/4) (2002) 212–219.
- [49] J. Sladek and V. Sladek, Application of local boundary integral equation method into micropolar elasticity, *Engrg. Anal. Bound. Elem.* 27(1) (2003) 81–90.
- [50] J. Sladek, V. Sladek and S.N. Atluri, Local boundary integral equation (LBIE) method for solving problems of elasticity with nonhomogeneous material properties, *Comput. Mech.* 24(6) (2000) 456–462.
- [51] J. Sladek, V. Sladek and S.N. Atluri, A pure contour formulation for the meshless local boundary integral equation method in thermoelasticity, *CMES: Comput. Modeling Engrg. Sci.* 2(4) (2001) 423–434.
- [52] J. Sladek, V. Sladek and S.N. Atluri, Application of local boundary integral equation method to solve boundary value problems, *Internat. Appl. Mech.* 38(9) (2002) 3–27.
- [53] V. Sladek, J. Sladek, S.N. Atluri and R. Keer, Numerical integration of singularities in meshless implementation of the LBIE, *Comput. Mech.* 25 (2000) 394–403.
- [54] J. Sladek, V. Sladek and H.A. Mang, Meshless local boundary integral equation method for simply supported and clamped plates resting on elastic foundation, *Comput. Methods Appl. Math.* 191(51/52) (2002) 5943–5959.
- [55] J. Sladek, V. Sladek and R. Van Keer, Global and local Trefftz boundary integral formulations for sound vibration, *Adv. Engrg. Software* 33(7–10) (2002) 469–476.
- [56] N. Sukumar, B. Moran and T. Belytschko, The natural element method in solid mechanics, *Internat. Numer. Methods Engrg.* 43 (1998) 839–887.
- [57] Z. Tang, S. Shen and S.N. Atluri, Analysis of materials with strain gradient effects: A meshless local Petrov–Galerkin approach with nodal displacements only, *CMES: Comput. Modeling Engrg. Sci.* 4(1) (2003) 177–196.

- [58] J.G. Wang and G.R. Liu, A point interpolation meshless method based on radial basis functions, *Internat. J. Numer. Methods Engrg.* 54(11) (2002) 1623–1648.
- [59] H. Wendland, Piecewise polynomial, positive definite and compactly supported radial basis functions of minimal degree, *Adv. Comput. Math.* 4 (1995) 389–396.
- [60] H. Wendland, Error estimates for interpolation by compactly supported radial basis functions of minimal degree, *J. Approx. Theory* 93 (1998) 258–272.
- [61] H. Wendland, Meshless Galerkin methods using radial basis function, *Math. Comp.* 68(228) (1999) 1521–1531.
- [62] Z. Wu, Hermite–Birkhoff interpolation of scattered data by radial basis functions, *Approx. Theory Appl.* 8 (1992) 1–10.
- [63] Z. Wu, Compactly supported positive definite radial functions, *Adv. Comput. Math.* 4 (1995) 283–292.
- [64] J.R. Xiao and M.A. McCarthy, Local variational inequality and meshless analysis of a beam involving unilateral contact conditions, in: *Proc. of the ACMC-UK 10th Anniversary Conference*, Swansea, 2002, pp. 223–226.
- [65] J.M. Zhang and Z.H. Yao, Meshless regular hybrid boundary node method, *CMES: Comput. Modeling Engrg. Sci.* 2(3) (2001) 307–318.
- [66] X. Zhang, K.Z. Song, M.W. Lu and X. Liu, Meshless methods based on collocation with radial basis functions, *Comput. Mech.* 26(4) (2000) 333–343.
- [67] T. Zhu and S.N. Atluri, A modified collocation and a penalty formulation for enforcing the essential boundary conditions in the element free Galerkin method, *Comput. Mech.* 21 (1998) 211–222.
- [68] T. Zhu, J.D. Zhang and S.N. Atluri, A local boundary integral equation (LBIE) method in computational mechanics, and a meshless discretization approach, *Comput. Mech.* 21 (1998) 223–235.
- [69] T. Zhu, J.D. Zhang and S.N. Atluri, A meshless local boundary integral equation (LBIE) method for solving nonlinear problems, *Comput. Mech.* 22 (1998) 174–186.

# Truly Meshless Local Petrov-Galerkin (MLPG) Solutions of Traction & Displacement BIEs

Z. D. Han<sup>1</sup> and S. N. Atluri<sup>1</sup>

**Abstract:** The numerical implementation of the truly Meshless Local Petrov-Galerkin (MLPG) type weak-forms of the displacement and traction boundary integral equations is presented, for solids undergoing small deformations. In the accompanying part I of this paper, the general MLPG/BIE weak-forms were presented [Atluri, Han and Shen (2003)]. The MLPG weak forms provide the most general basis for the numerical solution of the non-hyper-singular displacement and traction BIEs [given in Han, and Atluri (2003)], which are simply derived by using the gradients of the displacements of the fundamental solutions [Okada, Rajiyah, and Atluri (1989a,b)]. By employing the various types of test functions, in the MLPG-type weak-forms of the non-hyper-singular dBIE and tBIE over the local sub-boundary surfaces, several types of MLPG/BIEs are formulated, while also using several types of non-element meshless interpolations for trial functions over the surface of the solid. Specifically, three types of MLPG/BIEs are formulated in that paper, i.e. MLPG/BIE1, MLPG/BIE2, and MLPG/BIE6, as per the consistent categorizations of the MLPG domain methods [Atluri and Shen (2002a)]. As the accompanying part II, this paper is devoted to MLPG/BIE6. In particular, the moving least squares (MLS) method has been extended for the approximation on three dimensional surfaces, which makes it possible for the MLPG/BIE methods to be truly meshless. Numerical examples, including crack problems, are presented to demonstrate that the present methods are very promising, especially for solving the elastic problems in which the singularities in displacements, strains, and stresses, are of primary concern.

**keyword:** Meshless Local Petrov-Galerkin approach (MLPG), Boundary Integral Equations (BIE), Non-

Hypersingular dBIE/tBIE, Moving Least Squares (MLS), MLPG/BIE.

## 1 Introduction

The meshless local Petrov-Galerkin (MLPG) approach has become very attractive as a very promising method for solving partial differential equations. The MLPG method was originally applied for domain discretizations in Atluri and Zhu (1998). The main advantage of this method over the widely used finite element methods is that it does not need any mesh either for the interpolation of the solution variables or for the integration of the weak forms. The MLPG approach is very general, and can be based on the symmetric or unsymmetric local weak-forms of the PDEs, and uses a variety of interpolation methods (trial functions), test functions, integration schemes with/without background cells, and their flexible combinations. Such generality has been widely investigated [Atluri and Shen (2002a,b)]. The many research successes in solving PDEs, demonstrate that the MLPG method, and its variants, become some of the most promising alternative methods for computational mechanics.

The boundary integral equations (BIEs) have also been developed for solving PDEs, because of their efficiency in certain applications, in comparison to the domain-solution methods. They have been applied to solve linear elastic isotropic solid mechanics problems [Okada, Rajiyah, and Atluri (1990)], 3-D dynamic problems [Hatzigeorgiou, and Beskos (2002)], cracked plate problems [Wen, Aliabadi, and Young (2003), El-Zafrany (2001)], acoustic problems [Gaul, Fischer, and Nackenhorst (2003)], and biological systems [Muller-Karger, Gonzalez, Aliabadi and Cerrolaza] (2001)]. It is well known that the hyper-singularities of the traction BIEs, as derived directly from differentiating the displacement BIEs, hinder their applications in various numerical implementations. The hyper-singular BIEs need some spe-

<sup>1</sup> Center for Aerospace Research & Education  
University of California, Irvine  
5251 California Avenue, Suite 140  
Irvine, CA, 92612, USA

cial treatments, such as the various de-singularization techniques [Richardson and Cruse (1996)]. In contrast, as far back as 1989, Okada, Rajiyah, and Atluri (1989a,b, 1990) have proposed a simple way to *directly derive* the integral equations for the gradients of displacements. It resulted in “non-hyper-singular” boundary integral equations for the gradients of displacements, and these have been applied to solve the nonlinear problems successfully. Recently, this concept has been followed and extended for a *directly-derived* traction BIE [Han and Atluri (2002, 2003)], which is also “non-hyper-singular”  $[1/r^2]$ , as opposed to being “hyper-singular”  $[1/r^3]$ . Han and Atluri (2003) have also proposed a very straightforward and simple procedure to de-singularize the “non-hyper-singular” integrals, in order to render them numerically tractable, with only a weak singularity. These weakly-singular dBIE and tBIE are solved here by using the MLPG approaches, by writing their local weak-forms in the local sub-boundary surfaces. These meshless solution methods for solving BIEs are labeled as MLPG/BIE approaches. The generalities of the MLPG/BIE approaches have been discussed in the accompanying part I of the paper [Atluri, Han and Shen (2003)], in which various forms of MLPG/BIEs were proposed. Some issues in the numerical implementation have also been addressed there.

In the present paper, we implement the formulations proposed in Atluri, Han and Shen (2003) for the MLPG/BIE6 and solve some elastic problems, including fracture mechanics problems of non-planar crack-growth. The MLS method is used to construct the interpolation functions on the surface of a three-dimensional body. It is well unknown that the moment matrix becomes singular or nearly singular, if the 3-D Cartesian coordinates are used in the MLS over a general 3-D surface. For three dimensional surface cases, the curvilinear coordinates are used in the boundary node method (BNM) [Gowrishankar and Mukherjee (2002)], in which the background cells are required for the approximation, as well as for the integration. It prevents the meshless BIE methods to be truly meshless, since it still involves the mesh generation and re-meshing. As an alternate implementation, the varying polynomial basis may be chosen, with the use of Cartesian coordinates, so that the singularity in the MLS is eliminated, as proposed for the boundary cloud method (BCM) [Li and Aluru (2003)]. However, it is difficult to choose the polynomial basis

for the arbitrary 3D surfaces. Secondly, the local geometry information is required to help in choosing the basis. The idea of the varying basis is promising, but is difficult for the numerical implementation, as worse results were reported by the authors [Li and Aluru (2003)]. In the present paper, we check the singularity of the moment matrix, and determine the local normal direction of 3D surfaces from its lowest eigenvector. Then, the singularity of the moment matrix has been cancelled, by using this information on the local normal direction. *With this extension, the local geometry information or the background cells are not required for the MLS, to construct the interpolation functions.* It leads to truly meshless BIE methods, if the integration schemes are based on nodal influence domains, as discussed in [Atluri, Han and Shen (2003)]. In this paper, we focus on the displacement and traction MLPG/BIEs in their local symmetric weak-forms, with the combination of the enhanced MLS surface interpolation method.

The outline of the paper is as follows: Section 2 summarizes the non-hypersingular displacement and traction BIEs [Han and Atluri (2003)], and their MLGP approaches [Atluri, Han and Shen (2003)]; In Section 3, the MLS approximation is extended to recondition the singular or nearly singular moment matrix when it is applied for the approximation over the three dimensional surface; Section 4 discusses the numerical results by using the moving least squares in the MLPG/BIE6 method. Some conclusions are made in Section 5.

## 2 Non-Hyper-singular MLPG Displacement and Traction BIEs

This section summarizes, for the sake of completeness, the non-hypersingular MLPG displacement and traction BIEs for a linear elastic, homogeneous, isotropic solid. They were proposed and discussed in detail in [Atluri, Han and Shen (2003)], by extending the general non-hyper-singular dBIE and tBIEs through the MLPG approaches [Han and Atluri (2003)].

### 2.1 BIEs for elastic problems

Consider a linear elastic, homogeneous, isotropic body in a domain  $\Omega$ , with a boundary  $\partial\Omega$ . The Lamé constants of the linear elastic isotropic body are  $\lambda$  and  $\mu$ ; and the corresponding Young's modulus and Poisson's ratio are  $E$  and  $\nu$ , respectively. We use Cartesian coordinates  $\xi_i$ ,

and the attendant base vectors  $\mathbf{e}_i$ , to describe the geometry in  $\Omega$ . The solid is assumed to undergo infinitesimal deformations. The equations of balance of linear and angular momentum can be written as:

$$\nabla \cdot \boldsymbol{\sigma} + \mathbf{f} = \mathbf{0}; \quad \boldsymbol{\sigma} = \boldsymbol{\sigma}^t; \quad \nabla = \mathbf{e}_i \frac{\partial}{\partial \xi_i} \quad (1)$$

The strain-displacement relations are:

$$\boldsymbol{\varepsilon} = \frac{1}{2}(\nabla \mathbf{u} + \mathbf{u} \nabla) \quad (2)$$

The constitutive relations of an isotropic linear elastic homogeneous solid are:

$$\boldsymbol{\sigma} = \lambda \mathbf{I}(\nabla \cdot \mathbf{u}) + 2\mu \boldsymbol{\varepsilon} \quad (3)$$

The forms of the boundary integral equations, which are used in the present paper, are given by [Han and Atluri 2003], for displacement,

$$u_p(\mathbf{x}) = \int_{\partial\Omega} t_j(\xi) u_j^{*p}(\mathbf{x}, \xi) dS - \int_{\partial\Omega} n_i(\xi) u_j(\xi) \sigma_{ij}^{*p}(\mathbf{x}, \xi) dS \quad (4a)$$

and for traction

$$-t_b(\mathbf{x}) = \int_{\partial\Omega} t_q(\xi) n_a(\mathbf{x}) \sigma_{ab}^{*q}(\mathbf{x}, \xi) dS + \int_{\partial\Omega} D_p u_q(\xi) n_a(\mathbf{x}) \Sigma_{abpq}^{*}(\mathbf{x}, \xi) dS \quad (4b)$$

where  $u_j^{*p}$ ,  $\sigma_{ij}^{*p}$  and  $\Sigma_{abpq}^{*}$  are kernel functions, which were first given in Han and Atluri (2003) and listed in the appendix for 2D and 3D problems separately; the surface tangential operator  $D_t$  is defined as,

$$D_t = n_r e_{rst} \frac{\partial}{\partial \xi_s} \quad (5)$$

It should be pointed out that dBIE and tBIE in Eq. (4) are directly derived without hyper-singularities, as originally presented in [Okada, Rajiyah, and Atluri (1989a,b)]. They are both numerically tractable after desingularization by using the identities of the fundamental solution [Han and Atluri (2003)].

## 2.2 MLPG Approaches

The meshless approach for solving PDEs has attracted much attention during the past decades. As a general method, the MLPG approach was first proposed by Atluri and Zhu (1998) for solving linear potential problems, by using either a local symmetric weak form, or an unsymmetric weak form of the governing equation *over the local sub domain, and such local domains may overlap each other*. The generality of the MLPG, and its variants, are comprehensively investigated in Atluri and Shen (2002a,b). This approach can also be used for solving BIEs, instead of using traditional element-based methods, such as the Boundary Element Method. Following the general idea as presented in Atluri and Zhu (1998), one may consider a local sub-boundary surface  $\partial\Omega_L$ , with its boundary contour  $\Gamma_L$ , as a part of the whole boundary-surface, as shown in Figure 1, for a 3-D solid. Eq. (4) may be satisfied in weak-forms over the sub-boundary surface  $\partial\Omega_L$ , by using a Local Petrov-Galerkin scheme, as:

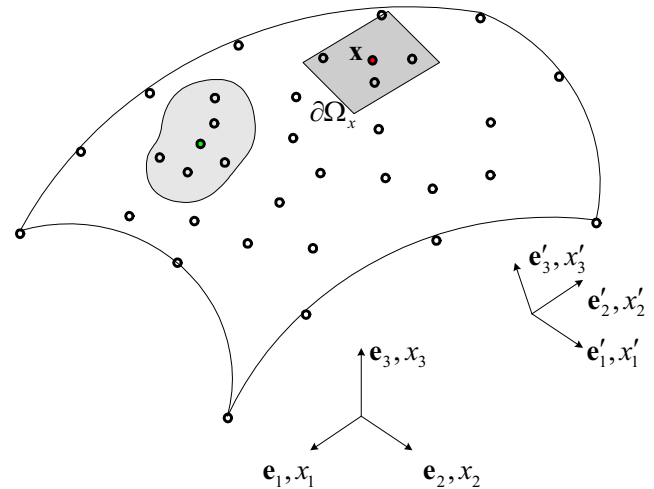


Figure 1 : A sub-part of the boundary around point  $\mathbf{x}$

$$\begin{aligned} & \int_{\partial\Omega_L} w_p(\mathbf{x}) u_p(\mathbf{x}) dS_x \\ &= \int_{\partial\Omega_L} w_p(\mathbf{x}) dS_x \int_{\partial\Omega} t_j(\xi) u_j^{*p}(\mathbf{x}, \xi) dS \\ & - \int_{\partial\Omega_L} w_p(\mathbf{x}) dS_x \int_{\partial\Omega} n_i(\xi) u_j(\xi) \sigma_{ij}^{*p}(\mathbf{x}, \xi) dS \end{aligned} \quad (6a)$$

$$\begin{aligned}
& - \int_{\partial\Omega_L} w_b(\mathbf{x}) t_b(\mathbf{x}) dS_x \\
& = \int_{\partial\Omega_L} w_b(\mathbf{x}) dS_x \int_{\partial\Omega} t_q(\xi) n_a(\mathbf{x}) \sigma_{ab}^{*q}(\mathbf{x}, \xi) dS_\xi \\
& + \int_{\partial\Omega_L} w_b(\mathbf{x}) dS_x \int_{\partial\Omega} D_p u_q(\xi) n_a(\mathbf{x}) \Sigma_{abpq}^*(\mathbf{x}, \xi) dS_\xi
\end{aligned} \quad (6b)$$

where  $\mathbf{w}(\mathbf{x})$  is a vector test function. If  $\mathbf{w}(\mathbf{x})$  is chosen as a Dirac delta function, i.e.  $w_b(\mathbf{x}) = \delta(\mathbf{x}, \mathbf{x}_m)$  at  $\partial\Omega_L$ , we obtain the standard “collocation” method for displacement and traction BIEs, at the collocation point  $\mathbf{x}_m$ . Their detail de-singularized forms have been presented in Atluri, Han and Shen (2003). One may also choose  $\mathbf{w}(\mathbf{x})$  in such way that it is continuous over the local sub boundary-surface  $\partial\Omega_L$  and zero at the contour  $\Gamma_L$ , and apply Stokes’ theorem to Eq. (6), and re-write it as:

$$\begin{aligned}
& \frac{1}{2} \int_{\partial\Omega_L} w_p(\mathbf{x}) u_p(\mathbf{x}) dS_x \\
& = \int_{\partial\Omega_L} w_p(\mathbf{x}) dS_x \int_{\partial\Omega} t_j(\xi) u_j^{*p}(\mathbf{x}, \xi) dS_\xi \\
& + \int_{\partial\Omega_L} w_p(\mathbf{x}) dS_x \int_{\partial\Omega} D_i(\xi) u_j(\xi) G_{ij}^{*p}(\mathbf{x}, \xi) dS_\xi \\
& + \int_{\partial\Omega_L} w_p(\mathbf{x}) dS_x \int_{\partial\Omega}^{CPV} n_i(\xi) u_j(\xi) \phi_{ij}^{*p}(\mathbf{x}, \xi) dS_\xi
\end{aligned} \quad (7a)$$

$$\begin{aligned}
& - \frac{1}{2} \int_{\partial\Omega_L} t_b(\mathbf{x}) w_b(\mathbf{x}) dS_x \\
& = \int_{\partial\Omega_L} D_a w_b(\mathbf{x}) dS_x \int_{\partial\Omega} t_q(\xi) G_{ab}^{*q}(\mathbf{x}, \xi) dS_\xi \\
& - \int_{\partial\Omega} t_q(\xi) dS_\xi \int_{\partial\Omega_L}^{CPV} n_a(\mathbf{x}) w_b(\mathbf{x}) \phi_{ab}^{*q}(\mathbf{x}, \xi) dS_x \\
& + \int_{\partial\Omega_L} D_a w_b(\mathbf{x}) dS_x \int_{\partial\Omega} D_p u_q(\xi) H_{abpq}^*(\mathbf{x}, \xi) dS_\xi
\end{aligned} \quad (7b)$$

where  $G_{ab}^{*q}$ ,  $\phi_{ab}^{*q}$  and  $H_{abpq}^*$  are fundamental solution related kernel functions and given in the appendix for both 2D and 3D problems.

In the present implementation, the test function  $w_b(\mathbf{x})$  is chosen to be identical to a function that is energy-conjugate to  $u_p$  (for dBIE) and  $t_b$  (for tBIE), namely, the nodal trial function  $\hat{t}_p(\mathbf{x})$  and  $\hat{u}_b(\mathbf{x})$ , respectively, we obtain the local symmetric Galerkin weak-forms of the weakly singular dBIE and tBIE, as:

$$\begin{aligned}
& \frac{1}{2} \int_{\partial\Omega_L} \hat{t}_p(\mathbf{x}) u_p(\mathbf{x}) dS_x \\
& = \int_{\partial\Omega_L} \hat{t}_p(\mathbf{x}) dS_x \int_{\partial\Omega} t_j(\xi) u_j^{*p}(\mathbf{x}, \xi) dS_\xi \\
& + \int_{\partial\Omega_L} \hat{t}_p(\mathbf{x}) dS_x \int_{\partial\Omega} D_i(\xi) u_j(\xi) G_{ij}^{*p}(\mathbf{x}, \xi) dS_\xi \\
& + \int_{\partial\Omega_L} \hat{t}_p(\mathbf{x}) dS_x \int_{\partial\Omega}^{CPV} n_i(\xi) u_j(\xi) \phi_{ij}^{*p}(\mathbf{x}, \xi) dS_\xi
\end{aligned} \quad (8a)$$

$$\begin{aligned}
& - \frac{1}{2} \int_{\partial\Omega_L} t_b(\mathbf{x}) \hat{u}_b(\mathbf{x}) dS_x \\
& = \int_{\partial\Omega_L} D_a \hat{u}_b(\mathbf{x}) dS_x \int_{\partial\Omega} t_q(\xi) G_{ab}^{*q}(\mathbf{x}, \xi) dS_\xi \\
& - \int_{\partial\Omega} t_q(\xi) dS_\xi \int_{\partial\Omega_L}^{CPV} n_a(\mathbf{x}) \hat{u}_b(\mathbf{x}) \phi_{ab}^{*q}(\mathbf{x}, \xi) dS_x \\
& + \int_{\partial\Omega_L} D_a \hat{u}_b(\mathbf{x}) dS_x \int_{\partial\Omega} D_p u_q(\xi) H_{abpq}^*(\mathbf{x}, \xi) dS_\xi
\end{aligned} \quad (8b)$$

### 3 Meshless Interpolation

The MLS method of interpolation is generally considered to be one of the best schemes to interpolate random data with a reasonable accuracy [Atluri and Zhu (1998)]. Although the nodal shape functions that arise from the MLS approximation have a very complex nature, they always preserve completeness up to the order of the chosen basis, and robustly interpolate the irregularly distributed nodal information. The MLS scheme has been widely used in domain discretization methods [Atluri and Shen (2002b)]. If we consider the MLS approximation on the boundary of a 3D solid domain, i.e., a 3D surface, the moment matrix in the MLS interpolation sometimes becomes singular, if global Cartesian coordinates are used in describing the surface, and if the surface containing the nodes in the domain of influence of the node in question becomes nearly planar. The two surface-curvilinear coordinates may be used here as an alternative choice, but it requires the background cells, which hinders it from being a true meshless implementation. In the present study,

we present a method to recondition the singular moment matrix, while still using the global Cartesian coordinates to approximate the trial function over a surface.

Consider a local sub-part of the boundary  $\partial\Omega$ , of a 3-D solid, denoted as  $\partial\Omega_x$ , the neighborhood of a point  $\mathbf{x}$ , which is a local region in the global boundary  $\partial\Omega$ . To approximate the function  $u$  in  $\partial\Omega_x$ , over a number of scattered points  $\{\mathbf{x}_I\}$ , ( $I = 1, 2, \dots, n$ ) (where  $\mathbf{x}$  is given, in the global Cartesian coordinates by  $x_1, x_2$  and  $x_3$ ), the moving least squares approximation  $u(\mathbf{x})$  of  $u$ ,  $\forall \mathbf{x} \in \partial\Omega_x$ , can be defined by

$$u(\mathbf{x}) = \mathbf{p}^T(\mathbf{x})\mathbf{a}(\mathbf{x}) \quad \forall \mathbf{x} \in \partial\Omega_x \quad (9)$$

where  $\mathbf{p}^T(\mathbf{x}) = [p_1(\mathbf{x}), p_2(\mathbf{x}), \dots, p_m(\mathbf{x})]$  is a monomial basis of order  $m$ ; and  $\mathbf{a}(\mathbf{x})$  is a vector containing coefficients, which are functions of the global Cartesian coordinates  $[x_1, x_2, x_3]$ , depending on the monomial basis. They are determined by minimizing a weighted discrete  $L_2$  norm, defined, as:

$$\begin{aligned} J(\mathbf{x}) &= \sum_{i=1}^m w_i(\mathbf{x}) [\mathbf{p}^T(\mathbf{x}_i)\mathbf{a}(\mathbf{x}) - \hat{u}_i]^2 \\ &\equiv [\mathbf{P} \cdot \mathbf{a}(\mathbf{x}) - \hat{\mathbf{u}}]^T \mathbf{W} [\mathbf{P} \cdot \mathbf{a}(\mathbf{x}) - \hat{\mathbf{u}}] \end{aligned} \quad (10)$$

where  $w_i(\mathbf{x})$  are the weight functions and  $\hat{u}_i$  are the fictitious nodal values.

The stationarity of  $J$  in Eq. (10), with respect to  $\mathbf{a}(\mathbf{x})$  leads to following linear relation between  $\mathbf{a}(\mathbf{x})$  and  $\hat{\mathbf{u}}$ ,

$$\mathbf{A}(\mathbf{x})\mathbf{a}(\mathbf{x}) = \mathbf{B}(\mathbf{x})\hat{\mathbf{u}} \quad (11)$$

where matrices  $\mathbf{A}(\mathbf{x})$  and  $\mathbf{B}(\mathbf{x})$  are defined by

$$\mathbf{A}(\mathbf{x}) = \mathbf{P}^T \mathbf{W} \mathbf{P} \quad \mathbf{B}(\mathbf{x}) = \mathbf{P}^T \mathbf{W} \quad \forall \mathbf{x} \in \partial\Omega_x \quad (12)$$

The MLS approximation is well defined only when the matrix  $\mathbf{A}(\mathbf{x})$  in Eq. (11) is non-singular. It needs to be reconditioned, if the monomial basis defined in the global Cartesian coordinate system for an approximation of  $u$  as in Eq. (9), becomes nearly linearly dependent on a 3-D surface. One may define a local set of orthogonal coordinates,  $x'_i$  as in Figure 1, on  $\partial\Omega_x$ . One may rewrite Eq. (9) as:

$$\begin{aligned} u &= [1; x_1; x_2; x_3; x_1^2; x_2^2; x_3^2; x_1x_2; x_2x_3; x_3x_1; \dots] \\ &\quad [a_1(\mathbf{x}); a_2(\mathbf{x}); a_3(\mathbf{x}); a_4(\mathbf{x}); \dots]^T \\ &\equiv [1; x'_1; x'_2; x'_3; x_1'^2; x_2'^2; x_3'^2; x'_1x'_2; x'_2x'_3; x'_3x'_1; \dots] \\ &\quad [a'_1(\mathbf{x}); a'_2(\mathbf{x}); a'_3(\mathbf{x}); a'_4(\mathbf{x}); \dots]^T \\ &\quad \text{for } \forall \mathbf{x} \in \partial\Omega_x \end{aligned} \quad (13)$$

Suppose  $\partial\Omega_x$  becomes nearly planar, which may be defined in the local-set of orthogonal coordinates, for instance, as  $x'_3 = \text{constant}$ . It is then clear that the monomial basis in Eq. (13), in terms of becomes linearly dependent. In fact, one may make the basis to be *linearly independent* again in Eq. (13), for instance, for  $x'_3 = \text{constant}$ , by setting the corresponding coefficients  $a'_i(\mathbf{x})$  to be zero. When this is done, the order of the vector  $\mathbf{p}'(\mathbf{x})$  is correspondingly reduced; and thus, correspondingly, the order of  $\mathbf{A}(\mathbf{x})$  in Eq. (11) is reduced. Thus, it can be seen that if one proceeds with a full monomial basis, with  $m$  basis functions in  $x_i$  coordinates in Eq. (9), and if the points on  $\partial\Omega_x$  are not all in the same plane, the matrix  $\mathbf{A}(\mathbf{x})$  in Eq. (11) will have the full rank of  $m$ . On the other hand, if  $\partial\Omega_x$  becomes almost planar, say normal to  $x'_3$ , then the rank of  $\mathbf{A}(\mathbf{x})$  is clearly only  $(m - n)$ , where  $n$  is the reduction in the number of basis due to the fact that  $x'_3 = \text{constant}$ . Thus, by simply monitoring the eigen-values of  $\mathbf{A}(\mathbf{x})$ , and if a set of eigen-values becomes nearly or precisely zero, we automatically detect that  $\partial\Omega_x$  is becoming nearly planar. In addition, it implies that the normal to the surface can be determined from the lowest eigenvalue of matrix  $\mathbf{A}(\mathbf{x})$  when it is singular or nearly-singular, without the local geometry information. It makes the present method to be truly meshless, which does need any background cells to define the geometry as well as the normal direction, if the boundary integrals are handled based on the nodal influence domain [Atluri, Han, and Shen (2003)].

Once coefficients  $\mathbf{a}(\mathbf{x})$  in Eq. (11) are determined, one may obtain the approximation from the nodal values at the local scattered points, by substituting them into Eq. (9), as

$$u(\mathbf{x}) = \Phi^T(\mathbf{x})\hat{\mathbf{u}} \quad \forall \mathbf{x} \in \partial\Omega_x \quad (14)$$

where  $\Phi(\mathbf{x})$  is the so-called shape function of the MLS approximation, defined as,

$$\Phi(\mathbf{x}) = \mathbf{p}^T(\mathbf{x})\mathbf{A}^{-1}(\mathbf{x})\mathbf{B}(\mathbf{x}) \quad (15)$$

The weight function in Eq. (10) defines the range of influence of node  $I$ . Normally it has a compact support. The possible choices are the Gaussian and spline weight functions with compact supports, which have been fully studied in Atluri and Shen (2002a).

It should be pointed out that the shape functions given in Eq. (15) are based on the fictitious nodal values. This

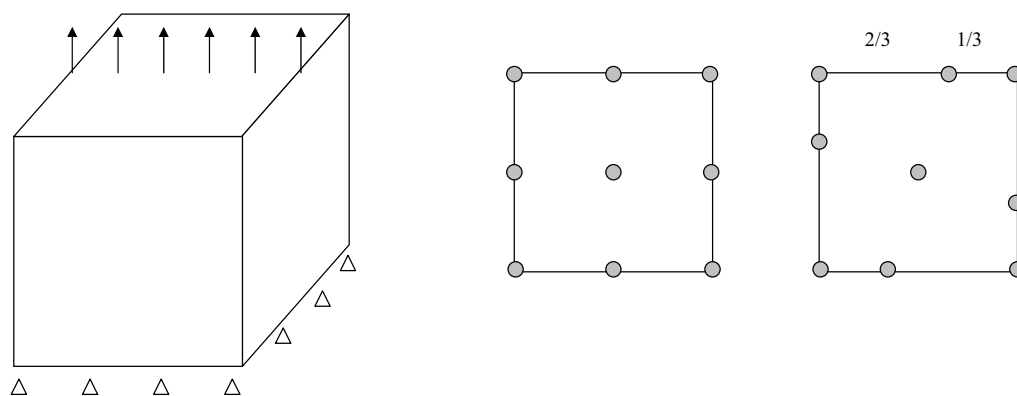


**Figure 2 :** A cube under uniform tension, and its nodal configurations

introduces an additional complication, since all the nodal values in BIEs are the direct boundary values, a situation which is totally different from the domain meshless methods. As a practical way, a conversion matrix is used to map the fictitious values to true values and applied to the system equations.

#### 4 Numerical Experiments

Several problems in three-dimensional linear elasticity are solved to illustrate the effectiveness of the present method. The numerical results of the MLPG/BIE6 method as applied to problems in 3D elasto-statics, specifically (i) a cube, (ii) a hollow sphere, (iii) a concentrated load on a semi-infinite space, and (iv) non-planar fatigue growth of an elliptical crack, are discussed.

##### 4.1 Cube under uniform tension

The first example is the standard patch test, shown in Figure 2. A cube under the uniform tension is considered. The material parameters are taken as  $E = 1.0$ , and  $\nu = 0.25$ . All six faces are modeled with the same configurations with 9 nodes. Two nodal configurations are used for the testing purpose: one is regular and another is irregular, as shown in Figure 2. In the patch tests, the uniform tension stress is applied on the upper face and the proper displacement constraints are applied to the lower face.

The satisfaction of the patch test requires that the displacements are linear on the lateral faces, and are constant on the upper face; and the stresses are constant on all faces. It is found that the present method passes the patch tests. The maximum numerical errors are

$1.7 \times 10^{-7}$  and  $3.5 \times 10^{-7}$  for two nodal configurations, respectively, which may be limited by the computer.

##### 4.2 3D Lamé problem

The 3D Lamé problem consists of a hollow sphere under internal pressure, as illustrated in Figure 3. The geometry is defined with the inner and outer radius of 1.0 and 4.0, respectively. The Young's modulus is chosen as and the Poisson ratio. The internal pressure is applied. The inner and outer surfaces are modeled with 772 nodes in the present analysis.

The radial displacement field is given in [Timoshenko &

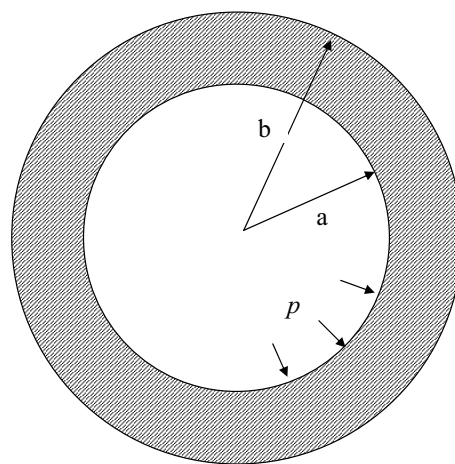


**Figure 3 :** A hollow sphere under internal pressure (Lamé problem)

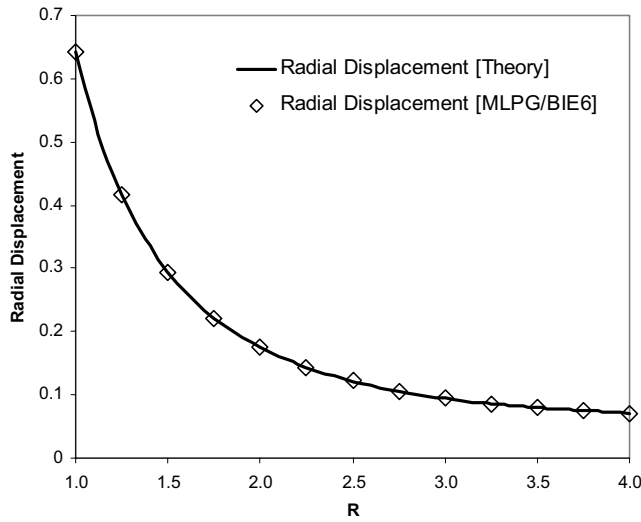


**Figure 4 :** Internal radial displacement for the Lamé problem

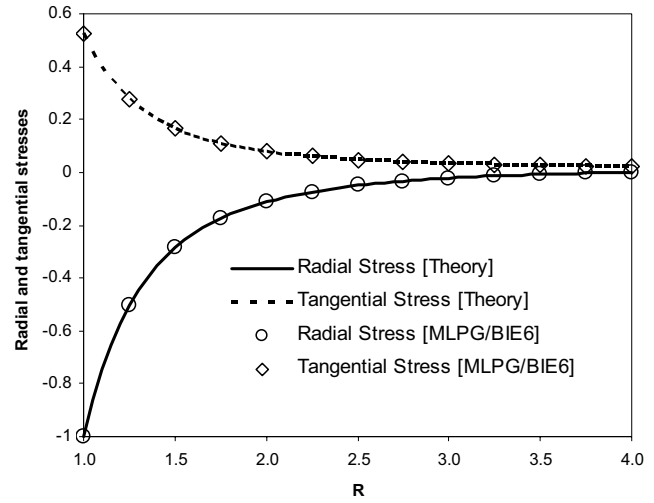


**Figure 5 :** Internal radial and tangential stresses for the Lamé problem

Goodier (1976)],

$$u_r = \frac{pRa^3}{E(b^3 - a^3)} \left[ (1 - 2\nu) + (1 + \nu) \frac{b^3}{2R^3} \right] \quad (16)$$

The radial and tangential stresses are

$$\begin{aligned} \sigma_r &= \frac{pa^3(b^3 - R^3)}{R^3(a^3 - b^3)} \\ \sigma_\theta &= \frac{pa^3(b^3 + 2R^3)}{2R^3(b^3 - a^3)} \end{aligned} \quad (17)$$

The displacements are shown in Figure 4, and are compared with the analytical solution. As shown in Figure 5, the radial and tangential stresses are compared with the analytical solution. They agree with each other very well.

#### 4.3 A concentrated load on a semi-infinite space (Boussinesq problem)

The Boussinesq problem can simply be described as a concentrated load acting on a semi-infinite elastic medium with no body force, as shown in Figure 6. Because of its strong singularity, it is difficult for mesh-based domain methods without special treatments. As one of the MLPG domain methods, MLPG5 was applied to this problem in [Li, Shen, Han and Atluri (2003)]. We

solve this problem here by using the MLPG/BIE methods to handle the strong singularity. A circular surface with a radius of 20 is used to simulate the semi-infinite space. It is modeled alternatively with two nodal configurations, as shown in Figure 7: one has 649 nodes and another has 1417 nodes. Young's modulus and Poisson's ratio are chosen to be 1.0 and 0.25, respectively.

The exact displacement field within the semi-infinite

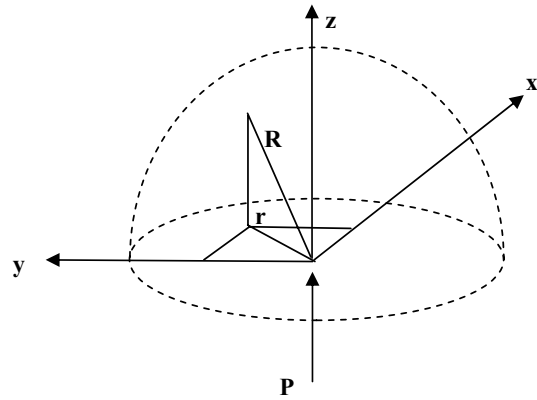
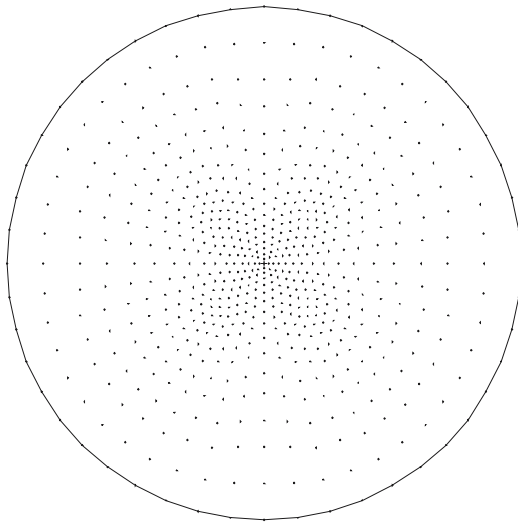
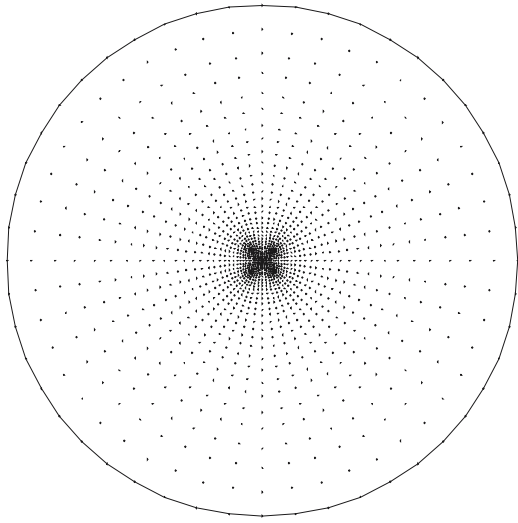


**Figure 6 :** A concentrated load on a semi-infinite space (Boussinesq Problem)



(a)



(b)

**Figure 7** : two nodal configurations for the Bossinesq Problem: (a) 672 nodes, and (b) 1417 nodes

medium is given in [Timoshenko & Goodier (1976)],

$$u_r = \frac{(1+\nu)P}{2E\pi R} \left[ \frac{zr}{R^2} - \frac{(1-2\nu)r}{R+z} \right]$$

$$u_w = \frac{(1+\nu)P}{2E\pi R} \left[ \frac{z^2}{R^2} + 2(1-\nu) \right] \quad (18)$$

where  $u_r$  is the radial displacement, and  $u_w$  is the verti-

cal one,  $R$  is the distance to the loading point,  $r$  is the projection of  $R$  on the loading surface.

The theoretical stresses field is:

$$\sigma_r = \frac{P}{2\pi R^2} \left[ -\frac{3r^2 z}{R^3} + \frac{(1-2\nu)R}{R+z} \right]$$

$$\sigma_\theta = \frac{(1-2\nu)P}{2\pi R^2} \left[ \frac{z}{R} - \frac{R}{R+z} \right]$$

$$\sigma_z = -\frac{3Pz^3}{2\pi R^5}$$

$$\tau_{zr} = \tau_{rz} = -\frac{3Prz^2}{2\pi R^5} \quad (19)$$

It is clear that the displacements and stresses are strongly singular and approach to infinity; with the displacement being  $O(1/R)$  and the stresses being  $O(1/R^2)$ .

The vertical displacement  $u_w$  along the  $z$ -axis is shown in Figure 8, and the radial and tangential stresses are shown in Figure 9 and Figure 10. The analytical solution for the displacement and stress are plotted on the same figures for comparison purpose. The zoom-in views within the shorter distance from the loading point are also shown in each figure. The shortest distance is 0.0025, where is very close the loading point and displacement and stresses increase rapidly. It can be clearly seen that both the MLPG/BIE displacement and stress results match the analytical solution very well, even within the very short distance, from the point of load application.

#### 4.4 Non-planar Crack Growth

An inclined elliptical crack with semi-axes  $c$  and  $a$ , subjected to fatigue loading, is shown in Figure 11. Its orientation is characterized by an angle,  $\alpha$ . This problem has been solved by using the boundary element method in [Nikishkov, Park, J.H., Atluri, S. N. (2001)] but it was reported that only  $K_I$  was obtained with the satisfactory agreement with the theoretical solution while failing in  $K_{II}$  and  $K_{III}$ . The present meshless method is applied to solve this problem, again. The nodal configuration is used to model the crack inclined at 45 degrees with 249 nodes, as shown in Figure 12. The exact solution for a tensile loading  $\sigma$  is given in [Tada, Paris and Irwin

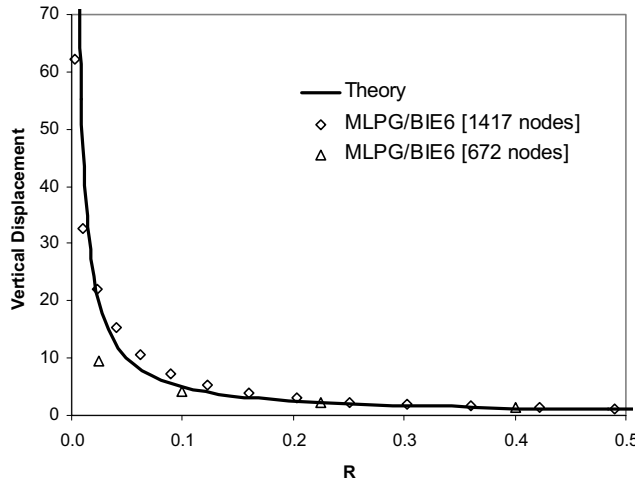
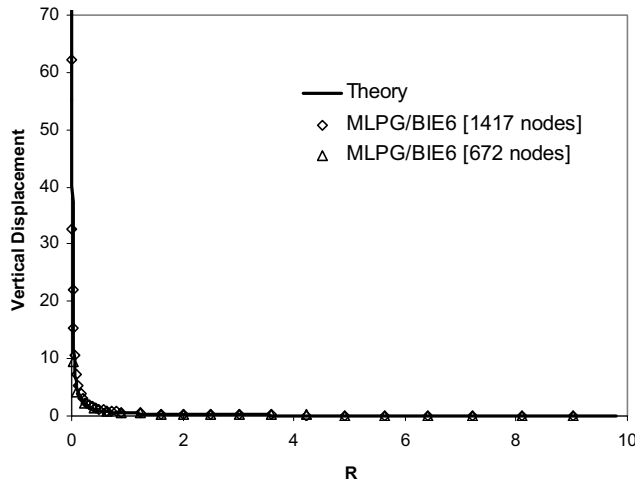


**Figure 8 :** Vertical displacement along z-axis for the Bossnesq problem

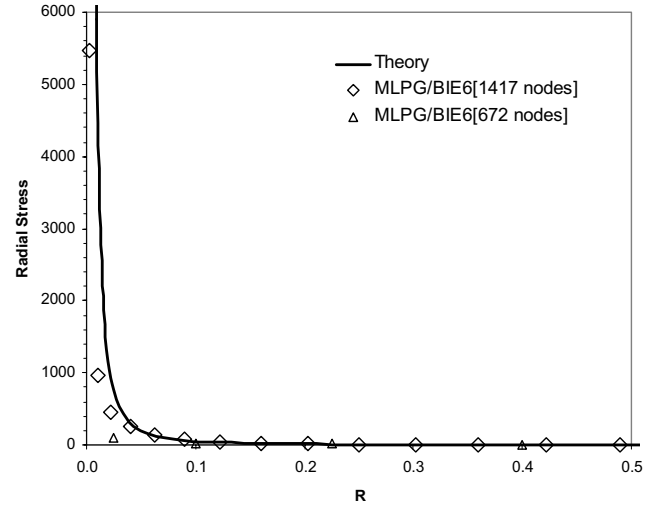
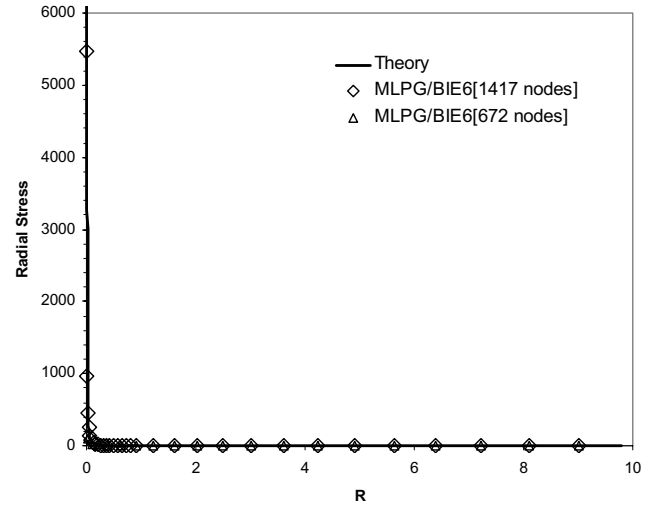


**Figure 9 :** Radial stress along z-axis for the Bossnesq problem

(2000)]:

$$K_I = K_0(1 + \cos 2\alpha) \frac{1}{E(k)} f(\varphi)$$

$$K_{II} = K_0 \sin 2\alpha \frac{k^2(a/c) \cos \varphi}{B f(\varphi)}$$

$$K_{III} = K_0 \sin 2\alpha \frac{k^2(1-\nu) \sin \varphi}{B f(\varphi)}$$

(20) The elliptical integrals of the first and second kind,  $E(k)$

where  $\varphi$  is the elliptical angle and

$$K_0 = \frac{\sigma \sqrt{\pi a}}{2}$$

$$f(\varphi) = (\sin^2 \varphi + (a/c)^2 \cos^2 \varphi)^{1/4}$$

$$k^2 = 1 - (a/c)^2$$

$$B = (k^2 - \nu)E(k) + \nu(a/c)^2 K(k) \quad (21)$$

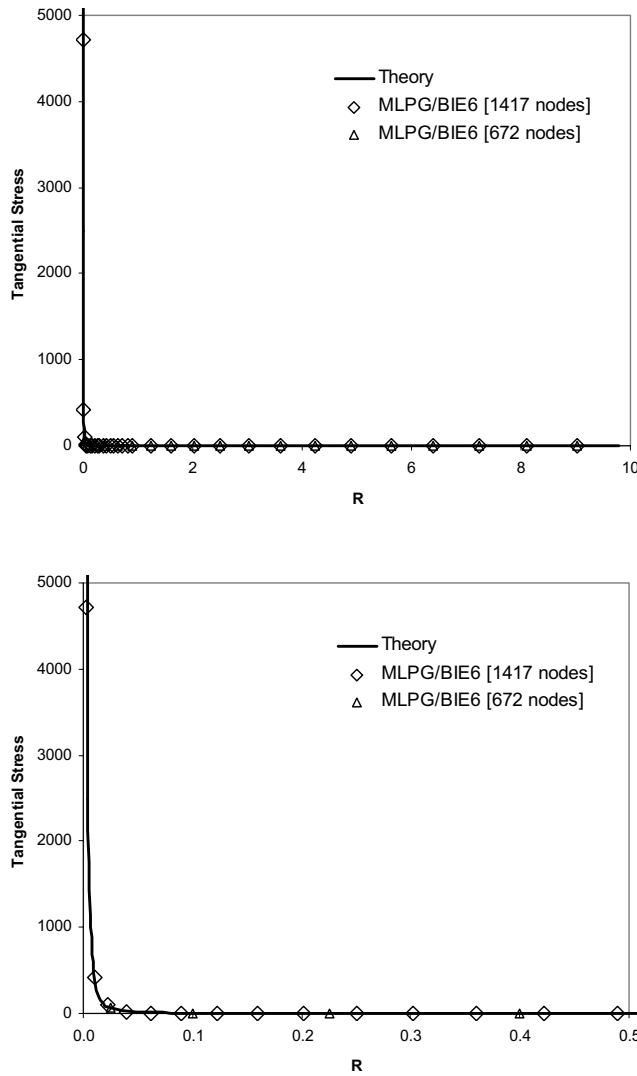


**Figure 10 :** Tangential stress along z-axis for the Bossi-esq problem

and  $K(k)$ , are defined as

$$K(k) = \int_0^{\pi/2} \frac{d\theta}{\sqrt{1 - k^2 \sin^2 \theta}}$$

$$E(k) = \int_0^{\pi/2} \sqrt{1 - k^2 \sin^2 \theta} d\theta \quad (22)$$

As a mixed-mode crack, the distribution of all three stress intensity factors,  $K_I$ ,  $K_{II}$  and  $K_{III}$ , along the crack front are shown in Figure 13, after being normalized by  $K_0$  as defined in Eq. (21). It can be seen that a good agree-

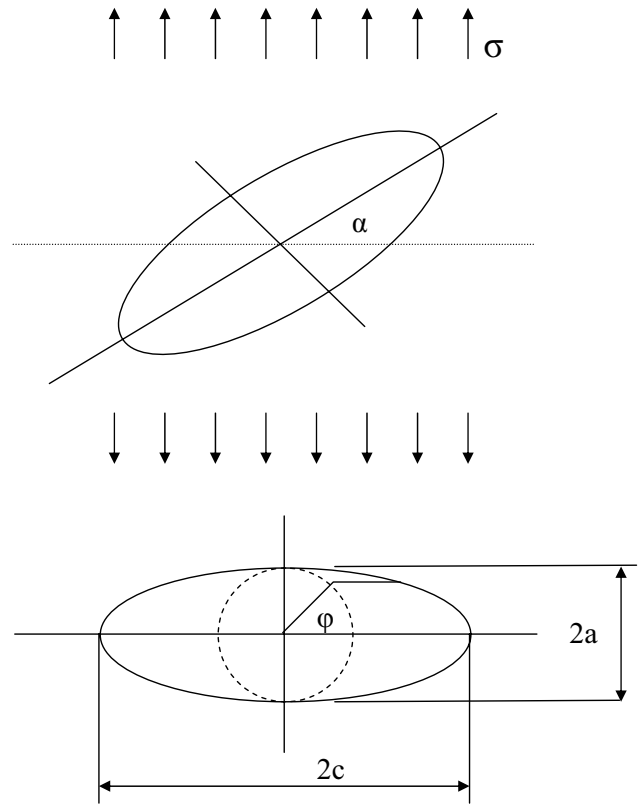


**Figure 11 :** Inclined elliptical crack under tension

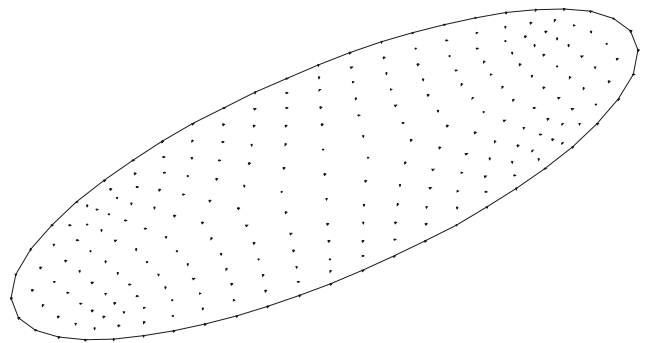


**Figure 12 :** Nodal configuration for an inclined elliptical crack

ment of the present numerical results with the theoretical solution is obtained.

The fatigue growth is also performed for this inclined crack. The Paris model is used to simulate fatigue crack growth. The crack growth rate with respect to the loading

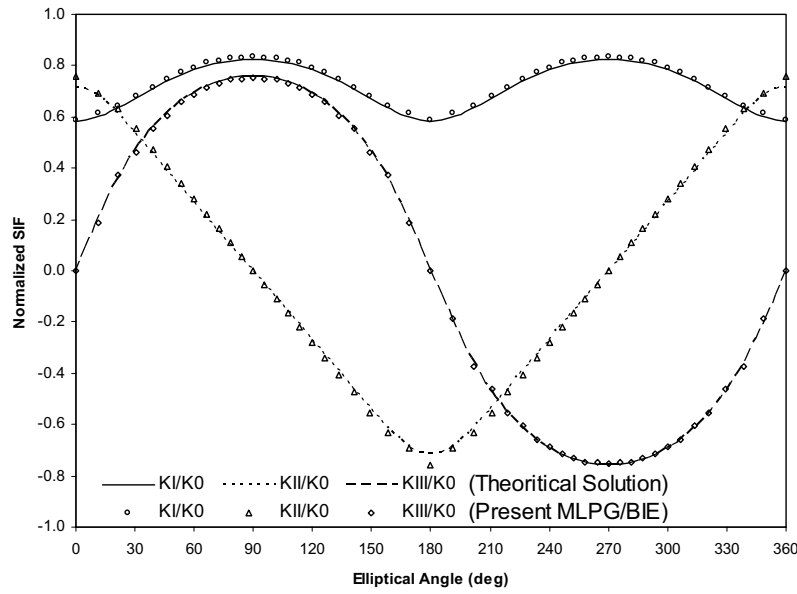


**Figure 13 :** Normalized stress intensity factors along the crack front of an inclined elliptical crack under tensile load

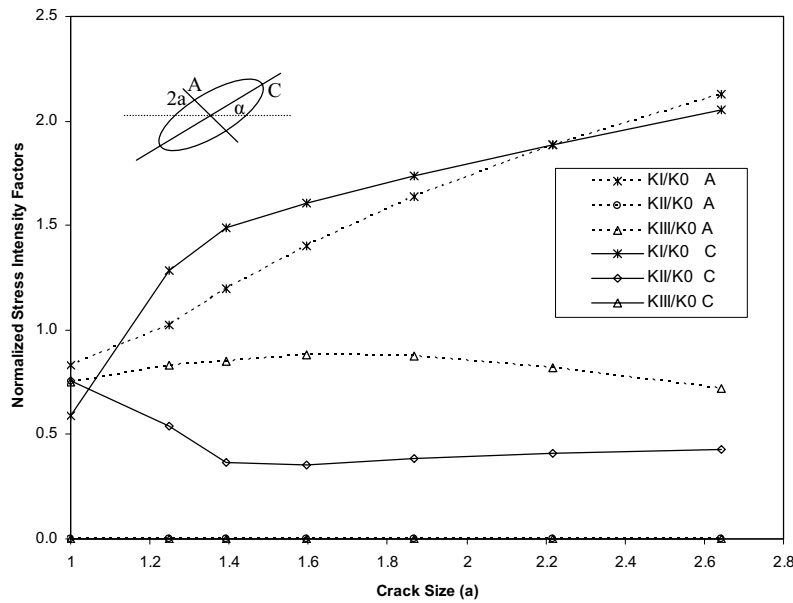


**Figure 14 :** Normalized stress intensity factors for the mixed-mode fatigue growth of an inclined elliptical crack

cycles,  $da/dN$ , is defined as:

$$\frac{da}{dN} = C(\Delta K_{eff})^n \quad (23)$$

in which the material parameters  $C$  and  $n$  are taken for 7075 Aluminum as  $C = 1.49 \times 10^{-8}$  and  $n = 3.21$  [Nikishkov, Park and Atluri(2001)]. The crack growth is simulated by adding nodes along the crack front. The

newly added points are determined through the  $K$  solutions. Seven increments are performed to grow the crack from the initial size  $a = 1$  to the final size  $a = 2.65$ . The normalized stress intensity factors during the crack growing are given in Figure 14, which are also normalized by  $K_0$  in Eq. (21). The results show that  $K_I$  keeps increasing while  $K_{II}$  and  $K_{III}$  are decreasing during the crack growth. It confirms that this mixed-mode crack

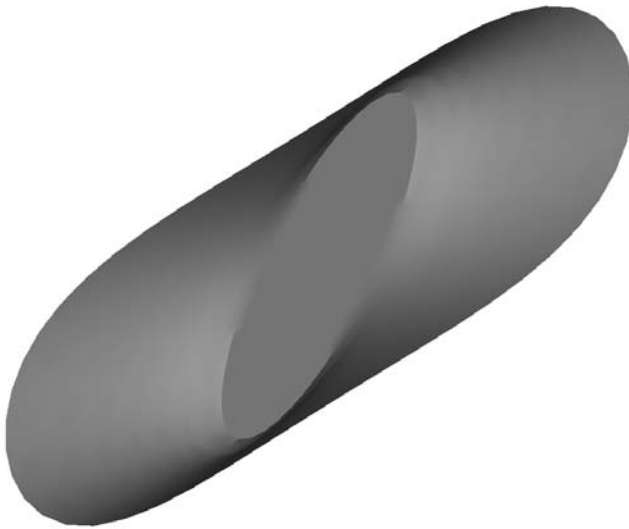


**Figure 15** : Final shape of an inclined elliptical crack after mixed-model growth

becomes a mode-I dominated one, while growing. The shape of the final crack is shown in Figure 15. It is clear that while the crack, in its initial configuration, starts out as a mixed-mode crack; and after a substantial growth, the crack configuration is such that it is in a pure mode-I state.

## 5 Closure

In this paper, we numerically implemented the specific symmetric form of “Meshless Local Petrov-Galerkin BIE Method” (MLPG/BIE6). It is one of the general MLPG/BIE methods, which are derived for displacement and traction BIEs, by using the concept of the general meshless local Petrov-Galerkin (MLPG) approach developed in Atluri et al [1998, 2002a,b, 2003]. The MLS surface-interpolation, with the use of Cartesian coordinates, is enhanced for the three dimensional surface without the requirement of a mesh or cells, to define the local geometry. It leads to the truly meshless BIE methods with the use of the nodal influence domain for the boundary integrations. The accuracy and efficiency of the present MLPG approach are demonstrated with numerical results.

**Acknowledgement:** This work was supported through a cooperative research agreement between the US Army Research Labs, and the University of California, Irvine,

through the US Army Research Office. Dr. R. Namburu is the cognizant program official. The many helpful discussions with Drs. R. Namburu, and A. M. Rajendran, are thankfully acknowledged.

## References

- Atluri, S. N.** (1985): Computational solid mechanics (finite elements and boundary elements) present status and future directions, *The Chinese Journal of Mechanics*.
- Atluri, S. N.; Han, Z. D.; Shen, S.** (2003): Meshless Local Petrov-Galerkin (MLPG) approaches for weakly-singular traction & displacement boundary integral equations, *CMES: Computer Modeling in Engineering & Sciences*, vol. 4, no. 5, pp. 507-517.
- Atluri, S. N.; Shen, S.** (2002a): The meshless local Petrov-Galerkin (MLPG) method. Tech. Science Press, 440 pages.
- Atluri, S. N.; Shen, S.** (2002b): The meshless local Petrov-Galerkin (MLPG) method: A simple & less-costly alternative to the finite element and boundary element methods. *CMES: Computer Modeling in Engineering & Sciences*, vol. 3, no. 1, pp. 11-52
- Atluri, S. N.; Zhu, T.** (1998): A new meshless local Petrov-Galerkin (MLPG) approach in computational mechanics. *Computational Mechanics*, Vol. 22, pp. 117-127.
- Cruse, T. A.; Richardson, J. D.** (1996): Non-singular Somigliana stress identities in elasticity, *Int. J. Numer. Meth. Engng.*, vol. 39, pp. 3273-3304.
- Fung, Y. C; Tong, P.** (2001): Classical and Computational Solid Mechanics, World Scientific, 930 pages.
- Gaul, L.; Fischer, M.; Nackenhorst, U.** (2003): FE/BE Analysis of Structural Dynamics and Sound Radiation from Rolling Wheels, *CMES: Computer Modeling in Engineering & Sciences*, vol. 3, no. 6, pp. 815-824.
- Gowrishankar, R.; Mukherjee S.** (2002): A ‘pure’ boundary node method for potential theory, *Communications in Numerical Methods*, vol. 18, pp. 411-427.
- Han. Z. D.; Atluri, S. N.** (2002): SGBEM (for Cracked Local Subdomain) – FEM (for uncracked global Structure) Alternating Method for Analyzing 3D Surface Cracks and Their Fatigue-Growth, *CMES: Computer Modeling in Engineering & Sciences*, vol. 3, no. 6, pp. 699-716.
- Han. Z. D.; Atluri, S. N.** (2003): On Simple For-

mulations of Weakly-Singular Traction & Displacement BIE, and Their Solutions through Petrov-Galerkin Approaches, *CMES: Computer Modeling in Engineering & Sciences*, vol. 4 no. 1, pp. 5-20.

**Hatzigeorgiou, G. D.; Beskos, D. E.** (2002): Dynamic Response of 3-D Damaged Solids and Structures by BEM, *CMES: Computer Modeling in Engineering & Sciences*, vol. 3, no. 6, pp. 791-802.

**Li, G.; Aluru, N. R.** (2003): A boundary cloud method with a cloud-by-cloud polynomial basis, *Engineering Analysis with Boundary Elements*, vol. 27, pp. 57-71.

**Muller-Karger, C. M.; Gonzalez, C.; Aliabadi, M. H.; Cerrolaza, M.** (2001): Three dimensional BEM and FEM stress analysis of the human tibia under pathological conditions, *CMES: Computer Modeling in Engineering & Sciences*, vol.2, no.1, pp.1-14.

**Nikishkov, G. P.; Park, J. H.; Atluri, S. N.** (2001): SGBEM-FEM alternating method for analyzing 3D non-planar cracks and their growth in structural components, *CMES: Computer Modeling in Engineering & Sciences*, vol.2, no.3, pp.401-422.

**Okada, H.; Atluri, S. N.** (1994): Recent developments in the field-boundary element method for finite/small strain elastoplasticity, *Int. J. Solids Struct.* vol. 31 n. 12-13, pp. 1737-1775.

**Okada, H.; Rajiyah, H.; Atluri, S. N.** (1989)a: A Novel Displacement Gradient Boundary Element Method for Elastic Stress Analysis with High Accuracy, *J. Applied Mech.*, April 1989, pp. 1-9.

**Okada, H.; Rajiyah, H.; Atluri, S. N.** (1989)b: Non-hyper-singular integral representations for velocity (displacement) gradients in elastic/plastic solids (small or finite deformations), *Computational. Mechanics.*, vol. 4, pp. 165-175.

**Okada, H.; Rajiyah, H.; Atluri, S. N.** (1990): A full tangent stiffness field-boundary-element formulation for geometric and material non-linear problems of solid mechanics, *Int. J. Numer. Meth. Eng.*, vol. 29, no. 1, pp. 15-35.

**Tada, H.; Paris, P. C.; Irwin, G. R.** (2000): *The Stress Analysis of Cracks Handbook*, ASME Press.

**Timoshenko, S. P.; Goodier, J. N.** (1976): *Theory of Elasticity*, 3<sup>rd</sup> edition, McGraw Hill.

**Tsai, C. C.; Young, D. L.; Cheng, A. H.-D.** (2002): Meshless BEM for Three-dimensional Stokes Flows,

*CMES: Computer Modeling in Engineering & Sciences*, vol.3, no.1, pp. 117-128.

**Wen, P. H.; Aliabadi, M. H.; Young, A.** (2003): Boundary Element Analysis of Curved Cracked Panels with Mechanically Fastened Repair Patches, *CMES: Computer Modeling in Engineering & Sciences*, vol. 3, no. 1, pp. 1-10.

**Zhang, J. M.; Yao, Z. H.** (2001): Meshless regular hybrid boundary node method. *CMES: Computer Modeling in Engineering & Sciences*, vol.2, no.3, pp.307-318.

## Appendix

The displacement solution corresponding to this unit point load is given by the Galerkin-vector-displacement-potential:

$$\Phi^{*p} = (1 - \nu)F^*e^p \quad (24)$$

The corresponding displacements are derived from the Galerkin-vector-displacement-potential as:

$$u_i^{*p}(\mathbf{x}, \xi) = (1 - \nu)\delta_{pi}F_{,kk}^* - \frac{1}{2}F_{,pi}^* \quad (25)$$

The gradients of the displacements are:

$$u_{i,j}^{*p}(\mathbf{x}, \xi) = (1 - \nu)\delta_{pi}F_{,kkj}^* - \frac{1}{2}F_{,pij}^* \quad (26)$$

The corresponding stresses are given by:

$$\begin{aligned} \sigma_{ij}^{*p}(\mathbf{x}, \xi) &\equiv E_{ijkl}u_{k,l}^{*p} \\ &= \mu[(1 - \nu)\delta_{pi}F_{,kkj}^* + \nu\delta_{ij}F_{,pkk}^* - F_{,pij}^*] \\ &\quad + \mu(1 - \nu)\delta_{pj}F_{,kki}^* \end{aligned} \quad (27)$$

Three functions  $\phi_{ij}^{*p}$ ,  $G_{ij}^{*p}$ ,  $\Sigma_{ijpq}^*$  and  $H_{ijpq}^*$  are defined as [Han and Atluri (2003)]

$$\phi_{ij}^{*p}(\mathbf{x}, \xi) \equiv -\mu(1 - \nu)\delta_{pj}F_{,kki}^* \quad (28)$$

$$G_{ij}^{*p}(\mathbf{x}, \xi) = \mu[(1 - \nu)e_{ipj}F_{,kk}^* - e_{ikj}F_{,pk}^*] \quad (29)$$

$$\Sigma_{ijpq}^*(\mathbf{x}, \xi) = E_{ijkl}e_{nlp}\sigma_{nq}^{*k}(\mathbf{x}, \xi) \quad (30)$$

$$\begin{aligned} H_{ijpq}^*(\mathbf{x}, \xi) &= \mu^2[-\delta_{ij}F_{,pq} + 2\delta_{ip}F_{,jq} + 2\delta_{jq}F_{,ip} - \delta_{pq}F_{,ij} \\ &\quad - 2\delta_{ip}\delta_{jq}F_{,bb} + 2\nu\delta_{iq}\delta_{jp}F_{,bb} + (1 - \nu)\delta_{ij}\delta_{pq}F_{,bb}] \end{aligned} \quad (31)$$

For 3D problems,

$$F^* = \frac{r}{8\pi\mu(1-\nu)} \quad (32)$$

where  $r = \|\xi - \mathbf{x}\|$

$$u_i^{*p}(\mathbf{x}, \xi) = \frac{1}{16\pi\mu(1-\nu)r} [(3-4\nu)\delta_{ip} + r_{,i}r_{,p}] \quad (33)$$

$$G_{ij}^{*p}(\mathbf{x}, \xi) = \frac{1}{8\pi(1-\nu)r} [(1-2\nu)e_{ipj} + e_{ikj}r_{,k}r_{,p}] \quad (34)$$

$$\sigma_{ij}^{*p}(\mathbf{x}, \xi) = \frac{1}{8\pi(1-\nu)r^2} [(1-2\nu)(\delta_{ij}r_{,p} - \delta_{ip}r_{,j} - \delta_{jp}r_{,i}) - 3r_{,i}r_{,j}r_{,p}] \quad (35)$$

$$H_{ijpq}^*(\mathbf{x}, \xi) = \frac{\mu}{8\pi(1-\nu)r} [4\nu\delta_{iq}\delta_{jp} - \delta_{ip}\delta_{jq} - 2\nu\delta_{ij}\delta_{pq} + \delta_{ij}r_{,p}r_{,q} + \delta_{pq}r_{,i}r_{,j} - 2\delta_{ip}r_{,j}r_{,q} - \delta_{jq}r_{,i}r_{,p}] \quad (36)$$

For 2D problems,

$$F^* = \frac{-r^2 \ln r}{8\pi\mu(1-\nu)} \quad (37)$$

$$u_i^{*p}(\mathbf{x}, \xi) = \frac{1}{8\pi\mu(1-\nu)} [-(3-4\nu)\ln r \delta_{ip} + r_{,i}r_{,p}] \quad (38)$$

$$G_{ij}^{*p}(\mathbf{x}, \xi) = \frac{1}{4\pi(1-\nu)} [-(1-2\nu)\ln r e_{ipj} + e_{ikj}r_{,k}r_{,p}] \quad (39)$$

$$\sigma_{ij}^{*p}(\mathbf{x}, \xi) = \frac{1}{4\pi(1-\nu)r} [(1-2\nu)(\delta_{ij}r_{,p} - \delta_{ip}r_{,j} - \delta_{jp}r_{,i}) - 2r_{,i}r_{,j}r_{,p}] \quad (40)$$

$$H_{ijpq}^*(\mathbf{x}, \xi) = \frac{\mu}{4\pi(1-\nu)} [-4\nu\ln r \delta_{iq}\delta_{jp} + \ln r \delta_{ip}\delta_{jq} + 2\nu\ln r \delta_{ij}\delta_{pq} + \delta_{ij}r_{,p}r_{,q} + \delta_{pq}r_{,i}r_{,j} - 2\delta_{ip}r_{,j}r_{,q} - \delta_{jq}r_{,i}r_{,p}] \quad (41)$$

# The Applications of Meshless Local Petrov-Galerkin (MLPG) Approaches in High-Speed Impact, Penetration and Perforation Problems

Z. D. Han<sup>1</sup>, H. T. Liu<sup>1</sup>, A. M. Rajendran<sup>2</sup>, S. N. Atluri<sup>3</sup>

**Abstract:** This paper presents the implementation of a three-dimensional dynamic code, for contact, impact, and penetration mechanics, based on the Meshless Local Petrov-Galerkin (MLPG) approach. In the current implementation, both velocities and velocity-gradients are interpolated independently, and their compatibility is enforced only at nodal points. As a result, the time consuming differentiations of the shape functions at all integration points is avoided, and therefore, the numerical process becomes more stable and efficient. The ability of the MLPG code for solving high-speed contact, impact and penetration problems with large deformations and rotations is demonstrated through several computational simulations, including the Taylor impact problem, and some ballistic impact and perforation problems. The computational times for the above simulations are recorded, and are compared with those of the popular finite element code (Dyna3D), to demonstrate the efficiency of the present MLPG approach.

**keyword:** Meshless method, MLPG, High-speed impact, Penetration

## 1 Introduction

With the dramatically increased high-performance computational power, computational mechanics has become an important tool in both civilian and military system design and analysis. Although the finite element method (FEM), as the most recognized approach, has achieved a phenomenal success, accurate and efficient numerical simulations of armor/anti-armor systems is still a challenging task, due to the fact that these applications always involve high strain rate, non-linear deformation and severe element distortion. Recently, a great effort has been put into this field. Johnson et al (2003) proposed an

“element to particle” conversion method to alleviate the problem of highly distorted meshes in fracture and fragmentation problems. This mixed mesh/particle method seems to provide stable and useful solutions to several impact problems; however, these types of numerical approaches tend to remain “phenomenological”, and are limited to a small class of problems. Ortiz and his colleagues developed FEM based fracture and fragmentation algorithms, in which cohesive zones are assumed between element boundaries, and cracks can be propagated between the elements using cohesive laws [Ortiz and Pandolfi (1999)]. They used advanced nonlinear error estimation and non smooth contact algorithms to assure numerical accuracy and stability. Unfortunately, this advanced FEM approach seems to suffer from mesh-influenced solutions. In addition, these element-based approaches require a tremendous effort in generating good quality meshes for complex geometries, and for component assemblies.

In contrast, the meshless methods have become very attractive for eliminating the mesh distortion problems due to large deformations. Some meshless methods are based on the global weak forms, such as the smooth particle hydrodynamics (SPH), and the element-free Galerkin methods (EFG). They may require a certain node distribution pattern, or background cells for integration, which may be not lead to satisfactory solutions when meshes are severely distorted during large deformations. In addition, in the usual meshless approaches, the shape functions are generally very complicated, which results in even more complicated derivatives. Thus, the accurate calculation of the shape function derivatives is always a time-consuming task, and many more Gaussian points are required in the domain integration. The high computational expense and complexity is a barrier that prevents the application of meshless method to large-scale simulations. Most of the current meshless codes and applications are restricted to two-dimensional demonstrations.

Recently, Atluri and his colleagues [Atluri and Zhu

<sup>1</sup> Knowledge Systems Research, LLC, Forsyth, GA 30253

<sup>2</sup> US Army Research Office (ARO), RTP, NC

<sup>3</sup> Center for Aerospace Research & Education, University of California, Irvine

(1998), Atluri and Shen (2002), and Atluri (2004)] proposed a general framework for developing the Meshless Local Petrov-Galerkin (MLPG) approach, which provides flexibility in choosing the local weak forms, the trial functions, and the independent test functions for solving systems of partial differential equations. The MLPG approach has the following advantages: (1) all weak forms are formulated locally; (2) various trial and test functions can be chosen and combined together for solving one problem; (3) overlapping local sub-domains can be chosen in such a way as to match problems and algorithms in any special cases. The flexibility in choosing and combining various trial and test functions make the simplification of meshless formulation possible. For example, by choosing the heavy-side function (a unity-valued function inside the sub-domain, and zero outside the sub-domain), the domain integration is eliminated and the local symmetric weak form is expressed as a boundary integration. This will reduce the number of integration points, and greatly increase the accuracy and efficiency. In the MLPG method, the equilibrium and energy conservation equations are written locally within the subdomains, which make the parallel computation straightforward. As an extension, a meshless mixed finite volume method is proposed [Atluri, Han and Rajendran (2004), Han, Rajendran and Atluri (2005)] to further simplify the meshless formulations. In the MLPG mixed method, the displacement-/velocity- gradients are interpolated independently from the displacement/velocity interpolations. The compatibility between the displacements/velocities and displacement-/velocity-gradients is enforced only at nodal points. The mixed MLPG does not require the calculation of the derivatives of the complex shape functions, and thus achieves more computational accuracy and efficiency. It should be pointed out that the MLPG mixed method is radically and fundamentally different from the finite-element mixed method, which is a saddle point variational problem and which is often plagued by the stability conditions such as the Brezzi-Babuska conditions (Xue, Karlovitz, and Atluri (1985)).

In the present paper, the above described MLPG mixed method is implemented in an explicit-time-integration computational code, with an updated Lagrangean description. For completeness purpose, a brief description of the MLPG mixed method is presented in the following section. Several numerical examples are presented to

show the applicability of the meshless program.

## 2 MLPG Formulation

### 2.1 Local Nodal Interpolation

An appropriate meshless interpolation scheme should satisfy the *locality*, *continuity*, and *consistency* requirements. Among a variety of local interpolation schemes, the Moving Least Squares (MLS) interpolation is generally considered to be one of the best schemes to interpolate random data with a reasonable accuracy, because of its completeness, robustness and continuity. With the MLS, a trial function  $u(\mathbf{x})$  can be expressed as

$$u(\mathbf{x}) = \sum_{I=1}^N \Phi^I(\mathbf{x}) \hat{u}^I \quad (1)$$

where  $\hat{u}^I$  and  $\Phi^I(\mathbf{x})$  are the fictitious nodal values, and the shape function of node  $I$ , respectively. The shape functions are obtained by minimizing the  $L_2$  norm of the weighted distance between the trial function value and its true values at nodal points. For a detailed derivation and explicit expressions for the shape functions, the readers are referred to Atluri (2004).

The MLS nodal shape function  $\Phi^I(\mathbf{x})$  has a rational form, and it is non-zero only inside the support domain of its corresponding node  $I$ . We define the nodes whose support domain covers  $\mathbf{x}$  as the neighbor node of  $\mathbf{x}$ . The trial function  $u(\mathbf{x})$  is only relying on its immediate neighbors' nodal values and thus the *locality* is preserved. The smoothness of the shape function  $\Phi^I(\mathbf{x})$  is determined by its basis functions and the weight functions. Therefore, it is easy for the MLS approximation to yield a high-order *continuity* for the shape functions and then the trial functions. In practice, polynomials are adopted as the basis functions and spline functions as the weight functions. Therefore, to construct a more continuous shape function will be a trivial task. The MLS interpolation constructed in Eq. (1) is able to represent the  $j$ th ( $j=1,2, \dots, m$ , with  $m$  is the number of the polynomial basis functions) component of monomials exactly. In other words, the shape function is consistent.

In the mixed method, we interpolate the velocities  $v_i$  and velocity gradients  $v_{i,j}$  independently using the same shape functions, namely

$$v_i(\mathbf{x}) = \sum_{J=1}^N \Phi^J(\mathbf{x}) v_i^J \quad (2)$$

$$v_{i,j}(\mathbf{x}) = \sum_{K=1}^N \Phi^K(\mathbf{x}) v_{i,j}^K \quad (3)$$

The compatibility condition between the velocities and velocity gradients is enforced only at the nodes by a standard collocation method as

$$v_{i,j}(\mathbf{x}^I) = \frac{\partial v_i(\mathbf{x}^I)}{\partial x_j} \quad (4)$$

By interpolating the velocity gradients, as one of the key features of the mixed method, we eliminate the differentiation operations of the shape functions in the local weak form integration. Therefore, the requirement of the completeness and continuity of the shape functions is reduced by one-order, and thus, lower-order polynomial terms can be used in the meshless approximations. This leads to a smaller nodal influence size and speeds up the calculation of the shape functions. The adoption of the mixed method in our implementation greatly improves the program efficiency.

## 2.2 Formulations for Finite Strain Problems

Since the purpose of the developed MLPG program is to simulate high-speed dynamic problems, we adopted an updated Lagrangian formulation in our implementation. Let  $x_i$  be the spatial coordinates of a material particle in the current configuration. Let  $\dot{S}_{ij}$  be the Truesdell stress-rate (the rate of second Piola-Kirchhoff stress as referred to the current configuration); and let  $\dot{\sigma}_{ij}^J$  be the Jaumann rate of Kirchhoff stress (which is  $J$  times the Cauchy stress, where  $J$  is the ratio of volumes). It is known [Atluri (1980)]:

$$\dot{S}_{ij} = \dot{\sigma}_{ij}^J - D_{ik}\sigma_{kj} - \sigma_{ik}D_{kj} \quad (5)$$

Here,  $D_{ij}$  and  $W_{ij}$  are the symmetric and skew-symmetric parts of the velocity gradient, respectively. Considering a 3D domain  $\Omega$  with a boundary  $\partial\Omega$ , the rate forms of the linear and angular momentum balances are [Atluri (1980)]:

$$(\dot{S}_{ij} + \tau_{ik}v_{j,k})_{,i} + \dot{f}_j = \rho\dot{a}_j \quad (6)$$

where,  $\rho$  is the mass density and  $\dot{a}_j$  the acceleration rate. In a dynamic problem,  $\dot{f}_j$  are appropriately defined in terms of the rate of change of inertia forces and  $(\cdot)_{,i} = \partial(\cdot)/\partial x_i$ ;  $x_i$  are current coordinates of a material particle. In Eq. (6),  $\tau_{ij}$  is the Cauchy stress in the current configuration.

## 2.3 Local weak form with the large deformations

In the MLPG approaches, the weak form is established over a local subdomain  $\Omega_s$ , which may have an arbitrary shape and contain a point  $\mathbf{x}$  in question. In our implementation, the local weak form is established for a spherical subdomain with the radius of  $r$  (we define it as the test-function size), namely

$$\int_{\Omega_s} [(\dot{S}_{ij} + \tau_{ik}v_{j,k})_{,i} + \dot{f}_j - \rho\dot{a}_j] w_j d\Omega = 0 \quad (7)$$

where  $w_j$  are the test functions. By applying the divergence theorem Eq. (7) may be rewritten in a symmetric weak form as:

$$\begin{aligned} & \int_{\partial\Omega_s} (\dot{S}_{ij} + \tau_{ik}v_{j,k}) n_i w_j d\Gamma \\ & - \int_{\Omega_s} [(\dot{S}_{ij} + \tau_{ik}v_{j,k}) w_{j,i} - \dot{f}_j w_j + \rho\dot{a}_j] d\Omega = 0 \end{aligned} \quad (8)$$

with the rate definition  $\dot{t}_j = (\dot{S}_{ij} + \tau_{ik}v_{j,k}) n_i$ , and with  $n_i$  being the components of a unit outward normal to the boundary of the local subdomain  $\Omega_s$ , in its current configuration. Thus the local symmetric weak form can be rewritten as

$$\begin{aligned} & \int_{L_s} \dot{t}_i w_i d\Gamma + \int_{\Gamma_{su}} \dot{t}_i w_i d\Gamma + \int_{\Gamma_{st}} \dot{t}_i w_i d\Gamma \\ & - \int_{\Omega_s} [(\dot{S}_{ij} + \tau_{ik}v_{j,k}) w_{j,i} - \dot{f}_j w_j + \rho\dot{a}_j] d\Omega = 0 \end{aligned} \quad (9)$$

where  $\Gamma_{su}$  is a part of the boundary  $\partial\Omega_s$  of  $\Omega_s$ , over which the essential boundary conditions are specified. In general,  $\partial\Omega_s = \Gamma_s \cup L_s$ , with  $\Gamma_s$  being a part of the local boundary located on the global boundary, and  $L_s$  is the other part of the local boundary which is inside the solution domain.  $\Gamma_{su} = \Gamma_s \cap \Gamma_u$  is the intersection between the local boundary  $\partial\Omega_s$  and the global displacement boundary  $\Gamma_u$ ;  $\Gamma_{st} = \Gamma_s \cap \Gamma_t$  is a part of the boundary over which the natural boundary conditions are specified.

To simplify the integration and speed up the numerical implementation, the Heaviside function is adopted as the test function in our program (Thus, the method is labeled here as the “finite-volume” MLPG method). Thus, the local symmetric weak form in Eq.(9) becomes

$$- \int_{L_s} \dot{t}_i d\Gamma - \int_{\Gamma_{su}} \dot{t}_i d\Gamma + \int_{\Omega_s} \rho\dot{a}_j d\Omega = \int_{\Gamma_{st}} \dot{t}_i d\Gamma + \int_{\Omega_s} \dot{f}_i d\Omega \quad (10)$$

This equation has the physical meaning that it represents the balance law of the local sub-domain  $\Omega_s$ , as in conventional finite volume methods.

### 3 Numerical Implementation

In this section, we will address some numerical issues in the implementation of the MLPG mixed method.

#### 3.1 Determination of the Support Sizes

The support size is an important parameter in the MLPG calculation. On the one hand, the support size should be large enough to include enough neighboring nodes to ensure the regularity and reduce the computational error; on the other hand, we should keep the support size relatively small to maintain the interpolation's locality. In the current implementation, the support size for each node is determined automatically from the neighbor nodes, on demand.

To ensure the regularity of the MLS interpolation, the minimum number of the linearly independent neighbor nodes is decided by the order of the polynomial basis. For the three-dimensional problems, the neighbor node number  $m$  is calculated from the order of the polynomial basis  $t$  as [Atluri (2004)]

$$m = (t+1)(t+2)(t+3)/6 \quad (11)$$

Eq. (11) means that for each point  $\mathbf{x}$ , it is required that there are  $m$  neighbor nodes whose support domains cover the point  $\mathbf{x}$ . On other words, for a node  $J$ , its support size should be large enough to cover all the nodes, of which the node  $J$  is a neighbor node. To increase the efficiency of the present implementation, the support sizes are not recalculated for each time step. Therefore, a scale factor, which is great than 1, is applied to the support sizes decided by the above procedure, to account for the effect of the nodal movement from the body's deformation.

#### 3.2 Determination of the Test Sizes

The test domains in the MLPG could be any overlapping local domains. A spherical domain centered at each node is adopted in the present implementation. For a node  $I$ , the radius of the spherical domain (the test size) is determined as

$$r_0^I = \alpha \min \{ \|\mathbf{x}^I - \mathbf{x}^J\| \}, \quad J = 1, 2, \dots, N \text{ and } I \neq J \quad (12)$$

where  $\alpha$  is the scale factor of the test size, which is a constant between 0 and 1. In addition, if node  $I$  is inside the solution domain, but close to the global boundary, a smaller radius may be used so that the local sphere has no intersection with the global boundary. In other words, the local test domains of all internal nodes are restricted to be inside the solution domain, and their local boundaries are also inside the solution domain. Therefore, the numerical implementation becomes much simpler, because the essential and natural boundary conditions appear in the integrals of the nodes on the global boundary only.

#### 3.3 Numerical Quadrature

In the present implementation, the integrations of the local symmetric weak form [Eq. (10)] are performed numerically by using the conventional Gaussian quadrature scheme. The boundary integration in Eq. (10) over a spherical surface involves the trigonometric functions. It is well known that the conventional numerical quadrature schemes are designed for polynomials, and are not efficient for trigonometric or rational functions. To improve the performance of the numerical integration, the local subdomain (i.e. a sphere) is partitioned by triangles for the surface integration [Han and Atluri (2004)].

#### 3.4 Time Integration

The well known and commonly accepted Newmark  $\beta$  method [Newmark (1959)] is used in the present implementation to integrate the governing equations in time. With the determined accelerations from the system equations based on the local symmetric weak form [Eq. (10)], the displacements and velocities are calculated from the standard Newmark  $\beta$  method as

$$\begin{aligned} \mathbf{u}^{t+\Delta t} &= \mathbf{u}^t + \Delta t \mathbf{v}^t + \frac{\Delta t^2}{2} [(1-2\beta) \mathbf{a}^t + 2\beta \mathbf{a}^{t+\Delta t}] \\ \mathbf{v}_c^{t+\Delta t} &= \mathbf{v}^t + \Delta t [(1-\gamma) \mathbf{a}^t + \gamma \mathbf{a}^{t+\Delta t}] \end{aligned} \quad (13)$$

For zero damping system, this method is unconditionally stable if

$$2\beta \geq \gamma \geq \frac{1}{2} \quad (14)$$

and conditionally stable if

$$\gamma \geq \frac{1}{2}, \quad \beta \leq \frac{1}{2} \text{ and } \Delta t \leq \frac{1}{\omega_{\max} \sqrt{\gamma/2 - \beta}} \quad (15)$$

where  $\omega_{\max}$  is the maximum frequency in the structural system.

This method can be used in the predictor-corrector mode, with specified initial conditions [Atluri (2004)]. In the present implementation, the central difference scheme is used by setting  $\beta = 0$  and  $\gamma = 1/2$ .

#### 4 Ceramic Constitutive Model with Damage

In the present implementation, the Rajendran and Grove (RG) ceramic damage model is adopted to model the material damage and failure during the impact and penetration process. The RG ceramic model [Rajendran (1994); Rajendran and Grove (1996)] is a sophisticated, three-dimensional, internal-state-variable-based constitutive model for ceramic materials, which incorporated both micro-crack propagation and void collapse. The proposed RG ceramic damage model has achieved a great success in describing the response of alumina (AD85) subjected to various stress/strain loading conditions [Rajendran (1994)]. In this section, the RG ceramic damage model is briefly reviewed and the main formulation is presented for completeness purposes.

##### 4.1 Constitutive Relationships

In the RG model, the total strain  $\epsilon_{ij}$  is decomposed into the elastic part  $\epsilon_{ij}^e$  and plastic part  $\epsilon_{ij}^p$ . The pressure is calculated through the Mie-Gruneisen equation of state as

$$P = [\bar{P}_H (1 - 0.5\Gamma\bar{\eta}) + \Gamma\rho_0 (I - I_0)] \quad (16)$$

with

$$\bar{P}_H = K_\gamma (\beta_1 \bar{\eta} + \beta_2 \bar{\eta}^2 + \beta_3 \bar{\eta}^3) \quad (17)$$

In the above equations,  $\beta_1$ ,  $\beta_2$  and  $\beta_3$  are empirical parameters;  $\Gamma$  is the Mie-Gruneisen parameter;  $K_\gamma = \bar{K}/K$  is the bulk modulus reduction ratio, with  $K$  being the bulk modulus for the intact matrix and  $\bar{K}$  the effective bulk modulus for the micro-crack containing material. Furthermore,  $\rho_0$  is the initial material density;  $I_0$  and  $I$  are the internal energy at the initial and current states, respectively. The engineering volumetric strain, with the consideration of the voids, is defined as

$$\bar{\eta} = \frac{(1 - f_0)V_0}{(1 - f)V} - 1 \quad (18)$$

Where  $V_0$  and  $V$  are the volumes of the initial and current states;  $f_0$  and  $f$  are the initial and current porosity densities, respectively.

The deviatoric stress is related with the deviatoric elastic strain  $e_{ij}^e$  as

$$S_{ij} = 2R_g \bar{G} e_{ij}^e \quad (19)$$

Here  $\bar{G}$  is the effective shear modulus for micro-crack containing material and  $R_g$  is the correction factor for shear modulus due to the existence of porosity, which is given in Rajendran and Grove's paper (1996). The porosity density is assumed to decrease due to void collapsing at pressures above the HEL as

$$\dot{f} = (1 - f) \dot{\epsilon}_v^p \quad (20)$$

with  $\epsilon_v^p$  the plastic volumetric strain and the dot means the temporal derivative.

When the materials are shocked above the HEL (Hugoniot Elastic Limit), plastic flow occurs. In the current model, Gurson's pressure dependent yield function, with considerations of the porosity, is adopted, namely

$$F = \frac{3J_2}{Y^2} + 2f \cosh\left(\frac{3P}{2Y}\right) - f^2 - 1 = 0 \quad (21)$$

with  $J_2 = 0.5S_{ij}S_{ij}$ . A simplified Johnson-Cook strain rate dependent strength model is used and can be expressed as

$$Y = C_1 \left(1 + C_3 \ln \frac{\dot{\epsilon}_p}{\dot{\epsilon}_0}\right) \quad (22)$$

where  $C_1$  and  $C_3$  are model constants.  $\dot{\epsilon}_p$  is the equivalent plastic strain rate and  $\dot{\epsilon}_0$  is the reference strain rate, which is assumed to be 1 in the current model.

##### 4.2 Damage Definition and Evolution

The micro-crack damage is measured in terms of a dimensionless micro-crack damage density  $\gamma$ , which is expressed as

$$\gamma = N_0^* a^3 \quad (23)$$

where  $N_0^*$  is the average number of micro-flaws per unit volume and  $a$  is the maximum micro-crack size at the

current state. The initial values of  $N_0^*$  and  $a_0$  are material constants. For simplicity, it is assumed that there is no crack nucleation during the loading, and therefore the damage evolution is represented by the growth of micro-crack size  $a$ , which follows a generalized Griffith criterion, as

$$\dot{a} = \begin{cases} 0 & G_s \leq G_C \\ n_1 C_R \left[ 1 - \left( \frac{G_C}{G_s} \right)^{n_2} \right] & G_s > G_C \end{cases} \quad (24)$$

where  $C_R$  is the Rayleigh wave speed,  $G_C$  is the critical strain energy release rate for micro-crack growth calculated from the fracture toughness  $K_{IC}$ , Young's modulus  $E$  and Poisson's ratio  $\nu$  as  $G_C = K_{IC}^2 (1 - \nu^2) / E$ .  $G_s$  is the applied strain energy release rate.  $n_1$  and  $n_2$  are the parameters controlling the crack growth rate. Four parameters are used for the micro-crack extension model:  $n_1^-$  and  $n_2^-$  for crack sliding, and  $n_1^+$  and  $n_2^+$  for crack opening.

### 4.3 Pulverization

When the micro-crack damage density  $\gamma$  reaches a critical value (usually set as 0.75) under compressive loading, the material becomes pulverized. The bulk and shear moduli for the pulverized material are set to the corresponding effective bulk and shear moduli at the pulverization point. The pulverized material does not support any tensile loading and the compressive strength of the pulverized material is described by the Mohr-Columb law as

$$Y = \begin{cases} 0 & , P \leq 0 \\ \alpha + \beta P & , P > 0 \end{cases} \quad (25)$$

where  $\alpha$  and  $\beta$  are model constants. The pressure is simply computed from the elastic volumetric strain  $\epsilon_v^e$  as

$$P = \begin{cases} 0 & , \epsilon_v^e \geq 0 \\ -\bar{K}_p \epsilon_v^e & , \epsilon_v^e < 0 \end{cases} \quad (26)$$

### 4.4 Determination of Model Constants

In the Rajendran-Grove ceramic model, there are eight material constants to describe the micro-crack behavior:  $N_0^*$ ,  $a_0$ ,  $\mu$ ,  $n_1^+$ ,  $n_2^+$ ,  $n_1^-$ ,  $n_2^-$ , and  $K_{IC}$ . Usually, several experiments such as the plate-on-plate and the bar-on-bar impact tests are needed to determine these constants for a specific material. Rajendran and Grove (1996) conducted a sensitivity study of the material constants, and calibrated the constants for several commonly used ceramic

**Table 1** : The material constants for Rajendran-Grove model

	AD85
Density ( $g/cm^3$ )	3.42
Shear Modulus (GPa)	88.0
Initial Porosity	10%
Material Strength Constants	
$C_1$ (GPa)	4.0
$C_3$	0.029
Equation of State Constants	
$\beta_1$ (GPa)	150.0
$\beta_2$ (GPa)	150.0
$\beta_3$ (GPa)	150.0
$\Gamma$	0
Damage Model Parameters	
$N_0^*$ ( $m^{-3}$ )	$1.83 \times 10^{10}$
$a_0$ ( $\mu m$ )	0.58
$\mu$	0.72
$n_1^+$	1.0
$n_2^+$	0.07
$n_1^-$	0.1
$n_2^-$	0.07
$K_{IC}$ ( $MPa\sqrt{m}$ )	3.25
Pulverized Material Constants	
$\alpha$ (GPa)	0.1
$\beta$	0.1

materials, like SiC, B<sub>4</sub>C, TiB<sub>2</sub>, AD85, and AD995. In the following numerical simulations, the AD85 ceramic is used and the material constants that we employed are listed in Table 1.

## 5 Numerical Examples

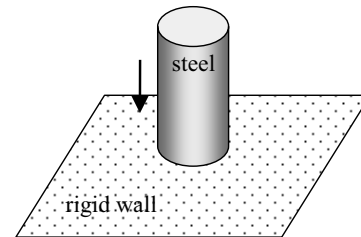


**Figure 1** : Taylor's problem: a solid cylinder impacting a rigid surface

Two numerical examples are presented here to show the applicability of the developed MLPG program in solv-

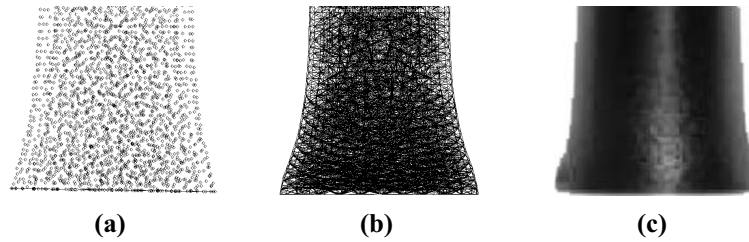


**Figure 2** : Deformed profile of the cylinder at 50 micro-seconds: (a) MLPG mixed method; (b) Finite element model; and (c) Test

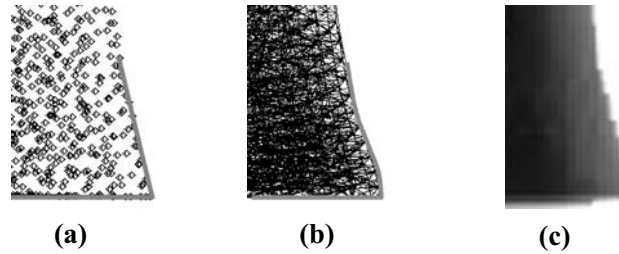


**Figure 3** : The lower corner of the deformed profile at 50 micro-seconds: (a) MLPG mixed method; (b) Finite element model; and (c) Test

ing contact, impact, penetration and perforation problems with large deformation. For the sake of readability and brevity, the details of the implementation of the MLPG contact, penetration, and perforation algorithms are omitted here, and will be reported elsewhere.

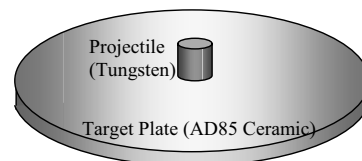
### 5.1 Taylor Impact Problem

The Taylor test is often used to determine the dynamic yield stress of a material in a state of uniaxial stress. The Taylor impact problem can simply be described as a solid cylinder impacting a rigid surface in the normal direction, shown in Figure 1. In the present study, a cylinder with a length of 12.7 cm and a radius of 76.2 cm is impacting a rigid surface with an initial impact velocity of 300 m/s. The solid cylindrical rod is modeled as being elasto-plastic, and the material is chosen as AISI 310 steel with the following material constants: density:  $8.027 \text{ g/cm}^3$ , Young's modulus: 199.95 GPa, Poisson's ratio: 0.28, yield strength: 310.26 MPa, and 1% hardening slope : 2.0 GPa.

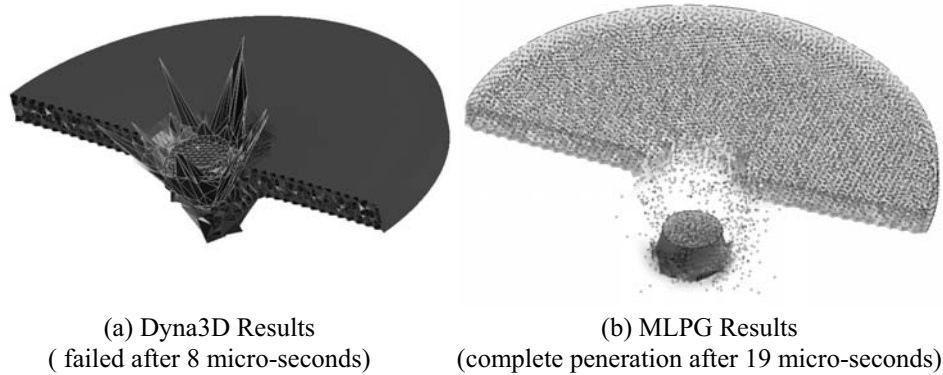
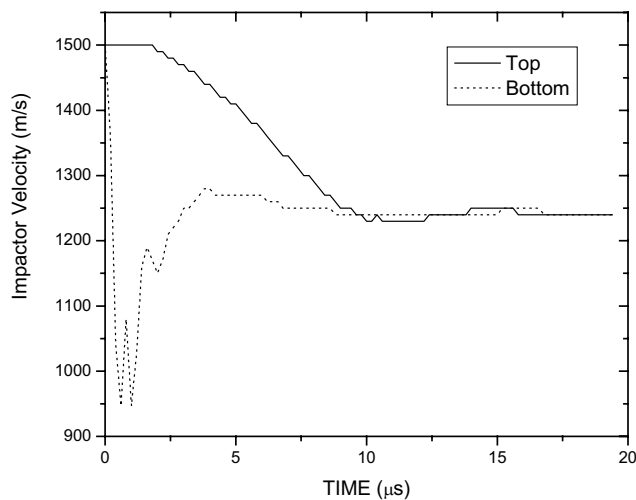
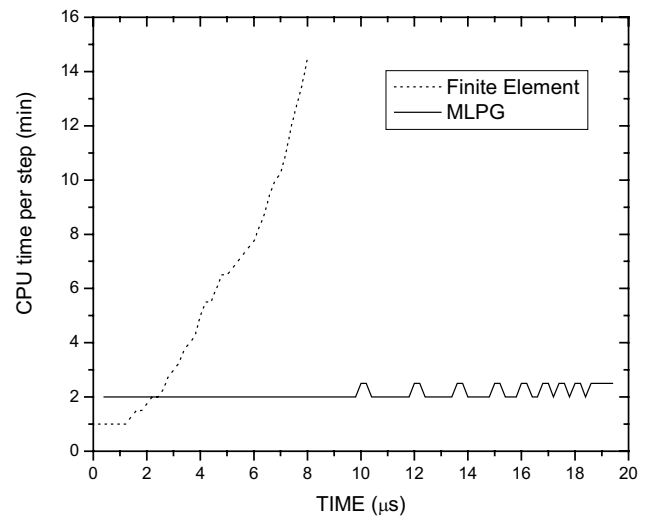
This Taylor impact problem is simulated using the present MLPG program. For comparison purposes, the finite element code Dyna3D (version 2000) is also used to analyze this problem, using the mesh generated from the same nodal configuration. The top surface of the cylinder reaches the lowest point at about 50 micro sec-

onds. The deformed profile of the cylinder is shown in Fig. 2(a) using the MLPG mixed method and in Fig. 2(b) using Dyna3D. Both codes give similar profiles. However, the MLPG method gives a straight corner while Dyna3D gives a curved one, for this *frictionless contact* impact. The corners of the deformed profiles are enlarged in Table 1.

In analyzing this problem, the present MLPG mixed method is used without any hour-glass control, or any other artificial numerical treatments. In contrast, one-point Gauss integration scheme is used in Dyna3D, along with hour-glass control. The total CPU times for the straightforward MLPG mixed method, and the Dyna3D with hour-glass control and artificial viscosity, are almost same. It clearly demonstrates the superior performance of the present MLPG mixed method as compared to the FEM methods.



**Figure 4** : Ballistic impact test configuration schematic

**Figure 5 : Ballistic Impact Penetration****Figure 6 : Remaining speed of the projectile after penetration****Figure 7 : CPU time comparison between MLPG and finite element approaches**

## 5.2 Ballistic Impact

In this simulation, we consider a cylindrical tungsten projectile to impact with an AD85 ceramic plate at the velocity of 1500 m/s. Both the length and diameter of the projectile are 10 mm. The target ceramic plate has a thickness of 5 mm and a diameter of 80 mm. Fig. 3 shows the experimental configuration. The tungsten is modeled as being elastoplastic, with the following material properties: density  $16.98 \text{ g/cm}^3$ , Young's modulus 299.6 GPa, Poisson's ratio 0.21 and yield strength 1.5 GPa. The target plate is modeled using the Rajendran-Grove ceramic damage model, which was implemented into the present MLPG implementation, as well as in Dyna3D.

The simulation using finite element method (Dyna3D)

stops at 8 micro-seconds due to severe element distortion, as shown in Figure 4(a). The *total simulation time with Dyna3D is over 5 hours*. As pointed out by Johnson and Robert (2003), the Lagrangian finite element algorithms are not always adequate when the distortions become very severe. The meshless method, which could be used to represent severe distortions in a Lagrangian framework, is more suitable to simulate the problems with severe distortions like ballistic penetration.

The same problem is re-simulated by using the MLPG method; and it is solved smoothly without any mesh distortion problems, because of the advantages of the truly meshless method. The total solution time is 20 micro-seconds, and *it takes about 1 hour for the first 8 micro-*

seconds, and 2.5 hours to carry out the whole analysis. The final deformation is shown in Figure 4(b), and the fragmentation is clearly formed after the projectile penetrates the target plate. The steady remaining speed of the projectile is about 1240 m/s after impact, with the velocity history chattered in Fig. 4. In addition, the MLPG method is more stable than the FEM as a steady CPU time is demonstrated during the whole solution time. However, the FEM is encountering a severe mesh distortion problem, and CPU time jumps up once the projectile and plate are undergoing the large deformation right after a few micro seconds of the solution time, shown in Fig. 5.

## 6 Closing Remarks

The meshless method has been a very active research area for over ten years in the computational mechanics field. However, due to the intrinsic complexity of the approach, most of the research is still at the academic level. The MLPG method, as a meshless framework, provides the flexibility to construct various meshless approaches by different choices and combinations of the trial and test functions; therefore, provides the possibility to simplify the numerical procedure and lead to an efficient and stable meshless implementation.

The present development of software is based on the MLPG mixed finite volume method for solving three-dimensional nonlinear problems. The MLS approximations are used for both velocity and velocity-gradients interpolations, independently. The adoption of the Heavy-side function as the test function eliminates the domain integration in the local weak form. In addition, the support size and test size are determined automatically by the program based on the nodal density and distribution. All of these efforts lead to a high-performance MLPG dynamic program, which shows the potential to replace the finite element method in some computational areas, such as solving the high-speed impact and penetration problems. These potentials are demonstrated through the two numerical examples. The 3D Taylor-impact example demonstrates that the present mixed method possesses an excellent accuracy and efficiency, as compared to the FEM. *The present method requires no special numerical treatments to handle the nonlinear static and dynamic problems, such as the reduced integration, hourglass control, and so on.* The ballistic-impact and perforation example demonstrates the ability of the MLPG

mixed method in solving high-speed problems with severe distortion and fragmentation. Compared with FEM, the MLPG is not only more stable but also more efficient.

## References

- Atluri, S. N.** (1980): On some new general and complementary energy theorems for the rate problems of finite strain, classical elastoplasticity. *Journal of Structure and Mechanics*, vol. 8, pp. 61-92.
- Atluri, S.N** (2004): *The Meshless Local Petrov-Galerkin (MLPG) Method for Domain & Boundary Discretizations*, Tech Science Press, 665 pages.
- Atluri S.N., Shen S.P.** (2002): The meshless local Petrov-Galerkin (MLPG) method: A simple & less-costly alternative to the finite element and boundary element methods, *CMES: Computer Modeling in Engineering and Sciences*, 3 (1) 11-51
- Atluri, S. N.; Han, Z. D.; Rajendran, A. M.** (2004): A New Implementation of the Meshless Finite Volume Method, Through the MLPG "Mixed" Approach, *CMES: Computer Modeling in Engineering & Sciences*, vol. 6, no. 6, pp. 491-514.
- Atluri, S. N.; Zhu, T.** (1998): A new meshless local Petrov-Galerkin (MLPG) approach in computational mechanics. *Computational Mechanics*, Vol. 22, pp. 117-127.
- Han. Z. D.; Atluri, S. N.** (2004): Meshless Local Petrov-Galerkin (MLPG) approaches for solving 3D Problems in elasto-statics, *CMES: Computer Modeling in Engineering & Sciences*, vol. 6 no. 2, pp. 169-188.
- Han Z. D.; Rajendran, A. M; Atluri, S. N.** (2005): Meshless Local Petrov-Galerkin (MLPG) Approaches for Solving Nonlinear Problems with Large Deformation and Rotation, *CMES: Computer Modeling in Engineering & Sciences*, vol. 10, no. 1, pp. 12.
- Johnson, G.R.; Robert, A.S.** (2003): Conversion of 3D Distorted Element into Meshless Particles During Dynamic Deformation. *Int. J. Impact Engng.*, vol. 28, pp. 947-966.
- Johnson, G. R.; Stryk, R. A.** (2003): Conversion of 3D distorted elements into meshless particles during dynamic deformation, *International Journal of Impact Engineering*, vol. 28, pp. 947-966.
- Newmark, N. M.** (1959): A method of computation for structural dynamics, *Journal of the Engineering mechan-*

*ics Division, ASCE*, vol. 86, pp. 67-95.

**Ortiz, M.; Pandolfi, A.** (1999): Finite-Deformation Irreversible Cohesive Elements for Three-Dimensional Crack-Propagation Analysis, *International Journal for Numerical Methods in Engineering*, Vol. 44, pp. 1267-1282.

**Rajendran, A.M.** (1994): Modeling the Impact Behavior of AD85 Ceramic under Multiaxial Loading. *Int. J. Impact Engng.*, Vol. 15, No. 3, pp. 749-768.

**Rajendran, A. M.; Grove, D.J.** (1996): Modeling the Shock Response of Silicon Carbide, Boron Carbide and Titanium Diboride. *Int. J. Impact Engng.*, Vol. 18, No. 6, pp. 611-631.

**Xue, W.-M., Karlovitz, L. A., and Atluri, S.N(1985):** On the Existences and Stability Conditions for Mixed-Hybrid Finite Element Solutions Based on Reissner's Variational Principle, *International Journal of Solids and Structures*, Vol. 21(1), pps. 97-116,

# Meshless Local Petrov-Galerkin (MLPG) Approaches for Solving Nonlinear Problems with Large Deformations and Rotations

Z. D. Han<sup>1</sup>, A. M. Rajendran<sup>2</sup> and S.N. Atluri<sup>1</sup>

**Abstract:** A nonlinear formulation of the Meshless Local Petrov-Galerkin (MLPG) finite-volume mixed method is developed for the large deformation analysis of static and dynamic problems. In the present MLPG large deformation formulation, the velocity gradients are interpolated independently, to avoid the time consuming differentiations of the shape functions at all integration points. The nodal values of velocity gradients are expressed in terms of the independently interpolated nodal values of displacements (or velocities), by enforcing the compatibility conditions directly at the nodal points. For validating the present large deformation MLPG formulation, two example problems are considered: 1) large deformations and rotations of a hyper-elastic cantilever beam, and 2) impact of an elastic-plastic solid rod (cylinder) on a rigid surface (often called as the Taylor impact test). The MLPG result for the cantilever beam problem was successfully compared with results from both analytical modeling and a commercial finite element code simulation. The final shapes of the plastically deformed rod obtained from a well-known finite element code, and the present MLPG code were also successfully compared. The direct comparison of computer run times between the finite element method (FEM) and the large deformation mixed MLPG method showed that the MLPG method was relatively more efficient than the FEM, at least for the two example problems considered in the present study.

**keyword:** Meshless Local Petrov-Galerkin approach (MLPG), Finite Volume Methods, Mixed Methods.

## 1 Introduction

Accurate description and modeling of large deformations has been a very challenging problem in computational

mechanics. However, during the past three decades, several researchers [Atluri (1980,1984), Belytshchko et al (1984), Malkus and Hughes(1978), Oden and Pires (1983)] have successfully developed algorithms to handle large deformations in finite element analyses. It is indeed well recognized that the FEM has certain inherent drawbacks: a) labor-intensive mesh-generation, b) shear locking, c) poor derivative solutions, and d) hour-glass effects, e) mesh distortion under very large deformations, and in f) problems of strain-localization, crack-propagation, and material penetration. Eventhough ad-hoc attempts are made to alleviate some of these problems, a thorough scientific basis is still necessary. Severe localizations such as adiabatic shear banding and coalescence of microcracks can often limit the FEM solutions. The so called shock propagation based FEM codes (“Hydrocodes”) provide numerical schemes that would allow the calculations to proceed smoothly through removal of highly distorted elements whose aspect ratios tend towards zero from the computations. Recently, Johnson et al (2003) proposed an “element to particle” conversion method to alleviate the problem of highly distorted meshes in fracture and fragmentation problems. This mixed mesh/particle method seems to provide stable and useful solutions to several impact problems; however, these types of numerical approaches tend to remain “phenomenological” and limited to a class of problems. Ortiz and his colleagues developed FEM based fracture and fragmentation algorithms in which cohesive zones are assumed between element boundaries and cracks can be propagated between the elements using cohesive laws [Ortiz and Pandolfi (1999)]. They used advanced nonlinear error estimation and non smooth contact algorithms to assure numerical accuracy and stability. Unfortunately, this advanced FEM approach seems to suffer from mesh-influenced solutions. The problem of time consuming mesh generation process and the need for intelligent mesh design make FEM based approaches more complicated and unattractive.

<sup>1</sup> University of California, Irvine Center for Aerospace Research & Education

5251 California Avenue, Suite 140  
Irvine, CA, 92612, USA

<sup>2</sup> Army Research Office, RTP, NC

In contrast, the meshless methods have become very attractive for eliminating the mesh distortion problems due to large deformations. Some meshless methods are based on the global weak forms, such as the smooth particle hydrodynamics (SPH) and the element-free Galerkin methods (EFG). They may require certain node distribution pattern or background cells for integration, which may be not satisfied while meshes are distorted during large deformations.

As a general framework for developing meshless methods, the MLPG approach provides the flexibility in choosing the local weak forms, the trial functions, and the independent test functions for solving PDEs, pioneered by Atluri and his colleagues [Atluri and Zhu(1998), and Atluri (2004)]. Some distinct advantages of the MLPG approach include: a) all weak forms are formulated locally; b) various trial and test functions can be chosen and combined together for solving one problem; c) overlapping local sub-domains can be chosen in a way to match problems and algorithms in any special cases; d) it is flexible to extend and incorporate the MLPG continuum methods with others, including molecular dynamics (MD). The MLPG approach has been used to solve various problems successfully, and has been demonstrated as to its suitability for computational mechanics, including the work in fracture mechanics [Atluri, Kim and Cho (1999)], fluid mechanics [Lin and Atluri (2001)], and 3D elasto- statics and dynamics [Han and Atluri (2004ab)] and so on. A very comprehensive summary has been presented in the monograph by Atluri [2004].

Most recently, a new meshless mixed finite volume method has been presented by [Atluri, Han and Rajendran (2004)], in which the strains are also interpolated independently from the displacements. The key feature of this new method is to interpolate the derivatives of the primary variables independently, which makes the MLPG method computationally more efficient. The calculation of the derivatives is required at each integration point in the primal MLPG methods, which is computationally costly. With the mixed method, the strain-displacement compatibility is enforced at nodal points by using the collocation method. In addition, it requires only  $C0$  continuities for the trial functions, instead of  $C1$  continuities. Thus a smaller support size can be used and the number of neighboring nodes is reduced dramatically, especially for 3D cases. At the same time, it still retains the simple physical meaning as the momentum balance law

of the local sub-domains, while the accuracy of the secondary variables has been improved. The mixed method has been applied to solve the elasto-static problems successfully [Atluri, Han and Rajendran (2004)].

In the present study, the mixed method is extended for the nonlinear analysis with large deformations. It is well known that the gradients of the displacements (or velocities) are widely used for the nonlinear analysis, such as the material constitutive models and the momentum balance law. The strain tensor is not enough to capture all deformation information, because the spin tensor plays an important role in the balance law, as well as the stress update [Atluri (1980)]. Therefore, the gradients of the velocities are chosen to be interpolated independently in the present study, instead of the strains. Thus the local weak forms are integrated based on the gradient interpolation, as well as the material constitutive models. As the primal variables, the velocities are chosen as the degrees of freedom for each node, and their gradients are mapped back by enforcing the compatibility conditions at nodal points through the collocation method. This special combination also demonstrates the flexibility of the general MLPG approach. The present MLPG mixed method is applied to solve some example nonlinear static and dynamic problems. An explicit algorithm is used in the present study to simulate the high-speed impact problems. The examples demonstrate the suitability of the MLPG mixed finite-volume method for nonlinear problems with large deformations and rotations.

The paper formulates the local weak forms for the nonlinear mechanics with large deformations in Section 2. It also includes the numerical implementation of the MLPG method through the mixed approach. Numerical examples are presented in Section 3, for both static and dynamic problems in 2D and 3D cases. Some conclusions and discussions are given in Section 4.

## 2 MLPG Mixed FVM for finite strain problems

### 2.1 Finite strain deformation

In the present study, we use an updated Lagrangian formulation. Let  $x_i$  be the spatial coordinates of a material particle in the current configuration. Let  $\dot{S}_{ij}$  be the Truesdell stress-rate (the rate of second Piola-Kirchhoff stress as referred to the current configuration); and let  $\dot{\sigma}_{ij}^J$  be the Jaumann rate of Kirchhoff stress (which is  $J$  times the Cauchy stress, where  $J$  is the ratio of volumes). It is

known [Atluri (1980)]:

$$\dot{S}_{ij} = \dot{\sigma}_{ij}^J - D_{ik}\sigma_{kj} - \sigma_{ik}D_{kj} \quad (1)$$

where  $D_{ij}$  is the symmetric part of the velocity gradient. The skew-symmetric part of the velocity gradients is denoted as  $W_{ij}$ , i.e.

$$W_{ij} = \frac{1}{2}(v_{i,j} - v_{j,i}) \quad (2)$$

Consider a body in a 3D domain  $\Omega$ , with a boundary  $\partial\Omega$ , the rate forms of the linear and angular momentum balances are [Atluri (1980)]:

$$(\dot{S}_{ij} + \tau_{ik}v_{j,k})_{,i} + \dot{f}_j = 0 \quad (3)$$

where, in a dynamic problem,  $\dot{f}_j$  are appropriately defined in terms of the rate of change of inertia forces and  $(\cdot)_{,i} = \partial(\cdot)/\partial x_i$ ;  $x_i$  are current coordinates of a material particle. In Eq. 2.2,  $\tau_{ij}$ , is the Cauchy stress in the current configuration.

Consistent theories of combined isotropic/kinematic hardening finite strain plasticity that are capable of modeling the available test data (at finite strain) are fully discussed in Im and Atluri (1984). Especially, in the case of kinematic hardening plasticity at finite strains, it is desirable [see Im and Atluri (1987), and the references cited therein] to introduce the so-called plastic spin, denoted by  $\mathbf{W}^p$ . As seen in Im and Atluri (1987) a combined isotropic/kinematic hardening plasticity may be characterized by the following evolution equations:

$$D_{ij}^p = f_{ij}(\sigma'_{ij}, D_{ij}, W_{ij}^p, \dots) \quad (4)$$

$$W_{ij}^p = g_{ij}(\sigma'_{ij}, r_{ij}, \dots) \quad (5)$$

$$r_{ij}^J = h_{ij}(D_{ij}^p, W_{ij}^p, \dots) \quad (6)$$

and

$$\dot{\sigma}_{ij}^J = k_{ij}(D_{ij}^p, W_{ij}^p, \dots) \quad (7)$$

Here,  $r_{ij}$  is the back-stress;  $r_{ij}^J$  the Jaumann rate of the back-stress;  $D_{ij}^p$  the plastic part of the velocity strain  $D_{ij}$ ; and  $\sigma'_{ij}$  is the deviator of the Kirchhoff stress.

Integral representations for the combined isotropic/kinematic hardening plasticity theories of the above type have been discussed in Im and Atluri

(1987b). It is noted here that  $r_{ij} = 0$ ;  $W_{ij}^p = 0$  in the case of isotropic hardening. The evolution equations for  $\dot{\sigma}_{ij}^J$  is given by:

$$\begin{aligned} \dot{\sigma}_{ij}^J &\equiv \dot{\sigma}_{ij} - W_{ik}\sigma_{kj} + \sigma_{ik}W_{kj} \\ &= E_{ijkl}(D_{kl} - D_{kl}^p) - W_{ik}^p\sigma_{kj} + \sigma_{ik}W_{kj}^p \end{aligned} \quad (8)$$

## 2.2 Local weak form with the large deformations

In the MLPG approaches, one may write a weak form over a local sub-domain  $\Omega_s$ , which may have an arbitrary shape, and contain the a point  $\mathbf{x}$  in question. A generalized local weak form of the differential equation in Eq. 2.2, over a local sub-domain  $\Omega_s$ , can be written as:

$$\int_{\Omega_s} [(\dot{S}_{ij} + \tau_{ik}v_{j,k})_{,i} + \dot{f}_j] w_j d\Omega = 0 \quad (9)$$

where  $w_j$  are the test functions.

By applying the divergence theorem, Eq. (9) may be rewritten in a symmetric weak form as:

$$\begin{aligned} &\int_{\partial\Omega_s} (\dot{S}_{ij} + \tau_{ik}v_{j,k}) n_i w_j d\Gamma \\ &- \int_{\Omega_s} [(\dot{S}_{ij} + \tau_{ik}v_{j,k}) w_{j,i} - \dot{f}_j w_j] d\Omega = 0 \end{aligned} \quad (10)$$

One may define the rate of tractions  $t_j$  as:

$$t_j = (\dot{S}_{ij} + \tau_{ik}v_{j,k}) n_i \quad (11)$$

where  $n_i$  are components of a unit outward normal to the boundary of the local subdomain  $\Omega_s$ , in its current configuration. Thus one may rewrite the local symmetric weak form as

$$\begin{aligned} &\int_{L_s} t_i w_i d\Gamma + \int_{\Gamma_{su}} t_i w_i d\Gamma + \int_{\Gamma_{st}} \dot{t}_i w_i d\Gamma \\ &- \int_{\Omega_s} [(\dot{S}_{ij} + \tau_{ik}v_{j,k}) w_{j,i} - \dot{f}_i w_i] d\Omega = 0 \end{aligned} \quad (12)$$

where  $\Gamma_{su}$  is a part of the boundary  $\partial\Omega_s$  of  $\Omega_s$ , over which the essential boundary conditions are specified. In general,  $\partial\Omega_s = \Gamma_s \cup L_s$ , with  $\Gamma_s$  being a part of the local boundary located on the global boundary, and  $L_s$  is the other part of the local boundary which is inside the solution domain.  $\Gamma_{su} = \Gamma_s \cap \Gamma_u$  is the intersection between the local boundary  $\partial\Omega_s$  and the global displacement boundary  $\Gamma_u$ ;  $\Gamma_{st} = \Gamma_s \cap \Gamma_t$  is a part of the boundary over which the natural boundary conditions are specified.

One may use the Heaviside function as the test function in the local symmetric weak form in Eq. (12), and obtain,

$$-\int_{L_s} \dot{t}_i d\Gamma - \int_{\Gamma_{su}} \dot{t}_i d\Gamma = \int_{\Gamma_{st}} \dot{\bar{t}}_i d\Gamma + \int_{\Omega_s} \dot{f}_i d\Omega \quad (13)$$

Eq. 2.3 has the physical meaning that it represents the balance law of the local sub-domain  $\Omega_s$ , as conventional finite volume methods.

### 2.3 Meshless interpolation for the mixed method

The MLS method of interpolation is generally considered to be one of the best schemes to interpolate random data with a reasonable accuracy, because of its completeness, robustness and continuity. With the MLS, the distribution of a function  $u$  in  $\Omega_s$  can be approximated, over a number of scattered local points  $\{\mathbf{x}_i\}$ , ( $i = 1, 2, \dots, n$ ), as,

$$u(\mathbf{x}) = \mathbf{p}^T(\mathbf{x})\mathbf{a}(\mathbf{x}) \quad \forall \mathbf{x} \in \Omega_s \quad (14)$$

where  $\mathbf{p}^T(\mathbf{x}) = [p_1(\mathbf{x}), p_2(\mathbf{x}), \dots, p_m(\mathbf{x})]$  is a monomial basis of order  $m$ ; and  $\mathbf{a}(\mathbf{x})$  is a vector containing coefficients, which are functions of the global Cartesian coordinates  $[x_1, x_2, x_3]$ , depending on the monomial basis. They are determined by minimizing a weighted discrete  $L_2$  norm, defined, as:

$$\begin{aligned} J(\mathbf{x}) &= \sum_{i=1}^m w_i(\mathbf{x}) [\mathbf{p}^T(\mathbf{x}_i)\mathbf{a}(\mathbf{x}) - \hat{u}_i]^2 \\ &\equiv [\mathbf{P} \cdot \mathbf{a}(\mathbf{x}) - \hat{\mathbf{u}}]^T \mathbf{W} [\mathbf{P} \cdot \mathbf{a}(\mathbf{x}) - \hat{\mathbf{u}}] \end{aligned} \quad (15)$$

where  $w_i(\mathbf{x})$  are the weight functions and  $\hat{u}_i$  are the fictitious nodal values.

One may obtain the shape function as,

$$u(\mathbf{x}) = \mathbf{p}^T(\mathbf{x})\mathbf{A}^{-1}(\mathbf{x})\mathbf{B}(\mathbf{x})\hat{\mathbf{u}} \equiv \Phi^T(\mathbf{x})\hat{\mathbf{u}} \quad \forall \mathbf{x} \in \partial\Omega_x \quad (16)$$

where matrices  $\mathbf{A}(\mathbf{x})$  and  $\mathbf{B}(\mathbf{x})$  are defined by

$$\mathbf{A}(\mathbf{x}) = \mathbf{P}^T \mathbf{W} \mathbf{P} \quad \mathbf{B}(\mathbf{x}) = \mathbf{P}^T \mathbf{W} \quad \forall \mathbf{x} \in \partial\Omega_x \quad (17)$$

The weight function in Eq. (15) defines the range of influence of node  $I$ . Normally it has a compact support. A fourth order spline weight function is used in the present study.

From the definition of the rate of tractions in Eq. (14), the integrals in the local weak form in Eq. 2.3 are based on the derivatives of the shape functions given in Eq. (16).

It is well known that the calculation of the derivatives of the shape functions is computationally costly. One may following the original idea reported by [Atluri, Han, and Rajendran (2004)] and interpolate the gradients of the velocities indecently. Thus no derivatives are required to perform the local weak form integration. One may use the same shape functions in Eq. (16) for the gradient interpolation, as

$$v_{i,j}(\mathbf{x}) = \sum_{K=1}^N \Phi^{(K)}(\mathbf{x}) v_{i,j}^{(K)} \quad (18)$$

where  $v_{i,j}^{(K)}$  are the gradients of the velocities at node  $K$ , which can be determined at the nodes by enforcing the compatibility condition through the standard collocation method. The interpolation of the velocities can be also written from the same shape functions, as

$$v_i(\mathbf{x}) = \sum_{J=1}^N \Phi^{(J)}(\mathbf{x}) v_i^{(J)} \quad (19)$$

Thereafter, the compatibility condition is enforced at node  $K$  by differentiating the velocity fields in Eq. (19), as

$$v_{i,j}(\mathbf{x}^{(I)}) = \frac{\partial v_i}{\partial x_j}(\mathbf{x}^{(I)}) \quad (20)$$

By interpolating the gradients of the velocities, as one of the key features of the mixed method, the integrals in the local weak form involve no derivatives, i.e. the differentiation operations of the shape functions. In addition, most nonlinear constitute equations are based on the gradients, and the stress measures are transformed through the gradients. By extending the mixed method by Atluri, Han, and Rajendran (2004)[wherein strains and displacements were independently interpolated], the present mixed method[wherein the displacement gradients and displacements are independently interpolated] still holds the same advantages: a) the efficiency of the present method is improved over the traditional MLPG [primal] displacement methods; b) the requirement of the completeness and continuity of the shape functions is reduced by one-order, because the gradients are interpolated independently. Thus, lower-order polynomial terms can be used in the meshless approximations, and leads to a smaller nodal influence size to speed up the calculation of the shape functions.

## 2.4 Small and finite strain elasto-plasticity for velocity gradients

The analyses of small and finite strain elasto-plasticity are presented, along with the detailed numerical implementations for the numerical evaluations of singular integrals. We consider a general type of elasto-plastic constitutive model, which includes the isotropic, the kinematic and the combined isotropic/kinematic hardening behavior of the solid at large strains. It is known that in a kinematic hardening large strain plasticity model, if the evolution equations for the Jaumann rates of the Kirchhoff stress and of the back-stress, respectively, are simply taken to be linear functions of the plastic component of the velocity strain, certain anomalous consequences, such as an oscillatory stress response of the material in finite simple shear, may result [Atluri (1984), Reed and Atluri (1985)]. More general evolution equations, especially to account for the noncoaxiality of the Cauchy stress and the Cauchy-like back-stress in shear and nonproportional loadings, have been attempted by Atluri (1984) and by Reed and Atluri (1985) to suppress the physically unacceptable oscillatory stress responses. Although these methods based on formal continuum mechanics were quite successful for the simple shear case, the physics and micromechanics of finite plastic flow indicate that a more consistent large strain elasto-plastic constitutive law should involve an evolution equation for the plastic component of the spin tensor. Such an elastic-plastic constitutive model has been developed, for instance, in Im and Atluri (1987), which is the finite strain version of the endochronic constitutive model of Watanabe and Atluri (1986). Here, the concept of a material director triad is introduced and the relaxed intermediate configuration is chosen to be isoclinic. The plastic spin tensor is defined through internal time. Such an endochronic constitutive model (for large strain elasto-plasticity) employed here, can be summarized as follows.

Let  $N_{ij}$  be the normal to the yield surface in the deviatoric Kirchhoff stress space. When the stress is on the yield surface and  $N_{ij}D_{ij} \geq 0$ , the process is a plastic process.

$$N_{ij} = (\tau'_{ij} - r_{ij}) / \|\tau'_{ij} - r_{ij}\| \quad (21)$$

$$\zeta = D_{ij}N_{ij}/C \quad (22)$$

$$D_{ij}^p = N_{ij}\zeta \quad (23)$$

$$W_{ij}^p = \Omega_{ij}\zeta \quad (24)$$

$$\Omega_{ij} = \left\{ \frac{m_1(r_{ik}\tau'_{kj} - \tau'_{ik}r_{kj})}{\tau_y^2 f^2(\zeta)}, \right. \\ \left. \frac{m_2(r_{ik}r_{kl}\tau'_{lj} - \tau'_{ik}r_{kl}r_{lj})}{\tau_y^3 f^3(\zeta)}, \right. \\ \left. \frac{m_3(r_{ik}\tau'_{kl}\tau'_{lj} - \tau'_{ik}\tau'_{kl}r_{lj})}{\tau_y^3 f^3(\zeta)} \right\} \quad (25)$$

$$(\tau'_{ij} - r_{ij})(\tau'_{ij} - r_{ij}) = \tau_y f^2(\zeta) \quad (26)$$

$$\dot{\tau}_{ij}^J = \lambda(D_{kk})\delta_{ij} + 2\mu(D_{ij} - D_{ij}^p) - W_{ik}^p\tau_{kj} + \tau_{ik}W_{kj}^p \quad (27)$$

$$\dot{r}_{ij}^J = 2\mu\rho_1 D_{ij}^p - \frac{\alpha r_{ij}(D_{kl}^p D_{kl}^p)^{1/2}}{f(\zeta)} - W_{ik}^p r_{kj} + r_{ik}W_{kj}^p \quad (28)$$

where,  $r_{ij}$  is the back-stress and  $\tau'_{ij}$  is the deviatoric part of Kirchhoff stress  $\tau_{ij}$ .  $f(\zeta)$  and  $r_{ij}$  represent the expansion and translation of von Mises type yield surface.  $D_{ij}^p$  and  $W_{ij}^p$  are the rate of plastic strain and the plastic spin, respectively.  $\zeta$  represents the internal time variable. It is seen that  $\Omega_{ij}$  accounts for the noncoaxiality of the tensors  $\tau'_{ij}$  and  $r_{ij}$ . The coefficient  $C$  is defined as a kernel function. The reader is referred to Im and Atluri (1987) for further details of the constitutive model.

## 2.5 Numerical quadrature

In the present study, the integrations are performed numerically by using the conventional Gauss quadrature scheme. To improve the performance of the numerical integration, the local subdomain (i.e. a circle for 2D problems) is divided into arcs, as in Atluri, Han, and Rajendran (2004). For 3D problems, the local subdomain (i.e. a sphere) is partitioned by triangles for the surface integration [Han and Atluri (2004a)]. The same algorithms are re-used in the present study.

## 3 Numerical Experiments

Several nonlinear problems in 2D and 3D are solved, to illustrate the effectiveness of the present method. The first two examples studied are 2D static problems, such as the patch tests, including (i) a tensile bar, (ii) a cantilever beam under shear load. The third example is the Taylor's impact problem, for explicit dynamics.

### 3.1 A tensile bar

A tensile bar is analyzed as the first example. The rectangular bar is subjected to tensile deformation (in plane strain) with shear free end conditions, as shown in Figure 1. It has a length of  $1.0m$  and a width of  $0.2m$ . The material behaviour is taken to be neo-Hookean hyperelastic. The strain energy is split into deviatoric and volumetric parts to account for the incompressibility condition as:



**Figure 1** : A bar under uniform tension

$$W_0 = W_{\text{deviatoric}} + W_{\text{volumetric}}$$

$$W_{\text{deviatoric}} = C_{10}(\bar{I}_1 - 3)$$

$$W_{\text{volumetric}} = \frac{9K}{2}(J^{\frac{1}{3}} - 1)^2 \quad (29)$$

where

$$\bar{I}_1 = I_1 I_3^{-\frac{1}{3}}, \quad I_1 = \text{tr}(\mathbf{C})$$

$$\bar{I}_2 = I_2 I_3^{-\frac{2}{3}}, \quad I_2 = \frac{1}{2}(\mathbf{C} : \mathbf{C} - I_1^2)$$

$$I_3 = \det(\mathbf{C})$$

$$J = \text{sqrt}(I_3)$$

and

$\mathbf{C} = \mathbf{F}^T \cdot \mathbf{F}$  is the right Cauchy-Green deformation tensor.

In the present study, the bulk modulus is taken as  $2 \times 10^7 \text{ MPa}$  and the shear modulus as  $7.5 \times 10^6 \text{ MPa}$ . The bar is modeled with 100 nodes as 25 nodes in 4 rows. The linear displacement fields are expected in the uniform deformations. The polynomials with first order completeness are used for the MLS approximation in the present study. Therefore, the present MLPG mixed method is expected to provide an accurate solution, in the patch test. The original MLPG mixed method passed this patch test for linear elastic problems [Atluri, Han and Rajendran (2004)].

The bar is stretched to 7 times of its original length. The numerical results obtained by using the present MLPG method are compared with the analytical solution and the FEM results, shown in Figure 2. A very good agreement is observed between these solutions.

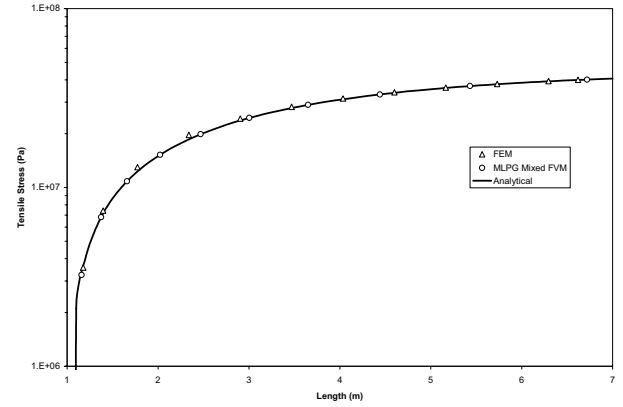


**Figure 2** : Tensile stress of a bar under uniform tension

### 3.2 Cantilever beam

The performance of the present MLPG formulations is also evaluated, using the cantilever beam problem under a transverse load, shown in Figure 3. The beam is considered to undergo large deformations, including large strains and rotations. The linear elastic solution is given in Timoshenko and Goodier (1970), as



**Figure 3** : A cantilever beam with an end load

$$u_x = -\frac{Py}{6EI} [3x(2L-x) + (2+\bar{\nu})(y^2 - c^2)]$$

$$u_y = \frac{P}{6EI} [x^2(3L-x) + 3\bar{\nu}(L-x)y^2 + (4+5\bar{\nu})c^2x] \quad (30)$$

where the moment of inertia  $I$  the beam is given as,

$$I = \frac{c^3}{3} \quad (31)$$

and

$$\bar{E} = \begin{cases} E & \\ E/(1-\nu)^2 & \end{cases}$$

$$\bar{\nu} = \begin{cases} \nu & \text{for plane stress} \\ \nu/(1-\nu) & \text{for plane strain} \end{cases} \quad (32)$$

The corresponding stresses are

$$\sigma_x = -\frac{P}{I}(L-x)y$$

$$\sigma_y = 0$$

$$\sigma_{xy} = -\frac{P}{2I}(y^2 - c^2) \quad (33)$$

The problem is solved for the plane strain case with  $L = 1.0$ , and  $c = 0.1$ . The same neo-Hookean hyperelastic material is taken for the beam as it in the first example. This problem has been used as an example by Atluri, Han and Rajendran (2004) in the linear elasto-static case. The effects of the MLS support and test sizes have also been investigated. In the present study, we revisit this example with for large deformations. Based on the numerical results by Atluri, Han and Rajendran (2004), a regular uniform nodal configuration with nodal distance,  $d$ , of 0.5 is used. The number of nodes is 105. The first order MLS is used for the meshless approximation, with a support size of  $1.15d$  and a test size of  $0.6d$ . For comparison purposes, a corresponding Quad-4 elements-based FE mesh has also been created, from the same nodes, for the FEM analysis with the commercial code MARC, .

A total transverse force of  $7.58 \times 10^5 N$  is applied at the free end of the beam. There are 10 constant increment steps to solve this problem by using the present MLPG mixed method. The final vertical displacement at the free end reaches 0.83, which is more than 4 times of the height of the beam. The final deformed beam is shown in Figure 5a. The problem is also solved by using MARC, as a full nonlinear analysis. The FE results give the same deformation shown in Figure 5b. The vertical displacements are shown in Figure 6. It can be seen that the numerical results agree well with those obtained by using the FE code.

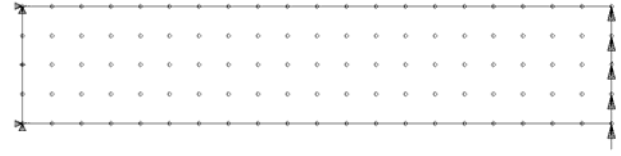
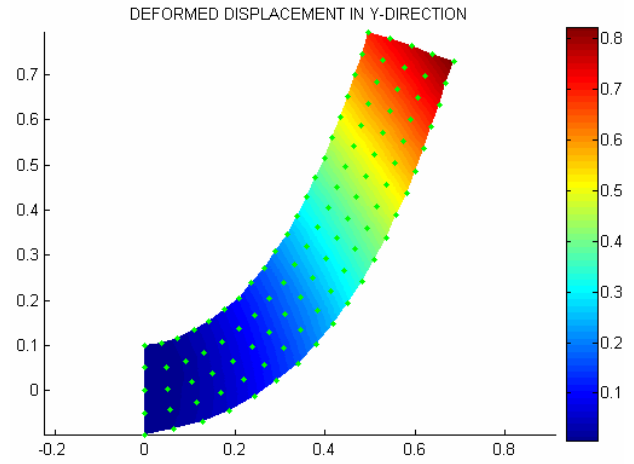
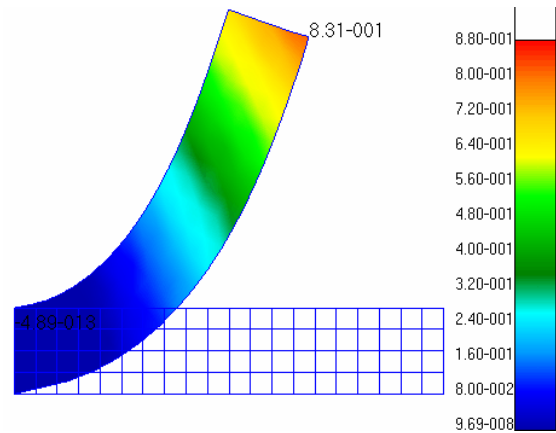


**Figure 4 :** Nodal configuration for a cantilever beam with 105 nodes



(a) The present MLPG mixed method



(b) FEM

**Figure 5 :** Vertical displacement field of the deformed cantilever beam under a transverse load.

The vertical stress distribution obtained by using the present MLPG method is shown in Figure 7a, and that

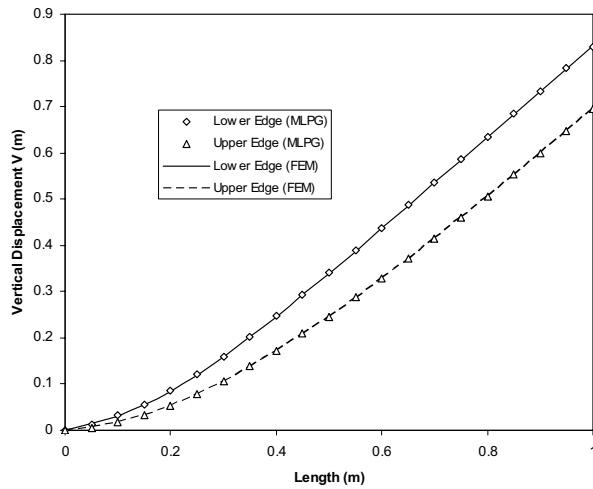
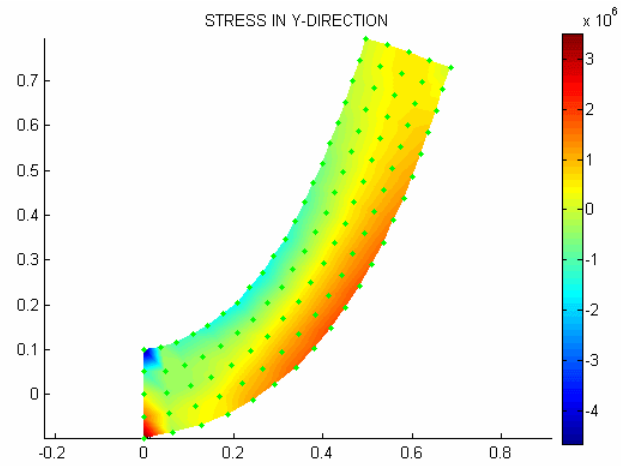


**Figure 6 :** Vertical displacements of a cantilever beam under a transverse load, along the lower and upper edges of the beam.

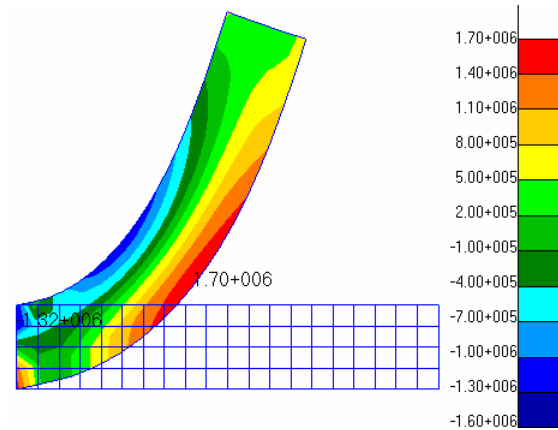
by using the FE method in Figure 7b. Both methods give the similar distributions. However, there is some difference at the corners of two ends of the beam. The stresses in the vertical direction at the lower and upper free edges are shown in Figure 8. It shows that the MLPG mixed method gives higher stresses at the fixed end, because of the stress concentration due to the fixed boundary conditions. At the free end, the MLPG mixed method gives the stress values that tend to zero as the parabolic transverse load is applied. Such numerical results confirm that the MLPG mixed method gives more accurate strain/stress (i.e. the derivative fields) results to enforce the balance laws locally. It should be pointed out that the current MLPG mixed method does not require any special numerical treatments to avoid any shear locking. It is straightforward to extend this method for other PDEs.

### 3.3 Taylor's problem: high speed impact

The Taylor test is often used to determine the dynamic yield stress of a material in a state of uniaxial stress. In this test, a right circular cylinder is impacted against a rigid wall. From measurements of the initial and final dimensions of the cylinder as well as the velocity of impact, the dynamic yield stress is calculated from an analytical relationship derived by Taylor (1948). However during 1990s, the Taylor test configuration has been routinely used to validate constitutive models developed for appli-



(a) The present MLPG mixed method



(b) FEM

**Figure 7 :** Stress distribution in the vertical direction of a cantilever beam under a transverse load code.

cations involving high strain rates. The high strain rate model parameters are often determined and calibrated using stress-strain curve data obtained from a number of conventional dynamic tests. Nicholas and Rajendran (1990) described these various dynamic tests and several high strain rate constitutive models. Most of the test configurations involve small strains and idealized stress / strain states, such as uni-axial stress and one-dimensional strain. The idea behind the Taylor test validation effort is to compare the high-speed-camera- measured time-resolved profiles (shapes or contours) of the plastically deforming cylinder with the profiles obtained from com-

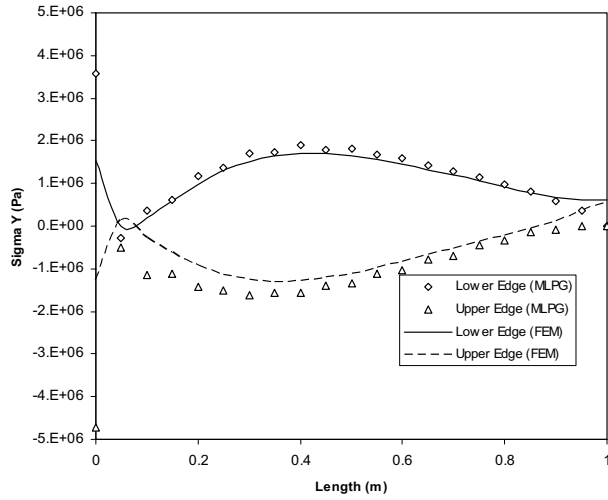


**Figure 8 :** Vertical stress of a cantilever beam under a transverse load, along the lower and upper edges of the beam.

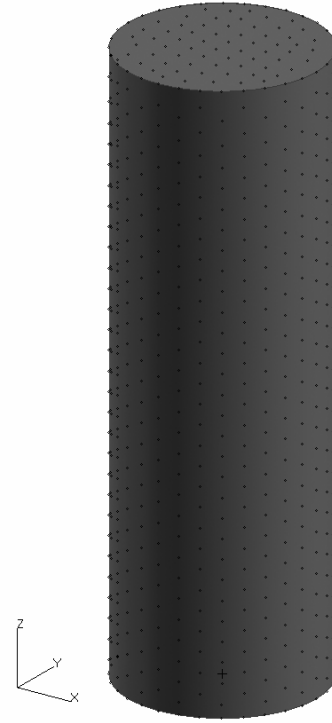


**Figure 10 :** A nodal configuration for the Taylor's problem: 3872 nodes.

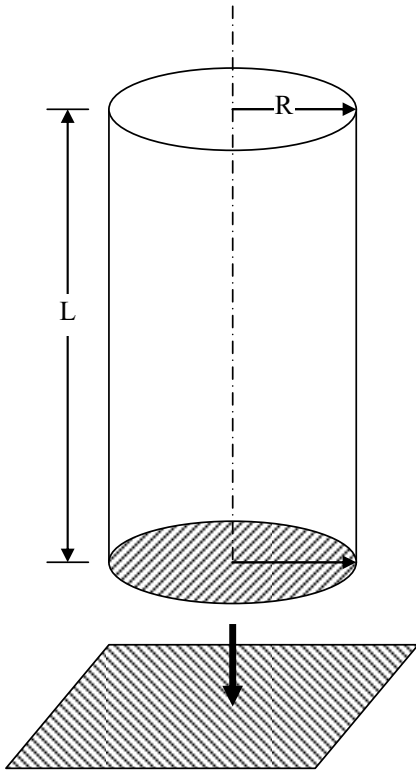
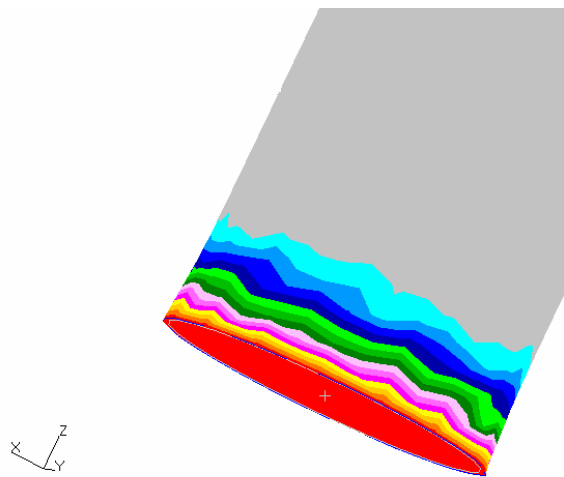


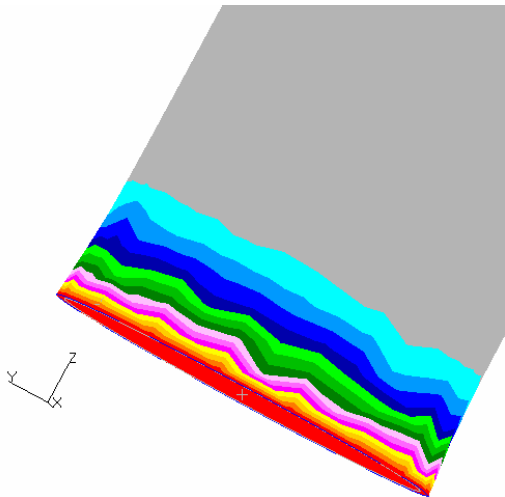
**Figure 9 :** Taylor's problem: a solid cylinder impacting a rigid surface

putational simulations. The loading conditions in Taylor tests involve very large deformation ( $>100$  percent), multi-axial stress/strain state, high temperature, and very high non-uniform strain rates.

The Taylor impact problem can simply be described as a solid cylinder impacting a rigid surface in the normal direction, shown in Figure 9. In the present study, a cylinder with a length of  $12.7\text{ cm}$  ( $0.5\text{ in}$ ) and a radius of  $76.2\text{ cm}$  ( $3\text{ in}$ ) is impacting a rigid surface with an initial impact velocity of  $300\text{ m/s}$ . It is assumed that there is no friction between the contact surfaces. The material is chosen as the isotropic-hardening elasto-plastic metal. The material properties are chosen as: the Young's modulus  $E = 199.948\text{ GPa}$ , the Poisson's ratio  $\nu = 0.28$ , the yield strength  $\sigma_s = 310.26\text{ MPa}$ , and the hardening tangent modulus  $H = E/100 = 1.99948\text{ GPa}$  for the nearly perfect plasticity. The cylinder is modeled with a nodal configuration with 3872 nodes, shown in Figure 10. There is an initial gap of  $0.1\text{ mm}$  between the bottom of the cylinder and rigid surface.



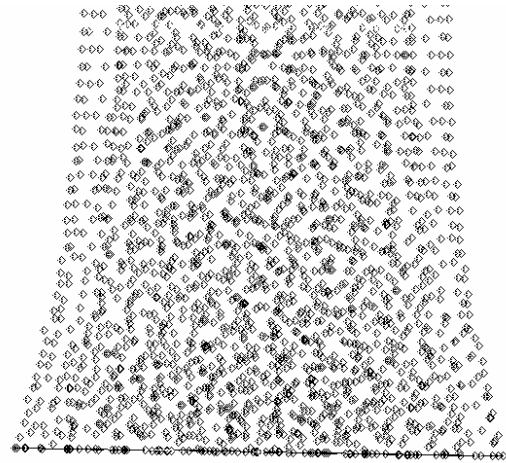
(a) MLPG Mixed Method



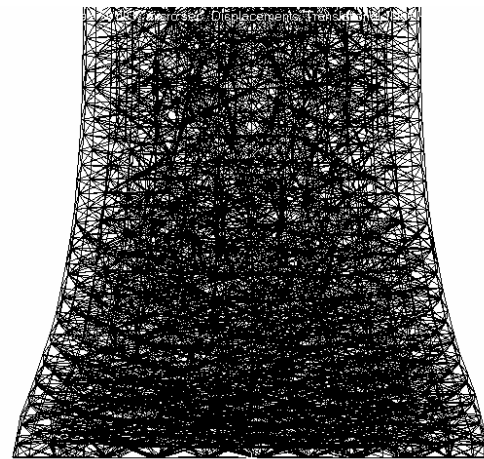
(b) Dyna3D

**Figure 11 :** Vertical displacement distribution of the Taylor's problem while starting contact (at  $t = 2$  micro seconds)

This Taylor impact problem is simulated using the present MLPG finite-volume mixed method, with a dynamic explicit algorithm for the direct time integration [Han and Atluri (2004b)]. The vertical displacements are shown in Figure 11a at 2 micro seconds, as the shock wave is propagating from the bottom surface towards the top surface of the cylinder. For comparison purposes, the LLNL Dyna3D (2000) is also used to analyze this problem, using the mesh generated from the same nodal



(a) MLPG Mixed Method



(b) Dyna3D

**Figure 12 :** Deformed profile of the cylinder (Taylor's problem) at  $t = 50$  micro seconds

configuration. Comparing Figs 11a and 11b, the wave propagation patterns from the MLPG and the Dyna3D simulations are quite similar.

The top surface of the cylinder reaches the lowest point at about 50 micro seconds. The deformed profile of the cylinder is shown in Figure 12a by using the MLPG mixed method, and in Figure 12b by using Dyna3D. Both codes give similar profiles. However, the MLPG method gives a straight corner while Dyna3D gives a curved one, for this *frictionless contact* impact. The corners of the deformed profiles are enlarged in Figure 13. After reaching the lowest point, the cylinder starts to bounce back. The

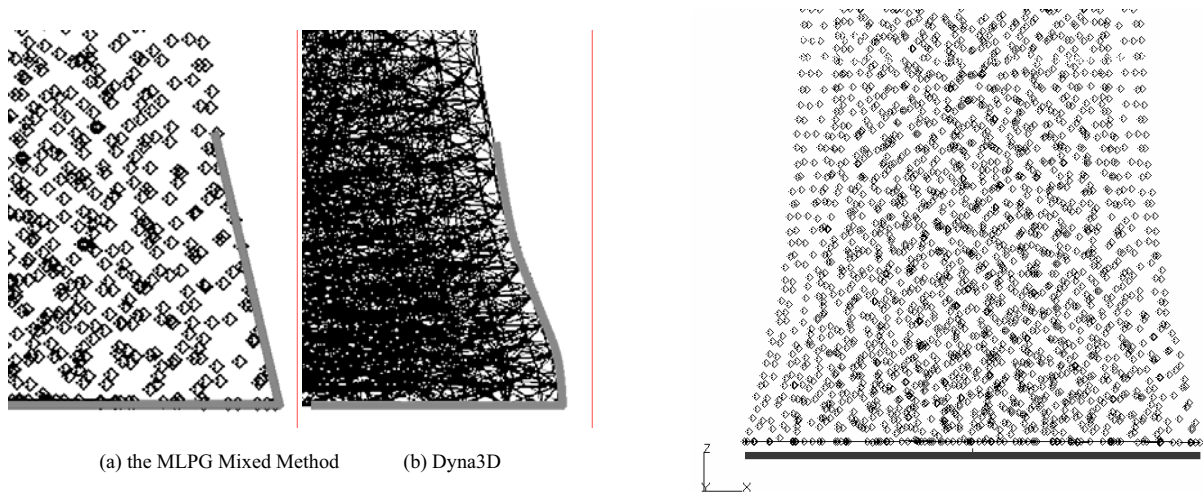


**Figure 13 :** The lower corner of the deformed profile of the cylinder (Taylor's problem) at  $t = 50$  micro seconds

final deformed profiles are shown in Figure 14 at the time of 100 micro seconds. The cylinder is entirely released from contact, and bounces back at a constant velocity, in both the simulations.

In analyzing this problem, the present MLPG mixed method is used without any hour-glass control, or any other artificial numerical treatments. In contrast, one-point Gauss integration scheme is used in Dyna3D with hour-glass control. The total CPU times for the straight-forward MLPG mixed method, and the Dyna3D with hour-glass control and artificial viscosity, are almost same. It clearly demonstrates the superior performance of the present MLPG mixed method as compared to the FEM methods.

#### 4 Closure

The mixed finite volume method (FVM) is developed for nonlinear problems, through the general MLPG approach. The MLS approximations are used for both velocity and velocity-gradients interpolations, independently. By enforcing the compatibility conditions only at nodal points, the present mixed method leads to an efficient quadrature scheme for performing the integrals in the local weak forms. The numerical examples in 2D statics show the suitability of the present MLPG mixed method for nonlinear problems with extremely large deformations and rotations. For the high-speed impact problems, the 3D Taylor-impact example demon-

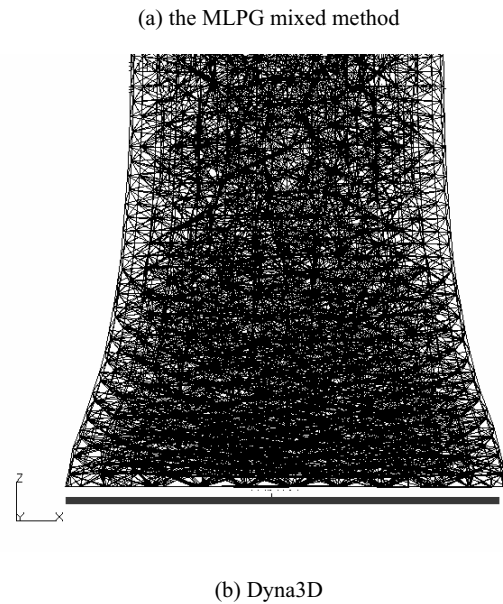


**Figure 14 :** Spring back of the cylinder (Taylor's problem) after impact at  $t = 50$  micro seconds

strates that the present mixed method possesses an excellent accuracy and efficiency, as compared to the FEM. *The present method requires no special numerical treatments to handle the nonlinear static and dynamic problems, such as the reduced integration, hour-glass control, and so on.* The present method is based on the local weak form and the nodal forces are assembled locally. It makes the present method suitable for parallel computation. With these distinct advantages, it can be concluded that the present MLPG mixed method is one of the most promising methods for the nonlinear problems with high-

speed large deformations.

**Acknowledgement:** The results presented in this paper were obtained during the course of investigations supported by the Army Research Office.

## References

- Atluri, S.N** (2004): *The Meshless Local Petrov-Galerkin (MLPG) Method for Domain & Boundary Discretizations*, Tech Science Press, 665 pages.
- Atluri, S. N.** (1980): On some new general and complementary energy theorems for the rate problems of finite strain, classical elastoplasticity. *Journal of Structure and Mechanics*, vol. 8, pp. 61-92.
- Atluri, S. N.** (1984). On constitutive relations at finite strain hypo-elasticity and elasto-plasticity with isotropic or kinematic hardening, *Camp. Meth. Appl. Mech. Engng*, vol. 43, pp. 137-171.
- Atluri, S. N.; Han, Z. D.; Rajendran, A. M.** (2004): A New Implementation of the Meshless Finite Volume Method, Through the MLPG "Mixed" Approach, *CMES: Computer Modeling in Engineering & Sciences*, vol. 6, no. 6, pp. 491-514.
- Atluri, S.N., Kim, H.G., Cho, J.Y.** (1999): A Critical Assessment of the Truly Meshless Local Petrov Galerkin (MLPG) and Local Boundary Integral Equation (LBIE) Methods, *Computational Mechanics*, 24:(5), pp. 348-372.
- Atluri, S. N.; Zhu, T.** (1998): A new meshless local Petrov-Galerkin (MLPG) approach in computational mechanics. *Computational Mechanics.*, Vol. 22, pp. 117-127.
- Belytschko, T.; Ong, J. S. J.; Liu, W. K.; Kennedy J. M.** (1984): Hourglass Control in Linear and Nonlinear Problems, *Computer Methods in Applied Mechanics and Engineering*, Vol. 43, No. 3, pp. 251-276.
- DYNA3D User Manual** (1999): A Nonlinear, Explicit, Three-Dimensional Finite Element Code for Solid and Structural Mechanics, Lawrence Livermore National Laboratory.
- Han. Z. D.; Atluri, S. N.** (2004a): Meshless Local Petrov-Galerkin (MLPG) approaches for solving 3D Problems in elasto-statics, *CMES: Computer Modeling in Engineering & Sciences*, vol. 6 no. 2, pp. 169-188.
- Han. Z. D.; Atluri, S. N.** (2004b): A Meshless Local Petrov-Galerkin (MLPG) Approach for 3-Dimensional Elasto-dynamics, *CMC: Computers, Materials & Continua*, vol. 1 no. 2, pp. 129-140.
- Im, S. and Atluri, S. N.** (1987). A study of two finite strain plasticity models: an internal time theory using Mandel's director concept, and a general isotropic/kinematic hardening theory. *International Journal of Plasticity*, vol. 3, pp.163-191.
- Johnson, G. R.; Stryk, R. A.** (2003) Conversion of 3D distorted elements into meshless particles during dynamic deformation, *International Journal of Impact Engineering*, Vol. 28, pp. 947-966.
- Lin, H., Atluri, S.N.** (2001): The Meshless Local Petrov-Galerkin (MLPG) Method for Solving Incompressible Navier-Stokes Equations *CMES: Computer Modeling in Engineering & Sciences*, vol. 2, no. 2, pp. 117-142.
- Malkus, D. S.; Hughes, T. J. R.** (1978): Mixed Finite-Element Methods – Reduced and Selective Integration Techniques – Unification of Concepts, *Computer Methods in Applied Mechanics and Engineering*, Vol. 15 No. 1, pp. 63-81.
- Oden, J. T.; Pires, E. B.** (1983): Nonlocal and Non-linear Friction Laws and Variational Principles for Contact Problems in Elasticity, *Journal of Applied Mechanics*, Vol. 50, No. 1, pp.67-76.
- Ortiz, M.; Pandolfi, A.** (1999): Finite-Deformation Irreversible Cohesive Elements for Three-Dimensional Crack-Propagation Analysis, *International Journal for Numerical Methods in Engineering*, Vol. 44, pp. 1267-1282.
- Reed, K. W. and Atluri, S. N.** (1985). Constitutive modeling and computational implementation for finite strain plasticity. *International Journal of Plasticity*, vol. 1, pp. 63~87.
- Taylor, G.I.** (1948) The use of flat-ended projectiles for determining dynamic yield stress. *Proc. Roy. Soc. Lond., A*, 194, pp. 289-299.
- Timoshenko, S. P.; Goodier, J. N.** (1976): *Theory of Elasticity*, 3<sup>rd</sup> edition, McGraw Hill.
- Watanabe, O. and Atluri, S. N.** (1986). Internal time, general internal variable, and multiyield surface theories of plasticity and creep: a unification of concepts. *International Journal of Plasticity*, vol. 2, pp.107-134.

# The MLPG Mixed Collocation Method for Material Orientation and Topology Optimization of Anisotropic Solids and Structures

Shu Li<sup>1</sup> and S. N. Atluri<sup>2</sup>

**Abstract:** In this paper, a method based on a combination of an optimization of directions of orthotropy, along with topology optimization, is applied to continuum orthotropic solids with the objective of minimizing their compliance. The spatial discretization algorithm is the so called Meshless Local Petrov-Galerkin (MLPG) “mixed collocation” method for the design domain, and the material-orthotropy orientation angles and the nodal volume fractions are used as the design variables in material optimization and topology optimization, respectively. Filtering after each iteration diminishes the checkerboard effect in the topology optimization problem. The example results are provided to illustrate the effects of the orthotropic material characteristics in structural topology-optimization.

**Keyword:** orthotropy, material-axes orientation optimization, topology optimization, meshless method, MLPG, collocation, mixed method

## 1 Introduction

The use of anisotropic materials in structural design provides superior physical and mechanical properties in a wide range of engineering applications such as complex aircraft: low-mass army ground-vehicles, simple sails: high speed and light rotating disks [Spalatel-Lazar, Léné and Turbé(2008), Khoshnood and Jalali (2008)]. Composite materials are used to design a material with properties which are impossible to be achieved by isotropic materials. It is well known that the characteristics and properties of composite structures made of orthotropic materials are di-

rectly related to the orientation of material principal axes. For complicated engineering structures with many design parameters, simple structural design is not sufficient for the desired structural performance. Topology optimization is becoming a potentially important tool for structural design. By adding material where it is required for desired performance, and by removing material where it is redundant, while keeping the volume of the structure constant, topology optimization methods transform the structural design problem into a material distribution optimization problem.

The conventional topology optimization of a structure proceeds in a sequential manner, and it simultaneously solves the equilibrium equations and optimizes the structure subjected to certain objectives and constraints [Norato, Bendsoe, Haber and Tortorelli (2007), Vemaganti and Lawrence (2005), Cisilino(2006), Wang, Lim, Khoo and Wang (2007), Zhou and Wang (2006)]. Simpler, convenient and efficient numerical methods are also mandatory, because of the intensive computation involved in topology optimization. With the potential benefits of the meshless methods, especially research in [Atluri and Zhu(1998), Atluri and Shen(2002a, 2002b), and Atluri(2004)] shows that the MLPG method is becoming the most effective numerical-analytical method for optimizing structures. In this paper, the equilibrium equations of the topology optimization problem are solved by a Meshless Local Petrov-Galerkin (MLPG) “mixed collocation” method which was presented by Atluri, Liu, and Han (2006). This meshless method avoids any numerical integration either over a local domain or over the local boundary and has inherent advantages such as the computational efficiency and the ease of implementation.

In the present work, we extend our previous work

<sup>1</sup> Department of Aircraft Engineering, Beijing University of Aeronautics and Astronautics, Beijing 100083, P.R. China

<sup>2</sup> Center for Aerospace Research & Education, University of California, Irvine, USA

[Li and Atluri (2008)] to perform topology optimization of orthotropic composite structures. This work focuses on a combination of the optimization of material-axes orientation, along with topology optimization, of orthotropic continuum solids. We deal with this problem in two stages. The first stage is based on ideas from optimization of orientation angles of an orthotropic material. The orientations of orthotropic materials are important design parameters, because they can change the structural mechanical behavior. In the “orientation-optimization” of an orthotropic material, one of the early works is due to Pedersen (1989). The objective of the optimization is to treat the compliance minimization as a measure of the material stiffness. To this end the compliance of the structure is evaluated using the Meshless Local Petrov-Galerkin (MLPG) “mixed collocation” method, the one already used by the authors for isotropic plane structures [Li and Atluri (2008)]. Finally, a topology optimization of the orthotropic composite structure, with the optimized material orientations, is performed. The methods can be easily extended to thick-section composite laminates, wherein each lamina can be modeled as an orthotropic material. *The methods that are developed in the present paper, and in Li and Atluri (2008) are germane to our overall goal of implementing multi-scale material and topology optimization strategies for maximizing the fracture and damage resistance of light weight structures subject to intense dynamic loading.*

The outline of this paper is as follows: the MLPG mixed collocation method is introduced in Section 2, where the moving least squares (MLS) approximation is briefly reviewed and the equilibrium equations for an anisotropic solid are discussed. An “optimal orientation-of-material-angles” problem of an anisotropic material is defined in Section 3. Section 4 gives the formulation for the structural topology optimization, a scheme for the Lagrange method and the filtering principle. Several examples are presented to illustrate the characteristics of topology optimization for orthotropic materials, in section 5. Finally, we summarize, discuss, and generalize the results of the paper in section 6.

## 2 MLPG Mixed Collocation Method

### 2.1 The moving least squares (MLS) approximation

The moving least squares (MLS) approximation is often chosen as the interpolation function in a meshless approximation of the trial function. The MLPG Mixed Collocation Method adopts the MLS interpolation [while other functions such as the Radial Basis Functions, MQ, etc. can also equally well be used] to approximate a function  $\mathbf{u}(\mathbf{x})$  over a number of nodes randomly spread within the domain of influence. The approximated function  $\mathbf{u}(\mathbf{x})$  can be written as [Atluri (2004)]

$$\mathbf{u}(\mathbf{x}) = \mathbf{p}^T(\mathbf{x})\mathbf{a}(\mathbf{x}) \quad (1)$$

where  $\mathbf{p}^T(\mathbf{x})$  is a monomial basis which can be expressed as  $\mathbf{p}^T(\mathbf{x}) = [1, x_1, x_2]$  for two-dimensional problems and  $\mathbf{p}^T(\mathbf{x}) = [1, x_1, x_2, x_3]$  for three dimensional problems, respectively.  $\mathbf{a}(\mathbf{x})$  is a vector of undetermined coefficients, which can be obtained by minimizing the weighted discrete  $L_2$  norm, defined as

$$J(\mathbf{x}) = \sum_{I=1}^m \mathbf{w}_I(\mathbf{x}) [\mathbf{p}^T(\mathbf{x}_I)\mathbf{a}(\mathbf{x}) - \hat{u}^I]^2 \quad (2)$$

where  $\{\mathbf{x}_I\} : (I = 1, 2, \dots, m)$  are scattered local points (nodes) to approximate the function  $\mathbf{u}(\mathbf{x})$ ,  $\mathbf{w}_I$  are the weight functions and  $\hat{u}^I$  are the fictitious nodal values. After the coefficient vector  $\mathbf{a}(\mathbf{x})$  is obtained, we substitute it into Eq. (1). The function  $\mathbf{u}(\mathbf{x})$  can be approximated by these fictitious nodal values, as

$$u(\mathbf{x}) = \sum_{I=1}^m \Psi^I(\mathbf{x})\hat{u}^I \quad (3)$$

where  $\hat{u}^I$  is the virtual nodal value at node  $I$ , and  $\Psi^I(\mathbf{x})$  is the shape function. The detailed formulations and discussions for the MLS interpolation, using the true nodal values can be found in Atluri (2004).

Generally speaking, the MLS shape function does not have the Dirac Delta property, namely

$$u^I \equiv u(\mathbf{x}^I) = \sum_{J=1}^m \Psi^J(\mathbf{x})\hat{u}^J \neq \hat{u}^I \quad (4)$$

However, with the mapping relationship between the virtual and true nodal values [Eq. (4)], it is straightforward to establish the trial functions in the true nodal-values space as

$$\mathbf{u}(\mathbf{x}) = \sum_{I=1}^m \Phi^I(\mathbf{x}) \mathbf{u}^I \quad (5)$$

## 2.2 Equilibrium equations

We consider a linear elastic body  $\Omega$  undergoing infinitesimal deformations. The equilibrium equation can be expressed as

$$\nabla \cdot \boldsymbol{\sigma} + \mathbf{f} = \mathbf{0} \quad (6)$$

subject to the boundary conditions:

$$\begin{aligned} \mathbf{u} &= \bar{\mathbf{u}} \quad \text{on } \Gamma_u \\ \mathbf{t} = \mathbf{n} \cdot \boldsymbol{\sigma} &= \bar{\mathbf{t}} \quad \text{on } \Gamma_t \end{aligned} \quad (7)$$

In which  $\boldsymbol{\sigma}$  is the stress tensor,  $\nabla$  is the gradient vector,  $\mathbf{f}$  is the body force vector;  $\mathbf{u}$  is the displacement vector,  $\mathbf{t}$  is the traction vector, and  $\mathbf{n}$  is the outward unit normal to the boundary  $\Gamma$ .

Within the general MLPG framework [Atluri(2004)], one may choose the Dirac Delta function as the test function for the unsymmetric local weak form, and apply it to each nodal point. The momentum balance equation is enforced at the nodal points, as

$$[\nabla \cdot \boldsymbol{\sigma}](\mathbf{x}^I) + \mathbf{f}(\mathbf{x}^I) = \mathbf{0} \quad (8)$$

where  $\{\mathbf{x}^I\}$  ( $I = 1, 2, \dots, N$ ) are the distributed nodes, and  $N$  is the number of total distributed nodes in the solution domain. In the present mixed scheme, we interpolate the displacement vector  $\mathbf{u}(\mathbf{x})$  and the stress tensor  $\boldsymbol{\sigma}(\mathbf{x})$  independently, using the same shape functions obtained from the MLS approximation [Eq. (3)], the displacement field  $\mathbf{u}(\mathbf{x})$  and the stress field  $\boldsymbol{\sigma}(\mathbf{x})$  can be represented in matrix form

$$\mathbf{u}(\mathbf{x}) = \sum_{J=1}^m \Phi^J(\mathbf{x}) \mathbf{u}^J \quad (9)$$

$$\boldsymbol{\sigma}(\mathbf{x}) = \sum_{J=1}^m \Phi^J(\mathbf{x}) \boldsymbol{\sigma}^J \quad (10)$$

Here,  $\mathbf{u}^J$  and  $\boldsymbol{\sigma}^J$  are the nodal displacement vector and stress vector [note that the stress tensor is now symbolically re-written as a stress-vector] at node  $J$ , respectively. In the case of the orthotropic linear elastic problem, the plane orthotropic constitutive relation is described by four independent material parameters and by a specified direction ( $Q_{11} > Q_{22}$ ) as

$$\begin{bmatrix} \sigma_1 \\ \sigma_2 \\ \sigma_{12} \end{bmatrix} = \begin{bmatrix} Q_{11} & Q_{12} & 0 \\ Q_{12} & Q_{22} & 0 \\ 0 & 0 & Q_{66} \end{bmatrix} \begin{bmatrix} \varepsilon_1 \\ \varepsilon_2 \\ \varepsilon_{12} \end{bmatrix}$$

$$Q_{11} = \frac{E_1}{1 - \nu_{12}\nu_{21}}, \quad Q_{22} = \frac{E_2}{1 - \nu_{12}\nu_{21}},$$

$$Q_{66} = G_{12}, \quad Q_{12} = \nu_{12}Q_{11} = \nu_{21}Q_{22}$$

With  $E_1$ ,  $E_2$  the Young's modulus,  $\nu_{12}$ ,  $\nu_{21}$  the Poisson's ratio.

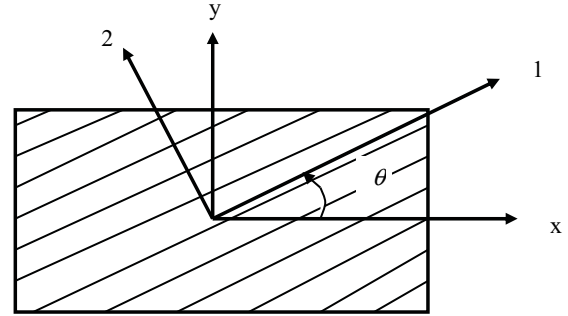


Figure 1: The orientation angle

Using a matrix expression for the rotated elastic coefficients, we can define

$$\begin{bmatrix} \sigma_1 \\ \sigma_2 \\ \sigma_{12} \end{bmatrix} = T \begin{bmatrix} \sigma_x \\ \sigma_y \\ \sigma_{xy} \end{bmatrix}$$

where the matrix  $T$  stands for the rotation matrix,  $\theta$  is the orientation angle of the materials' principle direction of orthotropy. The rotation matrix  $T$  can be given by

$$T = \begin{bmatrix} m^2 & n^2 & 2mn \\ n^2 & m^2 & -2mn \\ -mn & mn & (m^2 - n^2) \end{bmatrix}$$

and

$$T^{-1} = \begin{bmatrix} m^2 & n^2 & -2mn \\ n^2 & m^2 & 2mn \\ mn & -mn & (m^2 - n^2) \end{bmatrix}$$

$$m = \cos \theta, \quad n = \sin \theta$$

The relation between the stress vector  $\boldsymbol{\sigma}$  and strain vector the  $\boldsymbol{\varepsilon}$  can be written as

$$\boldsymbol{\sigma} = \bar{\mathbf{Q}} \cdot \boldsymbol{\varepsilon} \quad (11)$$

Where

$$\bar{\mathbf{Q}} = \mathbf{T}^{-1} \cdot \mathbf{Q} \cdot (\mathbf{T}^{-1})^T$$

$$\boldsymbol{\varepsilon} = \mathbf{L}^* \cdot \mathbf{u} \quad (12)$$

where,  $\mathbf{L}^*$  a differential operator, for the present 2D problem.

Upon substituting the stress interpolation Eq. (10) into Eq. (8), we have

$$\sum_{J=1}^m \nabla \cdot \Phi^J(\mathbf{x}^I) \cdot \boldsymbol{\sigma}^J + \mathbf{f}(\mathbf{x}^I) = 0;$$

$$\text{for } I = 1, 2, \dots, N \quad (13)$$

It clearly shows that there are no second derivatives of the shape functions for the displacements involved in the system equations, due to the independent interpolation of the stress variables. It is well known that in the meshless approximation, specifically the MLS, usually results in a very complex form of the second derivatives. The Eq. (13) has less number of equations than the number of the independent stress variables, because the nodal stress variables are more than the displacement ones. Therefore, we need to establish some more equations in addition to Eq. (11) through the stress displacement relation. The standard collocation method may be applied to enforce the stress displacement relation at each nodal point. For linear elasticity problems, this relation can be written as

$$\boldsymbol{\sigma}(\mathbf{x}^I) \bar{\mathbf{Q}} \cdot \boldsymbol{\varepsilon}(\mathbf{x}^I) = \bar{\mathbf{Q}} \cdot \mathbf{L}^* \cdot \mathbf{u}(\mathbf{x}^I) \quad (14)$$

After substituting the displacement interpolation Eq. (9) into Eq. (14), we have

$$\boldsymbol{\sigma}^J = \sum_{K=1}^m \bar{\mathbf{Q}} \mathbf{B}^J(\mathbf{x}^I) \mathbf{u}^K \quad (15)$$

where

$$\mathbf{B}^J(\mathbf{x}^I) = \begin{bmatrix} \Phi_{,x}^J(\mathbf{x}^I) & 0 \\ 0 & \Phi_{,y}^J(\mathbf{x}^I) \\ \Phi_{,y}^J(\mathbf{x}^I) & \Phi_{,x}^J(\mathbf{x}^I) \end{bmatrix} \quad (16)$$

$$\boldsymbol{\sigma}^J = [\sigma_x^J \quad \sigma_y^J \quad \tau_{xy}^J]^T$$

$$\mathbf{u}^J = [u_x^J \quad u_y^J]^T$$

Eq. (13) and Eq. (14) can be rewritten in the forms as follows, respectively:

$$\mathbf{K}_S \cdot \boldsymbol{\sigma} = \mathbf{f}_b \quad (17)$$

$$\boldsymbol{\sigma} = \mathbf{T} \cdot \mathbf{u} \quad (18)$$

in which  $\mathbf{f}_b$  is the body force vector.

We set  $\mathbf{B}_{IJ} = \mathbf{B}^J(\mathbf{x}^I)$ , thus

$$\mathbf{K}_S = \begin{bmatrix} \mathbf{B}_{11}^T & \mathbf{B}_{12}^T & \cdots & \mathbf{B}_{1n}^T \\ \mathbf{B}_{21}^T & \mathbf{B}_{22}^T & \cdots & \mathbf{B}_{2n}^T \\ \vdots & \vdots & \ddots & \vdots \\ \mathbf{B}_{n1}^T & \mathbf{B}_{n1}^T & \cdots & \mathbf{B}_{nn}^T \end{bmatrix}$$

$$\mathbf{T} = \bar{\mathbf{Q}} \cdot \begin{bmatrix} \mathbf{B}_{11} & \mathbf{B}_{12} & \cdots & \mathbf{B}_{1n} \\ \mathbf{B}_{21} & \mathbf{B}_{22} & \cdots & \mathbf{B}_{2n} \\ \vdots & \vdots & \ddots & \vdots \\ \mathbf{B}_{n1} & \mathbf{B}_{n1} & \cdots & \mathbf{B}_{nn} \end{bmatrix}$$

and

$$\boldsymbol{\sigma} = \begin{bmatrix} \sigma^1 \\ \sigma^2 \\ \vdots \\ \sigma^J \\ \vdots \\ \sigma^N \end{bmatrix} \quad \mathbf{u} = \begin{bmatrix} \mathbf{u}^1 \\ \mathbf{u}^2 \\ \vdots \\ \mathbf{u}^J \\ \vdots \\ \mathbf{u}^N \end{bmatrix}$$

Let

$$\bar{\mathbf{K}} = \mathbf{K}_S \cdot \mathbf{T} \quad (19)$$

which yields the well known formulation of equilibrium equation

$$\bar{\mathbf{K}} \mathbf{u} = \mathbf{f}_b \quad (20)$$

Where

$$\bar{\mathbf{K}}_{IJ} = \sum_{K=1}^m \mathbf{B}_{IK}^T \bar{\mathbf{Q}} \mathbf{B}_{KJ} \quad (21)$$

It should be noted that  $\mathbf{B}_{IK} = \mathbf{B}^K(\mathbf{x}^I)$  and  $\mathbf{B}_{KJ} = \mathbf{B}^J(\mathbf{x}^K)$ . We can write Eq.(21) as

$$\bar{\mathbf{K}}_{IJ} = \sum_{K=1}^m (\mathbf{B}^K(\mathbf{x}^I))^T \hat{\mathbf{Q}} \mathbf{B}^J(\mathbf{x}^K) \quad (22)$$

Obviously,  $\bar{\mathbf{K}}_{IJ}$  is not a symmetric matrix.

### 2.3 Boundary Conditions

The traction boundary conditions are enforced at each of the traction boundary nodes  $K$ , as:

$$\mathbf{n}^K \cdot \boldsymbol{\sigma}^K = \bar{\mathbf{t}}^K \quad \text{for } K = 1, \dots, S \quad (23)$$

where  $S$  is the number of total traction boundary nodes, the matrix  $\mathbf{n}^K$  is the transformation matrix between the coordinates, as

$$\mathbf{n}^K = \begin{bmatrix} n_x^K & 0 & n_y^K \\ 0 & n_y^K & n_x^K \end{bmatrix}$$

and

$$\boldsymbol{\sigma}^K = [\sigma_x^K \quad \sigma_y^K \quad \tau_{xy}^K]^T, \quad \bar{\mathbf{t}}^K = [\bar{t}_x^K \quad \bar{t}_y^K]^T$$

Assuming  $\boldsymbol{\sigma}_1$  and  $\boldsymbol{\sigma}_2$  represent the known and unknown stress vectors, respectively. Hence Eq.(20) can be written as

$$\bar{\mathbf{K}}_1 \cdot \boldsymbol{\sigma}_1 + \bar{\mathbf{K}}_2 \cdot \boldsymbol{\sigma}_2 = \mathbf{f}_b \quad (24)$$

where

$$\boldsymbol{\sigma}_1 = \mathbf{T}_1 \cdot \mathbf{u} \quad (25)$$

$$\boldsymbol{\sigma}_2 = \mathbf{T}_2 \cdot \mathbf{u} \quad (26)$$

Premultiplying Eq. (23) by the penalty number  $\alpha$  and the transpose of the transformation matrix  $\mathbf{n}$ , we obtain:

$$\alpha \mathbf{n}^T \cdot \mathbf{n} \cdot \boldsymbol{\sigma}_1 = \alpha \mathbf{n}^T \cdot \bar{\mathbf{t}} \quad (27)$$

where

$$\mathbf{n} = \begin{bmatrix} \mathbf{n}^1 & & & & 0 \\ & \mathbf{n}^2 & & & \\ & & \ddots & & \\ & & & \mathbf{n}^K & \\ & & & & \ddots \\ 0 & & & & & \mathbf{n}^S \end{bmatrix},$$

$$\boldsymbol{\sigma}_1 = \begin{bmatrix} \sigma^1 \\ \sigma^2 \\ \vdots \\ \sigma^K \\ \vdots \\ \sigma^S \end{bmatrix} \quad \bar{\mathbf{t}} = \begin{bmatrix} \bar{t}^1 \\ \bar{t}^2 \\ \vdots \\ \bar{t}^K \\ \vdots \\ \bar{t}^S \end{bmatrix}$$

It is easy to obtain

$$\boldsymbol{\sigma}_1 + \alpha \mathbf{n}^T \cdot \mathbf{n} \cdot \boldsymbol{\sigma}_1 = \mathbf{T}_1 \cdot \mathbf{u} + \alpha \mathbf{n}^T \cdot \bar{\mathbf{t}} \quad (28)$$

and

$$\boldsymbol{\sigma}_1 = (\mathbf{I} + \alpha \mathbf{n}^T \cdot \mathbf{n})^{-1} (\mathbf{T}_1 \cdot \mathbf{u} + \alpha \mathbf{n}^T \cdot \bar{\mathbf{t}}) \quad (29)$$

where  $\mathbf{I}$  is unit matrix.

Let

$$\mathbf{R} = (\mathbf{I} + \alpha \mathbf{n}^T \cdot \mathbf{n})^{-1} \quad (30)$$

then

$$\boldsymbol{\sigma}_1 = \mathbf{R} \cdot \mathbf{T}_1 \cdot \mathbf{u} + \alpha \mathbf{R} \cdot \mathbf{n}^T \cdot \bar{\mathbf{t}} \quad (31)$$

By substituting Eq. (31) into Eq.(24), we can obtain a discretized system which is expressed as

$$\mathbf{K} \cdot \mathbf{u} = \mathbf{f} \quad (32)$$

where

$$\begin{aligned} \mathbf{K} &= \bar{\mathbf{K}}_1 \cdot \mathbf{R} \cdot \mathbf{T}_1 + \bar{\mathbf{K}}_2 \cdot \mathbf{T}_2 \\ \mathbf{f} &= \mathbf{f}_b - \alpha \bar{\mathbf{K}}_1 \cdot \mathbf{R} \cdot \mathbf{n}^T \cdot \bar{\mathbf{t}} \end{aligned} \quad (33)$$

### 3 Optimal orientation of material axes

We consider the problem of optimal orientation of material axes in two different problems. In the first problem, the design domain consists of an orthotropic material with a fixed orientation angle. In the second problem, the orientation angles are functions of the spatial coordinates in the design domain. The orientation optimization problem is to search for the minimization of total compliance of orthotropic material structures. The design variable is the orientation of material axes. The mean compliance is the function to be minimized with respect to the variations of the orientation angles. Here, 'compliance' is defined as the product of the external loads and the corresponding displacements.

### 3.1 The fixed orientation angle case

According to Eq.(32), the objective function (the mean compliance of a structure) is formulated as follows:

$$C(\theta) = \mathbf{f}^T \cdot \mathbf{u} \quad (34)$$

where  $\mathbf{u}$  is the global displacement vector, and  $\mathbf{f}$  is the prescribed force vector. Considering  $C(\theta)$  as a scalar function, the above expression can also be written, for linear response, as:

$$C(\theta) = \mathbf{u}^T \mathbf{K}^T \mathbf{u} = \mathbf{u}^T \mathbf{K} \mathbf{u} \quad (35)$$

If we set  $\mathbf{K}^T \mathbf{u} = \mathbf{f}'$ , Eq.(35) means that the both systems of  $\mathbf{K} \mathbf{u} = \mathbf{f}$  and  $\mathbf{K}^T \mathbf{u} = \mathbf{f}'$  have the same compliance value under the same deformation condition.

The orientation optimization problem is treated as an unconstrained optimization problem. The mathematical statement of the orientation optimization problem is as follows:

$$\min_{\theta} C(\theta) \quad (36)$$

The optimization problem is solved using a sequential quadratic programming algorithm. This algorithm requires the sensitivity derivatives of the objective function with respect to the design variables to determine the optimal orientation of extreme compliance.

For the single orientation angle case, the orientation optimization problem only has a design variable  $\theta$ . We now differentiate Eq. (36) with respect to  $\theta$ :

$$\begin{aligned} \frac{dC(\theta)}{d\theta} &= \frac{d\mathbf{u}^T}{d\theta} \mathbf{K} \mathbf{u} + \mathbf{u}^T \frac{d\mathbf{K}}{d\theta} \mathbf{u} + \mathbf{u}^T \mathbf{K} \frac{d\mathbf{u}}{d\theta} \\ &= \mathbf{u}^T \frac{d\mathbf{K}}{d\theta} \mathbf{u} + \mathbf{u}^T (\mathbf{K} + \mathbf{K}^T) \frac{d\mathbf{u}}{d\theta} \end{aligned} \quad (37)$$

Using the fact that applied forces are design-independent of  $\mathbf{K} \mathbf{u} = \mathbf{f}$  and  $\mathbf{K}^T \mathbf{u} = \mathbf{f}'$ , we have

$$\begin{aligned} \mathbf{K} \frac{d\mathbf{u}}{d\theta} &= -\frac{d\mathbf{K}}{d\theta} \mathbf{u} \\ \mathbf{K}^T \frac{d\mathbf{u}}{d\theta} &= -\frac{d\mathbf{K}^T}{d\theta} \mathbf{u} \end{aligned}$$

Finally, the sensitivity derivatives of the compliance function is given by

$$\frac{dC(\theta)}{d\theta} = -\mathbf{u}^T \frac{d\mathbf{K}^T}{d\theta} \mathbf{u} \quad (38)$$

### 3.2 The distributed angles case

When the material-orientation angles are functions of spatial coordinates at discrete locations, the orientation optimization problem is a multi-variable  $\theta = (\theta_1, \theta_2, \dots, \theta_n)$  design problem. The orientation optimization problem is stated as:

$$\min_{\theta_i} C(\theta_i)$$

Eq.(38) can be extended to multiple variable cases as follows,

$$\frac{\partial C(\theta)}{\partial \theta_i} = -\mathbf{u}^T \frac{\partial \mathbf{K}^T}{\partial \theta_i} \mathbf{u} \quad (39)$$

A sequential quadratic programming algorithm is also used to solve the optimal design problem.

## 4 Topology optimization problem

### 4.1 General topology optimization

Topology-optimization implies the optimal distribution of material in a structure, so as to minimize its compliance, subject to the specified constraints of the total material to be used. According to Eq.(32), the mean compliance of a structure is formulated as follows:

$$C = \mathbf{f}^T \cdot \mathbf{u}$$

where  $\mathbf{u}$  is the global displacement vector,  $\mathbf{f}$  is the force vector. Also, the above expression can also be written, for linear response, as:

$$C = \mathbf{u}^T \mathbf{K} \mathbf{u} \quad (40)$$

In this paper, Eq.(40) is formed by using the MLPG Mixed Collocation Method. The design domain  $\Omega$  (Fig.1) is partitioned into randomly distributed  $N$  nodes which have no connectivity in the form of a mesh. For an arbitrary node  $i$ , if the number of nodes around point  $i$  which influence

the trial function at node  $i$  is  $r$ , a sub-system consists of these  $r$  nodes. In this sub-system, we have

$$\mathbf{k}_i \mathbf{u}_i = \mathbf{f}_i \quad (41)$$

where  $\mathbf{u}_i$  is the displacement vector and  $\mathbf{k}_i$  is the “stiffness” matrix constructed in the same way as Eq.(19). The MLPG form of Eq.(40) becomes

$$C = \sum_{i=1}^N \mathbf{u}_i^T \mathbf{k}_i \mathbf{u}_i \quad (42)$$

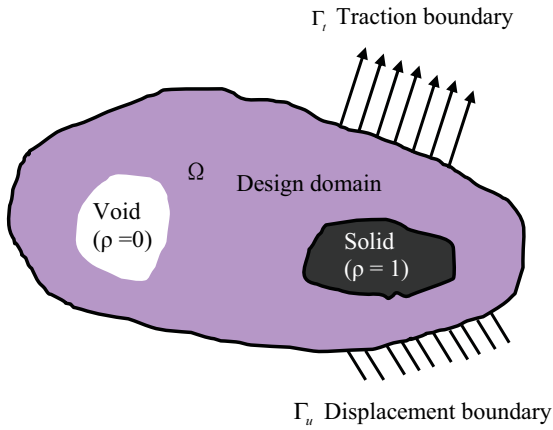


Figure 2: Topology optimization design domain

If we consider the nodal volume fractions  $\rho_i$  as the design variables, then the topology optimization problem for minimizing the compliance can thus be stated, with the volume constraint  $V^*$  as follows:

$$\begin{aligned} \min_{\boldsymbol{\rho}} C(\boldsymbol{\rho}) &= \mathbf{u}^T \mathbf{K} \mathbf{u} = \sum_{i=1}^N \mathbf{u}_i^T \mathbf{k}_i \mathbf{u}_i \\ \text{s.t. } V(\boldsymbol{\rho}) &= \sum_{i=1}^N \rho_i V_i = V^* \\ \mathbf{K} \mathbf{u} &= \mathbf{f} \\ 0 < \rho_{\min} &\leq \rho_i \leq 1 \end{aligned} \quad (43)$$

where  $\boldsymbol{\rho}$ , the vector consisting of design variable  $\rho_i$ ,  $\rho_{\min}$ , is the vector of minimum allowable relative volume fractions (non-zero to avoid singularity),  $N$  is the number of nodes to discretize the design domain, and  $V^*$  is the prescribed volume.  $V(\boldsymbol{\rho})$  is the total volume of material.

Setting  $\rho_{\min}$  to a small but positive value keeps the “stiffness” matrix  $\mathbf{k}_i$  from becoming singular. The artificial variable  $\rho_i$  is considered as an indicator of the local material volume  $V_i$ . The final material volume  $V^*$  is linearly related to the design variables.

The Solid Isotropic Material with Penalization (SIMP) model leads to a common and efficient called power-law approach. To avoid intermediate volume fraction values  $\rho_i$  (between 0 and 1), a SIMP-like model (Solid Isotropic Microstructure with Penalty) is adopted in the proposed topology optimization method. In this SIMP-like model, the penalized “stiffness” matrix  $\mathbf{k}_i$  is given by

$$\mathbf{k}_i = (\rho_i)^p \mathbf{k}_i^0 \quad (44)$$

$\mathbf{k}_i^0$  is the initial value of the matrix  $\mathbf{k}_i$ ,  $p$  is the penalization power (typically  $p = 3$ ). Fig.2 displays the relative “stiffness” ratio vs. volume fraction values  $\rho_i$ , for different values of the penalization power  $p$ .

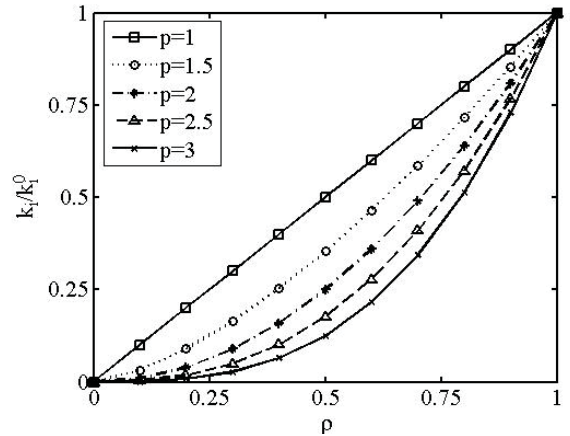


Figure 3: SIMP-like model for different values of the penalization power  $p$

The MLPG Mixed Collocation Method for topology optimization problem requires the computation of the sensitivity derivatives of the compliance with respect to the design variables. The sensitivities of the compliance respect to design variable  $\rho_i$  can be derived from the expression of Eq.(40) in the same manner as Eq.(39) as follows:

$$\frac{\partial C}{\partial \rho_i} = -\mathbf{u}^T \frac{\partial \mathbf{K}^T}{\partial \rho_i} \mathbf{u} \quad (45)$$

Considering the adaptation of the SIMP-like model as Eq.(44), the above expression of Eq.(45) is written as

$$\frac{\partial C}{\partial \rho_i} = -p(\rho_i)^{p-1} \mathbf{u}_i^T (\mathbf{k}_i^0)^T \mathbf{u}_i \quad (46)$$

#### 4.2 The Lagrange method

The classical Lagrangian method is called as the linear Lagrangian theory in [Goh and Yang (2001)]. In the linear Lagrangian theory, the Lagrangian function is a linear combination of the objective and constraint functions for solving constrained optimization problems. Based on linear Lagrangian theory, we consider the Lagrangean associated with the constrained topology optimization problem Eq.(43)

$$L(\boldsymbol{\rho}) = C + \lambda_1 \left( \sum_{i=1}^N \rho_i V_i - V^* \right) + \boldsymbol{\Lambda}^T (\mathbf{K}\mathbf{u} - \mathbf{f}) + \sum_{i=1}^N \mu_1^i (\rho_{\min} - \rho_i) + \sum_{i=1}^N \mu_2^i (\rho_i - 1) \quad (47)$$

where  $\lambda_1$  and  $\mu_i$  are Lagrange multipliers for the equality and inequality constraints, respectively.  $\boldsymbol{\Lambda}$  is the Lagrange multiplier vector.

To tackle this problem, the typical way of the Lagrangian method is the use the Kuhn-Tucker optimality condition which is a generalization of the first order optimality necessary conditions (FONC).

For a general classical single-objective nonlinear programming problem as:

$$\begin{aligned} & \min f(\mathbf{x}) \\ \text{s.t. } & g_i(\mathbf{x}) \leq 0 \quad \text{for } i = 1, 2, \dots, I \\ & h_j(\mathbf{x}) = 0 \quad \text{for } j = 1, 2, \dots, J \\ & \mathbf{x} = (x_1, x_2, \dots, x_N) \end{aligned}$$

The Kuhn-Tucker condition is:

$$\begin{cases} \nabla f(\mathbf{x}) + \sum \mu_i \nabla g_i(\mathbf{x}) + \sum \lambda_j \nabla h_j(\mathbf{x}) = 0 & \text{(optimality)} \\ g_i(\mathbf{x}) \leq 0 \text{ for } i = 1, 2, \dots, I & \text{(feasibility)} \\ h_j(\mathbf{x}) = 0 \text{ for } j = 1, 2, \dots, J & \text{(feasibility)} \\ \mu_i g_i(\mathbf{x}) = 0 \text{ for } i = 1, 2, \dots, I & \text{(complementary slackness condition)} \\ \mu_i \geq 0 \text{ for } i = 1, 2, \dots, I & \text{(non-negativity)} \end{cases}$$

(Note:  $\lambda_j$  is unrestricted in sign)

The Kuhn-Tucker condition is a necessary condition for optimality in constrained minimization (or maximization) under a constraint qualification. Here, the assumption is that  $\nabla g_i(\mathbf{x}^*)$  for  $i$  belonging to active constraints and  $\nabla h_j(\mathbf{x}^*)$  for  $j = 1, \dots, J$  are linearly independent. This is the so-called "constraint qualification".

The Kuhn-Tucker conditions not only give the necessary conditions for optimality but also provide a way of finding optimal solutions. So the Lagrange method essentially transforms a constrained problem to an unconstrained problem.

In this paper, the optimality criterion (OC) was formulated in a form suitable for incorporation in the meshless method codes. The necessary conditions for optimality can be obtained by using the Kuhn-Tucker conditions as follows:

$$\frac{\partial L}{\partial \rho_i} = 0, \quad i = 1, 2, \dots, N$$

Differentiating (47) with respect to  $\rho_i$  and manipulating the terms, the Kuhn-Tucker optimality condition can be written for problems [Eq.(43)] subject to multiple constraints as follows

$$\begin{cases} \frac{\partial L}{\partial \rho_i} = \frac{\partial C}{\partial \rho_i} + \lambda_1 \frac{\partial V}{\partial \rho_i} + \boldsymbol{\Lambda}^T \frac{\partial (\mathbf{K}\mathbf{u})}{\partial \rho_i} - \mu_1 + \mu_2 = 0 \\ V(\boldsymbol{\rho}) = \sum_{i=1}^N \rho_i V_i - V^* = 0 & \text{(the equality constraints)} \\ \mathbf{K}\mathbf{u} = \mathbf{f} & \text{(the equality constraints)} \\ \rho_{\min} - \rho_i \leq 0 & \text{(the inequality constraints)} \\ \rho_i - 1 \leq 0 & \text{(the inequality constraints)} \\ \mu_1 (\rho_{\min} - \rho_i) = 0 \\ \mu_2 (\rho_i - 1) = 0 \\ \mu_i \geq 0 \quad i = 1, 2 \end{cases}$$

(48)

Note:  $\lambda_1$  and  $\mathbf{\Lambda}$  are unrestricted in sign, corresponding to the equality constraints. It is clear that the efficiency of the OC method is determined mainly by the number of active constraints. If  $\rho_{\min} < \rho_i < 1$ , the lower and upper bounds of the design variables are inactive, then we have  $\mu_1 = \mu_2 = 0$ . If  $\rho_i = \rho_{\min}$ , the lower bound of the design variables are active, then we have  $\mu_1 \geq 0$ ,  $\mu_2 = 0$ . If  $\rho_i = \rho_{\max}$ , the upper bound of the design variables are active, then  $\mu_1 = 0$ ,  $\mu_2 \geq 0$ . and (48) yields:

$$\begin{cases} \frac{\partial C}{\partial \rho_i} + \lambda_1 \frac{\partial V}{\partial \rho_i} + \mathbf{\Lambda}^T \frac{\partial (\mathbf{K}\mathbf{u})}{\partial \rho_i} = 0 & \rho_{\min} < \rho_i < 1 \\ \frac{\partial C}{\partial \rho_i} + \lambda_1 \frac{\partial V}{\partial \rho_i} + \mathbf{\Lambda}^T \frac{\partial (\mathbf{K}\mathbf{u})}{\partial \rho_i} \geq 0 & \text{if } \rho_i = \rho_{\min} \\ \frac{\partial C}{\partial \rho_i} + \lambda_1 \frac{\partial V}{\partial \rho_i} + \mathbf{\Lambda}^T \frac{\partial (\mathbf{K}\mathbf{u})}{\partial \rho_i} \leq 0 & \text{if } \rho_i = \rho_{\max} \\ V(\boldsymbol{\rho}) = \sum_{i=1}^N \rho_i V_i - V^* = 0 & \text{(the equality constraints)} \\ \mathbf{K}\mathbf{u} = \mathbf{f} & \text{(the equality constraints)} \\ \mu_i \geq 0 & i = 1, 2 \end{cases} \quad (49)$$

The above sensitivity of a node is dependent on several surrounding points. For different positions, the number of nodes around one point may differ. So the sensitivity analysis is more complex and time consuming when compared with the case of element-based methods.

To derive the iterative formulation more conveniently, only the equality cases in Eq.(49) are used in the present illustration, i.e.

$$\frac{\partial C}{\partial \rho_i} + \lambda_1 \frac{\partial V}{\partial \rho_i} + \mathbf{\Lambda}^T \left( \frac{\partial \mathbf{K}}{\partial \rho_i} \mathbf{u} + \mathbf{K} \frac{\partial \mathbf{u}}{\partial \rho_i} \right) = 0$$

Utilizing the expression  $\mathbf{K}\mathbf{u} = \mathbf{f}$ , it is easy to obtain

$$\frac{\partial \mathbf{K}}{\partial \rho_i} \mathbf{u} + \mathbf{K} \frac{\partial \mathbf{u}}{\partial \rho_i} = 0$$

then

$$p(\rho_i)^{p-1} \mathbf{u}_i^T (\mathbf{k}_i^0)^T \mathbf{u}_i + \lambda_1 V_i = 0 \quad (50)$$

Set

$$B_i = \frac{p(\rho_i)^{p-1} \mathbf{u}_i^T (\mathbf{k}_i^0)^T \mathbf{u}_i}{\lambda_1 V_i} = 1 \quad (51)$$

Eq.(50) is regarded as an Optimally Criterion (OC) based on the discretization of the MLPG Mixed Collocation Method. Thus, we can update the design variables as follows:

$$\rho_i^{\text{new}} = \begin{cases} \max(\rho_{\min}, \rho_i - m) & \text{if } \rho_i B_i^\eta \leq \max(\rho_{\min}, \rho_i - m) \\ \rho_i B_i^\eta & \text{if } \max(\rho_{\min}, \rho_i - m) < \rho_i B_i^\eta < \min(1, \rho_i + m) \\ \min(1, \rho_i + m) & \text{if } \min(1, \rho_i + m) \leq \rho_i B_i^\eta \end{cases} \quad (52)$$

Where  $m$  is the limit ([Bendsøe and Kikuchi (1988)]), which represents the maximum allowable change in the relative nodal volume fractions  $\rho_i$  in the OC iteration.  $\eta$  is the damping coefficient. This updating scheme was often adopted in many presented papers. The values of  $m$  and  $\eta$  influence the convergence of the scheme, and they are chosen by experience ([Bendsøe and Kikuchi (1988)]).

The penalty parameter  $p$  is set to be 3, and the numerical damping coefficient  $\eta$  is set to 0.5. The Lagrange multiplier for the volume constraint  $\lambda_1$  is determined at each OC iteration using a bisectioning algorithm, as in the paper [Sigmund (2001)].

### 4.3 Filtering principle

Here we describe the principle of suppressing checkerboard patterns which is a familiar problem in topology optimization when numerical stability is not guaranteed. The appearance of checkerboarding causes difficulties in interpreting and fabricating topology-optimized structural components. Sigmund (1994, 1997) developed a sensitivity filter method for preventing numerical instabilities from occurring. Filtering techniques have become quite popular in topology optimization [Wang; Lim, Khoo and Wang (2008)]. To tackle checkerboarding, a scheme similar to the filtering method is incorporated in the optimization algorithms based on the meshless discretization. In

this scheme, we modify the design sensitivity of any specific node depending on a weighted average of the node sensitivities in a connected neighborhood. The principle works by modifying the nodal sensitivities as follows

$$\frac{\partial C}{\partial \rho_i} = \frac{1}{\rho_i \sum_{f=1}^m \hat{H}_f} \sum_{f=1}^m \hat{H}_f \rho_f \frac{\partial C}{\partial \rho_f} \quad (53)$$

Here, the convolution operator (weight factor) is written as

$$\hat{H}_f = r_{\min} - \text{dist}(n, f) \{f \in M | \text{dist}(n, f) \leq r_{\min}\}, \quad n = 1, \dots, m \quad (54)$$

and the operator  $\text{dist}(n, f)$  is defined as the distance between node  $n$  and node  $f$ . The convolution operator  $\hat{H}_f$  is zero outside the filter area, and decays linearly with the distance from node  $f$ .

## 5 Numerical examples

In this section, the examples concern two aspects of the problems with several subcases. The first aspect examines the results of the “material-axes orientation” optimization problem. The second aspect of examples examines the effect of topology optimization after finding the optimized “material-axes orientation”. We present several numerical examples (cantilever and MBB-beams). All the examples are treated here as being dimensionless.

### Example 1:

As shown in Fig. 4, the first example is that of a short cantilever beam. The material is orthotropic, with Young’s moduli  $E_1 = 30$ ,  $E_2 = 5$ , Poisson’s ratios  $\mu_{12} = 0.25$  and the shear moduli  $G_{12} = 2$ . The design domain is clamped along the left end and a concentrated vertical load  $P$  is acting at the point A, B and C respectively of the free (right) end of the beam.

The design domain  $\Omega$  is discretized by the MLPG Mixed Collocation Method using uniformly distributed nodes.

### Example 2:

The second example is that of a so-called MBB beam (Fig.7(a)) in which the right half-domain is

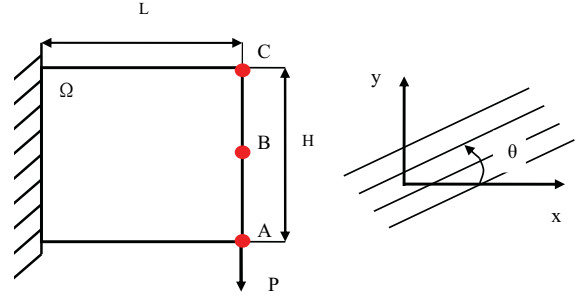


Figure 4: Cantilever beam

modeled as Fig.7(b). This is an orthotropic beam with Young’s moduli  $E_1 = 30$ ,  $E_2 = 5$ , Poisson’s ratios  $\mu_{12} = 0.25$  and the shear moduli  $G_{12} = 2$ . The design domain is discretized into  $60 \times 20$  uniformly distributed nodes in the half-domain. The left bottom is assumed to be fixed, and the right one is assumed to be on a roller.

In the Fig.7(b),  $A_t, B_t, C_t$  and  $A_b, B_b, C_b$  are the 3 points at top and bottom of the MBB beam, respectively, where the concentrated vertical load  $P$  is alternatively applied. The corresponding variations of the relative compliance vs the fixed material-orientation for various locations of the point of application of the load are displayed in Fig.8 and Fig.9. When the concentrated vertical load  $P$  is applied at the middle of the top of the MBB beam, fig.10 gives the curves of the relative compliance vs the fixed material-orientation for various  $L/H$  ratio case.

Figs.5-6 in example 1, and Figs.8-10 in example 2 illustrate that the load location and  $L/H$  ratio influence the compliance variation significantly. From these figures, it can be seen that the compliance has different extremums, which can be searched using the optimization method in the section 3.

### Example 3:

The example is the same cantilever beam as in Fig.4. The optimized material-orientation vs load position with  $L/H=1$  is shown in fig.11. The optimized material-orientation vs the  $L/H$  ratio under a concentrated vertical load  $P$  applied at the middle of the right end is shown in fig.12.

As a comparison, the considered problem was

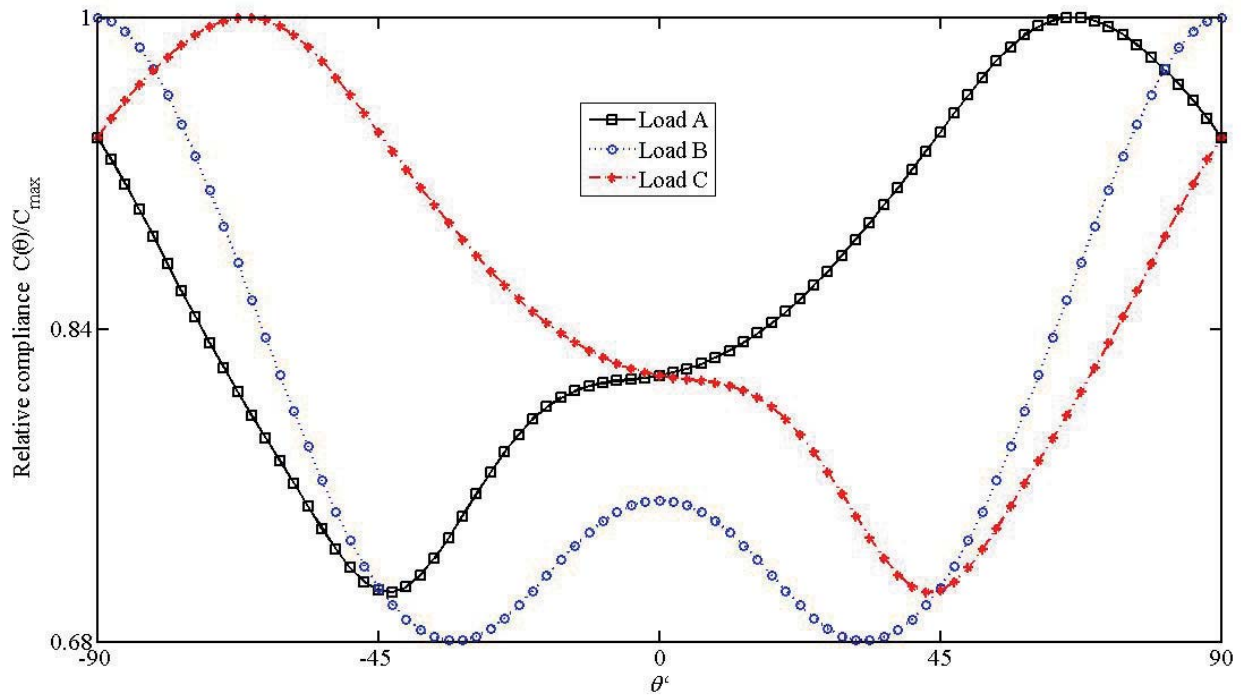


Figure 5: The relative compliance vs the fixed material-orientation for various locations of the point of application of the load ( $L/H=1$ )

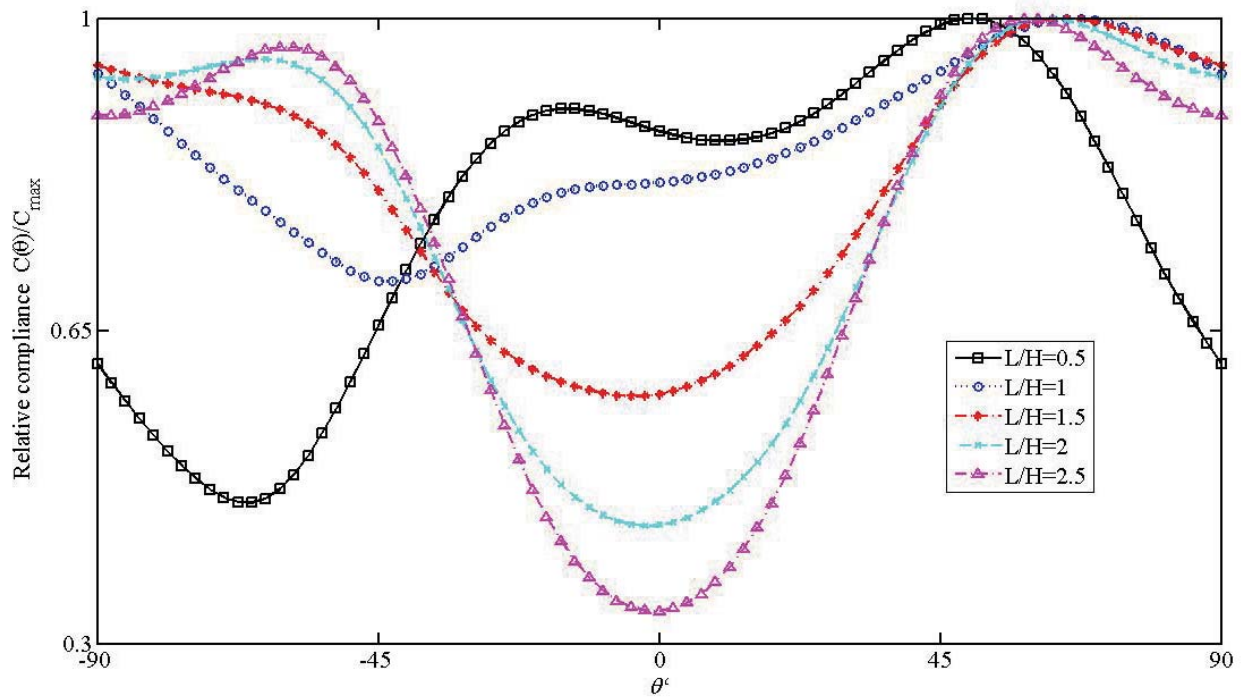


Figure 6: The relative compliance vs the fixed material-orientation for various  $L/H$  ratio cases (the load is applied at point A)

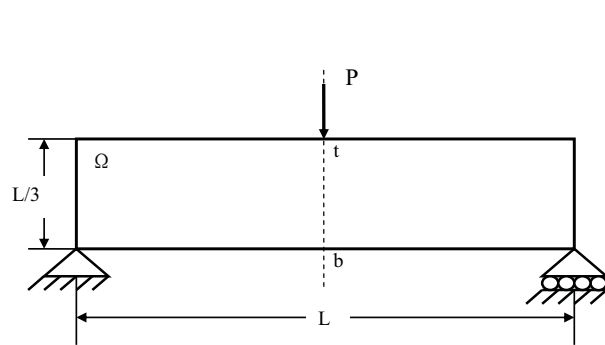


Figure 7(a): MBB beam

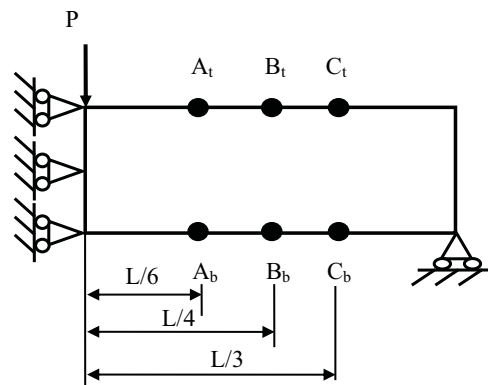


Figure 7(b): MBB beam (right half-domain)

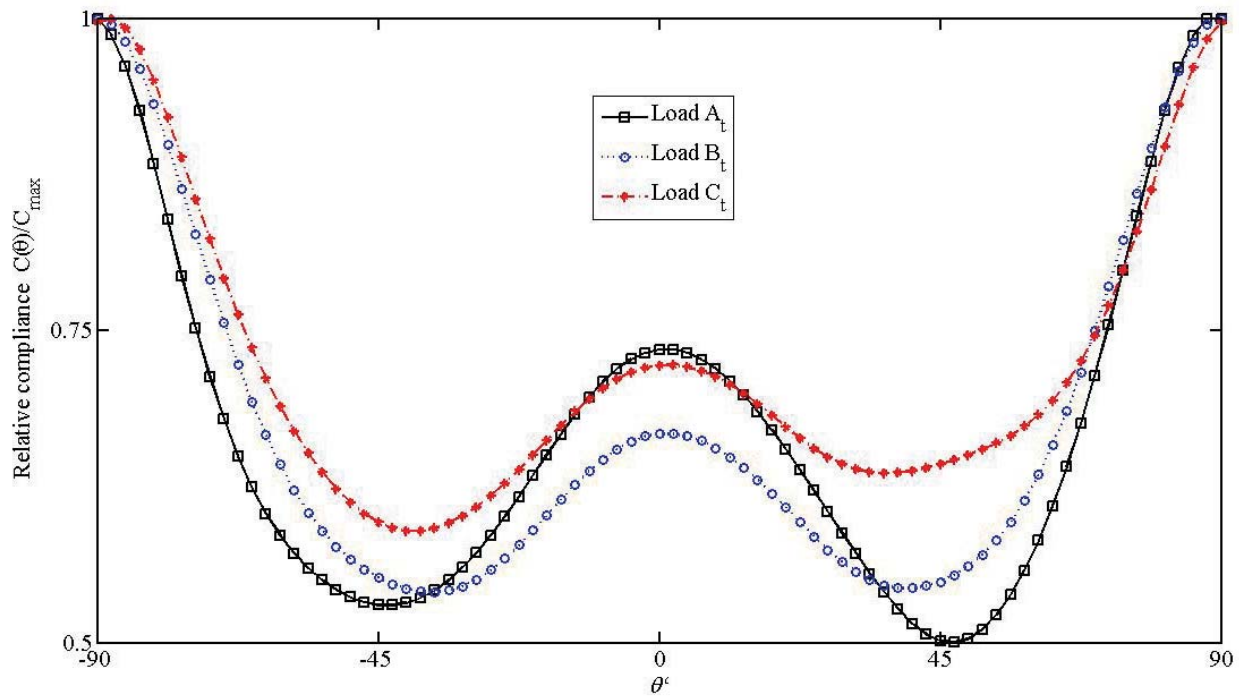


Figure 8: The relative compliance vs the fixed material-orientation for various locations of the point of application of the load (top)

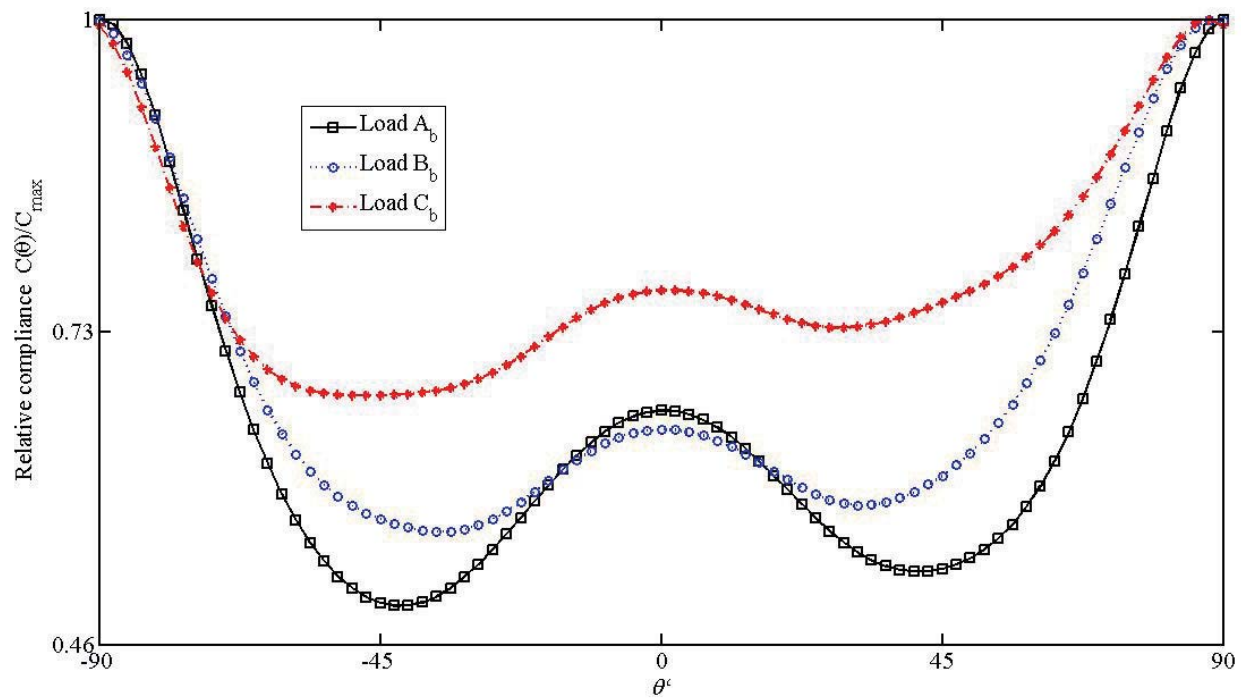


Figure 9: The relative compliance vs the fixed material-orientation for various locations of the point of application of the load (bottom)

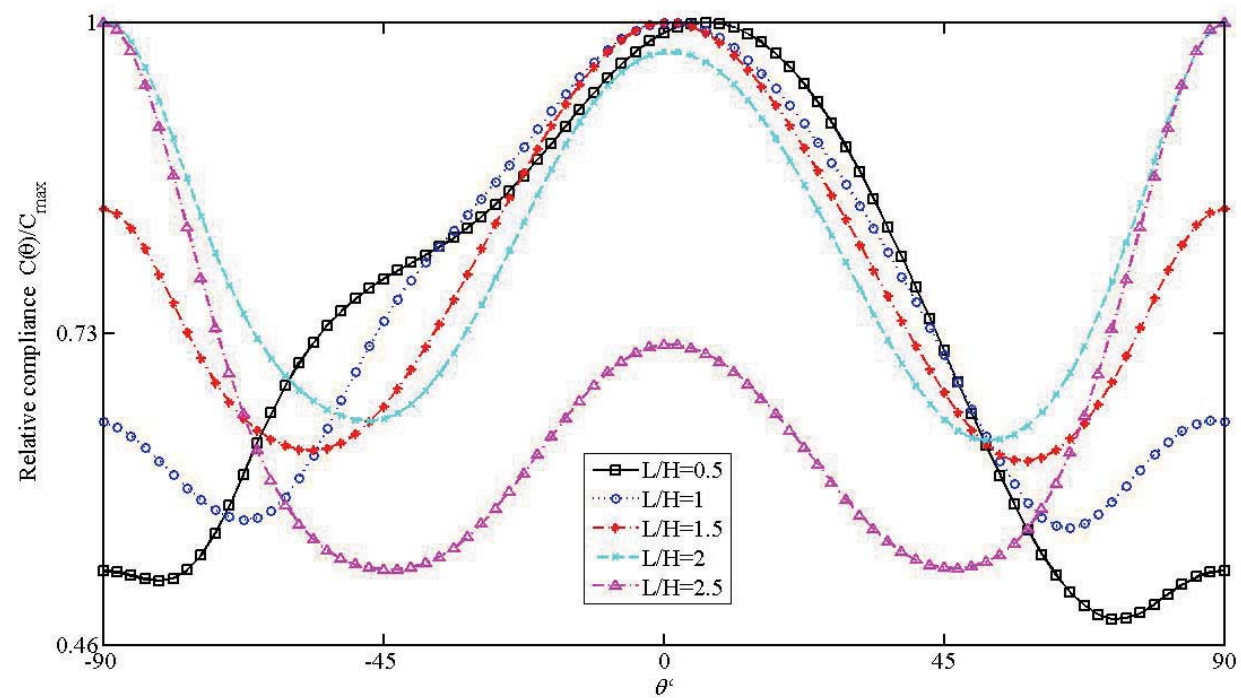


Figure 10: The relative compliance vs the fixed material-orientation for various  $L/H$  ratio cases

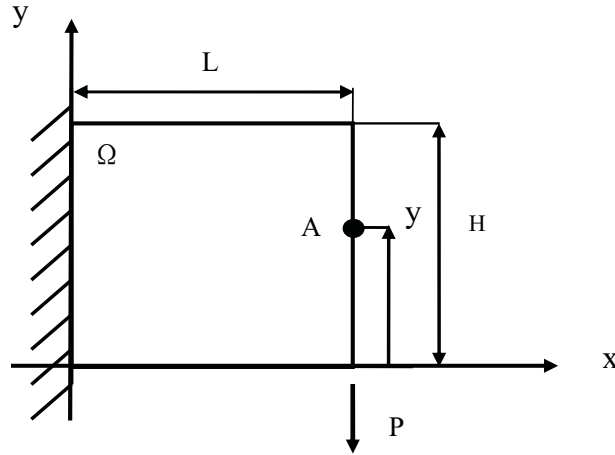


Figure 11(a): Cantilever beam model

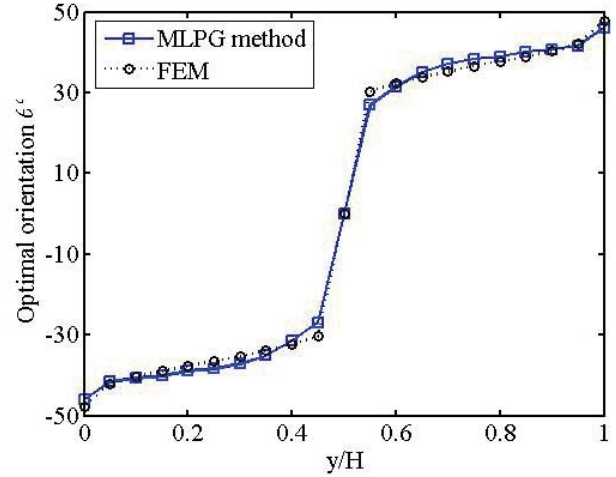


Figure 11(b): The optimized orientation angle vs load position

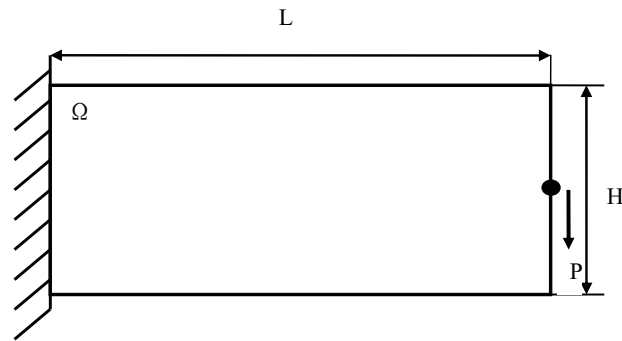


Figure 12(a): Cantilever beam model

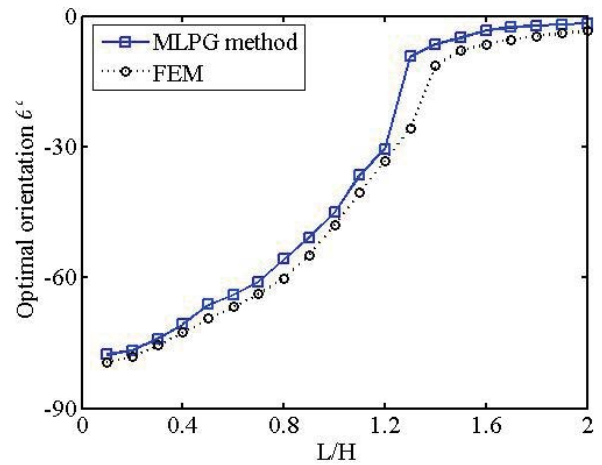


Figure 12(b): The optimized orientation angle vs the L/H ratio

also calculated by using finite element method (FEM). The results of the MLPG method are in good agreement with the solutions of the finite element method.

#### Example 4:

In this example of topology optimization, a cantilever beam as in fig. 4 is used. The design domain is discretized using 40 x 40 uniformly distributed. To compare the results of isotropic and orthotropic material cantilever beam, we choose an orthotropic material with orientation at 4 angles  $\theta = 0^\circ, 45^\circ, 90^\circ$  and the optimized angle, respectively.

#### Example 5:

In this example, a cantilever beam as in fig.

4 is used with  $L/H=1.5$ . The design domain is discretized using  $60 \times 40$  uniformly distributed nodes. To compare the results of isotropic and orthotropic material cantilever beam, results from topology design associated with an orthotropic material oriented at  $\theta = 0^\circ, \pm 60^\circ, 90^\circ$  and the optimized angle, respectively are presented.

The results shown in Fig.13 and fig.14 display topological similarities between the isotropic material and the orthotropic one, with material axes of  $\theta = 0^\circ$  and  $\theta = 90^\circ$ . We see that for orthotropic cases, the bending-tension coupling (i.e.,  $\bar{Q}_{16} = \bar{Q}_{26} = 0$ ) does not exist. However, the topological layouts are very different for other orthotropic material orientations since bending-tension cou-



MLPG



FEM

(a) Isotropic material



MLPG



FEM

(b) Orthotropic material ( $\theta = 0^\circ$ )



MLPG



FEM

(c) Orthotropic material ( $\theta = 45^\circ$ )



MLPG



FEM

(d) Orthotropic material ( $\theta = 90^\circ$ )

MLPG



FEM

(e) Orthotropic material (the optimized angle)

Figure 13: Comparison of topology optimization results

pling are significant enough to change the layouts. It is also shown that the result obtained by the MLPG method is identical to that of the finite element method. Furthermore, the MLPG can provide much better results in comparison with the finite element method at  $\theta = \pm 60^\circ$ .

#### Example 6:

This example is also that of an orthotropic cantilever beam with Young's moduli  $E_1 = 30$ ,  $E_2 = 5$ , Poisson's ratios  $\mu_{12} = 0.25$  and the shear moduli  $G_{12} = 2$ . The beam has the rectangular 'design domain' ( $L=2H$ ) as shown in Fig. 15. The load  $P$  is applied at the middle of the right end.

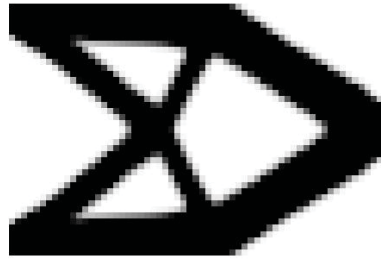
The design domain is discretized using  $40 \times 20$  uniformly distributed nodes. For the considered beam, optimized material directions (orientation angles) in minimum compliance design are shown in Fig.16.

Fig. 17 gives a comparison of the topology optimization results for isotropic and orthotropic material cantilever beam after the optimized orthotropic material directions are obtained.

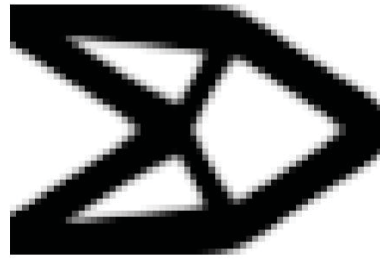
#### Example 7:

Optimized material directions (orientation angles) in minimum compliance design of orthotropic MBB beam as in Fig.7 when using continuous angles as design variables. The problem is then solved using MLPG method. This MBB beam is discretized using  $60 \times 20$  uniformly distributed nodes. The distribution of the optimized material directions is shown in fig.18 and topology optimization results in Fig.19.

Our displays of layouts for orthotropic planes reveal a very important effect of material directions for topology optimization results.



MLPG



FEM

(a) Isotropic material

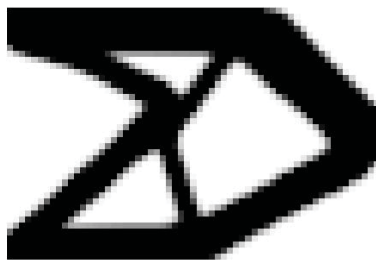


MLPG



FEM

(b) Orthotropic material ( $\theta = -60^\circ$ )



MLPG



FEM

(c) Orthotropic material ( $\theta = 60^\circ$ )

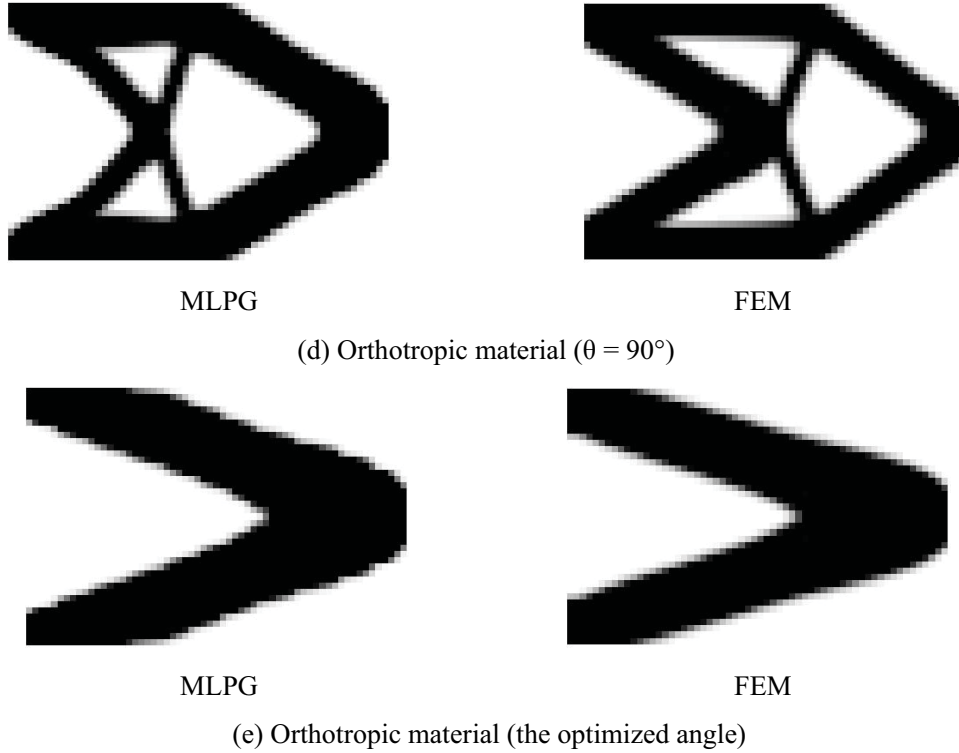


Figure 14: Comparison of topology optimization results

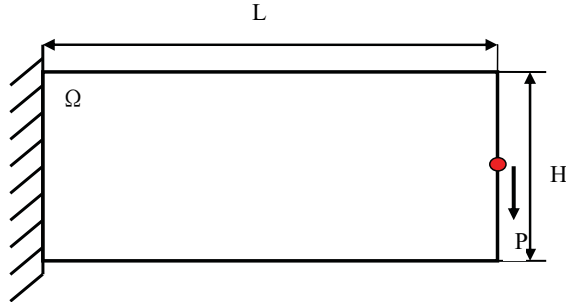
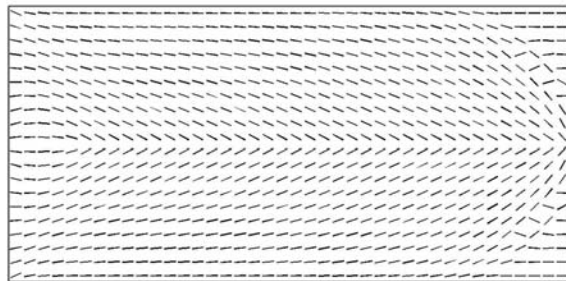
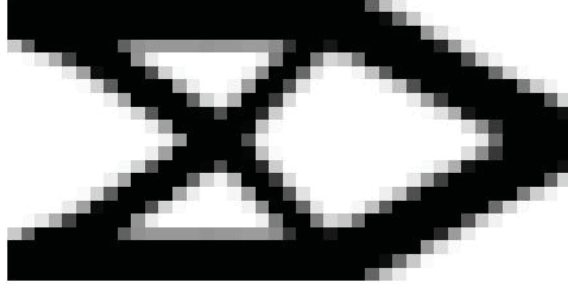
Figure 15: Cantilever beam ( $L=2H$ )

Figure 16: The distribution of orthotropic orientation

## 6 Conclusions

The structural design of an anisotropic solid involves an adaptation of the combined stages of the material-orientation optimization along with the topology optimization. Here we consider the optimization problem which minimizes the mean compliance of the structure. In the first stage, the material-orientation is the design variable without constraints (size optimization) and a sequential quadratic programming algorithm in which is a gradient based technique is used for efficient design. In the second stage, it is shown that different orientations of the same orthotropic material influence the optimal results of the global structure. The topology optimization problem is treated as the material distribution problem. The nodal values are used as the design variables, and the problem becomes one of finding the optimal values of the relative nodal volume fractions. In this paper, design domains are discretized by using the MLPG mixed collocation method, and a node with zero relative nodal volume fraction represents a void and a node with a relative nodal



(a) Isotropic material



(b) Orthotropic material with the optimized orientation

Figure 17: Comparison of topology optimization results

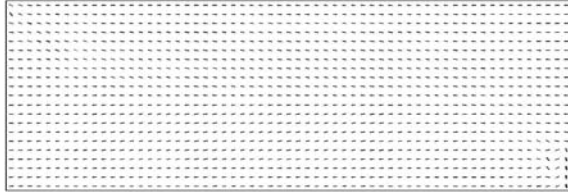
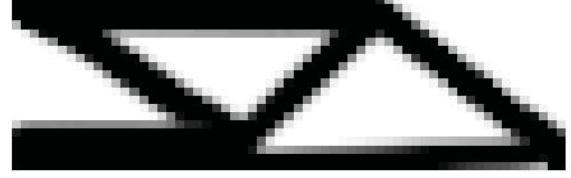


Figure 18: The distribution of orthotropic orientation

volume fraction of 1 represents a solid node. The goal is to find a distribution of relative nodal volume fractions that minimizes a compliance objective function, subject to volume constraints. To solve such a topology optimization problem, the popular optimality criteria (OC) based on the Lagrange method is employed with an iterative heuristic scheme for updating the design variables. In this paper, one of the significant findings is that of the topology optimized design for an orthotropic material results in a significantly different layout as compared to the isotropic material. This means that the solution space for the topology optimization problems is extended. So we



(a) Isotropic material



(b) Orthotropic material with the optimized orientation

Figure 19: Comparison of topology optimization results

have a considerably more flexible topology layout for an anisotropic solid, than when an isotropic material is used. The present method provides a physical insight into how the anisotropic material design variables interact to affect the topology properties of the structure.

We provide several numerical examples to demonstrate the versatility of the present method. For validation purposes, in some specific cases, the same topology optimization problem is solved using the finite element method, and the layouts can be compared with each other. The numerical instability problems related to a finite element mesh do not exist in the MLPG method. It need not cost extra CPU-time to deal with such numerical instabilities. The filtering technique is highly suitable for the present MLPG method.

**Acknowledgement:** This research was conducted during the study of Shu Li at UCI. The first author acknowledges the financial support of the National Natural Science Foundation of China (Grant No.10772013). This research was also partially supported by the Office of Naval Research and by the Office of the President of the University of California.

## References

- Atluri, S.N.; Zhu, T.** (1998): A New Meshless Local Petrov-Galerkin (MLPG) Approach in Computational Mechanics, *Computational Mechanics*, 22, 117-127.
- Atluri, S.N.; Shen, S.P.** (2002a): The meshless local Petrov-Galerkin (MLPG) method: A simple & less-costly alternative to the finite element and boundary element methods, *CMES: Computer Modeling in Engineering and Sciences*, 3 (1), 11-51.
- Atluri, S.N.; Shen, S.** (2002b): *The Meshless Local Petrov-Galerkin (MLPG) Method*, Tech Science Press.
- Atluri, S.N.** (2004): *The Meshless Method(MLPG) for Domain & BIE Discretizations*, Tech Science Press.
- Atluri, S.N.; Liu, H.T.; Han, Z.D.** (2006): Meshless local Petrov-Galerkin (MLPG) mixed collocation method for elasticity problems, *CMES: Computer Modeling in Engineering & Sciences*, 14 (3), 141-152.
- Bendsøe, M.P.; Kikuchi, N.** (1988): Generating optimal topologies in optimal design using a homogenization method, *Comp. Meth. Appl. Mech. Engrg.*, 71, 197-224.
- Cisilino, A.P.** (2006): Topology Optimization of 2D Potential Problems Using Boundary Elements, *CMES: Computer Modeling in Engineering & Sciences*, 15 (2), 99-106.
- Goh, C.J.; Yang, X.Q.** (2001): Nonlinear Lagrangian Theory for Nonconvex Optimization, *Journal of Optimization Theory and Applications*, 109 (1), 99-121.
- Khoshnood, A.; Jalali, M.A.** (2008): Normal oscillatory modes of rotating orthotropic disks, *Journal of Sound and Vibration*, 314, 147-160.
- Li, S.; Atluri, S.N.** (2008): Topology-optimization of structures based on the MLPG Mixed Collocation Method, *CMES: Computer Modeling in Engineering & Sciences*, 26 (1), 61-74.
- Norato, J.A.; Bendsøe, M.P.; Haber, R.B.; Tortorelli, D.A.** (2007): A topological derivative method for topology optimization, *Struct Multidisc Optim*, 33, 375-386.
- Pedersen, P.** (1989): On Optimal Orientation of Orthotropic Materials, *Struct. Optim.*, 1, 101-106.
- Sigmund, O.** (1994): Materials with prescribed constitutive parameters: An inverse homogenization problem, *Int. J. Solids Struct.*, 31, 2313-2329.
- Sigmund, O.** (1997): On the design of compliant mechanisms using topology optimization, *J. Mech. Struct. Mach.*, 25, 493-524.
- Sigmund, O.** (2001): A 99 line topology optimization code written in Matlab, *Struct Multidisc Optim.*, 21, 120-127.
- Spalatel-Lazar, M.; Léné, F; Turbé, N.** (2008): Modelling and Optimization of Sails, *Computers and Structures*, 86, 1486-1493.
- Vemaganti, K.; Lawrence, W.E.** (2005): Parallel methods for optimality criteria-based topology optimization, *Comput. Methods Appl. Mech. Engrg.*, 194, 3637-3667.
- Wang, S.Y.; Lim, K.M.; Khoo, B.C.; Wang, M.Y.** (2007): A Geometric Deformation Constrained Level Set Method for Structural Shape and Topology Optimization, *CMES: Computer Modeling in Engineering & Sciences*, 18, (3), 155-181.
- Wang S.Y.; Lim K.M.; Khoo B.C.; Wang M.Y.** (2008): A Hybrid Sensitivity Filtering Method for Topology Optimization, *CMES: Computer Modeling in Engineering & Sciences*, 24 (1), 21-50.
- Zhou, S.; Wang, M.Y.** (2006): 3D Multi-Material Structural Topology Optimization with the Generalized Cahn-Hilliard Equations, *CMES: Computer Modeling in Engineering & Sciences*, 16 (2), 83-101.

# Topology-optimization of Structures Based on the MLPG Mixed Collocation Method

Shu Li<sup>1</sup> and S. N. Atluri<sup>2</sup>

**Abstract:** The Meshless Local Petrov-Galerkin (MLPG) “mixed collocation” method is applied to the problem of topology-optimization of elastic structures. In this paper, the topic of compliance minimization of elastic structures is pursued, and nodal design variables which represent nodal volume fractions at discretized nodes are adopted. A so-called nodal sensitivity filter is employed, to prevent the phenomenon of checkerboarding in numerical solutions to the topology-optimization problems. The example results presented in the paper demonstrate the suitability and versatility of the MLPG “mixed collocation” method, in implementing structural topology-optimization.

**Keyword:** topology optimization, meshless method, MLPG, collocation, mixed method

## 1 Introduction

The quantity of engineering literature on the topology-optimization has grown very rapidly in the last two decades, starting with the so-called homogenization method for structural topology [Bendsøe and Kikuchi (1988)]. The topology optimization problem is usually described as a material distribution design problem, a so-called 0-1 problem in nature. By optimizing an objective function, subject to constraints on the design domain, one can employ topology-optimization techniques to engineer load-bearing structures with high strength, light weight and high fracture resistance [Chiandussi, Gaviglio and Ibba (2004), Hansen and Horst(2008)]. Topology optimization has been identified as one of the most challenging and potentially useful techniques in the field of

structural design. Most research work on topology optimization for continuum structures concerns new topology models, solutions of ill-posed problems, Optimality Criteria, etc. The earlier developments in the field of topology-optimization were described in an overview paper [Eschenauer and Olhoff(2001)], and in a monograph [Bendsøe and Sigmund (2003)]. Recently, with the increase of interest in this field, various models and methods for structural topology optimization were explored, with goals of improving the computational efficiency, and alleviating numerical instabilities [Norato, Bendsøe, Haber and Tortorelli (2007), Vemaganti and Lawrence (2005), Csilino(2006), Wang and Wang (2006b,c), Wang, Lim, Khoo and Wang (2007a, b, c, 2008), Zhou and Wang (2006)].

In practice, discretization and the use of numerical methods are unavoidable in order to design a complex and practical structure. Typically, approaches for solving topology optimization problems have been mostly based on the traditional element-based methods. Almost all of the approaches presented in prior literature employ finite element methods to discretize the topological domain. An exhaustive list of publications on subject of the topology and shape optimization of structures, using the finite element and boundary element techniques, is given in [Macklerle (2003)]. However, the use of finite element methods within the optimization procedures often leads to numerical instabilities, such as mesh-dependencies, etc [Sigmund and Petersson (1998)]. It is well known that topology optimization is a far more time-consuming task, because of its complicated evolutionary procedure and refinement of mesh density.

In recent years, substantial efforts have been made in the development of the meshless meth-

<sup>1</sup> Department of Aircraft Engineering, Beijing University of Aeronautics and Astronautics, Beijing 100083, P.R. China

<sup>2</sup> Center for Aerospace Research & Education, University of California, Irvine, USA

ods, especially the MLPG method [Atluri and Zhu(1998), Atluri and Shen(2002a, 2002b), and Atluri(2004)]. These meshless methods have inherent advantages over the element-based approaches, due to the elimination of the mesh, and the ease with which a high-order continuity of the trial functions is achieved. Atluri, Liu, and Han (2006) have recently proposed a very attractive and promising method which they call the MLPG “mixed collocation” method. In this method, a very simple formulation is achieved, and the computer implementation is very convenient. These benefits are realized, without any numerical integration either over a local domain or over the local boundary. This method improves the computational efficiency and the ease of implementation of the meshless method, especially for topology-optimization.

The present paper is dedicated to topology-optimization of continuum structures using the MLPG “mixed collocation” method. The main features of this paper are: the use of the MLPG “mixed collocation” method to discretize the design domain, and the choice of nodal volume fractions as the optimization design variables, instead of the element volume fractions. We employ the widely used density-like function called SIMP (Solid Isotropic Material with Penalization) model for the penalization. The objective of topology-optimization is to minimize the compliance for an optimal layout of structures, under a given set of loads and boundary conditions. The method of Optimality Criteria (OC) is employed to solve the topology optimization problem. Here, structural volume fractions become a function of the nodal volume fractions. Compared with the element-based methods such as in [Guest, Prévost and Belytschko (2004)], these nodal values need not be interpolated or projected onto the element, in order to obtain the familiar element-wise volume fractions which can determine the topology of structures. The numerical examples presented here demonstrate that the MLPG mixed collocation method renders the solution of the optimization problem to be highly accurate and computationally efficient.

The framework of this paper is as follows: Section

2 briefly reviews the major aspects of the MLPG mixed collocation method. Section 3 gives a formulation for the structural topology optimization, a heuristic scheme of the optimality criteria (OC) method, and the filtering principle. Section 4 presents some examples. Finally, we present some conclusions in Section 5.

## 2 MLPG Mixed Collocation Method

### 2.1 The moving least squares (MLS)

The moving least squares (MLS) approximation is often chosen as the interpolation function in a meshless approximation of the trial function. The MLPG Mixed Collocation Method adopts the MLS interpolation to approximate a function  $\mathbf{u}(\mathbf{x})$  over a number of nodes randomly spread within the domain of influence. The approximated function  $\mathbf{u}(\mathbf{x})$  can be written as [Atluri (2004)]

$$\mathbf{u}(\mathbf{x}) = \mathbf{p}^T(\mathbf{x})\mathbf{a}(\mathbf{x}) \quad (1)$$

where  $\mathbf{p}^T(\mathbf{x})$  is a monomial basis which can be expressed as  $\mathbf{p}^T(\mathbf{x}) = [1, x_1, x_2]$  for two-dimensional problems and  $\mathbf{p}^T(\mathbf{x}) = [1, x_1, x_2, x_3]$  for three dimensional problems, respectively.  $\mathbf{a}(\mathbf{x})$  is a vector of undetermined coefficients, which can be obtained by minimizing the weighted discrete  $L_2$  norm, defined as

$$J(\mathbf{x}) = \sum_{I=1}^m \mathbf{w}_I(\mathbf{x}) [\mathbf{p}^T(\mathbf{x}_I)\mathbf{a}(\mathbf{x}) - \hat{u}^I]^2 \quad (2)$$

where  $\{\mathbf{x}_I\}$ , ( $I = 1, 2, \dots, m$ ) are scattered local points (nodes) to approximate the function  $\mathbf{u}(\mathbf{x})$ ,  $\mathbf{w}_I$  are the weight functions and  $\hat{u}^I$  are the fictitious nodal values. After the coefficient vector  $\mathbf{a}(\mathbf{x})$  is obtained, we substitute it into Eq. (1). The function  $\mathbf{u}(\mathbf{x})$  can be approximated by these fictitious nodal values, as

$$u(\mathbf{x}) = \sum_{I=1}^m \Psi^I(\mathbf{x}) \hat{u}^I \quad (3)$$

where  $\hat{u}^I$  is the virtual nodal value at node  $I$ , and  $\Psi^I(\mathbf{x})$  is the shape function. The detailed formulations and discussions for the MLS interpolation, using the true nodal values can be found in Atluri (2004).

Generally speaking, the MLS shape function does not have the Dirac Delta property, namely

$$u^I \equiv u(\mathbf{x}^I) = \sum_{J=1}^m \Psi^J(\mathbf{x}) \hat{u}^I \neq \hat{u}^I \quad (4)$$

However, with the mapping relationship between the virtual and true nodal values [Eq. (4)], it is straightforward to establish the trial functions in the true nodal-values space as

$$u(\mathbf{x}) = \sum_{I=1}^m \Phi^I(\mathbf{x}) u^I \quad (5)$$

## 2.2 Equilibrium equations

We consider a linear elastic body  $\Omega$  undergoing infinitesimal deformations. The equilibrium equation can be expressed as

$$\nabla \cdot \boldsymbol{\sigma} + \mathbf{f} = \mathbf{0} \quad (6)$$

subject to the boundary conditions:

$$\begin{aligned} \mathbf{u} &= \bar{\mathbf{u}} \quad \text{on} \quad \Gamma_u \\ \mathbf{t} &= \bar{\mathbf{t}} \quad \text{on} \quad \Gamma_t \end{aligned} \quad (7)$$

In which  $\boldsymbol{\sigma}$  is the stress tensor,  $\nabla$  is the gradient vector,  $\mathbf{f}$  is the body force vector;  $\mathbf{u}$  is the displacement vector,  $\mathbf{t}$  is the traction vector, and  $\mathbf{n}$  is the outward unit normal to the boundary  $\Gamma$ .

Within the general MLPG framework [Atluri(2004)], one may choose the Dirac Delta function as the test function for the unsymmetric local weak form, and apply it to each nodal point. The momentum balance equation is enforced at the nodal points, as

$$[\nabla \cdot \boldsymbol{\sigma}](\mathbf{x}^I) + \mathbf{f}(\mathbf{x}^I) = \mathbf{0} \quad (8)$$

where  $\{\mathbf{x}^I\}$ ,  $(I = 1, 2, \dots, N)$  are the distributed nodes, and  $N$  is the number of total distributed nodes in the solution domain. In the present mixed scheme, we interpolate the displacement vector  $\mathbf{u}(\mathbf{x})$  and the stress tensor  $\boldsymbol{\sigma}(\mathbf{x})$  independently, using the same shape functions obtained from the MLS approximation [Eq. (3)], namely

$$\mathbf{u}(\mathbf{x}) = \sum_{J=1}^m \Phi^J(\mathbf{x}) \mathbf{u}^J \quad (9)$$

$$\boldsymbol{\sigma}(\mathbf{x}) = \sum_{J=1}^m \Phi^J(\mathbf{x}) \boldsymbol{\sigma}^J \quad (10)$$

Here,  $\mathbf{u}^J$  and  $\boldsymbol{\sigma}^J$  are the nodal displacement vector and stress vector [note that the stress tensor is now symbolically re-written as a stress-vector] at node  $J$ , respectively. In the case of the isotropic linear elastic problem, the relation between the stress vector  $\boldsymbol{\sigma}$  and the strain vector  $\boldsymbol{\varepsilon}$  can be written as

$$\boldsymbol{\sigma} = \mathbf{D} \cdot \boldsymbol{\varepsilon} \quad (11)$$

$$\boldsymbol{\varepsilon} = \mathbf{L}^* \cdot \mathbf{u} \quad (12)$$

where,  $\mathbf{L}^*$  a differential operator, for the present 2D problem,

$$\mathbf{D} = \frac{E}{1-\nu^2} \begin{bmatrix} 1 & \nu & 0 \\ \nu & 1 & 0 \\ 0 & 0 & \frac{1-\nu}{2} \end{bmatrix}$$

with  $E$  the Young's modulus,  $\nu$  the Poisson's ratio. Upon substituting the stress interpolation Eq. (10) into Eq. (8), we have

$$\sum_{J=1}^m \nabla \cdot \Phi^J(\mathbf{x}^I) \cdot \boldsymbol{\sigma}^J + \mathbf{f}(\mathbf{x}^I) = \mathbf{0}; \quad \text{for } \mathbf{I} = 1, 2, \dots, N \quad (13)$$

It clearly shows that there are no second derivatives of the shape functions for the displacements involved in the system equations, due to the independent interpolation of the stress variables. It is well known that in the meshless approximation, specifically the MLS, usually results in a very complex form of the second derivatives. The Eq. (13) has less number of equations than the number of the independent stress variables, because the nodal stress variables are more than the displacement ones. Therefore, we need to establish some more equations in addition to Eq. (11) through the stress displacement relation. The standard collocation method may be applied to enforce the stress displacement relation at each nodal point. For linear elasticity problems, this relation can be written as

$$\boldsymbol{\sigma}(\mathbf{x}^I) = \mathbf{D} \cdot \boldsymbol{\varepsilon}(\mathbf{x}^I) = \mathbf{D} \cdot \mathbf{L}^* \cdot \mathbf{u}(\mathbf{x}^I) \quad (14)$$

After substituting the displacement interpolation Eq. (9) into Eq. (14), we have

$$\boldsymbol{\sigma}^J = \sum_{J=1}^m \mathbf{D}\mathbf{B}^J(\mathbf{x}^I) \mathbf{u}^I \quad (15)$$

where

$$\mathbf{B}^J(\mathbf{x}^I) = \begin{bmatrix} \Phi_{,x}^J(\mathbf{x}^I) & 0 \\ 0 & \Phi_{,y}^J(\mathbf{x}^I) \\ \Phi_{,y}^J(\mathbf{x}^I) & \Phi_{,x}^J(\mathbf{x}^I) \end{bmatrix} \quad (16)$$

$$\boldsymbol{\sigma}^J = [\sigma_x^J \quad \sigma_y^J \quad \tau_{xy}^J]^T$$

$$\mathbf{u}^J = [u_x^J \quad u_y^J]^T$$

Eq. (13) and Eq. (14) can be rewritten in the form as follows, respectively:

$$\mathbf{K}_S \cdot \boldsymbol{\sigma} = \mathbf{f}_b \quad (17)$$

$$\boldsymbol{\sigma} = \mathbf{T} \cdot \mathbf{u} \quad (18)$$

In which  $\mathbf{f}_b$  is the body force vector.

We set  $\mathbf{B}_{IJ} = \mathbf{B}^J(\mathbf{x}^I)$ , thus

$$\mathbf{K}_S = \begin{bmatrix} \mathbf{B}_{11}^T & \mathbf{B}_{12}^T & \cdots & \mathbf{B}_{1n}^T \\ \mathbf{B}_{21}^T & \mathbf{B}_{22}^T & \cdots & \mathbf{B}_{2n}^T \\ \vdots & \vdots & \ddots & \vdots \\ \mathbf{B}_{n1}^T & \mathbf{B}_{n2}^T & \cdots & \mathbf{B}_{nn}^T \end{bmatrix}$$

$$\mathbf{T} = \mathbf{D} \cdot \begin{bmatrix} \mathbf{B}_{11} & \mathbf{B}_{12} & \cdots & \mathbf{B}_{1n} \\ \mathbf{B}_{21} & \mathbf{B}_{22} & \cdots & \mathbf{B}_{2n} \\ \vdots & \vdots & \ddots & \vdots \\ \mathbf{B}_{n1} & \mathbf{B}_{n2} & \cdots & \mathbf{B}_{nn} \end{bmatrix}$$

and

$$\boldsymbol{\sigma} = \begin{bmatrix} \boldsymbol{\sigma}^1 \\ \boldsymbol{\sigma}^2 \\ \vdots \\ \boldsymbol{\sigma}^J \\ \vdots \\ \boldsymbol{\sigma}^N \end{bmatrix}, \quad \mathbf{u} = \begin{bmatrix} \mathbf{u}^1 \\ \mathbf{u}^2 \\ \vdots \\ \mathbf{u}^J \\ \vdots \\ \mathbf{u}^N \end{bmatrix}$$

Let

$$\bar{\mathbf{K}} = \mathbf{K}_S \cdot \mathbf{T} \quad (19)$$

which yields the well known formulation of equilibrium equation

$$\bar{\mathbf{K}}\mathbf{u} = \mathbf{f}_b \quad (20)$$

where

$$\bar{\mathbf{K}}_{IJ} = \sum_{K=1}^m \mathbf{B}_{IK}^T \mathbf{D} \mathbf{B}_{KJ} \quad (21)$$

### 2.3 Boundary Conditions

The traction boundary conditions are enforced at each of the traction boundary nodes  $K$ , as:

$$\mathbf{n}^K \cdot \boldsymbol{\sigma}^K = \bar{\mathbf{t}}^K, \quad \text{for } K = 1, \dots, S \quad (22)$$

where  $S$  is the number of total traction boundary nodes, the matrix  $\mathbf{n}^K$  is the transformation matrix between the coordinates, as

$$\mathbf{n}^K = \begin{bmatrix} n_x^K & 0 & n_y^K \\ 0 & n_y^K & n_x^K \end{bmatrix}$$

and

$$\boldsymbol{\sigma}^K = [\sigma_x^K \quad \sigma_y^K \quad \tau_{xy}^K]^T, \quad \bar{\mathbf{t}}^K = [\bar{t}_x^K \quad \bar{t}_y^K]^T$$

Assuming  $\boldsymbol{\sigma}_1$  and  $\boldsymbol{\sigma}_2$  represent the known and unknown stress vectors, respectively. Hence Eq.(20) can be written as

$$\bar{\mathbf{K}}_1 \cdot \boldsymbol{\sigma}_1 + \bar{\mathbf{K}}_2 \cdot \boldsymbol{\sigma}_2 = \mathbf{f}_b \quad (23)$$

where

$$\boldsymbol{\sigma}_1 = \mathbf{T}_1 \cdot \mathbf{u} \quad (24)$$

$$\boldsymbol{\sigma}_2 = \mathbf{T}_2 \cdot \mathbf{u} \quad (25)$$

Premultiplying Eq. (22) by the penalty number  $\alpha$  and the transpose of the transformation matrix  $\mathbf{n}$ , we obtain:

$$\alpha \mathbf{n}^T \cdot \mathbf{n} \cdot \boldsymbol{\sigma}_1 = \alpha \mathbf{n}^T \cdot \bar{\mathbf{t}} \quad (26)$$

where

$$\mathbf{n} = \begin{bmatrix} \mathbf{n}^1 & & & 0 \\ & \mathbf{n}^2 & & \\ & & \ddots & \\ & & & \mathbf{n}^K \\ 0 & & & & \ddots & \\ & & & & & \mathbf{n}^S \end{bmatrix},$$

$$\boldsymbol{\sigma}_1 = \begin{bmatrix} \boldsymbol{\sigma}^1 \\ \boldsymbol{\sigma}^2 \\ \vdots \\ \boldsymbol{\sigma}^K \\ \vdots \\ \boldsymbol{\sigma}^S \end{bmatrix}, \quad \bar{\mathbf{t}} = \begin{bmatrix} \bar{\mathbf{t}}^1 \\ \bar{\mathbf{t}}^2 \\ \vdots \\ \bar{\mathbf{t}}^K \\ \vdots \\ \bar{\mathbf{t}}^S \end{bmatrix}$$

It is easy to obtain

$$\boldsymbol{\sigma}_1 + \alpha \mathbf{n}^T \cdot \mathbf{n} \cdot \boldsymbol{\sigma}_1 = \mathbf{T}_1 \cdot \mathbf{u} + \alpha \mathbf{n}^T \cdot \bar{\mathbf{t}} \quad (27)$$

and

$$\boldsymbol{\sigma}_1 = (\mathbf{I} + \alpha \mathbf{n}^T \cdot \mathbf{n})^{-1} (\mathbf{T}_1 \cdot \mathbf{u} + \alpha \mathbf{n}^T \cdot \bar{\mathbf{t}}) \quad (28)$$

where  $\mathbf{I}$  is unit matrix.

Let

$$\mathbf{Q} = (\mathbf{I} + \alpha \mathbf{n}^T \cdot \mathbf{n})^{-1} \quad (29)$$

then

$$\boldsymbol{\sigma}_1 = \mathbf{Q} \cdot \mathbf{T}_1 \cdot \mathbf{u} + \alpha \mathbf{Q} \cdot \mathbf{n}^T \cdot \bar{\mathbf{t}} \quad (30)$$

By substituting Eq. (30) into Eq.(23), we can obtain a discretized system which is expressed as

$$\mathbf{K} \cdot \mathbf{u} = \mathbf{f} \quad (31)$$

where

$$\begin{aligned} \mathbf{K} &= \bar{\mathbf{K}}_1 \cdot \mathbf{Q} \cdot \mathbf{T}_1 + \bar{\mathbf{K}}_2 \cdot \mathbf{T}_2 \\ \mathbf{f} &= \mathbf{f}_b - \alpha \bar{\mathbf{K}}_1 \cdot \mathbf{Q} \cdot \mathbf{n}^T \cdot \bar{\mathbf{t}} \end{aligned} \quad (32)$$

### 3 Topology optimization problem

#### 3.1 Problem formulation

Topology-optimization implies the optimal distribution of material in a structure, so as to minimize its compliance, subject to the specified constraints of the total material to be used. Here,

‘compliance’ is defined as the product of the external loads and the corresponding displacements. According to Eq.(31), the mean compliance of a structure is formulated as follows:

$$C = \mathbf{f}^T \cdot \mathbf{u} \quad (33)$$

where  $\mathbf{u}$  is the global displacement vector,  $\mathbf{f}$  is the force vector. Also, the above expression can also be written, for linear response, as:

$$C = \mathbf{u}^T \mathbf{K} \mathbf{u} \quad (34)$$

In practice, Eq.(34) is discretized using the MLPG Mixed Collocation Method. The design domain  $\Omega$  (Fig.1) is partitioned into  $N$  nodes. For an arbitrary node  $i$ , if the number of nodes around point  $i$  which influence the trial function at node  $i$  is  $r$ , a sub-system consists of these  $r$  nodes. In this sub-system, we have

$$\mathbf{k}_i \mathbf{u}_i = \mathbf{f}_i \quad (35)$$

where  $\mathbf{u}_i$  is the displacement vector and  $\mathbf{k}_i$  is the “stiffness” matrix constructed in the same way as Eq.(19). The discretized formulation of Eq.(34) becomes

$$C = \sum_{i=1}^N \mathbf{u}_i^T \mathbf{k}_i \mathbf{u}_i \quad (36)$$

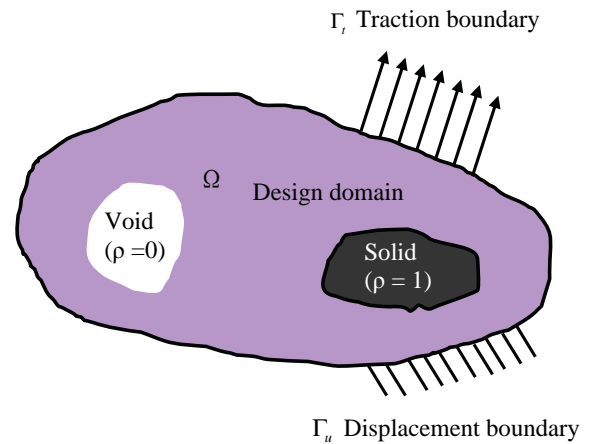


Figure 1: Two-dimensional design domain for topology optimization

If we consider the nodal volume fractions  $\rho_i$  as the design variables, then the topology optimization

problem for minimizing the compliance can thus be stated, with the volume constraint  $V^*$  as follows:

$$\begin{aligned} \min_{\boldsymbol{\rho}} \quad & C(\boldsymbol{\rho}) = \mathbf{u}^T \mathbf{K} \mathbf{u} = \sum_{i=1}^N \mathbf{u}_i^T \mathbf{k}_i \mathbf{u}_i \\ \text{subject to } & V(\boldsymbol{\rho}) = \sum_{i=1}^N \rho_i V_i = V^* \\ & \mathbf{K} \mathbf{u} = \mathbf{f} \\ & 0 < \rho_{\min} \leq \rho_i \leq 1 \end{aligned} \quad (37)$$

where  $\boldsymbol{\rho}$  is the vector consisted of design variable  $\rho_i$ ,  $\rho_{\min}$  is the minimum allowable relative volume fractions (non-zero to avoid singularity),  $N$  is the number of nodes to discretize the design domain, and  $V^*$  is the prescribed volume.  $V(\boldsymbol{\rho})$  is the total volume of material.

Setting  $\rho_{\min}$  to a positive value keeps the “stiffness” matrix  $\mathbf{k}_i$  from becoming singular. The artificial variable  $\rho_i$  is considered as an indicator of the local material volume  $V_i$ . The final material volume  $V^*$  is linearly related to the design variables.

To avoid intermediate volume fraction values  $\rho_i$  (between 0 and 1), a SIMP-like model (Solid Isotropic Microstructure with Penalty) is adopted in the proposed topology optimization method. In this SIMP-like model, the penalized “stiffness” matrix  $\mathbf{k}_i$  is given by

$$\mathbf{k}_i = (\rho_i)^p \mathbf{k}_i^0 \quad (38)$$

$\mathbf{k}_i^0$  is the initial value of the matrix  $\mathbf{k}_i$ ,  $p$  is the penalization power (typically  $p = 3$ ). Fig.2 displays the relative “stiffness” ratio vs. volume fraction values  $\rho_i$ , for different values of the penalization power  $p$ .

Due to the asymmetry of the matrix  $\mathbf{K}$  in the MLPG “Mixed Collocation” method, the sensitivities of the compliance respect to design variable  $\rho_i$  can be derived from the expression of Eq.(33), as follows:

$$\begin{aligned} \frac{\partial C}{\partial \rho_i} &= \mathbf{f}^T \cdot \frac{\partial \mathbf{u}}{\partial \rho_i} = (\mathbf{K} \mathbf{u})^T \frac{\partial \mathbf{u}}{\partial \rho_i} = \mathbf{u}^T \mathbf{K}^T \frac{\partial \mathbf{u}}{\partial \rho_i} \\ &= \mathbf{u}_i^T \mathbf{k}_i^T \frac{\partial \mathbf{u}_i}{\partial \rho_i} \end{aligned} \quad (39)$$

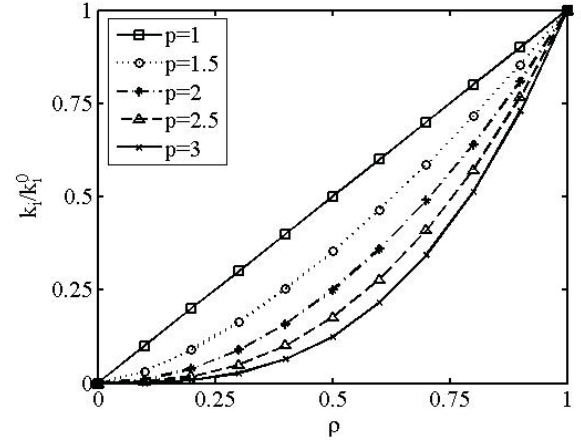


Figure 2: SIMP-like model for different values of the penalization power  $p$

We consider the discretized formulations  $\mathbf{k}_i \mathbf{u}_i = \mathbf{f}_i$  and  $C = \sum_{i=1}^N \mathbf{u}_i^T \mathbf{k}_i \mathbf{u}_i$ . Because the derivative of  $\mathbf{f}_i$  with respect to  $\rho_i$  is null, we can obtain:

$$\frac{\partial \mathbf{k}_i}{\partial \rho_i} \mathbf{u}_i = -\mathbf{k}_i \frac{\partial \mathbf{u}_i}{\partial \rho_i} \quad (40)$$

Substituting Eq.(38) into Eq.(40), we have

$$p(\rho_i)^{p-1} \mathbf{k}_i^0 \mathbf{u}_i = -(\rho_i)^p \mathbf{k}_i^0 \frac{\partial \mathbf{u}_i}{\partial \rho_i}$$

i.e.

$$\frac{\partial \mathbf{u}_i}{\partial \rho_i} = -\frac{1}{\rho_i} p \mathbf{u}_i \quad (41)$$

Finally, the expression of Eq.(39) is written as

$$\begin{aligned} \frac{\partial C}{\partial \rho_i} &= \mathbf{u}_i^T \mathbf{k}_i^T \frac{\partial \mathbf{u}_i}{\partial \rho_i} \\ &= \mathbf{u}_i^T ((\rho_i)^p \mathbf{k}_i^0)^T \left( -\frac{1}{\rho_i} p \mathbf{u}_i \right) \\ &= -p(\rho_i)^{p-1} \mathbf{u}_i^T (\mathbf{k}_i^0)^T \mathbf{u}_i \end{aligned} \quad (42)$$

### 3.2 The optimally criteria (OC) method

The discrete topology optimization problem (39) usually has a large number of design variables. It is natural to use iterative optimization methods for such a problem. Here, we choose the popular Optimality Criteria (OC) method for iterative optimization. Optimality Criteria methods seek the

optimum in the space of the Lagrange multipliers relevant to the active constraints based upon the Kuhn-Tucker (K-T) Conditions. These K-T Conditions are an extension of the Lagrangian theory to solve the general classical single-objective non-linear programming problem. They provide powerful tools to search optimal solutions. The computational time of the OC method is highly dependent on the number of active constraints. In this paper, the optimality criteria (OC) was formulated in a form suitable for incorporation in the meshless method codes.

The Lagrangian for the optimization problem [Eq.(39)] is defined as

$$L(\boldsymbol{\rho}) = C + \lambda_1 \left( \sum_{i=1}^N \rho_i V_i - V^* \right) + \boldsymbol{\Lambda}^T (\mathbf{K}\mathbf{u} - \mathbf{f}) + \sum_{i=1}^N \mu_1^i (\rho_{\min} - \rho_i) + \sum_{i=1}^N \mu_2^i (\rho_i - 1) \quad (43)$$

where  $\lambda_1$  and  $\mu_i$  are Lagrange multipliers for the equality and inequality constraints, respectively.  $\boldsymbol{\Lambda}$  is the Lagrange multiplier vector. The necessary conditions for optimality can be obtained by using the Kuhn-Tucker conditions as follows:

$$\frac{\partial L}{\partial \rho_i} = 0, \quad i = 1, 2, \dots, N$$

Differentiating (43) with respect to  $\rho_i$  and manipulating the terms, the Kuhn-Tucker optimality condition can be written for problems [Eq.(37)] subject to multiple constraints as follows

$$\begin{cases} \frac{\partial L}{\partial \rho_i} = \frac{\partial C}{\partial \rho_i} + \lambda_1 \frac{\partial V}{\partial \rho_i} + \boldsymbol{\Lambda}^T \frac{\partial (\mathbf{K}\mathbf{u})}{\partial \rho_i} - \mu_1 + \mu_2 = 0 \\ V(\boldsymbol{\rho}) = \sum_{i=1}^N \rho_i V_i - V^* = 0 \\ \quad \text{(the equality constraints)} \\ \mathbf{K}\mathbf{u} = \mathbf{f} \quad \text{(the equality constraints)} \\ \rho_{\min} - \rho_i \leq 0 \quad \text{(the inequality constraints)} \\ \rho_i - 1 \leq 0 \quad \text{(the inequality constraints)} \\ \mu_1 (\rho_{\min} - \rho_i) = 0 \\ \mu_2 (\rho_i - 1) = 0 \\ \mu_i \geq 0 \quad i = 1, 2 \end{cases} \quad (44)$$

Note:  $\lambda_1$  and  $\boldsymbol{\Lambda}$  are unrestricted in sign, corresponding to the equality constraints. It is clear that the efficiency of the OC method is determined mainly by the number of active constraints. If  $\rho_{\min} < \rho_i < 1$ , the lower and upper bounds of the design variables are inactive, then we have  $\mu_1 = \mu_2 = 0$ . If  $\rho_i = \rho_{\min}$ , the lower bound of the design variables are active, then we have  $\mu_1 \geq 0, \mu_2 = 0$ . If  $\rho_i = \rho_{\max}$ , the upper bound of the design variables are active, then  $\mu_1 = 0, \mu_2 \geq 0$ . and (44) yields:

$$\begin{cases} \frac{\partial C}{\partial \rho_i} + \lambda_1 \frac{\partial V}{\partial \rho_i} + \boldsymbol{\Lambda}^T \frac{\partial (\mathbf{K}\mathbf{u})}{\partial \rho_i} = 0 & \text{if } \rho_{\min} < \rho_i < 1 \\ \frac{\partial C}{\partial \rho_i} + \lambda_1 \frac{\partial V}{\partial \rho_i} + \boldsymbol{\Lambda}^T \frac{\partial (\mathbf{K}\mathbf{u})}{\partial \rho_i} \geq 0 & \text{if } \rho_i = \rho_{\min} \\ \frac{\partial C}{\partial \rho_i} + \lambda_1 \frac{\partial V}{\partial \rho_i} + \boldsymbol{\Lambda}^T \frac{\partial (\mathbf{K}\mathbf{u})}{\partial \rho_i} \leq 0 & \text{if } \rho_i = \rho_{\max} \\ V(\boldsymbol{\rho}) = \sum_{i=1}^N \rho_i V_i - V^* = 0 \\ \quad \text{(the equality constraints)} \\ \mathbf{K}\mathbf{u} = \mathbf{f} \quad \text{(the equality constraints)} \\ \mu_i \geq 0 \quad i = 1, 2 \end{cases} \quad (45)$$

The above sensitivity of a node is dependent on several surrounding points. For different positions, the number of nodes around one point may different. So the sensitivity analysis is more complex and time consuming when compared with the case of element-based methods.

To derive the iterative formulation more conveniently, only the equality cases in Eq.(45) are used in the present illustration, i.e.

$$\frac{\partial C}{\partial \rho_i} + \lambda_1 \frac{\partial V}{\partial \rho_i} + \boldsymbol{\Lambda}^T \left( \frac{\partial \mathbf{K}}{\partial \rho_i} \mathbf{u} + \mathbf{K} \frac{\partial \mathbf{u}}{\partial \rho_i} \right) = 0$$

Utilizing the expression  $\mathbf{K}\mathbf{u} = \mathbf{f}$ , it is easy to obtain

$$\frac{\partial \mathbf{K}}{\partial \rho_i} \mathbf{u} + \mathbf{K} \frac{\partial \mathbf{u}}{\partial \rho_i} = 0$$

then

$$-p(\rho_i)^{p-1} \mathbf{u}_i^T (\mathbf{k}_i^0)^T \mathbf{u}_i + \lambda_1 V_i = 0 \quad (46)$$

Set

$$B_i = \frac{p(\rho_i)^{p-1} \mathbf{u}_i^T (\mathbf{k}_i^0)^T \mathbf{u}_i}{\lambda_1 V_i} = 1 \quad (47)$$

Eq.(47) is regarded as an Optimally Criteria (OC) based on the discretization of the MLPG Mixed Collocation Method. Thus, we can update the design variables as follows:

$$\rho_i^{new} = \begin{cases} \max(\rho_{\min}, \rho_i - m) & \text{if } \rho_i B_i^\eta \leq \max(\rho_{\min}, \rho_i - m) \\ \rho_i B_i^\eta & \text{if } \max(\rho_{\min}, \rho_i - m) < \rho_i B_i^\eta < \min(1, \rho_i + m) \\ \min(1, \rho_i + m) & \text{if } \min(1, \rho_i + m) \leq \rho_i B_i^\eta \end{cases} \quad (48)$$

Where  $m$  is the limit ([Bendsøe and Kikuchi (1988)]), which represents the maximum allowable change in the relative nodal volume fractions  $\rho_i$  in the OC iteration.  $\eta$  is the damping coefficient. This updating scheme was often adopted in many presented papers. The values of  $m$  and  $\eta$  influence the convergence of the scheme, and they are chosen by experience ([Bendsøe and Kikuchi (1988)]).

The penalty parameter  $p$  is set to be 3, and the numerical damping coefficient  $\eta$  is set to 0.5. The Lagrange multiplier for the volume constraint  $\lambda_1$  is determined at each OC iteration using a bisectioning algorithm, as in the paper [Sigmund (2001)].

### 3.3 Filtering principle

Here we describe the principle of suppressing checkerboard patterns, which is a familiar problem in topology optimization when numerical stability is not guaranteed. The appearance of checkerboarding causes difficulties in interpreting and fabricating topology-optimized structural components. Sigmund (1994, 1997) developed a sensitivity filter method for preventing numerical instabilities from occurring. Filtering techniques have become quite popular in topology optimization [Wang; Lim, Khoo and Wang (2008)]. To tackle checkerboarding, a scheme similar to the filtering method is incorporated in the optimization algorithms based on the meshless discretization. In this scheme, we modify the de-

sign sensitivity of any specific node depending on a weighted average of the node sensitivities in a connected neighborhood. The principle works by modifying the nodal sensitivities as follows

$$\frac{\partial C}{\partial \rho_i} = \frac{1}{\rho_i \sum_{f=1}^m \hat{H}_f} \sum_{f=1}^m \hat{H}_f \rho_f \frac{\partial C}{\partial \rho_f} \quad (49)$$

Here, the convolution operator (weight factor) is written as

$$\begin{aligned} \hat{H}_f &= r_{\min} - \text{dist}(n, f) \\ \{f \in M \mid \text{dist}(n, f) \leq r_{\min}\}, \\ n &= 1, \dots, m \end{aligned} \quad (50)$$

and the operator  $\text{dist}(n, f)$  is defined as the distance between node  $n$  and node  $f$ . The convolution operator  $\hat{H}_f$  is zero outside the filter area, and decays linearly with the distance from node  $f$ .

## 4 Numerical examples

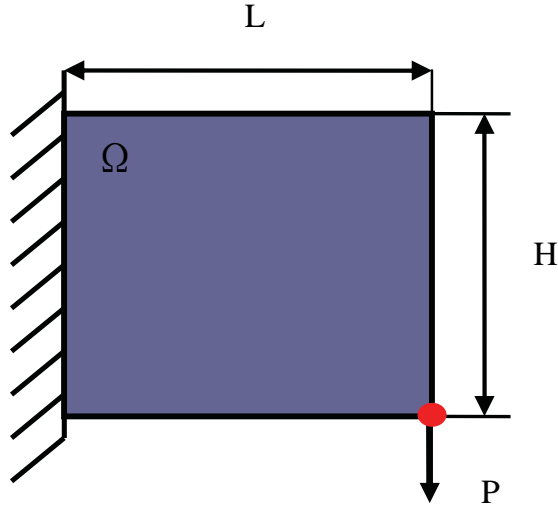
In this section, we present several numerical examples (cantilever and MBB-beams). They are used to illustrate the suitability of the MLPG Mixed Collocation Method for solving topology optimization problems with volume constraints. All the following examples are treated here as being dimensionless.

### 4.1 Verification of the validity and convergence

The topology-optimization problem is an ill-posed problem, with a lack of proof existence of solutions, since it often results in a complex material distribution [Eschenauer and Olhoff(2001)]. The convergence of solutions can not be guaranteed numerically. The validity and convergence are the important areas of concern for the solution of the topology optimization problem. We want to compare the results by the present method with the ones by finite element method (FEM).

#### Example 1:

The first example is that of a short cantilever beam as shown in Fig. 3. The design domain is fixed along the left edge and a concentrated vertical load  $P$  is applied at the bottom corner of the free (right) end of the beam.


 Figure 3: Cantilever beam I ( $L=H$ )

To determine an optimum structural layout, the square ‘design domain’ ( $L=H$ ) is discretized by the MLPG Mixed Collocation Method using  $20 \times 20$ ,  $40 \times 40$ ,  $80 \times 80$  uniformly distributed nodes, respectively.

The same problem is also solved by using the finite element method (FEM) by Sigmund(2001) for mesh refinements of  $20 \times 20$ ,  $40 \times 40$ ,  $80 \times 80$  elements. The optimized topology results using the meshless method and finite element method are shown in Fig. 4 and Fig.5, respectively. It can be seen that for this example, the similar topologies were obtained by two different algorithms.

### Example 2:

The second case is the so-called MBB beam [Zhou and Rozvany 1991] which only the right half-domain (Fig.7) is used for the analysis. The design domain is discretized into  $60 \times 20$ ,  $90 \times 30$ ,  $120 \times 40$  uniformly distributed nodes in the half-domain, respectively. The left bottom is assumed to be fixed, and the right one is assumed to be on a roller. The concentrated load  $P$  is applied at the middle of the top of the beam. As a comparison, the considered problem was also investigated by using finite element method (FEM). The mesh refinements are of  $60 \times 20$ ,  $90 \times 30$ ,  $120 \times 40$  elements in the half-domain, respectively. The solutions are given in Fig.8 and Fig.9. After comparing these solutions, it can be seen from that

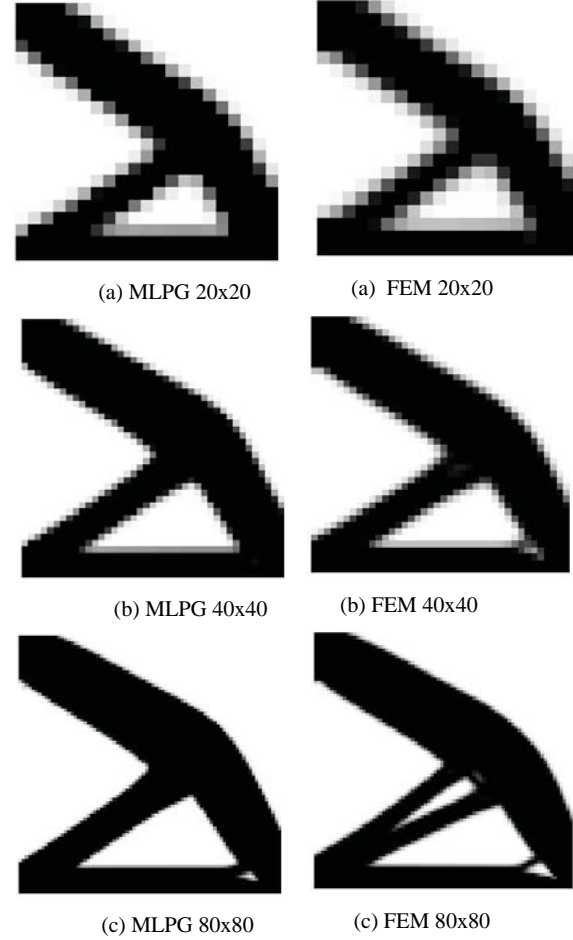


Figure 4: Topology optimization results of the cantilever beam by the MLPG Mixed Collocation Method

Figure 5: Topology optimization results of the cantilever beam by FEM methods

similar topologies can be obtained in the MLPG ‘Mixed Collocation’ method, as in the FEM.

Fig.6 and Fig.10 give three curves of convergence of the cantilever and MBB beams’ mean compliance, respectively. The almost monotonic and uniform convergence can be observed from these figures. The mean compliances steadily decrease as the iteration number is increased. Their convergence characteristics are very similar. Note that for both the above examples, the iterative performances of the discretization differ very little.

The validity and convergence of the present topology optimization method are verified by the ex-

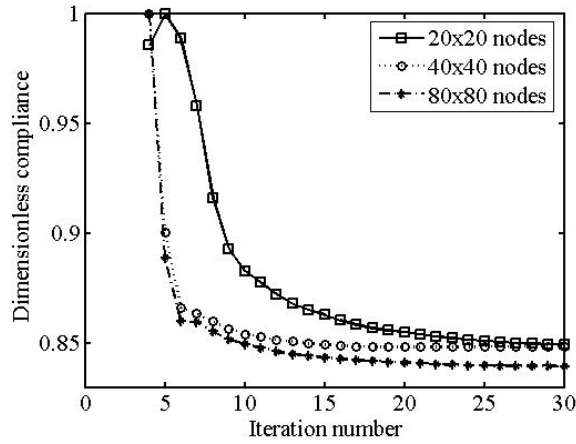


Figure 6: Convergence history of the cantilever beam compliance using the present method

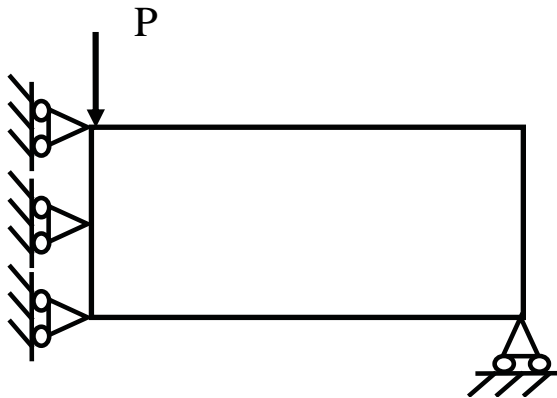


Figure 7: MBB beam (right half-domain)

cellent agreement between the results of meshless method and FEM. However, when FEM does converge to the same topology, the phenomena of mesh-dependency appears (Fig.10(c)) although a filter is applied. The appearance of mesh dependence is a common problem in topology optimization, wherein the solution to the topology optimization changes qualitatively as the mesh is refined. Fortunately, no phenomenon of mesh-dependence is found in the case of MLPG Mixed Collocation Method.

#### 4.2 Effectiveness of filtering

Checkerboard patterns are another common problem which are often present in optimal topologies generated by continuum topology optimization.

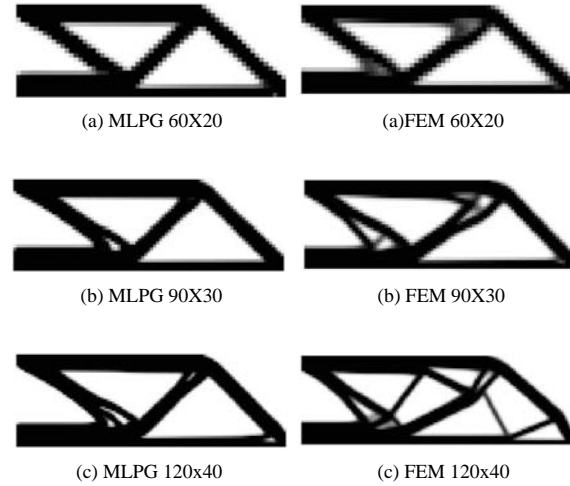


Figure 8: Optimal configuration of MBB beam (halves) by the MLPG Mixed Collocation Method

Figure 9: Optimal configuration of MBB beam (halves) by FEM methods

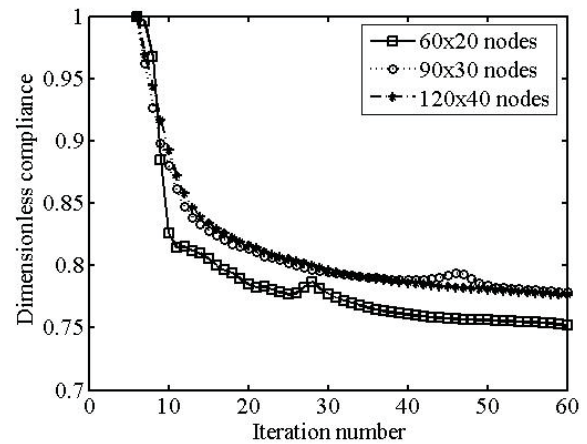


Figure 10: Convergence history of the MBB beam compliance using the present method

tion methods. Sigmund (1994) suggested a filtering method, which is shown to be effective in suppressing the formation of checkerboard patterns. To illustrate the filtering effect, we consider a cantilever beam in Fig. 11 and a MBB beam in Fig.14.

#### Example 3:

This example is also that of a short cantilever beam which has the rectangular 'design domain' ( $L=2H$ ) as shown in Fig. 11. The load  $P$  is applied

at the middle of the right end.

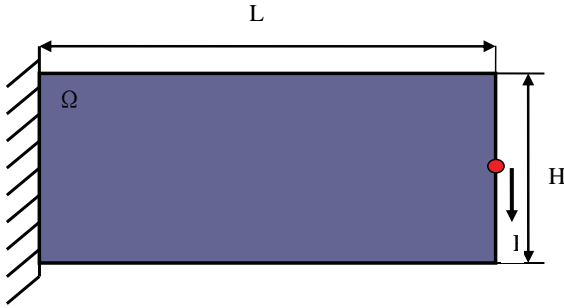


Figure 11: Cantilever beam II ( $L=2H$ )

The design domain is discretized using  $40 \times 20$ ,  $60 \times 30$ ,  $80 \times 40$  uniformly distributed nodes, respectively. For the considered beam, topologies are given in Fig. 12 and Fig.13.

We can see the effects of the filter. A sample MLPG solution with checkerboarding is shown in Fig.12. Fig.13 shows the final optimal layouts of the short cantilever beam after filtering. It can be seen that the checkerboard pattern disappears and optimal configurations became more clear. The filtering properties of the present method are thus verified.

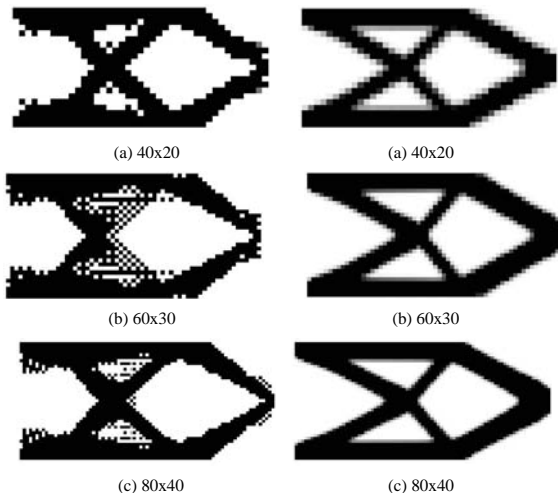


Figure 12: Optimal configuration before filtering

Figure 13: Optimal configuration after filtering

#### Example 4:

We now solve another simple topology optimization problem for various discretization cases, i.e.  $40 \times 20$ ,  $60 \times 30$ ,  $80 \times 40$  uniformly distributed nodes, respectively. The domain and boundary conditions for the problem chosen are shown in Fig. 14. In this case, the beam is of given length  $L$  and depth  $H$ , and both the ends are simply supported. The remaining volume ratio is 30%.

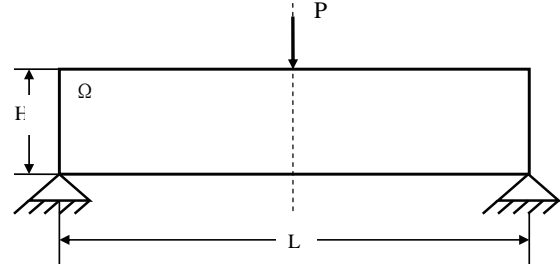


Figure 14: MBB-beam

Fig.15 shows that the algorithm finds a typical bar-design, The results are found to be similar to those in [Eschenauer and Olhoff(2001)]. In this example, we find that the optimum structural layouts are polluted by so-called checkerboard patterns. Figs.16 show that the checkerboards can be completely eliminated by the present nodal sensitivity filter. This example shows that the filter is good for eliminating checkerboarding. As a result of this, it is desirable to suppress the formation of checkerboard patterns in continuum topology optimization.

#### 4.3 Comparison of topology with different “remaining volume” ratio

##### Example 5:

The example is that of an MBB beam as in Fig. 17. This case is a bridge-structure with same boundary conditions and different load location as the MBB beam in Example 4. The beam has length  $L$  and depth  $H$  with ratio  $L/H=2$ .

These optimal designs have the “remaining volumes” of 60%, 50%, 40%, 30%, 20% and 10 % of the initial volume, respectively. The final topologies of MBB beam are shown in Fig.18. This design finds a classic Michell type structure and a typical bar-design. The same results can be ob-

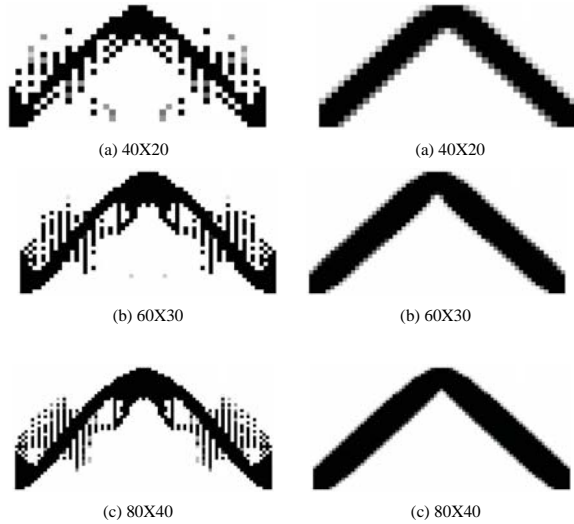


Figure 15: Optimal configuration before filtering

Figure 16: Optimal configuration after filtering

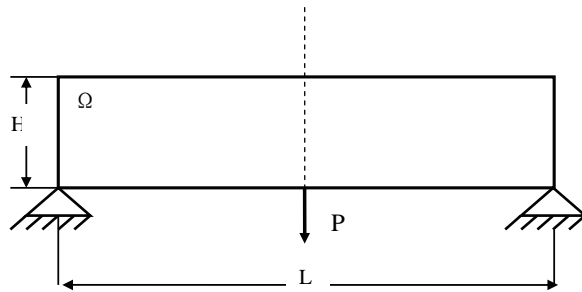


Figure 17: MBB-beam

tained by using Sigmund's 99 line code in Matlab [Sigmund (2001)].

#### Example 6:

In this example, we consider the initial design of a bridge structure for a prescribed (hatched) area subject to uniformly distributed load (Fig.19). The two points at the bottom surface corners are simply supported. The bridge-structure has a 2:1 ratio for the length:width. The whole structure is modelled by  $60 \times 30$  nodes. The hatched part is the required minimum thickness at the top of the bridge, which is specified as a non-design domain. We obtain the initial optimal designs for different "remaining volume" limits of 70, 60, 50, 40, 30 and 20 % of the initial volume.

Fig.20 displays an optimal design for the bridge

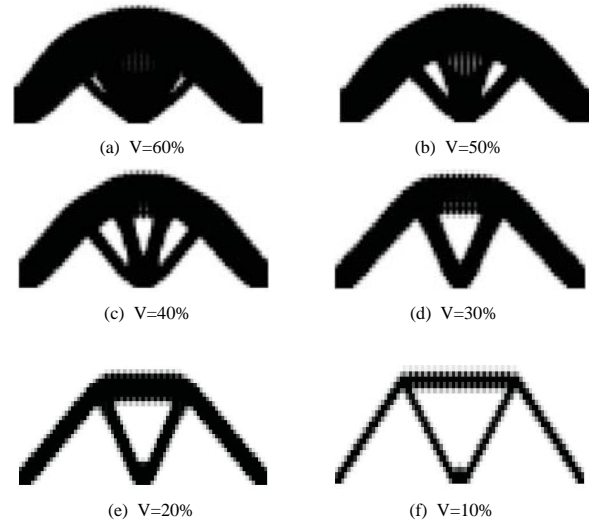


Figure 18: The final topologies of MBB beam with different volume

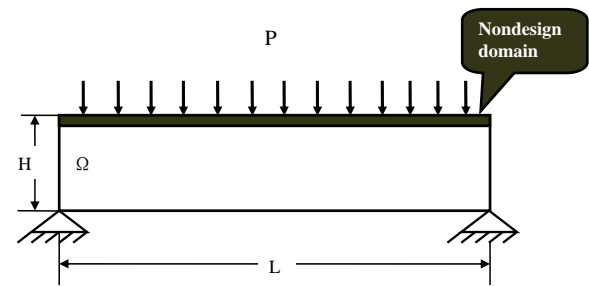


Figure 19: Bridge structure

structure using the conventional MLPG mixed collocation method. When the remaining material volume is less than 50%, the topologically optimized structure is becoming a typical arch truss system. This is a perfect construction that transfers the loads to the supports very efficiently through a reasonable path.

## 5 Conclusions

The MLPG method is implemented to solve the topology optimization problem. In this paper, design domains are discretized by using the MLPG mixed collocation method, and the material distribution problem becomes one of finding the optimal values of the relative nodal volume fractions. A node with zero relative nodal volume fraction represents a void and a node with a relative nodal

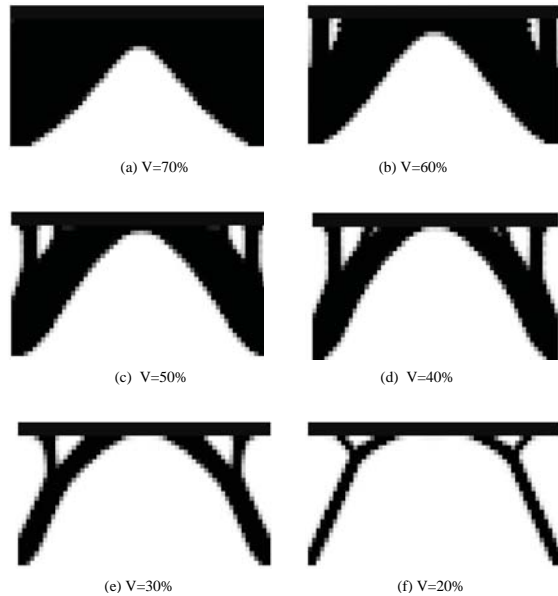


Figure 20: The final topologies of bridge structure with different volume

volume fraction of 1 represents a solid node. The goal is to find a distribution of relative nodal volume fractions that minimizes a compliance objective function, subject to volume constraints. To solve such a topology optimization problem, the popular optimality criteria (OC) method is employed with an iterative heuristic scheme for updating the design variables.

In this paper, we show several numerical examples to demonstrate the validity and convergence of the present method. We examine the effect of filtering on the resulting topology. We compare the various numerical results in solving topology optimization problems. Summarizing our research, the present method has the following advantages:

The filtering technique is not certain in general to suppress the mesh-dependency problem in the finite element method. The present method does not use a mesh of elements. The numerical instability problems related to mesh do not exist. It need not cost extra CPU-time to deal with such the numerical instabilities. The filtering technique is highly suitable for the present MLPG method.

The nodal values are used as the design variables. It can be seen, by comparing with the element-

based methods, that it is not necessary to interpolate or project those design variables onto an element space.

The formulation of the MLPG mixed collocation method is established at the nodal points. It is unnecessary to integrate over the design domain, during the optimization procedure. So the implementation becomes very convenient and efficient.

**Acknowledgement:** This research was conducted during the study of S. Li at UCI. This research was also partially supported by the office of Naval Research.

## References

- Atluri, S.N.; Zhu, T** (1998): A New Meshless Local Petrov-Galerkin (MLPG) Approach in Computational Mechanics, *Computational Mechanics*, Vol.22, pp. 117-127.
- Atluri, S.N., Shen, S.P.** (2002a): The meshless local Petrov-Galerkin (MLPG) method: A simple & less-costly alternative to the finite element and boundary element methods, *CMES: Computer Modeling in Engineering and Sciences*, 3 (1) 11-51.
- Atluri, S.N.; Shen, S.** (2002b): The Meshless Local Petrov-Galerkin (MLPG) Method, 2002, 440 pages, Tech Science Press.
- Atluri, S.N.** (2004) The Meshless Method(MLPG) for Domain & BIE Discretizations, 2004, 680 pages, Tech Science Press.
- Atluri, S.N.; Liu H.T.; Han Z.D.** (2006): Meshless local Petrov-Galerkin (MLPG) mixed collocation method for elasticity problems, *CMES: Computer Modeling in Engineering & Sciences*, vol. 14, no. 3, pp. 141-152.
- Bendsøe, M.P.; Kikuchi, N.** (1988): Generating optimal topologies in optimal design using a homogenization method, *Comp. Meth. Appl. Mech. Engrg*, vol. 71, pp.197-224.
- Bendsøe, M.P.** (1989), Optimal shape design as a material distribution problem, *Struct. Optim.*, vol. 1, pp.193-202.
- Bendsøe, M.P.; Sigmund, O.** (2003): Topology

optimization, theory, methods and applications, Springer.

**Chiandussi, G.; Gaviglio, I.; Ibba, A.** (2004): Topology optimisation of an automotive component without final volume constraint specification, *Advances in Engineering Software* vol. 35, pp.609-617.

**Cisilino, A.P.** (2006): Topology Optimization of 2D Potential Problems Using Boundary Elements, *CMES: Computer Modeling in Engineering & Sciences*, vol.15, no.2, pp.99-106.

**Eschenauer, H.A.; Olhoff, N.** (2001): Topology optimization of continuum structures: A review, *Appl Mech Rev*, vol. 54, no 4, pp.331-390.

**Guest, J.K.; J.H. Prévost, J.K.; Belytschko, T.** (2004): Achieving minimum length scale in topology optimization using nodal design variables and projection functions, *Int. J. Numer. Meth. Engng*; vol. 61, pp.238-254.

**Hansen, L.U.; Horst, P.** (2008): Multilevel optimization in aircraft structural design evaluation, *Computers and Structures*, vol.86, pp.104-118.

**Mackerle, J.** (2003): Topology and shape optimization of structures using FEM and BEM: A bibliography (1999-2001), *Finite Elements in Analysis and Design*, vol. 39, pp. 243-253.

**Norato, J.A.; Bendsøe, M.P.; Haber, R.B.; Tortorelli, D.A.** (2007): A topological derivative method for topology optimization, *Struct Multidisc Optim*, vol. 33, pp. 375-386.

**Sigmund, O.** (1994): Materials with prescribed constitutive parameters: An inverse homogenization problem, *Int. J. Solids Struct.*, vol. 31, pp.2313-2329.

**Sigmund, O.** (1997): On the design of compliant mechanisms using topology optimization, *J. Mech. Struct. Mach.*, vol. 25, pp.493-524.

**Sigmund, O.; Petersson, J.** (1998): Numerical instabilities in topology optimization: a survey on procedures dealing with checkerboards, mesh-dependencies and local minima. *Struct. Optim.*, vol. 16, pp.68-75.

**Sigmund, O.** (2001): A 99 line topology optimization code written in Matlab, *Struct Multidisc Optim.*, vol. 21, pp.120-127.

**Vemaganti, K.; Lawrence, W.E.** (2005): Parallel methods for optimality criteria-based topology optimization, *Comput. Methods Appl. Mech. Engng.*, Vol.194, pp.3637-3667.

**Wang, S.Y. and Wang, M.Y.** (2006): Structural Shape and Topology Optimization Using an Implicit Free Boundary Parametrization Method, *CMES: Computer Modeling in Engineering & Sciences*, vol.13, no.2, pp.119-147.

**Wang, S.Y.; Lim, K.M.; Khoo, B.C. and Wang, M.Y.** (2007a): A Geometric Deformation Constrained Level Set Method for Structural Shape and Topology Optimization, *CMES: Computer Modeling in Engineering & Sciences*, vol.18, no.3, pp.155-181.

**Wang, S.Y.; Lim, K.M.; Khoo, B.C. and Wang, M.Y.** (2007b): An Unconditionally Time-Stable Level Set Method and Its Application to Shape and Topology Optimization, *CMES: Computer Modeling in Engineering & Sciences*, Vol.21, No.1, pp.1-40.

**Wang, S.Y.; Lim, K.M.; Khoo, B.C. and Wang, M.Y.** (2007c): On Hole Nucleation in Topology Optimization Using the Level Set Methods, *CMES: Computer Modeling in Engineering & Sciences*, vol.21, no.3, pp.219-237.

**Wang, S.Y.; Lim, K.M.; Khoo, B.C. and Wang, M.Y.** (2008): A Hybrid Sensitivity Filtering Method for Topology Optimization, *CMES: Computer Modeling in Engineering & Sciences*, vol.24, no.1, pp.21-50.

**Zhou, M.; Rozvany, G.I.N.** (1991): COC algorithm, Part II: Topological, geometrical and generalized shape optimization, *Computer Methods in Applied Mechanics and Engineering*, vol. 89, pp.309-336.

**Zhou, S.; Wang M.Y.** (2006): 3D Multi-Material Structural Topology Optimization with the Generalized Cahn-Hilliard Equations, *CMES: Computer Modeling in Engineering & Sciences*, vol.16, no.2, pp.83-101.

# A Novel Time Integration Method for Solving A Large System of Non-Linear Algebraic Equations

Chein-Shan Liu<sup>1</sup> and Satya N. Atluri<sup>2</sup>

**Abstract:** Iterative algorithms for solving a nonlinear system of algebraic equations of the type:  $F_i(x_j) = 0$ ,  $i, j = 1, \dots, n$  date back to the seminal work of Issac Newton. Nowadays a Newton-like algorithm is still the most popular one due to its easy numerical implementation. However, this type of algorithm is sensitive to the initial guess of the solution and is expensive in the computations of the Jacobian matrix  $\partial F_i / \partial x_j$  and its inverse at each iterative step. In a time-integration of a system of nonlinear Ordinary Differential Equations (ODEs) of the type  $B_{ij}\dot{x}_j + F_i = 0$  where  $B_{ij}$  are nonlinear functions of  $x_j$ , the methods which involve an inverse of the Jacobian matrix  $B_{ij} = \partial F_i / \partial x_j$  are called “Implicit”, while those that do not involve an inverse of  $\partial F_i / \partial x_j$  are called “Explicit”. In this paper a natural system of explicit ODEs is derived from the given system of nonlinear algebraic equations (NAEs), by introducing a fictitious time, such that it is a mathematically equivalent system in the  $n + 1$ -dimensional space as the original algebraic equations system is in the  $n$ -dimensional space. The iterative equations are obtained by applying numerical integrations on the resultant ODEs, which do not need the information of  $\partial F_i / \partial x_j$  and its inverse. The computational cost is thus greatly reduced. Numerical examples given confirm that this fictitious time integration method (FTIM) is highly efficient to find the true solutions with residual errors being much smaller. Also, the FTIM is used to study the attracting sets of fixed points, when multiple roots exist.

**Keyword:** Nonlinear algebraic equations, Iterative method, Ordinary differential equations, Fictitious time integration method (FTIM)

## 1 Introduction

Numerical solution of algebraic equations is one of the main aspects of computational mathematics. In many practical nonlinear engineering problems, the methods such as the finite element method, boundary element method, finite volume method, the meshless method, etc., eventually lead to a system of nonlinear algebraic equations (NAEs). Many numerical methods used in computational mechanics, as demonstrated by Zhu, Zhang and Atluri (1998), Atluri and Zhu (1998a), Atluri (2002), Atluri and Shen (2002), and Atluri, Liu and Han (2006) lead to the solution of a system of linear algebraic equations for a linear problem, and of an NAEs system for a nonlinear problem. Collocation methods, as those used by Liu (2007a, 2007b, 2007c, 2008a) for the modified Trefftz method of Laplace equation also need to solve a large system of algebraic equations.

Over the past forty years two important contributions have been made towards the numerical solutions of NAEs. One of the methods has been called the “predictor-corrector” or “pseudo-arclength continuation” method. This method has its historical roots in the embedding and incremental loading methods which have been successfully used for several decades by engineers to improve the convergence properties when an adequate starting value for an iterative method is not available. Another is the so-called simplicial or piecewise linear method. The monographs by Allgower and Georg (1990) and Deuffhard (2004) are devoted to the continuation methods for solving NAEs.

<sup>1</sup> Department of Mechanical and Mechatronic Engineering, Taiwan Ocean University, Keelung, Taiwan. E-mail: csliu@mail.ntou.edu.tw

<sup>2</sup> Center for Aerospace Research & Education, University of California, Irvine

In this paper we introduce a novel continuation method, by embedding the NAEs into a system of nonautonomous first order ODEs (FOODEs). To motivate the present approach, we consider a single NAE:

$$F(x) = 0. \quad (1)$$

In the above equation, we only have an independent variable  $x$ . We transform it into a FOODE by introducing a time-like or fictitious variable  $t$  into the following transformation of variable from  $x$  to  $y$ :

$$y(t) = (1+t)x. \quad (2)$$

Here,  $t$  is a variable which is independent of  $x$ ; hence,  $\dot{y} = dy/dt = x$ . If  $v \neq 0$ , Eq. (1) is equivalent to

$$0 = -vF(x). \quad (3)$$

Adding the equation  $\dot{y} = x$  to Eq. (3) we obtain:

$$\dot{y} = x - vF(x). \quad (4)$$

By using Eq. (2) we can derive

$$\dot{y} = \frac{y}{1+t} - vF\left(\frac{y}{1+t}\right). \quad (5)$$

This is a FOODE for  $y(t)$ . The initial condition for the above equation is  $y(0) = x$ , which is however an unknown and requires a guess.

We demonstrate the above idea by a simple algebraic equation:

$$F(x) = x - 1 = 0, \quad (6)$$

which has the solution  $x = 1$ .

From Eqs. (5) and (6) it follows that

$$\dot{y} = \frac{1-v}{1+t}y + v. \quad (7)$$

Suppose that  $y(0) = y_0$ , then the solution of Eq. (7) can be written as

$$y(t) = \frac{y_0 - 1}{(1+t)^{v-1}} + 1 + t. \quad (8)$$

If we choose  $v > 1$ , the above  $y(t)$  approaches  $1+t$  with a power of  $(1+t)^{1-v}$ . At this moment

of convergence, by  $x = y/(1+t)$  we can get the solution  $x = 1$  of Eq. (6). We note that  $x = 1$  is also the asymptotic of the following FOODE:

$$\dot{x} = -\frac{v}{1+t}(x-1) = -\frac{v}{1+t}F(x), \quad (9)$$

where  $\dot{x} = dx/dt$ . The solution of Eq. (9) is

$$x(t) = \frac{x_0 - 1}{(1+t)^v} + 1, \quad (10)$$

where  $x(t=0) = x_0$ . The solution  $x = 1$  is recovered very fast from  $x(t)$  in Eq. (10), when  $v > 0$  is a large number.

Multiplying Eq. (5) by an integrating factor of  $1/(1+t)$  we can obtain

$$\frac{d}{dt} \left( \frac{y}{1+t} \right) = -\frac{v}{1+t} F\left(\frac{y}{1+t}\right). \quad (11)$$

Further using  $y/(1+t) = x$ , leads to

$$\dot{x} = -\frac{v}{1+t} F(x). \quad (12)$$

The roots of  $F(x) = 0$  are fixed points of the above equation. We should stress that the factor  $-v/(1+t)$  before  $F(x)$  is important.

We may employ a forward Euler scheme on Eq. (12) by starting from a chosen initial condition  $x_0$ :

$$x_{k+1} = x_k - \frac{hv}{1+t_k} F(x_k), \quad (13)$$

where  $h$  is a time stepsize and  $x_k = x(t_k)$  is the value of  $x$  at the  $k$ -th discrete time  $t_k$ .

Suppose that  $t_k = k$  is an integer time with a time increment  $h = 1$ , then we have

$$x_{k+1} = x_k - \frac{v}{1+k} F(x_k). \quad (14)$$

This bears certain similarity with the famous Newton method for Eq. (1):

$$x_{k+1} = x_k - \frac{F(x_k)}{F'(x_k)}. \quad (15)$$

But it can be seen that when there exists a danger in the Newton method of dividing by a zero

$F'(x_k)$ , the algorithm in Eq. (14) is always workable. If the function  $F$  is bounded, the algorithm (14) guarantees that the solution can be approached.

Now we turn to the discussions of the following algebraic equations:

$$F_i(x_1, \dots, x_n) = 0, \quad i = 1, \dots, n. \quad (16)$$

The Newton method for these equations is given by

$$\mathbf{x}_{k+1} = \mathbf{x}_k - [\mathbf{B}(\mathbf{x}_k)]^{-1} \mathbf{F}(\mathbf{x}_k), \quad (17)$$

where we use  $\mathbf{x} := (x_1, \dots, x_n)^T$  and  $\mathbf{F} := (F_1, \dots, F_n)^T$  to represent the vectors, and  $\mathbf{B}$  is an  $n \times n$  matrix with its  $ij$ -th component given by  $\partial F_i / \partial x_j$ .

The Newton method has a great advantage that it is quadratically convergent. However, it still has some drawbacks of not being easy to guess the initial point, the computational burden of  $[\mathbf{B}(\mathbf{x}_k)]^{-1}$ , and  $\mathbf{F}$  being required to be differentiable. Some quasi-Newton methods are thus developed to overcome these defects of the Newton method; see the discussions by Broyden (1965), Dennis (1971), Dennis and More (1974, 1977), and Spedicato and Huang (1997).

Davidenko (1953) was the first who developed a new idea of homotopy method to solve Eq. (16) by numerically integrating

$$\dot{\mathbf{x}}(t) = -\mathbf{H}_{\mathbf{x}}^{-1} \mathbf{H}_t(\mathbf{x}, t), \quad (18)$$

$$\mathbf{x}(0) = \mathbf{a}, \quad (19)$$

where  $\mathbf{H}$  is a homotopic vector function, for example,  $\mathbf{H} = (1-t)(\mathbf{x} - \mathbf{a}) + t\mathbf{F}(\mathbf{x})$ , and  $\mathbf{H}_{\mathbf{x}}$  and  $\mathbf{H}_t$  are respectively the partial derivatives of  $\mathbf{H}$  with respect to  $\mathbf{x}$  and  $t$ . This theory is later refined by Kellogg, Li and Yorke (1976), Chow, Mallet-Paret and Yorke (1978), Li and Yorke (1980), and Li (1997). At the same time, Hirsch and Smale (1979) also derived a continuous Newton method governed by the following differential equation:

$$\dot{\mathbf{x}}(t) = -\mathbf{B}^{-1}(\mathbf{x}) \mathbf{F}(\mathbf{x}), \quad (20)$$

$$\mathbf{x}(0) = \mathbf{a}. \quad (21)$$

It can be seen that the ODEs in Eqs. (18) and (20) are difficult to calculate, because they all include

an inverse matrix. Below we will develop a new ODEs system, which is equivalent to the original equation (16).

## 2 A fictitious time integration approach

### 2.1 Transformation into an ODEs system

First we propose the following variable transformation:

$$y_i(t) = (1+t)x_i, \quad i = 1, \dots, n, \quad (22)$$

and multiply Eq. (16) by a coefficient  $-v \neq 0$ :

$$0 = -vF_i(x_1, \dots, x_n). \quad (23)$$

Using Eq. (22) we have

$$0 = -vF_i\left(\frac{y_1}{1+t}, \dots, \frac{y_n}{1+t}\right). \quad (24)$$

Recalling that  $\dot{y}_i = x_i$  by Eq. (22), and adding it on both the sides of the above equation we obtain

$$\dot{y}_i = x_i - vF_i\left(\frac{y_1}{1+t}, \dots, \frac{y_n}{1+t}\right). \quad (25)$$

Then, by using  $x_i = y_i/(1+t)$ , we can change Eq. (16) into an ODEs system:

$$\dot{y}_i = \frac{y_i}{1+t} - vF_i\left(\frac{y_1}{1+t}, \dots, \frac{y_n}{1+t}\right). \quad (26)$$

Finally, multiplying each equation by the integrating factor  $1/(1+t)$  and using Eq. (22) again we obtain

$$\dot{x}_i = \frac{-v}{1+t} F_i(x_1, \dots, x_n), \quad i = 1, \dots, n. \quad (27)$$

It can be seen that this ODEs system is nonautonomous and is much simpler than those in Eqs. (18) and (20).

Furthermore, in terms of a logarithmic time scale

$$\tau = \ln(1+t), \quad (28)$$

Eq. (27) can be recast into a more elegant form:

$$\frac{dx_i}{d\tau} = -vF_i(x_1, \dots, x_n), \quad i = 1, \dots, n. \quad (29)$$

The above idea was first proposed by Liu (2008b) to treat an inverse Sturm-Liouville problem by

transforming an ODE into a PDE. Then, Liu and his coworkers [Liu (2008c, 2008d); Liu, Chang, Chang and Chen (2008)] extended this idea to develop new method for estimating parameters in the inverse vibration problems.

Eq. (22) is not the unique way to transform the algebraic equations (16) into the ODEs. We can adopt

$$y_i(t) = q(t)x_i, \quad i = 1, \dots, n, \quad (30)$$

and a similar derivation leads to

$$\dot{x}_i = \frac{-v}{q(t)} F_i(x_1, \dots, x_n), \quad i = 1, \dots, n. \quad (31)$$

The requirements on  $q(t)$  are that they be differentiable and  $q(0) = 1$ . A special case is  $q(t) = 1$  and  $v = -1$ , and then we have

$$\dot{x}_i = F_i(x_1, \dots, x_n). \quad (32)$$

Deuffhard (2004) has called the above equation a pseudo-transient continuation method. However, this equation is hard to work and usually leads to wrong solutions of  $F_i = 0$ .

From Eq. (29) we can understand that the so-called steady state must be considered in the logarithmic time scale  $\tau = \ln(1+t)$ , because this equation is no more a nonautonomous one as Eq. (27) is. In the logarithmic time scale, if the motion of  $x_i$  approaches a steady state, i.e.,  $dx_i/d\tau = 0$ , then the roots are reached. In this paper we focus on using Eq. (27) as our tool to compute the roots of algebraic equations. This is the most simple choice of  $q(t) = 1+t$  to meet the just mentioned requirements of  $q(t)$ . However, other choices are possible if they can provide better behavior than the present one.

## 2.2 GPS for differential equations system

As was done in Eq. (14), we may employ the Euler method for Eq. (27), and using  $h = 1$ , to obtain an iterative method to calculate the solutions of algebraic equations:

$$x_i^{k+1} = x_i^k - \frac{v}{1+k} F_i(x_1^k, \dots, x_n^k), \quad i = 1, \dots, n. \quad (33)$$

However, we find that this method is not so good, because sometimes  $h = 1$  may be too large to cause over-flow of the values of  $x_i$ .

Therefore we develop a more stable group preserving scheme (GPS) given as follows. Upon letting  $\mathbf{x} = (x_1, \dots, x_n)^T$ , and letting  $\mathbf{f}$  denote a vector with its  $i$ -th component being the right-hand side of Eq. (27) we can write Eq. (27) a vector form:

$$\dot{\mathbf{x}} = \mathbf{f}(\mathbf{x}, t) = \frac{-v}{1+t} \mathbf{F}(\mathbf{x}), \quad \mathbf{x} \in \mathbb{R}^n, \quad t > 0, \quad (34)$$

where  $n$  is the number of algebraic equations.

A GPS can preserve the internal symmetry group of the considered ODEs system. Although we do not know previously the symmetry group of differential equations system, Liu (2001) has embedded it into an augmented differential equations system, which concerns with not only the evolution of state variables themselves but also the evolution of the magnitude of the state variables vector. We note that

$$\|\mathbf{x}\| = \sqrt{\mathbf{x}^T \mathbf{x}} = \sqrt{\mathbf{x} \cdot \mathbf{x}}, \quad (35)$$

where the dot between two  $n$ -dimensional vectors denotes their inner product. Taking the derivatives of both the sides of Eq. (35) with respect to  $t$ , we have

$$\frac{d\|\mathbf{x}\|}{dt} = \frac{\dot{\mathbf{x}}^T \mathbf{x}}{\sqrt{\mathbf{x}^T \mathbf{x}}}. \quad (36)$$

Then, by using Eqs. (34) and (35) we can derive

$$\frac{d\|\mathbf{x}\|}{dt} = \frac{\mathbf{f}^T \mathbf{x}}{\|\mathbf{x}\|}. \quad (37)$$

It is interesting that Eqs. (34) and (37) can be combined together into a simple matrix equation:

$$\frac{d}{dt} \begin{bmatrix} \mathbf{x} \\ \|\mathbf{x}\| \end{bmatrix} = \begin{bmatrix} \mathbf{0}_{n \times n} & \frac{\mathbf{f}(\mathbf{x}, t)}{\|\mathbf{x}\|} \\ \frac{\mathbf{f}^T(\mathbf{x}, t)}{\|\mathbf{x}\|} & 0 \end{bmatrix} \begin{bmatrix} \mathbf{x} \\ \|\mathbf{x}\| \end{bmatrix}. \quad (38)$$

It is obvious that the first row in Eq. (38) is the same as the original equation (34), but the inclusion of the second row in Eq. (38) gives us a Minkowskian structure of the augmented state variables of  $\mathbf{X} := (\mathbf{x}^T, \|\mathbf{x}\|)^T$ , which satisfies the cone condition:

$$\mathbf{X}^T \mathbf{g} \mathbf{X} = 0, \quad (39)$$

where

$$\mathbf{g} = \begin{bmatrix} \mathbf{I}_n & \mathbf{0}_{n \times 1} \\ \mathbf{0}_{1 \times n} & -1 \end{bmatrix} \quad (40)$$

is a Minkowski metric, and  $\mathbf{I}_n$  is the identity matrix of order  $n$ . In terms of  $(\mathbf{x}, \|\mathbf{x}\|)$ , Eq. (39) becomes

$$\mathbf{X}^T \mathbf{g} \mathbf{X} = \mathbf{x} \cdot \mathbf{x} - \|\mathbf{x}\|^2 = \|\mathbf{x}\|^2 - \|\mathbf{x}\|^2 = 0. \quad (41)$$

It follows from the definition given in Eq. (35), and thus Eq. (39) is a natural result.

Consequently, we have an  $n+1$ -dimensional augmented differential equations system:

$$\dot{\mathbf{X}} = \mathbf{A} \mathbf{X} \quad (42)$$

with a constraint (39), where

$$\mathbf{A} := \begin{bmatrix} \mathbf{0}_{n \times n} & \frac{\mathbf{f}(\mathbf{x}, t)}{\|\mathbf{x}\|} \\ \frac{\mathbf{f}^T(\mathbf{x}, t)}{\|\mathbf{x}\|} & 0 \end{bmatrix}, \quad (43)$$

satisfying

$$\mathbf{A}^T \mathbf{g} + \mathbf{g} \mathbf{A} = \mathbf{0}, \quad (44)$$

is a Lie algebra  $so(n, 1)$  of the proper orthochronous Lorentz group  $SO_o(n, 1)$ . This fact prompts us to devise the GPS, whose discretized mapping  $\mathbf{G}$  must exactly preserve the following properties:

$$\mathbf{G}^T \mathbf{g} \mathbf{G} = \mathbf{g}, \quad (45)$$

$$\det \mathbf{G} = 1, \quad (46)$$

$$G_0^0 > 0, \quad (47)$$

where  $G_0^0$  is the 00-th component of  $\mathbf{G}$ .

Although the dimension of the new system is raised by one more, it has been shown that the new system permits a GPS given as follows [Liu (2001)]:

$$\mathbf{X}_{k+1} = \mathbf{G}(k) \mathbf{X}_k, \quad (48)$$

where  $\mathbf{X}_k$  denotes the numerical value of  $\mathbf{X}$  at  $t_k$ , and  $\mathbf{G}(k) \in SO_o(n, 1)$  is the group value of  $\mathbf{G}$  at  $t_k$ . If  $\mathbf{G}(k)$  satisfies the properties in Eqs. (45)-(47), then  $\mathbf{X}_k$  satisfies the cone condition in Eq. (39).

The Lie group can be generated from  $\mathbf{A} \in so(n, 1)$  by an exponential mapping,

$$\begin{aligned} \mathbf{G}(k) &= \exp[h\mathbf{A}(k)] \\ &= \begin{bmatrix} \mathbf{I}_n + \frac{(a_k-1)}{\|\mathbf{f}_k\|^2} \mathbf{f}_k \mathbf{f}_k^T & \frac{b_k \mathbf{f}_k}{\|\mathbf{f}_k\|} \\ \frac{b_k \mathbf{f}_k^T}{\|\mathbf{f}_k\|} & a_k \end{bmatrix}, \end{aligned} \quad (49)$$

where

$$a_k := \cosh\left(\frac{h\|\mathbf{f}_k\|}{\|\mathbf{x}_k\|}\right), \quad (50)$$

$$b_k := \sinh\left(\frac{h\|\mathbf{f}_k\|}{\|\mathbf{x}_k\|}\right). \quad (51)$$

Substituting Eq. (49) for  $\mathbf{G}(k)$  into Eq. (48), we obtain

$$\mathbf{x}_{k+1} = \mathbf{x}_k + \eta_k \mathbf{f}_k, \quad (52)$$

$$\|\mathbf{x}_{k+1}\| = a_k \|\mathbf{x}_k\| + \frac{b_k}{\|\mathbf{f}_k\|} \mathbf{f}_k \cdot \mathbf{x}_k, \quad (53)$$

where

$$\eta_k := \frac{b_k \|\mathbf{x}_k\| \|\mathbf{f}_k\| + (a_k - 1) \mathbf{f}_k \cdot \mathbf{x}_k}{\|\mathbf{f}_k\|^2}. \quad (54)$$

The group properties are preserved in this scheme for all  $h > 0$ , and is called a group-preserving scheme.

### 2.3 Runge-Kutta method

We have derived a GPS in the last section, which is however a first-order numerical integration scheme. In order to increase the accuracy in the integration of Eq. (34) sometimes we may employ the fourth-order Runge-Kutta method (RK4) by the following process:

$$\mathbf{x}_{k+1} = \mathbf{x}_k + \frac{h}{6} (\mathbf{f}_1 + 2\mathbf{f}_2 + 2\mathbf{f}_3 + \mathbf{f}_4), \quad (55)$$

where

$$\mathbf{f}_1 = \mathbf{f}(\mathbf{x}_k, t_k),$$

$$\mathbf{f}_2 = \mathbf{f}(\mathbf{x}_k + h/2 \mathbf{f}_1, t_k + h/2),$$

$$\mathbf{f}_3 = \mathbf{f}(\mathbf{x}_k + h/2 \mathbf{f}_2, t_k + h/2),$$

$$\mathbf{f}_4 = \mathbf{f}(\mathbf{x}_k + h \mathbf{f}_3, t_k + h).$$

## 2.4 Numerical procedure

Starting from an initial value of  $\mathbf{x}(0)$  which can be guessed in a rather free way, we employ the above GPS or RK4 to integrate Eq. (34) from  $t = 0$  to a selected final time  $t_f$ . In the numerical integration process we check the convergence of  $x_i$  at the  $k$ - and  $k + 1$ -steps by

$$\sum_{i=1}^n (x_i^{k+1} - x_i^k)^2 \leq \varepsilon^2, \quad (56)$$

where  $\varepsilon$  is a given convergent criterion. If at a time  $t_0 \leq t_f$  the above criterion is satisfied, then the solution of  $x_i$  is obtained. In practice, if a suitable  $t_f$  is selected we find that the numerical solution is also approached very well to the true solution, even the above convergent criterion is not satisfied before the time  $t < t_f$ . A suitable coefficient  $v$  introduced in Eq. (27) can increase the stability of numerical integration, and speeds up the rate of convergence.

In particular we would emphasize that the present method is a new fictitious time integration method (FTIM), which can calculate the solution very stably and effectively. Below we give numerical examples to display some advantages of the present FTIM.

## 3 Numerical tests of FTIM by examples

In this section we will apply the new method of FTIM on both single, as well as multiple nonlinear algebraic equations, and sometimes compare it with the Newton method (NM).

Before embarking the numerical tests we use the following case to compare the FTIM and continuous Newton method:

$$x^2 - 1 = 0. \quad (57)$$

Of course, it has two roots  $x = -1$  and  $x = 1$ .

From Eq. (20) we have

$$\dot{x} = -\frac{x^2 - 1}{2x}. \quad (58)$$

Similarly, from Eq. (12) we have

$$\dot{x} = -\frac{v(x^2 - 1)}{1 + t}. \quad (59)$$

While the integral of the first equation (58) leads to

$$x^2 = 1 + (x_0^2 - 1)e^{-t}, \quad (60)$$

the integral of the second equation (59) leads to

$$\frac{x-1}{x+1} = \frac{x_0-1}{x_0+1}(1+t)^{-2v}, \quad (61)$$

where  $x_0$  is an initial condition.

It is obvious that Eq. (60) quickly approaches  $x^2 = 1$  when  $t$  increases. However, because  $x^2$  is not a monotonic function, it cannot take the inverse of Eq. (60) to find  $x$ . Therefore, by applying a numerical integration method on Eq. (58) we need to decide which one of

$$x = \pm \sqrt{1 + (x_0^2 - 1)e^{-t}} \quad (62)$$

is selected.

Conversely, from Eq. (61) we have

$$x \rightarrow 1, \quad t \rightarrow \infty, \quad \text{if } v > 0, \quad (63)$$

$$x \rightarrow -1, \quad t \rightarrow \infty, \quad \text{if } v < 0. \quad (64)$$

The above convergence speed is dependent on the value of  $v$ . If we choose  $v > 0$  the FTIM will lead to a unique solution  $x = 1$ , no matter what  $x_0$  is selected; on the other hand, if we choose  $v < 0$  the FTIM will lead to a unique solution  $x = -1$ , no matter what  $x_0$  is selected. The convergence speed of FTIM is  $2v$  power of  $t$ , which is slower than the exponential convergence of Eq. (62), but its advantage is that we have a unique solution:  $x = 1$  if  $v > 0$ , and  $x = -1$  if  $v < 0$ . But the continuous NM cannot find these two solutions.

### 3.1 Example 1

We first consider a simple algebraic equation:

$$F(x) = x^3 - 3x^2 + 2x = 0. \quad (65)$$

The roots are 0, 1 and 2.

First we investigate the behavior in first 20 steps by tracing the paths in the plane of  $(x_k, x_{k+1})$ . As shown in Fig. 1(a), starting from  $x = -0.5$  the NM tends to the first root of  $x = 0$  very fast, while the FTIM with  $v = 1.5$  tends to the third root  $x = 2$

with an approximation value of 1.9996. It is interesting that when  $\nu = 1.6$  the FTIM tends to the second root of  $x = 1$  exactly, and when  $\nu = 1.7$  the FTIM tends to the first root of  $x = 0$  with a numerical value of  $-4.1 \times 10^{-7}$ .

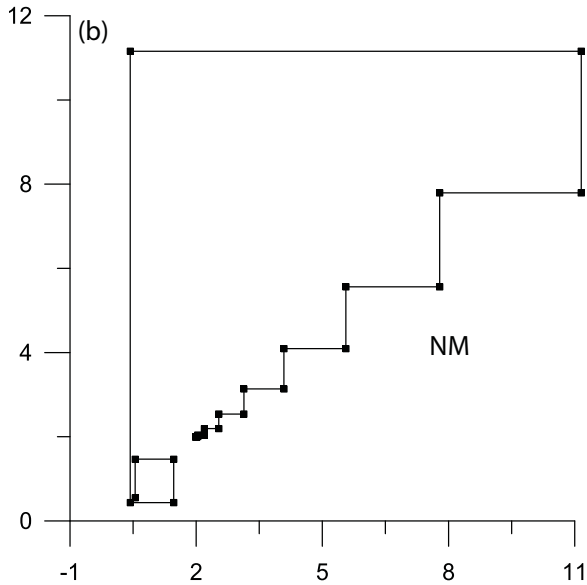
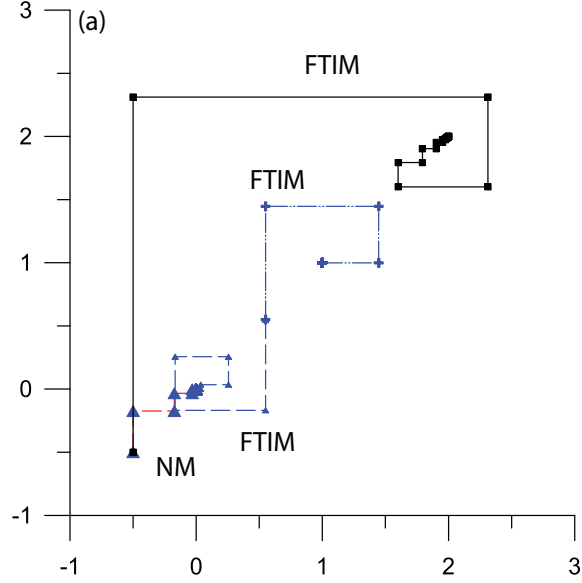


Figure 1: Comparing the iteration paths of Example 1 by FTIM and NM.

Next we start from  $x = 0.55$ . When the FTIM with  $\nu = -2.5$  tends to  $x = 1$  with a high accuracy of 0.999999992 and with  $\nu = 2$  tends to  $x = 0$  with a value of  $3.1 \times 10^{-7}$  as shown in Fig. 1(a), the NM

goes through a large range in the plane as shown separately in Fig. 1(b), and then tends to the third root of  $x = 2$ .

The above demonstration indicates that the solution by FTIM with a suitable choice of  $\nu$  can be very accurate even only through a few iterations. Between two roots with a same starting point the FTIM under different sign of  $\nu$  tend to different roots almost exactly.

### 3.2 Example 2

Then we consider a system of two algebraic equations in two-variables [Hirsch and Smale (1979)]:

$$\begin{aligned} F_1(x, y) &= x^3 - 3xy^2 + a_1(2x^2 + xy) + b_1y^2 \\ &\quad + c_1x + a_2y \\ &= 0, \end{aligned} \quad (66)$$

$$\begin{aligned} F_2(x, y) &= 3x^2y - y^3 - a_1(4xy - y^2) + b_2x^2 + c_2 \\ &= 0. \end{aligned} \quad (67)$$

The parameters used in this test are listed in Table 1. For these problems the initial guesses are respectively  $(x, y) = (5, 5)$ ,  $(x, y) = (0.25, 0.1)$  and  $(x, y) = (-1, -1)$ .

For problem 1 there are other solutions given by  $(x, y) = (50.46504, -37.2634179)$ , and  $(x, y) = (36.045402, 36.80750808)$ . For the former solution the parameters we use are given by  $(\nu, h, \epsilon) = (0.1, 0.0001, 10^{-10})$ , and the initial point is  $(50, -30)$ . Through 1341 iterations the result is obtained. For the latter solution the parameters are given by  $(\nu, h, \epsilon) = (0.01, 0.01, 10^{-10})$ , and the initial point is  $(40, 20)$ . Through 1474 iterations, the result is obtained.

For a vision of the convergent paths we also plotted the orbits of  $(x, y)$  for the above three problems in Figs. 2(a), 2(b) and 2(c), respectively. In Fig. 2(a) the left-side corresponds to the first root, while the right-side is for the second root. It can be seen that the first fixed point is a node, while the second one is a focus; similarly, the third fixed point is a focus. There appears a zig-zag of the path for problem 2; however, it spends only 52 iterations to reach a highly accurate solution of the

	Problem 1	Problem 2	Problem 3
$(a_1, b_1, c_1, a_2, b_2, c_2)$	$(25, 1, 2, 3, 4, 5)$	$(25, -1, -2, -3, -4, -5)$	$(200, 1, 2, 3, 1, 2)$
$(\nu, h, \varepsilon)$	$(0.1, 0.01, 10^{-10})$	$(1, 0.06, 10^{-11})$	$(0.02, 0.0001, 10^{-10})$
No. of Iterations	792	44	1274
$(x, y)$	$(-50.3970755, -0.8042426)$	$(0.134212, 0.811128)$	$(-400.0952897, -0.2000316)$
$(F_1, F_2)$	$(8.45 \times 10^{-7}, 6.67 \times 10^{-9})$	$(-7.77 \times 10^{-11}, -6.07 \times 10^{-10})$	$(4.26 \times 10^{-5}, 1.06 \times 10^{-8})$

Table 1: The parameters and results for Example 2

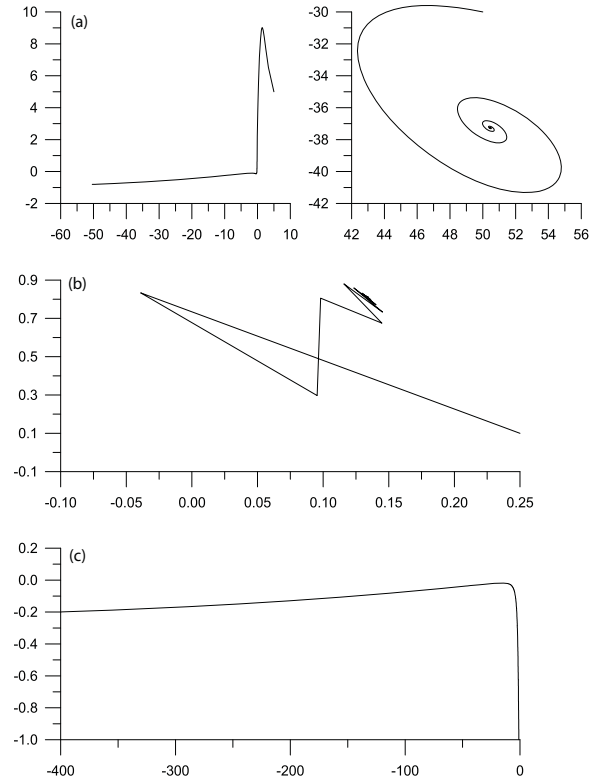


Figure 2: Two-dimensional solution orbits of Example 2 for three different problems.

roots with errors in the order of  $10^{-10}$ . The third problem is hard to solve because there appears a much large coefficient  $a_1 = 200$  than others. As reported by Hsu (1988), he could not calculate the third problem by using the homotopic algorithm with a Gordon-Shampine integrator, the Li-Yorke algorithm with Euler predictor and Newton corrector, and the Li-Yorke algorithm with Euler predictor and quasi-Newton corrector.

Hirsch and Smale (1979) used the continuous Newton algorithm to calculate the above three problems. For the first problem they obtained  $(x, y) = (36.0454, 36.8056)$ . However, inserting it into  $F_1$  and  $F_2$  we find that  $(F_1, F_2) = (13.315, 3.675)$ , which indicates that the result obtained by Hirsch and Smale (1979) is not an accurate root of Eqs. (66) and (67). For the second problem Hirsch and Smale (1979) obtained  $(x, y) = (39.0207, 38.2417)$ . Inserting it into  $F_1$  and  $F_2$  we find that  $(F_1, F_2) = (-0.339, -0.117)$ , which indicates that the result

obtained by Hirsch and Smale (1979) is not accurate. Finally, we check the third problem, of which Hirsch and Smale (1979) obtained  $(x, y) = (0.5115, 197.936)$ . Inserting it into  $F_1$  and  $F_2$  we find that  $(F_1, F_2) = (7.477, 26.964)$ , which indicates again that the result obtained by Hirsch and Smale (1979) is not an accurate root of Eqs. (66) and (67).

For problem 1 we have found three roots as shown above. It is interesting to investigate the attracting set of each fixed point in the plane of initial conditions of  $(x(0), y(0))$ . Starting from any initial condition in the domain of  $-60 < x(0) < 60$ ,  $-40 < y(0) < 40$  we apply the FTIM under a convergent criterion of  $\varepsilon = 10^{-7}$ , and with  $v = 0.01$  and  $h = 0.001$  to find its terminal location, and determines which attracting set it belongs by a small disk with a center on each fixed point. The most points in the left-side of Fig. 3 as shown by the diamonds are attracted by the fixed point  $(-50.3971, -0.8042)$ . At the right-side there are two fixed points  $(50.465, -37.263)$  and  $(36.045, 36.808)$ . The solid circular points as shown in Fig. 3 are the attracting set of the former one, while the square points are the attracting set of the latter one. This result reveals that the dynamics of the FTIM is rather simple, and it is convenient for us to choose suitable initial conditions to find the different roots. As we know the dynamics of Newton method is very complex, which usually makes the selection of initial condition being sensitive and difficult.

### 3.3 Example 3

Then we study the following system of two algebraic equations [Spedicato and Hunag (1997)]:

$$F_1(x, y) = x - y^2 = 0, \quad (68)$$

$$F_2(x, y) = (y - 1)^2(y - 2)^2 + (x - y^2)^2 = 0. \quad (69)$$

The two real roots are  $(x, y) = (1, 1)$  and  $(x, y) = (4, 2)$ .

In this test of the FTIM we study the attracting sets of these two fixed points. All nodes of a regular grid of 50 by 50 points with side length 5 in the region of  $[0, 5] \times [0, 5]$  are classified according to which fixed point is tended. In Fig. 4 the

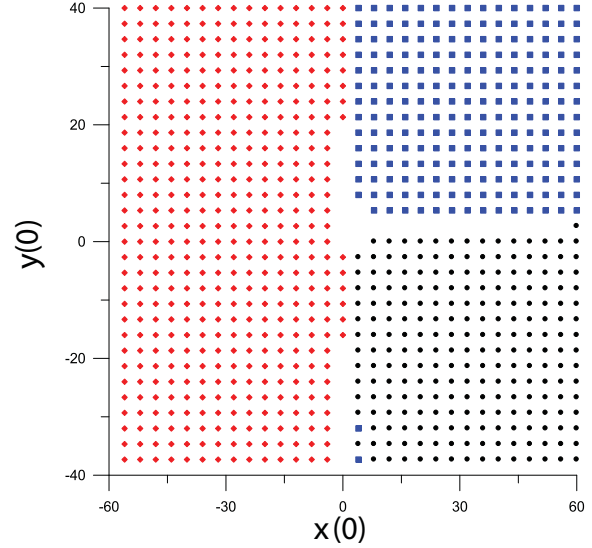


Figure 3: The attracting sets for three different fixed points of problem 1 in Example 2.

square points are those attracted by the fixed point  $(x, y) = (1, 1)$ , while the triangular points are those attracted by the fixed point  $(x, y) = (4, 2)$ . Under the convergent criterion  $\varepsilon = 10^{-4}$ , some points in the blank part of Fig. 4 are not convergent to any of the above fixed points.

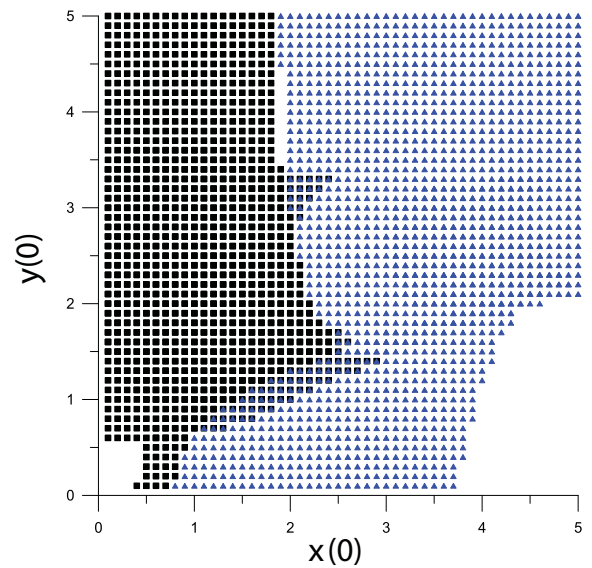


Figure 4: The attracting sets for two different fixed points of Example 3.

### 3.4 Example 4

We consider a system of three algebraic equations in three-variables:

$$F_1(x, y, z) = x + y + z - 3 = 0, \quad (70)$$

$$F_2(x, y, z) = xy + 2y^2 + 4z^2 - 7 = 0, \quad (71)$$

$$F_3(x, y, z) = x^8 + y^4 + z^9 - 3 = 0. \quad (72)$$

Obviously  $x = y = z = 1$  is the solution.

For this case we use a large  $v = 10$  to speed up the rate of convergence. In order to increase the accuracy we employ the RK4 method by using a small time stepsize  $h = 0.01$ , and a stringent convergent criterion with  $\varepsilon = 10^{-9}$  is used. Starting from an initial value of  $(x, y, z) = (0.5, 0.6, 0.6)$ , through 1264 iterations the orbit converges to the solution  $(x, y, z) = (1.000000037, 1.000000004, 0.999999955)$ , which is very near the true solution. The present method converges much faster than the above mentioned homotopic methods with the computational time smaller than 0.1 sec by using a PC586.

Because we do not use the steady-state concept in our formulation of the ODEs in Eq. (34), the final time spent by the present approach is not too long. For example, in this case the final time is  $t_f = 1264 \times 0.01 = 12.64$ .

### 3.5 Example 5

Now we consider a test example given by Roose, Kulla, Lomb and Meressoo (1990):

$$F_i = 3x_i(x_{i+1} - 2x_i + x_{i-1}) + \frac{1}{4}(x_{i+1} - x_{i-1})^2, \quad (73)$$

$$x_0 = 0, \quad x_{n+1} = 20. \quad (74)$$

Initial value is fixed to be  $x_i = 10$ ,  $i = 1, \dots, n$  as that used by Spedicato and Huang (1997).

For this case we use a large  $v = -100$  to speed up the rate of convergence, which needs 2381 iterations with a time stepsize  $h = 0.0002$  for the RK4 method. When the convergent criterion is given by  $10^{-15}$ , the residual error  $(\sum_{i=1}^n F_i^2)^{1/2}$  of numerical solution is about  $1.72 \times 10^{-13}$ . This is equivalent to spending a time of  $2381 \times 0.0002 = 0.4762$  that the dynamical system of Eq. (34)

reaches the fixed point, which is recorded in Table 2.

As compared with the methods reported by Spedicato and Huang (1997) for the Newton-like methods, the present approach is more accurate and time saving, where the computational time is smaller than 0.1 sec by using a PC586. For  $n = 50$  the numerical solutions are plotted in Fig. 5(a), where the error of each  $F_k$  is shown in Fig. 5(b). The residual error is about  $5.83 \times 10^{-12}$ .

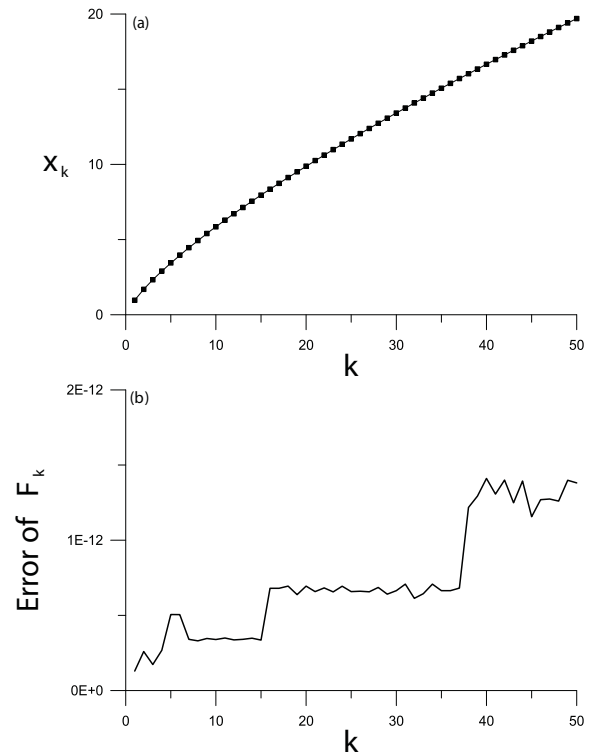


Figure 5: For Example 5 with  $n = 50$  the numerical solutions are plotted.

### 3.6 Example 6

In this example we apply the FTIM to solve the following boundary value problem [Liu (2006)]:

$$u'' = \frac{3}{2}u^2, \quad (75)$$

$$u(0) = 4, \quad u(1) = 1. \quad (76)$$

The exact solution is

$$u(x) = \frac{4}{(1+x)^2}. \quad (77)$$

Table 2: The numerical solutions of Example 5 with  $n = 10$ 

$x_1$	$x_2$	$x_3$	$x_4$	$x_5$	$x_6$	$x_7$	$x_8$	$x_9$	$x_{10}$
3.083	5.383	7.395	9.240	10.969	12.612	14.186	15.705	17.176	18.606

By introducing a finite difference discretization of  $u$  at the grid points we can obtain

$$F_i = \frac{1}{(\Delta x)^2}(u_{i+1} - 2u_i + u_{i-1}) - \frac{3}{2}u_i^2, \quad (78)$$

$$u_0 = 4, \quad u_{n+1} = 1, \quad (79)$$

where  $\Delta x = 1/(n+1)$  is the grid length.

Under the following parameters  $n = 49$ ,  $h = 0.001$ ,  $v = -0.3$  and  $\varepsilon = 10^{-10}$  we compute the roots of the above system, and compare them with the exact solutions in Fig. 6(a), which can be seen that the error as shown in Fig. 6(b) is very small in the order of  $10^{-4}$ .

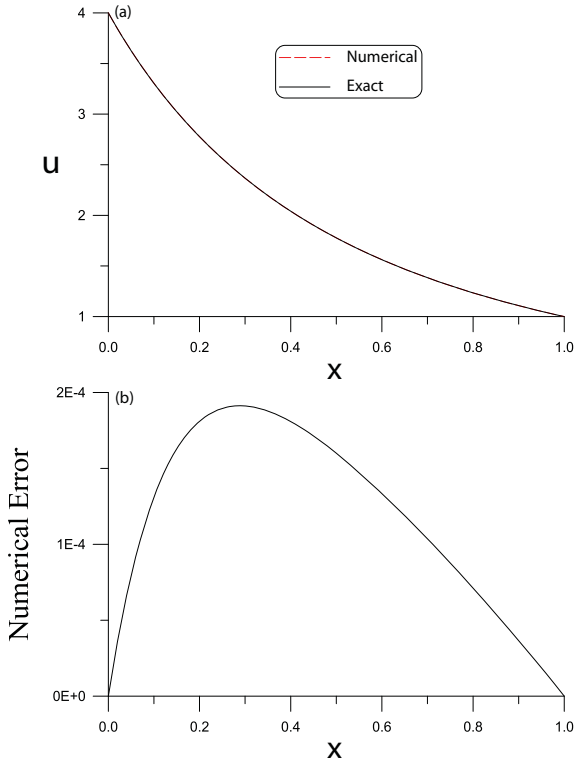


Figure 6: Applying the FTIM to a boundary value problem: (a) comparing numerical and exact solutions, and (b) displaying the numerical error.

### 3.7 Example 7

In this example we apply the FTIM to solve the following boundary value problem of nonlinear elliptic equation [Atluri and Zhu (1998a, 1998b); Zhu, Zhang and Atluri (1998, 1999)]:

$$\Delta u(x, y) + \omega^2 u(x, y) + \varepsilon u^3(x, y) = p(x, y). \quad (80)$$

The exact solution is

$$u(x, y) = \frac{-5}{6}(x^3 + y^3) + 3(x^2 y + x y^2). \quad (81)$$

The exact  $p$  can be obtained by inserting the above  $u$  into Eq. (80).

By introducing a finite difference discretization of  $u$  at the grid points we can obtain

$$\begin{aligned} F_{i,j} = & \frac{1}{(\Delta x)^2}(u_{i+1,j} - 2u_{i,j} + u_{i-1,j}) \\ & + \frac{1}{(\Delta y)^2}(u_{i,j+1} - 2u_{i,j} + u_{i,j-1}) \\ & + \omega^2 u_{i,j} + \varepsilon u_{i,j}^3 - p_{i,j}, \end{aligned} \quad (82)$$

where  $\Delta x = 1/(n+1)$  and  $\Delta y = 1/(n+1)$  are grid lengths. The boundary constraints can be obtained from the exact solution in Eq. (81).

Under the following parameters  $n = 29 \times 29$ ,  $h = 0.0005$ ,  $v = -2$ ,  $\varepsilon = 10^{-5}$ ,  $\omega = 1$  and  $\varepsilon = 0.001$  we compute the roots of the above system, and compare them with the exact solutions. Starting from an initial value of  $u_{i,j} = -0.1$ , the FTIM converges within 5488 steps. At the point  $y_0 = 0.75$  the error of  $u$  was plotted with respect to  $x$  in Fig. 7 by the dashed line, of which the maximum error is about  $5.4 \times 10^{-6}$ . At the point  $x_0 = 0.5$  the error of  $u$  was plotted with respect to  $y$  in Fig. 7 by the solid line, of which the maximum error is about  $4.4 \times 10^{-6}$ . For this highly nonlinear problem the FTIM is effective and gives very small error of the numerical solution.

## 4 Conclusions

Since the work of Newton, iterative algorithms were developed by many researchers, extending

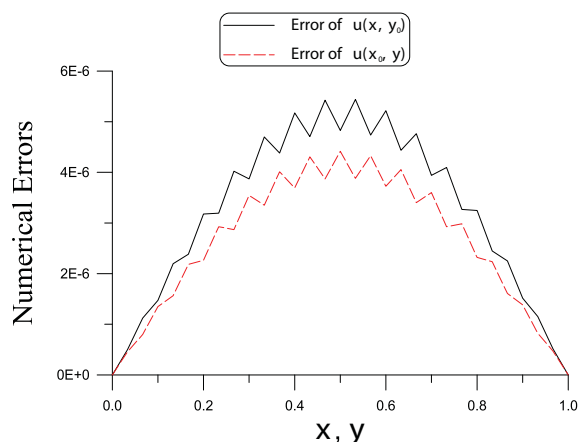


Figure 7: Applying the FTIM to a nonlinear elliptic boundary value problem, the errors are very small.

to continuous type by introducing an extra ad hoc artificial time. However, those ODEs are not intimately related to the original algebraic equations. The present paper very simply transforms the original nonlinear algebraic equations into an evolutionary system of equations by introducing a fictitious time, and had adding a coefficient to enhance the stability of numerical integration of the resulting ODEs and to speed up the convergence to the true roots. The main idea presented here is that the resulting system of ODEs is mathematically equivalent to the original equations, and no approximation is made. Hence, the present FTIM can work very effectively and accurately for the solution of nonlinear algebraic equations. Because no inverse of a matrix is required, the present method is very time efficient. Seven numerical examples were worked out, including the analysis of attracting sets and convergent paths. Some are compared with exact solutions revealing that high accuracy can be achieved by the FTIM. The new method is also applicable to the solutions of boundary value problems of elliptic type equation by discretizing them into high-dimensional nonlinear algebraic equations, revealing a high performance than other solvers.

## References

- Allgower, E. L.; Georg, K.** (1990): Numerical Continuation Methods: an Introduction. Springer, New York.
- Atluri, S. N.** (2002): Methods of Computer Modeling in Engineering and Sciences. Tech. Science Press, 1400 pages.
- Atluri, S. N.; Liu, H. T.; Han, Z. D.** (2006): Meshless local Petrov-Galerkin (MLPG) mixed collocation method for elasticity problems. *CMES: Computer Modeling in Engineering & Sciences*, vol. 14, pp. 141-152.
- Atluri, S. N.; Shen, S.** (2002): The meshless local Petrov-Galerkin (MLPG) method: a simple & less-costly alternative to the finite and boundary element methods. *CMES: Computer Modeling in Engineering & Sciences*, vol. 3, pp. 11-51.
- Atluri, S. N.; Zhu, T. L.** (1998a): A new meshless local Petrov-Galerkin (MLPG) approach in computational mechanics. *Comp. Mech.*, vol. 22, pp. 117-127.
- Atluri, S. N.; Zhu, T. L.** (1998b): A new meshless local Petrov-Galerkin (MLPG) approach to nonlinear problems in computer modeling and simulation. *Comp. Model. Simul. Eng.*, vol. 3, pp. 187-196.
- Broyden, C. G.** (1965): A class of methods for solving nonlinear simultaneous equations. *Math. Comp.*, vol. 19, pp. 577-593.
- Chow, S. N.; Mallet-Paret, J.; Yorke, J. A.** (1978): Finding zeroes of maps: homotopy methods that are constructive with probability one. *Math. Comp.*, vol. 32, pp. 887-889.
- Davidenko, D.** (1953): On a new method of numerically integrating a system of nonlinear equations. *Doklady Akad. Nauk SSSR*, vol. 88, pp. 601-604.
- Dennis, J. E.** (1971): On the convergence of Broyden's method for nonlinear systems of equations. A class of methods for solving nonlinear simultaneous equations. *Math. Comp.*, vol. 25, pp. 559-567.
- Dennis, J. E.; More, J. J.** (1974): A characterization of superlinear convergence and its application to quasi-Newton method. *Math. Comp.*, vol. 28,

pp. 549-560.

**Dennis, J. E.; More, J. J.** (1977): Quasi-Newton methods, motivation and theory. *SIAM Rev.*, vol. 19, pp. 46-89.

**Deuffhard, P.** (2004): Newton Methods for Non-linear Problems: Affine Invariance and Adaptive Algorithms. Springer, New York.

**Hirsch, M.; Smale, S.** (1979): On algorithms for solving  $f(x) = 0$ . *Commun. Pure Appl. Math.*, vol. 32, pp. 281-312.

**Hsu, S. B.** (1988): The Numerical Methods for Nonlinear Simultaneous Equations. Central Book Publisher, Taipei, Taiwan.

**Kellogg, R. B. T.; Li, T. Y.; Yorke, J. A.** (1976): A constructive proof of the Brouwer fixed-point theorem and computational results. *SIAM J. Num. Anal.*, vol. 13, pp. 473-483.

**Li, T. Y.; Yorke, J. A.** (1980): A simple reliable numerical algorithm for following homotopy paths. In *Analysis and Computation of Fixed Points*, Robinson, S. M. ed., pp. 73-91, Academic Press, New York.

**Li, T. Y.** (1997): Numerical solution of multivariate polynomial systems by homotopy continuation methods. *Acta Numerica*, vol. 6, pp. 399-436.

**Liu, C.-S.** (2001): Cone of non-linear dynamical system and group preserving schemes. *Int. J. Non-Linear Mech.*, vol. 36, pp. 1047-1068.

**Liu, C.-S.** (2006): The Lie-group shooting method for nonlinear two-point boundary value problems exhibiting multiple solutions. *CMES: Computer Modeling in Engineering & Sciences*, vol. 13, pp. 149-163.

**Liu, C.-S.** (2007a): A modified Trefftz method for two-dimensional Laplace equation considering the domain's characteristic length. *CMES: Computer Modeling in Engineering & Sciences*, vol. 21, pp. 53-66.

**Liu, C.-S.** (2007b): A highly accurate solver for the mixed-boundary potential problem and singular problem in arbitrary plane domain. *CMES: Computer Modeling in Engineering & Sciences*, vol. 20, pp. 111-122.

**Liu, C.-S.** (2007c): An effectively modified direct Trefftz method for 2D potential problems considering the domain's characteristic length. *Eng. Anal. Bound. Elem.*, vol. 31, pp. 983-993.

**Liu, C.-S.** (2008a): A highly accurate collocation Trefftz method for solving the Laplace equation in the doubly-connected domains. *Numer. Meth. Partial Diff. Eq.*, vol. 24, pp. 179-192.

**Liu, C.-S.** (2008b): Solving an inverse Sturm-Liouville problem by a Lie-group method. *Boundary Value Problems*, vol. 2008, Article ID 749865.

**Liu, C.-S.** (2008c): Identifying time-dependent damping and stiffness functions by a simple and yet accurate method. *J. Sound Vib.*, vol. 318, pp. 148-165.

**Liu, C.-S.** (2008d): A Lie-group shooting method for simultaneously estimating the time-dependent damping and stiffness coefficients. *CMES: Computer Modeling in Engineering & Sciences*, vol. 27, pp. 137-149.

**Liu, C.-S.; Chang, J. R.; Chang, K. H.; Chen, Y. W.** (2008): Simultaneously estimating the time-dependent damping and stiffness coefficients with the aid of vibrational data. *CMC: Computers, Materials & Continua*, vol. 7, pp. 97-107.

**Roose, A.; Kulla, V.; Lomb, M.; Meressoo, T.** (1990): Test examples of systems of non-linear equations. Estonian Software and Computer Service Company, Tallin 1990.

**Spedicato, E.; Hunag, Z.** (1997): Numerical experience with Newton-like methods for nonlinear algebraic systems. *Computing*, vol. 58, pp. 69-89.

**Zhu, T.; Zhang, J.; Atluri, S. N.** (1998): A meshless local boundary integral equation (LBIE) method for solving nonlinear problems. *Comp. Mech.*, vol. 22, pp. 174-186.

**Zhu, T.; Zhang, J.; Atluri, S. N.** (1999): A meshless numerical method based on the local boundary integral equation (LBIE) to solve linear and non-linear boundary value problems. *Eng. Anal. Bound. Elem.*, vol. 23, pp. 375-389.



# Computational Modeling of Impact Response with the RG Damage Model and the Meshless Local Petrov-Galerkin (MLPG) Approaches

H. T. Liu<sup>1</sup>, Z. D. Han<sup>1</sup>, A. M. Rajendran<sup>2</sup>, S. N. Atluri<sup>3</sup>

**Abstract:** The Rajendran-Grove (RG) ceramic damage model is a three-dimensional internal variable based constitutive model for ceramic materials, with the considerations of micro-crack extension and void collapse. In the present paper, the RG ceramic model is implemented into the newly developed computational framework based on the Meshless Local Petrov-Galerkin (MLPG) method, for solving high-speed impact and penetration problems. The ability of the RG model to describe the internal damage evolution and the effective material response is investigated. Several numerical examples are presented, including the rod-on-rod impact, plate-on-plate impact, and ballistic penetration. The computational results are compared with available experiments, as well as those obtained by the popular finite element code (Dyna3D).

**keyword:** Rajendran-Grove ceramic model, Material modeling, Ceramic damage, Meshless method, MLPG, High-speed impact, Penetration and perforation

## 1 Introduction

Ceramic materials are an important category of materials that have been widely used in armor elements, engine turbine blades and other structural components, because of their enhanced dynamic compressive strength and high temperature properties. Accurately modeling the constitutive behavior of ceramics, including their damage and failure, is essential in the device-design, and their deployment for dynamic structural and armor applications. Recently, Rajendran and Grove (Rajendran, 1994; Rajendran and Grove, 1996) proposed a three-dimensional, internal state variable based constitutive model (RG ceramic damage model) for ceramic materials, which incorporated both micro-crack propagation and void collapse. The proposed RG ceramic damage model has been im-

plemented into EPIC code for investigating the model's ability to describe the response of pure alumina (AD995) subjected to various stress/strain loading conditions (Rajendran and Grove, 2002).

In the present paper, the RG ceramic damage model is implemented into the newly developed computational code based on the Meshless Local Petrov-Galerkin (MLPG) method. The MLPG method is a truly meshless approach that establishes both the trial and test functions in local subdomains. Because of the total elimination of the mesh, it is a promising method in solving high-speed contact, impact and penetration problems with severe material-distortion. The detailed description of the MLPG and its applications can be found in the authors' other papers. For comparison and verification purpose, the RG model has also been implemented into the three-dimensional computational hydrodynamic code Dyna3D. Several numerical examples are solved, using either the Dyna3D or the MLPG method, with RG ceramic damage model implemented in them. Several numerical simulations are conducted: rod-on-rod impact, plate-on-plate impact, and the ballistic impact and penetration. The simulation results obtained from Dyna3D, MLPG and available experiments are compared. For completeness purpose, a brief introduction of the RG ceramic damage model is included.

## 2 Rajendran-Grove Ceramic Damage Model

In the Rajendran-Grove ceramic model, the following assumptions are made: 1) randomly distributed and oriented micro-cracks are pre-existing in the materials, 2) plastic flow occurs when the materials are shocked above the HEL (Hugoniot Elastic Limit), 3) pore collapse is due to the plastic flow in the matrix surrounding the pores, 4) no plastic flow happens when the material is under tensile loading, 5) micro-cracks propagate under both compression and tension, and 6) pulverization occurs under compressive loading, when the accumulated micro-crack density reaches a critical value. The micro-crack dam-

<sup>1</sup> Knowledge Systems Research, LLC, Forsyth, GA 30253

<sup>2</sup> US Army Research Office (ARO), RTP, NC

<sup>3</sup> Center for Aerospace Research & Education, University of California, Irvine

age is described using a dimensionless damage density parameter in terms of the maximum micro-crack size and the average number of micro-cracks per unit volume. The damage evolution in terms of crack growth is formulated based on a generalized Griffith criterion (Griffith, 1920). The stiffness reduction due to micro-cracking is modeled using the analytical formulation from Margolin (1983) and Budiansky and O'Connell (1976). The pore collapse effects are modeled using viscoplastic equations derived from Gurson's pressure dependent yield function (Gurson, 1977). In the following sections, the Rajendran-Grove ceramic model is briefly reviewed.

## 2.1 Constitutive Relationships

The total strain  $\epsilon_{ij}$  is decomposed into the elastic part  $\epsilon_{ij}^e$  and plastic part  $\epsilon_{ij}^p$  as

$$\epsilon_{ij} = \epsilon_{ij}^e + \epsilon_{ij}^p \quad (1)$$

Here, the elastic strain includes the elastic strain of the intact matrix material and the strain due to micro-crack opening/sliding. The plastic strain is associated with pore collapse and occurs only when the applied pressure exceeds the pressure at the Hugoniot Elastic Limit (HEL). The total stress  $\sigma_{ij}$  is decomposed into deviatoric stress  $S_{ij}$  and pressure  $P$  as

$$\sigma_{ij} = S_{ij} - P\delta_{ij} \quad (2)$$

The pressure is calculated through the Mie-Gruneisen equation of state which given by

$$P = [\bar{P}_H (1 - 0.5\Gamma\bar{\eta}) + \Gamma\rho_0 (I - I_0)] \quad (3)$$

where

$$\bar{P}_H = K_\gamma (\beta_1 \bar{\eta} + \beta_2 \bar{\eta}^2 + \beta_3 \bar{\eta}^3) \quad (4)$$

In the above equations,  $\beta_1$ ,  $\beta_2$  and  $\beta_3$  are empirical parameters;  $\Gamma$  is the Mie-Gruneisen parameter;  $K_\gamma = \bar{K}/K$  is the bulk modulus reduction ratio with  $K$  the bulk modulus for the intact matrix and  $\bar{K}$  the effective bulk modulus for the micro-crack containing material (Margolin, 1983; Budiansky and O'Connell 1976). Furthermore,  $\rho_0$  is the initial material density;  $I_0$  and  $I$  are the internal energy at the initial and current states, respectively. The

engineering volumetric strain, with the consideration of the voids, is defined as

$$\bar{\eta} = \frac{(1 - f_0)V_0}{(1 - f)V} - 1 \quad (5)$$

Where  $V_0$  and  $V$  are the volumes of the initial and current states;  $f_0$  and  $f$  are the initial and current porosity densities, respectively.

The deviatoric stress is related to the deviatoric elastic strain  $e_{ij}^e$ , as

$$S_{ij} = 2R_g \bar{G} e_{ij}^e \quad (6)$$

Here  $\bar{G}$  is the effective shear modulus for micro-crack containing material (Margolin, 1983; Budiansky and O'Connell, 1976) and  $R_g$  is the correction factor for shear modulus due to the existence of porosity, which is expressed as

$$R_g = (1 - f) \left[ 1 - \frac{(6K + 12G)f}{(9K + 8G)} \right] \quad (7)$$

with  $G$  the shear modulus for the intact matrix. The porosity density is assumed to decrease, due to void collapsing at pressures above the HEL, as

$$\dot{f} = (1 - f) \dot{\epsilon}_v^p \quad (8)$$

where  $\epsilon_v^p$  the plastic volumetric strain, and the dot above a symbol implies the temporal derivative.

When the materials are shocked above the HEL (Hugoniot Elastic Limit), plastic flow occurs. In the current model, Gurson's pressure dependent yield function (Gurson, 1977) when considerations of the porosity are included, namely

$$F = \frac{3J_2}{Y^2} + 2f \cosh\left(\frac{3P}{2Y}\right) - f^2 - 1 = 0 \quad (9)$$

with  $J_2 = 0.5S_{ij}S_{ij}$ . A simplified Johnson-Cook strain rate dependent strength model (Johnson and Cook, 1985) is used and can be expressed as

$$Y = C_1 \left( 1 + C_3 \ln \frac{\dot{\epsilon}_p}{\dot{\epsilon}_0} \right) \quad (10)$$

where  $C_1$  and  $C_3$  are model constants.  $\dot{\epsilon}_p$  is the equivalent plastic strain rate and  $\dot{\epsilon}_0$  is the reference strain rate, which is assumed to be 1 in the current model.

Figure 1 qualitatively shows the effect of the void collapse on the material response under a hydrostatic loading/unloading condition predicted by the RG model. With the increase of the compressive hydrostatic loading, the voids start to collapse at point **A**. At point **B**, the volume of the voids reduces to zero and the corresponding porosity  $f$  becomes 0. During the unloading process, at point **C**, the pressure reduces to zero, but the volumetric strain does not go to zero due to the collapsed void volume.

## 2.2 Damage Definition and Evolution

The micro-crack damage is measured in terms of a dimensionless micro-crack damage density  $\gamma$ , which is expressed as

$$\gamma = N_0^* a^3 \quad (11)$$

where  $N_0^*$  is the average number of micro-flaws per unit volume, and  $a$  is the maximum micro-crack size at the current state. The initial values of  $N_0^*$  and  $a_0$  are material constants. For simplicity, it is assumed that no cracks nucleate during the loading, and therefore the damage evolution is represented by the growth of micro-crack size  $a$ , which follows a generalized Griffith criterion (Griffith, 1920) as

$$\dot{a} = \begin{cases} 0 & , G_s \leq G_C \\ n_1 C_R \left[ 1 - \left( \frac{G_C}{G_s} \right)^{n_2} \right] & G_s > G_C \end{cases} \quad (12)$$

where  $C_R$  is the Rayleigh wave speed,  $G_C$  is the critical strain energy release rate for micro-crack growth calculated from the fracture toughness  $K_{IC}$ , Young's modulus  $E$  and Poisson's ratio  $\nu$  as  $G_C = K_{IC}^2 (1 - \nu^2) / E$ .  $G_s$  is the applied strain energy release rate.  $n_1$  and  $n_2$  are the parameters controlling the crack growth rate. Four parameters are used for the micro-crack extension model:  $n_1^-$  and  $n_2^-$  for crack sliding, and  $n_1^+$  and  $n_2^+$  for crack opening. The applied strain energy release rates are calculated in the principal directions, with  $\sigma_1, \sigma_2, \sigma_3$  being the three principal stress components. For crack opening

$$G_s^+ = \frac{4(1 - \nu^2)}{\pi E} \max(0, \sigma_1, \sigma_2, \sigma_3)^2 \quad (13)$$

and for crack sliding

$$G_s^- = \max(G_1^-, G_2^-, G_3^-) \quad (14)$$

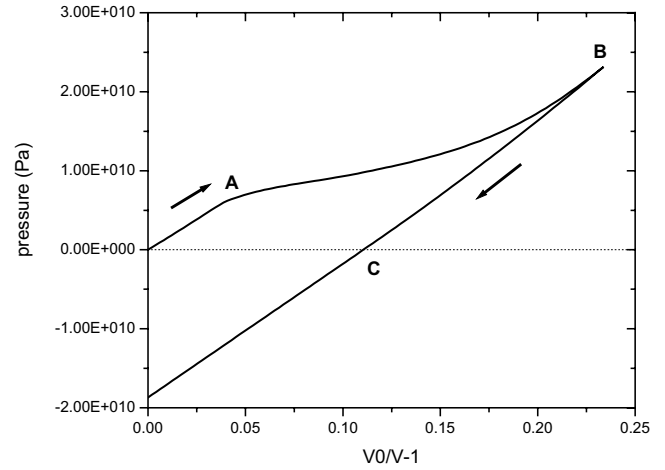


**Figure 1** : The hydrostatic loading/unloading of RG model with void collapse

with

$$G_i^- = \frac{8(1 - \nu^2)a}{\pi E(2 - \nu)} \left\{ \frac{|\sigma_j - \sigma_k|}{2} + \min \left[ 0, \mu \frac{\sigma_j + \sigma_k}{2} \right] \right\}^2 \quad (15)$$

In the above equation,  $i, j, k = 1, 2, 3$  and  $i \neq j \neq k$ .  $\mu$  is the dynamic friction coefficient.

As an example, we show the shear loading response with micro-crack evolution predicted by the RG model in Figure 2. With the increase of the applied shear loading, the strain energy release rate goes beyond the critical energy release rate at the point **A**, activating the micro-cracks sliding. The micro-crack damage density  $\gamma$  increases proportional to the growth of the micro-crack size and the effective shear modulus in Eq. (6) decreases. Therefore, a softening stage corresponding to the micro-cracks extension is form in this figure between point **A** and **B**.

## 2.3 Pulverization

When the micro-crack damage density  $\gamma$  reaches a critical value (usually set as 0.75) under compressive loading, the material becomes pulverized. The bulk and shear moduli for the pulverized material are set to the corresponding effective bulk and shear moduli at the pulverization point as

$$\bar{K}_p = \bar{K}, \bar{G}_p = \bar{G} \quad (16)$$

The pulverized material does not support any tensile loading and the compressive strength of the pulverized

material is described by the Mohr-Columb law as

$$Y = \begin{cases} 0 & , P \leq 0 \\ \alpha + \beta P & , P > 0 \end{cases} \quad (17)$$

where  $\alpha$  and  $\beta$  are model constants. The pressure is simply computed from the elastic volumetric strain  $\epsilon_v^e$  as

$$P = \begin{cases} 0 & , \epsilon_v^e \geq 0 \\ -\bar{K}_p \epsilon_v^e & , \epsilon_v^e < 0 \end{cases} \quad (18)$$

## 2.4 Determination of Model Constants

In the Rajendran-Grove ceramic model, there are eight material constants to describe the micro-crack behavior:  $N_0^*$ ,  $a_0$ ,  $\mu$ ,  $n_1^+$ ,  $n_2^+$ ,  $n_1^-$ ,  $n_2^-$ , and  $K_{IC}$ . Usually, several experiments like plate-on-plate and bar-on-bar impact tests are needed to determine these constants for a specific material. Rajendran and Grove (1996) conducted a sensitivity study of the material constants and calibrated the constants for several commonly used ceramic materials, like SiC, B<sub>4</sub>C, TiB<sub>2</sub>, AD85, and AD995 (Rajendran and Grove, 1996 and 2002; Grove, 1993). In the following numerical simulations, the AD995 and AD85 ceramic are used and the material constants that we employed are listed in Table 1.

## 3 Meshless Local Petrov-Galerkin Method

Meshless Local Petrov-Galerkin Method (MLPG) [Atluri and Zhu (1998), and Atluri (2004)] is a truly meshless approach, in which both the trial and test functions are established in local subdomains. As an extension to the primitive MLPG method, Atluri Han, and Rajendran proposed an MLPG mixed method to simplify the formulation and improve the efficiency and stability of the MLPG approach [Atluri, Han and Rajendran (2004), Han, Rajendran and Atluri (2005)]. In this MLPG mixed method, both displacement/velocity gradients and displacements/velocities are interpolated independently. Their compatibility is enforced only at the nodal points. Therefore, the continuity requirement of the trial function is reduced by one order, and the second derivatives of the shape functions are eliminated. This MLPG mixed method has been implemented to solve static problems with large deformation [Atluri, Han and Rajendran (2004)] and dynamic problems [Han, Rajendran and Atluri (2005)]. Recently, the authors have successfully applied the MLPG mixed method to

solve three-dimensional high-speed contact and impact problems with large deformation [Han, Liu, Rajendran, and Atluri (2006)].

In this section, a brief introduction of the MLPG mixed method is presented. Interested readers are encouraged to refer to the above mentioned MLPG papers for detailed formulations.

### 3.1 Local Nodal Interpolation

In the current implementation, the Moving Least Squares (MLS) is adopted as the local nodal interpolation scheme because of the reasonable accuracy, completeness, robustness and continuity of the MLS functions. With the MLS, a trial function  $u(\mathbf{x})$  can be expressed as

$$u(\mathbf{x}) = \sum_{I=1}^N \Phi^I(\mathbf{x}) \hat{u}^I \quad (19)$$

where  $\hat{u}^I$  and  $\Phi^I(\mathbf{x})$  are the fictitious nodal value and shape function of node  $I$ , respectively. The shape functions are obtained by minimizing the  $L_2$  norm of the weighted distance between the trial function value and its true values at nodal points. The explicit expressions for the shape functions can be found in Atluri (2004).

In the mixed method, we interpolate the velocities  $v_i$ , and the velocity gradients  $v_{i,j}$ , independently, using the same shape functions, namely

$$v_i(\mathbf{x}) = \sum_{J=1}^N \Phi^J(\mathbf{x}) v_i^J \quad (20)$$

$$v_{i,j}(\mathbf{x}) = \sum_{K=1}^N \Phi^K(\mathbf{x}) v_{i,j}^K \quad (21)$$

The compatibility condition between the velocities and velocity gradients is enforced only at the nodes by a standard collocation method, as

$$v_{i,j}(\mathbf{x}^I) = \frac{\partial v_i(\mathbf{x}^I)}{\partial x_j} \quad (22)$$

By interpolating the velocity gradients, as one of the key features of the mixed method, we eliminate the differentiation operations of the shape functions in the local weak form integration. Therefore, the requirement of the completeness and continuity of the shape functions

**Table 1** : The material constants for Rajendran-Grove model

	AD995	AD85
Density ( $g/cm^3$ )	3.89	3.42
Shear Modulus (GPa)	156	88.0
Initial Porosity	0	10%
Material Strength Constants		
$C_1$ (GPa)	2.3	4.0
$C_3$	0.2	0.029
Equation of State Constants		
$\beta_1$ (GPa)	231	150.0
$\beta_2$ (GPa)	-169	150.0
$\beta_3$ (GPa)	2774	150.0
$\Gamma$	0.1	0
Damage Model Parameters		
$N_0^*$ ( $m^{-3}$ )	$2 \times 10^{11}$	$1.83 \times 10^{10}$
$a_0$ ( $\mu m$ )	20	0.58
$\mu$	0.45	0.72
$n_1^+$	1.0	1.0
$n_2^+$	1.0	0.07
$n_1^-$	0.1	0.1
$n_2^-$	1.0	0.07
$K_{IC}$ ( $MPa\sqrt{m}$ )	3.0	3.25
Pulverized Material Constants		
$\alpha$ (GPa)	0	0.1
$\beta$	1.0	0.1

is reduced by one-order, and thus, lower-order polynomial terms can be used in the meshless approximations. This leads to a smaller nodal influence size and speeds up the calculation of the shape functions. The adoption of the mixed method in our implementation greatly improves the program efficiency.

### 3.2 Formulations for Finite Strain Problems

We adopted an updated Lagrangian formulation in our implementation for solving the high-speed dynamic problems. Let  $x_i$  be the spatial coordinates of a material particle in the current configuration. Let  $\dot{S}_{ij}$  be the Truesdell stress-rate (the rate of second Piola-Kirchhoff stress as referred to the current configuration); and let  $\dot{\sigma}_{ij}^J$  be the Jaumann rate of Kirchhoff stress (which is  $J$  times the Cauchy stress, where  $J$  is the ratio of volumes). It is

known [Atluri (1980)]:

$$\dot{S}_{ij} = \dot{\sigma}_{ij}^J - D_{ik}\sigma_{kj} - \sigma_{ik}D_{kj} \quad (23)$$

Here,  $D_{ij}$  and  $W_{ij}$  are the symmetric and skew-symmetric parts of the velocity gradient, respectively. Considering a 3D domain  $\Omega$  with a boundary  $\partial\Omega$ , the rate forms of the linear and angular momentum balances are [Atluri (1980)]:

$$(\dot{S}_{ij} + \tau_{ik}v_{j,k})_{,i} + \dot{f}_j = \dot{b}_j \quad (24)$$

where,  $\dot{b}_j = \rho \dot{a}_j$  is the inertia force rate with  $\rho$  is the mass density and  $\dot{a}_j$  the acceleration rate. In a dynamic problem,  $\dot{f}_j$  are appropriately defined in terms of the rate of change of inertia forces and  $(\ )_{,i} = \partial(\ )/\partial x_i$ ;  $x_i$  are current coordinates of a material particle. In Eq. (24),  $\tau_{ij}$  is the Cauchy stress in the current configuration.

### 3.3 Local weak form with the large deformations

In the MLPG approaches, the weak form is established over a local subdomain  $\Omega_s$ , which may have an arbitrary shape, and contain a point  $\mathbf{x}$  in question. In our implementation, the local weak form is established for a spherical subdomain with the radius of  $r$  (we define it as the test-function size), namely

$$\int_{\Omega_s} [(\dot{S}_{ij} + \tau_{ik} v_{j,k})_{,i} + \dot{f}_j - \dot{b}_j] w_j d\Omega = 0 \quad (25)$$

where  $w_j$  are the test functions. By applying the divergence theorem, Eq. (25) may be rewritten in a symmetric weak form, as:

$$\begin{aligned} \int_{\partial\Omega_s} (\dot{S}_{ij} + \tau_{ik} v_{j,k}) n_i w_j d\Gamma \\ - \int_{\Omega_s} [(\dot{S}_{ij} + \tau_{ik} v_{j,k}) w_{j,i} - \dot{f}_j w_j + \dot{b}_j] d\Omega = 0 \end{aligned} \quad (26)$$

wherein, the rate definition  $\dot{t}_j = (\dot{S}_{ij} + \tau_{ik} v_{j,k}) n_i$ , with  $n_i$  being the components of a unit outward normal to the boundary of the local subdomain  $\Omega_s$ , in its current configuration, is used. Thus the local symmetric weak form can be rewritten as

$$\begin{aligned} \int_{L_s} \dot{t}_i w_i d\Gamma + \int_{\Gamma_{su}} \dot{t}_i w_i d\Gamma + \int_{\Gamma_{st}} \dot{t}_i w_i d\Gamma \\ - \int_{\Omega_s} [(\dot{S}_{ij} + \tau_{ik} v_{j,k}) w_{j,i} - \dot{f}_i w_i + \dot{b}_j] d\Omega = 0 \end{aligned} \quad (27)$$

where  $\Gamma_{su}$  is a part of the boundary  $\partial\Omega_s$  of  $\Omega_s$ , over which the essential boundary conditions are specified. In general,  $\partial\Omega_s = \Gamma_s \cup L_s$ , with  $\Gamma_s$  being a part of the local boundary located on the global boundary, and  $L_s$  is the other part of the local boundary which is inside the solution domain.  $\Gamma_{su} = \Gamma_s \cap \Gamma_u$  is the intersection between the local boundary  $\partial\Omega_s$  and the global displacement boundary  $\Gamma_u$ ;  $\Gamma_{st} = \Gamma_s \cap \Gamma_t$  is a part of the boundary over which the natural boundary conditions are specified.

To simplify the integration and speed up the numerical implementation, the Heaviside function is adopted as the test function in our program. Thus, the local symmetric weak form in Eq.(27) becomes

$$\begin{aligned} - \int_{L_s} \dot{t}_i d\Gamma - \int_{\Gamma_{su}} \dot{t}_i d\Gamma + \int_{\Omega_s} \dot{b}_j d\Omega \\ = \int_{\Gamma_{st}} \dot{t}_i d\Gamma + \int_{\Omega_s} \dot{f}_i d\Omega \end{aligned} \quad (28)$$

## 4 Numerical Simulations

For the implementation of the Rajendran-Grove ceramic damage model, a material subroutine is developed. To maintain the stability of the explicit algorithm, an iterative scheme based on a second-order diagonally implicit Runge-Kutta method is employed to solve the coupled differential equations of the constitutive model. This material subroutine is linked to the Dyna3D (2000 version) hydrodynamic code and the newly developed MLPG mixed program. Numerical examples are conducted either under the Dyna3D (finite element method) and the meshless method (MLPG).

### 4.1 Beam Under Stretch and Rotation

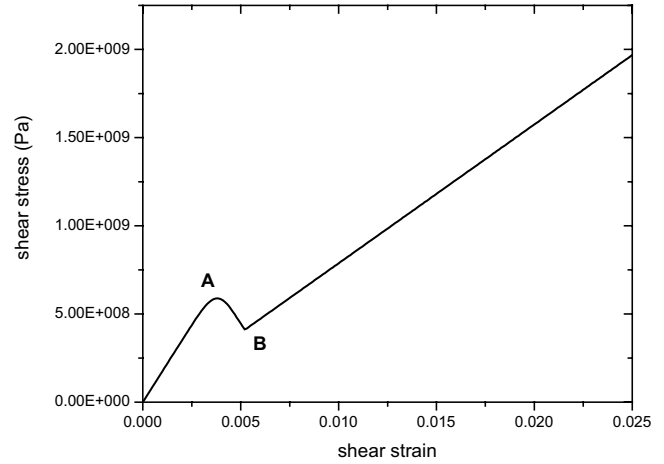


**Figure 2 :** The shear loading response of RG model with micro-crack evolution

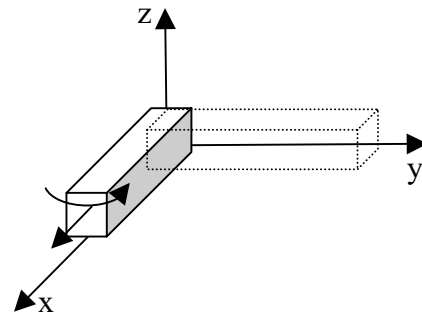


**Figure 3 :** A beam under stretch and rotation

In the first example, we consider a beam undertaking a uniaxial stretch in the x-direction, as shown in Figure 3.

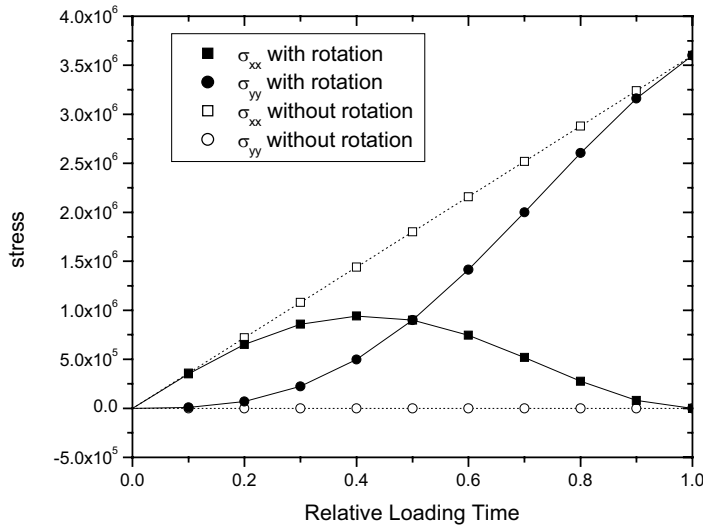


**Figure 4 :** The stress components of the beam under uniaxial stretch and rotation

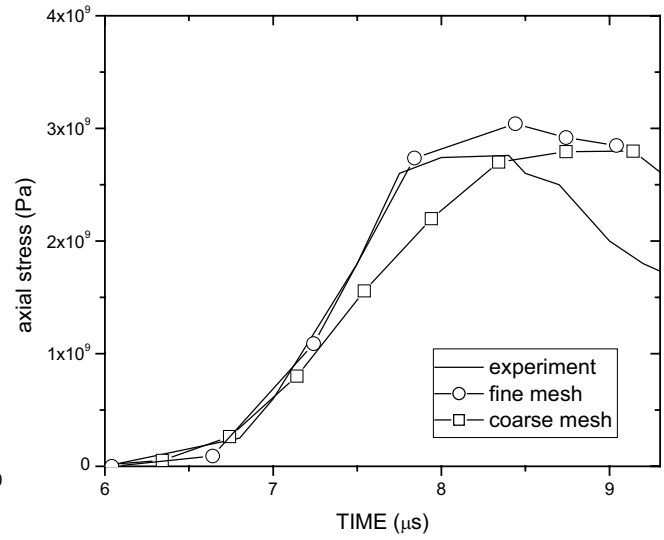


**Figure 7 :** Axial stress history in the rod-on-rod impact

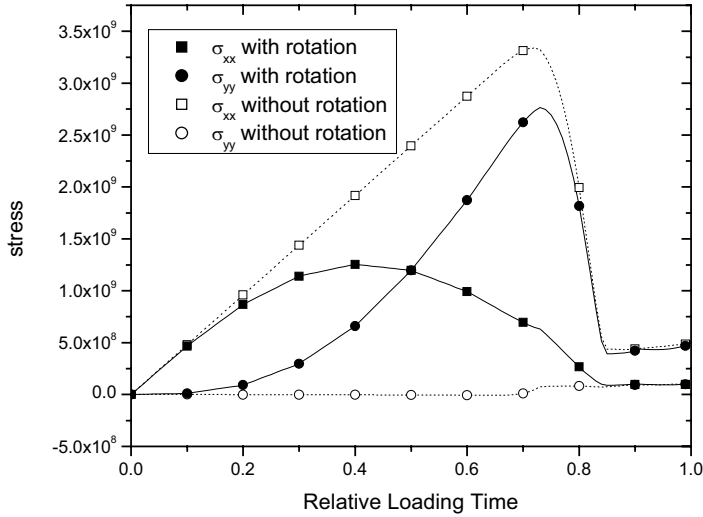


**Figure 5 :** The stress components of the beam under uniaxial stretch and rotation with micro-crack damage evolution

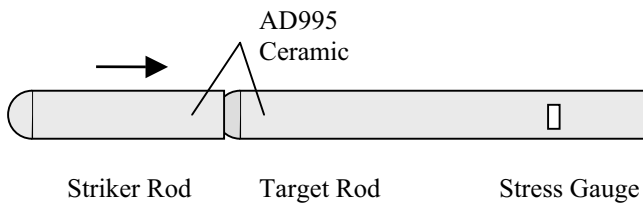


**Figure 6 :** Rod-on-rod impact test configuration schematic

To demonstrate the consistency of the RG model in dealing with large deformation problems, a rigid body rotation in z-direction is added to the beam. The rotation rate is set such that the beam will rotate a 90 degree in z-direction after the simulation. The stretching and rotation are applied slowly so that there is no inertia effect and a quasi-static state is maintained. The Poisson's ratio is set to be zero during the simulations.

Figure 4 shows elastic stress response obtained with RG model. The beam orientation rotates 90 degree with the uniaxial stretching, and therefore the stress tensors are rotated correspondingly. Figure 5 shows the same problem solved using RG model with micro-crack damage evolution. With the increase of the uniaxial stretching, the micro-crack opening is activated when the strain energy release rate goes beyond the critical energy release rate. The stress drops due to the micro-crack damage evolution.

#### 4.2 Rod-on-Rod Impact

Recently, Simha (1998) conducted rod-on-rod impact experiments at the impact velocity of 278 m/s, in which both the striker and the target rods were made of AD995 ceramic. The striker rod was 5 cm long and 1.25 cm in diameter, while the target rod was 10 cm long and 1.25 cm in diameter. A stress gauge was embedded in the target rod at the location of 2.5 cm from the free end to record the axial stress history. Figure 6 shows the test configuration.

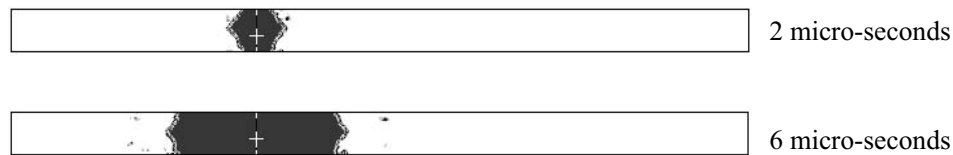


**Figure 8** : Crack density profile in the rod-on-rod impact

ration. In this experiment, fracture initiates at the impact end and propagates toward the gauge location. The measured peak stress from this experiment can be used in a qualitative sense to validate the model constants under uniaxial stress.

The same problem is simulated using Dyna3D with the RG ceramic damage model. Three-dimensional finite element mesh is constructed and a quarter of the striker and target rods are modeled by considering the configuration symmetry. 49499 nodes and 254021 Tet4 elements with the average nodal spacing of 0.5 mm are used in the finite element model. The initial crack size is reduced to  $a_0 = 2.3\mu\text{m}$  to avoid premature crack extension and catch the peak stress recorded in the experiment. Figure 7 compares the computed axial stress at the gauge location with the experimental data and a good agreement is obtained. A coarse mesh with average nodal spacing of 1 mm is used to re-simulate the same problem and the result is shown in Figure 7. The calculated stress from the coarse mesh increases slower than the one obtained with fine mesh, due to the loss of the high-frequency wave information of the stress wave. Figure 8 shows the micro-crack density profile, with the darkness scales of the micro-crack density. The micro-cracks begin to extend at the impact ends upon the collision of the striker and target rods. With the propagation of the stress wave, the micro-crack damage extends toward the free ends.

#### 4.3 Plate-on-Plate Impact

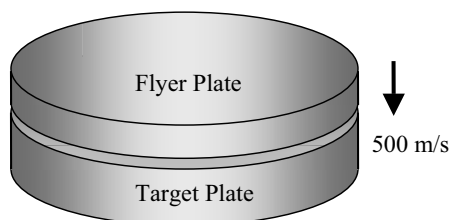


**Figure 9** : Plate-on-plate impact test configuration schematic

In the simulated plate impact problem, two thin ceramic plates collide at the velocity of 500 m/s (see Figure 9). The flyer and target plates have the same diameter of 50 mm and their thicknesses are 4 mm and 8 mm, respectively. Frictionless contact is assumed between the two plates. Both the flyer and the target plates are made of AD995 ceramic.

To simulate the described problem using the MLPG software, 32058 nodes are used with an averaged nodal spacing of 1 mm. The AD995 ceramic material is modeled using Rajendran-Grove (RG) ceramic model. The material constants for RG model are listed in Table 1. For comparison purpose, the plate impact problem is also solved, using the Dyna3D. The FEM modeling uses the same nodal arrangement, and thus, 163698 Tet4 elements are produced from these nodes.

Figure 10 reports the axial velocity profiles. In Figure 10(a), the axial velocities at the central points on the free surfaces of the flyer and target plates are drawn, respectively. The velocity of the flyer plate starts to decrease while the compressive wave initiated at the collision surface arrives at the free surface. The flyer velocity becomes positive representing the bouncing back of the flyer plate. Similarly, the free surface of the target plate begins to move when the first compressive wave arrives at around 0.6 micro-seconds. This time is twice the time taken for the wave to propagate to the flyer free surface, which reflects the fact that the target plate is twice as thick as the flyer plate. The speed changes due to the arrivals of the second wave peak can be clearly observed in the target free surface velocity profile. To investigate the momentum exchange between the flyer and target plates, the averaged axial velocities are drawn in Figure 10(b). The averaged velocity is obtained by the total momentum of the flyer or target plate, divided by the total mass of the corresponding plate. At around 1.5 micro-seconds, the momentum exchange completes, which represents the end of the collision process. The target plate attains an averaged axial velocity of 270 m/s, while the flyer plate bounces back at a velocity of 38 m/s. The ve-

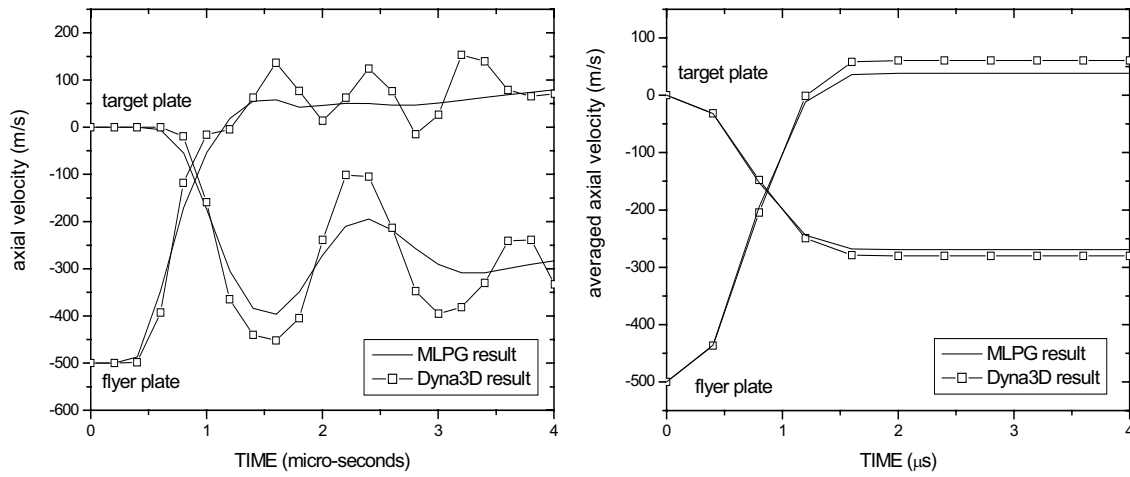


**Figure 10 :** (a) Axial velocities of the central points at the free surfaces of the flyer and target plates; and (b) the averaged axial velocities of the flyer and target plates

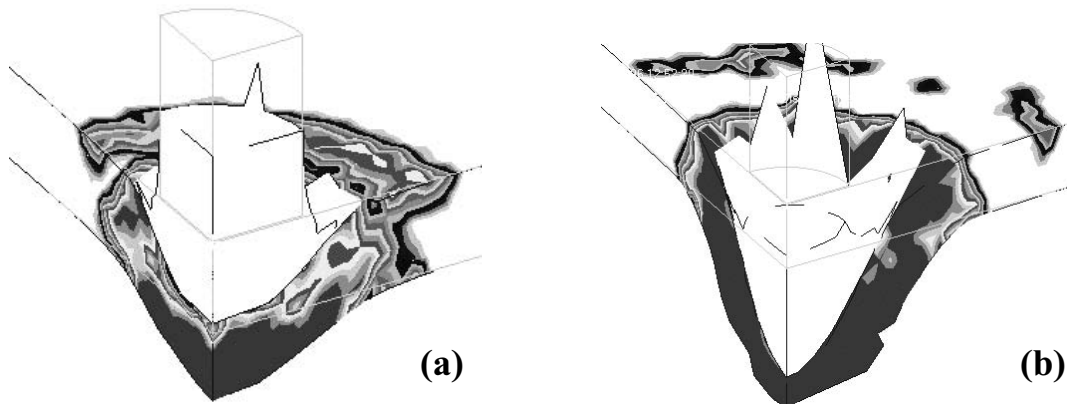


**Figure 11 :** Damage profiles of ballistic impact (a) 3.5 micro-seconds and (b) 10 micro-seconds

locity profiles calculated from Dyna3D are also shown in the same figures. From Figure 10(a), similar velocity histories are obtained from MLPG and Dyna3D and both of them show the same wave arrival time. The results from Dyna3D simulation are more oscillatory than the ones from MLPG. It shows that MLPG is able to obtain more stable results than the FEM, even while there are no hourglass control or other artificial “fixes” involved in the MLPG calculation. The averaged axial velocities computed from Dyna3D are shown in Figure 10(b). From this figure, it is seen that both the MLPG and Dyna3D results strictly follow the conservation of momentum. Although the Dyna3D calculation shows larger velocities for both flyer and target plates after the contact, the difference of the averaged velocities from MLPG and Dyna3D is insignificant.

#### 4.4 Ballistic Impact

To demonstrate the capacity of the RG model on simulating the damage and penetration problems, a ballistic impact problem is considered here. In this simulation, a cylindrical tungsten projectile impacts with an AD85 ceramic plate at the velocity of 1500 m/s. Both the length and diameter of the projectile are 10 mm. The target ceramic plate has a thickness of 5 mm and a diameter of 80 mm. The tungsten is modeled as elastoplastic with the following material properties: density  $16.98 \text{ g/cm}^3$ , Young’s modulus 299.6 GPa, Poisson’s ratio 0.21 and yield strength 1.5 GPa. The target plate is modeled using the Rajendran-Grove ceramic model, with the material constants as listed in Table 1.

This problem is simulated using both the Dyna3D and the MLPG. Figure 11 shows the damage profile from

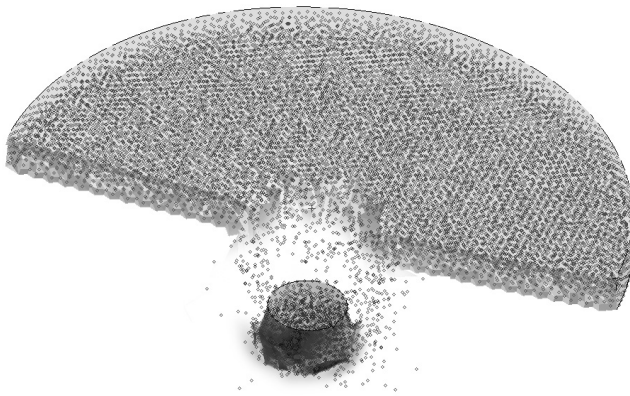


**Figure 12 :** Ballistic impact penetration

Dyna3D simulation, with the darkness referring to the damage density. At 3.5 micro-seconds, damage begins to form under and around the impact area. Inside these areas, the compressive stress or shear stress increases rapidly due to the collision, causing the strain energy release rate to go beyond the critical strain energy release rate. Thus, the micro-cracks begin to grow inside these areas. At 10 micro-seconds, these micro-cracks inside the whole impact area grow and cause the damage to accumulate very rapidly inside the whole impact area, to form a perforation hole. Due to the incapability of the element-based method in dealing with severe distortion, the Dyna3D simulation stops at the 10 micro-seconds.

The same problem is re-simulated by using the MLPG method. The problem has been solved smoothly without any mesh distortion problems, because of the advantages of the truly meshless method. The whole penetration process is simulated and the total solution time is 20 micro-seconds. The final deformation is shown in Figure 12, and the fragmentation is clearly formed after the projectile penetrates the target plate. The detailed simulation results and discussion is reported in the author another paper [Han, Liu, Rajendran, and Atluri, (2006)].

## 5 Closing Remarks

The ability and accuracy of the constitutive model plays an important role in the computational methodology. The Rajendran-Grove ceramic damage model is capable of predicting the micro-crack and void damage evolution, and the pulverization of ceramic materials. The MLPG method, as a truly meshless approach, enables a feasible computational framework for solving high-

speed dynamic problems with large deformation. The current mixed method, as an extension to the primal MLPG method, leads to a high-performance computational code, which can solve three-dimensional high-speed impact and penetration problems. The numerical examples demonstrate the capability of the MLPG method with RG ceramic damage model in solving the important class of impact and penetration problems, involving severe material deformation and fragmentation.

## References

- Atluri, S.N** (2004): *The Meshless Local Petrov-Galerkin ( MLPG) Method for Domain & Boundary Discretizations*, Tech Science Press, 665 pages.
- Atluri, S. N.; Zhu, T.** (1998): A new meshless local Petrov-Galerkin (MLPG) approach in computational mechanics. *Computational Mechanics*, Vol. 22, pp. 117-127.
- Budiansky, B.; O'Connell, R.J.** (1976): Elastic Moduli of Cracked Solid. *Int. J. Solids Structures*, Vol. 12, pp. 81-97.
- Griffith, A.A.** (1920): The Phenomena of Rupture and Flow in Solids. *Phil. Trans. R. Soc. London*, Vol. 221, pp. 163-198.
- Grove, D.J.** (1993): Research Report UDR-TR-93-133, University of Dayton Research Institute.
- Grady, D.E.; Moody, R.L.** (1996): Shock Compression Profiles in Ceramics. *Sandia Report, SAND96-0551*, Sandia National Laboratory, Albuquerque, NM.
- Gurson, A.L.** (1977): Porous Rigid-Plastic Materials Containing Rigid Inclusions-Yield Function, Plastic Potential and Void Nucleation. In *Adv. Res. Strength Fract. Matls. 2a* (edited by Tablin DMR), Pergamon Press, New York.
- Han. Z. D.; Atluri, S. N.** (2004): Meshless Local Petrov-Galerkin (MLPG) approaches for solving 3D Problems in elasto-statics, *CMES: Computer Modeling in Engineering & Sciences*, vol. 6 no. 2, pp. 169-188.
- Han Z. D.; Rajendran, A. M; Atluri, S. N.** (2005): Meshless Local Petrov-Galerkin (MLPG) Approaches for Solving Nonlinear Problems with Large Deformation and Rotation, *CMES: Computer Modeling in Engineering & Sciences*, vol. 10, no. 1, pp. 1-12.
- Han Z. D.; Liu H. T.; Rajendran, A. M; Atluri, S. N.** (2006): The Applications of Meshless Local Petrov-

Galerkin (MLPG) Approaches in High-Speed Impact, Penetration and Perforation Problems, *CMES: Computer Modeling in Engineering & Sciences*, vol. 14, no. 2, pp. 119-128.

**Johnson, G.R.; Robert, A.S.** (2003): Conversion of 3D Distorted Element into Meshless Particles During Dynamic Deformation. *Int. J. Impact Engng.*, Vol. 28, 947-966.

**Margolin, L.G.** (1983): Elastic Moduli of Cracked Body. *Int. J. Fract.*, Vol. 22, pp. 65-79.

**Rajendran, A.M.** (1994): Modeling the Impact Behavior of AD85 Ceramic under Multiaxial Loading. *Int. J. Impact Engng.*, Vol. 15, No. 3, pp. 749-768.

**Rajendran, A. M.; Grove, D.J.** (1996): Modeling the Shock Response of Silicon Carbide, Boron Carbide and Titanium Diboride. *Int. J. Impact Engng.*, Vol. 18, No. 6, pp. 611-631.

**Rajendran, A.M.; Grove, D.J.** (2002): Computational Modeling of Shock and Impact Response of Alumina. *CMES: Computer Modeling & Engng. Sci.*, Vol. 3, No. 3, 367-380.

**Resnyansk, A.D.** (2002): DYNA-Modeling of the High-Velocity Impact Problems with a Split-Element Algorithm, *Int. J. Impact Engng.*, Vol. 27, 709-727.

**Simha, C.H.M.** (1998): High Rate Loading of a High Purity Ceramic – One Dimensional Stress Experiments and Constitutive Modeling. Ph.D. thesis, University of Texas, Austin, Texas.



# The Optimal Radius of the Support of Radial Weights Used in Moving Least Squares Approximation

Y.F. Nie<sup>1,2</sup>, S.N. Atluri<sup>2</sup> and C.W. Zuo<sup>1</sup>

**Abstract:** Owing to the meshless and local characteristics, moving least squares (MLS) methods have been used extensively to approximate the unknown function of partial differential equation initial boundary value problem. In this paper, based on matrix analysis, a sufficient and necessary condition for the existence of inverse of coefficient matrix used in MLS methods is developed firstly. Then in the light of approximate theory, a practical mathematics model is posed to obtain the optimal radius of support of radial weights used in MLS methods. As an example, while uniform distributed particles and the 4<sup>th</sup> order spline weight function are adopted in MLS method in two dimension domain and two kinds of norms are used to measure error, optimal results for linear and quadratic basis are gained. Finally, the test data verify that the optimal values are correct. The research idea can be used in 3-dimension problems too.

**keyword:** MLS methods, Radius of support, Scaling, Sobolev norm, Mathematics model, Matrix analysis, Approximate theory.

## 1 Introduction

Comparing with the radial basis function interpolation approach, the moving least squares (MLS) method offers another kind of efficient scattered data approximation especially if the number of point is large and the data values contain noise. The MLS method is a variation on the classical least squares technique with the advantage allowing the nearest neighbors of the evaluation point  $x$  to influence the approximate value through a weight function with local compact support  $w(x, x_j) : R^d \times R^d \rightarrow R^+$  where  $x_j$  is one of the given particles (nodes) in set  $P_\Omega = \{x_j\}_{j=1}^n$  in the bounded domain  $\Omega \subset R^d$ . That is for every

point  $x$  we have to solve the following problem

$$\min_{s \in S} \left\{ \sum_{j=1}^n [s(x_j) - f_j]^2 w(x, x_j) \right\}, \quad (1)$$

where  $S$  is a finite-dimensional linear space and  $f_j = f(x_j)$  is the collected data. Weight function  $w(x, x_j)$  with the form  $w_0(\|x - x_j\|_2 / r_j)$  is generally used to simplify the form of weight function and help forward the independence of weight function on the dimension  $d$  of the domain  $\Omega$ . As function  $w_0(r)$  has a compact support  $[0, 1]$ , weight function  $w(x, x_j)$  has a disc support with center  $x_j$  and radius  $r_j$ . In this paper, we would like to take the radius as a constant  $r$  for simplicity.

The MLS approximation has its origin in the early paper [Lancaster and Salkauskas(1981)] with special cases going back to [McLain(1974), and Shepard(1968)], and some investigation about the approximation order is given in paper [Farwig(1986)]. Now MLS methods have emerged as the basis of numerous meshless (meshfree) approximation methods that being suggested as an alternative to the traditional finite element method in references [Atluri (2004), and Babuska, Banerjee and Osborn(2003), Liu, Han and Lu (2004)] and there referred. Especially, the generalized moving least squares methods is developed and successfully applied as a approximation methods to solve thin beam problem in paper [Atluri, Cho, Kim(1999)].

As we know, one of the crucial steps to solve partial differential equations system is the approximation to the unknown field function appeared in the system, i.e. how to ensure trial function being an effective approximation. The influence factors existing in MLS method include which kind of weight function  $w_0$  should be used and how much the size of compact support of the weight function  $r$  should be. Reference [Atluri (2004)] suggests to use 4<sup>th</sup> order spline type weight function in order to give smoothness to the derivatives of the trial function. About the second factor there is no definite answer up to now as our known.

<sup>1</sup> School of Science, Northwestern Polytechnical University, Xi'an 710072, China. E-mail: Yfnie@nwpu.edu.cn

<sup>2</sup> Center for Aerospace Research & Education, University of California at Irvine, Irvine, CA 92697, USA

In this paper, after a brief introduction of the MLS approximation in this section, a sufficient and necessary condition about the existence of the inverse of coefficient matrix of linear equations system used in MLS method is posed and proved when uniform distributed particle is exploited in section 2. The conclusions about the application in the case of linear and quadratic basis are specified in section 3. Then the model of optimal radius of the support of radial weight function is developed and solved in section 4 and 5 respectively. Some numerical tests about the optimal radius when linear bases and quadratics base being used are given in section 6. And the conclusions are shown in the end.

## 2 Sufficient and necessary

Let's assume that the finite dimension of linear space  $S$  used in formula (1) is expressed as

$$S = \text{span}\{p_1(x), p_2(x), \dots, p_m(x)\},$$

i.e. a series of linear independent functions  $p_1(x), p_2(x), \dots, p_m(x)$  defined on  $R^d$  are the basis of linear space  $S$ , and for any  $s \in S$  there exist a group of coefficients  $\{a_i\}_{i=1}^m \subset R$  such that  $s = \sum_{i=1}^m a_i p_i(x)$ . Then for any given point  $x \in \Omega \subset R^d$ , the moving least squares problem (1) can be written as

Find  $s^* = \sum_{i=1}^m a_i(x) p_i(x)$  such that

$$\begin{aligned} \min_{s \in S} & \left\{ \sum_{j=1}^n [s(x_j) - f_j]^2 w(x, x_j) \right\} \\ &= \min_{\substack{a_i \in R \\ 1 \leq i \leq m}} \left\{ \sum_{j=1}^n \left[ \sum_{i=1}^m a_i p_i(x_j) - f_j \right]^2 w(x, x_j) \right\} \\ &= \sum_{j=1}^n \left[ \sum_{i=1}^m a_i(x) p_i(x_j) - f_j \right]^2 w(x, x_j). \end{aligned} \quad (2)$$

According to least squares principle, for any point  $x \in \Omega \subset R^d$ , the coefficients  $\{a_i(x)\}_{i=1}^m \subset R$  of the solution function  $s^*$  should be the solution of the following linear equations system

$$\mathbf{A}(x) \mathbf{a}(x) = \mathbf{B}(x) \mathbf{u}, \quad (3)$$

where matrix

$$\begin{aligned} \mathbf{A}(x) &= \mathbf{P}^T \mathbf{W}(x) \mathbf{P}, \quad \mathbf{B}(x) = \mathbf{P}^T \mathbf{W}(x), \\ \mathbf{W}(x) &= \text{diag}\{w(x, x_1), w(x, x_2), \dots, w(x, x_n)\}, \end{aligned} \quad (4)$$

$$\begin{aligned} \mathbf{P} &= \begin{bmatrix} p_1(x_1) p_2(x_1) \dots p_m(x_1) \\ p_1(x_2) p_2(x_2) \dots p_m(x_2) \\ \dots \dots \dots \\ p_1(x_n) p_2(x_n) \dots p_m(x_n) \end{bmatrix}, \\ \mathbf{a}(x) &= \begin{bmatrix} a_1(x) \\ a_2(x) \\ \vdots \\ a_m(x) \end{bmatrix}, \\ \mathbf{u} &= \begin{bmatrix} f_1 \\ f_2 \\ \vdots \\ f_n \end{bmatrix}. \end{aligned} \quad (5)$$

In order to describe the solvability of the linear equations system (3) clearly, we need introduce the following definition as in reference [Zuo and Nie(2005)].

**Definition 1** Assuming that we have functions series  $\{\phi_i(x)\}_{i=1}^m$  and particles set  $X = \{x_j\}_{j=1}^n$ ,  $\{\phi_i(x)\}_{i=1}^m$  is said to be linear independent on the set  $X$  if equations  $\sum_{i=1}^m c_i \phi_i(x_j) = 0 \quad (1 \leq j \leq n)$  lead to  $c_1 = c_2 = \dots = c_m = 0$ .

**Remark 2** According to the definition, obviously the functions series  $\{\phi_i(x)\}_{i=1}^m$  is linear independent on the set  $X$  if and only if the rank of the matrix  $\Phi$  is  $m$ . The matrix  $\Phi$  is defined as

$$\Phi = \begin{bmatrix} \phi_1(x_1) \phi_2(x_1) \dots \phi_m(x_1) \\ \phi_1(x_2) \phi_2(x_2) \dots \phi_m(x_2) \\ \dots \dots \dots \\ \phi_1(x_n) \phi_2(x_n) \dots \phi_m(x_n) \end{bmatrix}.$$

In other words, the column vectors of matrix  $\Phi$  are linear independent. The geometric explanation is that there is a group of particles  $\{x_{ij}\}_{j=1}^m \subset X$  such that they do not locate in any same curve expressed by a function in space  $\text{span}\{\phi_1(x), \phi_2(x), \dots, \phi_m(x)\}$ .

Now, let us come back to the MLS approximation. For a fixed  $x \in \Omega$ , suppose that there are number of  $k$  particles,  $\{x_{i1}, x_{i2}, \dots, x_{ik}\} \triangleq P_x \subset P_\Omega$ , which satisfy condition

weight  $w(x, x_l) > 0$  for any  $x_l \in P_x$  in contrast with weight  $w(x, x_l) = 0$  for  $x_l \in P_\Omega \setminus P_x$ . Reference [Atluri (2004)] calls  $P_x$  as the influence domain of point  $x$  based on given particles set  $P_\Omega$ .

Take a permutation matrix  $\mathbf{T}_x$  which can be used to realize the following transformation

$$\mathbf{T}_x \mathbf{W}(x) \mathbf{T}_x^T = \begin{bmatrix} \mathbf{W}_{11}(x) & \mathbf{O}_{12} \\ \mathbf{O}_{21} & \mathbf{O}_{22} \end{bmatrix}, \quad (6)$$

where matrix

$$\mathbf{W}_{11}(x) = \text{diag}\{w(x, x_{i1}), w(x, x_{i2}), \dots, w(x, x_{ik})\},$$

and the sizes of the zero matrixes  $\mathbf{O}_{12}$ ,  $\mathbf{O}_{21}$ ,  $\mathbf{O}_{22}$  are  $k \times (n - k)$ ,  $(n - k) \times k$ ,  $(n - k) \times (n - k)$  respectively. Using the characteristic of permutation matrix, we have the alternative form of coefficient matrix of linear equations system (3) as follows

$$\begin{aligned} \mathbf{A}(x) &= \mathbf{P}^T \mathbf{W}(x) \mathbf{P} = \mathbf{P}^T \mathbf{T}_x^T \mathbf{T}_x \mathbf{W}(x) \mathbf{T}_x^T \mathbf{T}_x \mathbf{P} \\ &= (\mathbf{T}_x \mathbf{P})^T \mathbf{T}_x \mathbf{W}(x) \mathbf{T}_x^T (\mathbf{T}_x \mathbf{P}) \end{aligned} \quad (7)$$

Let's dispart the matrix  $(\mathbf{T}_x \mathbf{P})_{n \times m}$  into two parts, as follows

$$\mathbf{T}_x \mathbf{P} = \begin{pmatrix} \mathbf{P}_1 \\ \mathbf{P}_2 \end{pmatrix} \quad (8)$$

where matrix  $\mathbf{P}_2$  has the size of  $(n - k) \times m$  and matrix  $\mathbf{P}_1$  has the form

$$\mathbf{P}_1 = \begin{bmatrix} p_1(x_{i1})p_2(x_{i1}) \cdots p_m(x_{i1}) \\ p_1(x_{i2})p_2(x_{i2}) \cdots p_m(x_{i2}) \\ \dots \dots \dots \\ p_1(x_{ik})p_2(x_{ik}) \cdots p_m(x_{ik}) \end{bmatrix}_{k \times m} \quad (9)$$

Substitute formulas (6) and (8) into (7), and we obtain that coefficient matrix

$$\begin{aligned} \mathbf{A}(x) &= \begin{pmatrix} \mathbf{P}_1 \\ \mathbf{P}_2 \end{pmatrix}^T \begin{bmatrix} \mathbf{W}_{11}(x) & \mathbf{O}_{12} \\ \mathbf{O}_{21} & \mathbf{O}_{22} \end{bmatrix} \begin{pmatrix} \mathbf{P}_1 \\ \mathbf{P}_2 \end{pmatrix} \\ &= \mathbf{P}_1^T \mathbf{W}_{11}(x) \mathbf{P}_1. \end{aligned} \quad (10)$$

Due to diagonal matrix  $\mathbf{W}_{11}(x)$  being positive symmetry,  $\det(\mathbf{A}(x)) \neq 0$  if and only if  $\text{rank}(\mathbf{P}_1) = m$ . Using the Remark 2 and Definition 1, that is to say functions series  $\{p_i(x)\}_{i=1}^m$  should be linear independent on the influence

domain  $P_x = \{x_{i1}, x_{i2}, \dots, x_{ik}\}$ . Conclude this into the following theorem.

**Theorem 3** For any  $x \in \Omega$ , the linear equation system derived from moving least squares approximation exist unique solution if and only if the base functions  $\{p_i(x)\}_{i=1}^m$  is linear independent on the influence domain  $P_x$  of point  $x$  based on the given particles set  $P_\Omega$ .

**Remark 4** The expression (10) of coefficient matrix  $\mathbf{A}(x)$  show us that the coefficient matrix of MLS method is positive symmetry under the condition of Theorem 3. And the characteristic leads that much more methods can be used to solve equations system (3).

**Remark 5** The theorem is correct for any kind of weight function, random distributed particles, and any dimension of any shape of domain  $\Omega$  used in the MLS approximation.

**Remark 6** To ensure basis  $\{p_i(x)\}_{i=1}^m$  of linear space  $S$  being linear independence on the influence domain  $P_x$  of any point  $x \in \overline{\Omega}$ , all of the radius  $r_j$  ( $1 \leq j \leq n$ ) of the compact support of weight function  $W(x, x_j)$  must large enough such that  $P_x$  can contain number of  $m$  particles at least. That is to say for any point  $x \in \overline{\Omega}$  there are number of  $k \geq m = \dim(S)$  supports of weight functions which cover the point  $x$ , and among of the  $k$  centers of the supports, there are  $m$  center at least which do not locate on any curve defined by a function in space  $S$ .

Although satisfying the condition of the Theorem 3 ensures that the MLS method has unique analysis solution, it does not tell us what the best radius of the compact support of weight function should be to obtain a good approximation. This problem will be discussed in the following several sections.

### 3 Application to linear and quadric basis

Now we use the previous theory to the case of the linear space  $S$  with linear and quadric basis respectively and assuming that the particles  $P_\Omega = \{x_j\}_{j=1}^n$  are distributed uniformly on the bounded convex domain  $\Omega \subset R^2$  with particles step  $h$ , namely the distance along the coordinate axis between the adjacent particles.

In the case of linear basis, we have linear space  $S = \text{span}\{1, x, y\}$  and  $m = \dim(S) = 3$ . According to Theorem 3 and Remark 6, the influence domain  $P_x$  for any point  $x \in \Omega$  must include at least 3 particles not sharing any same straight line, then the MLS method can be used to evaluate the approximation of the unknown

function at point  $x$ . As the particles are distributed like Fig. 1, and weight functions take the form of  $w(x, x_j) = w_0(\|x - x_j\|_2/r)$ , the support radius  $r$  of the support should be greater than  $\sqrt{5}/2h \approx 1.11803h$ , which can be obtained by sampling several special point  $x$  along the domain boundary  $\partial\Omega$  only because the interior point  $x$  has more particles included in its influence domain.

In the case of quadratic basis, linear space  $S = \text{span}\{1, x, y, x^2, xy, y^2\}$  and the dimension  $m = \dim(S) = 6$ . Similarly discussion as in the linear case, we know that the influence domain  $P_x$  must include 6 particles not sharing any quadratic curve (two lines regards as a special quadratic curve), and further the support radius  $r$  should be greater than  $\sqrt{17}/2h \approx 2.0616h$ .

**Remark 7** Although the previous conditions about the radius of support can ensure the matrix inversion of the MLS approximation possible, a little larger support radius than the previous mentioned is needed to reduce the condition number of the coefficient matrix. Through computing simulation, reference [Zuo and Nie (2005)] suggests that  $r \geq 1.2h > \sqrt{5}/2h$  for linear basis and  $r \geq 2.5h > \sqrt{17}/2h$  for quadratic basis. We will search the best support radius based on a model in the coming section.

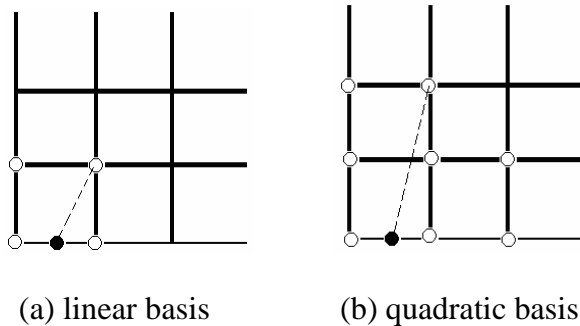


**Figure 1** : The positions where the minimum radius of influence domain needed by MLS method.  $\bullet$  point  $x \in \bar{\Omega}$   $\circ$  particle in  $P_x$

#### 4 Model of optimal radius

It is very hard just depending on the mathematical analysis to obtain the optimal radius of support of the weight function used in the MLS approximation. To our knowledge there is no a clear result about this problem up to

now. Here we try to develop a mathematic model and systemic numerical tests based on approximation theory to solve this problem partially.

According to reference [Atluri (2004)], the  $4^{th}$  order spline function which takes as the following form

$$w_0(t) = \begin{cases} 1 - 6t^2 + 8t^3 - 3t^4 & 0 \leq t \leq 1 \\ 0 & 1 < t \end{cases} \quad (11)$$

is suggested to use as the weight function in MLS method because it has better smoothness of the first derivative of the approximate function.

Owing to Weierstrass theorem that any continuous function can be approximated by a polynomial for any given accuracy requirement, we take the monomial basis, for example in  $R^2$  space they are

$$1, x, y, x^2, xy, y^2, x^3, x^2y, xy^2, y^3, \dots$$

to express the polynomial which is used to approximate a given functions. Thus a good approximation method should approximate monomials efficiently, and the reverse is correct because of the following fact

$$|f - s^*| \leq |f - p| + |p - s^*| \leq \varepsilon + |p - s^*|,$$

where  $f$  is any continuous function,  $s^*$  is the approximation function of function  $f$  by MLS methods, and  $p$  is the polynomial used to approximate  $f$  for a given accuracy requirement  $\varepsilon > 0$ .

For each monomial, we use MLS method to approximate it, and find the best radius through comparing the Sobolev norms of the approximate error. Considering the reproducing ability for polynomials of MLS which is decided by the linear space  $S$  used in formula (1), the first several monomials no need to be tested.

Sobolev norm  $\|\bullet\|_t$  is defined as follows

$$\|f\|_t = \left( \sum_{l=0}^t \sum_{|\alpha|=l} \int_{\Omega} [D^{\alpha} f(\mathbf{x})]^2 d\Omega \right)^{1/2},$$

$$f \in H^t(\Omega), \quad \Omega \subset R^d \quad (12)$$

where multi-index  $\alpha = (\alpha_1, \alpha_2, \dots, \alpha_d)$  is used,  $|\alpha| = \sum_{i=1}^d \alpha_i$ ,  $\{\alpha_i\}_{i=1}^d$  are nonnegative integers, and differential operator  $D^{\alpha} = \left(\frac{\partial}{\partial x_1}\right)^{\alpha_1} \left(\frac{\partial}{\partial x_2}\right)^{\alpha_2} \dots \left(\frac{\partial}{\partial x_d}\right)^{\alpha_d}$ .

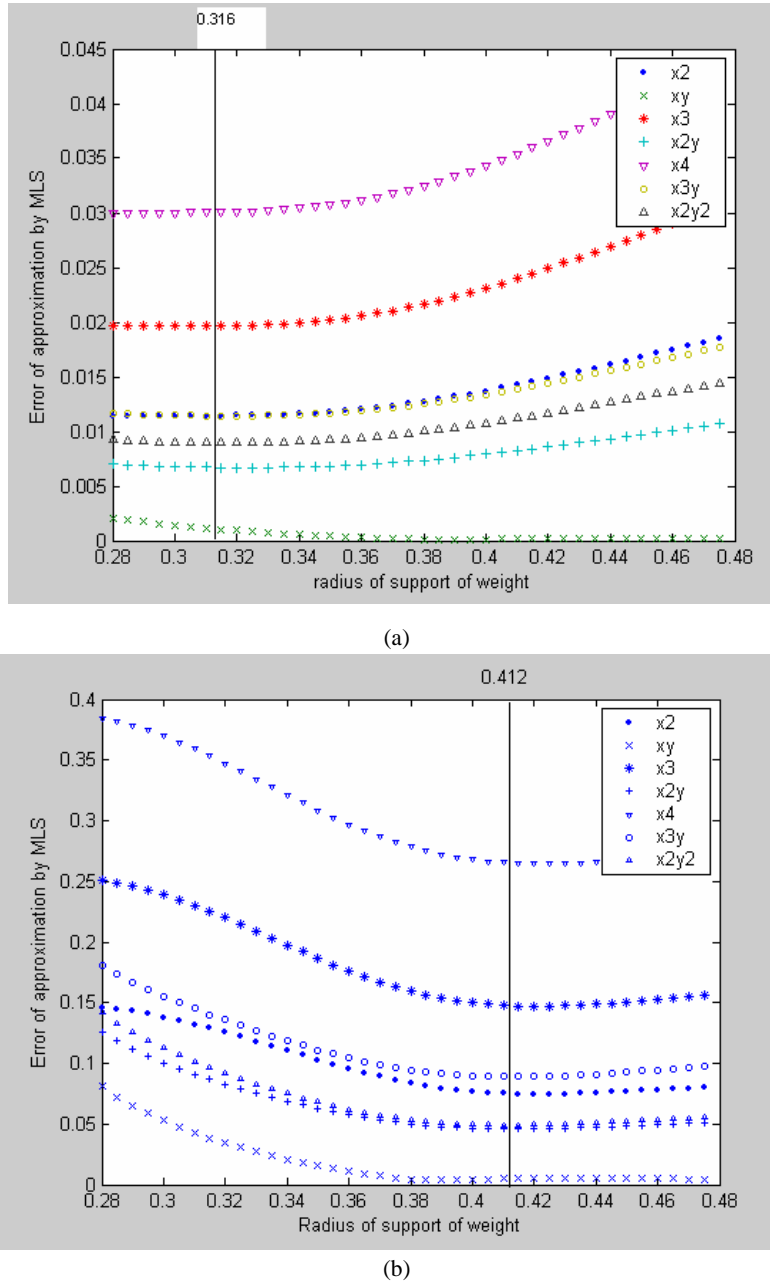


**Figure 2** : Errors of MLS method to monomials with varying support radius (Linear basis). (a)  $\|\bullet\|_0$ , (b)  $\|\bullet\|_1$  norms are used to measure errors respectively.

Denote the **monomial optimal radius** (MOR) of support of the weight used in MLS method as  $r_{opt}^{(t,\alpha)}$  while the approximated monomial is  $\mathbf{x}^\alpha = x_1^{\alpha_1} x_2^{\alpha_2} \dots x_d^{\alpha_d}$  and Sobolev norm  $\|\bullet\|_t$  is used to measure approximate error. MOR  $r_{opt}^{(t,\alpha)}$  can be gotten approximately through simple searching methods and the initial searching radius can be defined through the theory in section 2 (**Step 0**).

Generally, for different monomials, the MORs are different each other. So we need use these MORs to develop the optimal radius of MLS method  $r_{opt}^{(t)}$ . Assume that the MLS approximate has degree of  $(m^* - 1)$  polynomial reproducing. The following three steps can be used to obtain  $r_{opt}^{(t)}$ .

**Step 1** Develop the **group optimal radius** (GOR) of

**Table 1** : Evaluation of optimal radius in linear basis case (h=0.25)

h=0.25		n=2 x <sup>2</sup> xy		n=3 x <sup>3</sup> x <sup>2</sup> y		n=4 x <sup>4</sup> x <sup>3</sup> y x <sup>2</sup> y <sup>2</sup>			...
t=0	$r_{opt}^{(0,\alpha)}$	0.290	0.390	0.290	0.325	0.290	0.315	0.315	...
	$r_{opt}^{(0,n)}$	0.323		0.308		0.305			...
	$r_{opt,n}^{(0)}$	0.323		0.318		0.316			...
t=1	$r_{opt}^{(1,\alpha)}$	0.420	0.390	0.420	0.415	0.420	0.415	0.410	...
	$r_{opt}^{(1,n)}$	0.410		0.418		0.416			...
	$r_{opt,n}^{(1)}$	0.410		0.413		0.412			...

**Table 2** : Evaluation of optimal radius in quadratic basis case (h=0.25)

h=0.25		n=3 x <sup>3</sup> x <sup>2</sup> y		n=4 x <sup>4</sup> x <sup>3</sup> y x <sup>2</sup> y <sup>2</sup>			n=5 x <sup>5</sup> x <sup>4</sup> y x <sup>3</sup> y <sup>2</sup>			...
t=0	$r_{opt}^{(0,\alpha)}$	0.560	0.520	0.560	0.545	0.515	0.560	0.545	0.515	...
	$r_{opt}^{(0,n)}$	0.540		0.545			0.540			...
	$r_{opt,n}^{(0)}$	0.540		0.542			0.541			...
t=1	$r_{opt}^{(1,\alpha)}$	0.585	0.575	0.590	0.580	0.525	0.630	0.580	0.555	...
	$r_{opt}^{(1,n)}$	0.580		0.573			0.588			...
	$r_{opt,n}^{(1)}$	0.580		0.578			0.579			...

MLS method  $r_{opt}^{(t,n)}$  as simple arithmetic average of the MORs of monomials with the same degree  $n$ :

$$r_{opt}^{(t,n)} = \sum_{|\alpha|=n} r_{opt}^{(t,\alpha)} / C_n, \quad (13)$$

where  $C_n$  is the cardinality of multi-index set  $\{\alpha : |\alpha| = n\}$ .

**Step 2** Develop the **partial optimal radius** (POR) of MLS method  $r_{opt,n}^{(t)}$  as

$$r_{opt,n}^{(t)} = \sum_{l=m^*}^n w_l r_{opt}^{(t,l)} / \sum_{l=m^*}^n w_l. \quad (14)$$

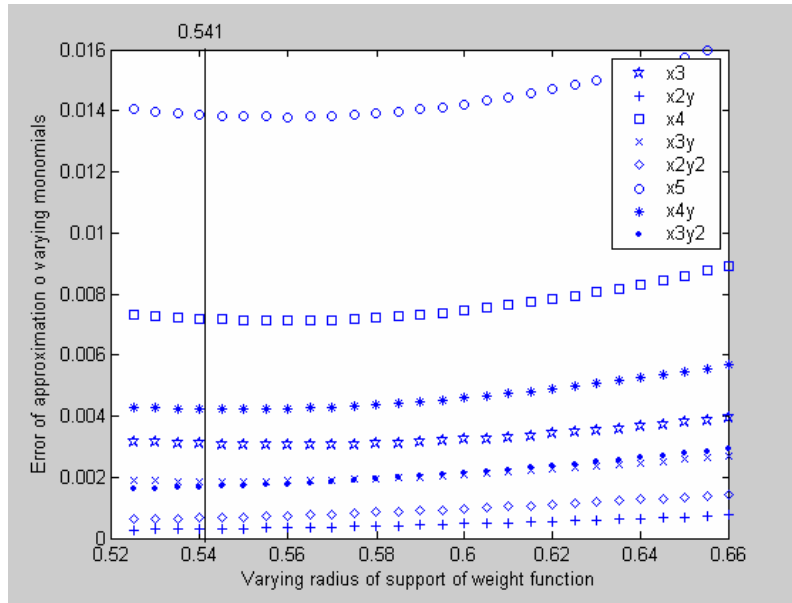
where  $\{w_l\}_{l=m^*}^n$  are a group of weights of GOR  $\{r_{opt}^{(t,l)}\}_{l=m^*}^n$ . For the first several degrees of monomials

less than  $m^*$ , any radius which satisfies the condition of Theorem 3 in this paper is optimal because of the zero error caused by the reproduction. So the optimal radius formula (14) does not include the contributions of those low orders of monomials. As the equal weights  $\{w_l\}_{l=m^*}^n$  are used for the GOR, formula (14) means the simple arithmetic average over the nonzero error groups. Otherwise, it is an average with weights on GOR. In order to ensure better approximate ability on a linear space, gradual reducing weights such as  $\{w_l = 1/2^l\}_{l=m^*}^n$  are suggested to use.

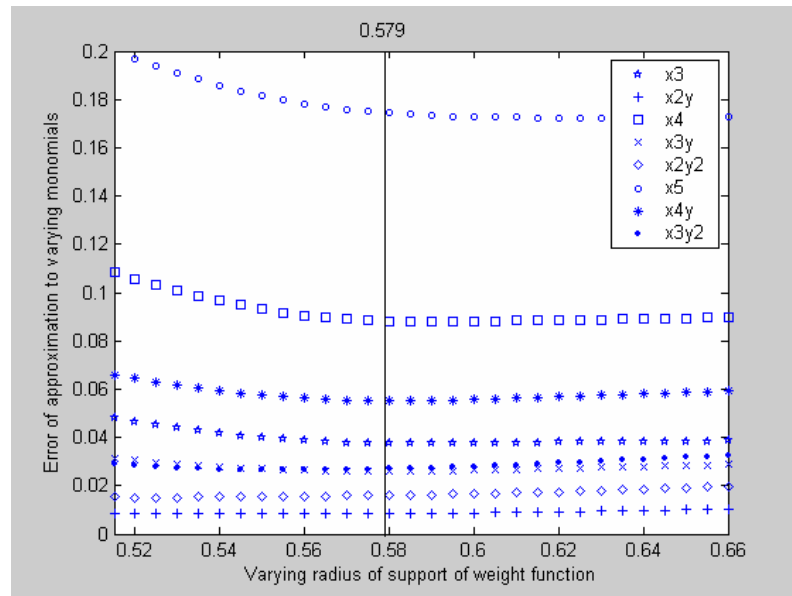
**Step 3** Develop the optimal radius of MLS method  $r_{opt}^{(t)}$  as the limit of POR

$$r_{opt}^{(t)} = \lim_{n \rightarrow \infty} r_{opt,n}^{(t)}. \quad (15)$$

As uniform particles are used,  $r_{opt}^{(t)}$  depends on particle



(a)



(b)

**Figure 3 :** Errors of MLS method to monomials with varying support radius (Quadratic basis). (a)  $\|\bullet\|_0$ , (b)  $\|\bullet\|_1$  norms are used to measure errors respectively.

step obviously. Let's name quantity  $r_{opt}^{(t)}/h = s^{(t)}$  as optimal scaling. The numerical results in section 6 will show that optimal scaling is independent on particle step  $h$ .

### 5 Optimal radius of linear and quadratic basis

Now we use the model posed in the previous section to develop the optimal scaling of MLS in the case of linear space  $S$  with linear and quadratic basis being used for 2 dimensional domain  $\Omega = [0, 1] \times [0, 1]$  with uniform distributed particles.

While the linear basis are used in MLS approximation, the errors of approximations to a group of monomials with varying radius in different norms are show in Fig.2, and the MORs  $r_{opt}^{(0,\alpha)}$  and  $r_{opt}^{(1,\alpha)}$  is given in Tab. 1. In the computing process, searching method is used with researching step 0.005 and initial radius value  $1.12h > \sqrt{5}/2h \approx 1.11803h$  that the reason has been discussed in details in section 3.

Considering the symmetry, we just show data about the partial monomials in a group in Fig. 2 and Tab. 1. GORs and PORs are evaluated due to formula (13) and (14) with weights  $\{w_l = 1/2^l\}_{l=m}^n$  respectively. Owing to formula (15), the optimal radius of MLS  $r_{opt}^{(0)} \approx 0.316$ ,  $r_{opt}^{(1)} \approx 0.412$  while particle step  $h = 0.25$  is used, and the optimal scalings  $s^{(0)} \approx 1.264$ ,  $s^{(1)} \approx 1.648$ . The reason that scaling  $s^{(1)} > s^{(0)}$  is that error measured by norm  $\|\bullet\|_1$  includes more items compared with norm  $\|\bullet\|_0$ , namely first order differentials, and this leads to more smooth requirement.

While the quadric bases are used, the same process as the linear case is followed except that for the initial searching radius is  $2.06h \approx \sqrt{17}/2h$ . The corresponding data are shown in Fig. 3 and Tab. 2. The optimal radius of MLS is  $r_{opt}^{(0)} \approx 0.541$ ,  $r_{opt}^{(1)} \approx 0.579$  while particle step  $h = 0.25$  is used, and the optimal scalings  $s^{(0)} \approx 2.164$ ,  $s^{(1)} \approx 2.316$ .

**Remark 8** Although the data we used is dependent on node step  $h$ , the optimal scaling  $s^{(t)}$  are independent of  $h$  which will be shown through numerical examples in next section. And the results can be applied to the other 2 dimensional domain with uniform nodes because linear map does not change the key characteristics of polynomials such as degree.

**Remark 9** The model can be used to three dimensional problem without any difficulty. As the quasi-uniform [Babuska, Banerjee and Osborn (2003)] distributed particles are used, it can be used with little modify which will be given in coming paper.

## 6 Numerical test

In this section, we check that the optimal scaling  $s^{(t)}$  has little dependent on node step  $h$  firstly. Then some complex functions are used to test the efficiency of the optimal scaling obtained by the model posed in this paper.

### 6.1 Optimal scaling independent on node step test

Two different node steps 0.2 and 0.125 compared with the step 0.25 are used to the model in section 5 to obtain the optimal scaling while linear and quadratic base are used respectively. The optimal scaling results evaluated from the data in Tab.5-6 and Tab. 7-8 are given in Tab. 3 and Tab. 4 for two kinds of linear space S respectively. The results show the optimal scaling of radius of support of weight function evaluated from different steps is equal each other approximately, and the little difference among them is caused mainly from searching step.

**Table 3** : Comparing of optimal scaling with varying particle steps (linear basis)

$h$	0.25	0.2	0.125	...
$s^{(0)}$	1.264	1.275	1.264	...
$s^{(1)}$	1.648	1.665	1.672	...

**Table 4** : Comparing of optimal scaling with varying particle steps (quadratic basis)

$h$	0.25	0.2	0.125	...
$s^{(0)}$	2.164	2.175	2.176	...
$s^{(1)}$	2.316	2.315	2.200	...

### 6.2 Efficient test

Three functions  $e^x \sin y \sin(x^2 y)$  and  $e^{xy^3}$  are used to test the efficiency of the optimal scaling of support radius of weight function in MLS method. And let particle step  $h=0.125$ . The error curves measured by two kinds of norms varying with support radius are displayed in Fig. 4 for linear basis case and Fig. 5 for quadratic basis.

Fig. 4 (a) and (b) show that while support radius

$$r = s^{(0)}h = 1.264 \times 0.125 = 0.158$$

and

$$r = s^{(1)}h = 1.672 \times 0.125 = 0.209$$

are used respectively MLS method with linear basis gives the three test functions the best approximations all-around in corresponding norm of  $\|\bullet\|_0$  and  $\|\bullet\|_1$ . Similarly, Fig. 5 (a) and (b) indicate that while MLS method with quadratic basis and support radius taken as

$$r = s^{(0)}h = 2.176 \times 0.125 = 0.272$$

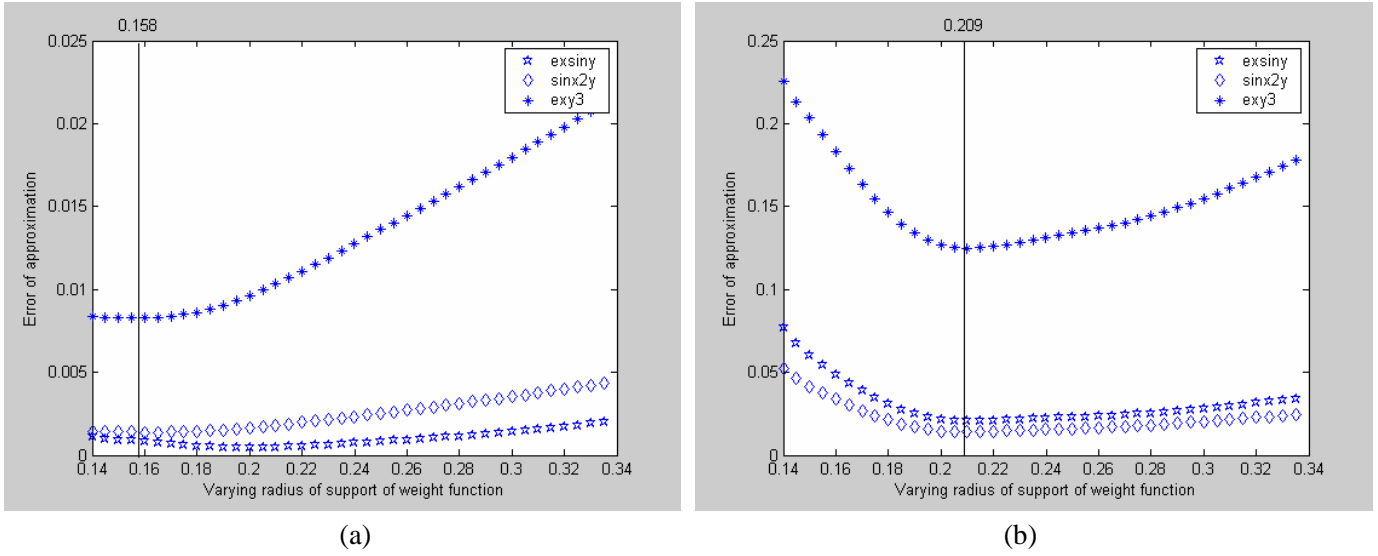


**Figure 4 :** Test about optimal radius (linear basis case). (a)  $\|\bullet\|_0$ , (b)  $\|\bullet\|_1$  norms are used to measure errors respectively.

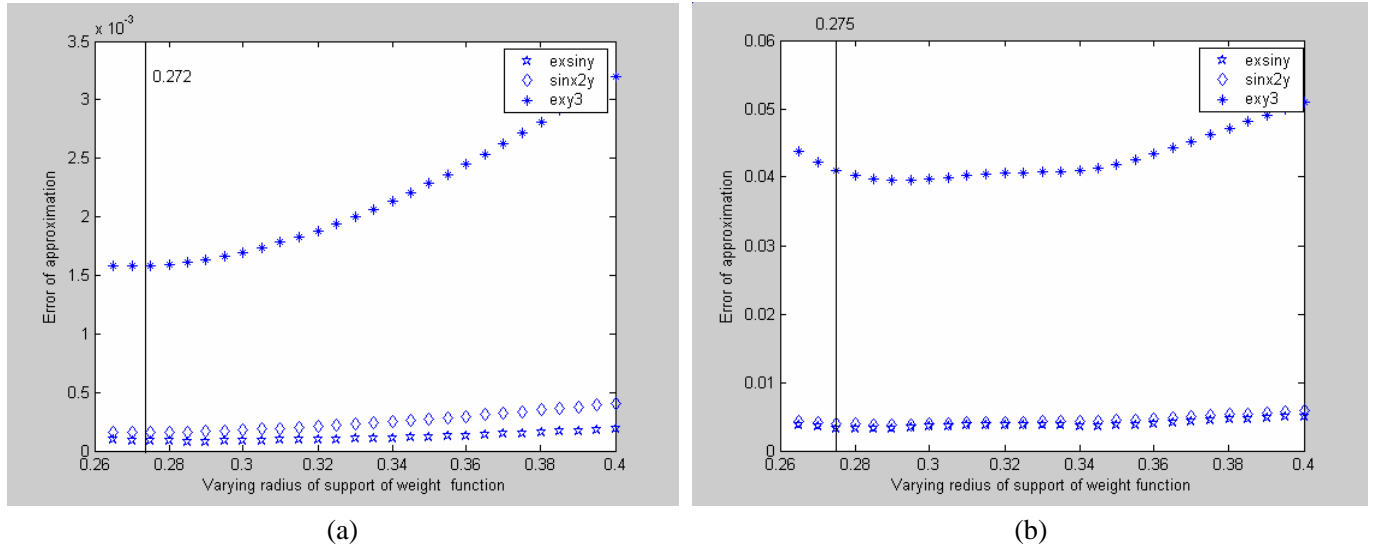


**Figure 5 :** Test about optimal radius (quadratic basis case). (a)  $\|\bullet\|_0$ , (b)  $\|\bullet\|_1$  norms are used to measure errors respectively.

and

$$r = s^{(1)}h = 2.200 \times 0.125 = 0.275 \quad ,$$

the best approximations all-around to the three test functions in norm of  $\|\bullet\|_0$  and  $\|\bullet\|_1$  are obtained respectively.

## 7 Conclusion

Based on matrix analysis and approximation theory, this paper develops an efficient approach to find the optimal

radius of support of radial weight function used in moving least squares method. As an example, while uniform distributed particles and the 4<sup>th</sup> order spline weight function are adopted in MLS method in two dimension domain, and two kinds of norms are used to measure error, optimal results for linear and quadratic basis are obtained, and then the test data verify that the optimal value are correct.

**Acknowledgement:** This work was supported by the

**Table 5** : Evaluation of optimal radius in linear basis case

h=0.2		n=2 $x^2$ $xy$		n=3 $x^3$ $x^2y$		n=4 $x^4$ $x^3y$ $x^2y^2$			...
t=0	$r_{opt}^{(0,\alpha)}$	0.235	0.310	0.235	0.260	0.235	0.255	0.255	...
	$r_{opt}^{(0,n)}$	0.260		0.248		0.247			...
	$r_{opt,n}^{(0)}$	0.260		0.256		0.255			...
t=1	$r_{opt}^{(1,\alpha)}$	0.340	0.310	0.340	0.335	0.340	0.335	0.330	...
	$r_{opt}^{(1,n)}$	0.330		0.338		0.336			...
	$r_{opt,n}^{(1)}$	0.330		0.333		0.333			...

**Table 6** : Evaluation of optimal radius in linear basis case

h=0.125		n=2 $x^2$ $xy$		n=3 $x^3$ $x^2y$		n=4 $x^4$ $x^3y$ $x^2y^2$			...
t=0	$r_{opt}^{(0,\alpha)}$	0.145	0.195	0.145	0.160	0.145	0.160	0.160	...
	$r_{opt}^{(0,n)}$	0.162		0.153		0.154			...
	$r_{opt,n}^{(0)}$	0.162		0.159		0.158			...
t=1	$r_{opt}^{(1,\alpha)}$	0.215	0.195	0.210	0.210	0.210	0.210	0.210	...
	$r_{opt}^{(1,n)}$	0.208		0.210		0.210			...
	$r_{opt,n}^{(1)}$	0.208		0.209		0.209			...

**Table 7** : Evaluation of optimal radius in quadratic basis case

h=0.2		n=3 $x^3$ $x^2y$		n=4 $x^4$ $x^3y$ $x^2y^2$			n=5 $x^5$ $x^4y$ $x^3y^2$			...
t=0	$r_{opt}^{(0,\alpha)}$	0.450	0.415	0.450	0.440	0.415	0.450	0.440	0.415	...
	$r_{opt}^{(0,n)}$	0.433		0.439			0.435			...
	$r_{opt,n}^{(0)}$	0.433		0.435			0.435			...
t=1	$r_{opt}^{(1,\alpha)}$	0.460	0.485	0.460	0.460	0.415	0.475	0.460	0.455	...
	$r_{opt}^{(1,n)}$	0.473		0.451			0.463			...
	$r_{opt,n}^{(1)}$	0.470		0.464			0.463			...

**Table 8** : Evaluation of optimal radius in quadratic basis case

h=0.125		n=3		n=4			n=5			...
		$x^3$	$x^2y$	$x^4$	$x^3y$	$x^2y^2$	$x^5$	$x^4y$	$x^3y^2$	
t=0	$r_k^{(0,n)}$	0.280	0.260	0.280	0.280	0.255	0.280	0.280	0.265	...
	$r_{opt}^{(0,n)}$	0.270		0.275			0.275			...
	$r_{opt,n}^{(0)}$	0.270		0.272			0.272			...
t=1	$r_k^{(1,n)}$	0.285	0.255	0.285	0.285	0.255	0.290	0.285	0.285	...
	$r_{opt}^{(1,n)}$	0.270		0.279			0.287			...
	$r_{opt,n}^{(1)}$	0.270		0.273			0.275			...

U.S. Army Research Laboratory under a cooperative research agreement with the University of California at Irvine. Partial support for this work was also provided by Chinese NNSFC Major Project.

**Zuo C.W., Nie Y.F.**(2005), The selection about the radius of influence in MLS, Chinese J. Engrg. Math., vol.21, pp.833-838

## References

**Atluri S.N.**(2004): The meshless methods (MLPG) for domain & BIE discretization. Tech. Science Press

**Atluri S.N., Cho J.Y., Kim H.G.**(1999): Analysis of the beams, using the meshless local Petrov-Galerkin method, with generalized moving least squares interpolations. *Comput. Mech.*, vol.24, pp.334-347

**Babuska I., Banerjee U., Osborn J.E.**(2003): Survey of meshless and generalized finite element methods: A unified approach. *Acta Numerica* . Vol. 1, pp.1–125

**Farwig R.**(1986): Multivariate interpolation of arbitrarily spaced data by moving least squares methods. *J. Comput. Appl. Math.*, vol. 16, pp.79-83

**Lancaster P., Salkauskas K.**(1981): Surfaces generated by moving least squares methods. *Math. Comput.*, vol 37, pp.141-158,

**Liu W.K., Han WM, Lu HS, et al** (2004).: Reproducing kernel element method. Part I: Theoretical formulation. *Comput. Meth. Appl. Mech. Engrg.*, vol.193, pp.933-951

**McLain D.H.**(1974): Drawing contours from arbitrary data points. *Comput. J.*, vol. 17, pp.318-324,

**Shepard D.**(1968): A two dimensional interpolation function for irregularly spaced data. Proc. 23<sup>rd</sup> Nat. Conf. ACM 517-523



# Atomic-level Stress Calculation and Continuum-Molecular System Equivalence

Shengping Shen<sup>1</sup> and S. N. Atluri<sup>1</sup>

**Abstract:** An atomistic level stress tensor is defined with physical clarity, based on the SPH method. This stress tensor rigorously satisfies the conservation of linear momentum, and is appropriate for both homogeneous and inhomogeneous deformations. The formulation is easier to implement than other stress tensors that have been widely used in atomistic analysis, and is validated by numerical examples. The present formulation is very robust and accurate, and will play an important role in the multiscale simulation, and in molecular dynamics. An equivalent continuum is also defined for the molecular dynamics system, based on the developed definition of atomistic stress and in conjunction with the SPH technique. The process is simple and easy to implement, and the fields are with high-order continuity. This equivalent continuum maintains the physical attributes of the atomistic system. This development provides a systematic approach to the continuum analysis of the discrete atomic systems.

**keyword:** Atomistic analysis, stress, SPH, continuum.

## 1 Introduction

The macroscopic behavior of solids is widely studied from a microscopic level, using the viewpoints of atomistic mechanics [Askar (1985), Bardenhagen and Triantafyllidis (1994)]. To bridge the atomistic mechanics and the continuum mechanics, it is important to know the relationships between the microscopic quantities of atoms, and the macroscopic quantities of continua. Atomic-level stress calculation plays a very important role in comparisons of continuum predictions with atomistic simulations, and it allows the intensity and nature of internal interactions in the discrete particle systems to be measured. The atomistic stress can be employed to interpret the results of atomistic simulation in light of contin-

uum mechanical calculations, which have been used in molecular dynamics simulations of solids in a variety of ways, such as characterization of defects, the determination of elastic constants, and the study of the local elastic properties of carbon nanotubes [Chandra, Namilae, and Shet (2004)]. There are different ways to calculate stress in atomistic simulations. Pioneering work has been done in this field by Born and Huang (1954) who used an elastic energy approach to evaluate the stress in lattices by means of the Cauchy-Born hypothesis for homogeneous deformation.

Another widely used stress measure at the atomic scale is the virial stress, which is based on a generalization of the virial theorem of Clausius (1870) for gas pressure. This quantity includes two parts, and can be expressed as:

$$\sigma^{virial}(\mathbf{r}) = \frac{1}{\Omega} \sum_i \left[ -m_i \dot{\mathbf{u}}_i \otimes \dot{\mathbf{u}}_i + \frac{1}{2} \sum_{j \neq i} \mathbf{r}_{ij} \otimes \mathbf{f}_{ij} \right] \quad (1)$$

Here  $i$  and  $j$  are the atomic indices. The summation is over all the atoms occupying the total volume  $\Omega$ .  $m_i$  is the mass of atom  $i$ ,  $\mathbf{u}_i$  is the displacement vector of atom  $i$  relative to a reference position,  $\dot{\mathbf{u}}_i = d\mathbf{u}_i/dt$  denotes the material time derivative of  $\mathbf{u}_i$ ,  $\mathbf{r}_{ij} = \mathbf{r}_j - \mathbf{r}_i$ , and  $\otimes$  represents the tensor product of two vectors.  $\mathbf{f}_{ij}$  is the interatomic force applied on atom  $i$  by atom  $j$ ,

$$\mathbf{f}_{ij} = \frac{\partial \phi(r_{ij})}{\partial r_{ij}} \frac{\mathbf{r}_{ij}}{r_{ij}} \quad (2)$$

where  $r_{ij} = \|\mathbf{r}_{ij}\|$ ,  $\phi(r_{ij})$  is the energy of the atomic ensemble. It is noted that this stress formulation is strictly valid only when a homogeneous stress state exists in the entire volume. The first term on the right-hand side of equation (1) is the kinetic-energy term, which accounts for mass transport across a fixed spatial surface. The second term comes from interatomic interactions. Based on the virial stress, some other formulations of stress in

<sup>1</sup> Center for Aerospace Research & Education  
University of California at Irvine  
5251 California Avenue, #140  
Irvine, CA 92617, USA

molecular dynamics such as BDT stress [Basinski, Duesbery, and Taylor (1971)], Lutsko stress [Lutsko (1988); Cormier, Rickman, and Delph (2001)], and mechanical stress [Cheung and Yip (1991)] are proposed. However, as pointed by Zhou (2003):

The virial, BDT, Lutsko and mechanical stresses, are not the Cauchy stresses or any other form of mechanical stresses. It must be clearly stated that the virial theorem for gas pressure is totally correct in the statistical sense. However, generalizing it to claim that mechanical stress also depends on mass transfer as well as internal interatomic force is unjustifiable and incorrect. The virial stress as defined in equation (1) has the geometric interpretation of being a measure for the momentum change in a fixed spatial region. This interpretation does not assign any physical significance to the virial stress as a possible measure of mechanical interaction. Stress is a measure of the effect of pure force on momentum change associated with a fixed amount of mass (not change in momentum contained in a spatial region). The “virial stress” is defined using a spatial cut which is fixed in space, and is related to the statistical average of the external forces between the system and a rigid non-deforming container. If the virial stress is treated as a measure of mechanical force, the balance of momentum would be violated.

However, if the kinetic-energy term in these expressions is thrown off, they reduce to Cauchy stress with a physical meaning. In this paper, we will not consider the kinetic-energy term in the formulations of BDT and Lutsko stresses. BDT stress is put forward by Basinski, Duesbery, and Taylor (1971), and is based on a volumetric partition of the homogeneous deformed bulk by extending the virial stress to one atomic volume. BDT stress is defined as:

$$\sigma^{BDT}(\mathbf{r}) = \frac{1}{2\Omega^i} \sum_{j \neq i} \mathbf{r}_{ij} \otimes \mathbf{f}_{ij} \quad (3)$$

where  $\Omega^i$  is a small volume around an atom  $i$ . Theoretically, the above definitions are valid only for a homogeneous system. In section 2, we will prove that the BDT stress in eq. (3) is equivalent to the Cauchy-Born hypothesis for homogeneous deformation. The total volume and the volume of a single atom are required in the calculation of virial and BDT stresses. The local stress proposed by Lutsko (1988) and extended by Cormier, Rickman, and Delph (2001) is based on the local stress tensor of

statistical mechanics. The Lutsko stress can be expressed as

$$\sigma^{Lutsko}(\mathbf{r}) = \frac{1}{2\Omega^{Avg}} \sum_i \sum_{j \neq i} \mathbf{r}_{ij} \otimes \mathbf{f}_{ij} l_{ij} \quad (4)$$

where  $\Omega^{Avg}$  is the averaging volume,  $l_{ij}$  ( $0 \leq l_{ij} \leq 1$ ) denotes the fraction of the length of the  $i-j$  bond lying inside the same averaging volume. For a homogeneously deformed system,  $\sigma^{Lutsko}$  approaches  $\sigma^{BDT}$  for large averaging volumes. Lutsko stress has been used to evaluate local elastic properties of grain boundaries in metals. Lutsko stress assumes that the stress state is homogenous in the averaging volume. The mechanical stress advanced by Cheung and Yip (1991) is calculated as the sum of the time rate of the change of the momentum flux and the forces divided by area across the particular surface of interest. The researchers interested in surface problems proposed the atomic stress based on force balance and the interplanar interaction, instead of the interatomic interaction [Machova (2001)].

Two years back, Atluri (2002) pointed out that in a multi-scale modeling, the forces on particles are simply different: those on an atomic particle arise due to atomic interactions, while those on a continuum particle arise due to the divergence of the stress-state around the particle, as pointed out by Navier. Thus, in any continuum-molecular dynamics equivalence, the atomic forces in MD should be made equivalent to the divergence of the stress-field in a continuum. Thus, in this paper, a new atomistic stress formulation is proposed with physical clarity, *which is appropriate for both homogeneous and inhomogeneous deformations*. In this paper, the formulation of the atomistic stress is derived directly based on the physics. Since the stress is a continuum concept, at first, the discrete atomistic force-field is smoothed by using the Smoothed Particle Hydrodynamics technique [Lucy (1977)]. Then, *by analyzing the force-state of an infinitesimal parallelepiped at point  $\mathbf{r}$ , a relationship between the stress and the atomistic force can be developed*. This formulation is useful and convenient for computational applications, and satisfies the conservation of linear momentum. The results are compared with the BDT and Lutsko stress. Based on the new formulation of the atomistic stress, an equivalent continuum for molecular system is defined, which conserves the momentum and mass of the discrete atomic system. The smoothed parti-

cle hydrodynamics (SPH) technique is employed to make the discrete atomic system to be an equivalent continuum system.

Smoothed Particle Hydrodynamics (SPH) has been introduced by Lucy (1977) to study self-gravitating fluids. The idea of the method is to consider the fluid as an ensemble of (smooth) particles. Each particle has a kernel which represents its mass distribution, and carries information on the average values of dynamical and thermodynamical quantities, as well as on their gradients. After then, it has become a widely used tool in astrophysics [Monaghan (1992)]. In astrophysics, the system is discrete. By means of a localized kernel function, a local continuous field is generated to avoid singularity. SPH provides a systematic method to obtain these quantities based on a “smoothed” estimate over neighboring particles. The idea for estimating the quantities using a kernel is at the heart of the SPH technique. We can employ this idea to obtain any physical quantity of a particle using a kernel-weighted estimate over neighboring particles. A primary reason for the popularity of SPH, despite its shortcomings, is its overall simplicity and ease of use. Due to its distinct advantage, the SPH method was widely adopted as one of the efficient computational techniques to solve applied mechanics problems.

## 2 The derivation of the stress tensor

As we discussed in the previous section, there are lots of atomistic stress tensors in volume-averaged form. Here, we will give an atomistic tensor in a nonvolume-averaged form with physical clarity.

Consider a discrete atomic system, wherein the interatomic force on atom  $i$  is  $\mathbf{f}_i$ . As well known, the concept of stress is a continuum concept. Hence, to derive the atomistic stress, at first, we should make the discrete atomic system to be an equivalent continuum system. The idea of the SPH method is employed here to smooth the discrete atomistic force field. SPH is very popular in astrophysics, where the real physical system is discrete. In order to avoid singularity, a local continuous field is generated by introducing a localized kernel function, which can serve as a smoothing interpolation field. The physical meaning of the kernel function can be interpreted as the probability of a particle’s position, as in a probabilistic method. The SPH is only a smoothing technique. In this paper, we will smooth the discrete atomic force field at first. In this case, the force per unit volume,

i.e. the force density  $\mathbf{g}(\mathbf{r})$ , can be obtained by means of the SPH, as

$$\mathbf{g}(\mathbf{r}) = \sum_i \mathbf{f}_i w(\mathbf{r} - \mathbf{r}_i, h) \quad (5)$$

where  $\mathbf{f}_i$  is the force on atom  $i$ ,  $w(\mathbf{x}, h)$  is the smooth kernel function, and the summation is over all the particles. Notice that we do not have to divide by volume, because the kernel is normalized to unite volume [ $w(\mathbf{x}, h)$  has the units of inverse volume, as in eq. (6)], the division by volume is effectively incorporate into  $w(\mathbf{x}, h)$ . A common choice for a kernel is a Gaussian, namely

$$w(\mathbf{x}, h) = \frac{1}{(\sqrt{\pi}h)^d} \exp\left(-\frac{\mathbf{x}^2}{h^2}\right) \quad (6)$$

where  $d$  is the number of spatial dimensions in the problem, and  $h$  is the smoothing length. The kernel is normalized such that its integral is unity, i.e.

$$\int w(\mathbf{x}, h) d\mathbf{x} = 1 \quad (7)$$

where the integration is over all the space. In general, the kernel function has to be a compact-supported positive function, and its integral is unity. Moreover, as  $h \rightarrow 0$ , the kernel function should approach to  $\delta(\mathbf{x})$ . It is important to realize that although the summations are formally over all the particles, only a small number actually contribute, because  $w(\mathbf{x}, h)$  can be chosen so that it falls off rapidly for appropriate  $h$ . Other commonly used compact-supported kernel functions include the cubic spline and the quartic spline [Atluri (2004), Atluri and Shen (2002)], in these cases, the smoothing length becomes the radius of the compact support.

Now, in the equivalent continuum system, we consider an infinitesimal parallelepiped at point  $\mathbf{r}$  with surfaces parallel to the coordinate planes (as shown in Fig. 1). In the infinitesimal volume, the volume of the infinitesimal parallelepiped is  $dv = dx_1 dx_2 dx_3$ , and the Cauchy stress at point  $\mathbf{r}$  is  $\boldsymbol{\sigma}(\mathbf{r})$ , then, the resultant forces at point  $\mathbf{r}$  in  $x_i$  direction are:  $\sigma_{ji,j} dv$ . On the other hand, from eq. (5), we can get the force density at point  $\mathbf{r}$ ,  $\mathbf{g}(\mathbf{r})$ , of the equivalent continuum system. Hence, the resultant forces at point  $\mathbf{r}$  should be equal to  $\mathbf{g}(\mathbf{r}) dv$ . Thus, we have the following

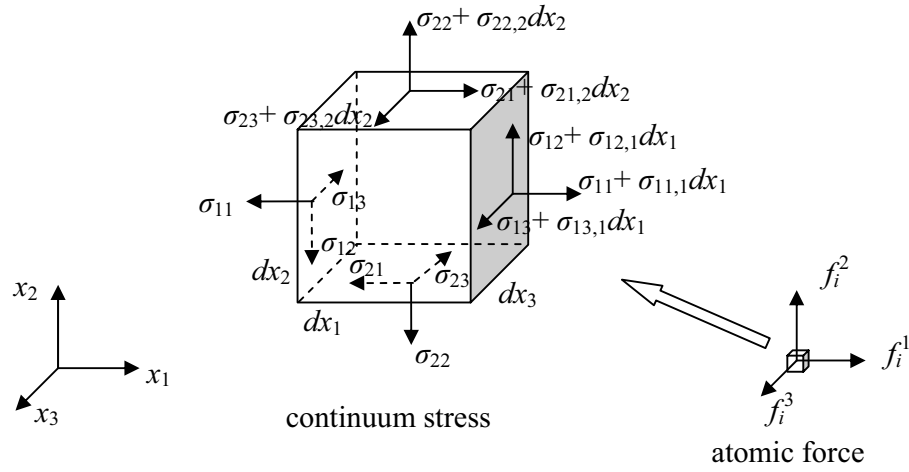


**Figure 1** : The definition of the stress tensor

equation to relate the equivalent-continuum stress and the atomic force,

$$\text{div} \boldsymbol{\sigma}(\mathbf{r}) dv = \mathbf{g}(\mathbf{r}) dv$$

Then, we have

$$\text{div} \boldsymbol{\sigma}(\mathbf{r}) = \sum_i \mathbf{f}_i w(\mathbf{r} - \mathbf{r}_i, h)$$

Defining the Fourier transform of a function  $F(\mathbf{r})$  as

$$\hat{F}(\mathbf{s}) = \int_V F(\mathbf{r}) e^{i\mathbf{s} \cdot \mathbf{r}} dV \quad (10)$$

and the inverse transform as

$$F(\mathbf{r}) = \frac{1}{(2\pi)^3} \int_{V^s} \hat{F}(\mathbf{s}) e^{-i\mathbf{s} \cdot \mathbf{r}} dV^s$$

where  $V^s$  is the transformed space. By using the Fourier transformation, equation (9) can be written as

$$\begin{aligned} i\mathbf{s} \cdot \hat{\boldsymbol{\sigma}}(\mathbf{s}) &= - \sum_i \mathbf{f}_i \hat{w}(\mathbf{s}) e^{i\mathbf{s} \cdot \mathbf{r}_i} \\ (8) \quad &= - \sum_i \sum_{j \neq i} \mathbf{f}_{ij} e^{i\mathbf{s} \cdot \mathbf{r}_i} \hat{w}(\mathbf{s}) \\ &= - \frac{1}{2} \sum_i \sum_{j \neq i} \left[ \mathbf{f}_{ij} e^{i\mathbf{s} \cdot \mathbf{r}_i} + \mathbf{f}_{ji} e^{i\mathbf{s} \cdot \mathbf{r}_j} \right] \hat{w}(\mathbf{s}) \\ (9) \quad &= i\mathbf{s} \cdot \frac{1}{2} \sum_i \sum_{j \neq i} \mathbf{r}_{ij} \otimes \mathbf{f}_{ij} \frac{e^{i\mathbf{s} \cdot \mathbf{r}_i} - e^{i\mathbf{s} \cdot \mathbf{r}_j}}{i\mathbf{s} \cdot \mathbf{r}_{ji}} \hat{w}(\mathbf{s}) \end{aligned} \quad (12)$$

Here, we use the following equation to deriving eq. (12),

$$\begin{aligned} &\int_V [\nabla \cdot \boldsymbol{\sigma}(\mathbf{r})] e^{i\mathbf{s} \cdot \mathbf{r}} dV \\ &= \int_V \left[ \nabla \cdot (e^{i\mathbf{s} \cdot \mathbf{r}} \boldsymbol{\sigma}) - \nabla (e^{i\mathbf{s} \cdot \mathbf{r}}) \cdot \boldsymbol{\sigma} \right] dV \\ (11) \quad &= \int_V \left[ \nabla \cdot (e^{i\mathbf{s} \cdot \mathbf{r}} \boldsymbol{\sigma}) - i\mathbf{s} \cdot (e^{i\mathbf{s} \cdot \mathbf{r}} \boldsymbol{\sigma}) \right] dV \\ &= \int_{\Gamma} \mathbf{n} \cdot (e^{i\mathbf{s} \cdot \mathbf{r}} \boldsymbol{\sigma}) d\Gamma - i\mathbf{s} \cdot \int_V e^{i\mathbf{s} \cdot \mathbf{r}} \boldsymbol{\sigma}(\mathbf{r}) dV \\ &= -i\mathbf{s} \cdot \hat{\boldsymbol{\sigma}}(\mathbf{s}) \end{aligned}$$

Noting that

$$\frac{e^{\mathbf{i}\mathbf{s}\cdot\mathbf{r}_i} - e^{\mathbf{i}\mathbf{s}\cdot\mathbf{r}_j}}{\mathbf{i}\mathbf{s}\cdot\mathbf{r}_{ji}} = e^{\mathbf{i}\mathbf{s}\cdot\mathbf{r}_j} \int_0^1 e^{(\mathbf{i}\mathbf{s}\cdot\mathbf{r}_{ji})c} dc \quad (13)$$

By means of eq. (13) and carrying out the inverse transform of eq. (12), the Cauchy stress of the atomic level can be obtained as

$$\begin{aligned} \boldsymbol{\sigma}(\mathbf{r}) &= \frac{1}{2} \sum_i \sum_{j \neq i} \mathbf{r}_{ij} \otimes \mathbf{f}_{ij} \\ &\left\{ \frac{1}{(2\pi)^3} \int_{V^s} e^{\mathbf{i}\mathbf{s}\cdot\mathbf{r}_j} \int_0^1 e^{(\mathbf{i}\mathbf{s}\cdot\mathbf{r}_{ji})c} dc \hat{w}(\mathbf{s}) e^{-\mathbf{i}\mathbf{s}\cdot\mathbf{r}} dV^s \right\} \\ &= \frac{1}{2} \sum_i \sum_{j \neq i} \mathbf{r}_{ij} \otimes \mathbf{f}_{ij} \\ &\left\{ \int_0^1 \left[ \frac{1}{(2\pi)^3} \int_{V^s} \hat{w}(\mathbf{s}) e^{\mathbf{i}\mathbf{s}\cdot(\mathbf{r}_{ji}c + \mathbf{r}_j - \mathbf{r})} dV^s \right] dc \right\} \\ &= \frac{1}{2} \sum_i \sum_{j \neq i} \mathbf{r}_{ij} \otimes \mathbf{f}_{ij} \int_0^1 w[\mathbf{r} - (\mathbf{r}_{ji}c + \mathbf{r}_j)] dc \end{aligned} \quad (14)$$

As  $h \rightarrow 0$ , the kernel function  $w(\mathbf{x}, h)$  should approach to  $\delta(\mathbf{x})$ , and eq. (14) will be reduced to

$$\boldsymbol{\sigma}(\mathbf{r}) = \frac{1}{2} \sum_i \sum_{j \neq i} \mathbf{r}_{ij} \otimes \mathbf{f}_{ij} \delta[\mathbf{r} - (\mathbf{r}_{ji}k + \mathbf{r}_j)] \quad (15)$$

where  $0 \leq k \leq 1$ .  $\delta[\mathbf{r} - (\mathbf{r}_{ji}k + \mathbf{r}_j)]$  is singular along the line segment between  $\mathbf{r}_i$  and  $\mathbf{r}_j$ , and is zero elsewhere. This singular expression can be used to obtain the average stress over any region of an atomistic ensemble, *i.e.* the Lutsko stress. For a region with volume  $\Omega^{Avg}$ , by integrating eq. (15), and divided by  $\Omega^{Avg}$ , eq. (4) is derived. Moreover, if one thinks that the singular atomic stress exists only at atomic positions, the physically significant interpretation of eq. (15) in the context of discrete atomic system is

$$\boldsymbol{\sigma}(\mathbf{r}) = \frac{1}{2} \sum_i \sum_{j \neq i} \mathbf{r}_{ij} \otimes \mathbf{f}_{ij} \delta(\mathbf{r} - \mathbf{r}_i) \quad (16)$$

This singular expression can be used to obtain the average stress over any region of an atomistic ensemble. For

a region with volume  $\Omega^i$  around atom  $i$  at the current configuration, the average stress can be derived as the BDT stress eq. (3). Equations (15) and (16) are useless for computational applications, but the coarse-grained average stress can be defined by integrating equations (15) and (16) over an appropriate averaging volume; while the stress formulation (14) is useful for computational applications. The virial, BDT and Lutsko stresses smear the effect of inhomogeneities due to volume averaging. The calculation of the Cauchy stress in eq. (14) does not involve *ad hoc* specification of a relevant volume, while the evaluation of the BDT stress (or the Cauchy-Born rule) for any set of atoms requires the identification of a proper volume whose extent is not always obvious: in atomic ensembles with irregular atom arrangement, the identification of this volume can be ambiguous.

For the finite deformation, we can also derive the first Piola-Kirchhoff stress  $\mathbf{T}$ , based on the initial configuration. We denote the initial position of the atom  $i$  as  $\mathbf{R}_i$ , then, in initial configuration, eq. (9) can be rewritten as

$$\text{div} \mathbf{T}(\mathbf{R}) = \sum_i \mathbf{f}_i w(\mathbf{R} - \mathbf{R}_i, h) \quad (17)$$

Similarly, the first Piola-Kirchhoff stress tensor can be obtained as

$$\mathbf{T}(\mathbf{R}) = \frac{1}{2} \sum_i \sum_{j \neq i} \mathbf{R}_{ij} \otimes \mathbf{f}_{ij} \int_0^1 w[\mathbf{R} - (\mathbf{R}_{ji}c + \mathbf{R}_j)] dc \quad (18)$$

As  $h \rightarrow 0$ , eq. (18) becomes

$$\mathbf{T}(\mathbf{R}) = \frac{1}{2} \sum_i \sum_{j \neq i} \mathbf{R}_{ij} \otimes \mathbf{f}_{ij} \delta[\mathbf{R} - (\mathbf{R}_{ji}c + \mathbf{R}_j)] \quad (19)$$

with  $0 \leq c \leq 1$ . For the discrete atomic system, the physically significant solution of eq. (19) is

$$\mathbf{T}(\mathbf{R}) = \frac{1}{2} \sum_i \sum_{j \neq i} \mathbf{R}_{ij} \otimes \mathbf{f}_{ij} \delta(\mathbf{R} - \mathbf{R}_i) \quad (20)$$

This singular expression can be used to obtain the average stress over any region of an atomistic ensemble. For a region with volume  $\Omega_0^i$  around atom  $i$  at initial configuration, the average stress is

$$\bar{\mathbf{T}}(\mathbf{R}) = \frac{1}{2\Omega_0^i} \sum_i \sum_{j \neq i} \mathbf{R}_{ij} \otimes \mathbf{f}_{ij} \quad (21)$$

Recognizing the relationship between stress, deformation and internal strain energy, Born and Huang (1954) used the Cauchy-Born hypothesis to evaluate the stress in lattices for homogeneous deformation. In that method, the gradient of the deformation  $\mathbf{F}$  is defined as

$$\mathbf{r}_{ij} = \mathbf{F}\mathbf{R}_{ij} \quad (22)$$

The strain density is  $W/\Omega_0^i$ , where  $W$  is the interatomic potential of the atomic volume  $\Omega_0^i$ . Then, the stress can be derived as

$$\begin{aligned} \bar{\mathbf{T}}(\mathbf{R}) &= \frac{1}{\Omega_0^i} \frac{\partial W}{\partial \mathbf{F}} \\ &= \frac{1}{2\Omega_0^i} \sum_i \sum_{j \neq i} \frac{\partial W}{\partial \mathbf{r}_{ij}} \frac{\partial \mathbf{r}_{ij}}{\partial \mathbf{F}} \\ &= \frac{1}{2\Omega_0^i} \sum_i \sum_{j \neq i} \mathbf{R}_{ij} \otimes \mathbf{f}_{ij} \end{aligned} \quad (23)$$

Here, we employed  $\partial \mathbf{r}_{ij} / \partial \mathbf{F} = \mathbf{R}_{ij}$  in derivation of eq. (23). From the finite deformation theory, we have

$$\boldsymbol{\sigma} = J\mathbf{F}\bar{\mathbf{T}} \quad (24)$$

where  $J$  is the Jacobian. Hence, by means of eq. (24), from eq. (23), we can get the Cauchy stress

$$\begin{aligned} \bar{\boldsymbol{\sigma}}(\mathbf{r}) &= J\mathbf{F}\bar{\mathbf{T}}(\mathbf{R}) \\ &= \frac{J}{2\Omega_0^i} \sum_i \sum_{j \neq i} \mathbf{F}\mathbf{R}_{ij} \otimes \mathbf{f}_{ij} \\ &= \frac{1}{2\Omega^i} \sum_i \sum_{j \neq i} \mathbf{r}_{ij} \otimes \mathbf{f}_{ij} \end{aligned} \quad (25)$$

If  $\Omega^i$  is taken to be the total volume of the system, this equation becomes the virial stress; if  $\Omega^i$  is taken to be a small volume around an atom  $i$ , this equation becomes the BDT stress. Eq. (25) confirms that the BDT stress

[or the second term of virial stress (1)] is identical to that based on the Cauchy-Born hypothesis, in homogeneous deformation. This also implies that the kinetic-energy term of eq. (1) should not be included in the expression of the atomic stress. However, there are a lot of limits in the Cauchy-Born hypothesis [Atluri (2004), Shen and Atluri (2004a, b)], while there are no limits on the formulation in (14).

It is important to point out that the derivation here is also appropriate for system with body forces, which can result from non-local effects of atoms or agents external to the system under consideration. The result would be the same, which will be shown in the next section.

### 3 Equivalent continuum for atomic system

It is important to know the relationships between the microscopic quantities of atoms, and the macroscopic quantities of continua, for nanoscale characterizations of material behavior. Molecular dynamics and continuum mechanics are on the opposite ends of the temporal and spatial scale spectrum, and consist of highly developed and reliable modeling methods. Continuum mechanics methods predict the macroscopic mechanical behavior of materials idealized as continuous media, based on known constitutive relationships of the bulk material, while molecular dynamic models predict molecular properties based on known quantum interactions. Each has its own advantages and limitations. Continuum analyses are appropriate only for a large enough system. Alternative to continuum analysis, the atomistic modeling and simulation calculates individual atoms explicitly, and follows them during their dynamic evolution. However, both continuum mechanics and molecular dynamics obey the same fundamental laws, including Newton's laws of motion and conservation of mass. These fundamental laws provide a bridge to link continuum mechanics and molecular dynamics. If a continuum is equivalent to a MD system, in addition that it contains the same amount of mass as the particle system, the Newton's laws of motion of the continuum system must be derived from the Newton's laws of motion of its corresponding MD system, vice versa, i.e. they are equivalent. The equivalent continuum development offers a high degree of fidelity to the discrete description.

An equivalent continuum is constructed by using the principle of the virtual work, and in conjunction with finite element interpolations in Zhou (2003), Zhou and

McDowell (2002); However, their formulations are very complicated. Their development is computationally intensive due to the construction of the finite elements. The determined fields are piecewise continuous, even for homogenous deformation. Moreover, the defined continuum deformation fields lack the consistency with the continuum differential requirement about the strain-displacement relations. In this section, an equivalent continuum is defined for molecular dynamics (MD) particle systems, based on the definition of atomistic stress (14) and in conjunction with the SPH technique. This process is simple and easy to implement, and the fields are with high-order continuity.

For the MD system, the Newton's laws of motion for each atom  $i$ , can be written as

$$\mathbf{f}_i = m_i \ddot{\mathbf{u}}_i \quad (26)$$

The force on atom  $i$  due to atoms or agents that are external to the system under consideration is denoted as  $\mathbf{f}_i^b$ , the total force on atom  $i$  is

$$\mathbf{f}_i = \sum_{j \neq i} \mathbf{f}_{ij} + \mathbf{f}_i^b = \mathbf{f}_i^s + \mathbf{f}_i^b \quad (27)$$

It is noted that  $\mathbf{f}_i^b$  also includes the non-local interactions.

Let  $\mathbf{b}$  denote the density of the continuum body force, and let  $\rho$  represent the density of the continuum mass. In this analysis, all the quantities are evaluated on the current configuration. Similar to the analysis in section 2, the resultant forces at point  $\mathbf{r}$  in the equivalent continuum system are:  $\text{div}\boldsymbol{\sigma} + \mathbf{b}$  then we have

$$\begin{aligned} \text{div}\boldsymbol{\sigma} + \mathbf{b} &= \sum_i \mathbf{f}_i w(\mathbf{r} - \mathbf{r}_i, h) \\ &= \sum_i \mathbf{f}_i^s w(\mathbf{r} - \mathbf{r}_i, h) + \sum_i \mathbf{f}_i^b w(\mathbf{r} - \mathbf{r}_i, h) \end{aligned} \quad (28)$$

Thus, the density of the continuum body force can be obtained as

$$\mathbf{b}(\mathbf{r}) = \sum_i \mathbf{f}_i^b w(\mathbf{r} - \mathbf{r}_i, h) \quad (29)$$

The associations of internal forces to the internal stress only, and the external force to the body force only, are

strictly required by the balance of momentum. And the stress is still expressed as in eq. (14). The density of the continuum mass can be expressed as

$$\rho(\mathbf{r}) = \sum_i m_i w(\mathbf{r} - \mathbf{r}_i, h) \quad (30)$$

Integrating eq. (30), and by means of eq. (7), we can confirm the conservation of the mass, *i.e.*  $\int \rho(\mathbf{r}) d\mathbf{r} = \sum_i m_i$ .

Substituting eq. (26) into eq. (28), the following equation can be derived

$$\text{div}\boldsymbol{\sigma}(\mathbf{r}) + \mathbf{b}(\mathbf{r}) = \sum_i m_i \ddot{\mathbf{u}}_i w(\mathbf{r} - \mathbf{r}_i, h) \quad (31)$$

On the other hand, the Newton's laws of motion for the equivalent continuum are

$$\text{div}\boldsymbol{\sigma}(\mathbf{r}) + \mathbf{b}(\mathbf{r}) = \rho(\mathbf{r}) \ddot{\mathbf{u}}(\mathbf{r}) \quad (32)$$

Then, the acceleration field  $\ddot{\mathbf{u}}$  of the equivalent continuum can be obtained as

$$\ddot{\mathbf{u}}(\mathbf{r}) = \frac{\sum_i m_i \ddot{\mathbf{u}}_i w(\mathbf{r} - \mathbf{r}_i, h)}{\rho(\mathbf{r})} = \frac{\sum_i m_i \ddot{\mathbf{u}}_i w(\mathbf{r} - \mathbf{r}_i, h)}{\sum_i m_i w(\mathbf{r} - \mathbf{r}_i, h)} \quad (33)$$

Thus, the equivalent continuum is constructed from the discrete MD system, which preserves the momentum, and conserves the mass. Moreover, from the Newton's laws of motion for the equivalent continuum, eq. (32), the Newton's laws of motion for each atom  $i$ , eq. (26), can also be derived.

A reinterpretation of the discrete atomistic force and deformation is reflected by the continuum field defined here, which maintains the physical effects of the atomistic system. This development provides a systematic approach to the continuum analysis of the discrete atomic system. It can also be applied to multiscale modeling of material behavior which combines both MD and continuum descriptions in the development of constitutive relations at different scales.

#### 4 Numerical examples

At first, we apply the stress formulation (14) to the case of a homogeneously deformed cubic, crystalline solid. Similar to Cormier, Rickman, and Delph (2001), we considered a collection of 2048 atoms, initially on the sites of a face centered cubic (fcc) lattice and confined to a periodic cubic simulation cell at temperature  $T=0$ . Employed is a modified (truncated) Lennard-Jones potential [Broughton and Gilmer (1983)],

$$\phi(r) = \begin{cases} 4\epsilon \left[ \left( \frac{\sigma}{r} \right)^{12} - \left( \frac{\sigma}{r} \right)^6 \right] + C_1, & r \leq 2.3\sigma \\ C_2 \left( \frac{\sigma}{r} \right)^{12} + C_3 \left( \frac{\sigma}{r} \right)^6 + C_4 \left( \frac{r}{\sigma} \right)^6 + C_5, & 2.3\sigma < r < 2.5\sigma \\ 0, & r \geq 2.5\sigma \end{cases} \quad (34)$$

with

$$C_1 = 0.016132\epsilon, C_2 = 3.1366 \times 10^3\epsilon, C_3 = -68.069\epsilon, \\ C_4 = -0.083312\epsilon, C_5 = 0.74689\epsilon$$

where  $\epsilon$  and  $\sigma$  are the energy and length parameters, respectively (not to be confused with the stress and strain). The perfect fcc crystal has a lattice parameter of  $a_0 = 1.550512\sigma$  and the corresponding energy per atom  $7.45\epsilon$ . The deformation can be imposed by simply changing the lattice parameter. The elastic constants can be deduced from the quadratic dependence of energy on strain, by using the Cauchy-Born hypothesis. We consider the simple case of uniform applied deformations, with corresponding strain tensor components  $\epsilon_{11} = \epsilon_{22} = \epsilon_{33} = 0.002$ , the remaining components are 0. In this case, the BDT stress (or the stress from Cauchy-Born hypothesis) is equal to the bulk stress. In the calculations, the kernel function  $w(\mathbf{x}, h)$  is truncated, by a truncated radius  $r_w$ , beyond which it falls off rapidly to zero for appropriate  $h$ , as

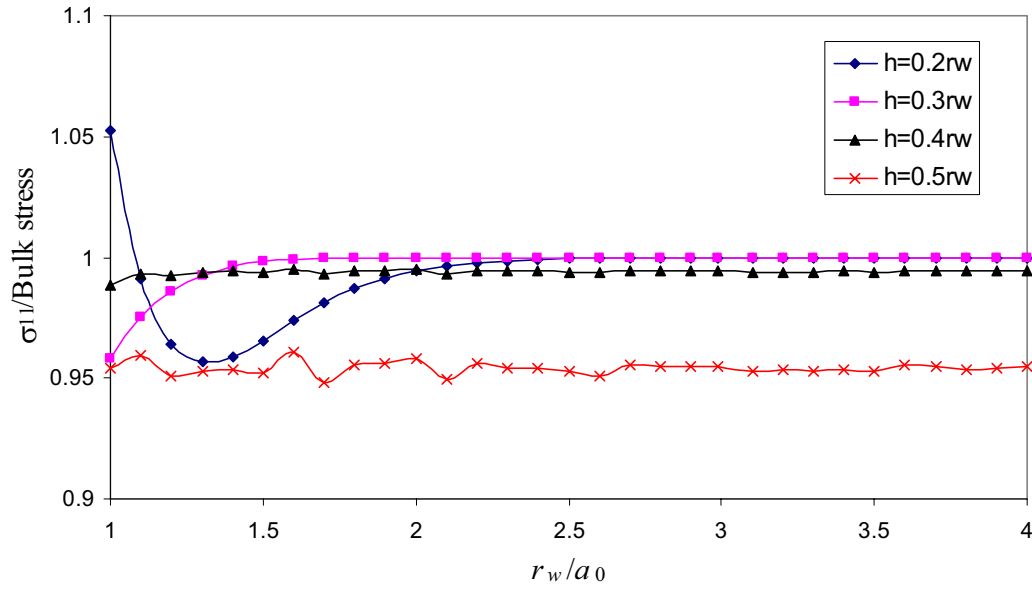
$$w(\mathbf{x}, h) = \begin{cases} \frac{1}{(\sqrt{\pi}h)^d} \exp\left(-\frac{\mathbf{x}^2}{h^2}\right), & |\mathbf{x}| \leq r_w \\ 0, & |\mathbf{x}| > r_w \end{cases} \quad (35)$$

Thus, the kernel function becomes compact-supported. The studies of SPH show that  $h = 0.4r_w$  or so give very

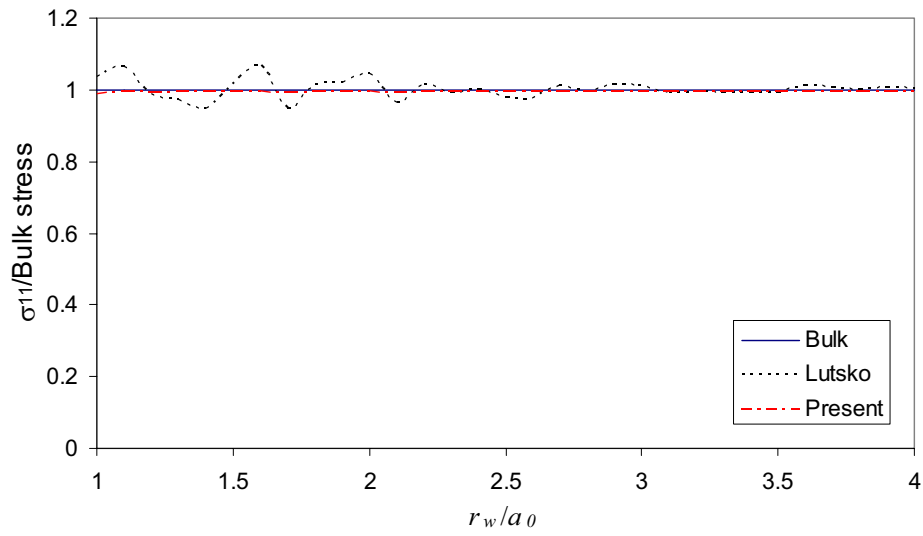
good results. Our numerical tests also confirm this statement. Fig.2 shows the effects of the ratio  $h/r_w$  on the stress value, the stress values of the formulation (14) are normalized by the bulk stress, which is equal to the BDT stress (or the stress from Cauchy-Born hypothesis) here. It can be seen that a larger  $r_w$  is needed for  $h = 0.2r_w$ , and the error is a little bigger for  $h = 0.5r_w$ . Hence, in this paper, we take  $h = 0.4r_w$  for all the calculations. For the purpose of comparison, we also compute the Lutsko stress. For Lutsko stress, the radius of the spherical averaging volume  $\Omega^{Avg}$  is taken to be  $r_w$ .

Fig. 3 shows the magnitude of the stress  $\sigma_{11}$  at an observation point versus the radius  $r_w$ , where the stresses are normalized by the bulk stress, which is equal to the BDT stress. The results of the present formulation are almost overlapped with the bulk stress value, while the Lutsko stress value oscillates around the bulk stress value. The Lutsko stress value converges to the bulk stress value for sufficiently large radii. However, the larger radius is computational costly. Hence, in the following calculations, we choose the radius  $r_w = 1.5a_0$ , at which the Lutsko stress value agrees with the bulk stress value very well in Fig. 3. Fig. 4 depicts the normalized stress  $\sigma_{11}$  at different observation points along the closed-packed [110] direction. This figure also shows the results of the present formulation agree with the bulk stress value very well, and the Lutsko stress value oscillates around the bulk stress value. From these figures, we can find that the present stress formulation (14) is very robust and accurate, while the accuracy of Lutsko stress depends on the radius of the spherical averaging volume and the position of the observation point.

Now, we apply the stress formulation (14) to the case of inhomogeneous deformation. A “big” atom replaces the atom at the origin of the previous fcc crystalline solid. The inhomogeneous elastic fields will arise due to the presence of the “big” atom. For the “big” atom, the energy and length parameters  $\epsilon^b$  and  $\sigma^b$  are assumed to be  $\epsilon^b = 1.2\epsilon$  and  $\sigma^b = 1.2\sigma$ , respectively. We employed the modified Newton-Raphson method to solve equations:  $\mathbf{f}_i(\mathbf{r}) = \mathbf{0}$ , to determine the equilibrium configuration (i.e. the minimum energy configuration) for this defected structure. This problem is similar to the inclusion problem in a continuum. As is well known, the continuum elastic field of an inclusion at the origin falls off with distance  $r$  from the origin as  $1/r^2$ , and the corresponding elastic stress field falls off with dis-



**Figure 2** : The effect of the ratio  $h/r_w$  on stress value for uniform deformation



**Figure 3** : The effect of the radius  $r_w$  on stress value for uniform deformation

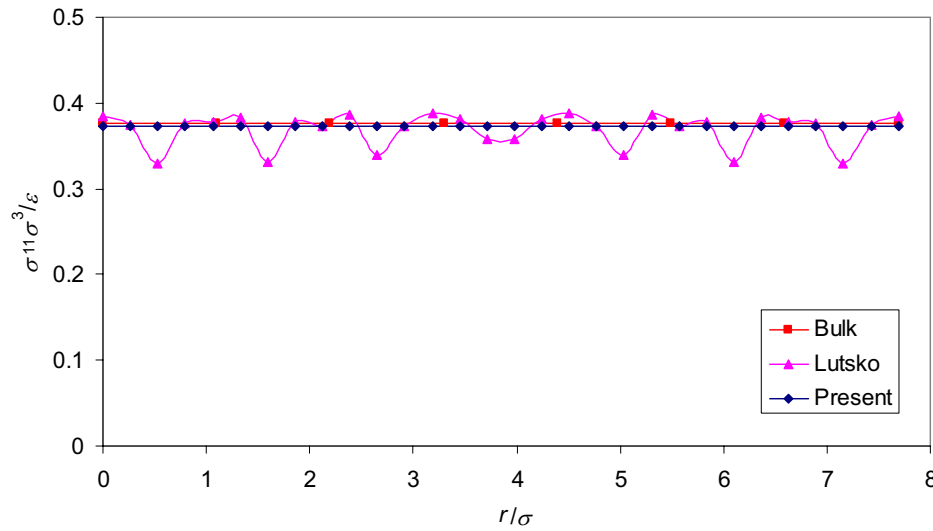


**Figure 4 :** The stress values at different position along [110] direction

tance  $r$  from the origin as  $1/r^3$  [Li, Shen, Han and Atluri (2003)]. Fig. 5 depicts the radial component of the discrete atomic displacement field in the close-packed [110] direction versus  $(\sigma/r)^2$ . We can find that the atomic displacement demonstrates the expected  $1/r^2$  behavior when  $(\sigma/r)^2 < 0.0924$ , i.e.  $r/\sigma > 1.5 \cdot \sqrt{2}a_0/\sigma = 3.288$  (i.e., beyond 1.5 times the lattice parameters from the origin). This is because the cut-off radius of the Lennard-Jones potential for the “big” atom is  $r_{cut} = 2.5\sigma^b = 3\sigma$ , and  $3.288\sigma$  is the nearest atomic site to  $r_{cut}$ , the boundary of the inclusion should be around this value.

Figs. 6, 7 and 8, respectively, show the variation of the normalized stress components  $\sigma_{11}$ ,  $\sigma_{12}$  and  $\sigma_{33}$  in the [110] direction versus  $(\sigma/r)^3$ . In these figures, the continuum solutions are plotted only for  $r/\sigma > 3.288$  (i.e.  $(\sigma/r)^3 < 0.0028$ ) due to the reason that we just discussed in the previous paragraph. The continuum solution is obtained by an approximate method. The displacement gradient is approximated from Fig. 5 at first, then using the elastic constants of the homogenous perfect fcc crystalline solid [Cormier, Rickman, and Delph (2001)] and the elastic constitutive relationship (Hook’s Law), the continuum elastic stress can be determined. For the purpose of comparison, we also plot here the corresponding values of the Lutsko and BDT stresses. For the BDT stress, we only calculate the values at the

atomic sites. Both of the Lutsko and BDT stress values are far away from the continuum solution. It can be seen that the stress values of the present formulation (14) agree with the continuum results very well beyond 2 times the lattice parameters from the origin (the “big atom”):  $(\sigma/r)^3 \leq 0.0017$  (i.e.,  $r/\sigma > 2 \cdot \sqrt{2}a_0/\sigma = 4.385$ ), which fall off with distance  $r$  from the origin as  $1/r^3$ . In range of 1.5-2 times the lattice parameters (i.e.  $0.0017 < (\sigma/r)^3 < 0.0028$ ), the stress values of the present formulation (14) deviate a little from the  $(\sigma/r)^3$  behavior. The deviations are due to the deviation of the elastic constants from those of the perfect fcc crystalline in this range [actually, in this range, the displacement shown in Fig. 5 already deviates from the  $(\sigma/r)^2$  behavior]. In the range of 0-1.5 times the lattice parameters, comparison with continuum theory is impossible, since the elastic constants cannot be well defined. However, the trend of the stress value of the present formulation (14) in this range is consistent with that of the displacements shown in Fig. 5. The results of the Lutsko stress show bad shapes, perhaps a larger averaging volume is required to improve its performance, even for homogeneous deformations. The requirement of a very large averaging volume inherently decreases its use for computational applications. Since the BDT stress is strictly valid only for homogeneous deformations, it is not surprising that it should not perform

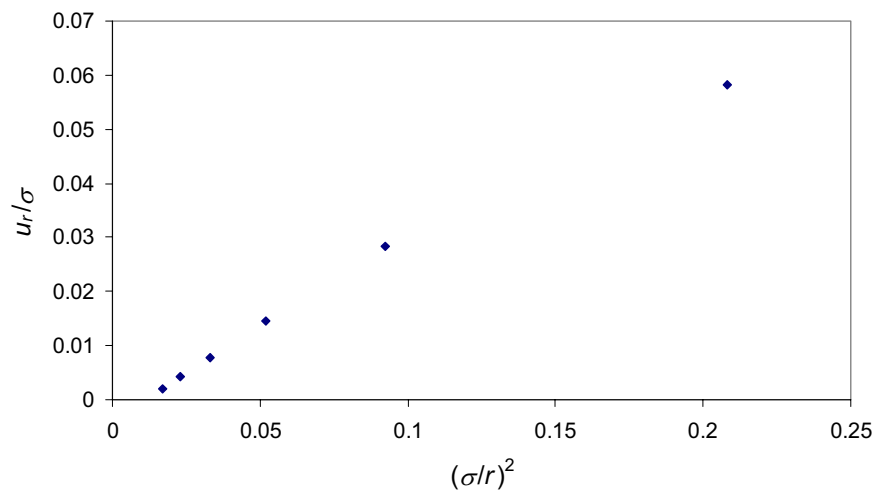


**Figure 5 :** Radial component of the displacement field in [110] direction

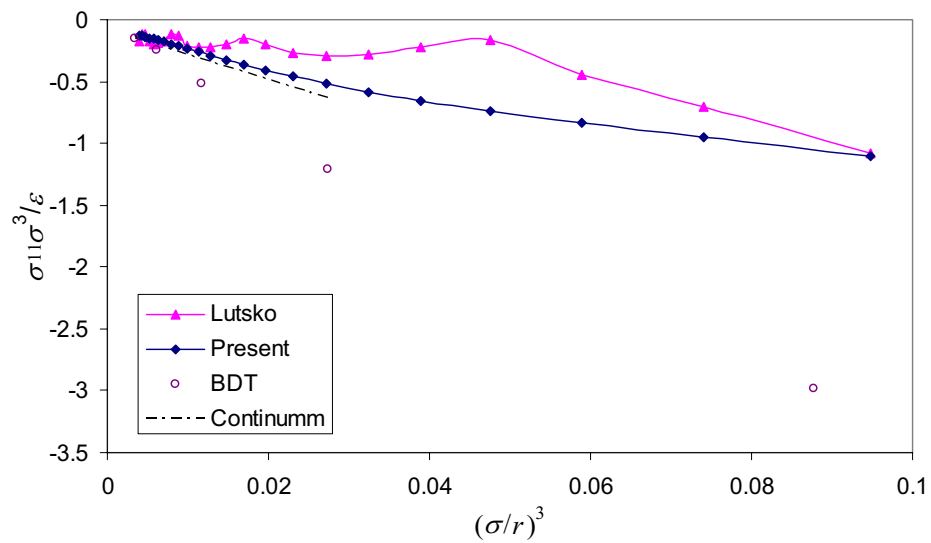


**Figure 6 :**  $\sigma_{11}$  values for inclusion in [110] direction

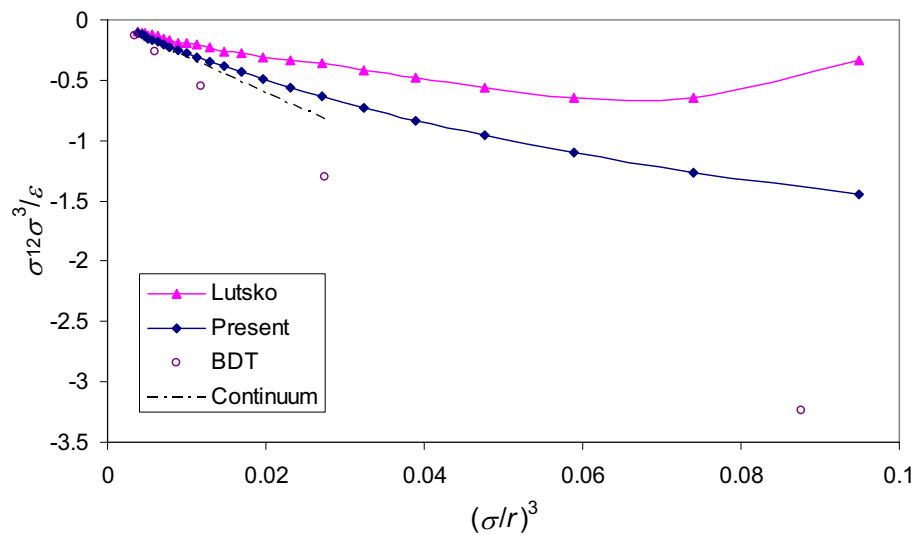


**Figure 7 :**  $\sigma_{12}$  values for inclusion in [110] direction

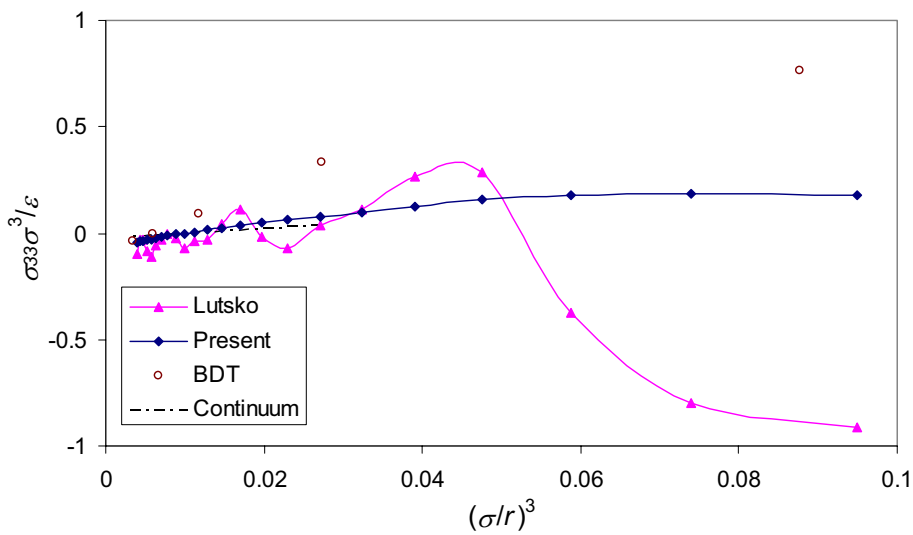


**Figure 8 :**  $\sigma_{33}$  values for inclusion in [110] direction

well in this case.

## 5 Conclusions

An atomistic level stress tensor is proposed with physical clarity, based on the SPH method. This stress tensor rigorously satisfies the conservation of linear momentum, and is appropriate for both homogeneous and inhomogeneous deformations. It is in a nonvolume-average form, and thus does not involve *ad hoc* specification of a relevant volume, whose extent is not always obvious: in atomic ensembles with irregular atom arrangement, the identification of this volume can be ambiguous. In contrast to this developed atomistic level stress tensor, other widely used stress tensors in atomistic analysis are in a volume-average form, and do not satisfy the conservation of linear momentum. The formulation is easy to implement, and is validated for both the homogeneous deformation, as well as defected crystalline solids. The numerical results show that the present formulation is very robust and accurate, and is superior to BDT and Lutsko stress formulations. Our numerical results also confirm that the BDT stress tensor is only appropriate for the homogeneously deformed system. The averaging volume and the location affect the Lutsko stress very much. A large averaging volume is required to get a stable value of the Lutsko stress, even for homogeneous deformations.

An equivalent continuum is also defined for molecular dynamics system, based on the developed definition of atomistic stress and in conjunction with the SPH technique. The process is simple and easy to implement, and the fields are with high-order continuity. This equivalent continuum is a reinterpretation of the discrete atomistic force and deformation fields of the MD system. This development provides a systematic approach to the continuum analysis of the discrete atomic system. It can also be applied to multiscale modeling of material behavior which combines both the MD and continuum descriptions in the development of constitutive relations at different scales.

The atomistic stress tensor derived in this paper will play an important role in the multiscale simulation [Srivastava, Atluri (2002a, b); Garikipati (2002); Ghoniem, Cho (2002)] and in molecular dynamics. The idea cannot be limited to mechanical properties, for it can be easily applied to multiscale modeling, directly linking the electronic structure level to the continuum level. A multiscale simulation based on this stress formulation is presented

in another companion paper. It is also noted that the use of the SPH approximation is not central to the idea of continuum-stress presented here. Alternate approximation will be discussed elsewhere.

**Acknowledgement:** This work was supported by the U. S. Army Research Office, and the U. S. Army Research Laboratory, under a cooperative research agreement with the University of California at Irvine. The Cognizant Program Official at the U. S. Army Research Labs is Dr. R. Namburu, and that at ARO is Dr. Bruce LaMattina. Partial support for this work was also provided by the Office of Naval Research, in the program directed by Dr. Y.D.S. Rajapakse.

## References

- Atluri, S. N. (2002): Seminars at the University of Florida, Virginia Tech, and the Office of Naval Research.
- Atluri, S. N. (2004): *The meshless method (MLPG) for domain & bie discretizations*. Tech Science Press, USA.
- Atluri, S. N.; Shen, S. (2002): The meshless local Petrov-Galerkin (MLPG) method: A simple & less-costly alternative to the finite element and boundary element method. *CMES: Computer Modeling in Engineering & Sciences* 3 (1): 11-52.
- Askar, A (1985): *Lattice dynamical foundations of continuum theories*. World Scientific, Singapore.
- Bardenhagen, S.; Triantafyllidis, N. (1994): Derivation of high order gradient continuum theories in 2, 3-D non-linear elasticity from periodic lattice models. *J. Mech. Phys. Solids* 42: 111-139.
- Basinski, Z. S.; Duesberry, M.S.; Taylor, R. (1971): Influence of shear stress on screw dislocations in a model sodium lattice. *Canadian J. of Phys.* 49: 2160.
- Born, M.; Huang, K. (1954): *Dynamical Theory of Crystal Lattices*. Oxford, Clarendon.
- Broughton, J. Q.; Gilmer, G. H. (1983): Molecular dynamics investigation of the crystal-fluid interface. I. Bulk properties. *J. Chem. Phys.* 79: 5095-5104.
- Chandra, N.; Namila, S.; Shet, C. (2004): Local elastic properties of carbon nanotubes in the presence of Stone-Wales defects. *Phys. Rev. B* 69: 094101.
- Cheung, K. S.; Yip, S. (1991): Atomic-level stress in an inhomogeneous system. *J. Appl. Phys.* 70: 5688-5690.
- Clausius, R. (1870): On a mechanical theory applicable

to heat. *Phil. Mag.* 40: 122-127.

**Cormier, J.; Rickman, J. M.; Delph, T. J.** (2001): Stress calculation in atomistic simulations of perfect and imperfect solids. *J. Appl. Phys.* 89: 99-104.

**Garikipati, K.** (2002): A variational multiscale method to embed micromechanical surface laws in the macromechanical continuum formulation. *CMES: Computer Modeling in Engineering & Sciences* 3(2): 175-184.

**Ghoniem, N.M.; Cho, K.** (2002): The emerging role of multiscale modeling in nano and micro-mechanics of materials. *CMES: Computer Modeling in Engineering & Sciences* 3 (2): 147-173.

**Li, Q.; Shen, S.; Han, Z-D.; Atluri, S. N.** (2003): Application of Meshless Local Petrov-Galerkin (MLPG) to Problems with Singularities, and Material Discontinuities, in 3-D Elasticity, *CMES: Computer Modeling in Engineering & Sciences* 4(5): 567-581.

**Lucy, L. B.** (1977): a numerical approach to the testing of the fassion hypothesis. *Astrophysical Journal* 82: 1013.

**Lutsko, J. F.** (1988): Stress and elastic constants in anisotropic solids: molecular dynamics techniques. *J. Appl. Phys.* 64: 1152-1154.

**Monaghan, J. J.** (1992): Smoothed particle hydrodynamics. *Annu. Rev. Astron. Astrophys.* 30: 543-574.

**Machova, A.** (2001): Stress calculations on the atomistic level. *Modeling Simul. Mater. Eng.* 9: 327-337.

**Shen, S.; Atluri, S. N.** (2004a): Multiscale simulation based on the meshless local Petrov-Galerkin (MLPG) method. *CMES: Computer Modeling in Engineering & Sciences* 5(3): 235-255.

**Shen, S.; Atluri, S. N.** (2004b): Computational nanomechanics and multiscale simulation. *CMC: Computers, Materials, & Continua* 1(1): 59-90.

**Srivastava, D.; Atluri, S. N.** (2002a): Computational Nanotechnology: A Current Perspective, *CMES: Computer Modeling in Engineering & Sciences* 3(5): 531-538

**Srivastava, D.; Atluri, S. N.** (2002b): Computational Nanotechnology, Special Issue, *CMES: Computer Modeling in Engineering & Sciences* 3(5).

**Zhou, M.** (2003): A new look at the atomic level virial stress: on continuum-molecular system equivalence. *Proc. R. Soc. Lond. A* 459: 2347-2392.

**Zhou, M; McDowell, D. L.** (2002): Equivalent contin-

uum for dynamically deforming atomistic particle systems. *Philosophical Magazine A* 82: 2547-2574.

# Computational Nano-mechanics and Multi-scale Simulation

Shengping Shen<sup>1</sup> and S. N. Atluri<sup>1</sup>

**Abstract:** This article provides a review of the computational nanomechanics, from the *ab initio* methods to classical molecular dynamics simulations, and multi-temporal and spatial scale simulations. The recent improvements and developments are briefly discussed. Their applications in nanomechanics and nanotubes are also summarized.

## 1 Introduction

Due to their potentially remarkable mechanical properties, nano-structured materials have stimulated a lot of interest in the materials research community in the last few years. The design and fabrication of these materials are performed on the nanometer scale, with the ultimate goal of obtaining highly desirable macroscopic properties. In particular, materials such as nanotubes, nanoparticle-reinforced polymers and metals, and nano-layered materials have shown considerable promise. With the advances in materials synthesis and device processing capabilities, the importance of developing and understanding nanoscale engineering devices has dramatically increased over the past decade. Nanotechnology deals with materials, devices, and their applications at the nanoscale, where many diverse enabling disciplines and associated technologies start to merge, because these are derived from the rather similar properties of the atomic or molecular level building blocks. The subject of nanoscience/technology is defined as the science and technology of the direct or indirect manipulation of atoms and molecules into functional structures, with applications that were never envisioned before [Srivastava and Atluri (2002)]. Nano-mechanics deals with mechanics problems associated with modeling, design, fabrication and application of three-dimensional structures and systems with nanometer-scale dimensions. Nanoscale systems have a number of interesting features which distin-

guish them from micro- and macro-scale systems.

An underlying issue in modeling the macroscopic mechanical behavior of nano-materials, based on molecular structure, is the large difference in temporal and spatial scales. Computational molecular dynamics and continuum mechanics are on the opposite ends of the temporal and spatial scale spectrum, and consist of highly developed and reliable modeling methods. Computational continuum mechanics methods predict the macroscopic mechanical behavior of materials idealized as continuous media, based on known constitutive relationships of the bulk material, while computational molecular dynamic models predict molecular properties based on known quantum interactions. However, a corresponding model does not exist in the intermediate time and length scale range, where the disparate length scales associated with molecular and continuum phenomena, and disparate time-scales of the molecular and continuum phenomena, may be present *simultaneously*. If a hierarchical approach is used to model the macroscopic behavior of nano-materials, then a methodology is needed to link the molecular structure and macroscopic properties.

However, systems with multiple length scales are ubiquitous in science, for example, the sub-micron Micro-Electro-Mechanical Systems (MEMS), or even Nano-Electro-Mechanical Systems (NEMS), where the behavior is determined by the interplay between the micron-scale continuum mechanics and the nanoscale atomistic processes. The continuum mechanics is governed largely by the geometry of the device, while the atomistic processes are important only in its smallest features. Continuum analyses are appropriate only for a large enough system. The nano-scale is the length scale of individual atoms, i.e. 1-10 nm. At such small length scales, continuum models are not flexible enough to accommodate the individual atomic scale processes. Alternative to continuum analysis, the atomistic modeling and simulation calculates, individual atoms explicitly, and follows them during their dynamic evolution. Even though

---

<sup>1</sup> Center for Aerospace Research & Education  
University of California at Irvine  
5251 California Avenue, #140, Irvine, CA 92612, USA

this atomistic method can trace all the details of atomic-scale processes explicitly, it still has time and length scale limitations from both small and large directions. When the length-scale cannot be accessed either by continuum methods, since it is too small for averaging, or by the atomistic methods (molecular dynamics or quantum mechanics), since it is too large for simulations on the current computers, these two approaches become inadequate, which has presented significant challenges to the scientific community.

The amount of computer resources needed to investigate a given volume of matter dramatically increases as one goes from the top down to the bottom, i.e. from the continuum, through the mesoscopic, the atomistic and to the quantum methods. Quantum mechanics solves Schrödinger's equation for the electrons in the system. Atomistic methods generally model atoms as spheres which may be linked together to form molecules. By assuming point charges on the nuclei of the atoms, electrostatic interactions are included. Mesoscopic methods are based on local groups of atoms, which generally represent many atoms with a considerable internal flexibility. Such groups can also be linked together to represent molecules. There exist a number of continuum approaches, such as the finite element method, the boundary element method and the meshless method *etc.* The length scales of the typical material system in multi-scale structures are shown in Fig. 1. Multiscale modeling is a unifying paradigm to enable the integration of the basic science and the engineering system. It allows for a rigorous correlation of different science and engineering models, representations, languages and metrics.

Carbon nanotubes have attracted considerable attention since they were discovered by Iijima (1991). The extraordinary properties of carbon nanotubes have motivated researchers worldwide to study the fundamentals of this novel material as well as to explore their applications in different fields [Ajayan and Zhou (2001)]. Application

of carbon nanotubes in nanoelectronics, nanocomposite materials, and NEMS is a typical multi-scale problem, which also impels the study on the multi-scale model that directly links the continuum theories to atomistic simulations.

This paper will review the current status of the progresses and developments in computational nanotechnology and multiscale simulation. The paper is organized as follows. Section 2 summarizes the simulation methods from quantum level to atom level; and the long range interactions are also included. Section 3 focuses on the multi-scale methods. Section 4 discusses the simulation methods for nanotubes. Finally, conclusions are made in Section 5.

## 2 Computational Techniques for Nanoscale Simulations

Since the spatial and temporal scales of nanoscale systems and phenomena have shrunk to the level where they can be directly addressed with high-fidelity computer simulations and theoretical modeling, computational nanotechnology [Srivastava and Atluri (2002a, b); Srivastava, Menon, and Cho (2001)] has become critically important in nanodevice development [Ajayan and Zhu (2001)]. *ab initio* methods are being used extensively, which can determine the electronic and atomic structures of different materials just from its atomic coordinates. However, the applications of *ab initio* methods are limited to very small-scale systems with only a few hundred atoms. Alternatively, tight-binding molecular dynamics (TBMD) and classical molecular dynamics (MD) offer powerful ways to treat even large-scale systems. Tight-binding molecular dynamics (TBMD) is a semi-empirical technique, which is a blend of certain features from both MD and *ab initio* methods. Molecular dynamics (MD) refers most commonly to the situation where the motion of atoms or molecules is treated in approximated finite difference equations of Newtonian mechanics. In fact, *ab initio* and TBMD are the quantum mechanics (QM) schemes. In this section, we summarize the main simulation approaches in computational nanotechnology.

### 2.1 Ab initio methods

Quantum mechanics is a means to understand and predict the interactions between atoms and molecules, and to model the chemical reactions at that scale. It uses

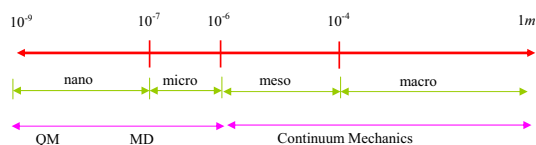


Figure 1 : The length scales of the material system

models based on the electronic structure. The solution of the Schrödinger's equation provides the electronic wave functions. Other properties are then obtained from these functions. The *ab initio* or first-principles method solves the complex quantum many-body Schrödinger equation with numerical algorithms [Payne, Teter, Allan, Arias, and Joannopoulos (1992)]. This method is to regard many-atom systems as many-body systems composed of electrons and nuclei, and to treat everything on the basis of first-principles of quantum mechanics, without introducing any empirical parameters [Ohno, Esfarjani and Kawazoe (1999)]. The *ab initio* method provides more accurate descriptions of quantum mechanical behavior of materials. However, currently the system sizes are limited to only about a few hundred atoms. In the general approach of quantum mechanics, atoms are represented as a collection of quantum mechanical particles, nuclei and electrons; the state of a particle is defined by a wave function  $\psi$ , based on the well-known wave-particle duality. The Schrödinger equation is [Born, and Huang (1954)]

$$H\psi(r_i, R_I) = E_{tot}\psi(r_i, R_I) \quad (1)$$

with the full quantum many-body Hamiltonian operator

$$H = \sum_I \frac{P_I^2}{2m_I} + \sum_{I,J} \frac{Z_I Z_J e^2}{R_{IJ}} + \sum_i \frac{p_i^2}{2m_e} + \sum_{i,j} \frac{e^2}{r_{ij}} - \sum_{I,i} \frac{Z_I e^2}{|R_I - r_i|} \quad (2)$$

where  $\psi$  is the energy eigenfunction corresponding to the energy eigenvalue  $E_{tot}$ , which represents the total energy of the system,  $R_I$  and  $r_i$  are the nuclei and electron coordinates, respectively,  $R_{IJ} = |R_I - R_J|$  and  $r_{ij} = |r_i - r_j|$ .  $P_I$  and  $p_i$  are the nuclei and electron momenta, respectively.  $m_I$  and  $m_e$  are nuclei and electron mass, respectively.  $e$  is the electric charge of an electron, and  $Z_I e$  is the electric charge of the nuclei of atom  $I$ . The Hamiltonian operator in equation (2) is composed of five parts. The first and third terms in equation (2) give the kinetic energy of the nucleus and electron, respectively; the second term gives the nucleus-nucleus Coulomb interaction, the fourth term gives the electron-electron Coulomb interaction, and the last terms gives the nucleus-electron Coulomb interaction.

After solving for the energy  $E_{tot}$ , the interatomic potential of the system can be obtained. Then, the interactions  $F_I$ , between atoms can be derived from

$$\mathbf{F}_I = -\frac{\partial V}{\partial \mathbf{R}_I} \quad (3)$$

where  $V$  is the atomic interaction potential. Since the kinetic energy of the nucleus is independent of its position,  $V$  can be replaced by  $E_{tot}$  in equation (3). Hence, as long as  $E_{tot}$  is determined, the interactions  $F_I$  can be obtained according to equation (3). The dynamic motion for the atomic positions is still governed by Newtonian or Hamiltonian mechanics, i.e.

$$m_I \ddot{\mathbf{R}}_I = \mathbf{F}_I = -\frac{\partial V}{\partial \mathbf{R}_I} \quad (4)$$

Equations (4) are approximated as finite-difference equations with discrete time step  $\Delta t$ . Due to the small scale involved, explicit integration algorithms such as the standard Gear's fifth-order predictor-corrector or Verlet's leapfrog methods [Verlet (1967), Berendsen, van Gunsteren (1986)], which will be described in detail in section 2.3, are commonly used to ensure high order accuracy.

In using the *ab initio* method, effective and applicable assumptions are necessary. The most commonly used approximation is the Born-Oppenheimer adiabatic approximation [Ohno, Esfarjani, and Kawazoe (1999)], which assumes that the electrons are always in a steady state, derived from their averaged motion, since their positions change rapidly compared to the nuclear motion. Hence, the motion of the electrons can be considered separately from the motion of the nuclei, as if the nuclei were stationary. Using this approximation, one can reduce the full quantum many-body problem to a quantum many-electron problem:

$$H_{el}(R_I)\psi(r_i) = E_{el}\psi(r_i) \quad (5)$$

where  $E_{el}$  is the ground state energy of a many-electron system and can be regarded as the atomic interaction potential, and

$$H = \sum_I \frac{P_I^2}{2m_I} + H_{el}(R_I) \quad (6)$$

It is very difficult to solve the eigen equation (5) exactly, and approximate methods have been developed. The most commonly used approaches are the Hartree-Fock approximation [Fock (1930), Hartree (1928)] and the density functional theory [Hohenberg and Kohn, 1964].

A detailed description and survey of the Hartree-Fock approximation can be found in Clementi (2000) and Ohno, Esfarjani and Kawazoe (1999). Here, we omit

the details. The Hartree-Fock approximation is usually used to describe electron-electron interaction effects. In the Hartree-Fock approximation, the ground state of the Hamiltonian  $H$  is obtained by means of the variational principle with a normalized set of wave functions. Actually, the methodology seeks the solution by minimizing the expected value of  $H$  with a trial function, similar to the Ritz method. Many *ab initio* simulations used the Hartree-Fock approximation, which translates a many-electronic problem into a single electronic problem. Then, the Hartree-Fock equation can be written as

$$H_{HF}\psi_i(r) = \epsilon_i\psi_i(r) \quad (7)$$

which is derived from the variational principle [Ohno, Esfarjani and Kawazoe (1999)], where  $H_{HF}$  is the Hartree-Fock operator, which consists of the one-electron Hamiltonian, the Hartree operator (or Coulomb term), and the Fock operator (or exchange term).  $\psi_i$  is the molecular orbit, and  $\epsilon_i$  is the orbital energy of the electron in this orbital. The molecular orbit is assumed to be the linear combination of atomic orbits (LAO), as

$$\psi_i = \sum_{\alpha} c_{\alpha}^i \phi_{\alpha} \quad (8)$$

where  $\phi_{\alpha}$  is the  $\alpha$ th atomic orbital and  $c_{\alpha}^i$  is the coefficient. Adopting the closed shell model, the Hartree-Fock equation can be conveniently written as a matrix form

$$\mathbf{FC} = \mathbf{SCE} \quad (9)$$

The above equation is called Roothaan-Hall equation. The Fock matrix  $\mathbf{F}$  can be written as [Leach (1996)]

$$F_{\alpha\beta} = \int d\nu \phi_{\alpha} \left[ -\frac{1}{2} \nabla_{\nu}^2 - \sum_{A=1}^M \frac{Z_A}{r_{\nu A}} \right] \phi_{\beta} + \sum_{\gamma=1}^K \sum_{\kappa=1}^K P_{\gamma\kappa} \left[ (\alpha\beta|\gamma\kappa) - \frac{1}{2} (\alpha\gamma|\beta\kappa) \right] + V_{\alpha\beta} \quad (10)$$

where the first term is the core energy, the second term is energy arising from the Coulomb and exchange interaction. It is noted that in this equation, the atomic units are used.  $\mathbf{P}$  is the charge density matrix and can be written as

$$P_{\gamma\kappa} = 2 \sum_{i=1}^{N/2} c_{\gamma}^i c_{\kappa}^i \quad (11)$$

$(\alpha\beta|\gamma\kappa)$  and  $(\alpha\gamma|\beta\kappa)$  are two-electron integrals that may involve up to four different basis functions ( $\phi_{\alpha}, \phi_{\beta}, \phi_{\gamma}, \phi_{\kappa}$ ), which may in turn be located at four different centers.  $V_{\alpha\beta}$  is the influence of external fields,  $\mathbf{S}$  is the overlap integrals matrix with

$$S_{\alpha\beta} = \int d\nu \phi_{\alpha} \phi_{\beta} \quad (12)$$

$\mathbf{C}$  is the coefficient matrix, and  $\mathbf{E}$  is the orbital energy diagonal matrix. The Hartree-Fock approximation does not include correlation effects. It is more tractable for a system of a small number of atoms and becomes more complex for crystals. A better approximation, the local-density approximation (LDA), gives ground-state properties almost perfectly and more efficiently. As an alternative to the Hartree-Fock approximation, the LDA replaces the electron-electron interactions by some effective potential acting on the electrons. The LDA is an approximating method, and cannot be applied to excited states and highly correlated systems.

The density functional theory [Hohenberg and Kohn, 1964] has a rigorous mathematical foundation, provided by two important works [Hohenberg and Kohn (1964), Kohn and Sham (1965)]. Hohenberg and Kohn (1964) have developed a theorem: the ground state energy ( $E_{el}$ ) of a many-electron system is a function of total electron density,  $\rho(r)$ , rather than the full electron wave function,  $\Psi(r_i)$ ,  $E_{el}(\Psi(r_i)) \equiv E_{el}(\rho(r))$ . The Hamiltonian operator  $H$  and Schrödinger equation are given by

$$H(R_I) = \sum_i \frac{p_i^2}{2m_e} + \sum_{i,j} \frac{e^2}{r_{ij}} - \sum_{I,i} \frac{Z_I e^2}{|R_I - r_i|} + \sum_{I,J} \frac{Z_I Z_J e^2}{R_{IJ}} \quad (13)$$

$$H(R_I)\psi(r_i) = E_{el}\psi(r_i) \quad (14)$$

The density functional theory (DFT) is derived from the fact that the ground state total electronic energy is a functional of the total electron density. However, it is very difficult to formulate  $E_{el}(\rho(r))$ . Kohn and Sham (1965) have shown that the DFT can be formulated as a single-electron problem with self-consistent effective potential including all the exchange-correlation effects of electronic interactions. Then the Kohn-Sham equation can be written as

$$H_1\psi_i(r) = \epsilon_i\psi_i(r), \quad i = 1, \dots, N_{tot} \quad (15)$$

which is the single-electron Schrödinger equation. Here,  $H_1$  is the effective one-electron Hamiltonian, and can be

written as

$$H_1 = \frac{p^2}{2m_e} + V_H(r) + V_{NE}(r) + V_{XC}(\rho(r)) \quad (16)$$

$$\rho(r) = \sum |\psi_i(r)|^2 \quad (17)$$

In equation (16), the first term represents the electron kinetic energy, the second term represents the electrostatic potential, the third term represents the nucleus-electron interaction potential, and the last term denotes the exchange-correlation potential and is a function of the electron density. While the first three terms can be obtained explicitly, the last one must be approximated. The local density approximation (LDA) has been introduced to approximate the unknown effective exchange-correlation potential by Kohn and Sham (1965). The LDA assumes that the exchange-correlation function corresponds to the homogeneous electron gas. This assumption is only valid locally, when the inhomogeneity due to the presence of the nuclei is small. Once  $\psi_i$  and  $\epsilon_i$  are solved from equation (15), the total energy can be obtained. The eigenvalues correspond to the quantum-mechanically possible electronic energy states of the system, and the eigenfunctions contain information about the electronic density distribution in the computed space. The DFT-LDA method has been very successful in predicting the properties of materials without using any experimental inputs other than the identity (i.e. atomic numbers) of constituent atoms [Car and Parrinello (1985)]. The major advantage of using LDA is that the error in the electron energy is second-order between any given electron density and ground state density.

For practical applications, a single electron wavefunction with a plane wave and pseudopotential have been implemented in the DFT-LDA method [Payne, Teter, Allan, Arias, and Joannopoulos (1992)]. These systematic approximations reduce the electronic structure problem to a self-consistent matrix diagonalization problem. The solution procedure requires an iterative diagonalization process, which in general involves  $O(N^3)$  order of computation and limits the DFT-LDA method to simple systems, and the system sizes currently are limited to only about a few hundred atoms.

The limitation of the DFT-LDA method mainly comes from two aspects: one is the use of plane waves as a basis to expand the electron wave functions; the other is the inclusion of degrees of freedom from the electron wave functions in the molecular dynamics. The former limits

the number of atoms used in the simulation due to the large number of basis functions required in the calculation, and the latter leads to that the simulation time step has to be chosen much smaller than that in simulations with classical potential (about ten times smaller).

To reduce the order of computation, over the last three decades, a lot of researchers attempted to develop rapid and effective methods for solving the Kohn-Sham equation [Li, Nunes and Vanderbilt (1993), Daw (1993), Mauri and Galli (1994), Kresse and Furthmüller (1996)]. Major improvements have been made using the Car-Parrinello MD (CPMD) method [Car and Parrinello (1985)], cluster variation method [Kawazoe (2001)], and conjugate gradient (CG) minimization methods [Payne, Teter, Allan, Arias, and Joannopoulos (1992)]. CPMD has significantly improved the computational efficiency by reducing the order from  $O(N^3)$  to  $O(N^2)$ . As shown by Payne, Teter, Allan, Arias, and Joannopoulos (1992), the CG method has further improved the efficiency by an additional factor 2-3.

The *ab initio* method makes it possible to model a few hundred atoms without any experimental inputs, and provides a powerful tool to investigate nanomaterials with predictive power. *Ab initio* method possesses high accuracy and transferability, due to there being no experimental inputs. However, the high order of computation limits the applicability of the *ab initio* method. Therefore, other methods, such as the tight-binding method or the classical molecular dynamics, are very important in order to overcome the complexities of some materials. In these methods, the potential parameters are extracted from the experiment or *ab initio* calculations. However, these methods are only valid in the region where they are fitted. Nevertheless, they are useful to study complex materials on the basis of these approximations.

A standard *Ab initio* routine is illustrated in Fig. 2.

## 2.2 Tight-binding methods

In the intermediate regime of a few hundred- to thousand-atom systems, where classical molecular dynamics method is not accurate enough, nor the *ab initio* computations are feasible, tight-binding [Slater and Koster (1954), Harrison (1980)], or semi-empirical quantum mechanics based methods, provide an important link between the *ab initio* quantum mechanics based approaches described above, and the classical atomistic force field based methods, that will be described below.

The tight binding method can handle a much larger system than the *ab initio* method, and has the information about the electronic structure of the system, while maintaining a better accuracy than the MD simulation. In its nature, the tight-binding method is very similar to Hartree-Fock methods, but the computations of the Hamiltonian and overlap matrix elements are based on semi-empirical formulae. In this method, the atoms are treated as classical particles that interact in part through an effective potential exerted by the electrons that are treated quantum mechanically. Hypothetical basis orbitals with the angular symmetries of single atom eigenstates are centered around each atom. In the tight binding method, the interatomic forces are evaluated in a straightforward way, based on the Hellmann-Feynman theorem and the rest of the procedure is almost identical to the MD simulation, that is the reason why the tight binding method is also referred to as tight binding MD method (TBMD).

The tight-binding method [Harrison (1980)] further simplifies the quantum many electron problem by assuming that the crystal potential is strong, such that when an ion captures an electron during its motion through the lattice, the electron remains at that site for a long time before

leaking, or tunneling, to the next ion site. During the capture interval, the electron orbits primarily around a single ion uninfluenced by other atoms, so that its state function is essentially that of an atomic orbital. Usually, the electron is tightly bound to its own atom. Hence, the total energy (or the interatomic potential) can be expressed as the sum of the eigenvalues of a set of occupied non-self-consistent one electron molecular eigenfunctions, in addition to certain analytical functions [Foulkes and Haydock (1989)]:

$$V_{TB} = \sum_{n=1}^{N_{occ}} \epsilon_n + \sum_{I < J} V^{rep}(\mathbf{R}_{IJ}) \quad (18)$$

The sum is over all occupied states  $N_{occ}$  up to the Fermi level. The first term on the right side is the sum of the energies of occupied orbits (i.e., band-structure energy), which can be solved from the Schrödinger equation (5).  $V^{rep}$  is the repulsive inter-atomic potential, and the double counting of the Coulomb and exchange-correlation terms inherent in the eigenvalue sum (the first term) are eliminated by the sum of the repulsive interatomic potential  $V^{rep}$  (the second term). Many papers [Wang and Ho (1993, 1996), Lewis and Mousseau (1998)] described how to obtain these two terms. Due to that  $V^{rep}$  is derived from the experiment, the TBMD method is a semi-empirical method. The eigenvalues  $\epsilon_n$  corresponding to the one-electron states of a first principles Hartree-Fock or density functional theory are obtained from a nonorthogonal one-electron Hamiltonian

$$\mathbf{H}\psi_n = \epsilon_n \mathbf{S}\psi_n \quad (19)$$

$$\psi_n = \sum_{I\alpha} c_{I\alpha}^n \phi_{I\alpha} \quad (20)$$

where  $\mathbf{S}$  is the overlap matrix. It is noted that, in equation (20), a linear combination of atomic orbitals (referred to LACO), which is modulated by a Bloch wave-function phase factor for a periodic lattice, is adopted in the wave function: the one-electron wave function  $\psi_n$  is expanded as a linear combination of atomic basis functions  $\phi_{I\alpha}$ , as discussed in Hartree-Fock approximations. This ensures that an electron in a tight-binding level will be found, with equal probability, in any cell of the crystal, since its wave function changes only by the phase factor, as one electron moves from one cell to another. Here,  $n$  denotes

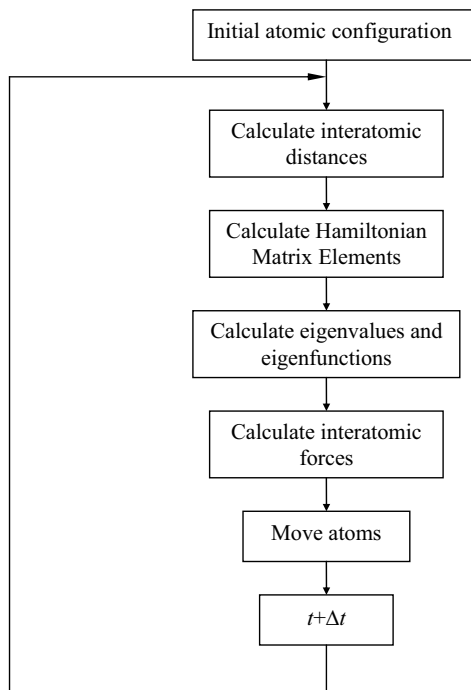


**Figure 2** : An illustration of *ab initio* routine

the orbital number, and  $\alpha$  denotes the basis functions (in the minimal basis of silicon, these represent  $s$ ,  $p_x$ ,  $p_y$ , and  $p_z$  atomic orbits). The details of the basis functions do not enter into the energy calculation, but only the interactions between basis elements  $\phi_{I\alpha}$  that from the overlap and Hamiltonian matrices. The matrix elements within the overlap  $\mathbf{S}$  and Hamiltonian  $\mathbf{H}$  matrices are obtained by fitting the equivalent integrals within an extensive database of the first-principles calculations to a particular parametric form

$$\begin{aligned} S_{\alpha\beta}(\mathbf{r}_{IJ}) &= \langle \phi_{I\alpha} | \phi_{J\beta} \rangle \\ H_{\alpha\beta}(\mathbf{r}_{IJ}) &= \langle \phi_{I\alpha} | H | \phi_{J\beta} \rangle \end{aligned} \quad (21)$$

The function  $V^{rep}$  is also obtained by fitting to a database involving the experimental indirect band gap. The parameters for this fit are given by Bernstein and Kaxiras (1997). Although the exact forms of the basis are not known, the Hamiltonian and overlap matrix can be parameterized, and the total energy and electronic eigenvalues can be easily extracted from the Hamiltonian matrix, which also contains the effects of angular forces in a natural way. There are two approaches to perform parameterization process, one is fitting to results from the *ab initio* methods [Xu, Wang, Chan and Ho (1992), Mehl and Papaconstantopoulos (1996)], the other is computing the matrix exactly based on the localized basis [Liu (1995), Porezag, Frauenheim, Kohler, Seifert, and Kaschner (1995), Taneda, Esfarjani, Li, Kawazoe (1998)].

The process of solving for the coefficient  $c_{I\alpha}^n$  is a generalized eigenvalue problem. For a given set of atomic coordinates, the coefficients are found by diagonalization. One-electron states are occupied up to Fermi level. The interatomic forces are evaluated in a straightforward way, based on the Hellmann-Feynman theorem, and the system's dynamic evolution is governed by Hamilton's classical equation of motion from Newton's second law:

$$m_I \ddot{\mathbf{R}}_I = \mathbf{F}_I = - \frac{\partial V_{TB}}{\partial \mathbf{R}_I} \quad (22)$$

After obtaining the force, atomic coordinates can be advanced through time, using the same algorithm as that used for the *ab initio* method or the classical MD, i.e., the standard Gear's fifth-order predictor-corrector or Verlet's leapfrog methods, which will be described in detail in section 2.3.

The TBMD is one of the fastest numerical quantum methods containing electronic structure information, and its application is extensive. Lewis and Mousseau (1998) used it to study defects and disorder in covalently bonded materials. Wang and Ho (1993) employed it to investigate the structure, dynamics and electronic properties of diamond-like amorphous carbon. Colombo (1998) provided a source code for TBMD simulations.

Since the brute force diagonalization is  $O(N^3)$ , which parallelizes poorly, in general, TBMD is an  $O(N^3)$  algorithm. To reduce the order of computation (i.e., improve the scale of computation), Khan and Broughton (1989) implemented a fictitious Lagrangian to reducing the order from  $O(N^3)$  to  $O(N^2)$ . There is much discussion in the literature about  $O(N)$  schemes for electronic structure [Li, Nunes, and Vanderbilt (1993), Daw (1993), Canning, Galli, Mauri, De Vita, and Car (1996), Ordejon (1998)]. However, such methods often have problems with situations in which states wander across the Fermi level. Another way to improve the scale of the TBMD is the parallel simulation [Kalia, Campbell, Chatterjee, Nakano, Vashishta, Ogata (2000)]. The parallelization of the TBMD code involves parallelizing the direct diagonalization (of the electronic Hamiltonian matrix) part as well as the MD part. Parallelizing a sparse symmetric matrix with many eigenvalues and eigenvectors is a complex bottleneck in the simulation of large intermediate-range system and requires new algorithms. A survey of the parallel simulation can be found in Heffelfinger (2000).

Although TBMD can consider the quantum structure of electron, its accuracy is less than that of *ab initio*. Hence, some researchers developed the first-principles molecular dynamics by combining the advantages of TBMD and DFT-LDA (*ab initio* method) [Demkov, Ortega, Sankey, and Grumbach (1995), Ortega (1998), Garcia-Vidal, Merino, Peerez, Rincon, Ortega, and Flores (1994), Pearson, Smargiassi, and Madden (1993), Smargiassi, and Madden (1994)]. This method showed a very good accuracy for the problems of defect [Smargiassi (1994)], and lattice dynamics [Pavone, Karch, Schutt, Windl, Strauch, Giannozzi, and Baroni (1993), Adler, Honke, Pavone, and Schroder (1998)].

A major problem with the TBMD method is the way that the parameterization of the Hamiltonian and the overlap matrices, and the function  $V^{rep}$  limits its applicability. Harrison (1989) has attempted to provide a mini-

mal tight-binding theory with a set of universal parameters that could describe qualitatively a wide range of materials and properties. However, this approach turns out to be neither transferable nor accurate. Although focusing on tetrahedral solids, he emphasized the necessity of including the nonorthogonality of the local environment in multi-coordinated structures. This important factor has generally been overlooked by those seeking a transferable scheme. After that, Menon and Subbaswami (1997) proposed a nonorthogonal tight-binding scheme with minimal number of adjustable parameters, resulting in a transferable scheme applicable to clusters as well as bulk systems. Although nonorthogonal tight-binding molecular dynamics schemes are more accurate, they are not easily converted to order  $O(N)$ , and can typically handle only systems with up to a few thousand atoms [Menon and Subbaswami (1997)].

A standard TBMD routine is illustrated in Fig. 3.

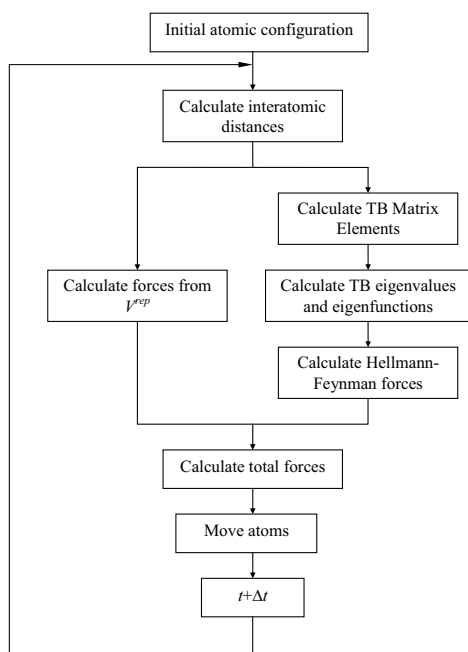


**Figure 3** : An illustration of the TBMD routine

### 2.3 Classical Molecular Dynamics

Up to now, we know that atomistic and electronic-scale simulations can be performed by means of *ab initio* or semi-empirical methods such as tight-binding. However,

these methods are still restricted in their capability with respect to both the number of atoms and the simulation timescale. Classical molecular dynamics is an important substitute to study longer-timescale phenomena of systems composed of larger numbers of particles, which is much simpler but still an atomic scale method. Molecular dynamics is a means to study matter at the atomic level and to predict the static and dynamic properties from the underlying interactions between the molecules. To go from quantum mechanics to molecular dynamics requires averaging over the electrons to obtain spring constants, discrete charges and van der Waals parameters. It is possible to construct realistic classical potentials based on *ab initio* calculations, experimental results or an empirical model. A possible way is to fit the classical potentials to contour maps of the total energy, which may be obtained with an *ab initio* method by changing the position of one atom while fixing the coordinates of all other atoms. With the increase in computing power, the connection between classical MD and *ab initio* calculations are being made in a clear and rigorous fashion. Classical molecular dynamics is an empirical method. Hence, it is easy to implement in larger systems (million to billion atoms). However, for different systems, different empirical parameters may be needed, which limits its transferability.

The method of classical molecular dynamics was first proposed by Alder and Wainwright (1957). Alder and Wainwright applied the method to the simplest system—hard spheres by first assuming an interatomic potential, and found a liquid-solid phase transition in this hard-sphere system. Later, the methods were also applied to various systems with soft potentials [Rahman (1963)] such as the Lennard-Jones potential. Classical MD describes system's atomic-scale dynamics, where atoms and molecules move, while interacting with many of the atoms and molecules in the vicinity. The system's dynamic evolution is governed by Hamilton's classical equation of motion from Newton's second law:

$$m_I \ddot{\mathbf{R}}_I = \mathbf{F}_I = -\frac{\partial V}{\partial \mathbf{R}_I} \quad (\text{no sum on } I) \quad (23)$$

which is derived from the classical Hamiltonian of the system,

$$H = \sum_I \frac{p_I^2}{2m_I} + V(\mathbf{R}_I) \quad (24)$$

where  $\mathbf{R}_I$  is the position of atom  $I$ , and  $V$  is the empirical potential for the system. Each atom moves and acts simply as a particle that is moving in many-body force field  $\mathbf{F}_I$  of other similar particles, which can also be obtained from more accurate quantum simulation as described in Sections 2.1 and 2.2. The atomic and molecular interactions describing the dynamics are given by classical many-body force-field functions. The atomic interaction energy function  $V(\mathbf{R}_I)$  can be written in terms of pair and many-body interactions, depending on the relative distances among different atoms [Daw and Baskes (1983, 1984)].

An alternate but equivalent approach is to solve the Hamiltonian system of ordinary differential equations

$$\frac{dP_I}{dt} = -\frac{\partial H}{\partial q_I} \quad (25)$$

$$\frac{dq_I}{dt} = \frac{\partial H}{\partial P_I} \quad (26)$$

where  $(q_I, P_I)$  are the set of canonically conjugate coordinates and momenta, respectively. Symplectic integrators [Gray, Noid, and Sumpter (1994)] have been developed to solve the above Hamiltonian equations of motion.

In MD simulations, the effects of finite system size and surfaces are always a severe problem. Periodic boundary conditions are usually employed to reduce these effects. All the particles are put inside a unit cell, and if the particle goes outside the cell boundary, it is brought back in from the opposite side of the cell. More descriptions of the general techniques used in molecular dynamics can be found in Allen and Tildesley (1989), Rapaport (1995), and Leach (1996).

Classical molecular dynamics have been applied extensively. Some computer codes can be available on the websites, such as CCP5 on <http://wserv1.dl.ac.uk/CCP/CCP5>, Amber/Sander on <http://www.amber.ucsf.edu/amber/amber.html> (or <http://amber.scipps.edu>), NAMD on <http://www.ks.uiuc.edu/Research/namd>, and LAMMPS on <http://www.cs.sandia.gov/sjplimp/lammps.html>.

### 2.3.1 Short range interactions

As the simplest interatomic potential in MD simulations, pair potentials are employed to qualitatively model diverse properties of materials, such as Buckingham potential [Wunderlich and Awaji (2001)], Morse potential [Ko-

manduri, Chandrasekaran, and Raff (1998)], and glue potential [Duan, Sun and Gong (2001)]. A very widely used inverse power model, the 12-6 Lennard-Jones (LJ) potential, was introduced by Lennard-Jones (1924a, b) for non-bond atomic interactions, as

$$V_{LJ} = 4\epsilon \left[ \left( \frac{\sigma}{R_{IJ}} \right)^{12} - \left( \frac{\sigma}{R_{IJ}} \right)^6 \right] \quad (27)$$

where  $\epsilon$  denotes the bind energy (the minimum of Lennard-Jones potential), and  $\sigma$  the equilibrium distance between two unbonded atoms or monomers,  $R_{IJ}$  denotes the inter-atomic distance between atoms  $I$  and  $J$ . The Lennard-Jones force (attraction or repulsion) between two atoms can be written as:

$$F_{IJ} = -\frac{\partial V_{LJ}}{\partial R_{IJ}} = -\frac{4\epsilon}{R_{IJ}} \left[ 12 \left( \frac{\sigma}{R_{IJ}} \right)^{12} - 6 \left( \frac{\sigma}{R_{IJ}} \right)^6 \right] \quad (28)$$

Girifalco and Lad (1956), and Girifalco (1992) employed the Lennard-Jones potential for the carbon-carbon system. Two sets of parameters have been used, one for a graphite system [Girifalco and Lad (1956)] and the second for an *fcc* crystal composed of  $C_{60}$  molecules [Girifalco (1992)]. The Lennard-Jones (LJ) potential is a non-bond order potential, which accounts for the steric and van der Waals non-bonded interaction.

To model more realistic materials, such as metals and semiconductors with complex many-body interactions, the pair potentials must be modified. Up to now, many approaches emerged, to improve the pair potentials. However, all of them fall into three categories, which are introduced below respectively.

The first one is to develop potentials by following the Born-Openheimer expansion (many-body potentials), i.e., besides the pair potential, many-body potentials should be added, such as Pearson [Pearson, Takai, Halicioglu and Tiller (1984)], and Stillinger-Weber (SW) [Stillinger, and Weber (1985)] potentials. The inter-atomic potential  $V$  as an infinite sum over pair, triplet, etc., can be expressed by the Born-Openheimer expansion as:

$$\begin{aligned} V(R_1, R_2, R_3, \dots) = & \frac{1}{2!} \sum_{J \neq I} \sum_I V^{(2)}(R_{IJ}) + \\ & \frac{1}{3!} \sum_{K \neq J \neq I} \sum_{J \neq I} \sum_I V^{(3)}(R_{IJ}, R_{JK}, R_{KI}) + \dots + \\ & \frac{1}{n!} \sum_{Q \neq J \neq M \neq J} \dots \sum_{J \neq I} \sum_I V^{(n)}(R_{IJ}, \dots, R_{IQ}, \dots, R_{MQ}, \dots) \end{aligned} \quad (29)$$

$V^{(2)}$ ,  $V^{(3)}$  ... and  $V^{(n)}$  are the interaction potentials of the two-, three- and  $n$ -body interactions, respectively; and  $R_{IJ}$  is the distance between atoms  $I$  and  $J$ . It is noted that the  $n$ -body potential decreases rapidly with the increase of  $n$ . Therefore, in practice, the Born-Openheimer potential is truncated at  $n=3$ . For covalently-bonded materials, Pearson takes the two-body component to be the Lennard-Jones potential, while triplet interactions are represented by an Axilrod-Teller-type three-body potential [Pearson, Takai, Halicioglu and Tiller (1984)]. The SW potential, which involves both two-body and three-body interatomic terms, is another example of the type of potential that is used to effectively deal with the directional nature of bonding in covalent materials. The SW potential can be written as

$$V_{SW}(R_1, R_2, R_3, \dots) = \sum_{J \neq I} \sum V^{(2)}(R_{IJ}) + \sum_{K \neq J \neq I} \sum V^{(3)}(R_{IJ}, R_{IK}) \quad (30)$$

The exact form of these interactions  $V^{(2)}$  and  $V^{(3)}$  are given in Stillinger, and Weber (1985). The potentials are assumed to have a cutoff radius, i.e., any atom interacts directly only with those atoms within a distance  $R_{cut}$  from it.

There are many different many-body empirical potentials developed during last decades, such as AMBER [Cornell, et al., (1995)], CFF95 [Peng et al. (1997)], CHARMM [Mackerell, et al. (1995)], Dreiding [Mayo, Olafson, and Goddard (1990)], MMFF [Halgren (1996)], MM2 [Allinger (1977), and Allinger, Yuh, Lii (1989)], MM3 [Cui, Li, and Allinger (1993)], MM4 [Nevins, Lii, and Allinger (1996)], OPLS [Jorgensen, et al. (1996)], SHARP [Bearpark, Robb, Bernardi, and Olivucci (1994)], UFF [Rappe, et al. (1992)], and VALBON [Cleveland, and Landis (1996)]. In these models, the total system potential energy  $V$  can be expressed as a sum of several individual energy terms [Burkert and Allinger (1982), Leach (1996), Rappe and Casewit (1997)]:

$$V = U_p + U_\theta + U_\omega + U_\tau + U_{vdW} + U_{es} \quad (31)$$

where  $U_p$ ,  $U_\theta$ ,  $U_\omega$ , and  $U_\tau$  are energies associated with bond stretching (two-body), angle variation (three-body), inversion and torsion (four-body), respectively;  $U_{vdW}$  and  $U_{es}$  are associated with van der Waals and electrostatic

interactions, respectively. Additional energy terms associated with electromechanical or optomechanical interactions can be included in the same way. Different models may include different terms. One can ignore or focus on some selective terms of the total potential energy according to the physics of a specific problem. MM2-MM4, SHAPE, VALBON and UFF models have been applied in the analysis of a variety of organic and inorganic systems. The Dreiding model has been used to analyze the structure of fullerene and carbon nano-tube [Guo, Karasawa, and Goddard (1991), Tuzun, Noid, Sumpter and Merklet (1996)].

The second one is to attempt to model the local environment using electron density distributions, which results in an addition energy, such as the embedded atom method (EAM) [Daw and Baskes (1983, 1984)], and variable charge molecular dynamics (VCMD) [Streitz and Mintmire (1994)]. VCMD is suitable to solving the boundary problems [Campbell, Kalia, Nakano, Vashishta, Ogata, and Rodgers (1999)]. However, it is more complicated than EAM. Based on the quasi-atom approach [Scott, and Zaremba (1980)], Daw and Baskes (1983) developed the EAM potential for metals. In this approach, the energy of an atom in the crystal is divided into two parts, which can be written as

$$E(R_{IJ}) = \sum_I \left\{ F_I(\rho_I) + \frac{1}{2} \sum_{J \neq I} \phi_{IJ}(R_{IJ}) \right\} \quad (32)$$

where the second term on the right side,  $\phi_{IJ}(R_{IJ})$ , is a two-body core-core interaction energy (pair potential), and the first term is an additional energy needed to embed the atom into the electron system in the lattice.  $\rho_I$  is the local electron density. The embedding energy is usually fit to the form

$$F_I = A_I E_I^0 \bar{\rho}_I \ln \bar{\rho}_I \quad (33)$$

where  $\bar{\rho}_I$  is obtained by functional fits to the electronic configuration surrounding atom  $I$ ,  $E_I^0$  is its sublimation energy, and  $A_I$  is a constant for atom  $I$ . Baskes (1992) proposed a modified embedded atom method by taking the non-sphere-symmetry of the electronic structure into account. Based on variations of the EAM and SW potentials, a wide variety of many-body potentials has been proposed and used in classical molecular dynamics simulations. These potentials are expected to work well within the range of physical parameters in which they were constructed.

EAM is applicable to interface and surface problems. Tan and Yang (1994) used the modified EAM to perform the atomistic simulation of interface fracture, and explained the origin of the crack-tip singularity. Baskes and his coworkers [Baskes, Angelo and Bison (1994), Gall, Horstemeyer, Van Schilfgaarde and Baskes (2000)] applied the modified EAM to study the tensile debonding and fracture of an aluminum-silicon interface, and analyzed the effect of the micro-defect on the interface. Fallis, Daw and Fong (1995) investigated the structure of small Pt clusters on Pt(111) by using EAM. Zhou, Lomdahl, Voter and Holian (1998) studied the three-dimensional fracture via large-scale molecular dynamics by appealing to EAM. Li, Gao, Qiao, Zhou and Chu (2001) simulated the microcrack healing in copper by means of EAM. Liu and Adams (1992), and Longo, Rey and Gallego (1999) used different EAM to simulate the structure of Ni clusters on Ni surface, respectively, and the results depended on the parameters of embedding energy.

The third one is to introduce the local electronic environment directly into pair potentials, such as the Tersoff potential [Tersoff (1986)]. The Tersoff potential was originally from Abell (1985), and then applied as a practical potential energy formalism for modeling covalent materials by Tersoff (1986, 1989). Tersoff potential is a sum of the energy on each bond. The energy of each bond consists of a repulsive and attractive part. A bond order function is embedded in the formulation. The bond order depends on the local atomic environment such as angular dependency due to the bond angles. Brenner (1990) modified the Tersoff potential by introducing additional terms into the bond order function, which is mainly to correct the overbinding of radicals. Wang, Tomanek and Bertsch (1991) introduced local density approximations (LDA) into a Morse-type potential for carbon systems, which derived a more reasonable binding energy than that from the Lennard-Jones potentials [Qian, Liu, and Ruoff (2001)].

A major distinguishing feature of the Tersoff-Brenner potential is that short-range bonded interactions are reactive, so that a chemical bond can form and break during simulation. The Tersoff-Brenner potentials [Brenner, Shenderova, Areshkin (1998)] are used to model carbon based systems using the type II parameterization, and have been used in a wide variety of scenarios. This potential has been successfully applied in the analysis of for-

mation of fullerenes and their properties [Brenner, Harrison, White, and Colton (1991), Robertson, Brenner, and Mintmire (1992), Robertson, Brenner, and White (1992, 1995)], surface patterning [Sinnott, Colton, White, and Brenner (1994)], indentation and friction at nanoscale [Harrison, White, Colton, and Brenner (1992, 1993a, b, 1995), Harrison, Colton, White, and Brenner (1993)], calculating properties of carbon nanostructures [Brenner, Shenderova, Areshkin, Schall, and Frankland (2002)], and energetics of nanotubes [Robertson, Brenner, and Mintmire (1992)].

Up to now, to authors' knowledge, there is no universal classical MD potential, which works for all the materials and in all the scenarios. EAM type potentials are suited for metals, while Stillinger-Weber (SW) and/or Tersoff-Brenner potentials are suited for semiconductors.

Hereinbefore, we only consider the short range interactions. In general, if the potential drops down to zero faster than  $R^{-d}$ , where  $R$  is the distance between two atoms and  $d$  the dimension of the problem, it is called short ranged. In short range interactions, a cutoff radius is introduced, only neighbored atoms up to the cutoff radius are taken into account for the calculation of interactions, beyond the cutoff radius mutual interactions between atoms are neglected. In order to compensate for the neglect of explicit calculations, long range corrections may be introduced. Energy modifying terms in a periodic molecular cell to account for long range interactions were studied in Madelung (1918), Ewald (1921), Deleeuw, Peram, and Smith (1980) and Heyes (1981) with additional references therein.

### 2.3.2 Long range interactions

In the case of short range potentials, it is easy to calculate the potential or force if one cuts it off at a certain range and uses a neighbor list, that is called a particle-particle method. The amount of calculation of this method is of  $O(N)$  for an  $N$ -particle system. However, in the case of long range potentials, like the Coulomb potential, interactions between all particles in the system must be taken into account, if treated without any approximation. This leads to an  $O(N^2)$  problem, which increases considerably the execution time of a program for larger systems.

The Ewald sum method [Ewald (1921)] is used to decrease the amount of calculation in Coulomb systems by accelerating the force calculation. The Ewald method is limited to fully or partially periodic systems, but has been

widely applied in studies of condensed matter, where it is important to eliminate surface effects arising in a small, isolated system. However, the computational task in this method is still heavy in large system.

There are many algorithms to deal with this problem by accelerating the force calculation, which can be classified into two categories: particle-mesh methods, and hierarchical or multipole methods [Gibbon, and Sutmann (2002)]. Particle-mesh models are more widely used in the field of cosmology than in MD. There are two principal types of particle-mesh simulation models: the particle-mesh (PM) model, and the particle-particle-particle-mesh (P<sup>3</sup>M) model [Birdsall, and Langdon (1985); Hockney and Eastwood (1981)]. The particle-particle (PP) model uses the action at a distance formulation of the force law, the PM model regards the force as a field quantity – approximating it on a mesh – and the P<sup>3</sup>M model is a hybrid of the PP model and PM models. The PP method can be used for small systems with long range forces or for large systems with short range forces. In the previous subsection the PP method is employed to calculate the short range forces. The PM method, on the other hand is computationally fast, but can only handle smoothly varying forces, and the result is generally less accurate. The P<sup>3</sup>M method combines the advantages of the PP and PM methods and enables large correlate systems with long range force to be simulated.

Recently, a PP-MLPG/BIE method is developed to simulate the long range force by Atluri (2004), which will be more accurate and faster than the P<sup>3</sup>M method. In PP-MLPG/BIE method, the MLPG/BIE (Meshless Local Petrov-Galerkin BIE) method replaces the particle mesh method in P<sup>3</sup>M method. The MLPG/BIE method was proposed by Atluri, Han and Shen (2003) by using the concept of the general meshless local Petrov-Galerkin (MLPG) approach developed in Atluri et al (1998, 2002a,b), and has been successfully applied in 3D fracture analysis and the crack growth [Han, Atluri (2003a, b)]. Then one will have the best of the worlds offered by pure MD and MLPG/BIE respectively: high resolution of individual encounters, combined with a rapid meshless evaluation of the long range forces.

In this case, the total potential (Coulomb's potential) of the system is

$$\Pi = \frac{1}{2} \sum_{i=1}^N \sum_{j \neq i}^N \frac{q_i q_j}{4\pi\epsilon |\mathbf{r}_i - \mathbf{r}_j|} \quad (34)$$

where  $N$  is the total number of the particles,  $\epsilon$  is the permittivity of free space, and  $q_j$  is the charge of the particle  $j$ . The force of particle  $j$  on particle  $i$  is give by Coulomb's law as

$$\mathbf{f}_{ij}^{coul} = \frac{q_i q_j}{4\pi\epsilon} \frac{\mathbf{r}_i - \mathbf{r}_j}{|\mathbf{r}_i - \mathbf{r}_j|^3} \quad (35)$$

The inter-particle force is initially split into two contributions:

$$\mathbf{f}_i = \sum_{\substack{j \neq i \\ j \in \Omega_i^{sr}}} \mathbf{f}_{ij}^{sr} + \mathbf{f}_i^{lr} \quad (36)$$

The first sum represents the direct forces of the particle  $j$  on particle  $i$  within the short range domain  $\Omega_i^{sr}$ , as shown in Fig. 4, the shaded box represents the short range domain  $\Omega_i^{sr}$ , the first sum is over all the black particles. The first term is obtained by the PP method. The second term represents the long range forces which are obtained from the MLPG/BIE method in the global domain.

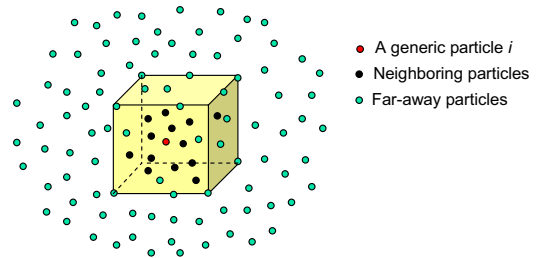


**Figure 4 :** Force splitting scheme

The long range interaction is assumed to be temporally and spatially smooth enough, so that the long range contribution to the interaction energy is found by solving the Poisson's equation for long range potential [Hockney, Eastwood (1981)] by employing the MLPG/BIE method [Atluri (2004)]. The derived boundary integral equations for the long range potential and the gradient of the potential are weakly singular. The PP-MLPG/BIE method will be faster and cheaper than the P<sup>3</sup>M method, although both of them are of  $O(N)$  computational complexity.

After obtaining the force on the particle  $i$ , we should solve the equation of motion. The multiple time scales method [Tuckerman et al. (1991)] in conjugation with

Verlet's leapfrog method is a natural choice to integrate the equation of motion  $m_i \ddot{\mathbf{r}}_i = \mathbf{f}_i$ , because the force is already subdivided into short and long range components,

$$\mathbf{f}_i = \mathbf{f}_i^{sr} + \mathbf{f}_i^{lr} \quad (37)$$

where  $\mathbf{f}_i^{sr}$  varies fast and  $\mathbf{f}_i^{lr}$  varies slow. In this multiple time step method, the short range forces are calculated every time step  $\delta t$  by means of PP method, while the long range forces are renewed every  $n$  time steps by using MLPG/BIE method. However, it should be pointed out that this multiple time scales method only focus on the calculation of the interaction of the particles, the equation of motion  $m_i \ddot{\mathbf{r}}_i = \mathbf{f}_i$  is still integrated every time step  $\delta t$ .

Multipole methods [Pfalzner, and Gibbon (1996)] are based on the observation that distant charges (or masses) may be grouped together and substituted by a single multipole expansion, that lead to a considerable saving in the number of interactions necessary to sum the potential or force. Two approaches proposed in mid-1980 belong to this category: hierarchical tree code method [Appel (1985); Barnes and Hut (1986)], and fast multipole method (FMM) [Greengard and Rohklin (1987)]. The hierarchical tree code method is  $O(N \log N)$ -schemes based on hierarchical grouping of distant particles. The fast multipole method (FMM) is  $O(N)$ -schemes with rounding-error accuracy. They serve a good basis for the accelerating calculation of many-body systems governed by long-range potentials. A detailed discussion about Multipole methods can be found in [Gibbon, and Sutmann (2002)].

Instead of accelerating the force calculation, the symplectic method [Channell and Scovel (1990); Candy and Rozmus (1991); and Wisdom and Holman (1991)] can also be employed to improve the accuracy and reduce the required computational time, which integrates the Hamiltonian rigorously and allow one to make the basic time step larger.

### 2.3.3 Time integrators

In order to obtain a trajectory through phase space for these atoms, an integrator is required for Newton's laws of motion. Numerical integration of the equations of motion is performed either by explicit or implicit methods, such as the Verlet [Verlet (1967)], leapfrog [Hockney (1970)], and velocity Verlet [Swope, et al. (1982)] methods. Because of the lack of numerical stability, the

simple Euler scheme is not appropriate for MD simulations. In Verlet method, the error will accumulate with the time steps and may lead to a serious error in the final results. The leapfrog method was proposed to avoid this accumulation of errors. The leapfrog method is more tractable than the Verlet method when one introduces velocity scaling in a system with periodic boundary conditions. However, the leapfrog method cannot handle the velocity properly, the velocity Verlet method is usually adopted. The explicit velocity Verlet method is very popular in MD simulations due to the fact that it is stable, memory-efficient, and easily augmented to handle multiple timescale MD. The following algorithm is iterated:

$$\dot{\mathbf{R}}_I \left( t + \frac{\Delta t}{2} \right) = \dot{\mathbf{R}}_I(t) + \frac{\Delta t}{2m_I} \mathbf{F}_I(t) \quad (38)$$

$$\mathbf{R}_I(t + \Delta t) = \mathbf{R}_I(t) + \Delta t \dot{\mathbf{R}}_I \left( t + \frac{\Delta t}{2} \right) \quad (39)$$

$$\mathbf{F}_I(t + \Delta t) = \frac{\partial V}{\partial \mathbf{R}_I(t + \Delta t)} \quad (40)$$

$$\dot{\mathbf{R}}_I(t + \Delta t) = \dot{\mathbf{R}}_I \left( t + \frac{\Delta t}{2} \right) + \frac{\Delta t}{2m_I} \mathbf{F}_I(t + \Delta t) \quad (41)$$

At each iteration, each of the four steps is performed sequentially for every atom  $I$  in the system. After exiting the last step, the simulation time is incremented by  $\Delta t$ . Another popular implicit integration method for MD is the predictor-corrector scheme, specially the Gear algorithm [Gear (1971)], which can integrate the temporal evolution equation for longer times with more accuracy. For detailed description for the technique of the molecular dynamics simulation, the readers are referred to Rapaport (1995). Tucker and his colleagues [Tucker, et al. (1991), and Tucker, and Berne (1992)] developed the multi-time-step method to improve the accuracy and reduce the required computational time.

The above descriptions are used for a microcanonical simulation (NVE ensemble), where the total energy is a conserved quantity. If the temperature or the pressure should keep constant (the NVT or NPT ensembles), it is not enough to only integrate Newton's equations of motion, the effect of a thermostat interacting with the system should be considered. In canonical simulations (NVT ensemble), to maintain the fixed temperature, one

should use the equipartition theorem and equate the kinetic energy to  $\frac{3}{2}Nk_B T$ , where  $N$  is the total number of the atoms in this system,  $k_B$  is the Boltzman constant, and  $T$  is the temperature. A number of more sophisticated thermostats have also been developed, such as the Langevin's algorithm or Nosé-Hoover thermostat [Nosé (1984)].

The standard molecular dynamics routine is illustrated in Fig. 5.

The previous treatments, *ab initio* molecular dynamics, tight binding, and classical molecular dynamics are all deterministic. The state of the system is determined completely by the initial condition. These approaches are useful in understanding stable structures, vibrations, and growth at the atomistic level. Another method for treating complex systems is the Monte Carlo method, which investigates problems by sampling from random distributions, and uses concepts of probability theory. It assumes very idealized or simplified interaction parameters and can treat larger number of atoms. Physical and chemical properties of large systems are obtained by statistically averaging over randomly moved particles. Hence, it is a stochastic method. These techniques are now routinely applied in almost every field, from biology to nuclear physics to social studies. The detailed discussion about this method is omitted here, interested readers are refer

to Ohno, Esfarjani and Kawazoe (1999). Some of its applications can be found in Battaile et al. (1997), Bortz et al. (1975), Huang et al. (1998), Gilmer et al. (2000) and Singh et al. (1997).

### 3 Multi-scale Simulation

Recently, an intense effort has been devoted to the modeling and simulations of physical phenomena occurring on a vast range of length scales. This endeavor has prompted the development of multiscale modeling and simulation strategies. Although constant increases in available computational power and improvement in numerical algorithms, even classical molecular dynamics methods with very simple potentials are still limited to simulating on the order of  $10^6$ - $10^8$  atoms for a few nanoseconds. However, real materials are composed of  $\sim 10^{23}$  atoms and molecules, and sometimes it becomes necessary to perform far-larger-scale simulations. For phenomena on a much larger space scale and longer time scale, one possible strategy is the multi-scale methods. The simulation of large systems must be left to continuum methods. Continuum mechanics is used to predict the phenomena described by uniform collective behavior of atoms, while nano-mechanics is used to predict the phenomena described by dramatic changes in the state of few atoms. Multiscale modeling and simulations are being used in diverse fields, such as materials science, nano/micro-electronics, environmental remediation, and biotechnology. The overall goal of multiscale modeling is to predict the response of complex systems across all relevant spatial and temporal scales. It is of interest to build models that can seamlessly simulate multi-scale systems. Several methods have been developed for the multiscale simulations. A recent review paper on the multiscale modeling in nano- and micro-mechanics of materials is written by Ghoniem and Cho (2002).

The traditional approaches to couple spatial and temporal scales are the hierarchical approaches in which a hierarchy of approaches and mathematical/computational models with different physical levels of description is pieced together, and the output of the smaller-scale models is used as input for the larger-scale models. Sinclair (1971) modeled a bcc dislocation core by equilibrating forces between atoms and continua with the continuum region modeled with analytical techniques. Clementi (1988) combined quantum mechanics, molecular dynamics, and fluid dynamics to predict the tidal circulations. In

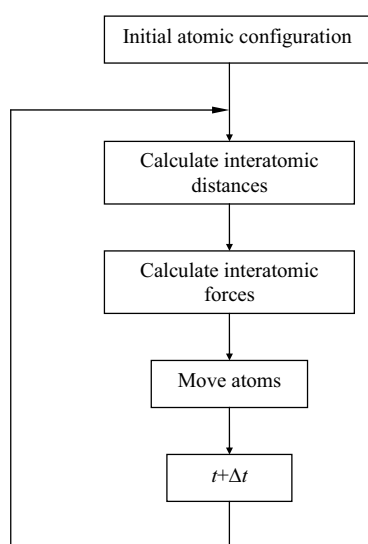


**Figure 5** : An illustration of classical MD routine

a series of calculations, each calculation was used as input to next up the length and time hierarchy. Kohlhoff, Gumbsch and Fishmeister (1991) proposed a method incorporating a non-local elasticity theory for a transition region connecting the lattice and continuum regions. Tan and Yang (1994) used the molecular dynamics (EAM) and finite element method to simulate interface fracture. Gumbsch (1996) used the molecular dynamics and finite element method to simulate brittle crack propagation. Noguchi and Furuya (1997) matched displacements between atomistic molecular dynamics and a micromechanics model to simulate elastic-plastic crack propagation. Sham and Tichy (1997) simulated thin film lubrication by means of molecular dynamics and finite element method. However, many gaps still exist in these models. Some of these methods were reviewed by Cleri, et al. (1998). So far, no rational way exists to relate the phenomena at the very small length scales with the macroscopic behavior.

An equivalent-continuum modeling approach was proposed to model structure-property relationships of nanostructured materials by [Odegard, Gates, Nicholson, and Wise (2002)]. This method replaced discrete molecular structures with equivalent-continuum representative volume models by equating the molecular potential energy of nano-structured materials with the mechanical strain energy of the representative volume element (equivalent-energy). This method has been applied to determine the effective geometry and effective bending rigidity of a graphene sheet [Odegard, Gates, Nicholson, and Wise (2002)]. The development of an equivalent-truss model may be used as intermediate step in establishing the equivalent-continuum model. Each atom in the molecular model is represented by a pin-joint, and each truss element represents an atomic bonded or non-bonded interaction. The moduli of the truss elements are based on the molecular mechanics force constants. If one stops at this equivalent-truss model instead establishing the equivalent-continuum model, the so-called molecular structural mechanics is developed [Wang, et al. (2002); Li, and Chou (2003)]. This method focuses mainly on simulating atom mechanics using linear continuum abstractions (trusses and bars). It preserves, and in some cases increases, the number of degrees of freedom compared to the full atomistic system. The expense is paid in order to make the problem quasi-static and linear before the application of a numerical solution procedure. So,

in the end, the atomic positions are easier to obtain than from full molecular dynamics. Wang, et al. (2002) derived the continuum mechanical properties of polymer networks using this molecular structural mechanics. The equivalent-continuum modeling is based on the equivalent-energy, it can not determine the geometry and material properties uniquely at the same time since all the quantities are mixed in the energy, only one of them can be determined given another one is predetermined from the literatures or assumed. Every independent material constant is determined by a different corresponding boundary condition. This method is not self-consistent, nor appropriate to large deformation.

With the advent of parallel computers, another approach to the coupling of length scales, the handshaking approach, appears. In this approach, the problem is divided into its natural components, each of which may be addressed by one or more processors. Then, the “handshaking” between the different regions plays a important role in this method. The “handshaking” is not just an algorithmic issue but also one that requires physical insight [Broughton, Abraham, Bernstein, and Kaxiras (1999)]. The FE/MD/TB model has recently been propounded by Abraham and coworkers [Broughton, Abraham, Bernstein, and Kaxiras (1999), Abraham (2000)]. An example of this handshaking approach for dynamic fracture analysis is shown in Fig. 6. In this model, the problem is divided into three regions: continuum mechanics, the implementation of which is via finite elements (FE); atomistic statistical mechanics, implemented by molecular mechanics; and mean-field quantum mechanics represented by semiempirical tight bind (TB) (or *ab initio* method). Each simulation is performed on a different region of the domain, with a coupling imposed in “handshake” regions where the different simulations overlap. The method is designed for implementation on supercomputers via parallel algorithms, allowing the solution of large problems. A Hamiltonian,  $H_{tot}$ , is defined for the entire system, which can be conceptually written as [Broughton, Abraham, Bernstein, and Kaxiras (1999)]

$$\begin{aligned}
 H_{tot} = & H_{FE}(\{\mathbf{u}, \dot{\mathbf{u}}\} \in FE) \\
 & + H_{FE/MD}(\{\mathbf{u}, \dot{\mathbf{u}}, \mathbf{R}, \dot{\mathbf{R}}\} \in FE/MD) \\
 & + H_{MD}(\{\mathbf{R}, \dot{\mathbf{R}}\} \in MD) \\
 & + H_{MD/TB}(\{\mathbf{R}, \dot{\mathbf{R}}\} \in MD/TB) \\
 & + H_{TB}(\{\mathbf{R}, \dot{\mathbf{R}}\} \in TB)
 \end{aligned} \tag{42}$$

The degrees of freedom are atomic positions,  $\mathbf{R}$ , and their velocity,  $\dot{\mathbf{R}}$ , for the TB and MD regions; and displacements,  $\mathbf{u}$ , and their time rates of change,  $\dot{\mathbf{u}}$ , for the FE regions. This equation states that there are three separate Hamiltonians for each subsystem as well as Hamiltonians that dictate the dynamics of variables in the handshake regions. The subscripts “FE/MD” and “MD/TB” denote such handshake regions.

Abraham, Broughton, Bernstein, and Kaxiras (1999) and Abraham, Bernstein, Broughton, and Hess (2000) used this method to simulate the propagation of a crack in a brittle material, where the TB method is used to simulate bond breaking at the crack tip, MD is used near the crack surface, and the surrounding medium is treated with FE. Rafii-Tabar, Hua, and Cross (1998) proposed a related method by a stochastic coupling of a molecular-dynamics region to a finite element region. The system is propagated in time using a stochastic differential equation so as to produce something resembling Langevin dynamics. Simirnova, Zhigilei, and Garrison (1999) studied the propagation of a laser-induced pressure wave in a solid by combining the molecular dynamics and finite element method. This method has been extensively applied in the field of laser of ablation by Zhigilei and his colleagues.

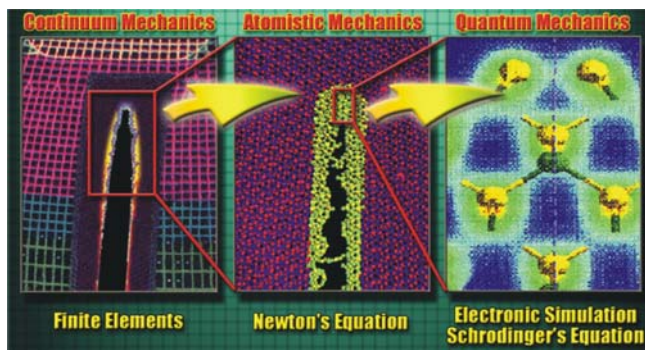


**Figure 6 :** The multiscale modeling approaches that attempt to link several computational approaches in a combined model for dynamic fracture analysis. In this model, electronic structure model (quantum mechanics) is combined with a molecular dynamics model, which in turn is embedded into a continuum model (discretized) by finite elements [Noor (2002)].

Fig. 6 The multiscale modeling approaches that attempt to link several computational approaches in a combined model for dynamic fracture analysis. In this model, electronic structure model (quantum mechanics) is combined

with a molecular dynamics model, which in turn is embedded into a continuum model (discretized) by finite elements [Noor (2002)].

In the handshaking approach, the standard technique is to a priori identify the atomistic and continuum regions and tie them together with some interface boundary conditions. The challenge for mesh generation is that the mesh should smoothly transition between the true atomic lattice in the MD region and the closely-packed FE meshes. Too abrupt a crossover leads to unphysical behavior, such as elastic wave reflections at the interface [Rudd and Broughton (1998, 2000)]. In addition to the disadvantage of introducing artificial numerical interfaces into the problem, a further drawback of these models is their inability to adapt to changes in loading an evolving state of deformation. To connect seamlessly to molecular dynamics in the atomic limit, Coarse Grained Molecular Dynamics (CGMD) has been developed as a substitute for finite elements Rudd and Broughton (1998, 2000)], which derived the equation of motion directly from finite temperature MD through a statistical coarse graining procedure. Although CGMD reduced unphysical scattering of waves traveling from the atomistic region into the CG region as compare to FE, the short-wavelength wave still reflected from the CG region. Moreover, the computational cost of the CG procedure is far beyond that of FE.

The quasicontinuum method was originally introduced by Tadmor, Ortiz, and Phillips (1996). The theory of the quasicontinuum furnishes a computational scheme for linking the atomistic and continuum realms, and regards that all the system is in the atomistic realm. The basic idea is that every point in a continuum corresponds to a region on the atomic scale, which is homogeneously distorted according to the deformation gradient at the point. The finite strain theory is employed in the continuum realms. The details about the finite strain analysis can be found in Atluri (1979, 1980). A hypothesis to connect the continuum displacement field and the motions of atoms must be employed. The Cauchy-Born hypothesis is the basis for developing the quasicontinuum elastic potentials, from the atomistic description of the system. The Cauchy-Born hypotheses for crystals are equivalent for homogeneous deformations [Born and Huang (1954), Ericksen (1984)].

For simple Bravais lattice that has the centrosymmetric atomic structure, the Cauchy-Born rule [Born and Huang

(1954), Ericksen (1984)] gives

$$\mathbf{r}_{IJ} = \mathbf{F}\mathbf{R}_{IJ} \quad (43)$$

where  $\mathbf{F}$  is the deformation gradient, and  $\mathbf{R}_{IJ}$  and  $\mathbf{r}_{IJ}$  represent the distances between two atoms  $I$  and  $J$  in the reference configuration and current configuration, respectively. However, it does not for complex Bravais lattice which can be given by means of a number of interpenetrating simple Bravais lattices (sub-lattices) and does not possess centrosymmetry, such as the hexagonal lattice. In this case, the Cauchy-Born rule gives [Zanzotto (1996), Martin (1975), Cousins (1978), Born and Huang (1954)]

$$\mathbf{r}_{IJ} = \mathbf{F}\mathbf{R}_{IJ} + \boldsymbol{\zeta}_k \quad (44)$$

where the internal variable  $\boldsymbol{\zeta}_k$  are shift vectors, with  $k$  ranging from 0 to some integer  $N$  (There are  $N+1$  sub-lattices in the complex Bravais lattice. If atoms  $I, J$  are in the same sub-lattices,  $\boldsymbol{\zeta}_k=0$ ).  $\boldsymbol{\zeta}_k$  and  $\mathbf{F}$  are independent variables. At the static equilibrium state, the vectors  $\boldsymbol{\zeta}_k$  are to be determined by the minimization of the energy function, so as to reach an equilibrium configuration in the deformed crystal. This means that the equilibrium values of  $\boldsymbol{\zeta}_k$  can be written as functions of  $\mathbf{F}$ . If focusing on dynamical problems, one will avoid making any specific hypothesis on the behavior of  $\boldsymbol{\zeta}_k$ , what one need is  $\partial\mathbf{r}_{IJ}/\partial\mathbf{F} = \mathbf{R}_{IJ}$  from either (43) or (44).

Once the geometry of the deformed lattice vectors is linked to the continuum deformation, a constitutive model based on atomistic description can be constructed by equating the continuum strain energy density to the potential energy of the atomic system for a representative cell, divided by its volume. A continuum finite element formulation is used to characterize the mechanical response of a given system. The difference from standard finite element methodologies is that the constitutive response of the system is obtained from an atomistic calculation rather than an empirical phenomenological rule. This type of approach is due to Kroner (1967). In this method, a set of atoms making up a Bravais lattice has selected from a subset. A triangulation of this subset allows the introduction of finite element-like shape functions at lattice points, allowing the interpolation of quantities at intermediate points in the lattice. The finite mesh permeates the entire system, right down to atomic dimensions. In the inhomogeneous deformation region (such as near defects), the atoms are expressed explicitly, while in

the homogeneous deformation region, the atoms are expressed implicitly by the representative atoms. An underlying atomistic Hamiltonian is used to determine the energy density of the system; a separate atomistic calculation is required for each cell in their finite element mesh. The energy of the atoms in inhomogeneous deformation region is calculated by building the appropriate complement of neighbors as in the classical MD method. In the homogeneous deformation regions, the energy is calculated using a single representative atom in the center of a uniformly deformed crystal in which the deformation gradient is  $\mathbf{F}$ . This crystal is always made sufficiently large that there are no boundary effects there. The problem of the minimization of energy to find equilibrium configurations can be written in terms of a reduced set of variables.

The method is made practical by approximating summations over all atoms, as using summation rules analogous to numerical quadrature. The rules rely on the smoothness of the quantities over the size of the triangulation to ensure accuracy. The adaptivity rules allow the reselection of representative lattice points in order to tailor the computational mesh to the structure of the deformation field. The criteria for adaptivity are designed to allow full atomic resolution in regions of large local strain, such as near a defect.

Different variants of the quasicontinuum theory have been developed in a series of publications where numerous examples of application have also been presented, such as the simulation of dislocations, grain boundary interactions, nanoindentation, fracture, and the response of ferroelectric materials to electrical and mechanical loading. Recently, Shenoy (2003) extended the method to dynamics at zero temperature, and a multiple-time-step method was also developed for the time integrating.

There are several limitations in the quasicontinuum method. In particular, cracks and defects are not allowed to form, and since the simulation is carried out at zero temperature, thermally-activated processes are not included [Smith, Tadmor, Bernstein, and Kaxiras (2001)]. Moreover, interface energies between different phases are not taken into account. Due to that the procedure focused on approximating the energy but not the forces, some non-physical forces are induced [Shenoy, Miller, Tadmor, Rodney, Phillips, and Ortiz (1999)]. Actually, another reason for these non-physical forces is the fact that the finite element interpolation is a local interpola-

tion, which disobeys the non-local physics property of the atoms. In addition, in these approaches, the nodes must coincide with atoms at the interface, therefore, the resolution of the discretized continuum nodal space down to the atom scale, that restrict the size of the continuum and leads to smaller overall dimension problem. Chung and Namburu (2003) circumvented the interface entirely through homogenization theory. A lattice statics based tangent-stiffness finite element method is developed for the interface/transition region by Chung, Namburu, and Henz (2004). Wagner and Liu (2003) presented a multiscale method for coupling molecular dynamics and continuum mechanics at finite temperature by using “bridging scale” decomposition and quasicontinuum method, where the entire system is treated as a coarse scale one, first; and then the entire system is treated as a fine scale one, later sequentially. Multiple time steps are employed for wave propagation in the coarse scale and fine scale. A recent review of the quasicontinuum method discussing its theory and applications can be found in Miller and Tadmor (2002).

Recent, by virtue of the dynamic principle of virtual work, an equivalent continuum is defined for dynamically deforming atomistic system by Zhou and his colleague [Zhou and McDowell (2002); Zhou (2003)]. Work-conjugate continuum stress and deformation fields, mass distribution, and all other work- and momentum-preserving kinetic quantities are specified for the equivalent continuum. The resulted equivalent continuum fields represent a continuum reinterpretation of the result of a discrete MD calculation, and have exactly the same number of independent degrees of freedom as the discrete atomistic system. Hence, this equivalent continuum fields is computationally intensive to obtain. This equivalent continuum may offer a theoretical basis for linking MD to continuum in multiscale simulation, just likes the role of the Cauchy-Born hypotheses in the quasicontinuum method.

Other studies describing methods for multi-scale simulations of the atomistic and the quantum regimes or continuum and the atomistic regimes can be found in Hoover, De Groot, and Hoover (1992), Capaz, Cho and Joannopoulos (1995), and Vanduijnen and Devries (1996). Friesecke and James (2000) proposed a scheme of bridging between continuum and atomic structure, focusing on nano-structures in which the size of one dimension is much larger than the other. Zhang, Klein, Huang,

Gao, and Wu (2002) developed virtual-internal-bond (VIB) model to apply continuum mechanics to multiscale material problems, which incorporated a cohesive-type law into constitutive equations. VIB model provides an effective method to investigate crack nucleation and propagation in engineering materials. Garikipati (2002) embedded micromechanical models in the macromechanical formulation by means of a variational multiscale method. The resulting macromechanical formulation is formed solely in terms of the coarse scale displacements, but is influenced by the fine scale, which is governed by micromechanical models; thereby it has a multiscale character. Insepov et al. (1997, 2000) used a multiscale method to study the effects of impact by atomic clusters on crystal surfaces. In this method, an ensemble averaging technique is employed to pass thermal and deformation from the atomistic region to the FE region.

As we know, in the multiscale simulation, the atomistic method is employed where the displacement field varies on an atomic scale, and the continuum approach is employed elsewhere. For the seamless multiscale simulation, it is important to ensure that the elastic waves generated in the atomistic region can propagate into the continuum region. The continuum region cannot support modes of short wavelength, which is less than the spacing of the nodes. One source of finite size effects is the short waves which are reflected back unphysically from an artificial interface or boundary, which may also produce uneven heating across the interface. In order to minimize such reflections, some interfacial conditions are proposed [Cai et al. (2000), E and Huang (2001), Wagner and Liu (2003)]. Cai et al. (2000), Wagner and Liu (2003) derived the interface conditions as a generalized Langevin equations. However, the time history integral is difficult to compute, especially for moving MD region. E and Huang (2001) minimized boundary reflection in an MD simulation with a reduced weighted sum of history terms. We developed a method for the seamlessly coupling of continuum and MD simulation at finite temperature [Shen, and Atluri (2004)], where alternate interfacial conditions between atomistic and continuum regions were proposed by considering the fluctuation of atoms in the continuum region. Their effectiveness in ensuring the accurate passage of information between atomistic and continuum regions was discussed.

Consider a multiscale system, including an atomistic region, which may contain inhomogeneities, and an equiv-

alent continuum mechanics (ECM) domain, which is defect-free. In the (ECM) region, the deformation is homogeneous, and thus can be approximated by an equivalent continuum mechanics model as in quasicontinuum method, where the individual atomic displacements are not being solved using molecular dynamics. The material in ECM is discretized into a set of nodes, which are not necessarily coincident with the atoms. The positions of the atoms in this region can be interpolated from those of the nodes. Effectively, the ECM model involves an averaging over the atomic degrees of the freedom that are missing from the node. The meshless local Petrov-Galerkin (MLPG) method is employed to solve for the displacements of the nodes in the ECM region. This is illustrated of in Fig. 7. In the ECM region, the nodes can be taken to be arbitrary, and not necessarily be coincident with the atoms. In MD region, the nodes are taken to be the atoms themselves. In the ECM region, the solid points represent the atoms, while the open points represent the nodes of the MLPG method. MLPG5 is implemented in “ECM” region and MLPG2 is implemented in MD region.

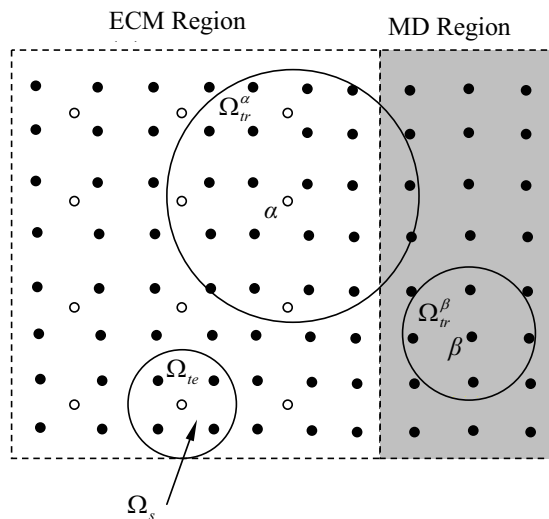


**Figure 7** : Illustration of ECM/MD multiscale simulation.

The MLPG method, a truly meshless method developed by Atluri and his colleagues, is a simple and less costly alternative to the FEM and BEM [Atluri and Zhu (1998), Atluri and Shen (2002a, b)]. Remarkable suc-

cesses of the MLPG method have been reported in solving the convection-diffusion problems [Lin and Atluri (2000)]; beam problems [Raju, Phillips (2003)]; fracture mechanics [Kim & Atluri (2000), Ching & Batra (2001)]; strain gradient materials [Tang, Shen and Atluri, (2003)]; three dimensional elasticity problems [Li, Shen, Han and Atluri (2003)]; elastodynamic problems [Batra, Ching (2002); Sellountos, and Polyzos (2003)]; elastodynamic problems in continuously nonhomogeneous solids [Sladek, Sladek, Zhang (2003)]; thermoelasticity [Sladek, Sladek, Atluri (2001)]; Navier-Stokes flows [Lin and Atluri (2001)]; and plate bending problems [Gu & Liu (2001), Long and Atluri (2002), Qian, Batra, and Chen (2003a, b)]. A comparison study of the efficiency and accuracy of a variety of meshless trial and test functions is presented in Atluri and Shen (2002a, b), based on the general concept of the meshless local Petrov-Galerkin (MLPG) method. The recent review of the MLPG method, regarding its theory and applications can be found in Atluri (2004), and Atluri and Shen (2003).

As mentioned before, the displacement  $\mathbf{u}_i$  of an atom in ECM region implies an average value of the atomic displacement, it can not catch the thermal fluctuations. To describe it more accurately, we assume that the “real” displacement  $\mathbf{q}_i$  of the atom in the ECM region can be expressed as:

$$\mathbf{q}_i = \mathbf{u}_i + \delta\mathbf{u}_i \quad (45)$$

where  $\delta\mathbf{u}_i$  denote the atomic thermal fluctuations, and it is assumed that  $\delta\mathbf{u}_i \ll \mathbf{u}_i$  in ECM region. This decomposition has the multiscale feature offered by pure MD and the continuum respectively: short-wavelength fluctuation of individual atom and long-wavelength wave of the continuum. By means of this decomposition, the effects of the thermal fluctuations on the MD region lead to the interface conditions. An optimal method was proposed [Shen and Atluri (2004)] in both reducing the reflection of phonons and in lowering computational cost, especially when the atomistic region moves with time. A multiple time step method was employed for the time integration in both MD and ECM region: the MD simulation is advanced by  $k$  steps of size  $\Delta t_A$ , when the ECM simulation is advanced for a step of size  $\Delta t_B = k\Delta t_A$ . The stability of multiple time step method was studied in Belytschko et al. (1979). Numerical experiments stated that this method was very accurate and efficient. More details about this multiscale method are given in Shen and Atluri

(2004), and Atluri (2004).

For more examples about the multi-scale simulations and their application, see the proceedings of the Training Workshop on Multiscale Modeling, Simulation and Visualization and Their Potential for Future Aerospace Systems [Noor (2002)]. In addition, two special issues of *CMES: Computer Modeling in Engineering & Sciences* (2002a, b) have been devoted to this topic. Srivastava, Menon and Cho (2001) briefly reviewed computational techniques and provided a few examples derived from computer simulations of carbon nanotube-based molecular nanotechnology. Chang and Guo (2002) also reviewed the recent advances in molecular dynamics and Monte Carlo simulations.

Although substantial progress has been made in recent years, multi-scale modeling method is still in its infancy, and it still requires intensive efforts. As pointed by many researchers, the main issues in the development of seamless multi-scale modeling methodology are still the limitations on the length and time scale, and the numerical accuracy and efficiency. Hence, a more accurate and efficient multi-scale modeling methodology is still desirable, and attracts many researchers.

#### 4 Numerical Simulations in Carbon Nanotube

Since the debut of carbon nanotube (CNT) in 1991 [Iijima (1991)], it has stimulated activities in the investigation of the physical and mechanical properties and their potential technological application. CNT can be produced by an array of techniques, such as laser ablation, arc discharge and chemical vapor deposition. They possess exceptional properties, such as high stiffness and strength, the ability to sustain large elastic strain, and high thermal and electric conductivity.

A single-walled carbon nanotube (SWNT) can be viewed as a result of rolling a graphene sheet, by specifying the direction of rolling and the circumference of the cross-section. A multi-walled carbon nanotube (MWNT) is composed of concentric graphitic cylinders with closed caps at both ends and the graphitic layer spacing is about 0.34 nm. In the graphene sheet, carbon atoms are arranged in a hexagonal array, and each has three nearest neighbors. The atomic structure of nanotube is described in terms of the tube chirality, or helicity, which is defined by the chiral vector  $\mathbf{C}_h$  and the chiral angle  $\theta$ , as shown in Fig. 8. After cutting the graphite sheet along the dotted

lines and rolling to form a nanotube, the two end nodes of the chiral vector coincide. The chiral vector, i.e. the roll-up vector can be expressed as a linear combination of base vectors  $\mathbf{a}_1$  and  $\mathbf{a}_2$  of the hexagon:

$$\mathbf{C}_h = n\mathbf{a}_1 + m\mathbf{a}_2 \quad (46)$$

where the integers  $(n, m)$ , which uniquely define the type of the nanotube, are the number of steps along the zigzag carbon bonds of the hexagonal lattice. Three major categories of nanotube are defined based on the chiral angle  $\theta$ . The chiral angles are  $0^\circ$  and  $30^\circ$  for the two limiting cases which are referred to as zigzag and armchair, respectively. The chiral angle is between  $0^\circ$  and  $30^\circ$  for chiral. The zigzag nanotube is denoted by  $(n, 0)$  and the armchair nanotube  $(n, n)$ . The roll-up vector of the nanotube also defines the diameter of the nanotube. The physical properties of CNTs are sensitive to their diameter, length and chirality [Dresselhaus, et al. (1997); Popov, et al. (2000); Hernandez, et al. (1998)]. A survey about the mechanics of carbon nanotubes can be found in Qian, Wagner, Liu, Yu and Ruoff (2002). Here, we only review the latest achievements in this field.

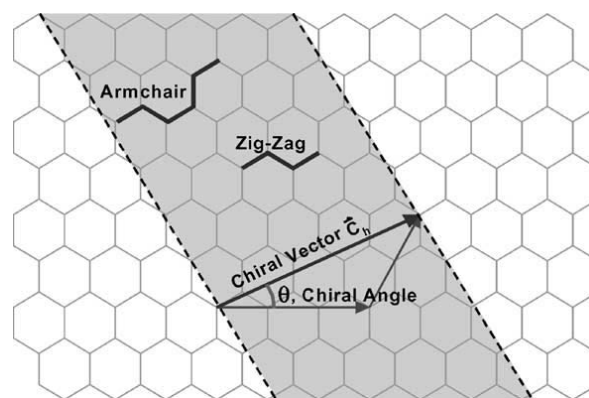


**Figure 8** : Schematic diagram of a hexagonal graphene sheet [Thostenson, et al. (2001)].

Ab initio, TBMD and classical MD methods were employed to perform the analysis of CNT. They are the “bottom up” methods. By means of MD, Iijima, et al. (1996) studied the structural flexibility of CNTs, and Yakobson, et al. (1997) simulated the high strain fracture in CNTs. Hernandez, et al. (1998) investigated the elastic properties of nanotubes using TBMD. Sanchez-Portal

(1999) studied the elastic and vibrational properties of CNTs resorting to density functional theory (ab initio). Belytschko et al. (2002) simulated the nanotube fracture using MD methods, and showed moderate dependence of fracture strength on chirality. Dumitrica et al. (2003) proposed a brittle bond-breaking CNT failure mechanism by using the density functional theory (DFT). Troya, et al. (2003) presented quantum mechanical studies of CNT fracture using two different semiempirical methods. The different fracture mechanisms from quantum mechanics and empirical potentials were explored. Guo and Guo (2003) investigated the coupled mechanical and electrostatic properties of single walled open CNTs under applied electric field and tensile loading by means of quantum mechanics and quantum-MD techniques. Quite different failure mechanisms in electric or mechanical loading were predicted. Guo and Guo (2003) simulated an exceptional large axial electrostrictive deformation in CNTs using Hartree-Fock and density functional theory. The volumetric and gravimetric work capacities are predicted to be three and six orders higher than those of the best known ferroelectric, electrostrictive, magnetostrictive materials and elastomers, respectively.

Multiwalled carbon nanotubes (MWNTs) have been proposed as candidates for nanoscale molecular bearings, spring, and oscillators. Zhao, et al. (2003) used MD to study the energy dissipation mechanism for isolated systems of two coaxial carbon nanotubes, which may serve as a nearly frictionless nano-oscillator. Guo, et al. (2003) also performed MD simulations of a double walled CNT oscillator to show that the rate of energy dissipation depends on the commensuration and relative morphology of the bitube. Zhang, et al. (2003) studied double-walled CNTs-based bearings using MD simulations. Their results showed that dynamic effects dominate the friction in these DWCNT bearings and the interlayer friction is very small. In their simulations, the intralayer interaction is described by a Brenner potential, and the interlayer interaction is represented by the registry-dependent graphitic potential developed by Kolmogorov and Crespi (2000). Qian et al. (2003) studied the nature of load transfer in a single walled carbon nanotube bundle using a Lennard-Jones potential for the inter-tube interactions. Their results revealed that the radial deformation strongly depended on the twist angle, which consequently changes the nature of the contact and contributes a new interlayer tribology. Zhang, et al. (2003) inves-

tigated the mechanical properties of SWNTs filled with small fullerenes (C<sub>20</sub>, C<sub>36</sub> and C<sub>60</sub>) using MD simulation. The interaction between carbon atoms was described by a combination of Brenner potential with a two-body pair potential. Their mechanical properties depended on the filling-density and the radius of the tube. Such peapod types of structures may use in functional nanoscale devices such as nano-pistons, nano-bearings, nano-writing implements, or as a nano-capsule storage system. Wei and Srivastava (2003) studied the transport of long polymer molecules through CNT channels using the MD simulations. A polymer molecule is adsorbed into a NT due to van der Waals interactions, which is modeled as Lennard-Jones potentials. Tersoff-Brenner potentials were used for carbon-carbon and hydrogen-carbon interactions.

As discussed in previous sections, these atomistic modeling techniques are limited to systems containing a small number of molecules or atoms and are usually confined to studies of relatively short-lived phenomena, from picoseconds to nanoseconds. Nanotubes dominated by atomistic effects exhibit continuum-like behavior. Continuum-like methods that have been developed for nanoscale devices rely on parameterizations of more detailed calculations, e.g. from molecular dynamics and/or ab initio, to be fed into existing continuum models such as shell [Yakobson, Brabec, and Bernholc (1996)] and beam [Wong, Sheehan, and Lieber (1997)] theories. Yakobson, Brabec, and Bernholc (1996) studied the nanotube instability problem by means of the shell theory. Pantano and his colleagues (2003) used a continuum/finite element approach to model the structure and the deformation of SWCNTs and MWCNTs. In their works, individual tubes are modeled using shell elements, the effects of van der Waals forces are simulated with special interaction elements. Vodenitcharova and Zhang (2003) investigated the effective wall thickness of a single-wall carbon nanotube using the continuum ring theory. Savinskii and Petrovskii (2002) calculated the vibration spectrum of a nanotube in the long-wavelength limit as a function of the radius and thickness of the nanotube, which was represented as an elastic cylindrical shell of a finite thickness. Harik (2002) analyzed the applicability of continuum-beam models and continuum shell theories to the global mechanical behavior of SWNTs, and concluded that the direct use of the beam theory should be limited to SWNTs with very small

diameters. Sudak (2003) presented a multiple column model for the linearized column buckling of multi-walled carbon nanotubes using the theory of nonlocal continuum mechanics. Gao and Li (2003) developed another continuum-based model for computing strain energies and Young's modulus of SWCNT, which is viewed as a continuum hollow cylinder by rolling up a flat graphite sheet that is treated as an isotropic continuum plate. In their model, kinematics of finite deformations was employed with the Hencky strain and the Cauchy stress. All these kinds of continuum models can be used to analyze the static or dynamic mechanical properties of nanotubes. However, these models neglect the detailed characteristics of nanotube chirality, and are unable to account for forces acting on the individual atoms. Moreover, developments such as these are difficult to extend to general computational methods due to the strict assumptions associated with shell and beam theories.

The equivalent-continuum modeling approach [Odegard, Gates, Nicholson, and Wise (2002)] and molecular structural mechanics method [Li, and Chou (2003)], as introduced in section 3, were also used to treat nanotubes. Odegard, et al. (2003) developed constitutive models for nanotube-reinforced polymer composite system, where the nanotube, the local polymer near the nanotube, and the nanotube/polymer interface were modeled as an effective continuum fiber using the equivalent-continuum modeling approach. Li and Chou (2003) used the molecular structural mechanics method to model the deformation of single-walled CNTs, the elastic properties was obtained. Then, they extended this method to simulate the elastic behavior of multi-walled CNTs under tension and torsion. The van der Waals interactions are accounted by introducing a nonlinear truss rod model. They also analyzed the interfacial load transfer in the carbon nanotube reinforced polymer composite by combining this method and continuum FEM, where the CNT is modeled by the molecular structural mechanics method, and the matrix is modeled by FEM. CNTs are regarded as ideal reinforcing materials for high-performance nanocomposites [Maryyama, and Alam (2002)], a review of nanotube-based composites can be found in Thostenson, et al. (2001).

Crystal elasticity theories based on the Cauchy-Born rule, as discussed in quasicontinuum method in section 3, have also been applied to CNTs. A continuum theory for modeling carbon nanotubes was proposed by directly in-

corporating interatomic potentials into a continuum-level constitutive relation on the basis of the Cauchy-Born rule in Zhang, Huang, Gao, et al. (2002), same as the quasicontinuum method. The SWCNT is assumed to be a cylindrical with vanishing thickness. The theory was first used to study the elastic modulus of a SWNT [Zhang, Huang, Geubelle, et al. (2002)], and then applied to the study of fracture nucleation in SWNTs [Zhang, Huang, Gao, et al. (2002)]. It was also employed to investigate the effect of nanotube radius on the constitutive model of SWCNTs [Jaing, et al. (2003)], and the influence of mechanical deformation on the electrical properties of SWCNTs via the k-space tight-binding method [Liu, et al. (2004)]. This method is limited to uniformly deformation, and the cross-section of the SWCNT must remain circular during the deformation (since this method required that the sequence of deforming a CNT and "un-roll" the deformed CNT to a plane can be exchanged). Therefore, this method can be applied to tension and torsion, but not bend. Qian, Liu and Ruoff (2001) proposed a combined continuum/MD models for the analysis of interaction between C60 and nanotube, where the nanotube is modeled as a cylindrical shell with finite thickness using the Cauchy-Born rule as in quasicontinuum method, and the C60 is modeled directly by MD. The direct application of the Cauchy-Born rule to CNT will result in inconsistency, since a CNT is not space-filling, but composed of a curved single-atom-thickness atomic layer. Arroyo and Belytschko (2002) corrected this inconsistency by introducing the exponential map from differential geometry. Using the modified Cauchy-Born rule, a quasicontinuum method was developed for single layer crystalline films, and the CNT is modeled as a continuum membrane with no thickness. Good results for the bending of nanotubes were presented [Arroyo and Belytschko (2002)]. However, it is not an easy task to evaluate the exponential map for a complicated configuration.

## 5 Conclusion

The recent developments and applications of the multi-scale modeling in nanomechanics and nanotubes are reviewed in this paper. Although many promising methods are proposed, a number of challenges still remain, such as the limitations on the length and time scale, the numerical accuracy and efficiency, the self-consistency (or non-reflection/seamless) of multiscale models. The numerical accuracy depends on the accuracy of interatomic poten-

tials, and the self-consistency depends on the interfacial condition between MD/continuum or QM/MD.

The Cauchy-Born rule and energy-equivalent assumption play important roles in reasonably bridging the continuum level to atomistic level. But the homogeneous-deformation assumption limits the application of the Cauchy-Born rule. The Cauchy-Born rule is only appropriate for bond interaction. For non-bond interaction, an accuracy, efficiency and reasonable continuum model is still lacking. The energy-equivalent assumption involves too many assumptions and mixed many quantities; these are the main reasons why there is a wide varieties in the values of Young's modulus/wall-thickness pair for SWCNTs in the literatures. Rather than Cauchy-Born rule and energy-equivalent assumption, possibly, a new generalized multiscale method should be directly based on the force (conservation of *local* linear momentum) and averaging techniques (constitutive equations represent some averaged behavior of collective atoms). For deriving the electric properties of the nanomaterials, the simulation must be taken down to quantum mechanics. An effective electromechanical multiscale model may be helpful.

Nanomechanics is a developing field which is rich of numerical, computational, physical and mathematical challenges. A novel and seamless multi-scale modeling methodology will play a key role in the simulation and design methodology for nanotechnology.

**Acknowledgement:** This work was supported by the U. S. Army Research Office, and the U. S. Army Research Laboratory, under a cooperative research agreement with the University of California at Irvine. The Cognizant Program Official at the U. S. Army Research Labs is Dr. R. Namburu. Partial support for this work was also provided by the Office of Naval Research, in the program directed by Dr. Y.D.S. Rajapakse.

## References

- Abell, G. C.** (1985): Empirical chemical pseudopotential theory of molecular and metallic bonding *Physical Review B* 31(10): 6184-6196.
- Abraham, F. F.** (2000): MAADLY spanning the length scales in dynamic fracture. *CMES: Computer Modeling in Engineering & Sciences* 1 (4): 63-69
- Abraham, F. F.; Bernstein, N.; Broughton, J. Q.; Hess, D.** (2000): Dynamic fracture of silicon: concurrent simulation of quantum electrons, classical atoms, and the continuum solid. *Materials Research Society Bulletin* 25:27-32.
- Abraham, F. F.; Broughton, J. Q.; Benstein, N.; Kaxiras, E.** (1998): Spanning the length scales in dynamic simulation. *Comput. Phys.* 12(6): 538-546.
- Adler, C.; Honke, R.; Pavone, P.; Schroder, V.** (1998): First-principles investigation of the lattice dynamics of epsilon-GaSe. *Phys. Rev. B* 57: 3726-3728.
- Ajayan, P. M.; Zhou, O. Z.** (2001): Applications of Carbon Nanotubes, in *Carbon Nanotubes*, Topics in Applied Physics; M.S. Dresselhaus, et al. (Eds); 80: 391-425, Springer
- Alder, B. J.; Wainwright, J.** (1957): Phase transition for a hard sphere system. *J. Chem. Phys.* 27(5): 1208-1209.
- Allen, M. P.; Tildesley, D. J.** (1989): *Computer simulation of liquids*. Clarendon, Oxford.
- Allinger, N. L.** (1977): Conformational-analysis. 130. MM2-Hydrocarbon force-field utilizing v1 and v2 torsional terms. *J. Am. Chem. Soc.* 99(25): 8127-8134.
- Allinger, N. L.; Yuh, Y. H.; Lii, J. H.** (1989): Molecular mechanics-The MM3 force-field for hydrocarbons. *J. Am. Chem. Soc.* 111(23): 8551-8566.
- Appel, A.** (1985): An efficient program for many-body simulation. *SIAM J. Sci. Statist. Comput.* 6: 85-103.
- Arroyo, M.; Belytschko, T.** (2002): An atomistic-based finite deformation membrane for single layer crystalline films. *Journal of Mechanics and Physics of Solids* 50: 1941-1977.
- Atluri, S. N.** (1979): On rate principles for finite strain analysis of elastic and inelastic nonlinear solids. In *Recent Research on Mechanical Behavior*, 79-107, University of Tokyo Press.
- Atluri, S. N.** (1980): On some new general and complementary energy theorems for the rate problems in finite strain, classical elastoplasticity. *Journal of Structural Mechanics* 8(1): 61-92.
- Atluri, S. N.** (2004): *The meshless local Petrov-Galerkin (MLPG) method for domain and boundary discretization*. Tech. Science Press, Los Angeles.
- Atluri, S. N.; Han, Z.D.; Shen, S.** (2003): The Meshless Local Petrov-Galerkin (MLPG) Approaches for Solving the Weakly-Singular Traction & Displacement Boundary Integral Equations. *CMES: Computer Modeling in Engineering & Sciences* 4(5), 507-516.

- Atluri, S. N.; Shen, S.** (2002a): *The meshless local Petrov-Galerkin (MLPG) method*. Tech. Science Press, Los Angeles, 440 pages.
- Atluri, S. N.; Shen, S.** (2002b): The meshless local Petrov-Galerkin (MLPG) method: A simple & less-costly alternative to the finite element and boundary element method. *CMES: Computer Modeling in Engineering & Sciences* 3 (1): 11-52.
- Atluri, S. N.; Shen, S.** (2004): The Basis of Meshless Domain Discretization: The Meshless Local Petrov Galerkin (MLPG) Method. *Advances in Computational Mathematics* (in press).
- Atluri, S. N.; Zhu, T.** (1998a): A new meshless local Petrov-Galerkin (MLPG) approach to nonlinear problems in computational modeling and simulation. *Comput. Modeling Simulation in Engrg.* 3: 187-196.
- Atluri, S. N.; Zhu, T.** (1998b): A new meshless local Petrov-Galerkin (MLPG) approach in computational mechanics. *Comput. Mech.* 22: 117-127.
- Barnes, J.; Hut, P.** (1986): A hierarchical  $O(N \log N)$  force-calculation algorithm. *Nature* 324: 446-449.
- Baskes, M. I.** (1992): Modified embedded-atom potentials for cubic materials and impurities. *Phys. Rev. B* 46: 2727-2742.
- Baskes, M. I.; Angelo, J. E.; Bison, C. L.** (1994): Atomistic calculations of composite interfaces. *Modell. Simul. Mater. Sci. Engng.* 2: 505-518.
- Batra, R. C.; Ching, H. K.** (2002): Analysis of elastodynamic deformations near a crack/notch tip by the meshless local Petrov-Galerkin (MLPG) method. *CMES: Computer Modeling in Engineering & Sciences* 3 (6): 717-730.
- Battaile, C. C.; Srolovitz, D. J.** (1997): A kinetic Monte Carlo method for the atomic-scale simulation of chemical vapor deposition: application to diamond. *J. Applied. Phys.* 82 (12): 6293-6300.
- Bearpark, M. J.; Robb, M. A.; Bernardi, F.; Olivucci, M.** (1994): Molecular mechanics valence-bond methods for large active spaces-application to conjugated polycyclic-hydrocarbons. *Chem. Phys. Lett.* 217: 513-519.
- Belytschko, T.; Xiao, S. P.; Schatz, G. C.; Ruoff, R.** (2002): Atomistic simulation of nanotube fracture. *Phys. Rev. B* 65(23): Art. No. 235430
- Belytschko, T.; Yen, H.; Mullen, R.** (1979): Mixed methods for time integration. *Comput. Meth. Appl. Mech. Eng.* 17-8: 258-275.
- Berendsen, H. J. C.; van Gunsteren, W. F.** (1986): *Dynamics simulation of statistical mechanical systems*, ed. Ciccotti GPF, Hoover, W.G. Vol. 63. North Holland. Amsterdam. 493.
- Bernstein, N.; Kaxiras, E.** (1997): Nonorthogonal tight-binding Hamiltonians for defects and interfaces in silicon. *Phys. Rev. B* 56: 10488-10496.
- Birdsall, C. K.; Langdon, A. B.** (1985): *Plasma physics via computer simulation*. McGraw-Hill, New York.
- Born, M.; Huang, K.** (1954): *Dynamical theory of crystal lattices*. Oxford University Press. Oxford.
- Bortz, A. B.; Kalos, M. H.; Lebowitz, J. L.** (1975): A new algorithm for Monte Carlo simulation of Ising spin systems. *J. Computational Phys.* 7(1): 10-18.
- Brenner, D. W.** (1990): Empirical potential for hydrocarbons for use in simulating the chemical vapor-deposition of diamond films. *Physical Review B* 42(15): 9458-9471.
- Brenner, D. W.; Harrison, J. A.; White, C. T.; Colton, R. J.** (1991): Molecular-dynamics simulations of the nanometer-scale mechanical-properties of compressed Buckminster fullerene. *Thin Solid Films* 206(1-2): 220-223.
- Brenner, D. W.; Shenderova, O. A.; Areshkin, D. A.** (1998): Quantum based analytic interatomic forces and materials simulation. *Reviews in Computational Chemistry*, VCH Publishers, New York: 213.
- Brenner, D. W.; Shenderova, O. A.; Areshkin, D. A.; Schall, J. D.; Frankland, S.-J.V.** (2002): Atomic modeling of carbon-based nanostructures as a tool for developing new materials and technologies. *CMES: Computer Modeling in Engineering & Sciences* 3 (5): 643-673.
- Broughton, J. Q.; Abraham, F. F.; Bernstein, N.; Kaxiras, E.** (1999): Concurrent coupling of length scales: Methodology and application. *Physical Review B* 60(4): 2391-2403.
- Burkert, U.; Allinger, N. L.** (1982): *Molecular mechanics*. ACS Monograph 177. American Chemical Society, Washington, DC.
- Cai, W.; de Koning, M.; Bulatov, V. V.; Yip, S.** (2000): Minimizing boundary reflections in coupled-domain simulations. *Phys. Rev. Lett.* 85: 3213-3216.
- Campbell, T.; Kalia, R. K.; Nakano, A.; Vashishta,**

- P.; Ogata, S.; Rodgers, S.** (1999): Dynamics of oxidation of aluminum nanoclusters using variable charge molecular-dynamics simulations on parallel computers. *Phys. Rev. Lett.* 82: 4866–4869.
- Candy, J.; Rozmus, W.** (1991): A symplectic integration algorithm for separable hamiltonian functions. *J. Comput. Phys.* 92: 230–256.
- Canning, A.; Galli, G.; Mauri, F.; De Vita, A.; Car, R.** (1996):  $O(N)$  tight-binding molecular dynamics on massively parallel computers: An orbital decomposition approach. *Computer Physics Communications* 94(2-3): 89–102.
- Capaz, R.; Cho, K.; Joannopoulos, J.** (1995): Signatures of bulk and surface arsenic antisite defects in  $gaas(110)$ . *Phys. Rev. Lett.* 75: 1811–1814.
- Car, R.; Parrinello, M.** (1985): Unified Approach for Molecular Dynamics and Density-Functional Theory. *Physical Rev. Letters* 55: 2471–2474.
- Chang, T.; Guo, W.** (2002): Recent advances in numerical simulation methods in nanomechanics. *Advances in Mechanics* 32(2): 175–188.
- Channell, P. J.; Scovel, C.** (1990): Symplectic integration of hamiltonian-systems. *Nonlinearity* 3: 231–259.
- Ching, H. K.; Batra, R. C.** (2001): Determination of Crack Tip Fields in Linear Elastostatics by the Meshless Local Petrov-Galerkin (MLPG) Method. *CMES: Computer Modeling in Engineering & Sciences* 2 (2): 273–290.
- Chung, P. W.; Namburu, R. R.** (2003): On a formulation for a multiscale atomistic-continuum homogenization method. *Int. J. Solids Struc.* 40: 2563–2588.
- Chung, P. W.; Namburu, R. R.; Henz, B. J.** (2004): A lattice statics based tangent stiffness finite element method. *CMES: Computer Modeling in Engineering & Sciences* 5(1): 45–62.
- Clementi, E.** (1988): Global scientific and engineering simulations on scalar, vector and parallel LCAP-type supercomputers. *Phil. Trans. Roy. Soc.* A326: 445–470.
- Clementi, E.** (2000): Ab initio computations in atoms and molecules. *IBM Journal of Research and Development*. 44(1-2): 228–245.
- Cleri, F.; Phillpot, S. R.; Wolf, D.; Yip, S.** (1998): Atomistic simulations of materials fracture and the link between atomic and continuum length scales. *J. Am. Ceramic Soc.* 81: 501–516.
- Cleveland, T.; Landis, C.R.** (1996): Valence bond concepts applied to the molecular mechanics description of molecular shapes. 2. Applications to hypervalent molecules of the P-block. *J. Am. Chem. Soc.* 118: 6020–6030. *CMES: Computer Modeling in Engineering & Sciences* (2002) 3 (2). *CMES: Computer Modeling in Engineering & Sciences* (2002) 3 (5).
- Colombo, L.** (1998): A source code for tight-binding molecular dynamics simulations. *Comput. Mat. Sci.* 12(3): 278–287.
- Cornell, W. D.; Cieplak, P.; Bayly, C. I.; Gould, I. R.; Merz, K. M.; Ferguson, D. M.; Spellmeyer, D. C.; Fox, T.; Caldwell, J. W.; Kollman, P. A.** (1995): A second generation force field for the simulation of proteins, nucleic acids, and organic molecules. *J. Am. Chem. Soc.* 117: 5179–5197.
- Cousins, C. S. G.** (1978): Inner elasticity. *J. Phys. C: Solid State Phys.* 11: 4867–4879.
- Cui, W. L.; Li, F. B.; Allinger, N. L.** (1993): Simulation of conformational dynamics with the mm3 force-field - the pseudorotation of cyclopentane. *J. Am. Chem. Soc.* 115: 2943–2951.
- Daw, M. S.** (1993): Model for energetics of solids based on the density matrix. *Phys. Rev. B* 47: 10895–10898.
- Daw, M.; Baskes, M.** (1983): Semiempirical, quantum-mechanical calculation of hydrogen embrittlement in metals. *Phys. Rev. Lett.* 50: 1285–1288.
- Daw, M. S.; Baskes, M. I.** (1984): Embedded-atom method: Derivation and application to impurities and other defects in metals. *Phys. Rev. B* 29: 6443–6453.
- DeLeeuw, S. W.; Perram, J. W.; Smith, E. R.** (1980): Simulation of electrostatic systems in periodic boundary conditions. i. lattice sums and dielectric constants. *Proc. Roy. Soc. London A* 373: 27–56.
- Demkov, A. A.; Ortega, J.; Sankey, O. F.; Grumbach, M. P.** (1995): Electronic structure approach for complex silicas. *Phys. Rev. B* 52: 1618–1630.
- Dresselhaus, M. S.** (1997): Future directions in carbon science. *Annu. Rev. Mater. Sci.* 27: 1–34.
- Duan, X. M.; Sun, D. Y.; Gong, X. G.** (2001): Hyper-molecular dynamics simulations of monovacancy diffusion. *Computational Materials Science*, 20(2): 151–156.
- Dumitrica, T.; Belytschko, T.; Yakobson, B. I.** (2003): Bond-breaking bifurcation states in carbon nanotube fracture. *J. Chem. Phys.* 118(21): 9485–9488.

- E, W.; Huang, Z.** (2001): Matching conditions in atomistic-continuum modeling of materials. *Phys. Rev. Lett.* 87, art. No.-135501.
- Ericksen, J. L.** (1984): *Phase transformations and material instabilities in solids*. Academic Press: 61-77.
- Ewald, P.** (1921): Die berechnung optischer und elektrostatischer gitterpotential. *Annalen der Physik* 64: 253-287.
- Fallis, M. C.; Daw, M. S.; Fong, C. Y.** (1995): Energetics of small Pt clusters on  $P_t(111)$ : Embedded-atom-method calculations and phenomenology. *Phys. Rev. B* 51: 7817-7826.
- Foulkes, C.; Haydock, R.** (1989): Tight-binding models and density functional theory. *Physical Review B*. 39(17): 12520-12536.
- Fock, V.** (1930): Naherungsmethode zur losung des quantenmechanis –chen mehrkorper problems. *Z. Physik.* 61: 126.
- Friesecke, G.; James, R. D.** (2000): A scheme for the passage from atomic to continuum theory for thin films, nanotubes and nanorodes. *J. Mech. Phys. Solids* 48: 1519-1540.
- Gall, K.; Horstemeyer, M. F.; Van Schilfgaarde, M.; Baskes, M. I.** (2000): Atomistic simulations on the tensile debonding of an aluminum–silicon interface. *Journal of the Mechanics and Physics of Solids*, 48(10): 2183-2212.
- Gao, X.-L.; Li, K.** (2003): Finite deformation continuum model for single-walled carbon nanotubes. *Int. J. Solids Struct.* 40: 7329-7337.
- Garcia-Vidal, F. J.; Merino, J.; Peerez, R.; Rincon, R.; Ortega, J.; Flores, F.** (1994): Density-functional approach to LCAO methods. *Phys. Rev. B* 50: 10537-10547.
- Garikipati, K.** (2002): A variational multiscale method to embed micromechanical surface laws in the macromechanical continuum formulation. *CMES: Computer Modeling in Engineering & Sciences* 3(2): 175-184.
- Gear, C. W.** (1971): *Numerical initial value problems in ordinary differential equations*. Prentice Hall, Englewood Cliffs, New Jersey.
- Ghoniem, N. M.; Cho, K.** (2002): The emerging role of multiscale modeling in nano and micro-mechanics of materials. *CMES: Computer Modeling in Engineering & Sciences* 3 (2): 147-173.
- Gibbon, P.** (2002): Classical molecular dynamics. Quantum Simulations of Complex Many-body Systems: from theory to algorithm. J. Grotendorst, D. Marx, A. Muramatsu (Eds.). John von Neumann Institute for Computing, Julich, NIC Series 10: 211-254.
- Gibbon P.; Sutmann, G.** (2002): Long-range interactions in many-particles simulation. Quantum Simulations of Complex Many-body Systems: from theory to algorithm. J. Grotendorst, D. Marx, A. Muramatsu (Eds.). John von Neumann Institute for Computing, Julich, NIC Series 10: 467-506.
- Gilmer, G. H.; Huang, H.; Diaz de la Rubia, T.; Torre, J. D.; Baumann, F.** (2000): Lattice Monte Carlo models of thin film deposition, an invited review. *Thin Solid Films* 365: 189-200.
- Girifalco, L. A.** (1992): Molecular-properties of c-60 in the gas and solid-phases. *Journal of Physical Chemistry.* 96(2): 858-861.
- Girifalco, L. A.; Lad, R. A.** (1956): Energy of cohesion, compressibility and the potential energy functions of the graphite system. *Journal of Chemical Physics.* 25(4): 693-697.
- Gray, S. K.; Noid, D. W.; Sumpter, B. G.** (1994): Symplectic integrators for large-scale molecular-dynamics simulations - a comparison of several explicit methods. *Journal of Chemical Physics.* 101(5): 4062-4072.
- Greengard, L.; Rokhlin, V.** (1987): A fast algorithm for particle simulations. *J. Comp. Phys.* 73: 325-348.
- Gu, Y. T.; Liu, G. R.** (2001): A meshless local Petrov-Galerkin (MLPG) formulation for static and free vibration analysis of thin plates. *CMES: Computer Modeling in Engineering & Sciences* 2 (4): 463-476.
- Gumbsch, P.** (1996): An atomistic study of brittle fracture: toward explicit failure criteria from atomistic modeling. *J. Mater. Res.* 10: 2897-2907.
- Guo, W.; Guo, F.** (2003): Giant Axial electrostrictive deformation in carbon nanotubes. *Phys. Rev. Lett.* 91: 115501.
- Guo, W.; Guo, F.; Gao, H.; Zheng, Q.; Zhong W.** (2003): Energy dissipation in gigahertz oscillators from multiwalled carbon nanotubes. *Phys. Rev. Lett.* 91: 125501.
- Guo Y.; Guo, W.** (2003): Mechanical and electrostatic properties of carbon nanotubes under tensile loading and electric field. *J. Phys. D: Appl. Phys.* 36: 805-811.

- Guo, Y. J.; Karasawa, N.; Goddard, W. A.** (1991): Prediction of fullerene packing in C<sub>60</sub> and C<sub>70</sub> crystals. *Nature* 351(6326): 464-467.
- Halgren, T. A.** (1996): Merck molecular force field. I. basis, form, scope, parameterization, and performance of MMFF94. *J. Comp. Chem.* 17: 490-519.
- Han, Z. D.; Atluri, S. N.** (2003a): On Simple Formulations of Weakly-Singular Traction & Displacement BIE, and Their Solutions through Petrov-Galerkin Approaches, *CMES: Computer Modeling in Engineering & Sciences* 4 (1): 5-20.
- Han, Z. D.; Atluri, S. N.** (2003b): Truly Meshless Local Petrov-Galerkin (MLPG) solutions of traction & displacement BIEs. *CMES: Computer Modeling in Engineering & Sciences* 4(6): 665-678.
- Harik, V. M.** (2002): Mechanics of carbon nanotubes: applicability of the continuum-beam models. *Comput. Mater. Sci.* 24: 328-342.
- Harrison, W. A.** (1989): *Electronic structure and the properties of solids: The physics of the chemical bond*. Dover. New York.
- Harrison, J. A.; White, C. T.; Colton, R. J.; Brenner, D. W.** (1992): Molecular-dynamics simulations of atomic-scale friction of diamond surfaces. *Physical Review B* 46(15): 9700-9708.
- Harrison, J. A.; Colton, R. J.; White, C. T.; Brenner, D. W.** (1993a): Effect of atomic-scale surface-roughness on friction - a molecular-dynamics study of diamond surfaces. *Wear* 168(1-2): 127-133.
- Harrison, J. A.; Colton, R. J.; White, C. T.; Brenner, D. W.** (1993b): Effects of chemically bound, flexible hydrocarbon species on the frictional-properties of diamond surfaces. *Journal of Physical Chemistry* 97(25): 6573-6576.
- Harrison, J. A.; White, C. T.; Colton, R. J.; Brenner, D. W.** (1995): Investigation of the atomic scale friction and energy-dissipation in diamond using molecular-dynamics. *Thin Solid Films* 260(2): 205-211.
- Hartree, D. R.** (1928): The wave mechanics of an atom with a non-coulomb central field, part I, theory and methods. *Proc. Cambridge Phil. Soc.* 24: 89.
- Heffelfinger, G. S.** (2000): Parallel atomistic simulations. *Comput. Phys. Commun.*, 128: 219-237.
- Hernandez, E.; Goze, C.; Bernier, P.; Rubio, A.** (1998): Elastic properties of C and BxCyNz composite nanotubes. *Phys. Rev. Lett.* 80: 4502-4505.
- Heyes, D. M.** (1981): Electrostatic potentials and fields in infinite point charge lattices. *J. Chem. Phys.* 74: 1924-1929.
- Hockney, R. W.** (1970): The potential calculation and some applications. *Methods Comput. Phys.* 9: 135-211.
- Hockney, R. L.; Eastwood, J. W.** (1981): Computer simulation using particles. McGraw-Hill, New York.
- Hohenberg, P.; Kohn, W.** (1964): Inhomogeneous electron gas. *Physical Review B*. 136: 864.
- Hoover, W. G.; De Groot, A.; Hoover, C.** (1992): Massively parallel computer simulation of plane-strain elastic-plastic flow via nonequilibrium molecular dynamics and Lagrangian continuum mechanics. *Computers in Physics* 6: 155-167.
- Huang, H.; Gilmer, G. H.; Diaz de la Rubia, T.** (1998): An atomistic simulator for thin film deposition in three dimensions. *J. Appl. Phys.* 84:3636-3649.
- Iijima, S.** (1991): Helical microtubules of graphitic carbon. *Nature* (London) 354(6348):56-58.
- Iijima, S.; Brabec, C.; Maiti, A.; Bernholc, J.** (1996): Structural flexibility of carbon nanotubes. *J. Chem. Phys.* 104: 2089-2092.
- Insepov, Z.; Sosnowski, M.; Yamada, I.** (1997): Simulation of cluster impacts on silicon surfaces. *Nuclear Instruments and Methods in Physics Research B* 127: 269-272.
- Insepov, Z.; Manory, R.; Matsuo, J.; Yamada, I.** (2000): Proposal for a hardness measurement technique without indenter by gas-cluster-beam bombardment. *Phys. Rev. B* 61(13): 8744-8752.
- Jiang, H.; Zhang, P.; Liu, B.; Huang, Y.; Geubelle, P. H.; Gao, H.; Huang, K. C.** (2003): The effect of nanotube radius on the constitutive model for carbon nanotubes. *Comput. Mater. Sci.* 28: 429-442.
- Jones, J. E.** (1924a): On the determination of molecular fields-I. From the variation of the viscosity of a gas with temperature. *Proc. Roy. Soc.* 106: 441-462.
- Jones, J. E.** (1924b): On the determination of molecular fields-ii. From the equation of state of a gas. *Proc. Roy. Soc.* 106: 463.
- Jorgensen, W. L.; Maxwell, D. S.; Tiradadorives, J.** (1996): Development and testing of the OPLS all-atom force field on conformational energetics and properties of

organic liquids. *J. Am. Chem. Soc.* 118: 11225-11236.

**Kalia, R. K.; Campbell, T. J.; Chatterjee, A.; Nakano, A.; Vashishta, P.; Ogata, S.** (2000): Multiresolution algorithms for massively parallel molecular dynamics simulations of nanostructured materials. *Computer Physics Communications* 128 (1-2): 245-259.

**Kawazoe, Y.** (2001): How well can physical, chemical, and mechanical properties of materials be predicted by ab initio techniques? *Materials and Design* 22: 61-67.

**Khan, F. S.; Broughton, J. Q.** (1989): Simulation of silicon clusters and surfaces via tight-binding molecular-dynamics. *Phys. Rev. B* 39: 3688-3700.

**Kim, H. G.; Atluri, S. N.** (2000): Arbitrary placement of secondary nodes, and error control, in the meshless local Petrov-Galerkin (MPLG) method. *CMES: Computer Modeling in Engineering & Sciences* 1(3): 11-32.

**Kohlhoff, S.; Gumbsch, P.; Fischmeister, H. F.** (1991): Crack propagation in bcc crystals studied with a combined finite element and atomistic model. *Phil. Mag. A* 64(4): 851-878.

**Kohn, W.; Sham, L. J.** (1965): Self-consistent equations including exchange and correlation effects. *Physical Review*. 140(4A): 1133.

**Kolmogorov, A. N.; Crespi, V. H.** (2000): Smoothest bearings: interlayer sliding in multiwalled carbon nanotubes. *Phys. Rev. Lett.* 85(22): 4727-4730.

**Komanduri, R.; Chandrasekaran, N.; Raff, L. M.** (1998): Effect of tool geometry in nanometric cutting: a molecular dynamics simulation approach. *Wear* 219(1): 84-97.

**Kresse, G.; Furthmüller, J.** (1996): Efficient iterative schemes for ab initio total-energy calculations using a plane-wave basis set. *Phys. Rev. B* 54: 11169-11186.

**Kroner, E.** (1967): Elasticity theory of materials with long range cohesive forces. *Int. J. Solids Struct.* 3: 731-742.

**Leach, A. R.** (1996): *Molecular Modeling Principles and Applications*. Addison Wesley Longman Limited, London.

**Lewis, L. J.; Mousseau, N.** (1998): Tight-binding molecular-dynamics studies of defects and disorder in covalently bonded materials. *Computational Materials Science* 12 (3): 210-241.

**Li, C.; Chou, T. W.** (2003): A structural mechanics approach for the analysis of carbon nanotubes. *Int. J. Solids*

*Struct.* 40: 2487-2499.

**Li, Q.; Shen, S.; Han, Z.-D.; Atluri, S. N.** (2003): Application of Meshless Local Petrov-Galerkin (MLPG) to Problems with Singularities, and Material Discontinuities, in 3-D Elasticity, *CMES: Computer Modeling in Engineering & Sciences* 4(5): 567-581.

**Li, S.; Gao, K. W.; Qiao, L. J.; Zhou, F. X.; Chu, W. Y.** (2001): Molecular dynamics simulation of microcrack healing in copper. *Computational Materials Science* 20(2): 143-150.

**Li, X. P.; Nunes, W.; Vanderbilt, D.** (1993): Density-matrix electronic-structure method with linear system-size scaling. *Phys. Rev. B* 47: 10891-10894.

**Lin, H.; Atluri, S. N.** (2000): Meshless local Petrov-Galerkin (MPLG) method for convection-diffusion problems. *CMES: Computer Modeling in Engineering & Sciences* 1 (2): 45-60

**Lin, H.; Atluri, S. N.** (2001): The meshless local Petrov-Galerkin (MPLG) method for solving incompressible Navier-stokes equations. *CMES: Computer Modeling in Engineering & Sciences* 2 (2): 117-142.

**Liu, B.; Jiang, H.; Johnson, H.T.; Huang, Y.** (2004): The influence of mechanical deformation on the electrical properties of single wall carbon nanotubes. *J. Mech. Phys. Solids* (in press)

**Liu, F.** (1995): Self-consistent tight-binding method. *Physical Review B*. 52(15): 10677- 10680.

**Liu, C. L.; Adams, J. B.** (1992): Structure and diffusion of clusters on Ni surfaces. *Surf. Sci.* 268: 73-86.

**Long, S. Y.; Atluri, S. N.** (2002): A meshless local Petrov-Galerkin method for solving the bending problem of a thin plate. *CMES: Computer Modeling in Engineering & Sciences* 3 (1): 53-63.

**Longo, R. C.; Rey, C.; Gallego, L. J.** (1999): Structure and melting of small Ni clusters on Ni surfaces. *Surface Science* 424(2-3): 311-321.

**Mackerell, A. D.; Wiorkiewicz-Kuczyńska, J.; Karplus, M.** (1995): An all-atom empirical energy function for the simulation of nucleic-acids. *J. Am. Chem. Soc.* 117: 11946-11975.

**Madelung, E.** (1918): Das elektrische field in systemen von regelmassig angeordneten punktladungen. *Zeitschrift für Physik* 19:524-533.

**Martin, J. W.** (1975): Many-body forces in solids and the Brugger elastic constants: II. Inner elastic constants.

*J. Phys. C: Solid State Phys.* 8: 2858-2868.

**Maruyama, B.; Alam, K.** (2002): Carbon nanotubes and nanofibers in composite materials. *SAMPE J.* 38(3): 59-68.

**Mauri, F.; Galli, G.** (1994): Electronic-structure calculations and molecular-dynamics simulations with linear system-size scaling. *Phys. Rev. B* 50: 4316-4326.

**Mayo, S. L.; Olafson, B. D.; Goddard, W. A.** (1990): Deriding - a generic force-field for molecular simulation., *Journal of Physical Chemistry.* 94(26): 8897-8909.

**Mehl, M. J.; Papaconstantopoulos, D. A.** (1996): Applications of a tight-binding total energy method for transition and noble metals: Elastic constants, vacancies, and surfaces of monatomic metals. *Physical Review B.* 54(7): 4519-4530.

**Menon, M.; Subbaswamy, K. R.** (1994): Transferable nonorthogonal tight-binding scheme for silicon. *Phys. Rev. B* 50: 11577-11582.

**Menon, M.; Subbaswamy, K. R.** (1997): Nonorthogonal tight-binding molecular dynamics scheme for silicon with improved transferability. *Physical Review B.* 55(15): 9231-9234.

**Miller, R. E.; Tadmor, E. B.** (2002): The quasicontinuum method: overview, applications and current direction. *J. Computer-Aided Materials Design* 9: 203-239.

**Nevins, N.; Lii, J. H.; Allinger, N. L.** (1996): Molecular mechanics (MM4) calculations on conjugated hydrocarbons. *J. Comp. Chem.* 17: 695-729.

**Noguchi, H.; Furuya, Y.** (1997): A method of seamlessly combining a crack tip molecular dynamics enclave with a linear elastic outer domain in simulating elastic-plastic crack advance. *Int. J. Frac.* 87: 309-329.

**Noor, A. K.** (2002): *Multiscale Modeling, Simulation and Visualization and Their Potential for Future Aerospace Systems.* NASA/CP-2002-211741.

**Nosé, S.** (1984): A unified formulation of the constant temperature molecular-dynamics methods. *J. Chem. Phys.* 81: 511-519.

**Odegard, G. M.; Gates, T. S.; Nicholson, L. M.; Wise, K. E.** (2002) Equivalent-continuum modeling of nanostructured materials. *Composites Sci. Tech.* 62: 1869-1880.

**Odegard, G. M.; Gates, T. S.; Wise, K. E.; Park, C.; Siochi, E. J.** (2003): Constitutive modeling of nanotube-reinforced polymer composites. *Composites Science and*

*Technology* 63: 1671-1687.

**Ohno, K.; Esfarjani, K.; Kawazoe, Y.** (1999): *Computational Materials Science: from ab initio to Monte Carlo Methods.* Springer.

**Ordejon, P.** (1998) Order-N tight-binding methods for electronic-structure and molecular dynamics. *Computational Materials Science* 12 (3): 157-191.

**Ortega, J.** (1998): First-principles methods for tight-binding molecular dynamics. *Comput. Mat. Sci.* 12(3): 192-209.

**Pantano, A.; Boyce, M. C.; Parks, D. M.** (2003): Non-linear structural mechanics based modeling of carbon nanotube deformation. *Phys. Rev. Lett.* 91(14): 145504.

**Payne, M. C.; Teter, M. P.; Allan, D. C.; Arias, T. A.; Joannopoulos, J. D.** (1992): Iterative Minimization Techniques for Ab Initio Total-Energy Calculations: Molecular-Dynamics and Conjugate Gradients. *Review of Modern Physics* 64(4): 1045-1097.

**Pavone, P.; Karch, K.; Schutt, O.; Windl, W.; Strauch, D.; Giannozzi, P.; Baroni, S.** (1993): Ab initio lattice dynamics of diamond. *Phys. Rev. B* 48: 3156-3163.

**Pearson, M.; Smargiassi, E.; Madden, P. A.** (1993): Ab initio molecular dynamics with an orbital-free density functional. *J. Phys. Condens. Matter* 5: 3321.

**Pearson, E.; Takai, T.; Halicioglu, T.; Tiller, W.** (1984): Computer modeling of Si and SiC surfaces and surface processes relevant to crystal-growth from the vapor. *J. Cryst. Growth* 70: 33-40.

**Peng, Z. W.; Ewig, C. S.; Huang, M.-J.; Waldman, M.; Hagler, A. T.** (1997): Derivation of class ii force fields. 4. van der Waals parameters of Alkali metal cations and Halide anions. *J. Phys. Chem.* 101: 7243-7252.

**Pfalzner S.; Gibbon, P.** (1996): *Many body tree methods in physics.* Cambridge University Press, New York.

**Popov, V. N.; Van Doren, V. E.; Balkanski, M.** (2000): Elastic properties of single-walled carbon nanotubes. *Phys. Rev. B* 61: 3078-3084.

**Porezag, D.; Frauenheim, T.; Kohler, T.; Seifert, G.; Kaschner, R.** (1995): Construction of tight-binding-like potentials on the basis of density-functional theory-application to carbon. *Physical Review B.* 51(19): 12947-12957.

**Qian, D.; Liu, W. K.; Ruoff, R. S.** (2001): Mechanics of

- C<sub>60</sub> in nanotubes. *Journal of Physical Chemistry B* 105: 10753-10758.
- Qian, D.; Liu, W. K.; Ruoff, R. S.** (2003): Load transfer mechanism in carbon nanotube ropes. *Compos. Sci. Technol.* 63 (11): 1561-1569.
- Qian, D.; Wagner, G. J.; Liu, W. K.; Yu, M. F.; Ruoff, R. S.** (2002): Mechanics of carbon nanotubes. *Applied Mechanics Reviews* 55(2): 495-533.
- Qian, L. F.; Batra, R. C.; Chen, L. M.** (2003a): Elastostatic Deformations of a Thick Plate by Using a Higher-Order Shear and Normal Deformable Plate Theory and two Meshless Local Petrov-Galerkin (MLPG) Method. *CMES: Computer Modeling in Engineering & Sciences* 4 (1): 161-176.
- Qian, L. F.; Batra, R. C.; Chen, L. M.** (2003b): Free and forced vibrations of thick rectangular plates using higher-order shear and normal deformable plate theory and meshless Petrov-Galerkin (MLPG) method. *CMES: Computer Modeling in Engineering & Sciences* 4 (5): 519-534.
- Rafii-Tabar, H.; Hua, L.; Cross, M.** (1998): Multi-scale numerical modeling of crack propagation in two-dimensional metal plate. *Materials Science and Technology* 14(6): 544-548.
- Rahman, A.** (1964): Correlations in motion of atoms in liquid argon. *Phys. Rev. A* 136: 405.
- Raju, I. S.; Phillips, D. R.** (2003): Further Developments in the MLPG Method for Beam Problems. *CMES: Computer Modeling in Engineering & Sciences* 4 (1): 141-160.
- Rapaport, D. C.** (1995): *The art of molecular dynamics simulation*. Cambridge University Press, 400 pages.
- Rapp, A. K.; Casewit, C. J.** (1997): *Molecular mechanics across chemistry*. University Science Books, Sausalito, CA.
- Rappe, A. K.; Casewit, C. J.; Colwell, K. S.; Goddard, W. A.; Skiff, W. M.** (1992): UFF, a full periodic-table force-field for molecular mechanics and molecular-dynamics simulations. *J. Am. Chem. Soc.* 114: 10024-10035.
- Robertson, D. H.; Brenner, D. W.; Mintmire, J. W.** (1992): Energetics of nanoscale graphitic tubules. *Physical Review B* 45(21): 12592-12595.
- Robertson, D. H.; Brenner, D. W.; White, C. T.** (1992): On the way to fullerenes - molecular-dynamics study of the curling and closure of graphitic ribbons. *Journal of Physical Chemistry* 96(15): 6133-6135.
- Robertson, D. H.; Brenner, D. W.; White, C. T.** (1995): Temperature-dependent fusion of colliding C<sub>60</sub> fullerenes from molecular-dynamics simulations. *Journal of Physical Chemistry* 99(43): 15721-15724.
- Rudd, R. E.; Broughton, J. Q.** (1998): Coarse-grained molecular dynamics and the atomic limit of finite elements. *Physical Review B* 58(10): R5893-R5896.
- Rudd, R. E.; Broughton, J. Q.** (2000): Concurrent coupling of length scales in solid state systems. *Phys. Stat. Solid B* 217(1): 251-291.
- Sanchez-Portal, D.** (1999): Ab ignition structural, elastic, and vibrational properties of carbon nanotubes. *Phys. Rev. B* 59: 12678-12688.
- Savinskii, S. S.; Petrovskii, V. A.** (2002): Discrete and continuum models for calculating the phonon spectra of carbon nanotubes. *Physics of the Solid State* 44(9): 1802-1807.
- Sham, T.-L.; Tichy, J.** (1997): A scheme for hybrid molecular dynamics/finite element analysis of thin film lubrication. *Wear* 207 (1-2) 100-106.
- Shen, S.; Atluri, S. N.** (2004): Multiscale simulation based on the meshless local Petrov-Galerkin (MLPG) method. *CMES: Computer Modeling in Engineering & Sciences* 5(3): 235-255.
- Sellountos, E. J.; Polyzos D.** (2003): A MLPG (LBIE) method for solving frequency domain elastic problems. *CMES: Computer Modeling in Engineering & Sciences* 4(6): 619-636.
- Shenoy, V. B.** (2003): Multiscale modeling strategies in materials science-the quasicontinuum method. *Bull. Mater. Sci.* 26(1): 53-62.
- Shenoy, V. B.; Miller, R.; Tadmor, E. B.; Rodney, D.; Phillips, R.; Ortiz, M.** (1999): An adaptive finite element approach to atomic-scale mechanics - the quasicontinuum method. *Journal of the Mechanics and Physics of Solids*. 47(3): 611-642.
- Sinclair, J.** (1971): Improved atomistic model of a bcc dislocation core. *J. Appl. Phys.* 42: 5321-5329.
- Singh, B.; Foreman, A. J. E.; Trinkaus, H.** (1997): Radiation hardening revisited: role of intracascade clustering. *J. Nul. Mater.* 249:103-115.
- Sinnott, S. B.; Colton, R. J.; White, C. T.; Brenner, D. W.** (1994): Surface patterning by atomically-controlled

- chemical forces - molecular-dynamics simulations. *Surface Science* 316(1-2): L1055-L1060.
- Sladek, J.; Sladek, V.; Zhang, C.** (2003): Application of Meshless Local Petrov-Galerkin (MLPG) Method to Elastodynamic Problems in Continuously Nonhomogeneous Solids. *CMES: Computer Modeling in Engineering & Sciences* 4 (6): 637-648.
- Sladek, J.; Sladek, V.; Atluri, S. N.** (2001): A pure contour formulation for the meshless local boundary integral equation method in thermoelasticity. *CMES: Computer Modeling in Engineering & Sciences* 2 (4): 423-434.
- Stott, M. J.; Zaremba, E.** (1980): Quasiatoms: An approach to atoms in nonuniform electronic systems. *Phys. Rev. B* 22: 1564-1533.
- Slater, J. C.; Koster, G. F.** (1954): Wave functions for impurity levels. *Physical Review* 94: 1498.
- Smargiassi, E.** (2001): Defect properties and diffusion in sodium using ab initio molecular dynamics. *Computational Materials Science* 20 : 416-422.
- Smargiassi, E.; Madden, P. A.** (1994): Orbital-free kinetic-energy functionals for first-principles molecular dynamics. *Phys. Rev. B* 49: 5220-5226.
- Smirnova, J. A.; Zhigilei, L. V.; Garrison, B. J.** (1999): A combined molecular dynamics and finite element method technique applied to laser induced pressure wave propagation. *Computer Physics Communication* 118: 11-16.
- Smith, G. S.; Tadmor, E. B.; Bernstein, N.; Kaxiras, E.** (2001): Multiscale simulation of silicon nanoindentation. *Acta Mater.* 49: 4089- 4101.
- Srivastava, D.; Atluri, S. N.** (2002): Computational Nanotechnology: A Current Perspective. *CMES: Computer Modeling in Engineering & Sciences* 3 (5): 531-538.
- Srivastava, D.; Menon, M.; and Cho, K.** (2001): Computational nanotechnology with carbon nanotubes and fullerenes. *Computing in Science & Engineering* 3: 42-55.
- Stillinger, F. H.; Weber, T. A.** (1985): Computer simulation of local order in condensed phases of silicon. *Phys. Rev. B* 31:5262-5271.
- Streitz, F. H.; Mintmire, J. W.** (1994): Electrostatic potentials for metal-oxide surfaces and interfaces. *Phys. Rev. B* 50: 11996-12003.
- Sudak, L. J.** (2003): Column buckling of multiwalled carbon nanotubes using nonlocal continuum mechanics. *J. Appl. Phys.* 94(11): 7281-7287.
- Swope W. C.; Andersen, H. C.; Berens, P. H.; Wilson, K. R.** (1982): A computer-simulation method for the calculation of equilibrium-constants for the formation of physical clusters of molecules - application to small water clusters. *J. Chem. Phys.* 76: 637-649.
- Tadmor, E. B.; Ortiz, M.; Phillips, R.** (1996): Quasi-continuum analysis of defects in solids. *Philosophical Magazine A* 73: 1529-1563.
- Tadmor, E. B.; Phillips, R.; Ortiz, M.** (1996): Mixed atomistic and continuum models of deformation in solids. *Langmuir* 12(19): 4529-4534.
- Tan, H. L.; Yang, W.** (1994): Atomistic/continuum simulation of interface fracture, Part II. *Acta Mechanica Sinica* 16: 237-249
- Taneda, A.; Esfarjani, K.; Li, Z. Q.; Kawazoe, Y.** (1998): Tight-binding parameterization of transition metal elements from lcao ab initio Hamiltonians. *Computational Materials Science.* 9(3-4): 343-347.
- Tang, Z.; Shen, S.; Atluri, S. N.** (2003): Analysis of materials with strain gradient effects: A Meshless local Petrov-Galerkin approach, with nodal displacements only. *CMES: Computer Modeling in Engineering & Sciences* 4(1): 177-196.
- Tersoff, J.** (1986): New empirical-model for the structural-properties of silicon. *Physical Review Letters* 56(6): 632-635.
- Tersoff, J.** (1989): Modeling solid-state chemistry - interatomic potentials for multi-component systems. *Physical Review B* 39(8): 5566-5568.
- Thostenson, E. T.; Ren, Z.; Chou, T.-W.** (2001): Advances in the science and technology of carbons and their composites: a review. *Composites Science and Technology* 61: 1899-1912.
- Troya, D.; Mielke, S. L.; Schatz, G. C.** (2003): Carbon nanotube fracture-differences between quantum mechanical mechanisms and those of empirical potentials. *Chem. Phys. Lett.* 382: 133-141.
- Tuckerman, M.; Berne, B. J.** (1992): Reversible multiple time scale molecular-dynamics. *J. Chem. Phys.* 97: 1990-2001.
- Tuckerman, M. E.; Berne, B. J.; Martyna, G. J.** (1991): Molecular dynamics algorithm for multiple time scales: systems with long range forces. *J. Chem. Phys.*

94(10): 6811-6815.

**Tuzun, R. E.; Noid, D. W.; Sumpter, B. G.; Merkle, R. C.** (1996): Dynamics of fluid flow inside carbon nanotubes. *Nanotechnology* 7(3): 241-246.

**Vanduijn, P.; Devries, A. H.** (1996): Direct reaction field force field: A consistent way to connect and combine quantum-chemical and classical descriptions of molecules. *Int. J. Quant. Chem.* 60: 1111-1132.

**Verlet, L.** (1967): Computer experiments on classical fluids .I. Thermodynamical properties of Lennard-Jones molecules, *Physical Review*. 159(1): 98.

**Vodenitcharova, T.; Zhang, L. C.** (2003): Effective wall thickness of a single-walled carbon nanotube. *Phys. Rev. B* 68: 165401.

**Wagner, G. J.; Liu, W. K.** (2003): Coupling of Atomistic and continuum simulations using a bridging scale decomposition. *J. Comput. Phys.* 190: 249-274.

**Wang, C. Z.; Ho, K. M.** (1996): Tight-binding molecular dynamics study of covalent systems, in: I. Prigogine, S.A. Rive (Eds.), *Advances in Chemical Physics*, Vol. XCIII, Wiley, New York.

**Wang, C. Z.; Ho, K. M.** (1993): Structure, dynamics, and electronic properties of diamond-like amorphous carbon. *Physical Review Letters*, 71 (8): 1184-1187.

**Wang, Y.; Sun, C.; Sun, X.; Hinkley, J.; Odegard, G. M.; Gates, T. S.** (2003): 2-D nano-scale finite element analysis of a polymer field. *Composites Science and Technology* 63(11): 1581-1590.

**Wang, Y.; Tomanek, D.; Bertsch, G. F.** (1991): Stiffness of a solid composed of C<sub>60</sub> clusters. *Physical Review B*. 44(12): 6562-6565.

**Wei, C.; Srivastava, D.** (2003): Theory of transport of long polymer molecules through carbon nanotube channels. *Phys. Rev. Lett.* 91: 235901.

**Wisdom, J.; Holman, M.** (1991): Symplectic maps for the n-body problem. *Astron. J.* 102: 1528-1538.

**Wong, E. W.; Sheehan, P. E.; Lieber, C. M.** (1997): Nanotube mechanics: elasticity, strength and toughness of nanorods and nanotubes. *Science* 277: 1971-1975.

**Wunderlich, W.; Awaji, H.** (2001): Molecular dynamics - simulations of the fracture toughness of sapphire. *Materials and Design*, 22: 53-59.

**Xu, C. H.; Wang, C. Z.; Chan, C. T.; Ho, K. M.** (1992): A transferable tight-binding potential for carbon. *Journal*

*of Physics-Condensed Matter*. 4(28): 6047-6054.

**Yakobson, B. I.; Brabec, C. J.; Bernholc, J.** (1996): Nanomechanics of carbon tubes: Instabilities beyond linear response. *Phys. Rev. Lett.* 76: 2511-2514.

**Yakobson, B. I.; Campbell, M. P.; Brabec, C. J.; Bernholc, J.** (1997): High strain rate fracture and C-chain unraveling in carbon tubes. *Comput. Mater. Sci.* 8: 341-348.

**Zanzotto, G.** (1996): The Cauchy-Born Hypothesis, nonlinear elasticity and mechanical twinning in crystals. *Acta Cryst.* A52: 839-849.

**Zhang, P.; Huang, Y.; Gao, H.; Hwang, K. C.** (2002): Fracture nucleation in single-wall carbon nanotubes under tension: a continuum analysis incorporating interatomic potentials. *J. Appl. Mech.* 69: 454-458.

**Zhang, P.; Klein, P.; Huang, Y.; Gao, H.; Wu, P. D.** (2002): Numerical simulation of cohesive fracture by the virtual-internal bond model. *CMES: Computer Modeling in Engineering & Sciences* 3(2): 263-278.

**Zhang, S.; Liu, W. K.; Ruoff, R. S.** (2004): Atomistic simulation of double-walled carbon nanotubes (DWCNTs) as rotational bearings. *Nano Letters* (in press)

**Zhang, Z. X.; Pan, Z. Y.; Wei, Q.; Li, Z. J.; Zang, L. K.; Wang, Y. X.** (2003): Mechanics of nanotubes filled with C60, C36 and C20. *Int. J. Modern Phys. B* 17(26): 4667-4674.

**Zhao, Y.; Ma, C.-C.; Chen, G.H.; Jiang, Q.** (2003): Energy dissipation mechanisms in carbon nanotube oscillators. *Phys. Rev. Lett.* 91: 175504.

**Zhou, M.; McDowell, D. L.** (2002): Equivalent continuum for dynamically deforming atomistic particles system. *Philosophical Magazine A* 82(13): 2547-2574.

**Zhou, M.** (2003): A new look at the atomic level virial stress: on continuum-molecular system equivalence. *Proc. R. Soc. Lond. A* 459: 2347-2392.

**Zhou, S. J.; Lomdahl, P. S.; Voter, A. F.; Holian, B. L.** (1998): Three-dimensional fracture via large-scale molecular dynamics. *Eng. Fract. Mech.* 61: 173-187.

# Multiscale Simulation Based on The Meshless Local Petrov-Galerkin (MLPG) Method

Shengping Shen<sup>1</sup> and S. N. Atluri<sup>1</sup>

**Abstract:** A multiscale simulation technique based on the MLPG methods, and finite deformation mechanics, is developed, implemented, and tested. Several alternate time-dependent interfacial conditions, between the atomistic and continuum regions, are systematically studied, for the seamless multiscale simulation, by decomposing the displacement of atoms in the equivalent-continuum region into long and short wave-length components. All of these methods for enforcing the interface conditions can ensure the passage of information accurately between the atomistic and continuum regions, while they lead to different performances at short wave-lengths. The presently proposed Solution Method 2 reduces the phonon reflections at the interface, without increasing the computational burden. Multiple length scale, multiple time step, and meshless local Petrov-Galerkin (MLPG) methods are used in the numerical examples.

## 1 Introduction

With the advances in materials synthesis and device processing capabilities, the importance of developing and understanding nanoscale engineering devices has dramatically increased over the past decade. *Computational Nanotechnology* [Srivastava and Atluri (2002a,b)] has become an indispensable tool not only in predicting, but also in *engineering* the properties of multi-functional nano-structured materials. The elasto-dynamics is governed largely by the geometry of the device, while the atomistic processes are important in its smallest features. Continuum approaches begin to fail as the system size approaches the atomic scale, and atomistic methods begin to reach their inherent time and length-scale limitations. The nano-scale is the length scale of individual

atoms, i.e. 1-10nm. At such length scales, continuum models are not flexible enough to accommodate the individual atomic scale processes. An alternative to continuum analysis is the atomistic modeling and simulation (MD), in which individual atoms are explicitly followed during their dynamic evolution. Even though this MD can trace all details of atomic-scale processes, it has its own set of limitations. When the length-scale cannot be accessed by either continuum methods because it is too small for averaging, or the atomistic methods [MD or quantum mechanics (QM)] because it is too large for simulations on the present day computers, these two approaches become inadequate, and that has presented significant challenges to the scientific community. The length scales of the typical material system in multi-scale structures are shown in Fig. 1.

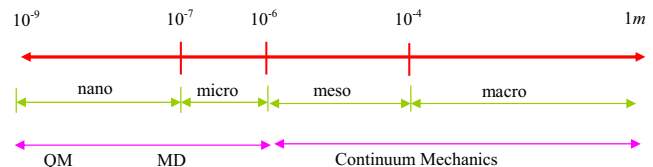


**Figure 1 :** The length scales of the material system

This paper is devoted to computational nanotechnology and multiscale simulations, in both length and time scales, as illustrated in Fig. 2, below [which is more fully discussed in Shen and Atluri (2004) and Atluri (2004)]. **Molecular Dynamics (MD) Domains, Equivalent Continuum Models (ECM), and Actual Continuum Domains (ACD)**, will be linked through the device of the Meshless Local Petrov-Galerkin (MLPG) Method [Atluri and Zhu(1998), and Atluri and Shen (2002a,b)], which is a cost-effective alternative to the traditional finite-element & boundary-element methods, and which offers the possibility of carrying out uniformly valid simulations of material properties for multi-scale systems at

<sup>1</sup> Center for Aerospace Research & Education  
University of California at Irvine  
5251 California Avenue, #140  
Irvine, CA 92612, USA

both larger length scales and longer times than the direct atomistic calculations, and permits a reduction of the full set of atomic degrees of freedom.

### Seamless MD to CM

#### Standard Newtonian MD Scheme:

1. Determine interatomic potential and forces (for long range interaction,  $O(n^2)$ ) ← PP-MLPG/BIE
2. Integrate the equations of motion  $-m_a \ddot{\mathbf{u}}_a + \mathbf{f}_a = 0$  ← ECM (atom by atom)

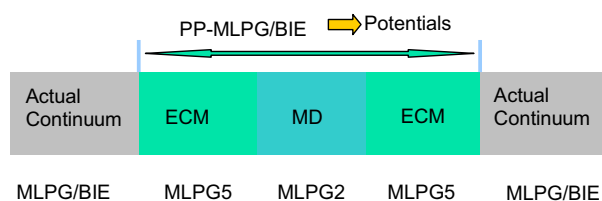


**Figure 2** : Seamless Multiscale Modeling

The role of **computational nanotechnology** [Srivastava and Atluri (2002a,b); Srivastava, Menon, and Cho (2001)], has become critically important in the nanodevice development [Ajayan and Zhu(2001)]. There are two major categories of molecular simulation methods for nanotechnology: classical molecular dynamics (MD) and *ab initio* methods. MD treats the motion of atoms or molecules in approximated finite difference equations of Newtonian mechanics. In general, *ab initio* methods give more accurate results than MD, but they are also much more computationally intensive. A hybrid method, tight-binding molecular dynamics (TBMD), is a blend of certain features from both MD and *ab initio* methods. In fact, *ab initio* and TBMD are the quantum mechanics (QM) schemes. Despite constant increases in available computational power and improvement in numerical algorithms, even classical MD computations are still limited to simulating on the order of  $10^6$ - $10^8$  atoms for a few nanoseconds. The simulation of large systems must be left to continuum methods. Several methods are developed for the multiscale simulation.

The quasicontinuum method, introduced by Tadmor et al. (1996), and Chung, Namburu, and Henz (2004), gives a theory for bridging the atomistic and continuum scales in *quasistatic problems*. In this method, a set of atoms making up a Bravais lattice is selected from a subset. A tri-

angulation of this subset allows the introduction of finite element-like shape functions at lattice points, allowing the interpolation of quantities at intermediate points in the lattice. Thus, the problem of the minimization of energy to find equilibrium configurations can be written in terms of a reduced set of variables. The method is made practical by approximating summations over all atoms, as using summation rules analogous to numerical quadrature. The rules rely on the smoothness of the quantities over the size of the triangulation to ensure accuracy. The final aspect of the method is therefore the prescription of adaptivity rules, allowing the reselection of representative lattice points in order to tailor the computational mesh to the structure of the deformation field. The criteria for adaptivity are designed to allow full atomic resolution in regions of large local strain, for example, very close to a dislocation in the lattice. This method is limited to the case of a zero temperature.

Another approach to the coupling of the length scales is the FE/MD/TB model of Abraham (2000). In this method, three simulations are run simultaneously, using the finite element method (FEM), molecular dynamics (MD), and semi-empirical tight binding (TB). Each simulation is performed on a different region of the domain, with a coupling imposed in “handshake” regions where the different simulations overlap. The method is designed for implementation on supercomputers via parallel algorithms, allowing the solution of large problems. One example of such a problem is the propagation of a crack in a brittle material. Here, the TB method is used to simulate bond breaking at the crack tip, MD is used near the crack surface, and the surrounding medium is treated with FE. The challenge for mesh generation is that the mesh should smoothly transition between the true atomic lattice in the MD region and the closely-packed FE meshes. Too abrupt a crossover leads to an unphysical behavior, such as elastic wave resonances at the interface. The coarse-grained MD method proposed by Rudd and Broughton (1998) derived a constitutive relationship for the continuum, directly from the interatomic potential by using a statistical coarse graining procedure. This method has high computational complexity. Wagner and Liu (2003) presented a multiscale method for coupling molecular dynamics and continuum mechanics by using “bridging scale” decomposition and the quasicontinuum method [Tadmor et al. (1996)].

Although substantial progress has been made in recent

years, the multi-scale modeling method is still in its infancy, and it still requires intensive efforts. As pointed by many researchers, the main issues in the development of seamless multi-scale modeling methodology are still the limitations on the length and time scale, and the numerical accuracy and efficiency. Hence, a more accurate and efficient multi-scale modeling methodology is still desirable, and such methodologies are currently being pursued by many researchers, in contemporary literature. In this paper, we propose a seamless multi-scale modeling methodology, based on the meshless local Petrov-Galerkin (MLPG) method.

## 2 The Meshless Local Petrov-Galerkin (MLPG) Method and Radial Basis functions

Meshless methods, as alternative numerical approaches to eliminate the well-known drawbacks in the finite element and boundary element methods, have attracted much attention in recent decades, due to their flexibility, and due to their potential in negating the need for the human-labor intensive process of constructing geometric meshes in a domain

The MLPG method is a simple and less-costly alternative to the FEM and BEM [Atluri and Zhu (1998), Atluri and Shen (2002a,b)]. The main objective of the meshless methods is to get rid of, or at least alleviate the difficulty of, meshing and remeshing the entire structure; by only adding or deleting nodes in the entire structure, instead. The meshless local Petrov-Galerkin (MLPG) method is truly meshless, as no finite element/or boundary element meshes are required in this approach, either for purposes of interpolation of the trial and test functions for the solution variables, or for the purpose of integration of the 'energy'. All pertinent integrals can be easily evaluated over over-lapping, regularly shaped, domains (in general, spheres in three-dimensional problems) and their boundaries. Remarkable successes of the MLPG method have been reported in solving the convection-diffusion problems; fracture mechanics; Navier-Stokes flows; and plate bending problems. Recently, the MLPG method has made some strides, and it is applied successfully in studying strain gradient materials [Tang, Shen and Atluri, (2003)], three dimensional elasticity problems [Li, Shen, Han and Atluri (2003)], and elastodynamics [Batra, Ching (2002)]. The MLPG method was also extended to solve the boundary integral equations [Atluri, Han and Shen (2003), and Han, Atluri (2003)].

Six different nodal-based local test functions may be selected, which lead to six different MLPG methods. Based on the MLPG concept, these variants of the MLPG method are labeled as MLPG1, MLPG2, MLPG3, MLPG4, MLPG5, and MLPG6, respectively. Among them, there are three methods that avoid the domain integral in the weak-form, over the nodal test-function domain  $\Omega_s$ : MLPG2 (wherein the local, nodal-based test function, over a local sub-domain  $\Omega_s$  centered at a node, is a Dirac's Delta function); MLPG4 (wherein the local, nodal-based test function, over a local sub-domain  $\Omega_s$  centered at a node, is the modified fundamental solution to the differential equation); and MLPG5 (wherein the local, nodal-based test function, over a local sub-domain  $\Omega_s$  centered at a node, is the Heaviside step function). MLPG4 (which is synonymous with the Local Boundary Integral Equation method) involves singular integrals; while the collocation method, (i.e. MLPG2), is notorious for the sensitivity of the solution to the choice of proper collocation points. However, MLPG5 does not involve either a domain, or a singular integral, to generate the stiffness matrix; it only involves the regular boundary integral. Thus, it is a highly promising MLPG method while, numerical examples validate that the MLPG5 method is fast, accurate and robust.

In summary, the MLPG is a truly meshless method, which involves not only a meshless interpolation for the trial functions [such as MLS, PU, Shepard function or Radial Basis Functions(RBF)], but also a meshless integration of the weak-form (i.e. all integrations are always performed over regularly shaped sub-domains such as spheres, parallelepipeds, and ellipsoids in 3-D). In the conventional Galerkin method, the trial and test functions are chosen from the same function-space. In MLPG, the nodal trial and test functions can be different: the nodal trial function may correspond to any one of MLS, PU, Shepard function, or RBF types of interpolations; and the test function may be totally different, and may correspond to any one of MLS, PU, Shepard function, RBF, a Heaviside step function, a Dirac delta function, the Gaussian weight function of MLS, a special form of the fundamental solution to the differential equation, or any other convenient function, in the support domain,  $\Omega_{te}$ , of the test function. Furthermore, the physical sizes of the supports ( $\Omega_{tr}$  and  $\Omega_{te}$ , respectively) of the nodal trial and test functions may be different. These features make the MLPG method very flexible. The MLPG method, based

on a local formulation, can include all the other meshless methods based on global formulation, as special cases [see Atluri, and Shen (2003)].

In this paper, we choose the local radial basis functions [Hardy (1971), Wendland (1999), Liu and Gu (2001)] to interpolate the trial functions, because of its Kronecker Delta property. Consider a continuous function  $u(\mathbf{x})$  defined in a domain  $\Omega$ , discretized by a set of nodes. An interpolation of  $u(\mathbf{x})$  from the neighboring nodes of a point  $\mathbf{x}_\alpha$  within the domain  $\Omega$ , using RBFs augmented by a polynomial basis, can be written as

$$\begin{aligned} u(\mathbf{x}) &= \sum_{i=1}^n R_i(\mathbf{x}) a_i(\mathbf{x}_\alpha) + \sum_{j=1}^m p_j(\mathbf{x}) b_j(\mathbf{x}_\alpha) \\ &= \mathbf{R}^T \mathbf{a} + \mathbf{P}^T \mathbf{b} \end{aligned} \quad (1)$$

where  $R_i(\mathbf{x})$  is the radial basis function,  $p_j(\mathbf{x})$  is a monomial in the space coordinates,  $n$  is the number of nodes in the neighborhood of  $\mathbf{x}_\alpha$ ,  $m$  is the number of polynomial basis functions (usually  $m < n$ ), and  $a_i(\mathbf{x}_\alpha)$  and  $b_j(\mathbf{x}_\alpha)$  are the coefficients for  $R_i(\mathbf{x})$  and  $p_j(\mathbf{x})$ , respectively, corresponding to the point  $\mathbf{x}_\alpha$ . The number of the neighbor nodes of  $\mathbf{x}_\alpha$  is not greater than the total number of nodes in the global domain. The vectors are defined as

$$\begin{aligned} \mathbf{a}^T &= [a_1, a_2, \dots, a_n] \\ \mathbf{b}^T &= [b_1, b_2, \dots, b_m] \\ \mathbf{R}^T &= [R_1(\mathbf{x}), R_2(\mathbf{x}), \dots, R_n(\mathbf{x})] \\ \mathbf{P}^T &= [p_1(\mathbf{x}), p_2(\mathbf{x}), \dots, p_m(\mathbf{x})] \end{aligned} \quad (2)$$

The radial basis function has the following general form

$$R_i(\mathbf{x}) = R_i(r_i) \quad (3)$$

where  $r_i = \|\mathbf{x} - \mathbf{x}_i\|$ . The polynomial term is added to ensure the consistency and the condition of the non-singularity of the RBFs approximation, which should satisfy the following constraints

$$\sum_{i=1}^n p_j(\mathbf{x}_i) a_i = 0, \quad j = 1, 2, \dots, m \quad (4)$$

The coefficients are determined by ensuring that the interpolation passes through all  $n$  scattered nodes within the influence domain:

$$u(\mathbf{x}_k) = \sum_{i=1}^n R_i(\mathbf{x}_k) a_i + \sum_{j=1}^m p_j(\mathbf{x}_k) b_j, \quad k = 1, 2, \dots, n$$

$$(5)$$

Equations (5) and (4) can be expressed in matrix form

$$\mathbf{A} \begin{Bmatrix} \mathbf{a} \\ \mathbf{b} \end{Bmatrix} = \begin{Bmatrix} \mathbf{u}_e \\ \mathbf{0} \end{Bmatrix} \quad (6)$$

where

$$\mathbf{A} = \begin{bmatrix} \mathbf{R}_0 & \mathbf{P}_0 \\ \mathbf{P}_0^T & \mathbf{0} \end{bmatrix} \quad (7)$$

$$\mathbf{R}_0 = \begin{bmatrix} R_1(\mathbf{x}_1) & R_2(\mathbf{x}_1) & \cdots & R_n(\mathbf{x}_1) \\ R_1(\mathbf{x}_2) & R_2(\mathbf{x}_2) & \cdots & R_n(\mathbf{x}_2) \\ \vdots & \vdots & \ddots & \vdots \\ R_1(\mathbf{x}_n) & R_2(\mathbf{x}_n) & \cdots & R_n(\mathbf{x}_n) \end{bmatrix}_{n \times n} \quad (8)$$

$$\mathbf{P}_0 = \begin{bmatrix} p_1(\mathbf{x}_1) & p_2(\mathbf{x}_1) & \cdots & p_m(\mathbf{x}_1) \\ p_1(\mathbf{x}_2) & p_2(\mathbf{x}_2) & \cdots & p_m(\mathbf{x}_2) \\ \vdots & \vdots & \ddots & \vdots \\ p_1(\mathbf{x}_n) & p_2(\mathbf{x}_n) & \cdots & p_m(\mathbf{x}_n) \end{bmatrix}_{n \times m} \quad (9)$$

$$\mathbf{u}_e = [u_1, u_2, \dots, u_n]^T \quad (10)$$

Then, from equation (6), the coefficients can be obtained. Finally, the interpolation is expressed as

$$u(\mathbf{x}) = [\mathbf{R}^T(\mathbf{x}) \quad \mathbf{P}^T(\mathbf{x})] \mathbf{A}^{-1} \begin{Bmatrix} \mathbf{u}_e \\ \mathbf{0} \end{Bmatrix} = \boldsymbol{\phi}(\mathbf{x}) \mathbf{u}_e \quad (11)$$

where the matrix of the shape functions  $\boldsymbol{\phi}(\mathbf{x})$  is defined by

$$\boldsymbol{\phi}(\mathbf{x}) = [\phi^1(\mathbf{x}), \phi^2(\mathbf{x}), \dots, \phi^i(\mathbf{x}), \dots, \phi^n(\mathbf{x})] \quad (12)$$

with

$$\phi^k(\mathbf{x}) = \sum_{i=1}^n R_i(\mathbf{x}) \hat{\mathbf{A}}_{ik} + \sum_{j=1}^m p_j(\mathbf{x}) \hat{\mathbf{A}}_{(n+j)k} \quad (13)$$

where  $\hat{\mathbf{A}}_{ik}$  represents the  $(i, k)$  element of matrix  $\mathbf{A}^{-1}$ .

The widely used RBFs include multiquadrics (MQ), Gaussian (EXP), and thin plate splines (TPS) forms, and so on. In this paper, we will employ the multiquadrics (MQ) form:

$$R_i(\mathbf{x}) = (r_i^2 + c^2)^\beta \quad (14)$$

$c$  and  $\beta$  are the shape parameters. Here, we choose  $c = 1$ ,  $\beta = 1.03$  or  $c = 2$ ,  $\beta = 1.99$ .

### 3 The MLPG Method for Multiscale Simulation

In this section, a finite deformation model based on the atomistic physics will be developed, for use in the ECM region.

In continuum mechanics, the stress at a material point is a function of the ‘state’ variables, such as strain, and its gradients, at the same point. In order to formulate a constitutive law for an *equivalent continuum model* (ECM) from the atomic forces, a hypothesis to connect the continuum displacement field and the motions of atoms must be employed. The Cauchy-Born hypothesis is the basis for developing the ECM elastic potentials, from the atomistic description of the system. In the absence of slips, phase transitions, twinning or other inelastic phenomena, the Cauchy-Born hypotheses for crystals are equivalent for homogeneous deformations (Ericksen, 1984). Once the geometry of the deformed lattice vectors is linked to the continuum deformation, a constitutive model based on atomistic description can be constructed by equating the continuum strain energy density to the potential energy of the atomic system for a representative cell, divided by its volume, as in Tadmor et al. (1996).

In this paper, first, we will develop an MLPG tangent-stiffness method for the ECM region, in which it is assumed that the state of deformation is homogeneous and can be well-characterized by the local deformation gradient  $\mathbf{F}$ . The inhomogeneous deformation, such as near defect cores, will be accounted for by the pure molecular dynamics (MD). The whole idea is that: in the ECM, MLPG5 or MLPG1 tangent-stiffness method will be employed; in the MD region, MLPG2 tangent-stiffness method will be employed.

Both of these, the ECM and MD regions, will be linked through the device of the meshless local Petrov-Galerkin (MLPG) method, which will thus offer the possibility of carrying out uniformly valid simulations of material properties for multi-scale systems at both larger length scales and longer times than direct atomistic calculations, and permits a reduction of the full set of atomic degrees of freedom; thus inching towards almost  $O(N)$  algorithms. This is illustrated of in Fig. 3. In the ECM region, the nodes can be taken to be arbitrary, and not necessarily be coincident with the atoms. In MD region, the nodes are taken to be the atoms themselves. In the ECM region, the solid points represent the atoms,

while the open points represent the nodes of the MLPG method. MLPG5 will be implemented in ‘ECM’ region and MLPG2 will be implemented in MD region.

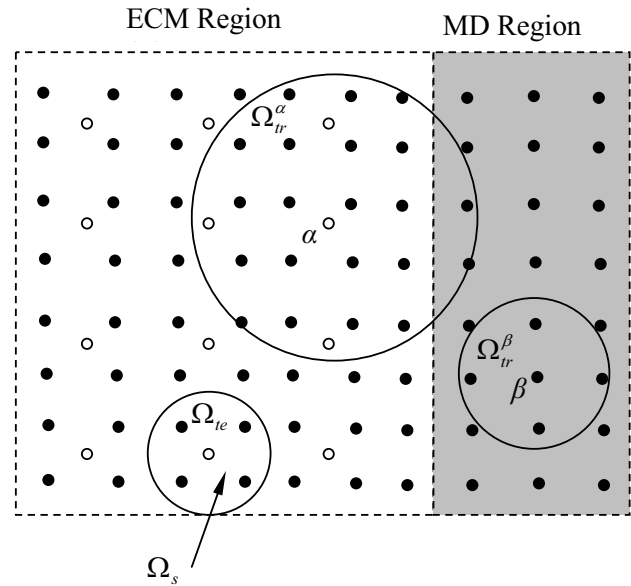


Figure 3 : Illustration of multiscale simulation.

The dynamic motion for atomic positions are governed by Newtonian mechanics and described by molecular dynamics. The multi-scale materials are discretized into a set of nodes. In the molecular dynamics region, the position of the atom can be interpolated by the meshless interpolation (the moving least square or radial basis functions) of the nodes, similar to the displacement in the continuum mechanics region. The atomic forces are analytic derivatives of the inter-atomic potential (Born-Oppenheimer expansion). In the ECM, the atomic environment is characterized by the deformation gradient there. *Each continuum point is taken to represent a large region on the atomic scale, which is homogeneously distorted according to the deformation gradient at the point.* The constitutive response in this region is obtained from the atomistic calculation rather than a phenomenological rule, in a way similar to the quasicontinuum method proposed by Tadmor et al. (1996), and Chung, Namburu, and Henz (2004).

By means of the concept of the MLPG, a local weak form (in subdomain  $\Omega_s$ , as in Fig. 3) for the Newton’s law of motion (conservation of linear momentum) will be used to derive a system of equations for multi-scale materials

modeling. In this paper, we choose radial basis function to be the interpolation scheme, due to its convenience in this case and their Kroneck Delta property [Atluri & Shen, (2002a, b, 2003)].

In classical continuum mechanics, a point  $\mathbf{X}$  in the undeformed body  $\Omega_0$  in the reference frame is mapped to a point  $\mathbf{x}$  in its current shape  $\Omega$  in the current frame. The deformed configuration of the body is described by a displacement function  $\mathbf{u}(\mathbf{X})$ , which represents the displacement at point  $\mathbf{X}$ , as

$$\mathbf{x} = \mathbf{X} + \mathbf{u}(\mathbf{X})$$

The deformation gradient is defined by

$$\mathbf{F} = \frac{\partial \mathbf{x}}{\partial \mathbf{X}} = \mathbf{I} + \frac{\partial \mathbf{u}}{\partial \mathbf{X}}$$

to map infinitesimal material vector from the undeformed body  $\Omega_0$  into the deformed one  $\Omega$ . Here,  $\mathbf{I}$  is the identity tensor.

In the molecular dynamics region, the initial position of an atom  $I$  is denoted as  $\mathbf{X}_I$ . The current configuration of the atom is described by a displacement  $\mathbf{u}$  which depends on  $\mathbf{X}$ , and can be written as

$$\mathbf{x}_I = \mathbf{X}_I + \mathbf{u}_I \quad (15)$$

where  $\mathbf{u}_I = \mathbf{u}(\mathbf{X}_I)$ .

The distance between two atoms  $I$  and  $J$  in the reference configuration can be written as

$$\mathbf{R}_{IJ} = \mathbf{X}_J - \mathbf{X}_I \quad (16)$$

The distance between two atoms  $I$  and  $J$  in the current configuration can be written as

$$\mathbf{r}_{IJ} = \mathbf{x}_J - \mathbf{x}_I \quad (17)$$

According to the Cauchy-Born rule (Ericksen, 1984), for simple Bravais lattice that has the centrosymmetric atomic structure, we have

$$\mathbf{r}_{IJ} = \mathbf{F}\mathbf{R}_{IJ} \quad (18)$$

However, it does not hold for a complex Bravais lattice, which can be described by means of a number of interpenetrating simple Bravais lattices (sub-lattices) and

does not possess centrosymmetry, such as the hexagonal lattice. In this case, the Cauchy-Born rule gives [Zanzotto (1996), Martin (1975), Cousins (1978), Born and Huang (1954)]

$$\mathbf{r}_{IJ} = \mathbf{F}\mathbf{R}_{IJ} + \boldsymbol{\zeta}_k \quad (19)$$

where the internal variables  $\boldsymbol{\zeta}_k$  are shift vectors, with  $k$  ranging from 0 to some integer  $N$  (There are  $N+1$  sub-lattices in the complex Bravais lattice. If atoms  $I, J$  are in the same sub-lattices,  $\boldsymbol{\zeta}_k = 0$ ).  $\boldsymbol{\zeta}_k$  and  $\mathbf{F}$  are independent variables. At the static equilibrium state, the vectors  $\boldsymbol{\zeta}_k$  are to be determined by the minimization of the energy function, so as to reach an equilibrium configuration in the deformed crystal. This means that the equilibrium values of  $\boldsymbol{\zeta}_k$  can be written as functions of  $\mathbf{F}$ . In this paper, which focuses on dynamical problems, we will avoid making any specific hypothesis on the behavior of  $\boldsymbol{\zeta}_k$ . As discussed later [see equation (98)], what we need is  $\partial \mathbf{r}_{IJ} / \partial \mathbf{F} = \mathbf{R}_{IJ}$  from either (18) or (19).

It is noted that, in order to apply the Cauchy-Born rule to nanotubes or fullerenes, a more general exponential mapping procedure like the one in Arroyo and Belytchko (2002) should be used. That will be taken into account as we apply the present multiscale simulation to nanotubes.

The right Cauchy-Green strain tensor is defined by

$$\mathbf{C} = \mathbf{F}^T \mathbf{F} \quad (20)$$

and the Green strain tensor is defined by

$$\mathbf{E} = \frac{1}{2} (\mathbf{C} - \mathbf{I}) \quad (21)$$

The kinematics of the deformation is characterized by the deformation gradient. The constitutive nature of the material is obtained through the strain energy density function  $W$  which relates the energy at a point to the local state of deformation there. It may be shown that  $W$  can only be a function of  $\mathbf{F}$ , from the hypothesis of locality and use the entropy production inequality. Moreover, according to the postulate of material frame indifference, it can be shown that the dependence of  $W$  on  $\mathbf{F}$  can only be through the right Cauchy-Green tensor  $\mathbf{C}$ .

Following the classical continuum mechanics, the second Piola-Kirchhoff stress  $\mathbf{S}$  can be defined as

$$\mathbf{S} = \frac{\partial W}{\partial \mathbf{E}} = 2 \frac{\partial W}{\partial \mathbf{C}} \quad (22)$$

$\mathbf{C}$  and  $\mathbf{S}$  are invariant with respect to rigid-body rotation. The conservation of linear momentum leads to:

$$\nabla \cdot (\mathbf{S}\mathbf{F}^T) + \mathbf{f} = \rho \mathbf{w} \quad (23)$$

where  $\nabla \cdot$  denotes the divergence taken with respect to the material frame,  $\mathbf{f}$  is the body force,  $\rho$  is the density, and  $\mathbf{w}$  is the acceleration, i.e.,  $\mathbf{w} = \frac{d^2 \mathbf{u}}{dt^2}$ .

The conservation of angular momentum leads to:

$$\mathbf{S} = \mathbf{S}^T \quad (24)$$

The tangent stiffness material-moduli can be defined as

$$\mathbf{D} = \frac{\partial^2 W}{\partial \mathbf{E} \partial \mathbf{E}} = 4 \frac{\partial^2 W}{\partial \mathbf{C} \partial \mathbf{C}} \quad (25)$$

More details about the finite strain analysis can be found in Atluri (1979, 1980).

The *local weak form* of equation (23) can be written as

$$\int_{\Omega_s} [\nabla \cdot (\mathbf{S}\mathbf{F}^T) + \mathbf{f} - \rho \mathbf{w}] \mathbf{V} d\Omega = 0 \quad (26)$$

where  $\mathbf{V}$  is the test function in the local domain  $\Omega_s$ . The local symmetric weak form can be written as

$$\begin{aligned} & \int_{\Omega_s} (S_{KLX_{l,L}}) V_{l,K} d\Omega + \int_{L_s} S_{KLX_{l,L}} n_K V_l d\Gamma \\ & + \int_{\Gamma_{su}} S_{KLX_{l,L}} n_K V_l d\Gamma \\ & = \int_{\Gamma_{st}} S_{KLX_{l,L}} n_K V_l d\Gamma + \int_{\Omega_s} (f_l - \rho w_l) V_l d\Omega \end{aligned} \quad (27)$$

where  $\mathbf{n}$  is the unit normal to the local boundary surface  $\Gamma_s$  of  $\Omega_s$ . The corresponding MLPG5 weak-form (when the test functions are taken to Heaviside functions) is:

$$\begin{aligned} & \int_{L_s} S_{KLX_{l,L}} n_K d\Gamma + \int_{\Gamma_{su}} S_{KLX_{l,L}} n_K d\Gamma \\ & = \int_{\Gamma_{st}} S_{KLX_{l,L}} n_K d\Gamma + \int_{\Omega_s} (f_l - \rho w_l) d\Omega \end{aligned} \quad (28)$$

Actually, the MLPG5 [equation (28)] can be directly derived from the conservation of linear momentum in an arbitrary local domain, which is the basis of the finite deformation theory. The physical basis of the MLPG5 is the conservation of linear momentum in an arbitrary local domain, and that of the MLPG2 is the conservation of linear momentum on arbitrary point.

A corresponding continuous interpolation will replace the piece-wise function for the position of the atom in the ECM region,

$$\mathbf{x} = \sum_{\alpha=1}^N \phi^\alpha(\mathbf{X}) \mathbf{x}_\alpha \quad (29)$$

$\mathbf{x}_\alpha, \alpha = 1, 2, \dots, N$ , in equation (29), are the nodal values.  $\phi^\alpha(\mathbf{X})$  is the RBF shape function.

Assume that there are  $N_1$  atoms in region A (MD), and  $N_2$  in region B (ECM). The displacements of atoms  $I$  in the Region A are denoted by  $\mathbf{q}_I$  ( $1 \leq I \leq N_1$ ). The displacements of atom  $i$  in the Region B are denoted by  $\mathbf{u}_i$  ( $1 \leq i \leq N_2$ ), which are interpolated from the displacements of the nodes in region B, as

$$\mathbf{u}_i = \mathbf{u}(\mathbf{X}_i) = \sum_{\alpha=1}^N \phi^\alpha(\mathbf{X}_i) \mathbf{u}_\alpha \quad (30)$$

Here,  $\mathbf{u}_\alpha, \alpha=1, 2, \dots, N$ , are the nodal values. It is noted that  $N$  is less than the amount of atoms of Region B, i.e.,  $N \leq N_2$ , and the node is not necessarily an atom. The displacement  $\mathbf{u}_i$  of an atom in region B implies an average value of the atomic displacement, and can not catch the thermal fluctuations.

### 3.1 The Atomistic Constitutive Law for Homogeneous Deformation and MLPG5, in ECM

The classical MD describes the system's atomic-scale dynamics, where atoms and molecules move, while interacting with many of the atoms and molecules in the vicinity. The system's dynamic evolution is governed by Hamilton's classical equation of motion from Newton's second law. Each atom moves and acts simply as a particle that is moving in a many-body force field of other similar particles. The atomic and molecular interactions describing the dynamics are thus given by classical many-body force-field functions, and the interatomic potential  $\Pi$  as an infinite sum over pair, triplet, etc., can be expressed by the Born-Oppenheimer expansion as:

$$\begin{aligned} \Pi = & \sum_I \left[ \frac{1}{2!} \sum_{J \neq I} V^{(2)}(\mathbf{r}_{IJ}) + \frac{1}{3!} \sum_{K \neq J \neq I} V^{(3)}(\mathbf{r}_{IJ}, \mathbf{r}_{KI}, \mathbf{r}_{KJ}) \right. \\ & \left. + \dots + \frac{1}{n!} \sum_{L \neq J} \dots \sum_{M \neq J} \sum_{J \neq I} V^{(n)}(\mathbf{r}_{IJ}, \dots, \mathbf{r}_{IL}, \dots, \mathbf{r}_{ML}, \dots) \right] \end{aligned} \quad (31)$$

$V^{(2)}$ ,  $V^{(3)}$  ... and  $V^{(n)}$  are the interaction potentials of the two-, three- and  $n$ -body interactions, respectively.

As an example, we consider a two-body and three-body separable potential here. The energy can be expressed as,

$$\Pi = \sum_I \left[ \frac{1}{2} \sum_{J \neq I} V^{(2)}(\mathbf{r}_{IJ}) + \sum_{K \neq J \neq I} V^{(3)}(\mathbf{r}_{IJ}, \mathbf{r}_{Ik}, \mathbf{r}_{Jk}) \right] \quad (32)$$

In this paper, an important procedure is to estimate the strain energy density in the ECM. If we sum over all the atoms as in the classical molecular dynamics, we can certainly get the energy density by evaluating  $\Pi / \Omega$ . However, this is very expensive. In the quasicontinuum method [Tadmor et al. (1996)], for a homogeneously distorted crystal, the continuum strain energy density is obtained by equating to the potential energy of the atomic system for a representative cell divided by its volume, which means that the calculation of equation (32) is limited to a single unit cell. This method will be used in regions that are very far from the inhomogeneous region, in this paper. In the MLPG method, it is natural to limit the calculation of equation (32) to a local domain  $\Omega_s$ , i.e.,

$$W = \frac{1}{\Omega_s} \sum_{I \in \Omega_s} \left[ \frac{1}{2} \sum_{J \neq I} V^{(2)}(\mathbf{r}_{IJ}) + \sum_{K \neq J \neq I} V^{(3)}(\mathbf{r}_{IJ}, \mathbf{r}_{Ik}, \mathbf{r}_{Jk}) \right] - \frac{\Pi_r}{\Omega_s} = \frac{\Pi_s}{\Omega_s} \quad (33)$$

where  $\Omega_s$  is the volume of the local domain, and  $\Pi_r$  is the potential energy of the reference configuration. It is noted that the atoms  $K$  and  $J$  are located in the local domain  $\Omega_s$ , and within the cutoff radius of the boundary of the local domain  $\Omega_s$ . It is noted that both the interatomic potential energy and the strain energy, involve reference states. The former is referenced to infinitely separated atoms, and the latter is referenced to the unstrained configuration. Hence, the constant offset energy  $\Pi_r$ , representing the potential energy in the unstrained state, which does not affect the dynamics is subtracted in equation (33).

If the energy can be written in a form that is additively decomposed, such that  $\Pi = \sum_{I=1} \Pi_I$ , with  $\Pi_I$  denotes the potential energy for each atom, another way to derive the strain energy density is to assume that each atom can be assigned a volume  $\Delta\Omega_I$  in the undeformed configuration

( $\Omega = \sum_{I=1} \Delta\Omega_I$ ). Then, the strain energy density can be derived as  $W = \Pi_I / \Delta\Omega_I$ . In our numerical examples, we proceed in this way.

After obtaining the strain energy density (33) by the Cauchy-Born rule, the second Piola-Kirchhoff stress  $\mathbf{S}$ , and the tangent stiffness moduli  $\mathbf{D}$ , in the ECM can be expressed, respectively, as

$$\begin{aligned} \mathbf{S} &= \frac{\partial W}{\partial \mathbf{E}} = \frac{2}{\Omega_s} \frac{\partial \Pi_s}{\partial \mathbf{C}} \\ &= \frac{2}{\Omega_s} \sum_{I \in \Omega_s} \left[ \frac{1}{2} \sum_{J \neq I} \frac{\partial V^{(2)}(\mathbf{r}_{IJ})}{\partial \mathbf{r}_{IJ}} \frac{\partial \mathbf{r}_{IJ}}{\partial \mathbf{C}} \right] \\ &\quad + \frac{2}{\Omega_s} \sum_{I \in \Omega_s} \left[ \sum_{K \neq J \neq I} \frac{\partial V^{(3)}(\mathbf{r}_{IJ}, \mathbf{r}_{Ik}, \mathbf{r}_{Jk})}{\partial \mathbf{r}_{IJ}} \frac{\partial \mathbf{r}_{IJ}}{\partial \mathbf{C}} \right. \\ &\quad \left. + \frac{\partial V^{(3)}(\mathbf{r}_{IJ}, \mathbf{r}_{Ik}, \mathbf{r}_{Jk})}{\partial \mathbf{r}_{Ik}} \frac{\partial \mathbf{r}_{Ik}}{\partial \mathbf{C}} \right. \\ &\quad \left. + \frac{\partial V^{(3)}(\mathbf{r}_{IJ}, \mathbf{r}_{Ik}, \mathbf{r}_{Jk})}{\partial \mathbf{r}_{Jk}} \frac{\partial \mathbf{r}_{Jk}}{\partial \mathbf{C}} \right] \end{aligned} \quad (34)$$

$$\mathbf{D} = 4 \frac{\partial^2 W}{\partial \mathbf{C} \partial \mathbf{C}} = \frac{4}{\Omega_s} \frac{\partial^2 \Pi_s}{\partial \mathbf{C} \partial \mathbf{C}} \quad (35)$$

where

$$\frac{\partial \mathbf{r}_{IJ}}{\partial \mathbf{F}} = \mathbf{R}_{IJ}, \quad \frac{\partial \mathbf{F}}{\partial \mathbf{C}} = \mathbf{F}^{-1}, \quad \frac{\partial \mathbf{r}_{IJ}}{\partial \mathbf{C}} = \mathbf{R}_{IJ} \mathbf{F}^{-1} \quad (36)$$

The equations from the nonlinear local Petrov-Galerkin formulation (27), can be solved by employing an incremental algorithm. The total Lagrangean method (T. L.) will be employed in this paper. Assuming that the equation (27) is at time  $t$ , then from time  $t$  to time  $t + \Delta t$ , the incremental constitutive relation in the ECM can be expressed as

$$\Delta \mathbf{S} = \mathbf{D} : \Delta \mathbf{E} = \mathbf{D} : (\nabla \Delta \mathbf{u} + \nabla \mathbf{u}^T \cdot \nabla \Delta \mathbf{u}) \quad (37a)$$

or

$$\Delta S_{KL} = D_{KLMN} (\Delta u_{M,N} + u_{P,M} \Delta u_{P,N}) \quad (37b)$$

where  $\Delta \mathbf{u}$  is the discernment of the displacement, i.e.,

$$\Delta \mathbf{u} = {}^{t+\Delta t} \mathbf{u} - {}^t \mathbf{u} \quad (38)$$

with  ${}^t\mathbf{u}$  denotes the displacement  $\mathbf{u}$  at time  $t$ . The equation (27) at time  $t + \Delta t$  can be linearized as

$$\begin{aligned} & \int_{\Omega_s} \Delta(S_{KL}x_{l,L}) V_{l,K} d\Omega + \int_{L_s} \Delta(S_{KL}x_{l,L}) n_K V_l d\Gamma \\ & + \int_{\Gamma_{su}} \Delta(S_{KL}x_{l,L}) n_K V_l d\Gamma - \int_{\Omega_s} \rho({}^t w_l + \Delta w_l) V_l d\Omega \\ & = Q \end{aligned} \quad (39)$$

where the density is defined as

$$\rho = \frac{1}{\Omega_s} \sum_{l \in \Omega_s} m_l \quad \text{or} \quad \rho = \frac{m_l}{\Delta\Omega_l} \quad (40)$$

and

$$\begin{aligned} Q &= \int_{\Gamma_{st}} S_{KL}x_{l,L} n_K V_l d\Gamma + \int_{\Omega_s} f_l V_l d\Omega \\ &+ \int_{\Gamma_{st}} \Delta(S_{KL}x_{l,L}) n_K V_l d\Gamma + \int_{\Omega_s} \Delta f_l V_l d\Omega \\ &- \int_{\Omega_s} S_{KL}x_{l,L} V_{l,K} d\Omega - \int_{L_s} S_{KL}x_{l,L} n_K V_l d\Gamma \\ &- \int_{\Gamma_{su}} S_{KL}x_{l,L} n_K V_l d\Gamma \end{aligned} \quad (41)$$

If we adopt the MLPG5 method, equation (39) and (41) can be rewritten as

$$\begin{aligned} & \int_{L_s} \Delta(S_{KL}x_{l,L}) n_K d\Gamma + \int_{\Gamma_{su}} \Delta(S_{KL}x_{l,L}) n_K d\Gamma \\ & - \int_{\Omega_s} \rho({}^t w_l + \Delta w_l) d\Omega \\ & = Q_l \end{aligned} \quad (42)$$

and

$$\begin{aligned} Q_l &= \int_{\Gamma_{st}} S_{KL}x_{l,L} n_K d\Gamma + \int_{\Omega_s} f_l d\Omega + \int_{\Gamma_{st}} \Delta(S_{KL}x_{l,L}) n_K d\Gamma \\ &+ \int_{\Omega_s} \Delta f_l d\Omega - \int_{L_s} S_{KL}x_{l,L} n_K d\Gamma - \int_{\Gamma_{su}} S_{KL}x_{l,L} n_K d\Gamma \end{aligned} \quad (43)$$

By using the natural boundary on  $\Gamma_t$ ,  $S_{KL}x_{l,L} n_K = \bar{T}_l$ , equation (43) can be written as

$$\begin{aligned} Q_l &= \int_{\Gamma_{st}} \bar{T}_l d\Gamma + \int_{\Omega_s} f_l d\Omega + \int_{\Gamma_{st}} \Delta \bar{T}_l d\Gamma + \int_{\Omega_s} \Delta f_l d\Omega \\ &- \int_{L_s} S_{KL}x_{l,L} n_K d\Gamma - \int_{\Gamma_{su}} S_{KL}x_{l,L} n_K d\Gamma \end{aligned} \quad (44)$$

According to equation (37), equation (39) or (42) is a linear equation in terms of  $\Delta\mathbf{u}$ . The increment of displacement,  $\Delta\mathbf{u}$ , can be interpolated in the MLPG method as

$$\Delta\mathbf{u} = \sum_{\alpha=1}^N \phi^\alpha(\mathbf{X}) \Delta\mathbf{u}_\alpha \quad (45)$$

$\Delta\mathbf{u}_\alpha, \alpha = 1, 2, \dots, N$ , in equation (45), are the nodal values. Again, it is noted that  $N$  is less than the amount of atoms of the system, and the node is not necessarily the atom. For convenience, we rewrite equation (45) as

$$\Delta u_I = \sum_{\alpha=1}^N \phi_{IJ}^\alpha(\mathbf{X}) \Delta u_{\alpha J} \quad (46)$$

with  $\phi_{IJ}^\alpha = \phi^\alpha \delta_{IJ}$ .

Substitution of equation (45) into equation (42), for all nodes, leads to the following discretized system of linear equations:

$$-\sum_{\beta=1}^N [\mathbf{M}_{\alpha\beta}]^{t+\Delta t} \ddot{\mathbf{u}}_\beta + \sum_{\beta=1}^N [{}^t\mathbf{K}_{\alpha\beta}] \Delta\mathbf{u}_\beta = \mathbf{Q}_\alpha \quad (47)$$

where

$$\begin{aligned} & [{}^t\mathbf{K}_{\alpha\beta}]_{JI} \\ &= \int_{L_s} \left[ D_{KLMN} (\delta_{JL} + {}^t u_{J,L}) n_K (\delta_{PM} + {}^t u_{P,M}) \phi_{PI,N}^\beta \right. \\ & \quad \left. + S_{KL} n_K \phi_{JI,L}^\beta \right] d\Gamma \\ & \quad + \int_{\Gamma_{su}} \left[ D_{KLMN} (\delta_{JL} + {}^t u_{J,L}) n_K (\delta_{PM} + {}^t u_{P,M}) \phi_{PI,N}^\beta \right. \\ & \quad \left. + S_{KL} n_K \phi_{JI,L}^\beta \right] d\Gamma \end{aligned} \quad (48)$$

$$[\mathbf{M}_{\alpha\beta}]_{JI} = \int_{\Omega_s} \rho \phi_{JI}^\beta d\Omega \quad (49)$$

$$\begin{aligned} & \{\mathbf{Q}_\alpha\}_J \\ &= \int_{\Gamma_{st}} \bar{T}_J d\Gamma + \int_{\Omega_s} f_J d\Omega + \int_{\Gamma_{st}} \Delta \bar{T}_J d\Gamma + \int_{\Omega_s} \Delta f_J d\Omega \\ & \quad - \int_{L_s} S_{KL} (\delta_{JL} + {}^t u_{J,L}) n_K d\Gamma \\ & \quad - \int_{\Gamma_{su}} S_{KL} (\delta_{JL} + {}^t u_{J,L}) n_K d\Gamma \end{aligned} \quad (50)$$

The integration in equation (48)-(50) can employ the Gaussian quadrature. It is shown that no domain integration is involved in equation (48), which is an important advantage of MLPG5.

The linearized equations (47) will be very effective for static or implicit time integration schemes. However, if an explicit time integration scheme is employed, we can directly use equations (28), and do not need to linearize them. In this paper, we will use the central difference rule to integrate time, and not linearize equations (28).

In this case, equation (28) can be rewritten as

$$\mathbf{M}_{\alpha\beta}\ddot{\mathbf{u}}_\beta = \mathbf{t}_\alpha \quad (51)$$

for node  $\alpha$  or

$$\mathbf{M}_C \ddot{\mathbf{d}} = \mathbf{t}_C \quad (52)$$

for the whole region B, with

$$\begin{aligned} \mathbf{t}_\alpha &= \int_{\Gamma_{st}} (\mathbf{S}\mathbf{F}^T) \cdot \mathbf{n} d\Gamma - \int_{L_s} (\mathbf{S}\mathbf{F}^T) \cdot \mathbf{n} d\Gamma - \int_{\Gamma_{su}} (\mathbf{S}\mathbf{F}^T) \cdot \mathbf{n} d\Gamma \\ &= \int_{\Gamma_{st}} \frac{\partial W}{\partial \mathbf{F}} \cdot \mathbf{n} d\Gamma - \int_{L_s} \frac{\partial W}{\partial \mathbf{F}} \cdot \mathbf{n} d\Gamma - \int_{\Gamma_{su}} \frac{\partial W}{\partial \mathbf{F}} \cdot \mathbf{n} d\Gamma \end{aligned} \quad (53)$$

$$\mathbf{M}_{\alpha\beta} = \int_{\Omega_s} \rho \phi^\beta \mathbf{I} d\Omega \quad (54)$$

and

$$\begin{aligned} \mathbf{d} &= [\mathbf{u}_1, \mathbf{u}_2, \dots, \mathbf{u}_\alpha, \dots, \mathbf{u}_N]^T \\ \mathbf{t}_C &= [\mathbf{t}_1, \mathbf{t}_2, \dots, \mathbf{t}_\alpha, \dots, \mathbf{t}_N]^T \end{aligned}$$

Gaussian quadrature is employed to compute the integral in equation (53) numerically.  $\mathbf{M}_{\alpha\beta}$  is the sub-matrix of the global mass matrix  $\mathbf{M}_C$  in region B. Here, the body force is not considered. Equation (54) is for the consistent mass matrix. It is noted that we can also use the lumped mass in equation (52) same as that in FEM. The lumping procedure can be same as that in FEM. Then, we will obtain a diagonal mass matrix. Actually, in MLPG method, to lump the mass matrix is simpler and more convenient than in FEM, we can just assign the mass on the node instead of distributing it continuously within the local domain, i.e.

$$\rho = \bar{m}_\alpha \delta(\mathbf{X} - \mathbf{X}_\alpha) \quad (55)$$

with  $\bar{m}_\alpha = \int_{\Omega_s} \rho d\Omega$ . Then, we have the diagonal mass matrix

$$\mathbf{M}_{\alpha\beta} = \bar{m}_\alpha \delta_{\alpha\beta} \mathbf{I} \quad (56)$$

This reduces to the correct description in the atomic limit, where nodes coincide with atoms. It is noted that equation (56) can also be obtained by means of the row-sum technique, because of the zero-order consistency, i.e.,  $\sum_{\beta=1}^n \phi^\beta = 1$ .

#### 4 Atomistic (MD) Simulation in the Inhomogeneous Deformation Region

In the inhomogeneous-deformation region, we will employ the MLPG2 by letting the node to be the atom itself. Assume that there are  $N_1$  atoms in this region (MD). The displacement of atom  $I$  in this region is denoted as  $\mathbf{q}_I$  ( $1 \leq I \leq N_1$ ). Now, the control equation will be

$$-m_I \ddot{\mathbf{q}}_I + \mathbf{f}_I = 0 \quad (57)$$

$$\mathbf{f}_I = -\frac{\partial \Pi}{\partial \mathbf{x}_I} = -\frac{\partial \Pi}{\partial \mathbf{q}_I} \quad (58)$$

The force  $\mathbf{f}_I$  is computed, as it would be in a standard atomistic calculation. In molecular dynamics, these equations are approximated as finite-difference equations with discrete time step  $\Delta t$  and are solved by the standard Gear's fifth-order predictor-corrector or Verlet's leapfrog method. The evaluation of the interatomic potential energy, and forces, is performed by taking advantage of the neighbor-list of atoms, so that the time for the computation scales with the number of atoms in region A, i.e. it is of order- $N_1$ . The neighbor list is renewed every several time steps.

Similar to that in section 3, we can also linearize equation (57). Although we will not employ it in the numerical examples, we still list the equations here. Equation (57) can be rewritten as

$$-m_I {}^{t+\Delta t}\ddot{\mathbf{q}}_I + {}^{t+\Delta t}\mathbf{f}_I = 0 \quad (59)$$

Then, equation (59) is written as

$$\begin{aligned} &-m_I {}^{t+\Delta t}\ddot{\mathbf{q}}_I + {}^{t+\Delta t}\mathbf{f}_I \\ &\approx -m_I {}^{t+\Delta t}\ddot{\mathbf{q}}_I + {}^t\mathbf{f}_I + \sum_{j=1}^t \left( \frac{\partial \mathbf{f}_I}{\partial \mathbf{q}_j} \right) \Delta \mathbf{q}_j = 0 \end{aligned} \quad (60)$$

The above equation can be rewritten as

$$-m_I {}^{t+\Delta t}\ddot{\mathbf{q}}_I + \sum_{J=1}^N [{}^t\mathbf{K}_{IJ}\Delta\mathbf{q}_J] = \Delta\mathbf{Q}_I \quad (61)$$

where the tangent stiffness matrix  ${}^t\mathbf{K}_{IJ}$  is defined as

$${}^t\mathbf{K}_{IJ} = \frac{\partial \mathbf{f}_I}{\partial \mathbf{q}_J} \quad (62)$$

and

$$\Delta\mathbf{Q}_I = -{}^t\mathbf{f}_I \quad (63)$$

Now, a unified formulation for the multiscale system can be developed, based on the MLPG method, and the tangent stiffness concept. The equation (47) and (61) can be written as

$$\mathbf{M} {}^{t+\Delta t}\ddot{\mathbf{u}} + {}^t\mathbf{K}\Delta\mathbf{u} = {}^{t+\Delta t}\mathbf{Q} \quad (64)$$

This method should be very effective due to the fact that adaptive remeshing, which is an important factor in multiscale dynamics, is very convenient in the MLPG method. This computational methodology provides a unified method for simulation in MD and equivalent continuum mechanics regions.

## 5 Interfacial Conditions between Atomistic Simulation (MD) Region and the Equivalent Continuum Mechanics (ECM) Region

In the multiscale simulation, the atomistic method is employed where the displacement field varies on an atomic scale, and the continuum approach is employed elsewhere. For the seamless multiscale simulation, it is important to ensure that the elastic waves generated in the atomistic region can propagate into the continuum region. The continuum region cannot support modes of short wavelength, which is less than the spacing of the nodes. One source of finite size effects is the short waves which are reflected back unphysically from an artificial interface or boundary, which may also produce uneven heating across the interface. In order to minimize such reflections, some interfacial conditions are proposed [Cai et al. (2000), E and Huang (2001), Wagner and Liu (2003)]. In this paper, alternate interfacial conditions between atomistic and continuum regions are proposed. Their effectiveness in ensuring the accurate passage of

information between atomistic and continuum regions is discussed.

As mentioned before, the displacement  $\mathbf{u}_i$  of an atom in region B [ECM] implies an average value of the atomic displacement, it can not catch the thermal fluctuations. To describe it more accurately, we assume that the “real” displacement  $\mathbf{q}_i$  of the atom in the region B can be expressed as:

$$\mathbf{q}_i = \mathbf{u}_i + \delta\mathbf{u}_i \quad (65)$$

where  $\delta\mathbf{u}_i$  denote the atomic thermal fluctuations, and it is assumed that  $\delta\mathbf{u}_i \ll \mathbf{u}_i$  in region B. Now, the total potential energy of the system (A+B) [wherein Region A is of MD] can be written as:

$$\begin{aligned} \Pi(\mathbf{q}_1, \dots, \mathbf{q}_{N_1+N_2}) &\approx \Pi(\mathbf{u}_i; \mathbf{q}_I) + \sum_{i=1}^{N_2} \left. \frac{\partial \Pi}{\partial \mathbf{q}_i} \right|_{\mathbf{q}_i=\mathbf{u}_i} \delta\mathbf{u}_i \\ &= \Pi_0 + \sum_{i=1}^{N_2} \frac{\partial \Pi_0}{\partial \mathbf{u}_i} \delta\mathbf{u}_i = \Pi_0(\mathbf{u}_B; \mathbf{q}_A) + \frac{\partial \Pi_0}{\partial \mathbf{u}_B} \cdot \delta\mathbf{u}_B \end{aligned} \quad (66)$$

( $I = 1, \dots, N_1$  in A;  $i = 1, \dots, N_2$  in B)

Here  $\Pi_0$  denotes the zeroth-order approximation of the potential energy;  $\mathbf{q}_A$  and  $\mathbf{u}_B$  are the atomic displacement vectors with dimensions  $3N_1$  (for 3 dimensions) in region A, and  $3N_2$  in region B, respectively;  $\delta\mathbf{u}_B$  is atomic thermal fluctuation vector with dimension  $3N_2$ . We can also expand the potential energy to a higher order, which will be at the expense of an additional computational cost. However, in the region B, the deformation is homogeneous, and  $\delta\mathbf{u}_i$  is very small compared to  $\mathbf{u}_i$ , so that equation (66) is accurate enough. Effectively, the MLPG algorithm involves an average over the atomic degrees of freedom that are missing from the nodes in region B. The second term in right side of equation (66) accounts for the missing degrees of atomic freedom.

In many of the existing multiscale modeling methods, the thermal fluctuation is generally neglected, as in Rudd and Broughton (1998), Shenoy (2003), Abraham (2000). In this case, in region A, the Newton's Second law can be written in a matrix form as

$$\mathbf{M}_A \ddot{\mathbf{q}}_A = \mathbf{f}_A^0; \quad \mathbf{f}_A^0 = -\partial \Pi_0 / \partial \mathbf{q}_A \quad (67)$$

where the atomic mass matrix  $\mathbf{M}_A$  is a diagonal matrix of size  $3N_1$  with the atomic masses on the diagonal, and

the force vector  $\mathbf{f}_A^0$  is of dimension  $3N_1$ . Eq. (67) is valid only for classical  $0^\circ\text{K}$ . We denote the solution of eq. (67) as “Solution Method 1”. The degrees of freedom (DOF)  $N_1$  in A are in general greater than these in B, viz.,  $N_2$  [i.e.,  $N_1 \gg N_2$ ]. Thus, in Solution Method 1, which is computationally inexpensive, has the potential drawback that higher frequencies waves will reflect back from the interface between A and B.

To improve the performance at higher frequencies and assure that the energy in region A can pass through the interface between A and B, the thermal fluctuation of atoms in region B must be considered. Thus, we will use the first-order approximation of the potential energy, i.e.  $\Pi$  in eq. (66), to replace  $\Pi_0$  in eq. (67), which leads to:

$$\mathbf{M}_A \ddot{\mathbf{q}}_A = \mathbf{f}_A^0 - \mathbf{K}_{AB} \delta \mathbf{u}_B \quad (68)$$

where

$$\mathbf{K}_{AB} = \partial^2 \Pi_0 / \partial \mathbf{u}_B \partial \mathbf{q}_A.$$

It is noted that the tangent stiffness matrix  $\mathbf{K}_{AB}$  is of order  $3N_1 \times 3N_2$ , and its entries are nonzero, only when the atoms in region A are directly coupled to atoms in region B.  $\delta \mathbf{u}_B$  can be obtained from the equation of motion in region B, viz.,

$$\mathbf{M}_B \delta \ddot{\mathbf{u}}_B = \mathbf{f}_B^0 - \mathbf{M}_B \ddot{\mathbf{u}}_B \quad (69)$$

where the atomic mass matrix  $\mathbf{M}_B$  is a diagonal matrix of size  $3N_2$ , and the force vector  $\mathbf{f}_B^0$  of dimension  $3N_2$  is approximated as

$$\mathbf{f}_B^0 = -\partial \Pi_0 / \partial \mathbf{u}_B \quad (70)$$

In equations (68) and (69), we note that  $\mathbf{f}_A$  in region A is approximated as  $\mathbf{f}_A = -\partial \Pi / \partial \mathbf{q}_A \approx -\partial \Pi_0 / \partial \mathbf{q}_A - \partial^2 \Pi_0 / \partial \mathbf{u}_B \partial \mathbf{q}_A \delta \mathbf{u}_B$ ; that in region B is approximated as  $\mathbf{f}_B = -\partial \Pi / \partial \mathbf{q}_B$ . By integrating eq. (69) twice,  $\delta \mathbf{u}_B$  can be solved for, and substituting this solution into eq. (68), we have

$$\mathbf{M}_A \ddot{\mathbf{q}}_A = \mathbf{f}_A^0(\mathbf{u}_B, \mathbf{q}_A) - \mathbf{K}_{AB} \int_0^t (t - \tau) \mathbf{Y}(\tau) d\tau - \mathbf{R}(t) \quad (71)$$

where

$$\mathbf{Y}(t) = \mathbf{M}_B^{-1} \mathbf{f}_B^0(\mathbf{u}_B, \mathbf{q}_A) - \ddot{\mathbf{u}}_B(t)$$

$$\mathbf{R}(t) = \mathbf{K}_{AB} [\delta \mathbf{u}_B(0) + t \delta \dot{\mathbf{u}}_B(0)] \quad (73)$$

$\mathbf{Y}(t)$  simply represents  $\delta \ddot{\mathbf{u}}_B$ .  $\mathbf{R}(t)$  represents the effects on region A due to the initial thermal fluctuation, and the velocity in region B and is usually treated as a vector of random forces to describe the effects of statistical fluctuation in region B at nonzero temperature. In the example problems in section 7, it is assumed that the temperature is  $0^\circ\text{K}$ , so that  $\mathbf{R}(t)$  can be ignored. The solution of eq. (71), which is originally proposed here, is denoted as “Solution Method 2”. It is noted that only a few of the entries in vector  $\mathbf{Y}(t)$  are necessary, since the matrix  $\mathbf{K}_{AB}$  is nonzero only for the atomic pairs in the cutoff of the interface. That makes presently proposed Solution Method 2 is computationally inexpensive.

Now, we will give a brief discussion about the second term on the right hand side of equation (71). Assuming that the time step is  $\Delta t$ , and all the quantities are obtained at the  $i$ th time step, then at the  $(i+1)$ th time step, we have

$$\begin{aligned} \mathbf{J}_{i+1} &= \int_0^{t_{i+1}} (t_{i+1} - \tau) \mathbf{Y}(\tau) d\tau \\ &= t_{i+1} \int_0^{t_{i+1}} \mathbf{Y}(\tau) d\tau - \int_0^{t_{i+1}} \tau \mathbf{Y}(\tau) d\tau \\ &= t_{i+1} \int_0^{t_i} \mathbf{Y}(\tau) d\tau + t_{i+1} \int_{t_i}^{t_{i+1}} \mathbf{Y}(\tau) d\tau - \int_0^{t_i} \tau \mathbf{Y}(\tau) d\tau \\ &\quad - \int_{t_i}^{t_{i+1}} \tau \mathbf{Y}(\tau) d\tau \\ &= t_{i+1} \hat{\mathbf{Y}}_i + t_{i+1} \int_{t_i}^{t_{i+1}} \mathbf{Y}(\tau) d\tau - \tilde{\mathbf{Y}}_i - \int_{t_i}^{t_{i+1}} \tau \mathbf{Y}(\tau) d\tau \\ &= (t_i \hat{\mathbf{Y}}_i - \tilde{\mathbf{Y}}_i) + \Delta t \hat{\mathbf{Y}}_i + t_{i+1} \int_{t_i}^{t_{i+1}} \mathbf{Y}(\tau) d\tau - \int_{t_i}^{t_{i+1}} \tau \mathbf{Y}(\tau) d\tau \\ &= \mathbf{J}_i + \Delta t \hat{\mathbf{Y}}_i + t_{i+1} \Delta \hat{\mathbf{Y}} - \Delta \tilde{\mathbf{Y}} = \mathbf{J}_i + t_i \Delta \hat{\mathbf{Y}} - \Delta \tilde{\mathbf{Y}} \\ &\quad + (\Delta t \hat{\mathbf{Y}}_i + \Delta \hat{\mathbf{Y}}) \\ &= \mathbf{J}_i + t_i \Delta \hat{\mathbf{Y}} - \Delta \tilde{\mathbf{Y}} + \Delta t \hat{\mathbf{Y}}_{i+1} \end{aligned}$$

with

$$\hat{\mathbf{Y}}_i = \int_0^{t_i} \mathbf{Y}(\tau) d\tau$$

$$\hat{\mathbf{Y}}_{i+1} = \hat{\mathbf{Y}}_i + \Delta \hat{\mathbf{Y}}$$

$$t_{i+1} = t_i + \Delta t$$

and

$$\Delta \hat{\mathbf{Y}} = \int_{t_i}^{t_{i+1}} \mathbf{Y}(\tau) d\tau = \frac{\Delta t}{2} [\mathbf{Y}(t_i) + \mathbf{Y}(t_{i+1})]$$

$$(72) \quad \Delta \tilde{\mathbf{Y}} = \int_{t_i}^{t_{i+1}} \tau \mathbf{Y}(\tau) d\tau = \frac{\Delta t}{2} [t_i \mathbf{Y}(t_i) + t_{i+1} \mathbf{Y}(t_{i+1})]$$

From the above equations, it can be seen that they only used the results at the  $i$ th and the  $(i+1)$ th time steps, to calculate the second term on the right hand side of equation (71) [only the entries for the atomic pairs in the cut-off of the interface are needed] at  $(i+1)$  time step. Hence, a complete time history of the trajectory is not needed to evaluate the second term on the right hand side of equation (71).

In equations (68) and (69), which are based on the potential energy, we note that the force in the region A is expanded to the first order of  $\delta \mathbf{u}_B$ , while the force in the region B is only of the zeroth order. To increase the accuracy of the results, we can also expand the force in the region B to the first order, as

$$\mathbf{f}_B = \mathbf{f}_B^0 + \mathbf{K}_{BB} \delta \mathbf{u}_B \quad (74)$$

with the  $3N_2 \times 3N_2$  tangent stiffness matrix

$$\mathbf{K}_{BB} = \partial^2 \Pi_0 / \partial \mathbf{u}_B \partial \mathbf{u}_B$$

Then, eq. (69) can be rewritten as

$$\mathbf{M}_B \delta \ddot{\mathbf{u}}_B = \mathbf{f}_B^0 + \mathbf{K}_{BB} \delta \mathbf{u}_B - \mathbf{M}_B \ddot{\mathbf{u}}_B \quad (75)$$

Similar to Adelman and Doll (1976), by means of Laplace transforms, the intermediate-variable  $\delta \mathbf{u}_B$  can be solved for, and substituting it back into eq. (68), we have

$$\mathbf{M}_A \ddot{\mathbf{q}}_A = \mathbf{f}_A^0(\mathbf{u}_B, \mathbf{q}_A) - \int_0^t \boldsymbol{\Phi}(t-\tau) \mathbf{Y}(\tau) d\tau + \mathbf{R}(t) \quad (76)$$

where

$$\boldsymbol{\Phi}(t) = L^{-1} \left\{ \mathbf{K}_{AB} \left[ s^2 \mathbf{I} + \mathbf{M}_B^{-1} \mathbf{K}_{BB} \right]^{-1} \right\} \quad (77)$$

$$\mathbf{R}(t) = \dot{\boldsymbol{\Phi}}(t) \delta \mathbf{u}_B(0) + \boldsymbol{\Phi}(t) \delta \dot{\mathbf{u}}_B(0) \quad (78)$$

The matrix  $\boldsymbol{\Phi}(t)$  denotes the time-dependent memory kernel. The Operator  $L^{-1}$  indicates the inverse Laplace transform. Eq. (76) is similar to the Generalized Langevin Equation (GLE) boundary condition derived in Adelman and Doll (1976) for the single-scale problem, and in Wagner and Liu (2003) for the multiscale problem by using a “bridging scale” decomposition [i.e., the entire system is treated as a coarse scale one, B, first; and then the entire system is treated as a fine scale one, A, later sequentially. In the present paper, the system is treated as a combination of parts A and B simultaneously]. We denote the solution of eq. (75) as “Solution Method 3”.

The second term on the right hand side of equations (71) and (75), the time history integral, implies the dissipation of energy from region A into region B, which results in non-reflecting boundary conditions, supporting short wavelengths that cannot be represented by the interpolations in region B.

It is noted that the computation of the of the matrix  $\boldsymbol{\Phi}(t)$  involves not only an inverse Laplace transform, but also the inversion of an  $N_2 \times N_2$  matrix, which appears to be impractical, although only a few of the entries in this inverted matrix are necessary, since the matrix  $\mathbf{K}_{AB}$  is nonzero only for atomic pairs in the cutoff of the interface. The necessary entries of the matrix  $\boldsymbol{\Phi}(t)$  can be approximated as that in Adelman and Doll (1976), or computed numerically as in Cai et al. (2000). However, the computation of the matrix  $\boldsymbol{\Phi}(t)$  is costly. Moreover, a complete time history of the trajectory is required to evaluate the second term on the right hand side of equation (76). In our numerical examples, we will not consider Solution Method 3.

## 6 Multiple Time Steps for Time Integration

In this paper, a multiple time step method is employed for the time integration in both region A and B. The stability of multiple time step method was studied in Belytschko et al. (1979), Belytschko and Smolinski (1985), Belytschko and Lu (1993). The standard method would be to use the central difference rule. In region B, the time step is taken to be  $\Delta t_B$ . In region A, the time step is  $\Delta t_A = \Delta t_B / k$ , where  $k$  is a positive integer and determined by the spacing of the nodes. Hence, the MD simulation in region A is advanced by  $k$  steps of size  $\Delta t_A$ , when the ECM simulation in region B is advanced for a step of size  $\Delta t_B$ .

The scheme for time integration in region A from time step  $nk + i$  to  $nk + i + 1$  is as follows:

$$\mathbf{d}^{nk+i+1} = \mathbf{d}^{nk+i} + \Delta t_A \dot{\mathbf{d}}^{nk+i} + \frac{1}{2} \Delta t_A^2 \ddot{\mathbf{d}}^{nk} \quad (79)$$

$$\dot{\mathbf{d}}^{nk+i+1} = \dot{\mathbf{d}}^{nk+i} + \Delta t_A \ddot{\mathbf{d}}^{nk} \quad (80)$$

Then, the displacements  $\mathbf{u}_B^{nk+i+1}$ , of atom in the cutoff of the interface, in region B are interpolated by equation (30), and then

$$\mathbf{q}_A^{nk+i+1} = \mathbf{q}_A^{nk+i} + \Delta t_A \dot{\mathbf{q}}_A^{nk+i} + \frac{1}{2} \Delta t_A^2 \ddot{\mathbf{q}}_A^{nk+i} \quad (81)$$

$$\ddot{\mathbf{q}}_A^{nk+i+1} = \mathbf{M}_A^{-1} \mathbf{f}_A^R(\mathbf{u}_B^{nk+i+1}, \mathbf{q}_A^{nk+i+1}) \quad (82)$$

$$\dot{\mathbf{q}}_A^{nk+i+1} = \dot{\mathbf{q}}_A^{nk+i} + \frac{1}{2} \Delta t_A (\ddot{\mathbf{q}}_A^{nk+i+1} + \ddot{\mathbf{q}}_A^{nk+i}) \quad (83)$$

where  $0 \leq i < k$ ,  $\mathbf{f}_A^R(\mathbf{u}_B^{nk+i+1}, \mathbf{q}_A^{nk+i+1})$  represents the entire right hand side of equation (67) or (71) or (76). It is noted that in equations (79) and (80), only the quantities in the cutoff of the interface are needed. For all the  $k$  steps from step  $nk$ , the acceleration of the nodes in region B is assumed to be constant.

Once  $\mathbf{q}_A^{(n+1)k}$  are obtained at  $(n+1)k$  time step, the node-displacement in region B is advanced from time step  $nk$  to  $(n+1)k$ . The scheme for time integration in region B from time step  $nk$  to  $(n+1)k$  is as follows

$$\mathbf{d}^{(n+1)k} = \mathbf{d}^{nk} + \Delta t_B \dot{\mathbf{d}}^{nk} + \frac{1}{2} \Delta t_B^2 \ddot{\mathbf{d}}^{nk} \quad (84)$$

$$\ddot{\mathbf{d}}^{(n+1)k} = \mathbf{M}_C^{-1} \mathbf{t}_C(\mathbf{d}^{(n+1)k}, \mathbf{q}_A^{(n+1)k}) \quad (85)$$

$$\dot{\mathbf{d}}^{(n+1)k} = \dot{\mathbf{d}}^{nk} + \frac{1}{2} \Delta t_B (\ddot{\mathbf{d}}^{nk} + \ddot{\mathbf{d}}^{(n+1)k}) \quad (86)$$

It is noted that equations (79) and (80) give the same node-displacement at  $(n+1)k$  time step as equation (84). Once these quantities at  $(n+1)k$  time step are determined, they will be used in equations (79) and (80).

## 7 Numerical Examples

### 7.1 one-dimensional chains

As a demonstration of the effectiveness of the multiscale simulation method and the interfacial conditions proposed here, we consider the same example as in Rudd and Broughton (1998), Cai, et al. (2000), and Wagner and Liu (2003): one-dimensional chains of identical atoms with nearest-neighbor interactions. The spring constants, mass, and equilibrium distances are set equal to unity. There are 151 atoms in region A, which is bracketed by two semi-infinite chains (region B). The lumped mass matrix is used. The time integration uses multiple time steps: the equivalent continuum simulation in region B is advanced by a time step  $\Delta t_B = 0.1$ , while the MD simulation in region A is advanced by  $\Delta t_A = \Delta t_B/5$ . The distance between the nodes in region B is  $h=7.8$ . The radius

of the trial function domain is taken to be  $3.2h$ , and the radius of the test domain is  $0.85h$ . The Solution Methods denoted as 1 and 2 earlier, are used to simulate the time evolution, after introducing initial displacements according to the wave packet [Rudd and Broughton (1998), Cai, et al. (2000)]:

$$u(X, t=0) = \cos(kX) \exp(-X^2/2\sigma^2) \quad (87)$$

Here,  $X$  denotes the equilibrium position of atoms. The center of region A is  $X = 0$ . A full MD simulation is also performed, in which the entire system is treated in an atomistic scale. As a measure of the effectiveness of Solution Methods 1 and 2, the wave reflection at the interface between region A and B is evaluated. The reflectivity  $R$  is defined as the maximum difference between the instantaneous energies stored in region A during the simulation and the full MD run, divided by initial energy in region A [Cai, et al. (2000)].

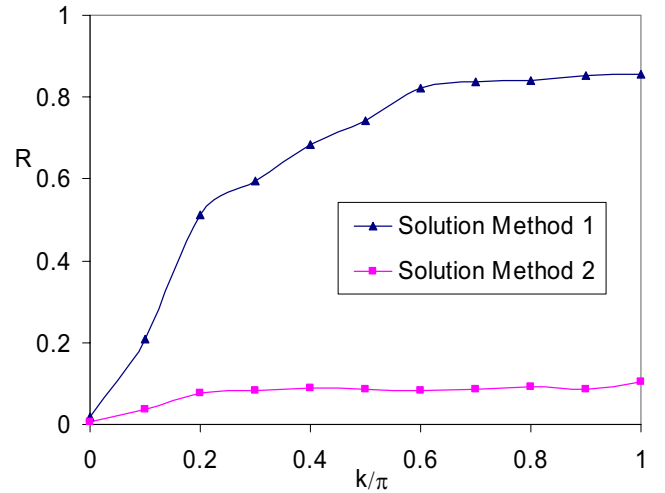


**Figure 4** : Comparison of the phonon reflectivity  $R$  in two solution methods.

Fig. 4 shows the variation of phonon reflectivity  $R$  versus the wave number  $k$  with  $\sigma = 5$ . In both cases shown,  $R$  approaches to zero in the long wave-length limit. As the wave number increases,  $R$  increases greatly, and is over 0.8 at the boundary of Brillouin zone in Solution Method 1, while it is less than 0.1 in all the Brillouin zone in Solution Method 2. Solution Method 1 obtains lower  $R$  than that in Rudd and Broughton (1998), and Abraham (2000), that means MLPG will be a better method for a seamless multiscale simulation than the finite element

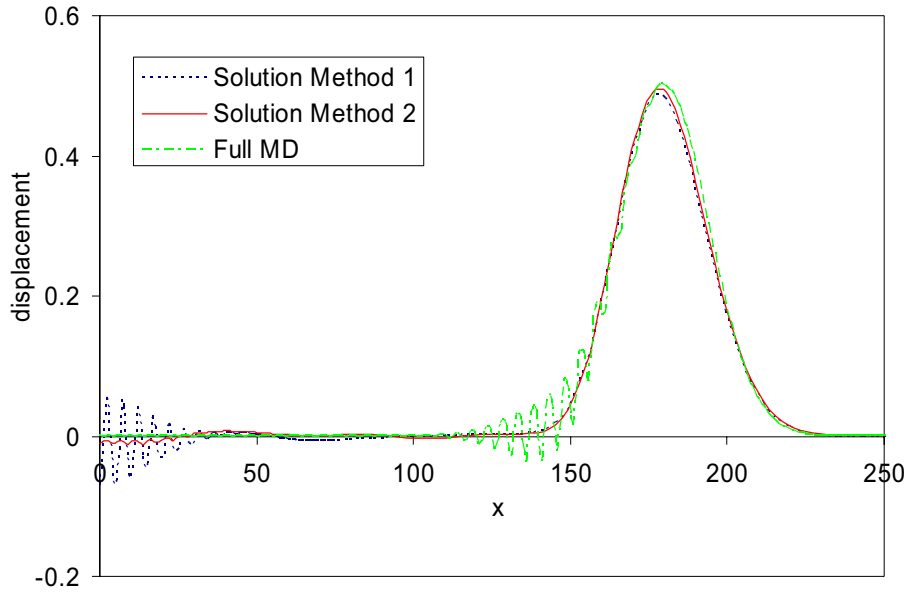


**Figure 5** : Comparison of the displacement profiles computed using the multiscale methods and the full MD, at  $t=18$ .

method. However, Solution Method 1 is much less effective than the Solution Method 2. Although lower  $R$  can be reached in the Solution Method 3 [Cai, et al. (2000)], due to its high computational cost, Solution Method 3 should not be an appropriate choice among the three solutions in most problems.

Another example is the same problem as in Wagner and Liu (2003). A short wave-length perturbation is multiplied to a Gaussian pulse. The resulting initial displacement is

$$u(X, t=0) = \frac{[\exp(-X^2/\sigma^2) - u_c]}{1 - u_c} [1 + 0.1\cos(kX)] \quad (88)$$

Here,  $u_c = \exp(-l^2/\sigma^2)$ ,  $l = 50$ ,  $\sigma = 20$ ,  $k = 0.4\pi$ . All the other parameters are same as in the first example. Fig. 5 shows the displacements obtained by Solution Methods 1 and 2, and full MD at  $t = 18$ . Because of the configurational symmetry about  $X = 0$ , only the right plane is plotted. An internal reflection of the short wave-length perturbation appears in Solution Method 1, which looks like the mirror image of the short wave-length perturbation in full MD with the mirror located on the interface of region A and B ( $X = 75$ ). In Solution Method 2, the short wave-length waves almost pass out of region A at the same time as the long wave-length Gaussian pulse prop-

agates into region B. In region B, both cases simulate the long wave-length Gaussian wave very well. Compared with the full MD solution, there is an apparent smoothing of the wave profile as the Gaussian pulse propagates in region B, due to the large node space.

To make sure that the mass-lumping procedure (55)-(56) are correct, we also used the consistent mass matrix in Solution Method 2 in this example. The results show that both the lumped and consistent mass work very well. A Comparison of the displacement profiles computed using the consistent and lumped mass in Solution Method 2, at  $t=18$  is plotted in Fig. 6. The initial displacement profile is also plotted in Fig. 6.

## 7.2 Two-dimensional graphene sheet

This multiscale method can be generalized to multiaxial problems. In this subsection, a planar problem is considered to demonstrate the method without loss of generality. The formulations can be extended to more complicated 3-D systems. The problem is of a graphene sheet of one-atom thickness.

In this example, the Tersoff-Brenner potential [Tersoff (1988), Brenner (1990)] is used for the energy associated with the deformation of the atoms. It is given as a sum

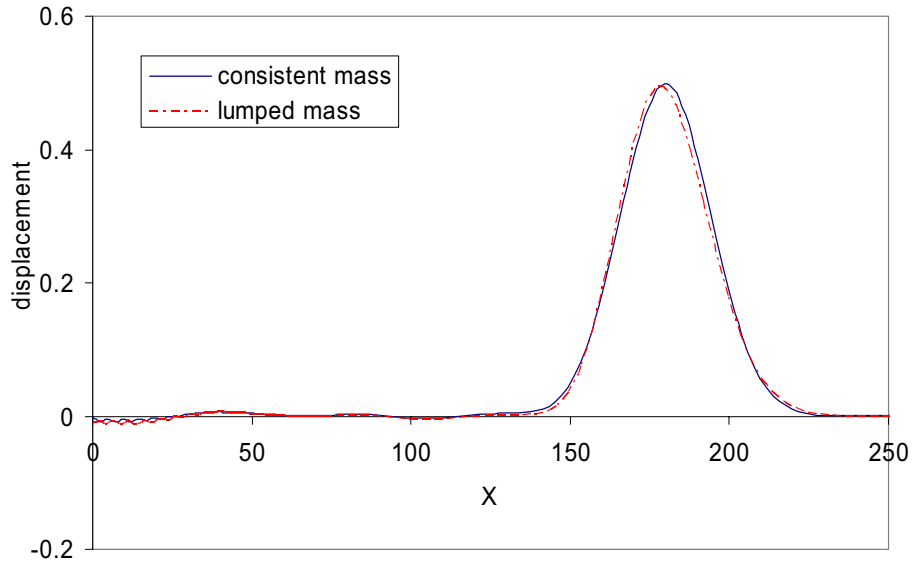


**Figure 6 :** Comparison of the displacement profiles computed using the consistent and lumped mass in Solution Method 2, at  $t=18$ , and the initial displacement profile.

over bonds as

$$\Pi = \sum_I \sum_{J(>I)} [V_R(r_{IJ}) - \bar{B}V_A(r_{IJ})] \quad (89)$$

where the constants for carbon are

$$V_R(r_{IJ}) = \frac{f_{IJ}(r)D^{(e)}}{(S-1)} e^{-\sqrt{2S}\beta(r-R^{(e)})} \quad (90)$$

$$V_A(r_{IJ}) = \frac{f_{IJ}(r)D^{(e)}S}{(S-1)} e^{-\sqrt{\frac{2}{S}}\beta(r-R^{(e)})} \quad (91)$$

with the functions of the bond angle

$$\bar{B} = \frac{1}{2}(B_{IJ} + B_{JI}) \quad (92)$$

$$B_{IJ} = \left[ 1 + \sum_{K(\neq I,J)} G(\theta_{IJK}) f_{IK}(r_{IK}) \right]^{-\delta} \quad (93)$$

$$G(\theta) = a_0 \left\{ 1 + \frac{c_0^2}{d_0^2} - \frac{c_0^2}{d_0^2 + (1 + \cos\theta)^2} \right\} \quad (94)$$

and the cut-off function which limits the rang of the interactions

$$f_{IJ}(r) = \begin{cases} 1, & r < R^{(1)} \\ \frac{1}{2} + \frac{1}{2} \cos \left[ \frac{\pi(r-R^{(1)})}{(R^{(2)}-R^{(1)})} \right], & R^{(1)} < r < R^{(2)} \\ 0, & r > R^{(2)} \end{cases}$$

$$\begin{aligned} R^{(e)} &= 1.39 \text{ \AA}, \quad D^{(e)} = 6.0 \text{ eV}, \quad S = 1.22, \\ \beta &= 2.1 \text{ \AA}^{-1}, \quad \delta = 0.5, \quad R^{(1)} = 1.7 \text{ \AA}, \quad R^{(2)} = 2.0 \text{ \AA}, \\ a_0 &= 2.0813 \times 10^{-4}, \quad c_0 = 330, \quad d_0 = 3.5 \end{aligned}$$

and the mass of the carbon atom is  $m_I = 12.01115 \times 1.65979 \times 10^{-27}$  kg, and  $1 \text{ eV} = 1.602 \times 10^{-19}$  J.

As discussed in section 3, in this method, the energy will be written in a form that is additively decomposed. Hence, equation (89) will be rewritten as sum over atomic site  $I$ ,

$$\Pi = \sum_{I=1} \Pi_I \quad (96)$$

where each contribution  $\Pi_I$  is written as

$$\Pi_I = \frac{1}{2} \sum_{J(\neq I)} [V_R(r_{IJ}) - B_{IJ}V_A(r_{IJ})] \quad (97)$$

Then, the stress in equation (53) can be written as

$$\begin{aligned} \frac{\partial W}{\partial \mathbf{F}} &= \frac{1}{\Delta \Omega_I} \frac{\partial \Pi_I}{\partial \mathbf{F}} \\ &= \frac{1}{2\Delta \Omega_I} \sum_{J(\neq I)} \left[ V'_R \frac{\partial r_{IJ}}{\partial \mathbf{r}_{IJ}} - V_A \frac{\partial B_{IJ}}{\partial \mathbf{r}_{IJ}} - B_{IJ} V'_A \frac{\partial r_{IJ}}{\partial \mathbf{r}_{IJ}} \right] \otimes \frac{\partial \mathbf{r}_{IJ}}{\partial \mathbf{F}} \\ &\quad + \frac{1}{2\Delta \Omega_I} \sum_{J(\neq I)} \left[ -V_A \frac{\partial B_{IJ}}{\partial \mathbf{r}_{IK}} \otimes \frac{\partial \mathbf{r}_{IK}}{\partial \mathbf{F}} \right] \end{aligned} \quad (98)$$

and the force on the atom  $I$  can be obtained as

$$\begin{aligned} \mathbf{f}_I &= -\frac{\partial \Pi}{\partial \mathbf{x}_I} = -\frac{\partial \Pi}{\partial \mathbf{q}_I} \\ &= \frac{1}{2} \sum_{J(\neq I)} \left[ -V'_R \frac{\partial r_{IJ}}{\partial \mathbf{r}_{IJ}} + V_A \frac{\partial \bar{B}_{IJ}}{\partial \mathbf{r}_{IJ}} + \bar{B}_{IJ} V'_A \frac{\partial r_{IJ}}{\partial \mathbf{r}_{IJ}} \right] \\ &\quad + \frac{1}{2} \sum_{J(\neq I)} \sum_{K(\neq I, J)} \left[ -V_A(r_{JK}) \frac{\partial B_{JK}}{\partial \mathbf{r}_{JI}} \right] \end{aligned} \quad (99)$$

The example is that of a 2D graphene sheet of one-atom thickness, with 452.2764 Å length, 68.1819 Å width, which has 11,552 atoms. The thickness of the sheet is taken to be 3.4 Å, which is the standard layer separation thickness for graphite. At the equilibrium state, which is taken to be the reference frame, the nearest neighbor bond length is  $b=1.4507$  Å. The sheet is fixed at left and right edges. Periodic boundary conditions in the direction parallel to the surface are imposed, thus the effects of the upper and lower surface are neglected. Initial displacements are introduced, according to the plane wave packet

$$\begin{aligned} u_1(X_1, X_2, t=0) &= \frac{[\exp(-X_1^2/\sigma^2) - u_c]}{1 - u_c} \left[ 1 + 0.1 \cos\left(\frac{kX_1}{a}\right) \right] \\ u_2(X_1, X_2, t=0) &= 0 \end{aligned} \quad (100)$$

where  $u_c = \exp(-l^2/\sigma^2)$ ,  $l = 40a$ ,  $\sigma = 15a$ ,  $a = \sqrt{3}b/2$ ,  $k = 0.5\pi$ . Here,  $X_1$  and  $X_2$  denote the positions of atoms in the reference frame, and  $u_1$  and  $u_2$  denote the displacement in the  $X_1$  and  $X_2$  direction, respectively. The center line of the sheet is  $X_1 = 0$ . Because of the configurational symmetry about  $X_1 = 0$ , only the right plane is considered in this numerical example. The computational domain is  $[0, 226.1382] \times [0, 68.1819]$ . The region A is  $[0, 74.1242] \times [0, 68.1819]$ ; this region contains

1920 atoms. The region B containing 5792 atoms, is discretized into a set of nodes. Two sets of nodes are used in this paper, the coarse one includes  $19 \times 10$  nodes, and the fine one includes  $38 \times 20$  nodes. Fig. 6 is a part of the distribution of the atoms and nodes in the reference frame for the coarse one. The nodes in the region B are distributed evenly, although it is unnecessary. However, on the interface of region A and B, the nodes are taken to be the atoms, as show in Fig. 7. Actually, these nodes are only used for the interpolation, their motions is still governed by atomic motion equation (57).

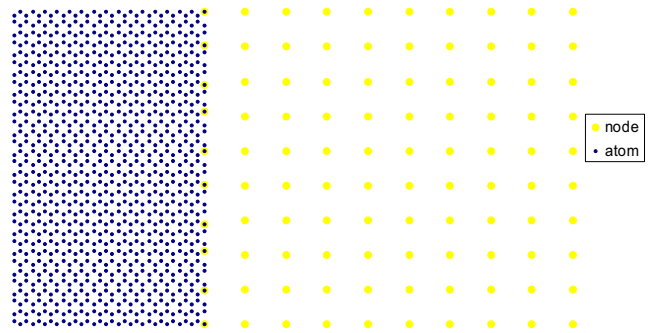
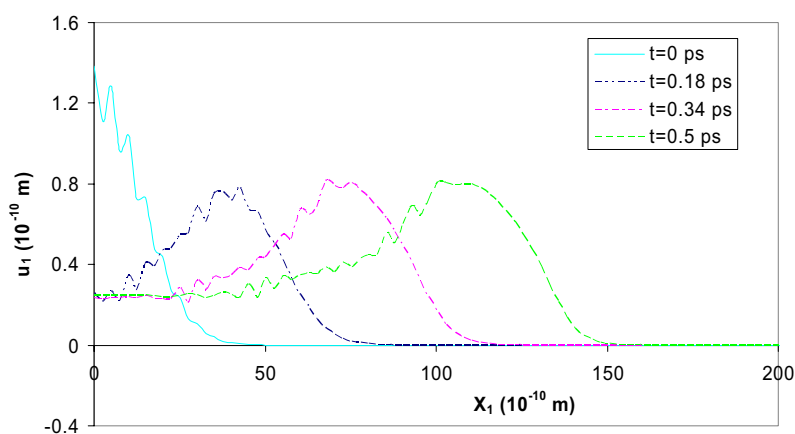


**Figure 7 :** The distribution of the atoms and nodes in the reference frame.

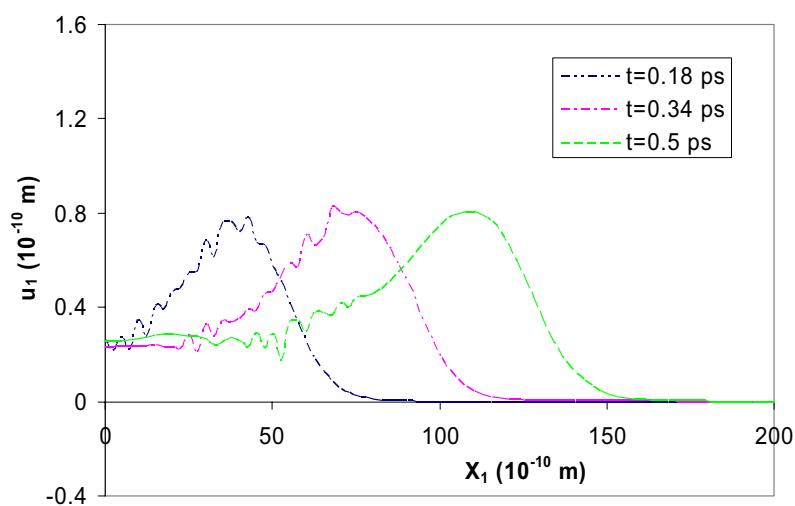
The computational setup described above is used to simulate the propagation of a plane wave packet (100). The equivalent continuum simulation in region B is advanced by a time step  $\Delta t_B = 5 \times 10^{-15}$ s, while the MD simulation in region A is advanced by  $\Delta t_A = \Delta t_B/10 = 5 \times 10^{-16}$ s. The radius of the trial function domain in Region B is taken to be  $4.2h$ , where  $h$  represents the distance between the nodes in region B, and the radius of the test domain is  $0.85h$ . The Solution Method 2, with the lumped mass matrix, is used to simulate the time evolution. A full MD simulation is also performed to verify our numerical results.

Fig. 8 shows the displacement profiles of  $u_1$  for the atoms along  $X_2=34.8168$  Å at different moments by using the full MD simulation. The displacement  $u_2$  should be 0 in this case. Fig. 9 and Fig. 10 are the corresponding displacement profiles obtained from the multiscale simulation by using the coarse and fine nodes, respectively.

Comparing Fig. 8 - Fig. 10, we can find that both coarse and fine cases can obtain good results. In Fig. 11, the comparison of the displacement profiles at  $t=0.5$  ps from



**Figure 8 :** The displacement profiles of  $u_1$  along  $X_2=34.8168$  Å at different moments (full MD)



**Figure 9 :** The displacement profiles of  $u_1$  along  $X_2=34.8168$  Å at different moments (Coarse)

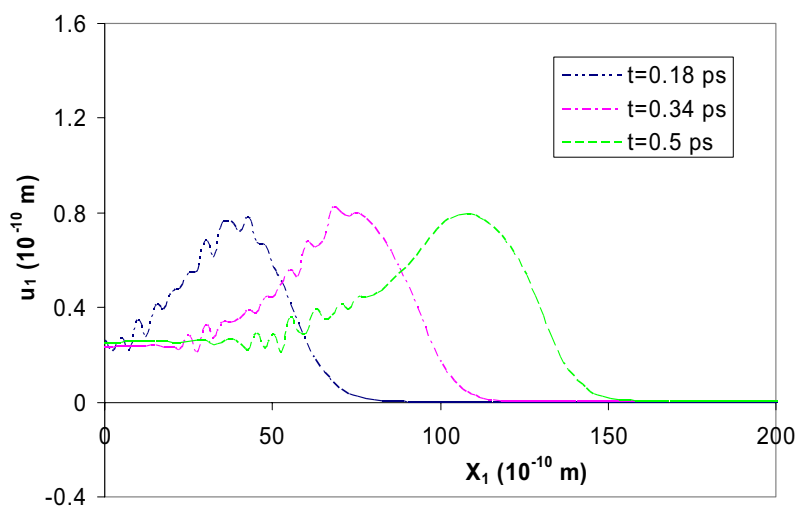


**Figure 10 :** The displacement profiles of  $u_1$  along  $X_2=34.8168$  Å at different moments (fine)

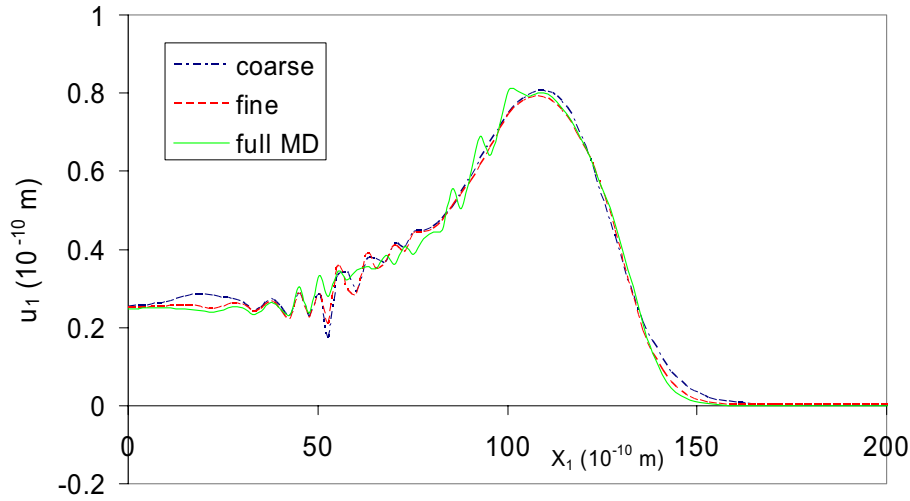


**Figure 11** : Comparison of the displacement profiles of  $u_1$  along  $X_2=34.8168 \text{ \AA}$ , computed using the multiscale methods and the full MD, at  $t=0.5 \text{ ps}$ .

these 3 figures, are plotted. Compared with the full MD solution, there is an apparent smoothing of the wave profile as the wave propagates in region B, due to the large node spacing. Certainly, the fine one can get better results than the coarse one. We also choose two atoms, one in region A with coordinates (61.5608, 34.8186), another in region B with coordinates (87.6876, 34.8186), to compare their trajectories. The results are plotted in Fig. 12. Obviously, in region B, we can only obtain the average displacements of the atoms, the fluctuation cannot be captured. Hence, the trajectory of the atom in region B is smoothed, but it does not lose the essential characteristics of the trajectory. Fig. 13 is the displacement profile of the right half sheet at  $t=0.5 \text{ ps}$ . The three coordinates in this figure are  $X_1$ ,  $X_2$ , and  $u_1$ , respectively. This result was obtained by using the coarse space resolution.

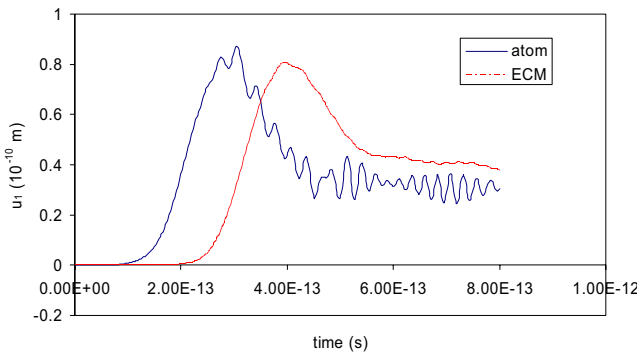


**Figure 12** : The trajectories of two atoms

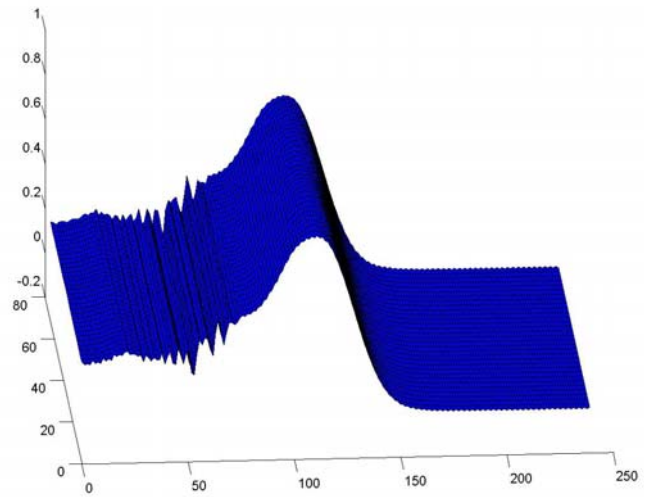


**Figure 13** : The displacement profiles of  $u_1$  at  $t=0.5 \text{ ps}$ .

## 8 Conclusion

A multiscale simulation technique, based on a combination of MD and MLPG methods has been implemented and tested. Multiple length scale, multiple time steps technique are used in the numerical examples. Good agreement of wave profile in MD and ECM parts is observed in the simulation. Three alternate interfacial conditions are derived, for the multiscale simulation, by considering the fluctuation of atoms in the continuum region. Solution Method 2, proposed in this paper, is found to

be optimal in both reducing the reflection of phonons and in lowering computational cost, especially when the atomistic region moves with time, which is the case that intrigues us. The MLPG method is also found to be very effective in seamless multiscale simulations. In this method, a wave can be transported from the MD region to the ECM region without losing the essential characteristics of the wave profile.

This multiscale simulation method allows one to balance the level of details necessary to provide reasonable accuracy in some regions of the model, with computational cost. The applications of this methodology will be many and varied. This method will play a key role in the simulation and design methodology for nanodevices.

**Acknowledgement:** This work was supported by the U. S. Army Research Office, and the U. S. Army Research Laboratory, under a cooperative research agreement with the University of California at Irvine. The Cognizant Program Official at the U. S. Army Research Labs is Dr. R. Namburu. Partial support for this work was also provided by the Office of Naval Research, in the program directed by Dr. Y.D.S. Rajapakse.

## References

- Abraham, F. F.** (2000): MAADLY spanning the length scales in dynamic fracture. *CMES: Computer Modeling in Engineering & Sciences* 1(4): 63-69
- Adelman, S. A.; Doll, J. D.** (1976): Generalized Langevin equation approach for atom-solid-surface scattering –general formulation for classical scattering off harmonic solids. *J. Chem. Phys.* 64: 2375-2388.
- Ajayan, P. M.; Zhou, O. Z.** (2001): “ Applications of Carbon Nanotubes”, in *Carbon Nanotubes*, Topics in Applied Physics; M.S. Dresselhaus, et al ( Eds); 80, 391-425, Springer
- Arroyo, M.; Belytschko, T.** (2002): An atomistic based finite deformation membrane for crystalline films one atom thick. *Journal of the Mechanics and Physics of Solids* 50(9): 1941-1977
- Atluri, S. N.** (1979): On rate principles for finite strain analysis of elastic and inelastic nonlinear solids. In *Recent Research on Mechanical Behavior*, 79-107, University of Tokyo Press.
- Atluri, S. N.** (1980): On some new general and complementary energy theorems for the rate problems in finite strain, classical elastoplasticity. *Journal of Structural Mechanics* 8(1): 61-92.
- Atluri, S. N.** (2004): *The meshless local Petrov-Galerkin (MLPG) method for domain and boundary discretization*. Tech. Science Press (in press).
- Atluri, S. N.; Zhu, T.** (1998): A new meshless local Petrov-Galerkin (MLPG) approach in computational mechanics. *Comput. Mech.* 22: 117-127.
- Atluri, S. N.; Shen, S.** (2002a): *The meshless local Petrov-Galerkin (MLPG) method*. Tech. Science Press, 440 pages.
- Atluri, S. N.; Shen, S.** (2002b): The meshless local Petrov-Galerkin (MLPG) method: A simple & less-costly alternative to the finite element and boundary element method. *CMES: Computer Modeling in Engineering & Sciences* 3(1): 11-52
- Atluri, S. N.; Shen, S.** (2004): The Basis of Meshless Domain Discretization: The Meshless Local Petrov Galerkin (MLPG) Method. *Advances in Computational Mathematics* (in press)
- Atluri, S. N.; Han, Z. D.; Shen, S.** (2003): Meshless Local Petrov-Galerkin (MLPG) approaches for weakly-singular traction & displacement boundary integral equations, *CMES: Computer Modeling in Engineering & Sciences* 4(5): 507-516.
- Batra, R. C.; Ching, H. K.** (2002): Analysis of elastodynamic deformations near a crack/notch tip by the meshless local Petrov-Galerkin (MLPG) method. *CMES: Computer Modeling in Engineering & Sciences* 3(6): 717-730.
- Belytschko, T.; Smolinski, P.; Liu, W. K.** (1985): Stability of multi-time step partitioned integrators for 1st-order finite-element systems. *Comput. Meth. Appl. Mech. Eng.* 49: 281-297.
- Belytschko, T.; Lu, Y. Y.** (1993): Explicit multi-time step integration for 1st and 2nd-order finite-element semidiscretizations. *Comput. Meth. Appl. Mech. Eng.* 108: 353-383.
- Belytschko, T.; Yen, H.; Mullen, R.** (1979): Mixed methods for time integration. *Comput. Meth. Appl. Mech. Eng.* 17-8: 258-275.
- Born, M.; Huang, K.** (1954): Dynamical theory of crystal lattices. Oxford: Clarendon Press.
- Brenner, D. W.** (1990): Empirical potential for hydrocarbons for use in simulating the chemical vapor deposi-

- tion of diamond films. *Phys. Rev. B* 42(15): 9458-9471.
- Cai, W.; de Koning, M.; Bulatov, V. V.; Yip, S.** (2000): Minimizing boundary reflections in coupled-domain simulations. *Phys. Rev. Lett.* 85: 3213-3216.
- Chung, P. W.; Namburu, R. R.; Henz, B. J.** (2004): A Lattice Statics Based Tangent Stiffness Finite Element Method, *CMES: Computer Modeling in Engineering & Sciences* 5(1): 45-62.
- Cousins, C. S. G.** (1978): Inner elasticity. *J. Phys. C: Solid State Phys.* 11: 4867-4879.
- E, W.; Huang, Z.** (2001): Matching conditions in atomistic-continuum modeling of materials. *Phys. Rev. Lett.* 87, art. No.-135501.
- Ericksen, J. L.** (1984): *Phase transformations and material instabilities in solids*. Academic Press: 61-77.
- Ghoniem, N. M.; Cho, K.** (2002): The emerging role of multiscale modeling in nano and micro-mechanics of materials. *CMES: Computer Modeling in Engineering & Sciences* 3(2): 147-173.
- Han, Z. D.; Atluri, S. N.** (2003): On Simple Formulations of Weakly-Singular Traction & Displacement BIE, and Their Solutions through Petrov-Galerkin Approaches. *CMES: Computer Modeling in Engineering & Sciences* 4(1): 5-20
- Hardy, R. L.** (1971): Multiquadric equations of topography and other irregular surfaces. *J. Geophys. Res.* 76: 1905-1915.
- Li, Q.; Shen, S.; Han, Z. D.; Atluri, S. N.** (2003): Application of Meshless Local Petrov-Galerkin (MLPG) to Problems with Singularities, and Material Discontinuities, in 3-D Elasticity, *CMES: Computer Modeling in Engineering & Sciences* 4(5): 567-581.
- Liu, G. R.; Gu, Y. T.** (2001): A local radial point interpolation method for free vibration analysis of 2D solids. *J. Sound Vibration* 246: 29-46.
- Martin, J. W.** (1975): Many-body forces in solids and the Brugger elastic constants: II. Inner elastic constants. *J. Phys. C: Solid State Phys.* 8: 2858-2868.
- Rudd, R. E.; Broughton, J. Q.** (1998): Coarse-grain molecular dynamics and the atomic limit of finite elements. *Phys. Rev. B* 58: R5893-R5896.
- Shen, S.; Atluri, S. N.** (2004): Computational nanomechanics and multiscale simulation. *CMC: Computers, Materials, & Continua* (in press)
- Shenoy, V. B.** (2003): Multiscale modeling strategies in materials science-the quasicontinuum method. *Bull. Mater. Sci.* 26(1): 53-62.
- Srivastava, D.; Menon, M.; Cho, K.** (2001): Computational nanotechnology with carbon nanotubes and fullerenes. *Computing in Science & Engineering* 3: 42-55.
- Srivastava, D.; Atluri, S. N.** (2002a): Computational Nanotechnology: A Current Perspective, *CMES: Computer Modeling in Engineering & Sciences* 3(5): 531-538
- Srivastava, D.; Atluri, S. N.** (2002b): Computational Nanotechnology, Special Issue, *CMES: Computer Modeling in Engineering & Sciences* 3(5).
- Tadmor, E. B.; Ortiz, M.; Phillips, R.** (1996): Quasi-continuum analysis of defects in solids. *Philosophical Magazine A* 73: 1529-1563.
- Tadmor, E. B.; Phillips, R.; Ortiz, M.** (1996): Mixed atomistic and continuum models of deformation in solids. *Langmuir* 12(19): 4529-4534.
- Tang, Z.; Shen, S.; Atluri, S. N.** (2003): **Analysis of materials** with strain gradient effects: A Meshless local Petrov-Galerkin approach, with nodal displacements only. *CMES: Computer Modeling in Engineering & Sciences* 4(1): 177-196.
- Tersoff, J.** (1988): Empirical interatomic potential for carbon, with applications to amorphous carbon. *Phys. Rev. Lett.* 61(25): 2879-2882.
- Tuckerman, M. E.; Berne, B. J.; Martyna, G. J.** (1991): Molecular dynamics algorithm for multiple time scales: systems with long range forces. *J. Chem. Phys.* 94(10): 6811-6815.
- Wagner, G. J.; Liu, W. K.** (2003): Coupling of Atomistic and continuum simulations using a bridging scale decomposition. *J. Comput. Phys.* 190: 249-274.
- Wendland, H.** (1999): Meshless Galerkin method using radial basis functions. *Math. Comput.* 68: 1521-1531.
- Zanzotto, G.** (1996): The Cauchy-Born Hypothesis, nonlinear elasticity and mechanical twinning in crystals. *Acta Cryst.* A52: 839-849.



# Modeling of Piezoelectric and Piezomagnetic Solids by the MLPG

J. Sladek<sup>1</sup>, V. Sladek<sup>1</sup>, P. Sölek<sup>2</sup> and S.N. Atluri<sup>3</sup>

<sup>1</sup>Institution of Construction and Architecture, Slovak Academy of Sciences, 84503  
Bratislava, Slovakia, sladek@savba.sk

<sup>2</sup> Department of Mechanics, Slovak Technical University, Bratislava, Slovakia

<sup>3</sup> Department of Mechanical and Aerospace Engineering, University of California, Irvine, USA

## Abstract:

A meshless method based on the local Petrov-Galerkin approach is proposed to solve 2-D and 3-D axisymmetric boundary value problems in piezoelectric and magneto-electric-elastic solids with continuously varying material properties. Axial symmetry of geometry and boundary conditions reduces the original 3-D boundary value problem into a 2-D problem in the axial cross section. Stationary and transient dynamic problems are considered in this paper. The mechanical fields are described by the equations of motion with an inertial term. To eliminate the time-dependence in the governing partial differential equations the Laplace-transform technique is applied to the governing equations, which are satisfied in the Laplace-transformed domain in a weak-form on small subdomains. Nodal points are spread on the analyzed domain and each node is surrounded by a small circle for simplicity. The spatial variation of the displacements and the electric potential are approximated by the Moving Least-Squares (MLS) scheme. After performing the spatial integrations, one obtains a system of linear algebraic equations for unknown nodal values. The boundary conditions on the global boundary are satisfied by the collocation of the MLS-approximation expressions for the displacements and the electric potential at the boundary nodal points. The Stehfest's inversion method is applied to obtain the final time-dependent solutions.

**Keyword:** Meshless local Petrov-Galerkin method (MLPG), Moving least-squares interpolation, piezoelectric and piezomagnetic solids, Laplace-transform, Stehfest's inversion

## 1. Introduction

Modern smart structures made of piezoelectric and piezomagnetic materials offer certain potential performance advantages over conventional ones due to their capability of converting the energy from one type to other (among magnetic, electric, and mechanical) [Avellaneda and G. Harshe (1994); Berlingcourt et al. (1964); Landau et al. (1984); Nan (1994)]. Former activities were focused on modeling piezoelectric problems [Tiersten (1969); Ha et al. (1992); Gaudenzi and Bathe (1995); Lee (1995); Chen and Lin (1995); Batra and Liang (1997); Ding and Liang (1999); Liew et al. (2002)]. Later, there are also some efforts to model magneto-electric-elastic fields [Alshits et al. (1992); Chung and Ting (1995); Pan (2001); Liu et al. (2001); Wang and Shen (2002)]. Recently, increasing interest is devoted to fracture mechanics of piezoelectric [Beom and Atluri (1996, 2002), Gruebner et al. (2003); Govorukha and Kamlah

(2004); Enderlein et al. (2005), Kuna (2006); Pan (1999); Gross et al. (2005); Garcia-Sanchez et al. (2005, 2007a); Saez et al. (2006); Sheng and Sze (2006)] and magneto-electric-elastic materials [Beom and Atluri (2003), Gao et al. (2003); Song and Sih (2003); Zhou et al. (2004); Hu et al. (2006); Wang et al. (2006); Tian and Gabbert (2005); Tian and Rajapakse, (2005); Garcia-Sanchez et al. (2007b); Wang and Mai (2007)]. Applications are mostly made under a static deformation assumption. Dynamic fracture analyses are occurring in literature very seldom. Also 3-D initial-boundary value analyses are occurring rarely. For homogeneous piezoelectric materials the axisymmetric free and forced vibrations of piezoceramic hollow spheres have been studied in [Loza and Shulga (1984, 1990)]. Analytical solution for stationary and transient dynamic load of a nonhomogeneous spherically isotropic piezoelectric hollow sphere is given by Chen et al. (2002) and Ding et al. (2003), respectively. The laminate model with radial dependence of physical fields is transformed to 1D problem. A piezoelectric solid under coupled thermal, mechanical and electrical loads have been studied [Tzou and Ye (1994); Gornandt and Gabbert (2002); Shang et al. (1996); Kuna (2006)]. Three-dimensional (3-D) penny-shaped crack problem in magneto-electro-elastic solids under a static load has been analyzed by Zhao et al. (2006). Recently, Feng et al. (2007) have investigated the transient response of a penny-shaped crack embedded in a magneto-electro-elastic layer of a finite thickness. Coupling of magneto-electro-thermo-elastic fields is investigated in works (Niraula and Wang, 2006; Zhu and T. Qin, 2007).

While the piezoelectric and piezomagnetic effects are due to electro-elastic and magneto-elastic interaction, respectively, the magnetoelectric effect is the induction of the electrical polarization by magnetic field and the induction of magnetization by electric field via electro-magneto-elastic interactions. Magnetoelectric coupling plays an important role in the dynamic behaviour of certain materials, especially compounds which possess simultaneously ferroelectric and ferromagnetic phases [Eringen and Maugin, (1990)]. The electric and magnetic symmetry groups for certain crystals permit the piezoelectric and piezomagnetic as well as magnetoelectric effects. In centrosymmetric crystals neither of these effects exists. However, remarkably large magnetoelectric effects are observed for composites than for either composite constituent [Nan, (1994); Feng and Su, (2006)]. If the volume fraction of constituents is varying in a predominant direction we are talking about functionally graded materials (FGMs). Originally these materials have been introduced to benefit from the ideal performance of its constituents, e.g. high heat and corrosion resistance of ceramics on one side, and large mechanical strength and toughness of metals on the other side. A review on various aspects of FGMs can be found in the monograph of Suresh and Mortensen (1998). Later, the demand for piezoelectric materials with high strength, high toughness, low thermal expansion coefficient and low dielectric constant encourages the study of functionally graded piezoelectric materials [Zhu et al. (1995); Han et al. (2006)]. According the best of authors' knowledge there is available only one paper [Feng and Su, (2006)] with applications to continuously nonhomogeneous magneto-electric materials.

The solution of general boundary value problems for continuously nonhomogeneous magneto-electric-elastic solids requires advanced numerical methods due to the high mathematical complexity. Besides this complication, the magnetic, electric and mechanical fields are coupled with each other in the constitutive equations. In spite of the great success of the finite element method (FEM) and boundary element method (BEM) as effective numerical tools for the solution of boundary value problems in mainly elastic solids, there is still a growing interest in the development of new advanced numerical methods. In recent years, meshless formulations are

becoming popular due to their high adaptability and low costs to prepare input and output data in numerical analysis. The moving least squares (MLS) approximation is generally considered as one of many schemes to interpolate discrete data with a reasonable accuracy. The continuity of the MLS approximation is given by the minimum between the continuity of the basis functions and that of the weight function. So continuity can be tuned to a desired value. In conventional discretization methods it is a discontinuity of secondary fields (gradients of primary fields) on the interface of elements. For modeling of continuously nonhomogeneous solids the approach based on piecewise continuous elements can bring some inaccuracies. Therefore, modeling based on  $C^1$  continuity, like meshless methods, is expected to be more accurate than conventional discretization techniques. The meshless or generalized FEM methods are also very convenient for modeling of cracks. One can embed particular enrichment functions at the crack tip so the stress intensity factor can be predicted accurately [Fleming et al, (1997)].

A variety of meshless methods has been proposed so far with some of them applied only to piezoelectric problems [Ohs and Aluru, (2001); Liu et al., (2002)]. They can be derived from a weak-form formulation either on the global domain or on a set of local subdomains. In the global formulation, background cells are required for the integration of the weak-form. In methods based on local weak-form formulation, no background cells are required and therefore they are often referred to as truly meshless methods. The meshless local Petrov-Galerkin (MLPG) method is a fundamental base for the derivation of many meshless formulations, since trial and test functions can be chosen from different functional spaces [Zhu et al. (1998); Atluri and Zhu(1998), Atluri et al. (2000); Atluri (2004); Sladek et al., (2000, 2001, 2003a,b); Sellountos and Polyzos (2003); Sellountos et al., (2005)]. Recently, the MLPG method with a Heaviside step function as the test functions [Atluri et al. (2003); Sladek et al., (2004, 2006a)] has been applied to solve two-dimensional (2-D) homogeneous and continuously nonhomogeneous piezoelectric solids [Sladek et al., (2006b, 2007a,b)]. In the present paper, the MLPG method is applied to 2-D continuously nonhomogeneous piezoelectric and magneto-electric-elastic solids. The coupled governing partial differential equations are satisfied in a weak form on small fictitious subdomains. Nodal points are introduced and spread on the analyzed domain and each node is surrounded by a small circle for simplicity, but without loss of shape generality. For a simple shape of subdomains like circles applied in this paper, numerical integrations over them can be easily carried out. The integral equations have a very simple nonsingular form. The spatial variations of the displacements and the electric potential are approximated by the moving least-squares scheme [Belytschko et al., (1996); Atluri, (2004)]. After performing the spatial integrations, a system of linear algebraic equations for the unknown nodal values is obtained.

## 2. Local integral equations for 2-D problems

Basic equations of phenomenological theory of nonconducting elastic materials consist of the governing equations (Maxwell's equations, the balance of momentum) and the constitutive relationships. An electro-elastic problem can be considered as a special case of a general magneto-electric-elastic problem. Therefore, further formulation is given for a general magneto-electric-elastic problem. The governing equations completed by the boundary and initial conditions should be solved for unknown primary field variables such as the elastic displacement vector field  $u_i(\mathbf{x}, \tau)$ , the electric potential  $\psi(\mathbf{x}, \tau)$  (or its gradient called the electric vector field  $E_i(\mathbf{x}, \tau)$ ), and the magnetic potential  $\mu(\mathbf{x}, \tau)$  (or its gradient called the magnetic intensity field

$H_i(\mathbf{x}, \tau)$ ). The constitutive equations co-relate the primary fields  $\{u_i, E_i, H_i\}$  with the secondary fields  $\{\sigma_{ij}, D_i, B_i\}$  which are the stress tensor field, the electric displacement vector field, and the magnetic induction vector field, respectively. The governing equations give not only the relationships between conjugated fields in each of the pairs  $(\sigma_{ij}, \varepsilon_{ij})$ ,  $(D_i, E_i)$ ,  $(B_i, H_i)$ , but describe also the electro-magneto-elastic interactions in the phenomenological theory of continuous solids.

Taking into account the typical material coefficients, it can be found that characteristic frequencies for elastic and electromagnetic processes are  $f_{el} = 10^4 \text{ Hz}$  and  $f_{elm} = 10^7 \text{ Hz}$ , respectively. Thus, if we consider such bodies under transient loadings with temporal changes corresponding to  $f_{el}$ , the changes of the electromagnetic fields can be assumed to be immediate, or in other words the electromagnetic fields can be considered like quasi-static [Parton and Kudryavtsev, (1988)]. Then, the Maxwell equations are reduced to two scalar equations

$$D_{j,j}(\mathbf{x}, \tau) = 0, \quad (1)$$

$$B_{j,j}(\mathbf{x}, \tau) = 0, \quad (2)$$

The rest vector Maxwell's equations in quasi-static approximation,  $\nabla \times \mathbf{E} = 0$  and  $\nabla \times \mathbf{H} = 0$ , are satisfied identically by appropriate representation of the fields  $\mathbf{E}(\mathbf{x}, \tau)$  and  $\mathbf{H}(\mathbf{x}, \tau)$  as gradients of scalar electric and magnetic potentials  $\psi(\mathbf{x}, \tau)$  and  $\mu(\mathbf{x}, \tau)$ , respectively,

$$E_j(\mathbf{x}, \tau) = -\psi_{,j}(\mathbf{x}, \tau), \quad (3)$$

$$H_j(\mathbf{x}, \tau) = -\mu_{,j}(\mathbf{x}, \tau). \quad (4)$$

To complete the set of governing equations, eqs. (1) and (2) need to be supplied by the equation of motion in elastic continuum

$$\sigma_{ij,j}(\mathbf{x}, \tau) + X_i(\mathbf{x}, \tau) = \rho \ddot{u}_i(\mathbf{x}, \tau), \quad (5)$$

where  $\ddot{u}_i$ ,  $\rho$  and  $X_i$  denote the acceleration of displacements, the mass density, and the body force vector, respectively. A comma after a quantity represents the partial derivatives of the quantity and a dot is used for the time derivative.

Finally, we extend the constitutive equations involving the general electro-magneto-elastic interaction [Nan, (1994)] to media with spatially dependent material coefficients for continuously non-homogeneous media

$$\sigma_{ij}(\mathbf{x}, \tau) = c_{ijkl}(\mathbf{x}) \varepsilon_{kl}(\mathbf{x}, \tau) - e_{kij}(\mathbf{x}) E_k(\mathbf{x}, \tau) - d_{kij}(\mathbf{x}) H_k(\mathbf{x}, \tau), \quad (6)$$

$$D_j(\mathbf{x}, \tau) = e_{jkl}(\mathbf{x}) \varepsilon_{kl}(\mathbf{x}, \tau) + h_{jk}(\mathbf{x}) E_k(\mathbf{x}, \tau) + \alpha_{jk}(\mathbf{x}) H_k(\mathbf{x}, \tau), \quad (7)$$

$$B_j(\mathbf{x}, \tau) = d_{jkl}(\mathbf{x}) \varepsilon_{kl}(\mathbf{x}, \tau) + \alpha_{kj}(\mathbf{x}) E_k(\mathbf{x}, \tau) + \gamma_{jk}(\mathbf{x}) H_k(\mathbf{x}, \tau), \quad (8)$$

with the strain tensor  $\varepsilon_{ij}$  being related to the displacements  $u_i$  by

$$\varepsilon_{ij} = \frac{1}{2}(u_{i,j} + u_{j,i}). \quad (9)$$

The functional coefficients  $c_{ijkl}(\mathbf{x})$ ,  $h_{jk}(\mathbf{x})$ , and  $\gamma_{jk}(\mathbf{x})$  are the elastic coefficients, dielectric permittivities, and magnetic permeabilities, respectively;  $e_{kij}(\mathbf{x})$ ,  $d_{kij}(\mathbf{x})$ , and  $\alpha_{jk}(\mathbf{x})$  are the piezoelectric, piezomagnetic, and magnetoelectric coefficients, respectively. Owing to transient loadings, inertial effects and coupling, the elastic fields as well as electromagnetic fields are time dependent, though the fields  $E_i$  and  $H_i$  are treated in quasi-static approximation.

In case of some crystal symmetries, one can formulate also the plane-deformation problems [Parton and Kudryavtsev, (1988)]. For instance, in the crystals of hexagonal symmetry with  $x_3$  being the 6-order symmetry axis and assuming  $u_2 = 0$  as well as the independence on  $x_2$ , i.e.  $\square_{,2} = 0$ , we have  $\varepsilon_{22} = \varepsilon_{23} = \varepsilon_{12} = E_2 = H_2 = 0$ . Then, the constitutive equations (6) - (8) are reduced to the following form

$$\begin{aligned} \begin{bmatrix} \sigma_{11} \\ \sigma_{33} \\ \sigma_{13} \end{bmatrix} &= \begin{bmatrix} c_{11} & c_{13} & 0 \\ c_{13} & c_{33} & 0 \\ 0 & 0 & c_{44} \end{bmatrix} \begin{bmatrix} \varepsilon_{11} \\ \varepsilon_{33} \\ 2\varepsilon_{13} \end{bmatrix} - \begin{bmatrix} 0 & e_{31} \\ 0 & e_{33} \\ e_{15} & 0 \end{bmatrix} \begin{bmatrix} E_1 \\ E_3 \end{bmatrix} - \begin{bmatrix} 0 & d_{31} \\ 0 & d_{33} \\ d_{15} & 0 \end{bmatrix} \begin{bmatrix} H_1 \\ H_3 \end{bmatrix} = \\ &= \mathbf{C}(\mathbf{x}) \begin{bmatrix} \varepsilon_{11} \\ \varepsilon_{33} \\ 2\varepsilon_{13} \end{bmatrix} - \mathbf{L}(\mathbf{x}) \begin{bmatrix} E_1 \\ E_3 \end{bmatrix} - \mathbf{K}(\mathbf{x}) \begin{bmatrix} H_1 \\ H_3 \end{bmatrix}, \end{aligned} \quad (10)$$

$$\begin{aligned} \begin{bmatrix} D_1 \\ D_3 \end{bmatrix} &= \begin{bmatrix} 0 & 0 & e_{15} \\ e_{31} & e_{33} & 0 \end{bmatrix} \begin{bmatrix} \varepsilon_{11} \\ \varepsilon_{33} \\ 2\varepsilon_{13} \end{bmatrix} + \begin{bmatrix} h_{11} & 0 \\ 0 & h_{33} \end{bmatrix} \begin{bmatrix} E_1 \\ E_3 \end{bmatrix} + \begin{bmatrix} \alpha_{11} & 0 \\ 0 & \alpha_{33} \end{bmatrix} \begin{bmatrix} H_1 \\ H_3 \end{bmatrix} = \\ &= \mathbf{G}(\mathbf{x}) \begin{bmatrix} \varepsilon_{11} \\ \varepsilon_{33} \\ 2\varepsilon_{13} \end{bmatrix} + \mathbf{H}(\mathbf{x}) \begin{bmatrix} E_1 \\ E_3 \end{bmatrix} + \mathbf{A}(\mathbf{x}) \begin{bmatrix} H_1 \\ H_3 \end{bmatrix}, \end{aligned} \quad (11)$$

$$\begin{aligned} \begin{bmatrix} B_1 \\ B_3 \end{bmatrix} &= \begin{bmatrix} 0 & 0 & d_{15} \\ d_{31} & d_{33} & 0 \end{bmatrix} \begin{bmatrix} \varepsilon_{11} \\ \varepsilon_{33} \\ 2\varepsilon_{13} \end{bmatrix} + \begin{bmatrix} \alpha_{11} & 0 \\ 0 & \alpha_{33} \end{bmatrix} \begin{bmatrix} E_1 \\ E_3 \end{bmatrix} + \begin{bmatrix} \gamma_{11} & 0 \\ 0 & \gamma_{33} \end{bmatrix} \begin{bmatrix} H_1 \\ H_3 \end{bmatrix} = \\ &= \mathbf{R}(\mathbf{x}) \begin{bmatrix} \varepsilon_{11} \\ \varepsilon_{33} \\ 2\varepsilon_{13} \end{bmatrix} + \mathbf{A}(\mathbf{x}) \begin{bmatrix} E_1 \\ E_3 \end{bmatrix} + \mathbf{M}(\mathbf{x}) \begin{bmatrix} H_1 \\ H_3 \end{bmatrix}, \end{aligned} \quad (12)$$

Recall that  $\sigma_{22}$  does not influence the governing equations, although it is not vanishing in general, since  $\sigma_{22} = c_{12}\varepsilon_{12} + c_{13}\varepsilon_{33} - e_{13}E_3$ .

The following essential and natural boundary conditions are assumed for the mechanical field

$$\begin{aligned} u_i(\mathbf{x}, \tau) &= \tilde{u}_i(\mathbf{x}, \tau), & \text{on } \Gamma_u, \\ t_i(\mathbf{x}, \tau) &= \sigma_{ij} n_j = \tilde{t}_i(\mathbf{x}, \tau), & \text{on } \Gamma_t, \quad \Gamma = \Gamma_u \cup \Gamma_t. \end{aligned}$$

For the electrical field, we assume

$$\begin{aligned} \psi(\mathbf{x}, \tau) &= \tilde{\psi}(\mathbf{x}, \tau), & \text{on } \Gamma_p, \\ n_i(\mathbf{x}) D_i(\mathbf{x}, \tau) &\equiv Q(\mathbf{x}, \tau) = \tilde{Q}(\mathbf{x}, \tau), & \text{on } \Gamma_q, \quad \Gamma = \Gamma_p \cup \Gamma_q \end{aligned}$$

and for the magnetic field

$$\begin{aligned} \mu(\mathbf{x}, \tau) &= \tilde{\mu}(\mathbf{x}, \tau), & \text{on } \Gamma_a, \\ n_i(\mathbf{x}) B_i(\mathbf{x}, \tau) &\equiv S(\mathbf{x}, \tau) = \tilde{S}(\mathbf{x}, \tau), & \text{on } \Gamma_b, \quad \Gamma = \Gamma_a \cup \Gamma_b \end{aligned}$$

where  $\Gamma_u$  is the part of the global boundary  $\Gamma$  with prescribed displacements, while on  $\Gamma_t$ ,  $\Gamma_p$ ,  $\Gamma_q$ ,  $\Gamma_a$ , and  $\Gamma_b$  the traction vector, the electric potential, the normal component of the electric displacement vector, the magnetic potential and the magnetic flux are prescribed, respectively. Recall that  $\tilde{Q}(\mathbf{x}, \tau)$  can be considered approximately as the surface density of free charge, provided that the permittivity of the solid is much greater than that of the surrounding medium (vacuum).

The initial conditions for the mechanical displacements are assumed as

$$u_i(\mathbf{x}, \tau)|_{\tau=0} = u_i(\mathbf{x}, 0) \text{ and } \dot{u}_i(\mathbf{x}, \tau)|_{\tau=0} = \dot{u}_i(\mathbf{x}, 0) \text{ in } \Omega.$$

The Laplace transform technique is applied to eliminate the time variable in the differential equation. Applying to the governing equations (5) one obtains

$$\bar{\sigma}_{ij,j}(\mathbf{x}, p) - \rho(\mathbf{x}) p^2 \bar{u}_i(\mathbf{x}, p) = -\bar{F}_i(\mathbf{x}, p), \quad (13)$$

where  $p$  is the Laplace-transform parameter and

$$\bar{F}_i(\mathbf{x}, p) = \bar{X}_i(\mathbf{x}, p) + p u_i(\mathbf{x}, 0) + \dot{u}_i(\mathbf{x}, 0)$$

is the re-defined body force in the Laplace-transformed domain with the initial boundary conditions for the displacements  $u_i(\mathbf{x}, 0)$  and velocities  $\dot{u}_i(\mathbf{x}, 0)$ . Recall that the subscripts take now values  $i \in \{1, 3\}$ .

Instead of writing the global weak-form for the above governing equations, the MLPG method constructs a weak-form over the local fictitious subdomains such as  $\Omega_s$ , which is a small region constructed for each node inside the global domain [Atluri, (2004)]. The local subdomains overlap each other, and cover the whole global domain  $\Omega$ . The local subdomains could be of any geometrical shape and size. In the present paper, the local subdomains are taken to be of a circular shape for simplicity. The local weak-form of the governing equation (13) can be written as

$$\int_{\Omega_s} \left[ \bar{\sigma}_{ij,j}(\mathbf{x}, p) - \rho(\mathbf{x}) p^2 \bar{u}_i(\mathbf{x}, p) + \bar{F}_i(\mathbf{x}, p) \right] u_{ik}^*(\mathbf{x}) d\Omega = 0, \quad (14)$$

where  $u_{ik}^*(\mathbf{x})$  is a test function.

Applying the Gauss divergence theorem to eq. (14) one obtains

$$\int_{\partial\Omega_s} \bar{\sigma}_{ij}(\mathbf{x}, p) n_j(\mathbf{x}) u_{ik}^*(\mathbf{x}) d\Gamma - \int_{\Omega_s} \bar{\sigma}_{ij}(\mathbf{x}, p) u_{ik,j}^*(\mathbf{x}) d\Omega + \int_{\Omega_s} [\bar{F}_i(\mathbf{x}, p) - \rho(\mathbf{x}) p^2 \bar{u}_i(\mathbf{x}, p)] u_{ik}^*(\mathbf{x}) d\Omega = 0, \quad (15)$$

where  $\partial\Omega_s$  is the boundary of the local subdomain which consists of three parts  $\partial\Omega_s = L_s \cup \Gamma_{st} \cup \Gamma_{su}$  [Atluri, (2004)]. Here,  $L_s$  is the local boundary that is totally inside the global domain,  $\Gamma_{st}$  is the part of the local boundary which coincides with the global traction boundary, i.e.,  $\Gamma_{st} = \partial\Omega_s \cap \Gamma_t$ , and similarly  $\Gamma_{su}$  is the part of the local boundary that coincides with the global displacement boundary, i.e.,  $\Gamma_{su} = \partial\Omega_s \cap \Gamma_u$ .

By choosing a Heaviside step function as the test function  $u_{ik}^*(\mathbf{x})$  in each subdomain as

$$u_{ik}^*(\mathbf{x}) = \begin{cases} \delta_{ik} & \text{at } \mathbf{x} \in \Omega_s \\ 0 & \text{at } \mathbf{x} \notin \Omega_s \end{cases},$$

the local weak-form (15) is converted into the following local boundary-domain integral equations

$$\int_{L_s + \Gamma_{su}} \bar{t}_i(\mathbf{x}, p) d\Gamma - \int_{\Omega_s} \rho(\mathbf{x}) p^2 \bar{u}_i(\mathbf{x}, p) d\Omega = - \int_{\Gamma_{st}} \tilde{t}_i(\mathbf{x}, p) d\Gamma - \int_{\Omega_s} \bar{F}_i(\mathbf{x}, p) d\Omega. \quad (16)$$

Equation (16) is recognized as the overall force equilibrium conditions on the subdomain  $\Omega_s$ .

Note that the local integral equation (16) is valid for both the homogeneous and nonhomogeneous solids. Nonhomogeneous material properties are included in eq. (16) through the elastic, piezoelectric and piezomagnetic coefficients in the traction components.

Similarly, the local weak-form of the governing equation (2) can be written as

$$\int_{\Omega_s} \bar{D}_{j,j}(\mathbf{x}, p) v^*(\mathbf{x}) d\Omega = 0, \quad (17)$$

where  $v^*(\mathbf{x})$  is a test function.

Applying the Gauss divergence theorem to the local weak-form (17) and choosing the Heaviside step function as the test function  $v^*(\mathbf{x})$  one can obtain

$$\int_{L_s + \Gamma_{sp}} \bar{Q}(\mathbf{x}, p) d\Gamma = - \int_{\Gamma_{sq}} \tilde{Q}(\mathbf{x}, p) d\Gamma, \quad (18)$$

where

$$\bar{Q}(\mathbf{x}, p) = \bar{D}_j(\mathbf{x}, p) n_j(\mathbf{x}) = [e_{jkl} \bar{u}_{k,l}(\mathbf{x}, p) - h_{jk} \bar{\psi}_{,k}(\mathbf{x}, p) - \alpha_{jk} \bar{\mu}_{,k}(\mathbf{x}, p)] n_j.$$

The local integral equation corresponding to the third governing equation (3) has the form

$$\int_{L_s + \Gamma_{sa}} \bar{S}(\mathbf{x}, p) d\Gamma = - \int_{\Gamma_{sb}} \tilde{S}(\mathbf{x}, p) d\Gamma, \quad (19)$$

where magnetic flux is given by

$$\bar{S}(\mathbf{x}, p) = \bar{B}_j(\mathbf{x}, p) n_j(\mathbf{x}) = \left[ d_{jkl} \bar{u}_{k,l}(\mathbf{x}, p) - \alpha_{kj} \psi_{,k}(\mathbf{x}, p) - \gamma_{jk} \mu_{,k}(\mathbf{x}, p) \right] n_j.$$

In the MLPG method the test and the trial functions are not necessarily from the same functional spaces. For internal nodes, the test function is chosen as a unit step function with its support on the local subdomain. The trial functions, on the other hand, are chosen to be the MLS approximations by using a number of nodes spreading over the domain of influence. According to the MLS [Belytschko et al., (1996)] method, the approximation of the displacement can be given as

$$\mathbf{u}^h(\mathbf{x}) = \sum_{i=1}^m p_i(\mathbf{x}) a_i(\mathbf{x}) = \mathbf{p}^T(\mathbf{x}) \mathbf{a}(\mathbf{x}),$$

where  $\mathbf{p}^T(\mathbf{x}) = \{p_1(\mathbf{x}), p_2(\mathbf{x}), \dots, p_m(\mathbf{x})\}$  is a vector of complete basis functions of order  $m$  and  $\mathbf{a}(\mathbf{x}) = \{a_1(\mathbf{x}), a_2(\mathbf{x}), \dots, a_m(\mathbf{x})\}$  is a vector of unknown parameters that depend on  $\mathbf{x}$ . For example, in 2-D problems

$$\mathbf{p}^T(\mathbf{x}) = \{1, x_1, x_2\} \text{ for } m=3$$

and

$$\mathbf{p}^T(\mathbf{x}) = \{1, x_1, x_2, x_1^2, x_1 x_2, x_2^2\} \text{ for } m=6$$

are linear and quadratic basis functions, respectively. The basis functions are not required to be polynomials. It is convenient to introduce  $r^{-1/2}$  singularity for secondary fields at the crack tip vicinity for modelling of fracture problems [Fleming et al., (1997)]. Then, the basis functions can be considered in the following form

$$\mathbf{p}^T(\mathbf{x}) = \{1, x_1, x_2, \sqrt{r} \cos(\theta/2), \sqrt{r} \sin(\theta/2), \sqrt{r} \sin(\theta/2) \sin \theta, \sqrt{r} \cos(\theta/2) \sin \theta\} \text{ for } m=7$$

where  $r$  and  $\theta$  are polar coordinates with the crack tip as the origin.

The approximated functions for the Laplace transforms of the mechanical displacements, the electric and magnetic potentials can be written as [Atluri, (2004)]

$$\bar{\mathbf{u}}^h(\mathbf{x}, p) = \mathbf{u}^T(\mathbf{x}) \cdot \sum_{a=1}^n \phi^a(\mathbf{x}) \hat{\mathbf{u}}^a(p),$$

$$\bar{\psi}^h(\mathbf{x}, p) = \sum_{a=1}^n \phi^a(\mathbf{x}) \hat{\psi}^a(p),$$

$$\bar{\mu}^h(\mathbf{x}, p) = \sum_{a=1}^n \phi^a(\mathbf{x}) \hat{\mu}^a(p), \quad (20)$$

where the nodal values  $\hat{\mathbf{u}}^a(p) = (\hat{u}_1^a(p), \hat{u}_3^a(p))^T$ ,  $\hat{\psi}^a(p)$  and  $\hat{\mu}^a(p)$  are fictitious parameters for the Laplace transforms of the displacements, the electric and magnetic potentials, respectively, and  $\phi^a(\mathbf{x})$  is the shape function associated with the node  $a$ . The number of nodes  $n$  used for the approximation is determined by the weight function  $w^a(\mathbf{x})$ . A 4<sup>th</sup> order spline-type weight function is applied in the present work

$$w^a(\mathbf{x}) = \begin{cases} 1 - 6\left(\frac{d^a}{r^a}\right)^2 + 8\left(\frac{d^a}{r^a}\right)^3 - 3\left(\frac{d^a}{r^a}\right)^4, & 0 \leq d^a \leq r^a \\ 0, & d^a \geq r^a \end{cases}, \quad (21)$$

where  $d^a = \|\mathbf{x} - \mathbf{x}^a\|$  and  $r^a$  is the size of the support domain. It is seen that the  $C^1$ -continuity is ensured over the entire domain, and therefore the continuity conditions of the tractions, the electric charge and the magnetic flux are satisfied.

The Laplace transform of traction vectors  $\bar{t}_i(\mathbf{x}, p)$  at a boundary point  $\mathbf{x} \in \partial\Omega_s$  are approximated in terms of the same nodal values  $\hat{\mathbf{u}}^a(p)$  as

$$\bar{\mathbf{t}}^h(\mathbf{x}, p) = \mathbf{N}(\mathbf{x})\mathbf{C}(\mathbf{x}) \sum_{a=1}^n \mathbf{B}^a(\mathbf{x}) \hat{\mathbf{u}}^a(p) + \mathbf{N}(\mathbf{x})\mathbf{L}(\mathbf{x}) \sum_{a=1}^n \mathbf{P}^a(\mathbf{x}) \hat{\psi}^a(p) + \mathbf{N}(\mathbf{x})\mathbf{K}(\mathbf{x}) \sum_{a=1}^n \mathbf{P}^a(\mathbf{x}) \hat{\mu}^a(p), \quad (22)$$

where the matrices  $\mathbf{C}(\mathbf{x})$ ,  $\mathbf{L}(\mathbf{x})$ , and  $\mathbf{K}(\mathbf{x})$  are defined in eq. (10), the matrix  $\mathbf{N}(\mathbf{x})$  is related to the normal vector  $\mathbf{n}(\mathbf{x})$  on  $\partial\Omega_s$  by

$$\mathbf{N}(\mathbf{x}) = \begin{bmatrix} n_1 & 0 & n_3 \\ 0 & n_3 & n_1 \end{bmatrix}$$

and finally, the matrices  $\mathbf{B}^a$  and  $\mathbf{P}^a$  are represented by the gradients of the shape functions as

$$\mathbf{B}^a(\mathbf{x}) = \begin{bmatrix} \phi_{,1}^a & 0 \\ 0 & \phi_{,3}^a \\ \phi_{,3}^a & \phi_{,1}^a \end{bmatrix}, \quad \mathbf{P}^a(\mathbf{x}) = \begin{bmatrix} \phi_{,1}^a \\ \phi_{,3}^a \end{bmatrix}.$$

Similarly the Laplace-transform of the normal component of the electric displacement vector  $\bar{Q}(\mathbf{x}, p)$  can be approximated by

$$\bar{Q}^h(\mathbf{x}, p) = \mathbf{N}_1(\mathbf{x})\mathbf{G}(\mathbf{x}) \sum_{a=1}^n \mathbf{B}^a(\mathbf{x}) \hat{\mathbf{u}}^a(p) - \mathbf{N}_1(\mathbf{x})\mathbf{H}(\mathbf{x}) \sum_{a=1}^n \mathbf{P}^a(\mathbf{x}) \hat{\psi}^a(p) - \mathbf{N}_1(\mathbf{x})\mathbf{A}(\mathbf{x}) \sum_{a=1}^n \mathbf{P}^a(\mathbf{x}) \hat{\mu}^a(p), \quad (23)$$

where the matrices  $\mathbf{G}(\mathbf{x})$ ,  $\mathbf{H}(\mathbf{x})$ , and  $\mathbf{A}(\mathbf{x})$  are defined in eq. (11) and

$$\mathbf{N}_1(\mathbf{x}) = \begin{bmatrix} n_1 & n_3 \end{bmatrix}.$$

Eventually, the Laplace-transform of the magnetic flux  $\bar{S}(\mathbf{x}, p)$  is approximated by

$$\bar{S}^h(\mathbf{x}, p) = \mathbf{N}_1(\mathbf{x})\mathbf{R}(\mathbf{x}) \sum_{a=1}^n \mathbf{B}^a(\mathbf{x}) \hat{\mathbf{u}}^a(p) - \mathbf{N}_1(\mathbf{x})\mathbf{A}(\mathbf{x}) \sum_{a=1}^n \mathbf{P}^a(\mathbf{x}) \hat{\psi}^a(p) - \mathbf{N}_1(\mathbf{x})\mathbf{M}(\mathbf{x}) \sum_{a=1}^n \mathbf{P}^a(\mathbf{x}) \hat{\mu}^a(p), \quad (24)$$

with the matrices  $\mathbf{R}(\mathbf{x})$  and  $\mathbf{M}(\mathbf{x})$  being defined in eq. (12).

Obeying the essential boundary conditions and making use of the approximation formula (20), one obtains the discretized form of these boundary conditions as

$$\begin{aligned}\sum_{a=1}^n \phi^a(\zeta) \hat{\mathbf{u}}^a(p) &= \tilde{\mathbf{u}}(\zeta, p) \quad \text{for } \zeta \in \Gamma_u, \\ \sum_{a=1}^n \phi^a(\zeta) \hat{\psi}^a(p) &= \tilde{\psi}(\zeta, p) \quad \text{for } \zeta \in \Gamma_p, \\ \sum_{a=1}^n \phi^a(\zeta) \hat{\mu}^a &= \tilde{\mu}(\zeta, p) \quad \text{for } \zeta \in \Gamma_a.\end{aligned}\tag{25}$$

Furthermore, in view of the MLS-approximation (22) - (24) for the unknown quantities in the local boundary-domain integral equations (16), (18) and (19), we obtain their discretized forms as

$$\begin{aligned}\sum_{a=1}^n \left( \int_{L_s + \Gamma_{st}} \mathbf{N}(\mathbf{x}) \mathbf{C}(\mathbf{x}) \mathbf{B}^a(\mathbf{x}) d\Gamma - \mathbf{I} p^2 \int_{\Omega_s} \phi^a(\mathbf{x}) d\Omega \right) \hat{\mathbf{u}}^a(p) &+ \sum_{a=1}^n \left( \int_{L_s + \Gamma_{sq}} \mathbf{N}(\mathbf{x}) \mathbf{L}(\mathbf{x}) \mathbf{P}^a(\mathbf{x}) d\Gamma \right) \hat{\mathbf{u}}^a(p) + \\ &+ \sum_{a=1}^n \left( \int_{L_s + \Gamma_{sb}} \mathbf{N}(\mathbf{x}) \mathbf{K}(\mathbf{x}) \mathbf{P}^a(\mathbf{x}) d\Gamma \right) \hat{\mathbf{u}}^a(p) = - \int_{\Gamma_{st}} \tilde{\mathbf{F}}(\mathbf{x}, p) d\Gamma - \int_{\Omega_s} \tilde{\mathbf{f}}(\mathbf{x}, p) d\Omega,\end{aligned}\tag{26}$$

$$\begin{aligned}\sum_{a=1}^n \left( \int_{L_s + \Gamma_{sp}} \mathbf{N}_1(\mathbf{x}) \mathbf{G}(\mathbf{x}) \mathbf{B}^a(\mathbf{x}) d\Gamma \right) \hat{\mathbf{u}}^a(p) &- \sum_{a=1}^n \left( \int_{L_s + \Gamma_{sp}} \mathbf{N}_1(\mathbf{x}) \mathbf{H}(\mathbf{x}) \mathbf{P}^a(\mathbf{x}) d\Gamma \right) \hat{\mathbf{u}}^a(p) - \\ &- \sum_{a=1}^n \left( \int_{L_s + \Gamma_{sp}} \mathbf{N}_1(\mathbf{x}) \mathbf{A}(\mathbf{x}) \mathbf{P}^a(\mathbf{x}) d\Gamma \right) \hat{\mathbf{u}}^a(p) = - \int_{\Gamma_{sq}} \tilde{\mathbf{Q}}(\mathbf{x}, p) d\Gamma,\end{aligned}\tag{27}$$

$$\begin{aligned}\sum_{a=1}^n \left( \int_{L_s + \Gamma_{sp}} \mathbf{N}_1(\mathbf{x}) \mathbf{R}(\mathbf{x}) \mathbf{B}^a(\mathbf{x}) d\Gamma \right) \hat{\mathbf{u}}^a(p) &- \sum_{a=1}^n \left( \int_{L_s + \Gamma_{sp}} \mathbf{N}_1(\mathbf{x}) \mathbf{A}(\mathbf{x}) \mathbf{P}^a(\mathbf{x}) d\Gamma \right) \hat{\mathbf{u}}^a(p) - \\ &- \sum_{a=1}^n \left( \int_{L_s + \Gamma_{sp}} \mathbf{N}_1(\mathbf{x}) \mathbf{M}(\mathbf{x}) \mathbf{P}^a(\mathbf{x}) d\Gamma \right) \hat{\mathbf{u}}^a(p) = - \int_{\Gamma_{sq}} \tilde{\mathbf{S}}(\mathbf{x}, p) d\Gamma,\end{aligned}\tag{28}$$

which are considered on the sub-domains adjacent to the interior nodes as well as to the boundary nodes on  $\Gamma_{st}$ ,  $\Gamma_{sq}$  and  $\Gamma_{sb}$ . In equation (26),  $\mathbf{I}$  is a unit matrix defined by

$$\mathbf{I} = \begin{pmatrix} 1 & 0 \\ 0 & 1 \end{pmatrix}.$$

Collecting the discretized local boundary-domain integral equations together with the discretized boundary conditions for the displacements, the electrical and magnetic potentials results in the complete system of linear algebraic equations for computation of the nodal unknowns, namely, the Laplace-transforms of the fictitious parameters  $\hat{\mathbf{u}}^a(p)$ ,  $\hat{\psi}^a(p)$  and  $\hat{\mu}^a(p)$ . The time

dependent values of the transformed quantities can be obtained by an inverse Laplace-transform. In the present analysis, the Stehfest's inversion algorithm [Stehfest, (1970)] is used. If  $\bar{f}(p)$  is the Laplace-transform of  $f(t)$ , an approximate value  $f_a$  of  $f(t)$  for a specific time  $t$  is given by

$$f_a(t) = \frac{\ln 2}{t} \sum_{i=1}^N v_i \bar{f}\left(\frac{\ln 2}{t} i\right), \quad (29)$$

where

$$v_i = (-1)^{N/2+i} \sum_{k=\lceil (i+1)/2 \rceil}^{\min(i, N/2)} \frac{k^{N/2} (2k)!}{(N/2 - k)! k! (k-1)! (i-k)! (2k-i)!}. \quad (30)$$

In numerical analyses, we have considered  $N = 10$  for double precision arithmetic. It means that for each time  $t$  we need to solve  $N$  boundary value problems for the corresponding Laplace-transform parameters  $p_i = i \ln 2 / t$ , with  $i = 1, 2, \dots, N$ . If  $M$  denotes the number of the time instants in which we are interested to know  $f(t)$ , the number of the Laplace-transform solutions  $\bar{f}(p_i)$  is then  $M \times N$ . It should be noted that the present computational method can be easily reformulated into the real time formulation as it was shown recently for 3-D axisymmetric piezoelectric problems in functionally graded materials [Sladek et al., (2008)].

### 3. Local integral equations for 3-D axisymmetric problems

Let us consider a 3-D axisymmetric magneto-electro-elastic body generated by the rotation of the planar domain  $\Omega$  bounded by the boundary  $\Gamma$  around the axis of symmetry as depicted in Fig.1. Let us consider solids with hexagonal symmetry and the z-axis being oriented in the poling direction. Moreover, we assume the body to be transversely isotropic, i.e. the additional symmetry is the rotational symmetry with respect to the z-axis. For axisymmetric problems it is convenient to use cylindrical coordinates  $\mathbf{x} \equiv (r, \varphi, z)$ . Owing to the hexagonal symmetry, the tensors of material coefficients are the same as in the previous section and their cylindrical components can be identified with the Cartesian ones by equating the indices as  $(r, \varphi, z) = (1, 2, 3)$  in the axial plane  $(x_1, x_3) = (r, z)$ . Furthermore, the angular component of the displacements vanishes and all physical field quantities are independent on the angular coordinate  $\varphi$  because of the axial symmetry. Thus, in the cylindrical coordinates also with the representation of tensors being with respect to the cylindrical unit basis vectors, the nonzero strains are given as

$$\varepsilon_{rr} = u_{r,r}, \quad \varepsilon_{\varphi\varphi} = u_r / r, \quad \varepsilon_{rz} = (u_{r,z} + u_{z,r}) / 2, \quad \varepsilon_{zz} = u_{z,z},$$

and the nonzero electrical and magnetic fields are  $E_a = -\psi_{,a}$ ,  $H_a = -\mu_{,a}$  with  $a \in \{r, z\}$ .

Thus, selecting the considered planar domain  $\Omega$  in the axial plane  $(x_1, x_3) = (r, z)$ , we can apply the constitutive equations valid for crystals exhibiting hexagonal to nonzero components of the fields  $\{\varepsilon_{ab}, E_a, H_a\}$  (Parton and Kudryavtsev, 1988). Then bearing in mind  $c_{22} = c_{11}$ ,  $c_{23} = c_{13}$ , etc, we have

$$\begin{aligned}
\begin{pmatrix} \sigma_{rr} \\ \sigma_{\varphi\varphi} \\ \sigma_{zz} \\ \sigma_{rz} \end{pmatrix} &= \begin{bmatrix} c_{11} & c_{12} & c_{13} & 0 \\ c_{12} & c_{11} & c_{13} & 0 \\ c_{13} & c_{13} & c_{33} & 0 \\ 0 & 0 & 0 & c_{44} \end{bmatrix} \begin{pmatrix} u_{r,r} \\ u_r/r \\ u_{z,z} \\ u_{r,z} + u_{z,r} \end{pmatrix} - \begin{bmatrix} 0 & e_{31} \\ 0 & e_{31} \\ 0 & e_{33} \\ e_{15} & 0 \end{bmatrix} \begin{pmatrix} E_r \\ E_z \end{pmatrix} - \begin{bmatrix} 0 & d_{31} \\ 0 & d_{31} \\ 0 & d_{33} \\ d_{15} & 0 \end{bmatrix} \begin{pmatrix} H_r \\ H_z \end{pmatrix}, \\
\begin{pmatrix} D_r \\ D_z \end{pmatrix} &= \begin{bmatrix} 0 & 0 & 0 & e_{15} \\ e_{31} & e_{31} & e_{33} & 0 \end{bmatrix} \begin{pmatrix} u_{r,r} \\ u_r/r \\ u_{z,z} \\ u_{r,z} + u_{z,r} \end{pmatrix} + \begin{bmatrix} h_{11} & 0 \\ 0 & h_{33} \end{bmatrix} \begin{pmatrix} E_r \\ E_z \end{pmatrix} + \begin{bmatrix} \alpha_{11} & 0 \\ 0 & \alpha_{33} \end{bmatrix} \begin{pmatrix} H_r \\ H_z \end{pmatrix}, \\
\begin{pmatrix} B_r \\ B_z \end{pmatrix} &= \begin{bmatrix} 0 & 0 & 0 & d_{15} \\ d_{31} & d_{31} & d_{33} & 0 \end{bmatrix} \begin{pmatrix} u_{r,r} \\ u_r/r \\ u_{z,z} \\ u_{r,z} + u_{z,r} \end{pmatrix} + \begin{bmatrix} \alpha_{11} & 0 \\ 0 & \alpha_{33} \end{bmatrix} \begin{pmatrix} E_r \\ E_z \end{pmatrix} + \begin{bmatrix} \gamma_{11} & 0 \\ 0 & \gamma_{33} \end{bmatrix} \begin{pmatrix} H_r \\ H_z \end{pmatrix}. \tag{31}
\end{aligned}$$

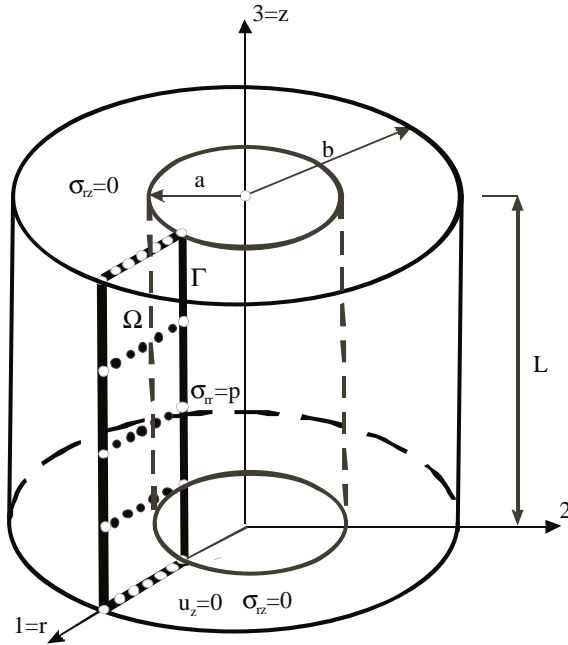


Fig. 1 A 3-D axisymmetric body

In the cylindrical coordinate system, the governing equations (1), (2) and (5) take the form

$$\begin{aligned}
\sigma_{rr,r}(r,z,\tau) + \sigma_{rz,z}(r,z,\tau) + \frac{1}{r} [\sigma_{rr}(r,z,\tau) - \sigma_{\varphi\varphi}(r,z,\tau)] - \rho(\mathbf{x}) \ddot{u}_r(r,z,\tau) &= -X_r(r,z,\tau), \\
\sigma_{rz,r}(r,z,\tau) + \sigma_{zz,z}(r,z,\tau) + \frac{1}{r} \sigma_{rz}(r,z,\tau) - \rho(\mathbf{x}) \ddot{u}_z(r,z,\tau) &= -X_z(r,z,\tau), \\
D_{r,r}(r,z,\tau) + D_{z,z}(r,z,\tau) + \frac{1}{r} D_r(r,z,\tau) &= 0,
\end{aligned}$$

$$B_{r,r}(r, z, \tau) + B_{z,z}(r, z, \tau) + \frac{1}{r} B_r(r, z, \tau) = 0, \quad (32)$$

Note that  $c_{12} \neq c_{11}$  (and consequently  $\sigma_{rr} - \sigma_{\varphi\varphi} \neq 0$ ) even in the case of the axial symmetry. The opposite has been assumed implicitly in eqs. (3.28) and (3.29) of the book (Parton and Kudryavtsev, 1988).

In the present analysis, all material parameters in the constitutive equations (31) are considered to be dependent on the  $(r, z)$ -coordinates.

Applying the Laplace transform to the first two eqs. in (32), we get

$$\begin{aligned} \bar{\sigma}_{rr,r}(r, z, p) + \bar{\sigma}_{rz,z}(r, z, p) + \frac{1}{r} [\bar{\sigma}_{rr}(r, z, p) - \bar{\sigma}_{\varphi\varphi}(r, z, p)] - \rho(\mathbf{x}) p^2 \bar{u}_r(r, z, p) &= -\bar{F}_r(r, z, p), \\ \bar{\sigma}_{rz,r}(r, z, p) + \bar{\sigma}_{zz,z}(r, z, p) + \frac{1}{r} \bar{\sigma}_{rz}(r, z, p) - \rho(\mathbf{x}) p^2 \bar{u}_z(r, z, p) &= -\bar{F}_z(r, z, p). \end{aligned} \quad (33)$$

Recall that the third and fourth eqs. in (32) remain unchanged by the Laplace transformation, i.e.

$$\begin{aligned} \bar{D}_{r,r}(r, z, p) + \bar{D}_{z,z}(r, z, p) + \frac{1}{r} \bar{D}_r(r, z, p) &= 0, \\ \bar{B}_{r,r}(r, z, p) + \bar{B}_{z,z}(r, z, p) + \frac{1}{r} \bar{B}_r(r, z, p) &= 0. \end{aligned} \quad (34)$$

In numerical solution, we apply again the MLPG method to construct the weak form over local subdomains such as  $\Omega_s$ , which is a small region taken for each node inside the global domain (Atluri, 2004). The local subdomains overlap each other, and cover the whole global domain  $\Omega$ . The local subdomains could be of any geometric shape and size. In the present paper, the local subdomains are taken to be of circular shape. The local weak forms of the governing equations (33) and (34) can be written as

$$\begin{aligned} \int_{\Omega_s} (\bar{\sigma}_{rr,r} + \bar{\sigma}_{rz,z}) u^* d\Omega + \int_{\Omega_s} \frac{1}{r} (\bar{\sigma}_{rr} - \bar{\sigma}_{\varphi\varphi}) u^* d\Omega - \int_{\Omega_s} \rho(\mathbf{x}) p^2 \bar{u}_r(r, z, p) u^* d\Omega &= - \int_{\Omega_s} \bar{F}_r(r, z, p) u^* d\Omega, \\ \int_{\Omega_s} (\bar{\sigma}_{rz,r} + \bar{\sigma}_{zz,z}) v^* d\Omega + \int_{\Omega_s} \frac{1}{r} \bar{\sigma}_{rz}(r, z, p) v^* d\Omega - \int_{\Omega_s} \rho(\mathbf{x}) p^2 \bar{u}_z(r, z, p) v^* d\Omega &= - \int_{\Omega_s} \bar{F}_z(r, z, p) v^* d\Omega, \\ \int_{\Omega_s} (\bar{D}_{r,r} + \bar{D}_{z,z}) m^* d\Omega + \int_{\Omega_s} \frac{1}{r} \bar{D}_r(r, z, p) m^* d\Omega &= 0, \\ \int_{\Omega_s} (\bar{B}_{r,r} + \bar{B}_{z,z}) \beta^* d\Omega + \int_{\Omega_s} \frac{1}{r} \bar{B}_r(r, z, p) \beta^* d\Omega &= 0, \end{aligned} \quad (35)$$

where  $u^*(\mathbf{x})$ ,  $v^*(\mathbf{x})$ ,  $m^*(\mathbf{x})$  and  $\beta^*(\mathbf{x})$  are test functions.

Applying the Gauss divergence theorem to the first domain integrals of eqs. (35) and selecting Heaviside unit step functions as test functions  $u^*(\mathbf{x})$ ,  $v^*(\mathbf{x})$ ,  $m^*(\mathbf{x})$  and  $\beta^*(\mathbf{x})$  in each subdomain, one can recast equations into the following forms

$$\begin{aligned}
& \int_{\partial\Omega_s} \bar{\sigma}_{rb}(r, z, p) n_b d\Gamma + \int_{\Omega_s} \frac{1}{r} (\bar{\sigma}_{rr} - \bar{\sigma}_{\varphi\varphi}) d\Omega - \int_{\Omega_s} \rho(\mathbf{x}) p^2 \bar{u}_r(r, z, p) d\Omega = - \int_{\Omega_s} \bar{F}_r(r, z, p) d\Omega, \\
& \int_{\partial\Omega_s} \bar{\sigma}_{zb}(r, z, p) n_b d\Gamma + \int_{\Omega_s} \frac{1}{r} \bar{\sigma}_{rz}(r, z, p) d\Omega - \int_{\Omega_s} \rho(\mathbf{x}) p^2 \bar{u}_z(r, z, p) d\Omega = - \int_{\Omega_s} \bar{F}_z(r, z, p) d\Omega, \\
& \int_{\partial\Omega_s} \bar{D}_b(r, z, p) n_b d\Gamma + \int_{\Omega_s} \frac{1}{r} \bar{D}_r(r, z, p) d\Omega = 0, \\
& \int_{\partial\Omega_s} \bar{B}_b(r, z, p) n_b d\Gamma + \int_{\Omega_s} \frac{1}{r} \bar{B}_r(r, z, p) d\Omega = 0,
\end{aligned} \tag{36}$$

where the subscript  $b$  in eqs. (36) is considered as a summation index with  $b = r, z$ .

As in 2-D problems the displacement and the potential fields are approximated by the MLS approximation. Substituting the approximation formula (20) into the local integral equations (36) a system of linear algebraic equations for the unknown fictitious parameters  $\{\hat{u}_r^a, \hat{u}_z^a, \hat{\psi}^a, \hat{\mu}^a\}$  is obtained as

$$\begin{aligned}
& \sum_{a=1}^n \hat{u}_r^a(p) \left\{ \int_{\partial\Omega_s} \left[ c_{11}(\mathbf{x}) n_r(\mathbf{x}) \phi_{,r}^a(\mathbf{x}) + \frac{c_{12}(\mathbf{x})}{r} n_r(\mathbf{x}) \phi^a(\mathbf{x}) + c_{44}(\mathbf{x}) n_z(\mathbf{x}) \phi_{,z}^a(\mathbf{x}) \right] d\Gamma + \right. \\
& \left. + \int_{\Omega_s} \left[ \frac{1}{r} (c_{11}(\mathbf{x}) - c_{12}(\mathbf{x})) \left( \phi_{,r}^a(\mathbf{x}) - \frac{1}{r} \phi^a(\mathbf{x}) \right) - \rho(\mathbf{x}) p^2 \phi^a(\mathbf{x}) \right] d\Omega \right\} + \\
& + \sum_{a=1}^n \hat{u}_z^a(p) \int_{\partial\Omega_s} (c_{13}(\mathbf{x}) n_r(\mathbf{x}) \phi_{,z}^a(\mathbf{x}) + c_{44}(\mathbf{x}) n_z(\mathbf{x}) \phi_{,r}^a(\mathbf{x})) d\Gamma + \\
& + \sum_{a=1}^n \hat{\psi}^a(p) \int_{\partial\Omega_s} (e_{31}(\mathbf{x}) n_r(\mathbf{x}) \phi_{,z}^a(\mathbf{x}) + e_{15}(\mathbf{x}) n_z(\mathbf{x}) \phi_{,r}^a(\mathbf{x})) d\Gamma + \\
& + \sum_{a=1}^n \hat{\mu}^a(p) \int_{\partial\Omega_s} (d_{31}(\mathbf{x}) n_r(\mathbf{x}) \phi_{,z}^a(\mathbf{x}) + d_{15}(\mathbf{x}) n_z(\mathbf{x}) \phi_{,r}^a(\mathbf{x})) d\Gamma = - \int_{\Omega_s} \bar{F}_r(r, z, p) d\Omega,
\end{aligned} \tag{37}$$

$$\begin{aligned}
& \sum_{a=1}^n \hat{u}_z^a(p) \left\{ \int_{\partial\Omega_s} [c_{33}(\mathbf{x}) n_z(\mathbf{x}) \phi_{,z}^a(\mathbf{x}) + c_{44}(\mathbf{x}) n_r(\mathbf{x}) \phi_{,r}^a(\mathbf{x})] d\Gamma + \int_{\Omega_s} \left[ \frac{c_{44}(\mathbf{x})}{r} \phi_{,r}^a(\mathbf{x}) - \rho(\mathbf{x}) p^2 \phi^a(\mathbf{x}) \right] d\Omega \right\} + \\
& + \sum_{a=1}^n \hat{u}_r^a(p) \left\{ \int_{\partial\Omega_s} \left( c_{44}(\mathbf{x}) n_r(\mathbf{x}) \phi_{,z}^a(\mathbf{x}) + c_{13}(\mathbf{x}) n_z(\mathbf{x}) \left( \phi_{,r}^a(\mathbf{x}) + \frac{1}{r} \phi^a(\mathbf{x}) \right) \right) d\Gamma + \int_{\Omega_s} \frac{c_{44}(\mathbf{x})}{r} \phi_{,z}^a(\mathbf{x}) d\Omega \right\} +
\end{aligned}$$

$$\begin{aligned}
& + \sum_{a=1}^n \hat{\psi}^a(p) \left\{ \int_{\partial\Omega_s} (e_{15}(\mathbf{x})n_r(\mathbf{x})\phi_{,r}^a(\mathbf{x}) + e_{33}(\mathbf{x})n_z(\mathbf{x})\phi_{,z}^a(\mathbf{x})) d\Gamma + \int_{\Omega_s} \frac{1}{r} e_{15}(\mathbf{x})\phi_{,r}^a(\mathbf{x}) d\Omega \right\} + \\
& + \sum_{a=1}^n \hat{\mu}^a(p) \left\{ \int_{\partial\Omega_s} (d_{15}(\mathbf{x})n_r(\mathbf{x})\phi_{,r}^a(\mathbf{x}) + d_{33}(\mathbf{x})n_z(\mathbf{x})\phi_{,z}^a(\mathbf{x})) d\Gamma + \int_{\Omega_s} \frac{1}{r} d_{15}(\mathbf{x})\phi_{,r}^a(\mathbf{x}) d\Omega \right\} = \\
& = - \int_{\Omega_s} \bar{F}_z(r, z, p) d\Omega, \tag{38}
\end{aligned}$$

$$\begin{aligned}
& \sum_{a=1}^n \hat{u}_r^a(p) \left\{ \int_{\partial\Omega_s} \left[ e_{15}(\mathbf{x})n_r(\mathbf{x})\phi_{,z}^a(\mathbf{x}) + e_{31}(\mathbf{x})n_z(\mathbf{x}) \left( \phi_{,r}^a(\mathbf{x}) + \frac{1}{r} \phi^a(\mathbf{x}) \right) \right] d\Gamma + \int_{\Omega_s} \frac{1}{r} e_{15}(\mathbf{x})\phi_{,z}^a d\Omega \right\} + \\
& + \sum_{a=1}^n \hat{u}_z^a(p) \left\{ \int_{\partial\Omega_s} [e_{15}(\mathbf{x})n_r(\mathbf{x})\phi_{,r}^a(\mathbf{x}) + e_{33}(\mathbf{x})n_z(\mathbf{x})\phi_{,z}^a(\mathbf{x})] d\Gamma + \int_{\Omega_s} \frac{1}{r} e_{15}(\mathbf{x})\phi_{,r}^a(\mathbf{x}) d\Omega \right\} - \\
& - \sum_{a=1}^n \hat{\psi}^a(p) \left\{ \int_{\partial\Omega_s} (h_{11}(\mathbf{x})n_r(\mathbf{x})\phi_{,r}^a(\mathbf{x}) + h_{33}(\mathbf{x})n_z(\mathbf{x})\phi_{,z}^a(\mathbf{x})) d\Gamma + \int_{\Omega_s} \frac{1}{r} h_{11}(\mathbf{x})\phi_{,r}^a(\mathbf{x}) d\Omega \right\} - \\
& - \sum_{a=1}^n \hat{\mu}^a(p) \left\{ \int_{\partial\Omega_s} (\alpha_{11}(\mathbf{x})n_r(\mathbf{x})\phi_{,r}^a(\mathbf{x}) + \alpha_{33}(\mathbf{x})n_z(\mathbf{x})\phi_{,z}^a(\mathbf{x})) d\Gamma + \int_{\Omega_s} \frac{1}{r} \alpha_{11}(\mathbf{x})\phi_{,r}^a(\mathbf{x}) d\Omega \right\} = 0, \tag{39}
\end{aligned}$$

$$\begin{aligned}
& \sum_{a=1}^n \hat{u}_r^a(p) \left\{ \int_{\partial\Omega_s} \left[ d_{15}(\mathbf{x})n_r(\mathbf{x})\phi_{,z}^a(\mathbf{x}) + d_{31}(\mathbf{x})n_z(\mathbf{x}) \left( \phi_{,r}^a(\mathbf{x}) + \frac{1}{r} \phi^a(\mathbf{x}) \right) \right] d\Gamma + \int_{\Omega_s} \frac{1}{r} d_{15}(\mathbf{x})\phi_{,z}^a d\Omega \right\} + \\
& + \sum_{a=1}^n \hat{u}_z^a(p) \left\{ \int_{\partial\Omega_s} [d_{15}(\mathbf{x})n_r(\mathbf{x})\phi_{,r}^a(\mathbf{x}) + d_{33}(\mathbf{x})n_z(\mathbf{x})\phi_{,z}^a(\mathbf{x})] d\Gamma + \int_{\Omega_s} \frac{1}{r} d_{15}(\mathbf{x})\phi_{,r}^a(\mathbf{x}) d\Omega \right\} - \\
& - \sum_{a=1}^n \hat{\psi}^a(p) \left\{ \int_{\partial\Omega_s} (\alpha_{11}(\mathbf{x})n_r(\mathbf{x})\phi_{,r}^a(\mathbf{x}) + \alpha_{33}(\mathbf{x})n_z(\mathbf{x})\phi_{,z}^a(\mathbf{x})) d\Gamma + \int_{\Omega_s} \frac{1}{r} \alpha_{11}(\mathbf{x})\phi_{,r}^a(\mathbf{x}) d\Omega \right\} - \\
& - \sum_{a=1}^n \hat{\mu}^a(p) \left\{ \int_{\partial\Omega_s} (\gamma_{11}(\mathbf{x})n_r(\mathbf{x})\phi_{,r}^a(\mathbf{x}) + \gamma_{33}(\mathbf{x})n_z(\mathbf{x})\phi_{,z}^a(\mathbf{x})) d\Gamma + \int_{\Omega_s} \frac{1}{r} \gamma_{11}(\mathbf{x})\phi_{,r}^a(\mathbf{x}) d\Omega \right\} = 0, \tag{40}
\end{aligned}$$

Equations (37)-(40) are considered in the subdomains  $\Omega_s$  around each interior node  $\mathbf{x}^s$  and at boundary nodes with prescribed natural boundary conditions ( $\Gamma_t$ ,  $\Gamma_q$  and  $\Gamma_b$ ). On the parts of the global boundary  $\Gamma_u$  with prescribed elastic displacements,  $\Gamma_p$  with prescribed electric

potentials and  $\Gamma_a$  with prescribed magnetic potential the collocation equations are applied like in 2-D problem.

## 4 Numerical examples

### 4.1 Cantilever beam

In this section, numerical results for the bending of a square piezoelectric panel are presented to illustrate the accuracy of the proposed method. The square panel with a size  $a \times a = 1\text{mm} \times 1\text{mm}$  made of a PZT-4 material is subjected to a pure bending moment arising from a linearly varying stress at the right boundary (Fig. 1). The lower boundary of the panel is earthed and vanishing electrical potential is assumed on this side of panel. The other boundaries have prescribed vanishing electrical charge.

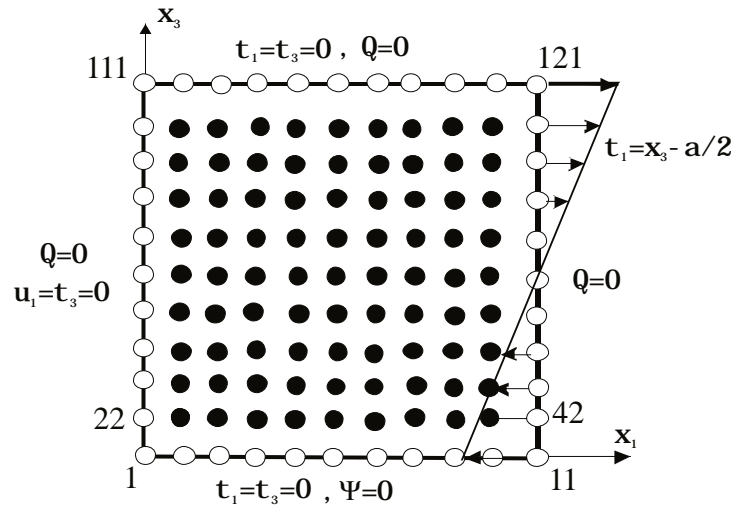


**Fig. 2** Bending of a square piezoelectric panel

The material coefficients corresponding to PZT-4 material are following

$$c_{11} = 13.9 \cdot 10^{10} \text{ Nm}^{-2}, \quad c_{13} = 7.43 \cdot 10^{10} \text{ Nm}^{-2}, \quad c_{33} = 11.3 \cdot 10^{10} \text{ Nm}^{-2}, \quad c_{44} = 2.56 \cdot 10^{10} \text{ Nm}^{-2},$$

$$e_{15} = 13.44 \text{ Cm}^{-2}, \quad e_{31} = -6.98 \text{ Cm}^{-2}, \quad e_{33} = 13.84 \text{ Cm}^{-2},$$

$$h_{11} = 6.0 \cdot 10^{-9} \text{ C(Vm)}^{-1}, \quad h_{33} = 5.47 \cdot 10^{-9} \text{ C(Vm)}^{-1}.$$

The mechanical displacement and the electrical potential fields on the finite square panel are approximated by using 121 (11x11) nodes equidistantly distributed. The local subdomains are considered to be circular with a radius  $r_{loc} = 0.08\text{mm}$ . First, the static boundary conditions are considered. The analytical solution of the problem is given by Parton et al. (1989). Numerical results for the displacement component  $u_3$  and the electric potential along the line  $x_3 = a/2$  are presented in Figs. 3 and 4. One can observe an excellent agreement of the present results and the exact solution in the whole interval considered. To see the influence of the electrical field on the

mechanical displacements the results for a pure elastic panel (without electro-elastic interaction  $e_{15} = e_{31} = e_{33} = 0$ ) are given in Fig. 3 too. For the considered boundary conditions, the mechanical displacement component  $u_3$  is reduced in the piezoelectric panel compared to a pure elastic one.

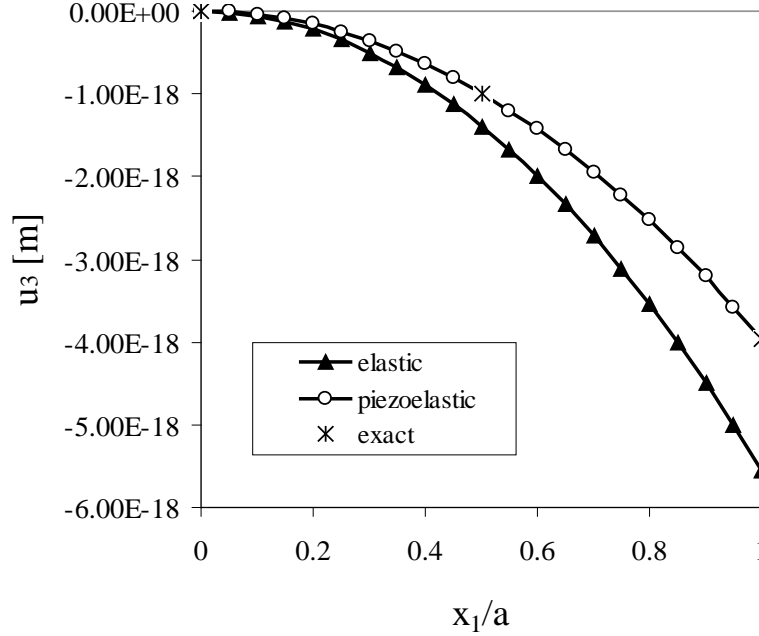


**Fig. 3** Variation of the mechanical displacement  $u_3$  with normalized coordinate  $x_1/a$

In the next example, we consider the same piezoelectric panel subject to a harmonic load with the angular frequency  $\omega$ . Both the geometrical and the material parameters are the same as in the previous static case. For the numerical calculations we have used again 441 nodes with a regular distribution. The mass density for PZT4 piezoelectric material is  $\rho = 7500 \text{ kg/m}^3$ . Numerical results are compared with those obtained by the FEM-ANSYS computer code. The FEM results have been obtained by using 3600 quadratic eight-noded elements. One can observe quite good agreement of the normalized amplitudes of the beam deflection at the considered angular frequency interval in Fig. 5. The amplitudes are normalized by the static value deflection value  $u_3^{stat} = 3.96 \cdot 10^{-18} \text{ m}$ . The first eigen-value frequency is  $3.8 \cdot 10^6 \text{ s}^{-1}$ .

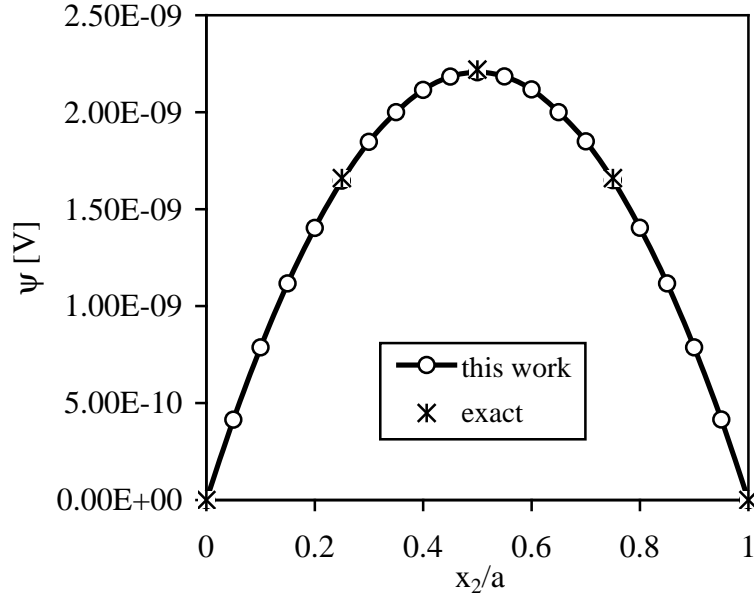


**Fig. 4** Variation of the electrical potential with normalized coordinate  $x_2/a$

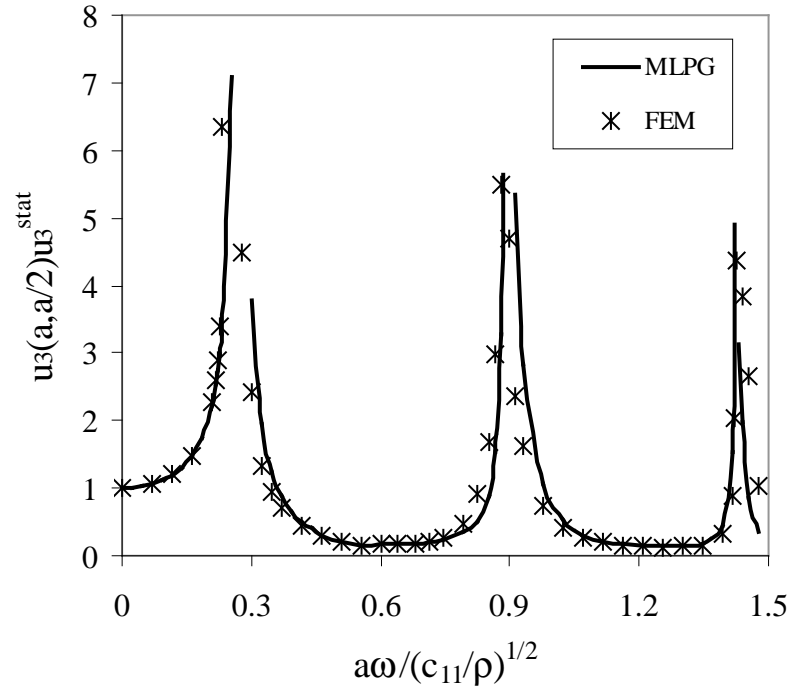


**Fig. 5** Influence of the angular frequency on the beam deflection

In the next example the PZT4 actuator is bonded on the upper surface of the steel cantilever beam. The width of the beam and actuators are 40 mm. Other sizes are given in Fig.6. When an external voltage 200V is applied across the thickness of the actuator, the induced strain generates

moments that bend the beam. The variation of the beam deflection with  $x_1$  coordinate is presented in Fig. 7. A quite good agreement of FEM and MLPG results is observed there. This example is an illustration that the present MLPG method can be successfully applied to problems in piecewise homogeneous structures too.

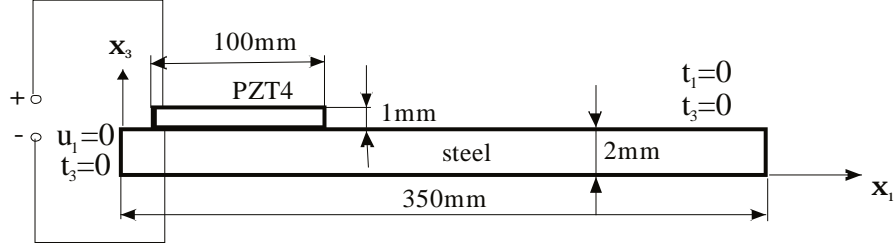


**Fig. 6** A cantilever beam with piezoelectric actuator

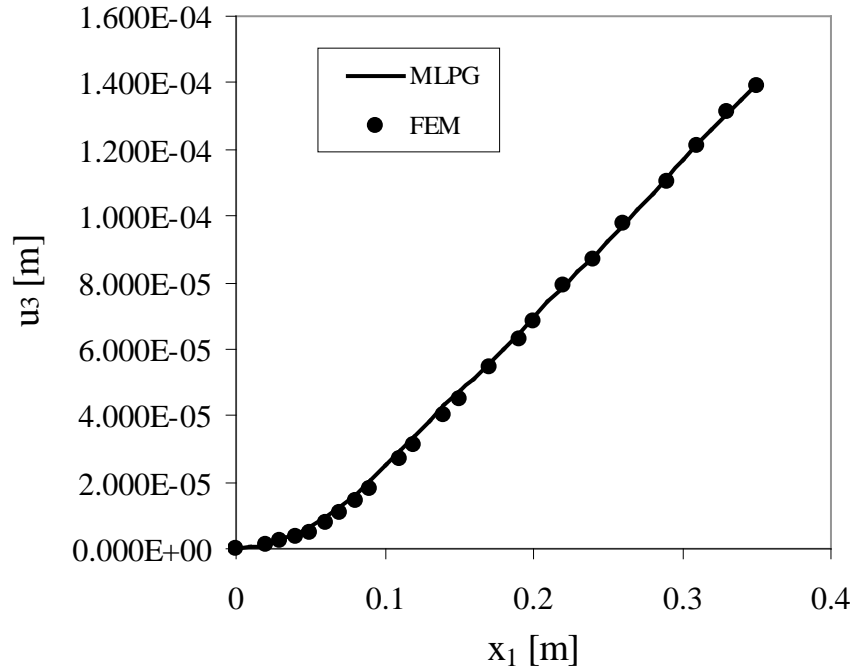


**Fig. 7** Variation of the beam deflection  $u_3$  with normalized coordinate  $x_1$

#### 4.2 Edge crack in a piezoelectric solid

An edge crack in a finite strip is analyzed in the next example. The sample geometry is given in Fig. 8 with following values:  $a = 0.5$ ,  $a/w = 0.4$  and  $h/w = 1.2$ . Due to the symmetry with respect to  $x_1$  only a half of the specimen is modeled. We have used 930 nodes equidistantly distributed for the MLS approximation of physical fields. On the top of the strip a uniform impact tension  $\sigma_0$  and electrical displacement  $D_0$  (Heaviside time variation) are applied, respectively. Impermeable electrical boundary conditions on crack surfaces are considered here.

Functionally graded material properties in  $x_1$  coordinate are considered. An exponential variation for the elastic, piezoelectric and dielectric tensors is used

$$\begin{aligned} c_{ijkl}(\mathbf{x}) &= c_{ijkl0} \exp(\gamma x_1), \\ e_{ijk}(\mathbf{x}) &= e_{ijk0} \exp(\gamma x_1) \\ h_{ij}(\mathbf{x}) &= h_{ij0} \exp(\gamma x_1), \end{aligned} \quad (41)$$

where  $c_{ijkl0}$ ,  $e_{ijk0}$  and  $h_{ij0}$  correspond to parameters used in the previous example.

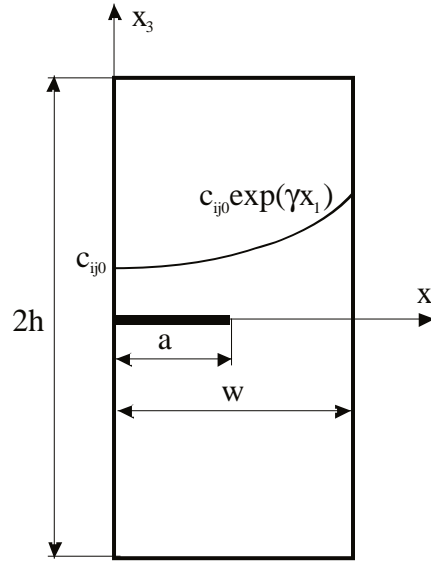


**Fig. 8** An edge crack in a finite strip with graded material properties in  $x_1$

For cracks in homogeneous and linear piezoelectric and piezomagnetic solids the asymptotic behaviour of the field quantities has been given by Wang and Mai (2003). In the crack tip vicinity, the displacements and potentials show the classical  $\sqrt{r}$  asymptotic behaviour. Hence, correspondingly, stresses, the electrical displacement and magnetic induction exhibit  $1/\sqrt{r}$  behaviour, where  $r$  is the radial polar coordinate with origin at the crack tip. Garcia-Sanchez et al. (2007b) extended the approach used in piezoelectricity to magnetoelectroelasticity to obtain asymptotic expression of generalized intensity factors

$$\begin{pmatrix} K_{II} \\ K_I \\ K_E \\ K_M \end{pmatrix} = \sqrt{\frac{\pi}{2r}} [\text{Re}(\mathbf{B})^{-1}] \begin{pmatrix} u_1 \\ u_3 \\ \psi \\ \mu \end{pmatrix} \quad (42)$$

where the matrix  $\mathbf{B}$  is determined by the material properties (Garcia-Sanchez et al., 2007b; Garcia-Sanchez and Saez, 2005) and

$$K_I = \lim_{r \rightarrow 0} \sqrt{2\pi r} \sigma_{33}(r, 0),$$

$$K_{II} = \lim_{r \rightarrow 0} \sqrt{2\pi r} \sigma_{13}(r, 0),$$

$$K_E = \lim_{r \rightarrow 0} \sqrt{2\pi r} D_3(r, 0),$$

$$K_M = \lim_{r \rightarrow 0} \sqrt{2\pi r} B_3(r, 0),$$

are the stress intensity factors (SIF)  $K_I$  and  $K_{II}$ ,  $K_E$  is the electrical displacement intensity factor (EDIF), and  $K_M$  is the magnetic induction intensity factor (MIIF), respectively.

The influence of the material gradation on the stress intensity factor and electrical displacement intensity factor is analyzed. The temporal variation of the SIF and the EDIF in the cracked strip under a pure mechanical load is presented in Fig. 9 and Fig. 10, respectively. The static stress intensity factor for the considered load and geometry is equal to  $K_I^{stat} = 2.642 \text{ Pa m}^{1/2}$ . Numerical results for a homogeneous strip are compared with FEM ones, and a quite good agreement is observed. For a gradation of mechanical material properties with  $x_1$  coordinate and a uniform mass density, the wave propagation is growing with  $x_1$ . Therefore, the peak value of the SIF is reached in a shorter time instant in FGPM strip than in a homogeneous one. The maximum value of the SIF is only slightly reduced for the FGPM cracked strip.

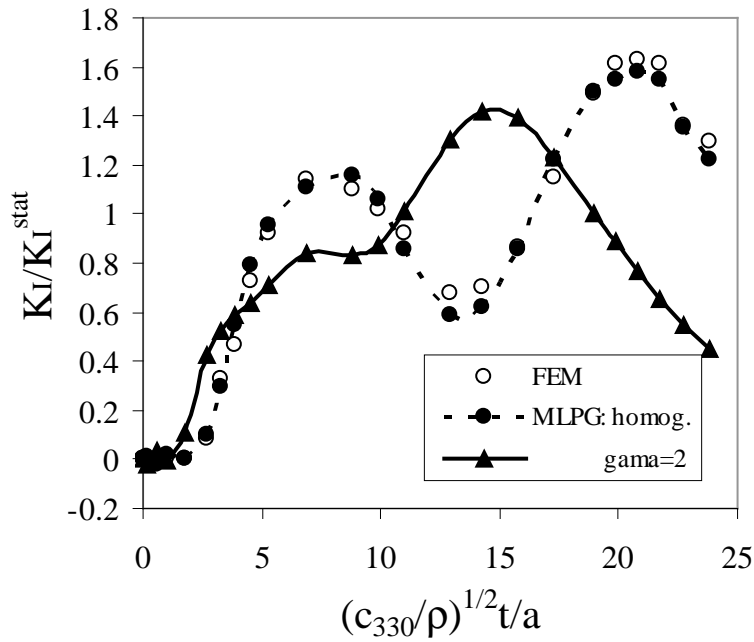


**Fig. 9** Influence of the material gradation on the stress intensity factor in a cracked strip under a pure mechanical impact load  $\sigma_0 H(t-0)$

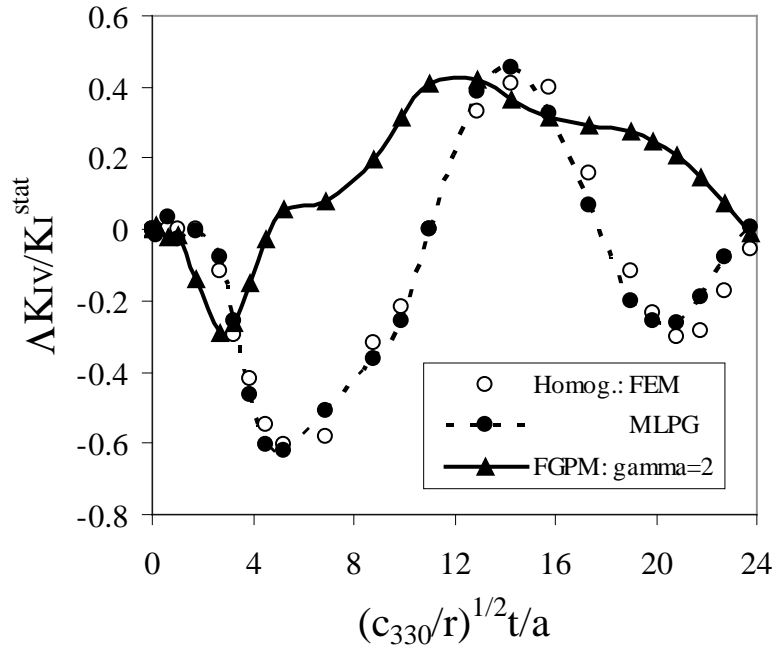


**Fig. 10** Influence of the material gradation on the EDIF in the cracked strip under a pure mechanical impact load  $\sigma_0 H(t-0)$

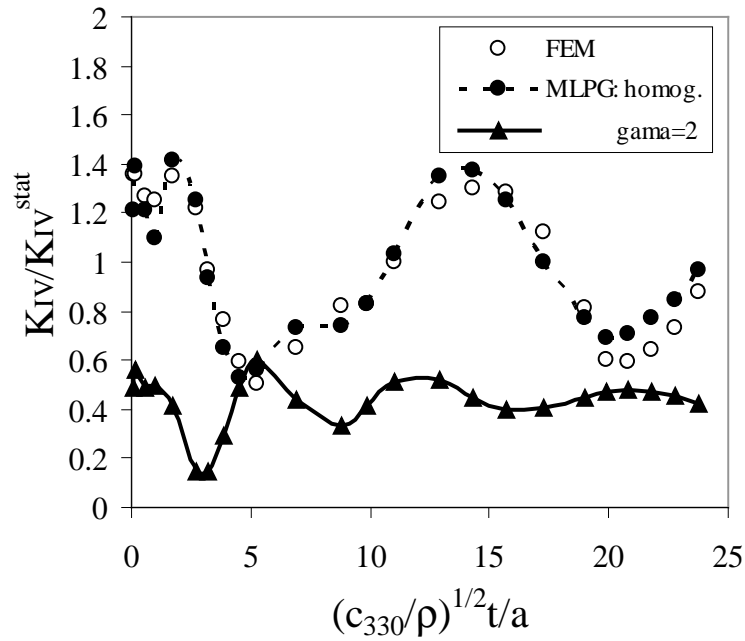


**Fig. 11** Temporal variation of the EDIF in the cracked strip under a pure electrical displacement impact load  $D_0 H(t-0)$

Next, the cracked strip under a pure electrical displacement impact load is analyzed. Since static SIF and EDIF are uncoupled it has to be valid  $K_{IV}^{stat} = K_I^{stat}$ . The temporal variation of the EDIF

is given in Fig. 11. The EDIF is significantly reduced for a cracked FGPM compared to a homogeneous strip. The oscillation of amplitudes for EDIF is again faster in an FGPM strip. Similar phenomena are observed for SIF in Fig. 12.

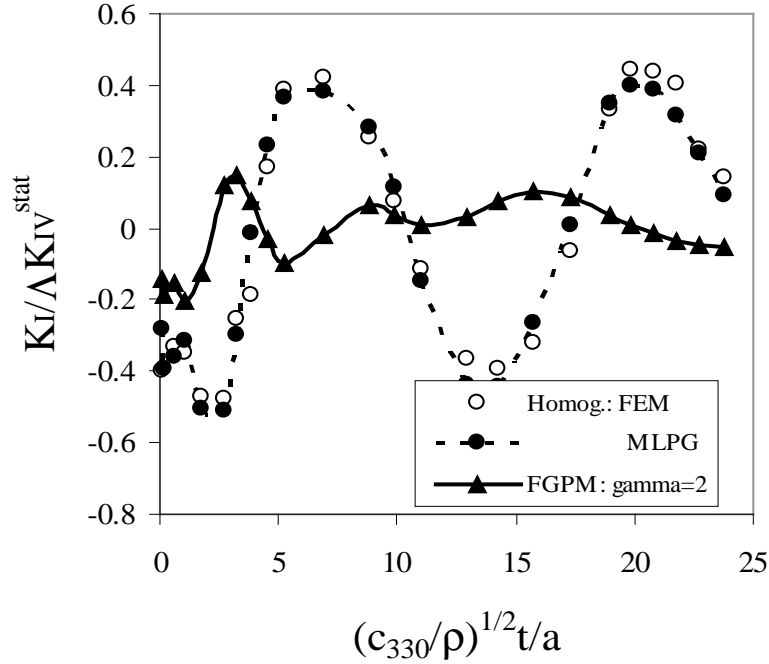


**Fig. 12** Temporal variation of the SIF in the cracked strip under a pure electrical displacement impact load  $D_0 H(t-0)$

### 4.3 Hollow piezoelectric sphere

A hollow sphere with continuously nonhomogeneous spherically symmetric and radially dependent piezoelectric material coefficients exhibits transversally isotropic properties. The sphere is radially polarized and either the static or impact loads are considered as spherically symmetric too. The temperature field is assumed to be uniformly distributed. The inner  $a = 0.4m$  and outer radii  $b = 1m$  are considered, respectively. The analytical solution is given by Chen et al. (2002) and Ding et al.(2003) and it is used as a benchmark to test the accuracy of the present method. The boundary conditions with prescribed pressures and vanishing electrical displacements on both surfaces correspond to pressured sphere embedded into nonconductive media (the open-circuit electric condition). A half of the hollow sphere can be created by the rotation of the cross section given in Fig. 13 around the  $z$ -axis. Note that the radial and axial directions are fixed as shown in Fig.13 according to the definition in the cylindrical coordinate system. The unit basis vectors of the spherical coordinate system  $\{\mathbf{e}_{r'}, \mathbf{e}_\varphi, \mathbf{e}_\omega\}$  are related to those of the cylindrical coordinate system  $\{\mathbf{e}_r, \mathbf{e}_\varphi, \mathbf{e}_z\}$  as

$$\mathbf{e}_{r'} = \mathbf{e}_r \cos \omega + \mathbf{e}_z \sin \omega, \quad \mathbf{e}_\omega = -\mathbf{e}_r \sin \omega + \mathbf{e}_z \cos \omega.$$

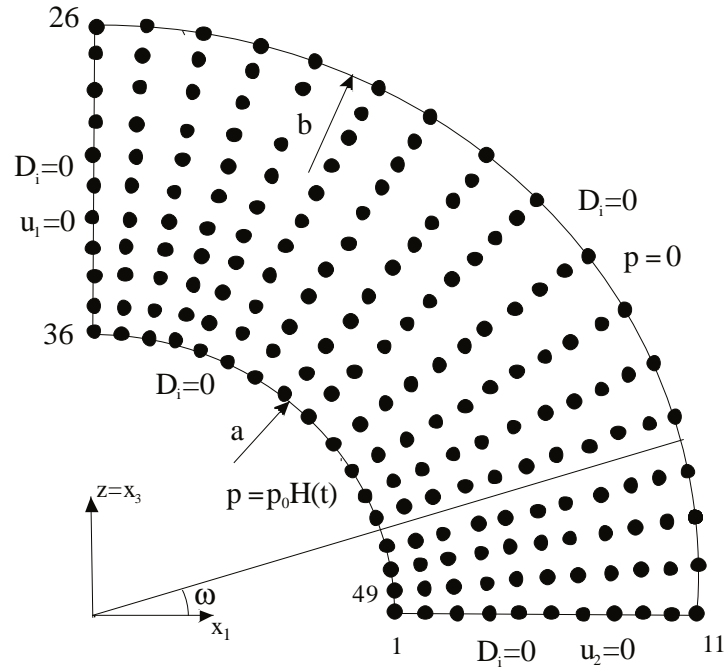
Thus, the radial directions in two considered coordinate systems are not identical in general.

For the numerical calculations, 176 nodes with a regular distribution in the radial and azimuthal directions in the section with  $\varphi=0$  are employed. An exponential variation of the elastic, piezoelectric and dielectric coefficients on the radial distance  $r' = \sqrt{(x_1^2 + x_3^2)}$  is assumed by

$$\begin{aligned} c_{ij}(\mathbf{x}) &= c_{ij}^0 \exp \gamma(r' - a), \\ e_{ij}(\mathbf{x}) &= e_{ij}^0 \exp \gamma(r' - a) \\ h_{ij}(\mathbf{x}) &= h_{ij}^0 \exp \gamma(r' - a), \end{aligned} \quad (43)$$

where the values on the inner radius  $r' = a$  are taken under the given temperature as

$$\begin{aligned} c_{11}^0 &= 13.9 \cdot 10^{10} \text{ Nm}^{-2}, & c_{13}^0 &= 7.43 \cdot 10^{10} \text{ Nm}^{-2}, & c_{12}^0 &= 7.78 \cdot 10^{10} \text{ Nm}^{-2}, \\ c_{33}^0 &= 11.5 \cdot 10^{10} \text{ Nm}^{-2}, & c_{44}^0 &= 2.56 \cdot 10^{10} \text{ Nm}^{-2}, \\ e_{44}^0 &= 12.7 \text{ Cm}^{-2}, & e_{31}^0 &= -5.2 \text{ Cm}^{-2}, & e_{33}^0 &= 15.1 \text{ Cm}^{-2}, \\ h_{11}^0 &= 6.46 \cdot 10^{-9} \text{ C(Vm)}^{-1}, & h_{33}^0 &= 5.62 \cdot 10^{-9} \text{ C(Vm)}^{-1}, & \rho &= \text{const} = 7500 \text{ kg/m}^3. \end{aligned}$$

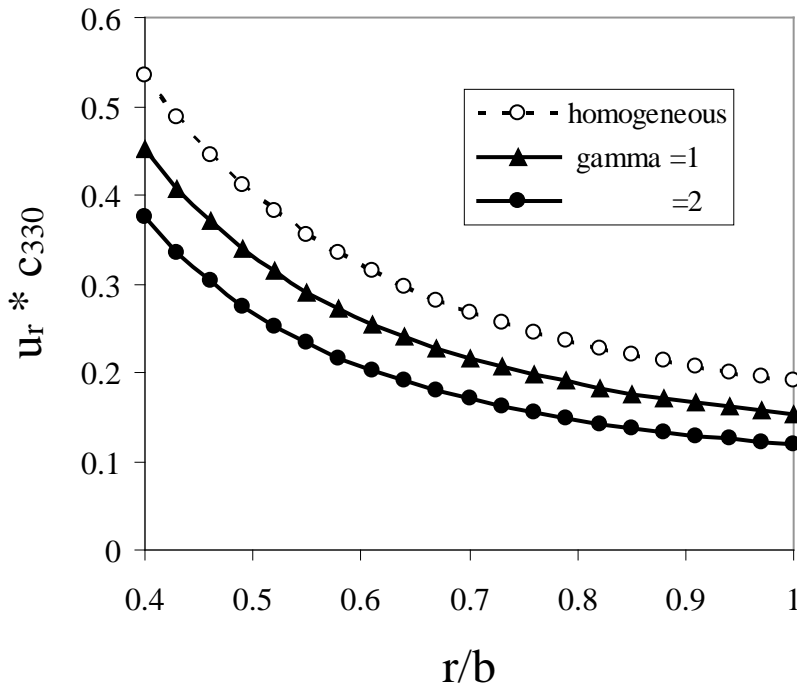


**Fig. 13** Analyzed domain for a hollow sphere

It should be noted that proposed computational method works for all continuously nonhomogeneous materials. In derivation of local integral equations no limitation is made with respect to spatial variation of material properties. The exponential variation in numerical example is selected only for comparative purposes since for such kind of nonhomogeneity numerical results are available. The mass density in this example is considered to be uniform,

however, a general spatial variation can be considered. No restriction is put on the variation of mass density in proposed local integral equations. A static uniform pressure load  $p_0 = 1N/m^2$  is considered on the inner radius  $r' = a$ , in the first step. Variation of the radial displacements  $u_r = u_1(x_1, x_3 = 0)$ , radial and hoop stresses  $[\sigma_{rr} = \sigma_{11}(x_1, x_3 = 0), \sigma_{\varphi\varphi}(x_1, x_3 = 0)]$  with the radial coordinate  $r = x_1$  are presented in Figs. 14-16. Owing to the spherical symmetry the presented results correspond to the following spherical components:

$$u_{r'}(r', \varphi, \omega) = u_r(x_1, \varphi = 0, x_3 = 0), \quad \sigma_{r'r'}(r', \varphi, \omega) = \sigma_{rr}(x_1, \varphi = 0, x_3 = 0),$$

$$\sigma_{\varphi\varphi}(r', \varphi, \omega) = \sigma_{\varphi\varphi}(x_1, \varphi = 0, x_3 = 0).$$


**Fig. 14** Variation of radial displacements with the radial coordinate

The results for radial stresses are compared also with the analytical solution (Chen et al., 2002) for constant material coefficients. One can observe that functionally graded material properties have a stronger influence on radial displacement values than on the radial stresses. With increasing gradation of elastic parameters the radial displacements are reduced. However, the influence of the material gradation on the hoop stresses is different on the inner and outer radii. On the outer radius the hoop stresses are enhanced with increasing material gradation while on the inner radius they are reduced.

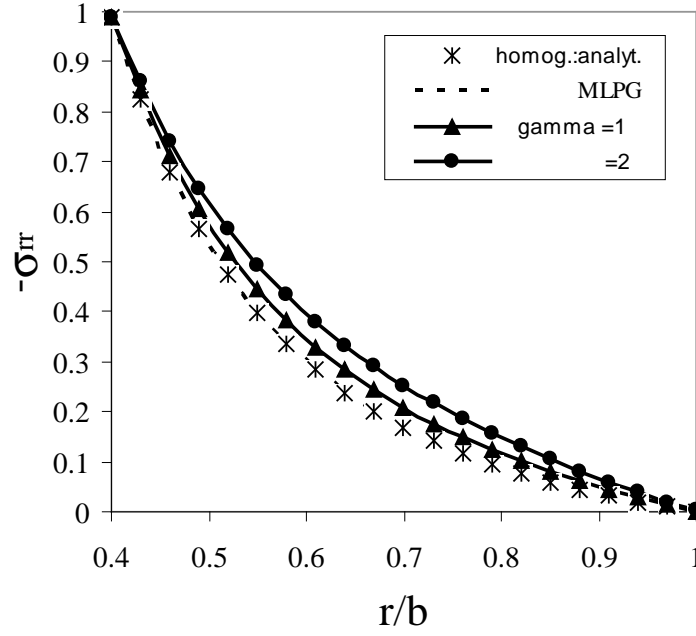


**Fig. 15** Variation of radial stresses with the radial coordinate

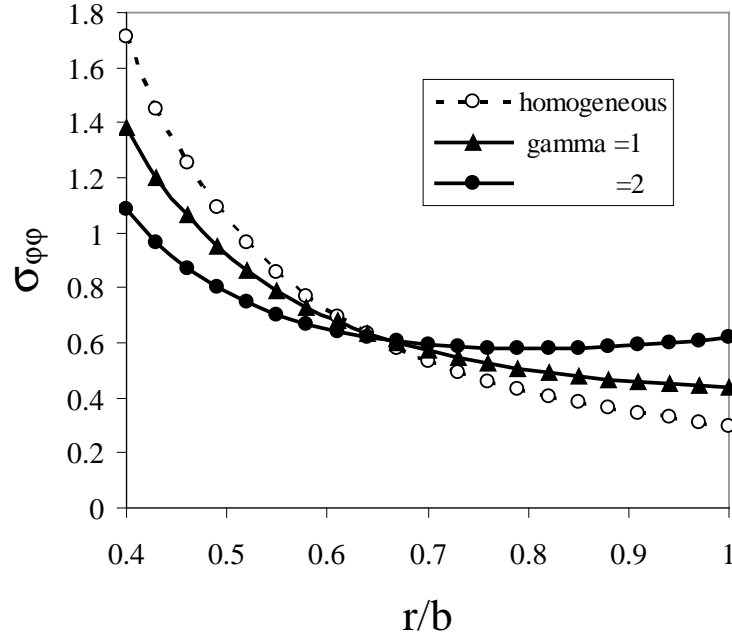


**Fig. 16** Variation of hoop stresses with the radial coordinate

Next, a uniform electrical load on the outer radius  $D_r = 1C/m^2$  and traction-free surfaces are considered. Variation of the radial displacements, hoop stresses, the electrical potential and the electrical displacement with the radial coordinate are presented in Figs. 17-20.

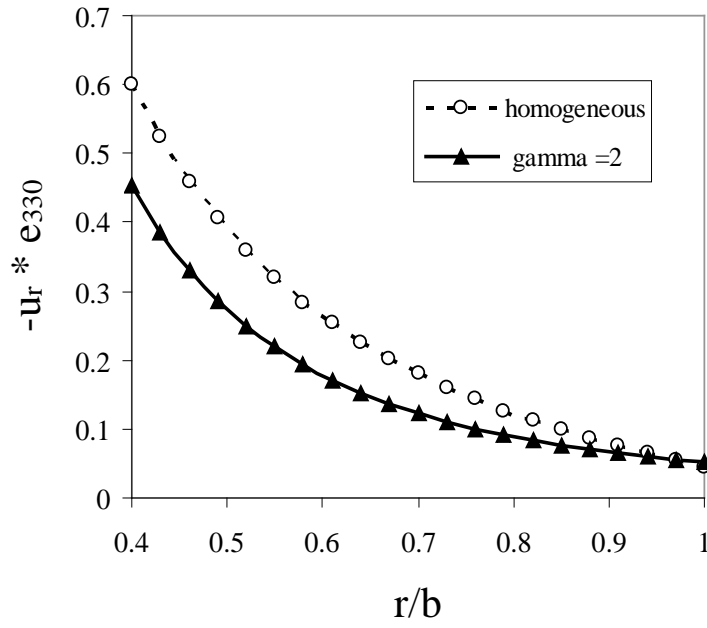


**Fig. 17** Variation of radial displacements with the radial coordinate in the hollow sphere under a static electrical displacement on the outer radius

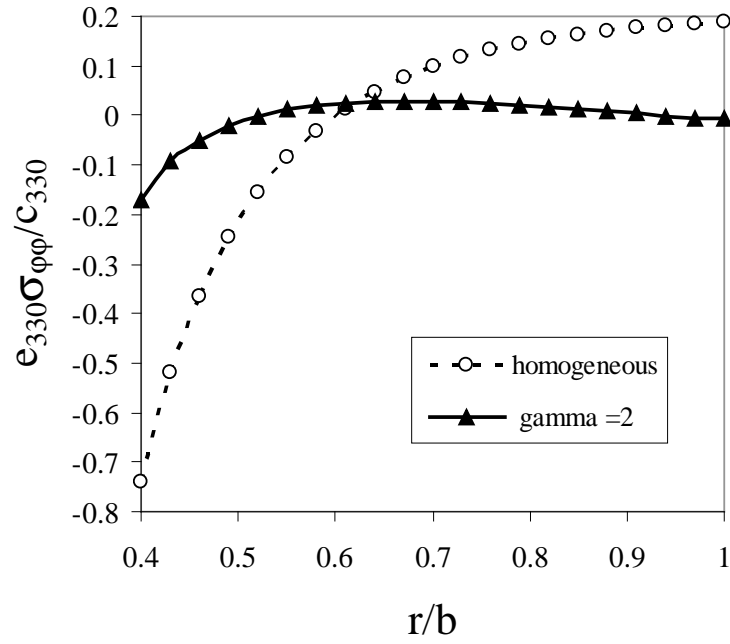


**Fig. 18** Variation of hoop stresses with the radial coordinate in the hollow sphere under a static electrical displacement on the outer radius

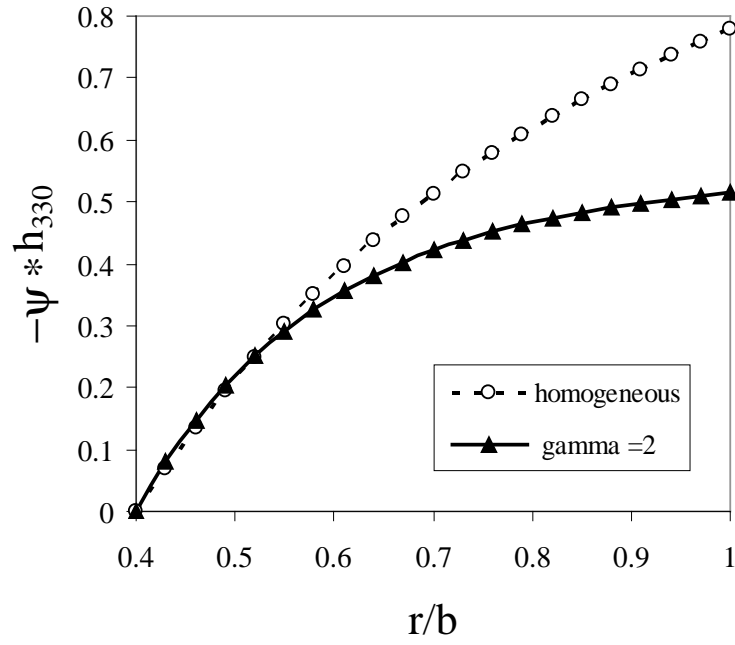


**Fig. 19** Variation of the electrical potential with the radial coordinate in the hollow sphere under a static electrical displacement on the outer radius

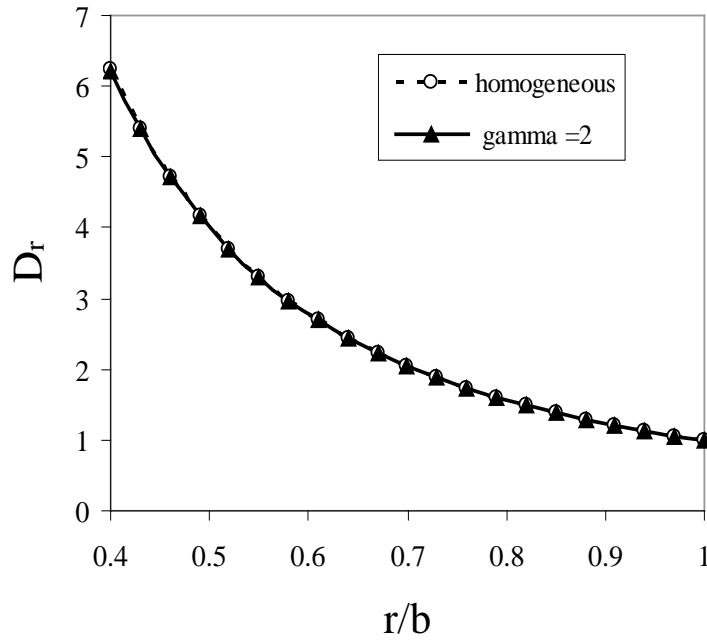


**Fig.20** Variation of electrical displacements with the radial coordinate in the hollow sphere under a static electrical displacement on the outer radius

The impact pressure load with a uniform distribution on the inner radius is considered too. Vanishing electrical potentials are considered on both spherical surfaces (the closed-circuit electric condition). The numerical results for radial displacements and hoop stresses are presented in Figs. 21 and 22. Both quantities are normalized by corresponding static ones,  $u_r^{stat}(a) = 0.465 \cdot 10^{-11} m$  and  $\sigma_{\varphi\varphi}^{stat}(a) = 1.71 N / m^2$ , respectively. The Laplace transform approach was applied in the numerical analysis. The mass density is considered to be uniform even for functionally graded material.

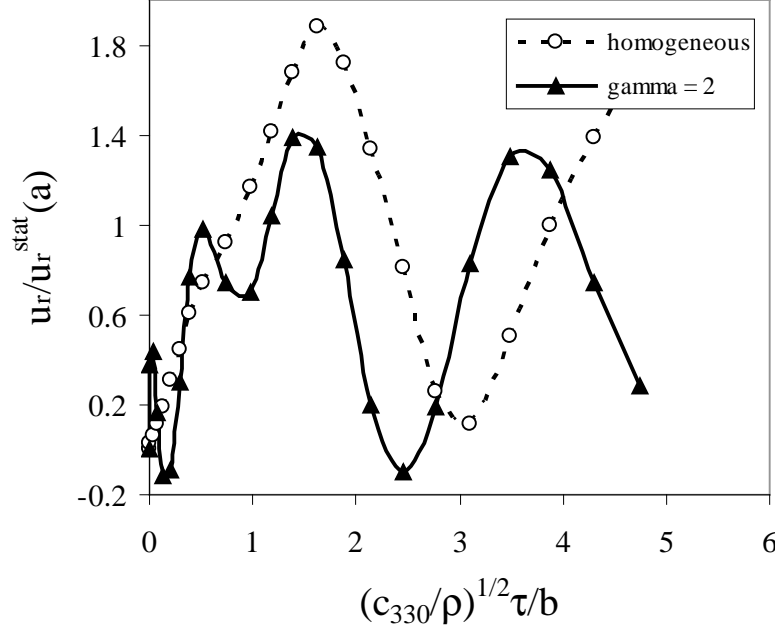


**Fig. 21** Time variation of radial displacements in the hollow sphere under an impact pressure load on the inner radius

The time evolution of the hoop stresses on the inner radius  $r' = a$  is compared also with the analytical results given by Ding et al. (2003) in case of homogeneous medium. One can observe a good agreement of analytical and MLPG results for a homogeneous piezoelectric sphere. For the gradual increase of mechanical material properties with radial coordinate and a uniform mass density, the wave propagation velocity is increasing with  $r$ . Therefore, the peak value of the radial displacements and hoop stresses are reached in an earlier time instant in FGPM hollow sphere than in a homogeneous one. The maximum quantities are reduced for the FGPM sphere.

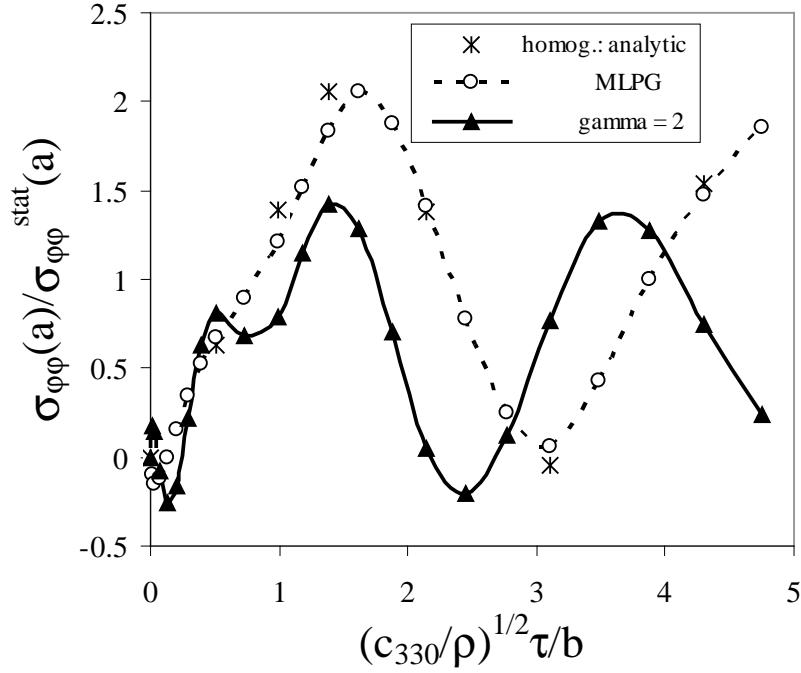


**Fig. 22** Time variation of hoop stresses in the hollow sphere under an impact pressure load on the inner radius

#### 4.4 Edge crack in a finite magneto-electric-elastic strip

Next, an edge crack in a finite magneto-electric-elastic strip is analyzed. The geometry of the cracked specimen is the same as in the previous example. We have used again 930 equidistantly distributed nodes for the MLS approximation of the physical fields. On the top of the strip either a uniform tension  $\sigma_0$ , or a uniform magnetic induction  $B_0$  is applied. Firstly, the static loadings are considered. The functionally graded material properties in the  $x_1$ -direction are considered. An exponential variation of the elastic, piezoelectric, dielectric, paramagnetic, electromagnetic and magnetic permeability coefficients are assumed as

$$f_{ij}(\mathbf{x}) = f_{ij0} \exp(\gamma_f x_1), \quad (44)$$

where the symbol  $f_{ij}$  is commonly used for particular material coefficients with  $f_{ij0}$  corresponding to the material coefficients for the  $\text{BaTiO}_3\text{-CoFe}_2\text{O}_4$  composite and being given by Li (2000) as

$$\begin{aligned} c_{11} &= 22.6 \times 10^{10} \text{ Nm}^{-2}, \quad c_{13} = 12.4 \times 10^{10} \text{ Nm}^{-2}, \quad c_{33} = 21.6 \times 10^{10} \text{ Nm}^{-2}, \quad c_{66} = 4.4 \times 10^{10} \text{ Nm}^{-2}, \\ e_{15} &= 5.8 \text{ Cm}^{-2}, \quad e_{31} = -2.2 \text{ Cm}^{-2}, \quad e_{33} = 9.3 \text{ Cm}^{-2}, \\ h_{11} &= 5.64 \times 10^{-9} \text{ C}^2 / \text{Nm}^2, \quad h_{33} = 6.35 \times 10^{-9} \text{ C}^2 / \text{Nm}^2, \end{aligned}$$

$$d_{15} = 275.0 N / Am , \quad d_{21} = 290.2 N / Am , \quad d_{22} = 350.0 N / Am ,$$

$$\alpha_{11} = 5.367 \times 10^{-12} Ns / VC , \quad \alpha_{33} = 2737.5 \times 10^{-12} Ns / VC ,$$

$$\gamma_{11} = 297.0 \times 10^{-6} Ns^2 C^{-2} , \quad \gamma_{33} = 83.5 \times 10^{-6} Ns^2 C^{-2} , \quad \rho = 5500 kg / m^3$$

and the origin  $x_1 = 0$  is assumed at the crack tip.

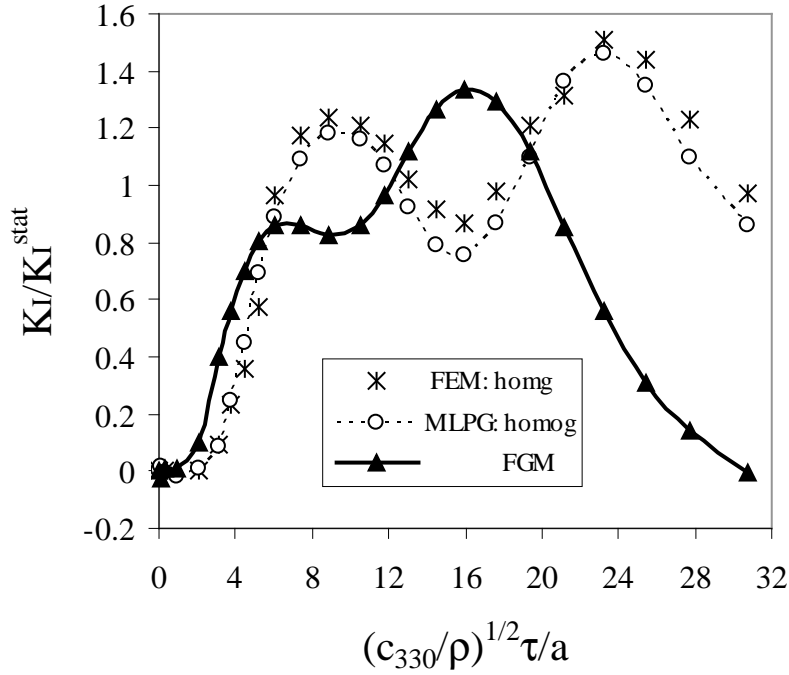


**Fig. 23** Normalized stress intensity factor for an edge crack in a strip under a pure mechanical load  $\sigma_0 H(\tau-0)$

We have considered the same exponential gradient for all coefficients with value  $\gamma=2$  in the numerical calculations. Then, all material parameters at the crack tip are  $e^1 = 2.718$  times larger than in the homogeneous material. Then, the crack opening displacement and potentials are significantly reduced in the nonhomogeneous material with gradually increasing material properties in  $x_1$ -direction. The normalized stress intensity factors for homogeneous and nonhomogeneous cracked specimen have the following values,  $f_I = K_I / \sigma_0 \sqrt{\pi a} = 2.105$  and 1.565, respectively. With increasing gradient parameter  $\gamma$  the SIF is decreasing. A similar phenomenon is observed for an edge crack in an elastic FGM strip under a mechanical loading (Dolbow and Gosz, 2002) and for a cracked piezoelectric FGM specimen (Sladek et al., 2007a). For a crack in a homogeneous magneto-electric-elastic solid analyzed in the previous example the SIF, EDIF, magnetic induction intensity factor (MIIF) are uncoupled. However, this conclusion is not valid generally for a continuously nonhomogeneous solid. We have obtained the following normalized quantities:  $\Lambda_e K_E / K_I^{stat} = 0.04866$  and  $\Lambda_m K_M / K_I^{stat} = 0.00412$ . For

normalized electrical displacement and magnetic induction intensity factor we have used parameters  $\Lambda_e = e_{33} / h_{33}$  and  $\Lambda_m = d_{33} / \gamma_{33}$ , respectively.

Next, the strip is subjected to an impact mechanical load with Heaviside time variation and the intensity  $\sigma_0 = 1Pa$ . The impermeable boundary conditions for the electric displacement and magnetic flux on crack surfaces are considered. The time variation of the normalized stress intensity factor is given in Fig. 23, where  $K_I^{stat} = 2.642Pa \cdot m^{1/2}$ . The boundary value problem for a homogeneous material has been analyzed also by the FEM computer code ANSYS. One can observe a quite good agreement of results. For graded elasticity coefficients along the  $x_1$  - coordinate and a uniform mass density, the wave propagation is growing with  $x_1$ . Therefore, the peak value of the SIF is reached in a shorter time instant in functionally graded strip than in a homogeneous one. The maximum value of the SIF is only slightly reduced for the FGM cracked strip.

#### 4.5 A penny-shaped crack in a finite cylinder

A penny-shaped crack in a finite cylinder as depicted in Fig. 24 is analyzed as the third example. The following geometry is considered: crack radius  $a = 0.5$ , cylinder radius  $w = 1.25$ , and cylinder length  $2L = 3.0$ . On the top of the cylinder either a uniform tension  $\sigma_0$ , or a uniform magnetic induction  $B_0$  are applied, firstly as static loads.

Also in this example, an exponential variation of the magneto-electro-elastic material parameters in radial direction is assumed, i.e.,

$$f_{ij}(r) = f_{ij0} \exp(\gamma_f r) .$$

The material coefficients at the axis of symmetry corresponding to the  $BaTiO_3$ - $CoFe_2O_4$  composite are given by (Wang and Mai, 2007)

$$c_{11} = 22.6 \times 10^{10} Nm^{-2} , \quad c_{13} = 12.4 \times 10^{10} Nm^{-2} , \quad c_{33} = 21.6 \times 10^{10} Nm^{-2} , \quad c_{44} = 4.4 \times 10^{10} Nm^{-2} ,$$

$$c_{12} = 12.5 \times 10^{10} Nm^{-2} , \quad e_{15} = 5.8 Cm^{-2} , \quad e_{31} = -2.2 Cm^{-2} , \quad e_{33} = 9.3 Cm^{-2} ,$$

$$h_{11} = 5.64 \times 10^{-9} C^2 / Nm^2 , \quad h_{33} = 6.35 \times 10^{-9} C^2 / Nm^2 ,$$

$$d_{15} = 275.0 N / Am , \quad d_{31} = 290.2 N / Am , \quad d_{33} = 350.0 N / Am ,$$

$$\alpha_{11} = 5.367 \times 10^{-12} Ns / VC , \quad \alpha_{33} = 2737.5 \times 10^{-12} Ns / VC ,$$

$$\gamma_{11} = 81.0 \times 10^{-6} Ns^2 C^{-2} , \quad \gamma_{33} = 83.5 \times 10^{-6} Ns^2 C^{-2} , \quad \rho = 5500 kg / m^3 .$$

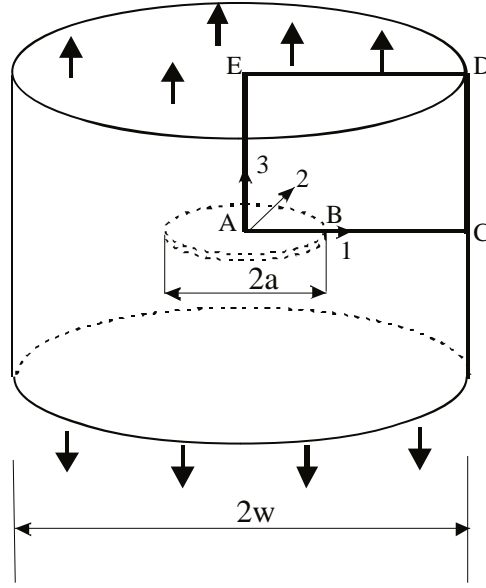


**Fig. 24** A penny-shaped crack in a finite magneto-electro-elastic cylinder

Numerical calculations are carried out for the gradient parameter  $\gamma=2$ . A regular node distribution with 930 (31x30) nodes is used for the MLS-approximation of the displacements and the potentials in the analyzed domain ABCDE (see Fig.24).

The static values of the SIF for the homogeneous and FGM cracked cylinder are  $K_I^{stat} = 0.813 \text{Pa} \cdot \text{m}^{1/2}$  and  $K_I^{FGM} = 0.353 \text{Pa} \cdot \text{m}^{1/2}$ , respectively. The SIF in the cracked cylinder with positive material properties gradient is significantly reduced in comparison with the SIF for the corresponding homogeneous cylinder. This is due to the significant reduction of the crack opening displacement in the FGM cylinder as presented in Fig. 25. One can also see a good agreement of numerical results obtained by the MLPG method and the FEM for a cracked homogeneous cylinder.

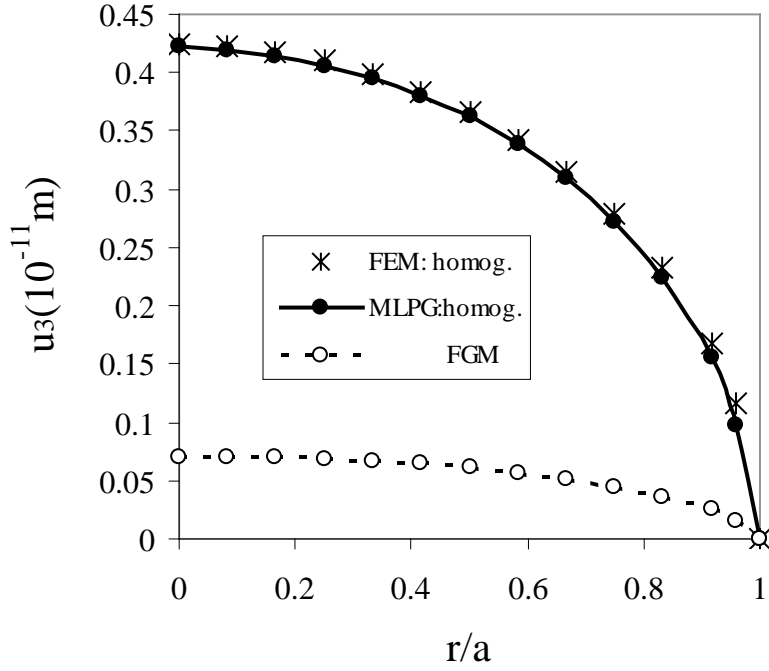
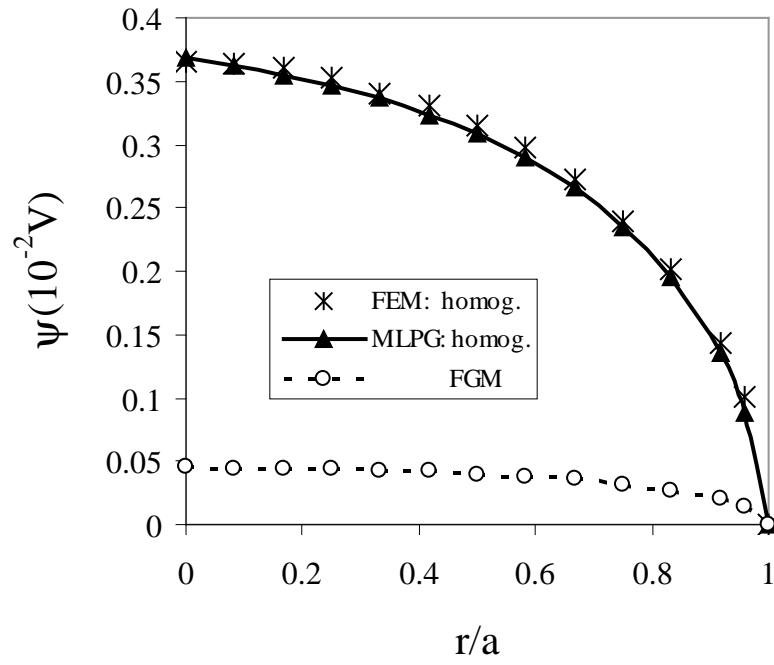
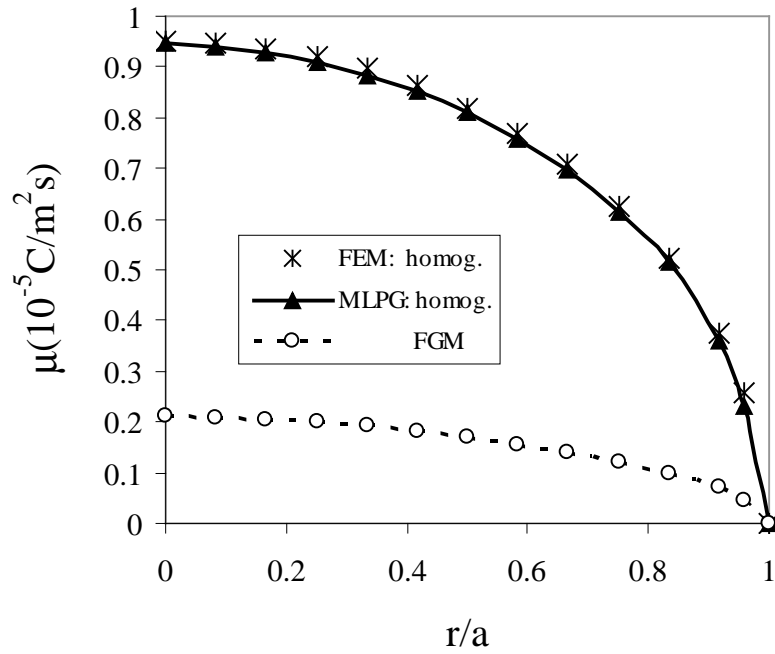


**Fig. 25** Variation of the crack opening displacement with the normalized coordinate  $r/2a$  in the cracked cylinder under a pure mechanical loading  $\sigma_0 = 1Pa$ .

Variation of the electric and magnetic potentials with the radial coordinate under a pure mechanical loading  $\sigma_0 = 1Pa$  is presented in Fig. 26. The EDIF and MIIF vanish in the static case with a pure mechanical load in the homogeneous cylinder. Both the electrical and magnetic potentials are significantly reduced in the FGM cylinder with respect to the homogeneous one. A good agreement between the MLPG and FEM results is again observed for both potentials in a homogeneous cylinder.



a)



b)

**Fig. 26** Variation of a) the electric, and b) magnetic potentials with the normalized coordinate  $r/2a$  under a pure mechanical loading  $\sigma_0 = 1Pa$  in the cracked cylinder.

Next, the cracked cylinder is subjected to an impact mechanical load with Heaviside time variation and the intensity  $\sigma_0 = 1 \text{ Pa}$ . Impermeable boundary conditions for the electric displacement and magnetic flux on crack surfaces are considered. The time variation of the normalized stress intensity factor is given in Fig. 27, where  $K_I^{stat} = 0.813 \text{ Pa} \cdot \text{m}^{1/2}$  corresponds to the corresponding homogeneous case.

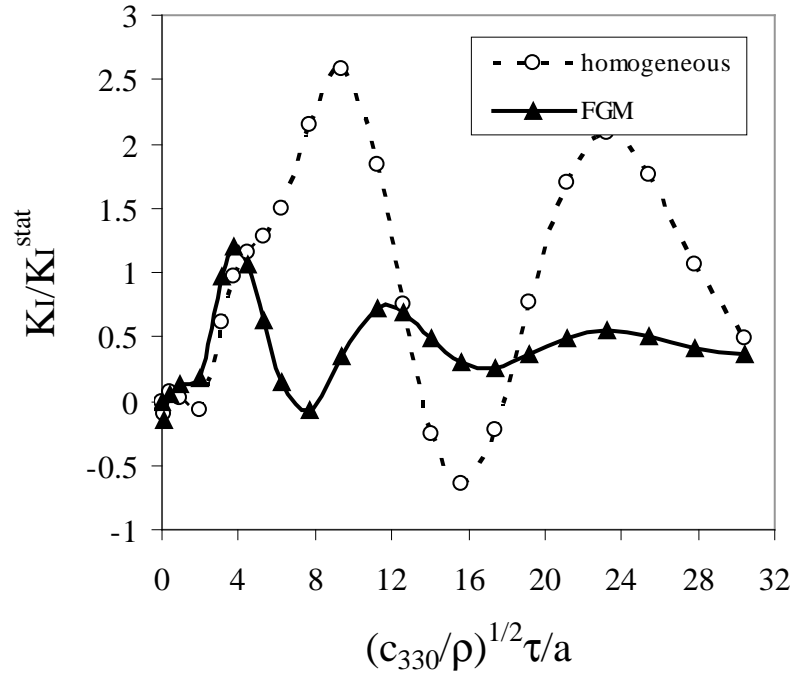
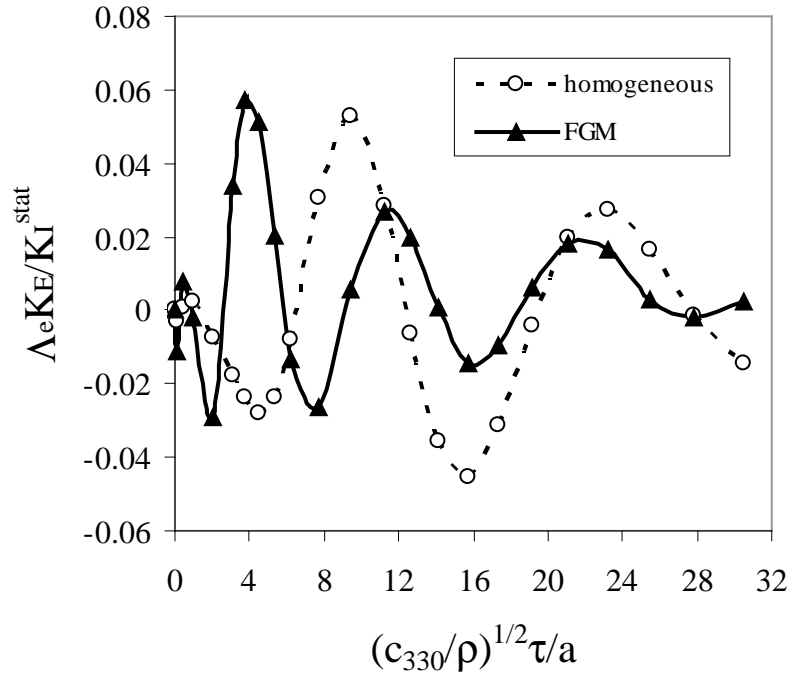
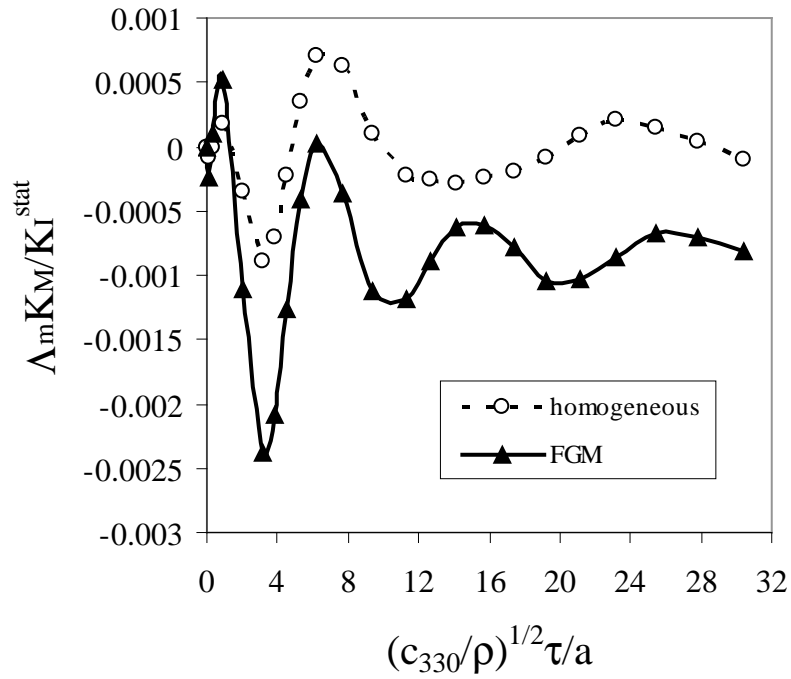


**Fig. 27** Normalized stress intensity factor for a penny-shaped crack in a cylinder under a pure mechanical load  $\sigma_0 H(\tau - 0)$

The picks of the SIF in Fig. 27 for the FGM cylinder are significantly reduced with respect to the homogeneous case. The reduction is proportional to the reduction of the static stress intensity factors in both cases. If the dynamic SIF in the FGM cylinder is normalized by the corresponding static value  $K_I^{FGM} = 0.353 \text{ Pa} \cdot \text{m}^{1/2}$  one obtains almost the same pick value as in the homogeneous case. The peak value of the SIF in FGM cylinder is reached at a shorter time instant than in the corresponding homogeneous one. It is due to the higher value of the wave velocity in the FGM cylinder than in the homogeneous one.



a)



b)

**Fig. 28** Normalized a) electric, and b) magnetic intensity factors for a penny-shaped crack in a cylinder under a pure mechanical load  $\sigma_0 H(\tau-0)$

For normalized electrical displacement and magnetic induction intensity factors we have used parameters  $\Lambda_e = e_{33} / h_{33}$  and  $\Lambda_m = d_{33} / \gamma_{33}$ , respectively. Numerical results are presented in Fig. 28. Opposite to the static case, finite values of EDIF and MIIF are obtained under a pure mechanical impact load in the homogeneous cylinder too. Both dynamic quantities for FGM cylinder are oscillating around the static values which are:  $\Lambda_e K_E / K_I^{stat} = 0.00655$  and  $\Lambda_m K_M / K_I^{stat} = -0.831 \cdot 10^{-3}$ .

## 5. Conclusions

A meshless local Petrov-Galerkin method (MLPG) is presented for modelling 2-D and 3-D axisymmetric piezoelectric and magneto-electric-elastic problems. Both static and impact loads are considered. The Laplace-transform technique is applied to eliminate the time variable in the coupled governing partial differential equations. The analyzed domain is divided into small overlapping circular subdomains. A unit step function is used as the test function in the local weak-form of the governing partial differential equations. The derived local boundary-domain integral equations are non-singular. The moving least-squares (MLS) scheme is adopted for the approximation of the physical field quantities. The proposed method is a truly meshless method, which requires neither domain elements nor background cells in either the interpolation or the integration.

The present method is an alternative numerical tool to many existing computational methods like FEM or BEM. The main advantage of the present method is its simplicity. Compared to the conventional BEM, the present method requires no fundamental solutions and all integrands in the present formulation are regular. Thus, no special numerical techniques are required to evaluate the integrals. It should be noted here that the fundamental solutions are not available for magneto-electric-elastic solids with continuously varying material properties in general cases. The present formulation also possesses the generality of the FEM. Therefore, the method is promising for numerical analysis of multi-field problems like piezoelectric, electro-magnetic or thermoelastic problems, which cannot be solved efficiently by the conventional BEM.

## Acknowledgement

The authors acknowledge the support by the Slovak Science and Technology Assistance Agency registered under number APVV-0427-07, the Slovak Grant Agency VEGA-2/0039/09.

## References

- Alshits, V.I., Darinski, A.N., Lothe, J.** (1992): On the existence of surface waves in half-anisotropic elastic media with piezoelectric and piezomagnetic properties. *Wave Motion* 16: 265-283.
- Atluri, S.N.** (2004): *The Meshless Method, (MLPG) For Domain & BIE Discretizations*, Tech Science Press.
- Atluri, S.N., and Zhu, T.** (1998): A New Meshless Local Petrov-Galerkin (MLPG) Approach in Computational Mechanics, *Computational Mechanics*, Vol.22, pp. 117-127, 1998.

- Atluri, S.N.; Sladek, J.; Sladek, V.; Zhu, T.** (2000): The local boundary integral equation (LBIE) and its meshless implementation for linear elasticity. *Comput. Mech.*, 25: 180-198.
- Atluri, S.N.; Han, Z.D.; Shen, S.** (2003): Meshless local Petrov-Galerkin (MLPG) approaches for solving the weakly-singular traction & displacement boundary integral equations. *CMES: Computer Modeling in Engineering & Sciences*, 4: 507-516.
- Avellaneda, M.; Harshe, G.** (1994): Magnetolectric effect in piezoelectric/magnetostrictive multilayer (2-2) composites, *Journal of Intelligent Material Systems and Structures* 5: 501-513.
- Batra, R.C.; Liang, X.Q.** (1997): The vibration of a rectangular laminated elastic plate with embedded piezoelectric sensors and actuators. *Computers and Structures*, 63: 213-216.
- Belytschko, T.; Krogauz, Y.; Organ, D.; Fleming, M.; Krysl, P.** (1996): Meshless methods; an overview and recent developments. *Comp. Meth. Appl. Mech. Engn.*, 139: 3-47.
- Beom, H.G.; Atluri, S.N.** (1996)., "Near-Tip Fields & Intensity Factors for Interfacial Cracks in Dissimilar Anisotropic Piezoelectric Media," *Int. Journal of Fracture*, 75: 163-183,
- Beom H.G.; Atluri S.N.** (2002): "Conducting cracks in dissimilar piezoelectric media" *International Journal of Fracture*, 118 (4): 285-301
- Beom H.G.; Atluri S.N.** (2003): "Effect of electric fields on fracture behavior of ferroelectric ceramics", *Journal of Mechanics and Physics of Solids*, 51 (6): 1107-1125
- Berlingcourt, D.A.; Curran, D.R.; Jaffe, H.** (1964): Piezoelectric and piezomagnetic materials and their function in transducers, *Physical Acoustics* 1: 169-270.
- Chen, T.; Lin, F.Z.** (1995): Boundary integral formulations for three-dimensional anisotropic piezoelectric solids. *Computational Mechanics*, 15: 485-496.
- Chen, W.Q, Lu, Y., Ye, R., Cai, J.B.** (2002): 3D electroelastic fields in a functionally graded piezoceramic hollow sphere under mechanical and electric loadings. *Archives of Applied Mechanics*, 72: 39-51.
- Chung, M.Y., Ting, T.C.T.** (1995): The Green function for a piezoelectric piezomagnetic anisotropic elastic medium with an elliptic hole or rigid inclusion. *Philos. Mag. Lett.* 72: 405-410.
- Ding, H.; Liang, J.** (1999): The fundamental solutions for transversely isotropic piezoelectricity and boundary element method. *Computers & Structures*, 71: 447-455.
- Ding, H.J., Wang, H.M., Chen, W.Q.** (2003): Analytical solution for the electroelastic dynamics of a nonhomogeneous spherically isotropic piezoelectric hollow sphere. *Archives of Applied Mechanics*, 73: 49-62.
- Dolbow, J.E., Gosz, M.** (2002): On computation of mixed-mode stress intensity factors in functionally graded materials. *Int. J. Solids Structures* 39: 7065-7078.
- Enderlein, M.; Ricoeur, A.; Kuna, M.** (2005): Finite element techniques for dynamic crack analysis in piezoelectrics. *International Journal of Fracture*, 134: 191-208.
- Eringen, C.E.; Maugin M.A.** (1990): *Electrodynamics of Continua*. Springer-Verlag, Berlin.

- Feng, W.J.; Su, R.K.L.** (2006): Dynamic internal crack problem of a functionally graded magneto-electro-elastic strip. *Int. J. Solids Structures* 43: 5196-5216.
- Feng, W.J., Pan, E., Wang, X.** (2007): Dynamic fracture analysis of a penny-shaped crack in a magnetoelectroelastic layer. *Int. J. Solids Structures* 44: 7955-7974.
- Fleming, M.; Chu, Y.A.; Moran, B.; Belytschko, T.** (1997): Enriched element-free Galerkin methods for crack tip fields. *International Journal for Numerical Methods in Engineering* 40: 1483-1504.
- Gao, C.F., Kessler, H., Balke, H.** (2003): Crack problems in magnetoelectroelastic solids. Part I: exact solution of a crack. *International Journal of Engineering Science* 41: 969-981.
- Garcia-Sanchez, F.; Saez, A.; Dominguez, J.** (2005): Anisotropic and piezoelectric materials fracture analysis by BEM. *Computers & Structures*, 83: 804-820.
- Garcia-Sanchez, F.; Zhang, Ch.; Sladek, J.; Sladek, V.** (2007a): 2-D transient dynamic crack analysis in piezoelectric solids by BEM. *Computational Materials Science*, 39: 179-186.
- Garcia-Sanchez, F., Rojas-Diaz, R., Saez, A., Zhang, Ch.** (2007b): Fracture of magnetoelectroelastic composite materials using boundary element method (BEM). *Theoretical and Applied Fracture Mechanics* 47: 192-204.
- Gaudenzi, P.; Bathe, K.J.** (1995): An iterative finite element procedure for the analysis of piezoelectric continua. *Journal of Intelligent Material Systems and Structures*, 6: 266-273.
- Gornandt, A., Gabbert, U.** (2002): Finite element analysis of thermopiezoelectric smart structures. *Acta Mechanica*, 154: 129-140.
- Govorukha, V.; Kamlah, M.** (2004): Asymptotic fields in the finite element analysis of electrically permeable interfacial cracks in piezoelectric bimaterials. *Archives Applied Mechanics*, 74: 92-101.
- Gruebner, O.; Kamlah, M.; Munz, D.** (2003): Finite element analysis of cracks in piezoelectric materials taking into account the permittivity of the crack medium. *Eng. Fracture Mechahamics*, 70: 1399-1413.
- Gross, D.; Rangelov, T.; Dineva, P.** (2005): 2D wave scattering by a crack in a piezoelectric plane using traction BIEM. *SID: Structural Integrity & Durability*, 1: 35-47.
- Ha, S.K.; Keilers, C.; Chang, F.K.** (1992): Finite element analysis of composite structures containing distributed piezoceramic sensors and actuators. *AIAA Journal*, 30: 772-780.
- Han, F.; Pan, E.; Roy, A.K.; Yue, Z.Q.** (2006): Responses of piezoelectric, transversally isotropic, functionally graded and multilayered half spaces to uniform circular surface loading. *CMES: Computer Modeling in Engineering & Sciences*, 14: 15-30.
- Hu, K.Q., Li, G.Q., Zhong, Z.** (2006) Fracture of a rectangular piezoelectromagnetic body. *Mech. Res. Comm.* 33: 482-492.
- Kuna, M.** (2006): Finite element analyses of cracks in piezoelectric structures – a survey. *Archives of Applied Mechanics*, 76: 725-745.

- Landau, L.D., Lifshitz, E.M.**, In: Lifshitz, E.M., Pitaevskii, L.P. (Eds.) *Electrodynamics of Continuous Media* (second edition), Pergamon Press, New York, 1984.
- Lee, J.S.** (1995): Boundary element method for electroelastic interaction in piezoceramics. *Engineering Analysis with Boundary Elements*, 15: 321-328.
- Li, J.Y.** (2000): Magneto-electroelastic multi-inclusion and inhomogeneity problems and their applications in composite materials. *International Journal of Engineering Science* 38: 1993-2011.
- Liew, K.M.; Lim, H.K.; Tan, M.J. ; He, X.Q.** (2002): Analysis of laminated composite beams and plates with piezoelectric patches using the element-free Galerkin method. *Computational Mechanics*, 29: 486-497.
- Liu, J.X., Liu, X.L., Zhao, Y.B.** (2001): Green's functions for anisotropic magneto-electro-elastic solids with an elliptical cavity or a crack. *International Journal of Engineering Sciences* 39: 1405-1418.
- Liu, G.R.; Dai, K.Y.; Lim, K.M.; Gu, Y.T.** (2002): A point interpolation mesh free method for static and frequency analysis of two-dimensional piezoelectric structures. *Computational Mechanics*, 29: 510-519.
- Loza, I.A., Shulga, N.A.** (1984): Axisymmetric vibrations of a hollow piezoceramic sphere with radial polarization. *Soviet Applied Mechanics*, 20: 113-117.
- Loza, I.A., Shulga, N.A.** (1990): Forced axisymmetric vibrations of a hollow piezoceramic sphere with an electrical method of excitation. *Soviet Applied Mechanics*, 26: 818-822.
- Nan, C.W.** (1994): Magneto-electric effect in composites of piezoelectric and piezomagnetic phases. *Phys. Rev. B*, 50: 6082-6088.
- Niraula, O.P., Wang, B.L.** (2006): A magneto-electro-elastic material with a penny-shaped crack subjected to temperature loading. *Acta Mechanica* 187: 151-168.
- Ohs, R.R.; Aluru, N.R.** (2001): Meshless analysis of piezoelectric devices. *Computational Mechanics*, 27: 23-36.
- Pan, E.** (1999): A BEM analysis of fracture mechanics in 2D anisotropic piezoelectric solids. *Engineering Analysis with Boundary Elements* 23, 67-76.
- Pan, E.** (2001) Exact solution for simply supported and multilayered magneto-electro-elastic plates. *ASME J. Applied Mechanics* 68: 608-618.
- Parton, V.Z., Kudryavtsev, B.A.** (1988): *Electromagnetoelasticity, Piezoelectrics and Electrically Conductive Solids*. Gordon and Breach Science Publishers, New York.
- Parton, V.Z.; Kudryavtsev, B.A.; Senik, N.A.** (1989): Electroelasticity. *Applied Mechanics: Soviet Review*, 2: 1-58.
- Saez, A., Garcia-Sanchez, F., Dominguez, J.** (2006): Hypersingular BEM for dynamic fracture in 2-D piezoelectric solids. *Computer Methods in Applied Mechanics and Engineering*, 196, pp. 235-246.

- Sellountos, E.J.; Polyzos, D.** (2003): A MLPG (LBIE) method for solving frequency domain elastic problems. *CMES: Computer Modeling in Engineering & Sciences*, 4: 619-636.
- Sellountos, E.J.; Vavourakis, V.; Polyzos, D.** (2005): A new singular/hypersingular MLPG (LBIE) method for 2D elastostatics. *CMES: Computer Modeling in Engineering & Sciences*, 7: 35-48.
- Shang, F., Wang, Z., Li, Z.** (1996): Thermal stress analysis of a three-dimensional crack in a thermopiezoelectric solid. *Engineering Fracture Mechanics*, 55: 737-750.
- Sheng, N.; Sze, K.Y.** (2006): Multi-region Trefftz boundary element method for fracture analysis in plane piezoelectricity. *Computational Mechanics*, 37: 381-393.
- Sladek, J.; Sladek, V.; Atluri, S.N.** (2000): Local boundary integral equation (LBIE) method for solving problems of elasticity with nonhomogeneous material properties. *Computational Mechanics*, 24: 456-462.
- Sladek, J.; Sladek, V.; Atluri, S.N.** (2001): A pure contour formulation for meshless local boundary integral equation method in thermoelasticity, *CMES: Computer Modeling in Engr. & Sciences*, 2: 423-434.
- Sladek, J.; Sladek, V.; Van Keer, R.** (2003a): Meshless local boundary integral equation method for 2D elastodynamic problems. *Int. J. Num. Meth. Engr.*, 57: 235-249
- Sladek, J.; Sladek, V.; Zhang, Ch.** (2003b): Application of meshless local Petrov-Galerkin (MLPG) method to elastodynamic problems in continuously nonhomogeneous solids. *CMES: Computer Modeling in Engr. & Sciences*, 4: 637-648.
- Sladek, J.; Sladek, V.; Atluri, S.N.** (2004): Meshless local Petrov-Galerkin method in anisotropic elasticity. *CMES: Computer Modeling in Engr. & Sciences*, 6: 477-489.
- Sladek, J.; Sladek, V.; Wen, P.H.; Aliabadi, M.H.** (2006a): Meshless Local Petrov-Galerkin (MLPG) Method for shear deformable shells analysis, *CMES: Computer Modeling in Engr. & Sciences*, 13: 103-118.
- Sladek, J.; Sladek, V.; Zhang, Ch.; Garcia-Sanchez, F.; Wunsche, M.** (2006b): Meshless local Petrov-Galerkin method for plane piezoelectricity. *CMC: Computers, Materials & Continua*, 4: 109-118.
- Sladek, J.; Sladek, V.; Zhang, Ch.; Solek, P.; Starek, L.** (2007a): Fracture analyses in continuously nonhomogeneous piezoelectric solids by the MLPG. *CMES: Computer Modeling in Engr. & Sciences*, 19: 247-262 .
- Sladek, J., Sladek, V., Zhang, Ch., Solek, P.** (2007b): Application of the MLPG to thermopiezoelectricity. *CMES: Computer Modeling in Engr. & Sciences*, 22: 217-233.
- Sladek, J., Sladek, V., Solek, P., Saez, A.** (2008): Dynamic 3-D Axisymmetric Problems in Continuously Nonhomogeneous Piezoelectric Solids, *International Journal of Solids and Structures* 45: 4523-4542.
- Song, Z.F., Sih, G.C.** (2003) Crack initiation behavior in magnetoelectroelastic composite under in-plane deformation. *Theoretical Applied Fracture Mechanics* 39: 189-207.

- Stehfest, H.** (1970): Algorithm 368: numerical inversion of Laplace transform. *Comm. Assoc. Comput. Mach.*, 13: 47-49.
- Suresh, S.; Mortensen A.** (1998): *Fundamentals of Functionally Graded Materials*. Institute of Materials, London.
- Tian, W.Y., Gabbert, U.** (2005) Macro-crack-micro-crack problem interaction problem in magneto-electroelastic solids. *Mech. Mater.* 37: 565-592.
- Tian, W.Y., Rajapakse, R.K.N.D.** (2005) Fracture analysis of magneto-electroelastic solids by using path independent integrals. *International Journal of Fracture* 131: 311-335.
- Tiersten, H.F.** (1969): *Linear Piezoelectric Plate Vibrations*, Plenum Press, New York.
- Tzou, H.S., Ye, R.** (1994): Piezothermoelasticity and precision control of piezoelectric systems: Theory and finite element analysis. *Journal of Vibration and Acoustics*, 116: 489-495.
- Wang, X., Shen, Y.P.** (2002): The general solution of three-dimensional problems in magneto-electroelastic media, *International Journal of Engineering Sciences* 40: 1069-1080.
- Wang, B.L., Mai, Y.W.** (2003): Crack tip field in piezoelectric/piezomagnetic media. *European Journal of Mechanics A/Solids* 22: 591-602.
- Wang, B.L., Han, J.C., Mai, Y.W.** (2006): Mode III fracture of a magneto-electroelastic layer: exact solution and discussion of the crack face electromagnetic boundary conditions. *International Journal of Fracture* 139: 27-38.
- Wang, B.L., Mai, Y.W.** (2007): Applicability of the crack-face electromagnetic boundary conditions for fracture of magneto-electroelastic materials. *Int. J. Solids Structures* 44: 387-398.
- Zhao, M.H., Yang, F., Liu, T.** (2006): Analysis of a penny-shaped crack in a magneto-electro-elastic medium. *Philos. Mag.* 86: 4397-4416.
- Zhou, Z.G., Wang, B., Sun, Y.G.** (2004): Two collinear interface cracks in magneto-electro-elastic composites. *International Journal of Engineering Sciences* 42: 1155-1167.
- Zhu, T.; Zhang, J.D.; Atluri, S.N.** (1998): A local boundary integral equation (LBIE) method in computational mechanics, and a meshless discretization approaches. *Computational Mechanics*, 21: 223-235.
- Zhu, X.; Wang, Z.; Meng, A.** (1995): A functionally gradient piezoelectric actuator prepared by metallurgical process in PMN-PZ-PT system. *J. Mater. Sci Lett.*, 14: 516-518.
- Zhu, B., Qin, T.** (2007): Application of hypersingular integral equation method to three-dimensional crack in electromagnetothermoelastic multiphase composites. *Int. J. Solids Structures* 44: 5994-6012.

# The Eulerian–Lagrangian method of fundamental solutions for two-dimensional unsteady Burgers’ equations

D.L. Young<sup>a,\*</sup>, C.M. Fan<sup>a</sup>, S.P. Hu<sup>a</sup>, S.N. Atluri<sup>b</sup>

<sup>a</sup>*Department of Civil Engineering and Hydrotech Research Institute, National Taiwan University, Taipei, Taiwan*

<sup>b</sup>*Department of Mechanical and Aerospace Engineering, University of California, Irvine, CA, USA*

Received 27 October 2006; accepted 17 August 2007

Available online 24 October 2007

## Abstract

The Eulerian–Lagrangian method of fundamental solutions is proposed to solve the two-dimensional unsteady Burgers’ equations. Through the Eulerian–Lagrangian technique, the quasi-linear Burgers’ equations can be converted to the characteristic diffusion equations. The method of fundamental solutions is then adopted to solve the diffusion equation through the diffusion fundamental solution; in the meantime the convective term in the Burgers’ equations is retrieved by the back-tracking scheme along the characteristics. The proposed numerical scheme is free from mesh generation and numerical integration and is a truly meshless method. Two-dimensional Burgers’ equations of one and two unknown variables with and without considering the disturbance of noisy data are analyzed. The numerical results are compared very well with the analytical solutions as well as the results by other numerical schemes. By observing these comparisons, the proposed meshless numerical scheme is convinced to be an accurate, stable and simple method for the solutions of the Burgers’ equations with irregular domain even using very coarse collocating points.

© 2007 Elsevier Ltd. All rights reserved.

**Keywords:** Eulerian–Lagrangian method; Method of fundamental solutions; Burgers’ equations; Diffusion fundamental solution; Meshless method

## 1. Introduction

The Burgers’ equation was initially studied for the weather problem in 1915 by Bateman [1] and was extended to model turbulence and shock wave by Burgers [2]. Besides, the Burgers’ equation is a useful model for many interesting physical problems [3], such as shock wave, acoustic transmission, traffic and aerofoil flow theory, turbulence and supersonic flow as well as a prerequisite to the Navier–Stokes equations. The problems modeled by the Burgers’ equation can be considered as an evolutionary process in which a convective phenomenon is in contrast with a diffusive phenomenon. It is possible to obtain the exact solutions of the Burger’s equation for simple geometry by the Cole–Hopf transformation [4,5]. The known exact solutions of the Burgers’ equation are tabulated by Benton and Platzman [6] as well as Fletcher [7].

Although there are some analytic solutions available in the literature, the exact solutions for the practical applications are very limited due to the complex geometry and complicated initial and boundary conditions. The numerical methods developed more than three decades seem to serve as a satisfactory alternative to solve the unsteady Burger’s equations. Most of the existing numerical methods in previous studies were reported successfully to be able to solve the Burgers’ equations, such as the finite difference method (FDM) [8–10], the finite element method (FEM) [11,12] and the boundary element method (BEM) [13,14]. For example, for the Burgers’ equation Bahadir [8] proposed a fully implicit finite difference scheme and Radwan [10] used a fourth-order compact scheme and the fourth-order Du Fort Frankel algorithm. In addition, Froncioni et al. [11] proposed the discontinuous-Galerkin space–time finite element formulation using the simplex-type meshes. In the meantime, Kutluay et al. [12] used the least-squares quadratic B-spline FEM to handle the unsteady Burgers’ equations. In comparing with FDM and FEM, the BEM appears to be a better alternative to

\*Corresponding author. Fax: +886 2 23626114.

E-mail address: [dlyoung@ntu.edu.tw](mailto:dlyoung@ntu.edu.tw) (D.L. Young).

simulate the physical problems due to the reduction of one dimension. Kakuda and Tosaka [14] adopted the generalized BEM to treat the Burgers' equations while Chino and Tosaka [13] used the dual reciprocity BEM. The numerical methods discussed above can be used to solve the unsteady Burgers' equations; however the large amount of efforts should be paid during the numerical implementation. The time-consuming mesh generation of FDM and FEM as

well as the complicated singular integrals of BEM always bothered researchers. The drawbacks make these conventional numerical methods very difficult to efficiently deal with the Burgers' equations especially for treating the nonlinear, multidimensional flows and irregular domain problems.

The developments of the so-called meshless or meshfree methods catch the researchers' attentions recently. There

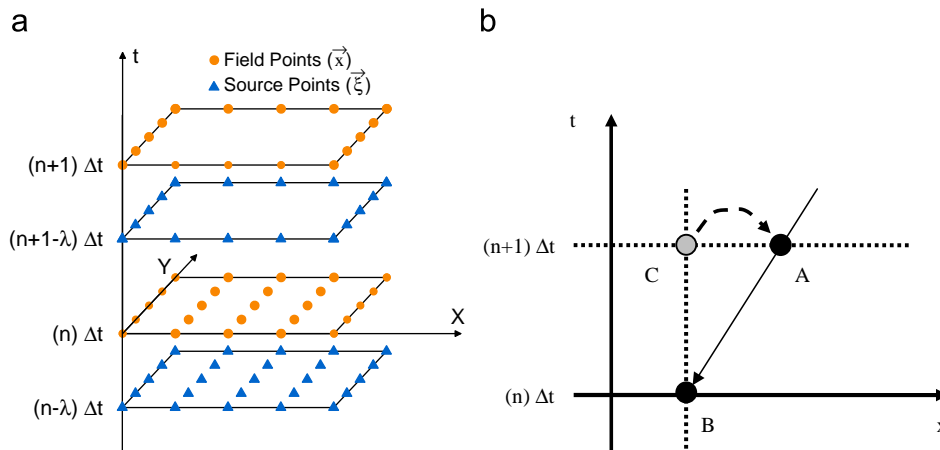


Fig. 1. (a) Schematic diagram for the location of source and field points on the space-time domain in 2-D problem. (b) Schematic diagram for the characteristic  $AB$ .

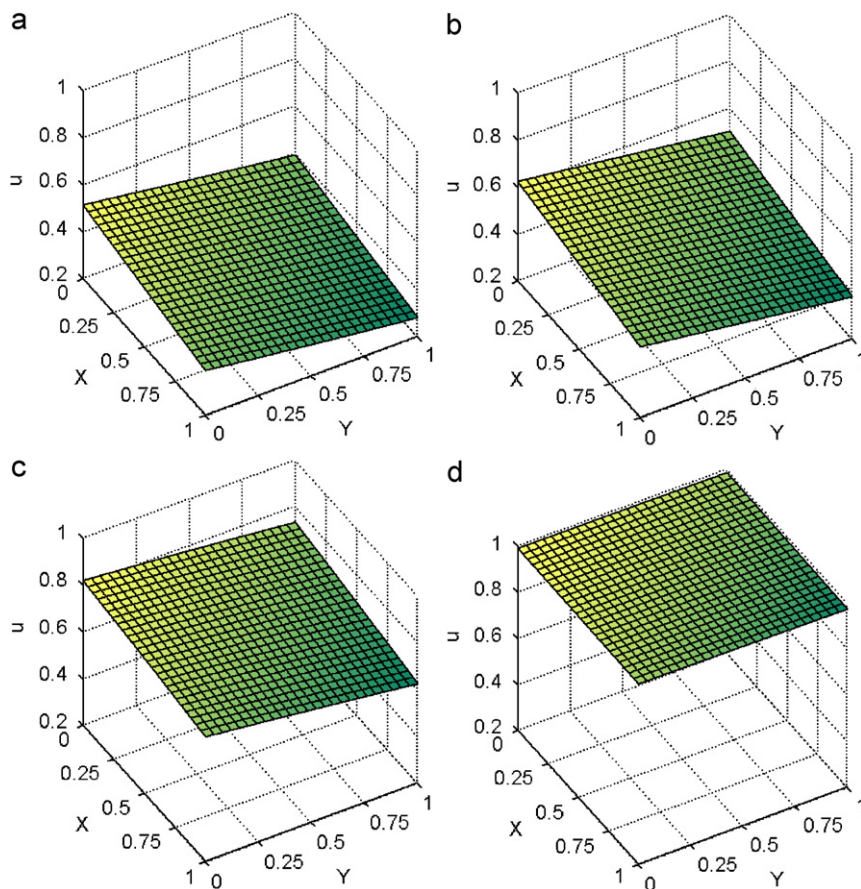


Fig. 2. Velocity profiles of problem 1 at different time levels ( $Re = 1$ ,  $\Delta t = 0.01$ ,  $N = 64$ ). (a)  $t = 0.10$ ; (b)  $t = 1.00$ ; (c)  $t = 3.00$ ; (d)  $t = 9.00$ .

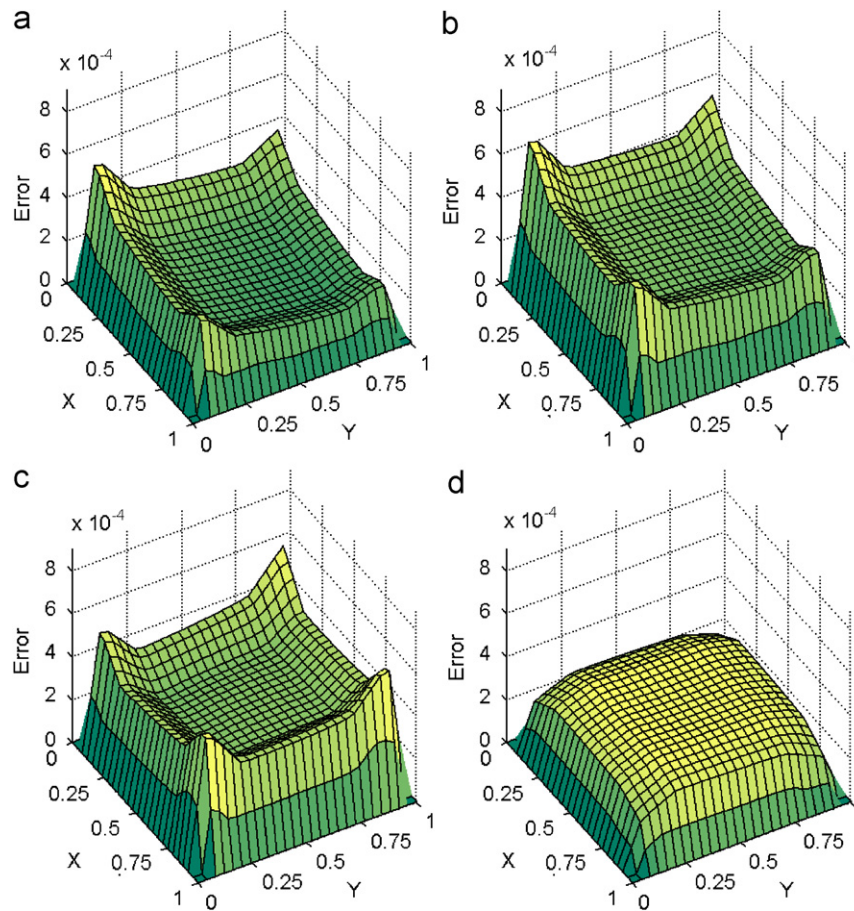


Fig. 3. Error profiles of problem 1 at different time levels ( $Re = 1$ ,  $\Delta t = 0.01$ ,  $N = 64$ ). (a)  $t = 0.10$ ; (b)  $t = 1.00$ ; (c)  $t = 3.00$ ; (d)  $t = 9.00$ .

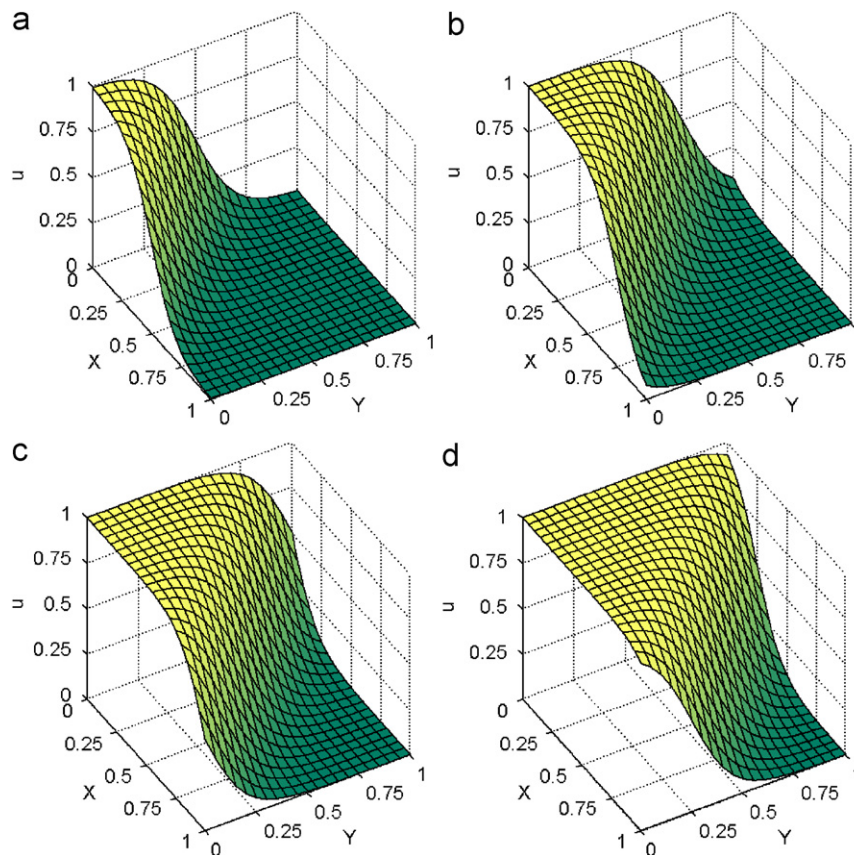


Fig. 4. Velocity profiles of problem 1 at different time levels ( $Re = 20$ ,  $\Delta t = 0.001$ ,  $N = 441$ ). (a)  $t = 0.50$ ; (b)  $t = 0.75$ ; (c)  $t = 1.00$ ; (d)  $t = 1.25$ .

are several meshless methods developed in the past decade and some available methods are the multiquadrics (MQ) method [15,16], the meshless local Petrov-Galerkin (MLPG) method [17–20] and the method of fundamental solutions (MFS) [21–29]. Hon and Mao [15] applied the MQ method to the one-dimensional unsteady Burgers' equation, while Li et al. [16] used the MQ method to solve two-dimensional problems. Though the MQ method can simply solve the Burgers' equations, the choice of a suitable shape parameter which will influence the stability of the numerical scheme is still an open topic. This handicap drastically limits the developments and applications of the MQ method. The MFS, which is similar to the BEM due to the reduction of one dimension, is free from the mesh generation and numerical integration. The MFS was originally proposed by Kupradze and Aleksidze [24] and has been extended to the solution of Poisson's equation by Golberg [21]. Karageorghis and Fairweather [23] adopted the MFS to model the biharmonic equation. On the other hand, Young and Ruan [26] analyzed the electromagnetic waves scattering problems by MFS, and Young et al. [27] used the Stokeslets and MFS to simulate the Stokes flow in a rectangular cavity with cylinders. Under the novel concept of time-space unification, Young et al. [28,29] solved the time-dependent diffusion equations by the

diffusion fundamental solution and MFS which can avoid the Laplace transform or finite difference method in discretizing the time state. The time-dependent MFS is further applied to the Stokes' first and second problems in a semi-infinite domain by Hu et al. [22].

The MFS is successfully applied to solve the linear diffusion equation since the numerical results are assumed to be the linear combination of the time-dependent diffusion fundamental solutions. Due to the existence of the convective term in the Burgers' equations, the MFS cannot be used directly for the Burgers' equations. The convective term of the unsteady Burgers' equation can be dealt with by the Eulerian–Lagrangian method (ELM) [25,30]. The ELM combines the computational powers of the Eulerian and Lagrangian approaches, so as to incorporate the merits of a fixed Eulerian coordinate and a moving Lagrangian coordinate. The combination of the ELM and BEM has been successfully applied to the advection–diffusion equations [30], while the same problems are also simulated by using the Eulerian–Lagrangian method of fundamental solutions (ELMFS) [25]. The use of ELM can be regarded as changing the physical viewpoint of the problem from a fixed to moving path. In this study, the Burgers' equations will be converted to the characteristic diffusion equations by ELM, and then

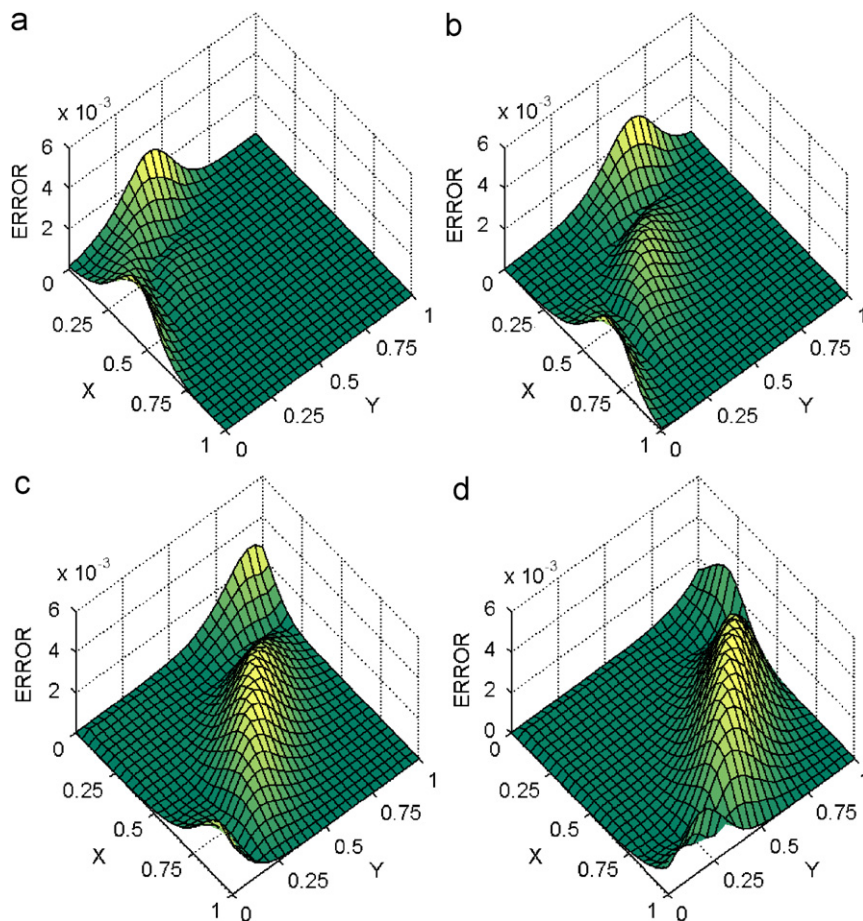


Fig. 5. Error profiles of problem 1 at different time levels ( $Re = 20$ ,  $\Delta t = 0.001$ ,  $N = 441$ ). (a)  $t = 0.50$ ; (b)  $t = 0.75$ ; (c)  $t = 1.00$ ; (d)  $t = 1.25$ .

Table 1

Numerical solutions of different time levels in some specific points of problem 1 ( $Re = 20$ ,  $\Delta t = 0.001$ ,  $N = 441$ )

x	y	t = 0.50				t = 0.75				t = 1.00				t = 1.25			
		Analytical solution	ELMFS	ERROR		Analytical solution	ELMFS	ERROR		Analytical solution	ELMFS	ERROR		Analytical solution	ELMFS	ERROR	
0.1	0.1	0.9526	0.9532	6.07E-04		0.9959	0.9961	1.70E-04		0.9997	0.9997	6.08E-06		1.0000	1.0000	3.29E-05	
0.5	0.1	0.2689	0.2694	4.66E-04		0.8176	0.8186	1.05E-03		0.9820	0.9822	1.95E-04		0.9985	0.9986	4.77E-05	
0.9	0.1	0.0067	0.0067	1.59E-06		0.0759	0.0759	6.60E-05		0.5000	0.5009	9.45E-04		0.9241	0.9248	6.38E-04	
0.3	0.3	0.2689	0.2686	3.79E-04		0.8176	0.8177	7.88E-05		0.9820	0.9821	9.11E-05		0.9985	0.9986	5.43E-05	
0.7	0.3	0.0067	0.0067	9.98E-07		0.0759	0.0756	2.55E-04		0.5000	0.4983	1.75E-03		0.9241	0.9238	2.99E-04	
0.1	0.5	0.2689	0.2694	4.66E-04		0.8176	0.8186	1.05E-03		0.9820	0.9822	1.95E-04		0.9985	0.9986	4.77E-05	
0.5	0.5	0.0067	0.0067	8.07E-06		0.0759	0.0753	5.18E-04		0.5000	0.4970	2.99E-03		0.9241	0.9235	6.45E-04	
0.9	0.5	0.0001	0.0001	2.00E-07		0.0015	0.0015	3.93E-06		0.0180	0.0179	1.18E-04		0.1824	0.1803	2.13E-03	
0.3	0.7	0.0067	0.0067	9.98E-07		0.0759	0.0756	2.55E-04		0.5000	0.4983	1.75E-03		0.9241	0.9238	2.99E-04	
0.7	0.7	0.0001	0.0001	1.95E-08		0.0015	0.0015	3.16E-06		0.0180	0.0178	1.82E-04		0.1824	0.1794	3.03E-03	
0.1	0.9	0.0067	0.0067	1.59E-06		0.0759	0.0759	6.60E-05		0.5000	0.5009	9.45E-04		0.9241	0.9248	6.38E-04	
0.5	0.9	0.0001	0.0001	2.00E-07		0.0015	0.0015	3.93E-06		0.0180	0.0179	1.18E-04		0.1824	0.1803	2.13E-03	
0.9	0.9	0.0000	0.0000	3.92E-08		0.0000	0.0000	2.40E-07		0.0003	0.0003	1.96E-06		0.0041	0.0040	5.04E-05	

the diffusion equations will be solved by the MFS. After the diffusion solutions are found by MFS, the convective term of the Burgers' equations can be obtained by the back-tracking scheme through the characteristics [25,30]. This ELMFS technique has been successfully applied to the one-dimensional unsteady Burgers' equations by Young [31].

The aim of this study is to demonstrate the capability and simplicity of the ELMFS to solve the unsteady nonlinear two-dimensional Burgers' equations. The governing equations and numerical method will be explained in Sections 2 and 3, respectively. The numerical results and conclusions will be provided, respectively, in Sections 4 and 5. There are three case study problems adopted in this article and the numerical results are compared very well with the analytical solutions as well as other numerical solutions.

## 2. Governing equations

The two-dimensional Burgers' equations with two variables are similar to the incompressible Navier–Stokes equations without considering pressure term and continuity equation. We will consider the following system of the two-dimensional Burgers' equations:

$$\frac{\partial u}{\partial t} + u \frac{\partial u}{\partial x} + v \frac{\partial u}{\partial y} = \frac{1}{Re} \left( \frac{\partial^2 u}{\partial x^2} + \frac{\partial^2 u}{\partial y^2} \right), \quad (1)$$

$$\frac{\partial v}{\partial t} + u \frac{\partial v}{\partial x} + v \frac{\partial v}{\partial y} = \frac{1}{Re} \left( \frac{\partial^2 v}{\partial x^2} + \frac{\partial^2 v}{\partial y^2} \right) \quad (2)$$

subject to the initial conditions:

$$u(x, y, t_0) = \phi_1(x, y) \quad (x, y) \in \Omega, \quad (3)$$

$$v(x, y, t_0) = \phi_2(x, y) \quad (x, y) \in \Omega \quad (4)$$

and the boundary conditions:

$$Lu(x, y, t) = \phi_3(x, y, t) \quad (x, y) \in \partial\Omega, \quad (5)$$

$$Lv(x, y, t) = \phi_4(x, y, t) \quad (x, y) \in \partial\Omega, \quad (6)$$

where  $\Omega$  and  $\partial\Omega$  denote the computational domain and the associated boundary.  $L$  is a boundary differential operator.  $u(x, y, t)$  and  $v(x, y, t)$  are the two unknown variables which can be regarded as the velocities in fluid-related problems.  $\phi_1(x, y)$ ,  $\phi_2(x, y)$ ,  $\phi_3(x, y, t)$  and  $\phi_4(x, y, t)$  are all known functions.  $Re$  is the Reynolds number, and  $t_0$  is the initial time.

According to the relative weighting of the diffusive and convective terms ( $Re$ ) in the Burgers' equations, the Burgers' equations will behave as elliptic, parabolic or hyperbolic type of partial differential equations.

## 3. Numerical method

The two-dimensional Burgers' equations, Eqs. (1) and (2), can be transferred to the following two characteristic

diffusion equations using the ELM:

$$\frac{Du}{Dt} = \frac{1}{Re} \left( \frac{\partial^2 u}{\partial x^2} + \frac{\partial^2 u}{\partial y^2} \right), \quad (7)$$

$$\frac{Dv}{Dt} = \frac{1}{Re} \left( \frac{\partial^2 v}{\partial x^2} + \frac{\partial^2 v}{\partial y^2} \right), \quad (8)$$

where the total or material derivative including the convective term is defined as [25,30]

$$\frac{D}{Dt} = \frac{\partial}{\partial t} + u \frac{\partial}{\partial x} + v \frac{\partial}{\partial y}. \quad (9)$$

Since the two-dimensional Burgers' equations are converted to the characteristic diffusion equations, the MFS

first adopted to solve the diffusion equations [28,29]. In MFS, the diffusion solution can be represented as the linear combination of the diffusion fundamental solutions with different source intensities. The fundamental solution of the linear diffusion equation is governed by

$$\frac{\partial G(\vec{x}, t; \vec{\xi}, \tau)}{\partial t} = \frac{1}{Re} \nabla^2 G(\vec{x}, t; \vec{\xi}, \tau) + \delta(\vec{x} - \vec{\xi}) \delta(t - \tau), \quad (10)$$

where  $G(\vec{x}, t; \vec{\xi}, \tau)$  is the fundamental solution of the linear diffusion equation.  $\vec{x} = (x, y)$  and  $\vec{\xi} = (\xi, \eta)$  are the spatial coordinates of the field and source points.  $t$  and  $\tau$  are the temporal coordinates of the field and source points.  $\delta()$  is the well-known Dirac delta function.

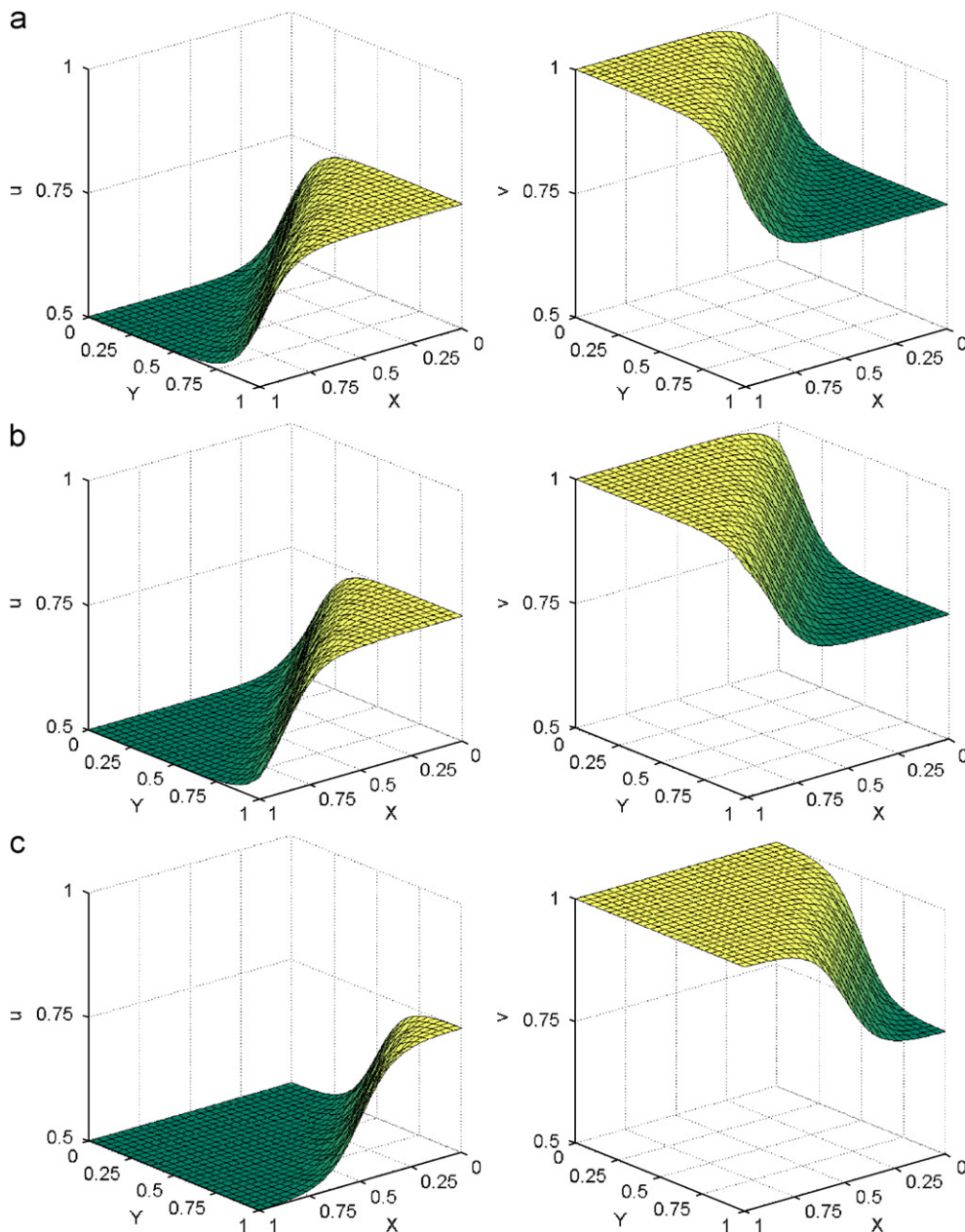


Fig. 6. Velocity profiles of problem 2 at different time levels ( $Re = 100$ ,  $\Delta t = 0.005$ ,  $N = 441$ ). (a)  $t = 0.01$ ; (b)  $t = 0.50$ ; (c)  $t = 2.00$ .

By using the integral transform theory of Eq. (10), the free-space Green's function or the fundamental solution of the linear diffusion equation can be obtained as

$$G(\vec{x}, t; \vec{\xi}, \tau) = \frac{e^{-|\vec{x}-\vec{\xi}|^2/[4(1/Re)(t-\tau)]}}{[4\pi(1/Re)(t-\tau)]^{d/2}} H(t-\tau), \quad (11)$$

where  $d$  is the dimension of the problem and is equal to two in this study.  $H()$  is the Heaviside step function.

Based on the time-dependent MFS concept, we can express the diffusion solutions of Eqs. (7) and (8) by the combination of the diffusion fundamental solutions,

Eq. (11), as

$$u(\vec{x}, t) = \sum_{j=1}^N \alpha_j G(\vec{x}, t; \vec{\xi}_j, \tau_j), \quad (12)$$

$$v(\vec{x}, t) = \sum_{j=1}^N \beta_j G(\vec{x}, t; \vec{\xi}_j, \tau_j), \quad (13)$$

where  $N$  is the number of source point.  $\alpha_j$  and  $\beta_j$  are the unknown coefficients which denote the source intensities of the corresponding fundamental solutions. Once the coefficients are obtained, the velocity of any field points in the

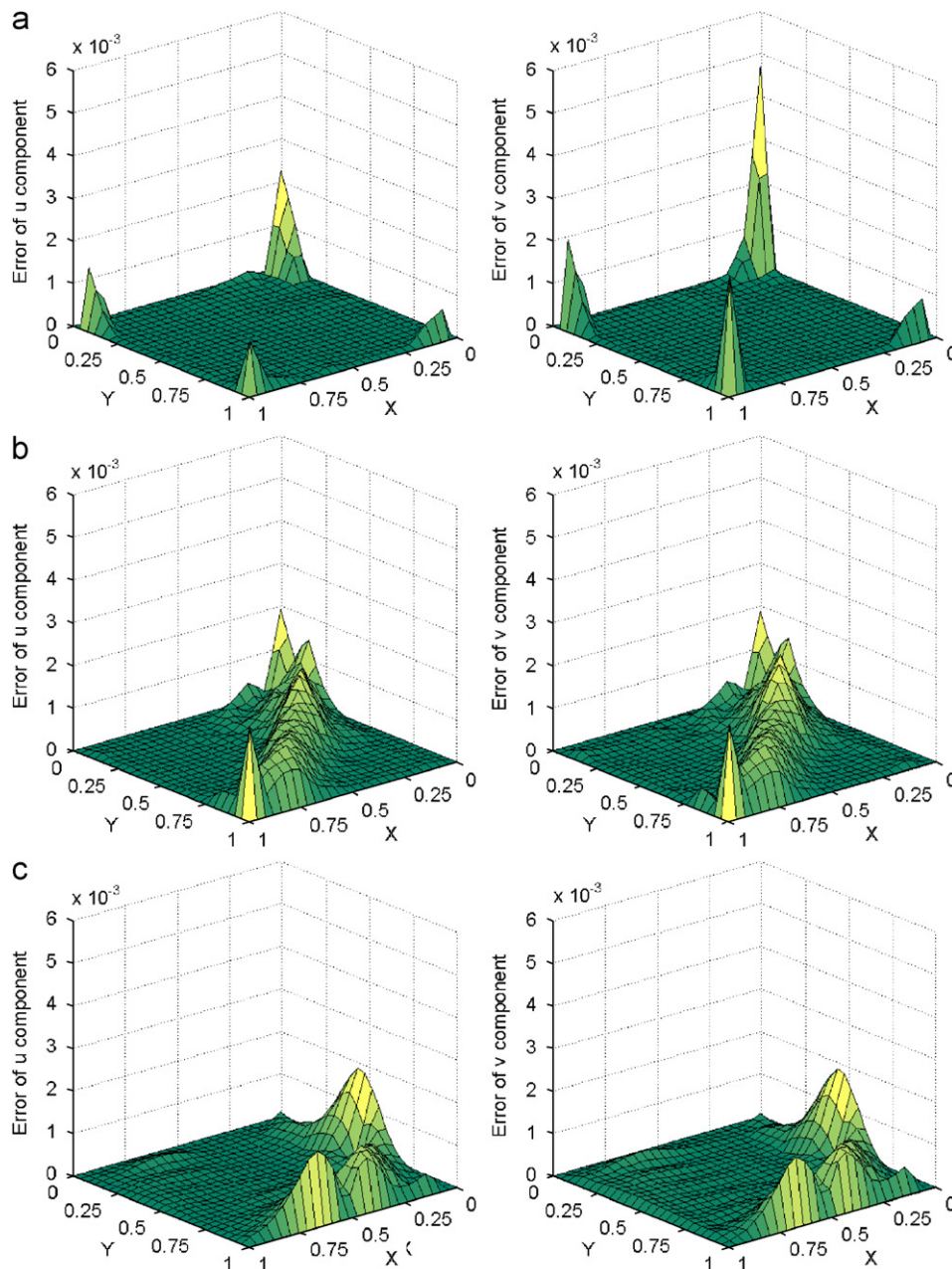


Fig. 7. Error profiles of problem 2 at different time levels ( $Re = 100$ ,  $\Delta t = 0.005$ ,  $N = 441$ ). (a)  $t = 0.01$ ; (b)  $t = 0.50$ ; (c)  $t = 2.00$ .

time–space domain can be acquired by using Eqs. (12) and (13) accordingly.

In our numerical experiments, the numbers of field and source points are chosen the same, and both are equal to  $N$  so that square matrices are formed. The locations of field and source points are illustrated in Fig. 1(a), and the field and source points are located at the same spatial positions but at different time levels. In Fig. 1(a), the parameter,  $\lambda$ , is chosen as a function of the maximum distance of the spatial domain ( $R$ ) and it can be expressed as  $\lambda(\Delta t) = \mu R$ . By observing the diffusion fundamental solution, it is noted that the temporal difference ( $t - \tau$ ) between field and source points is proportional to their spatial distance ( $|\vec{x} - \vec{\xi}|$ ). Hence we will use the empirical formula to determine the temporal location of the source points. In the section of numerical results, it will be elaborated that the proposed formula performs well and provides a useful guide to determine the time level of the source points.  $\mu$  is an adaptive parameter which can be chosen by the trial and error process. By collocating the initial and boundary conditions, two matrices are formed by utilizing Eqs. (3)–(6), (12) and (13):

$$[A_u]\{\alpha\} = [f_u], \quad (14)$$

$$[A_v]\{\beta\} = [f_v]. \quad (15)$$

The components of  $[A_u]$  and  $[A_v]$  are the representation of the fundamental solutions.  $\{f_u\}$  is the combination of  $\phi_1(x, y)$  and  $\phi_3(x, y, t)$ , and  $\{f_v\}$  is the combination of  $\phi_2(x, y)$  and  $\phi_4(x, y, t)$ . The unknown coefficients, or the source intensities of the fundamental solutions, can be obtained by inverting the above two matrices, Eqs. (14) and (15). The function values inside the time–space box at  $t = (n + 1)\Delta t$  can thus be acquired from Eqs. (12) and (13).

The results of the Burgers' equations with convective term can be retrieved from the numerical diffusion results by back-tracking the particles along the line of characteristics. In the ELM, the convective velocities in the Burgers' equations are expressed in terms of the spatial and time increments as follows:

$$u = \frac{dx}{dt} = \frac{x^{n+1} - x^n}{\Delta t}, \quad (16)$$

$$v = \frac{dy}{dt} = \frac{y^{n+1} - y^n}{\Delta t}, \quad (17)$$

$$x^n = x^{n+1} - u\Delta t, \quad (18)$$

$$y^n = y^{n+1} - v\Delta t. \quad (19)$$

In Fig. 1(b), the line AB is the characteristic path on which the transport of the scalar quantity can be traced. If the velocities at point A are required, the spatial location of point B can be traced by Eqs. (18) and (19). When the spatial location of point B is determined, the solutions along characteristics AB will follow the characteristic diffusion operators, Eqs. (7) and (8), according to the

material derivative and the diffusion equations. After the diffusion process is calculated by the time-dependent MFS, the velocities at point C can be obtained to represent the velocities at point A. Points B and C are located at the same spatial position but at different time levels (Fig. 1(b)). The velocities at point A are properly replaced by the diffusion results at point C, and then the results of the Burgers' equations at  $t = (n + 1)\Delta t$  thus can be acquired. This procedure can be repeated until either the terminal time or steady-state solution is achieved.

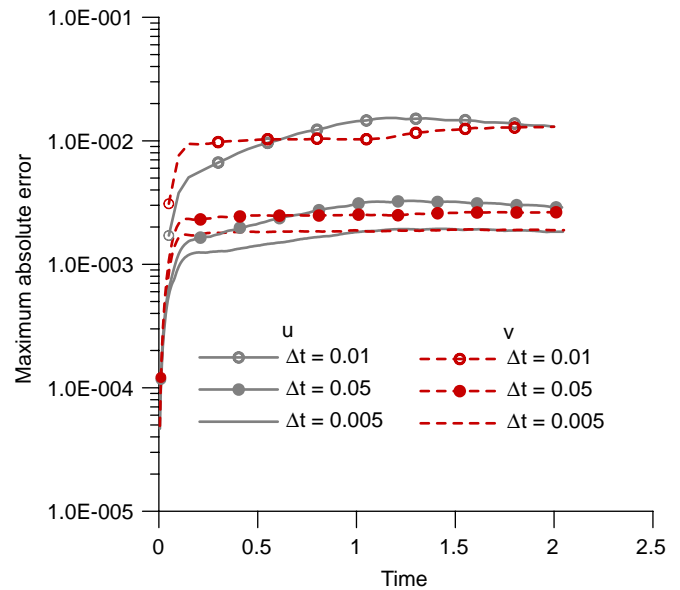


Fig. 8. Time history of maximum absolute errors of  $u$  and  $v$  of problem 2 for different size of time step ( $Re = 100$ ,  $N = 441$ ).

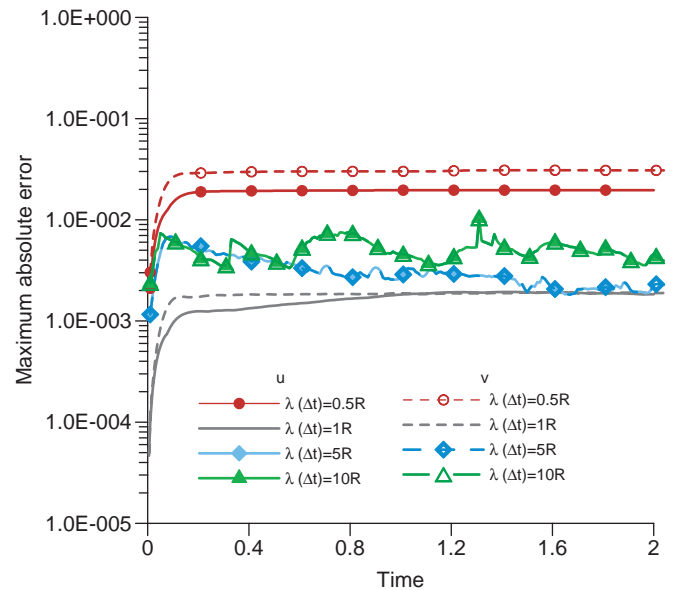


Fig. 9. Time evolution history of maximum absolute errors of  $u$  and  $v$  of problem 2 for temporal locations of source point ( $Re = 100$ ,  $N = 441$ ).

#### 4. Numerical results

To illustrate the high performance of ELMFS described in the previous section, three Burgers' problems will be considered. The first one is the two-dimensional Burgers' equation in one variable and the numerical results are compared with the analytical solutions. The second and the third ones are the two-dimensional Burgers' equations in two variables with regular and irregular domains. The results of the second problem are in good agreement with the analytical solutions and show better performance than the FDM [8]. In the second problem the study of the disturbance of noisy initial and boundary data is also taken into consideration. In order to demonstrate the flexibility of the ELMFS, the third problem is devoted to an irregular computational domain which is nontrivial by the conventional numerical methods.

##### 4.1. Problem 1

The first validation problem is the unsteady Burgers' equation in one variable which is described as below:

$$\frac{\partial u}{\partial t} + u \frac{\partial u}{\partial x} + u \frac{\partial u}{\partial y} = \frac{1}{Re} \left( \frac{\partial^2 u}{\partial x^2} + \frac{\partial^2 u}{\partial y^2} \right) \quad (20)$$

and the analytical solution is [16]

$$u(x, y, t) = \frac{1}{1 + \exp(Re(x + y - t)/2)}. \quad (21)$$

The computational domain is  $\Omega = \{(x, y) : 0 \leq x \leq 1, 0 \leq y \leq 1\}$ . The numerical results of velocity for  $Re = 1$  are shown in Fig. 2. The evolutionary process can be observed in the figure and the absolute errors are depicted in Fig. 3. Since the convective term is not large in comparing with the diffusion term, the diffusion process varies smoothly. The absolute errors in Fig. 3 are quite small, so it is proven that ELMFS can handle the Burgers' equation at low Reynolds number. Additionally, the numerical results in  $Re = 20$  are displayed in Fig. 4 and the absolute errors are depicted in Fig. 5. It is easy to find conspicuously a sharp gradient which moves with time in Fig. 4 as  $Re$  increases and the absolute errors in Fig. 5 also move with that front. The errors will occur near the sharp front in any numerical method and the absolute errors in this test are acceptable. The complete numerical results, absolute errors and analytical solutions are tabulated in Table 1. By observing the detailed comparison of numerical and analytical results, it is convinced that the proposed scheme is very simple, stable and accurate for the solutions of the Burgers' equation. There is no iteration

Table 2

Numerical solutions of (a)  $u$  and (b)  $v$  at different time levels in some specific points of problem 2 ( $Re = 10$ ,  $\Delta t = 0.01$ ,  $N = 441$ )

x	y	t = 0.01			t = 0.5			t = 2.0		
		Analytical solution	MFS	ERROR	Analytical solution	MFS	ERROR	Analytical solution	MFS	ERROR
(a)										
0.10	0.10	0.62481	0.62481	3.59E-07	0.61525	0.61526	3.10E-06	0.58716	0.58716	2.63E-06
0.50	0.10	0.59420	0.59420	2.05E-07	0.58540	0.58540	3.57E-06	0.56127	0.56127	2.80E-06
0.90	0.10	0.56708	0.56708	1.53E-07	0.55984	0.55984	2.15E-06	0.54113	0.54113	1.97E-06
0.30	0.30	0.62481	0.62480	3.26E-07	0.61525	0.61526	7.62E-06	0.58716	0.58717	6.02E-06
0.70	0.30	0.59420	0.59420	1.81E-07	0.58540	0.58540	6.44E-06	0.56127	0.56128	4.98E-06
0.10	0.50	0.65543	0.65543	3.04E-07	0.64628	0.64628	5.38E-06	0.61720	0.61720	5.17E-06
0.50	0.50	0.62480	0.62480	2.96E-07	0.61525	0.61527	1.14E-05	0.58716	0.58717	9.83E-06
0.90	0.50	0.59420	0.59420	1.75E-07	0.58540	0.58540	5.91E-06	0.56127	0.56128	5.12E-06
0.30	0.70	0.65543	0.65543	3.15E-07	0.64628	0.64629	1.13E-05	0.61720	0.61721	1.10E-05
0.70	0.70	0.62480	0.62480	2.76E-07	0.61525	0.61527	1.24E-05	0.58716	0.58717	1.22E-05
0.10	0.90	0.68261	0.68261	3.13E-07	0.67481	0.67482	4.77E-06	0.64817	0.64817	5.26E-06
0.50	0.90	0.65543	0.65543	3.10E-07	0.64628	0.64629	1.02E-05	0.61720	0.61721	1.09E-05
0.90	0.90	0.62480	0.62481	3.07E-07	0.61525	0.61526	6.57E-06	0.58716	0.58717	6.73E-06
(b)										
0.10	0.10	0.87520	0.87520	1.98E-07	0.88475	0.88475	9.89E-07	0.91284	0.91284	1.71E-06
0.50	0.10	0.90580	0.90580	1.82E-07	0.91460	0.91461	6.70E-07	0.93873	0.93873	1.73E-06
0.90	0.10	0.93292	0.93292	4.56E-09	0.94016	0.94016	1.39E-06	0.95887	0.95887	2.22E-06
0.30	0.30	0.87520	0.87520	2.74E-07	0.88475	0.88474	3.35E-06	0.91284	0.91284	1.06E-06
0.70	0.30	0.90580	0.90580	2.24E-07	0.91460	0.91460	2.90E-06	0.93873	0.93873	4.00E-07
0.10	0.50	0.84457	0.84457	3.73E-07	0.85372	0.85372	1.66E-06	0.88280	0.88280	2.98E-07
0.50	0.50	0.87520	0.87519	3.13E-07	0.88475	0.88474	7.58E-06	0.91284	0.91283	4.37E-06
0.90	0.50	0.90580	0.90580	2.32E-07	0.91460	0.91460	3.21E-06	0.93873	0.93873	9.19E-07
0.30	0.70	0.84457	0.84457	3.69E-07	0.85372	0.85372	7.51E-06	0.88280	0.88280	6.12E-06
0.70	0.70	0.87520	0.87519	3.42E-07	0.88475	0.88474	9.96E-06	0.91284	0.91283	7.09E-06
0.10	0.90	0.81739	0.81739	2.29E-07	0.82519	0.82519	6.48E-07	0.85183	0.85183	4.19E-07
0.50	0.90	0.84457	0.84457	3.61E-07	0.85372	0.85372	7.91E-06	0.88280	0.88280	6.89E-06
0.90	0.90	0.87520	0.87520	2.83E-07	0.88475	0.88474	4.23E-06	0.91284	0.91284	2.69E-06

process required by the ELMFS as far as the nonlinear Burgers’ problem is concerned

#### 4.2. Problem 2

The second validation problem is the unsteady Burgers’ equations in two variables, Eqs. (1) and (2). The analytical solutions can be obtained by the Cole–Hopf transformation [4,5,7] and have been used as a test problem by Bahadir [8]:

$$u(x,y,t)=\frac{3}{4}-\frac{1}{4[1+\exp((-4x+4y-t)(Re/32))]}, \quad (22)$$

$$v(x,y,t)=\frac{3}{4}+\frac{1}{4[1+\exp((-4x+4y-t)(Re/32))]}.\quad (23)$$

The computational domain is  $\Omega=\{(x,y):0\leq x\leq 1,0\leq y\leq 1\}$ . The initial and boundary conditions are taken from the analytical solutions. The numerical results are shown in Fig. 6 when  $Re=100$ . It is noted that there are sharp gradients which move toward the same direction in the  $u$  and  $v$  distributions, respectively. The nonlinear term dominates the evolutionary process and there appears a wave-like profile in Fig. 6 at  $Re=100$ . The absolute errors are displayed in Fig. 7 and the same phenomenon is revealed clearly that errors will move with the fronts. The

Table 3  
Numerical solutions of  $u$  at different time levels in some specific points of problem 2 ( $Re=100, \Delta t=0.005$ )

x	y	Analytical solution	$N = 11 \times 11$		$N = 21 \times 21$		$N = 21 \times 21$	
			ELMFS	ERROR	ELMFS	ERROR	FDM [8]	ERROR
$t = 0.01$								
0.1	0.1	0.62305	0.62323	1.87E−04	0.62229	7.58E−04	0.62310	5.30E−05
0.5	0.1	0.50162	0.50141	2.11E−04	0.50154	8.37E−05	0.50161	1.21E−05
0.9	0.1	0.50001	0.50035	3.36E−04	0.49995	6.01E−05	0.50000	1.10E−05
0.3	0.3	0.62305	0.62306	1.79E−05	0.62308	2.98E−05	0.62311	6.30E−05
0.7	0.3	0.50162	0.50201	3.84E−04	0.50164	2.17E−05	0.50162	2.07E−06
0.1	0.5	0.74827	0.74863	3.59E−04	0.74826	1.27E−05	0.74827	4.04E−06
0.5	0.5	0.62305	0.62321	1.60E−04	0.62307	2.68E−05	0.62311	6.30E−05
0.9	0.5	0.50162	0.50143	1.95E−04	0.50159	3.68E−05	0.50162	2.07E−06
0.3	0.7	0.74827	0.74774	5.39E−04	0.74827	7.19E−06	0.74827	4.04E−06
0.7	0.7	0.62305	0.62302	2.56E−05	0.62308	3.53E−05	0.62311	6.30E−05
0.1	0.9	0.74999	0.74969	2.94E−04	0.74992	6.74E−05	0.74998	8.29E−06
0.5	0.9	0.74827	0.74854	2.71E−04	0.74826	1.29E−05	0.74827	4.04E−06
0.9	0.9	0.62305	0.62305	1.04E−06	0.62269	3.62E−04	0.62311	6.30E−05
$t = 0.5$								
0.1	0.1	0.54332	0.53566	7.66E−03	0.54241	9.12E−04	0.54235	9.72E−04
0.5	0.1	0.50035	0.50150	1.14E−03	0.50024	1.17E−04	0.49964	7.13E−04
0.9	0.1	0.50000	0.50432	4.32E−03	0.49999	7.65E−06	0.49931	6.92E−04
0.3	0.3	0.54332	0.54905	5.73E−03	0.54427	9.48E−04	0.54207	1.25E−03
0.7	0.3	0.50035	0.50193	1.58E−03	0.50030	5.40E−05	0.49961	7.43E−04
0.1	0.5	0.74221	0.73665	5.56E−03	0.74222	4.84E−06	0.74130	9.14E−04
0.5	0.5	0.54332	0.54347	1.51E−04	0.54366	3.39E−04	0.54222	1.10E−03
0.9	0.5	0.50035	0.50025	9.80E−05	0.50030	5.60E−05	0.49997	3.83E−04
0.3	0.7	0.74221	0.74263	4.14E−04	0.74220	1.51E−05	0.74145	7.64E−04
0.7	0.7	0.54332	0.54331	1.08E−05	0.54367	3.45E−04	0.54243	8.92E−04
0.1	0.9	0.74995	0.75128	1.34E−03	0.74991	3.92E−05	0.74913	8.16E−04
0.5	0.9	0.74221	0.74218	3.82E−05	0.74230	8.93E−05	0.74201	2.04E−04
0.9	0.9	0.54332	0.54338	5.66E−05	0.54377	4.44E−04	0.54232	1.00E−03
$t = 2.0$								
0.1	0.1	0.50048	0.49845	2.03E−03	0.50012	3.59E−04	0.49983	6.52E−04
0.5	0.1	0.50000	0.50142	1.41E−03	0.49996	3.95E−05	0.49930	7.03E−04
0.9	0.1	0.50000	0.50201	2.01E−03	0.49995	4.57E−05	0.49930	7.00E−04
0.3	0.3	0.50048	0.49020	1.03E−02	0.50042	6.05E−05	0.49977	7.12E−04
0.7	0.3	0.50000	0.49589	4.11E−03	0.49999	1.53E−05	0.49930	7.03E−04
0.1	0.5	0.55568	0.55469	9.86E−04	0.55516	5.15E−04	0.55461	1.07E−03
0.5	0.5	0.50048	0.49774	2.74E−03	0.50041	7.31E−05	0.49973	7.52E−04
0.9	0.5	0.50000	0.49878	1.22E−03	0.49999	1.18E−05	0.49931	6.93E−04
0.3	0.7	0.55568	0.56310	7.42E−03	0.55587	1.95E−04	0.55429	1.39E−03
0.7	0.7	0.50048	0.49998	4.98E−04	0.50045	3.45E−05	0.49970	7.82E−04
0.1	0.9	0.74426	0.74114	3.12E−03	0.74416	9.21E−05	0.74340	8.56E−04
0.5	0.9	0.55568	0.55848	2.81E−03	0.55637	6.95E−04	0.55413	1.55E−03
0.9	0.9	0.50048	0.50063	1.44E−04	0.50051	2.69E−05	0.50001	4.72E−04

maximum absolute errors of  $u$  and  $v$  at three different time increments are shown in Fig. 8. When a smaller time step is used, the numerical accuracy is systematically improved. It seems that only accuracy instead of stability problem is involved in the selection of time step. At the previous section, we suggest that the time level of source points can be determined by the empirical function  $\lambda(\Delta t) = \mu R$ . When  $\mu$  is set to 0.5, 1, 5 or 10 and  $R$  is equal to  $\sqrt{2}$ , the results of time history of maximum absolute errors are demonstrated in Fig. 9. The numerical solution with  $\mu = 0.5$  is the worst one and the result with  $\mu = 1$  is the best case in this numerical test. Therefore, we suggest choosing  $\mu = 1$  and all numerical results in this investigation are obtained by

$\mu = 1$ . The numerical results in this study show that the empirical formula is very useful and provides a valuable guide to determine the optimal temporal location of the source point in the unsteady MFS. The theoretical study and more numerical tests of the proposed formula will be thoroughly examined in the future research.

The detailed velocity results and associated errors at some specified points are listed in Table 2 for  $Re = 10$  and the proposed numerical scheme is very stable and accurate when the evolutionary process happened. The results of  $u$  and  $v$  components for  $Re = 100$  are listed in Tables 3 and 4, respectively, and the problem is also solved by FDM [8]. The numerical computations were preformed using

Table 4

Numerical solutions of  $v$  at different time levels in some specific points of problem 2 ( $Re = 100$ ,  $\Delta t = 0.005$ )

x	y	Analytical solution	$N = 11 \times 11$		$N = 21 \times 21$		$N = 21 \times 21$	
			ELMFS	ERROR	ELMFS	ERROR	FDM [8]	ERROR
$t = 0.01$								
0.1	0.1	0.87695	0.87678	1.75E-04	0.87750	5.51E-04	0.87688	7.30E-05
0.5	0.1	0.99838	0.99860	2.20E-04	0.99836	1.84E-05	0.99837	7.93E-06
0.9	0.1	0.99999	0.99966	3.28E-04	0.99988	1.06E-04	0.99998	9.00E-06
0.3	0.3	0.87695	0.87694	1.72E-05	0.87694	1.56E-05	0.87689	6.30E-05
0.7	0.3	0.99838	0.99799	3.84E-04	0.99837	5.37E-06	0.99838	2.07E-06
0.1	0.5	0.75173	0.75137	3.52E-04	0.75164	8.13E-05	0.75172	5.96E-06
0.5	0.5	0.87695	0.87679	1.59E-04	0.87692	2.92E-05	0.87689	6.30E-05
0.9	0.5	0.99838	0.99857	1.95E-04	0.99836	1.46E-05	0.99838	2.07E-06
0.3	0.7	0.75173	0.75227	5.39E-04	0.75175	2.46E-05	0.75173	4.04E-06
0.7	0.7	0.87695	0.87698	2.53E-05	0.87694	1.52E-05	0.87689	6.30E-05
0.1	0.9	0.75001	0.75031	2.99E-04	0.74993	7.84E-05	0.75001	1.71E-06
0.5	0.9	0.75173	0.75145	2.73E-04	0.75170	2.97E-05	0.75173	4.04E-06
0.9	0.9	0.87695	0.87695	2.96E-06	0.87723	2.74E-04	0.87689	6.30E-05
$t = 0.5$								
0.1	0.1	0.95668	0.96467	7.99E-03	0.95717	4.93E-04	0.95577	9.08E-04
0.5	0.1	0.99965	0.99878	8.67E-04	0.99952	1.24E-04	0.99827	1.38E-03
0.9	0.1	1.00000	0.99592	4.07E-03	0.99974	2.60E-04	0.99861	1.39E-03
0.3	0.3	0.95668	0.95127	5.41E-03	0.95551	1.16E-03	0.95596	7.18E-04
0.7	0.3	0.99965	0.99834	1.30E-03	0.99952	1.23E-04	0.99827	1.38E-03
0.1	0.5	0.75779	0.76366	5.87E-03	0.75748	3.01E-04	0.75699	7.96E-04
0.5	0.5	0.95668	0.95667	3.55E-06	0.95621	4.73E-04	0.95685	1.72E-04
0.9	0.5	0.99965	0.99990	2.52E-04	0.99957	8.09E-05	0.99903	6.17E-04
0.3	0.7	0.75779	0.75763	1.58E-04	0.75760	1.86E-04	0.75723	5.56E-04
0.7	0.7	0.95668	0.95669	1.61E-05	0.95632	3.58E-04	0.95746	7.82E-04
0.1	0.9	0.75005	0.74897	1.09E-03	0.74984	2.15E-04	0.74924	8.14E-04
0.5	0.9	0.75779	0.75786	6.92E-05	0.75769	9.33E-05	0.75781	2.40E-05
0.9	0.9	0.95668	0.95661	6.97E-05	0.95630	3.79E-04	0.95777	1.09E-03
$t = 2.0$								
0.1	0.1	0.99952	1.00191	2.40E-03	0.99946	6.02E-05	0.99826	1.26E-03
0.5	0.1	1.00000	0.99902	9.72E-04	0.99980	1.95E-04	0.99860	1.40E-03
0.9	0.1	1.00000	0.99845	1.55E-03	0.99978	2.18E-04	0.99861	1.39E-03
0.3	0.3	0.99952	1.01020	1.07E-02	0.99938	1.42E-04	0.99820	1.32E-03
0.7	0.3	1.00000	1.00454	4.54E-03	0.99984	1.56E-04	0.99860	1.40E-03
0.1	0.5	0.94432	0.94571	1.38E-03	0.94450	1.70E-04	0.94393	3.95E-04
0.5	0.5	0.99952	1.00268	3.16E-03	0.99941	1.07E-04	0.99821	1.31E-03
0.9	0.5	1.00000	1.00164	1.64E-03	0.99984	1.56E-04	0.99862	1.38E-03
0.3	0.7	0.94432	0.93727	7.06E-03	0.94387	4.56E-04	0.94409	2.35E-04
0.7	0.7	0.99952	1.00043	9.14E-04	0.99937	1.47E-04	0.99823	1.29E-03
0.1	0.9	0.75574	0.75928	3.54E-03	0.75558	1.66E-04	0.75500	7.44E-04
0.5	0.9	0.94432	0.94188	2.45E-03	0.94345	8.72E-04	0.94441	8.50E-05
0.9	0.9	0.99952	0.99977	2.49E-04	0.99938	1.42E-04	0.99846	1.06E-03

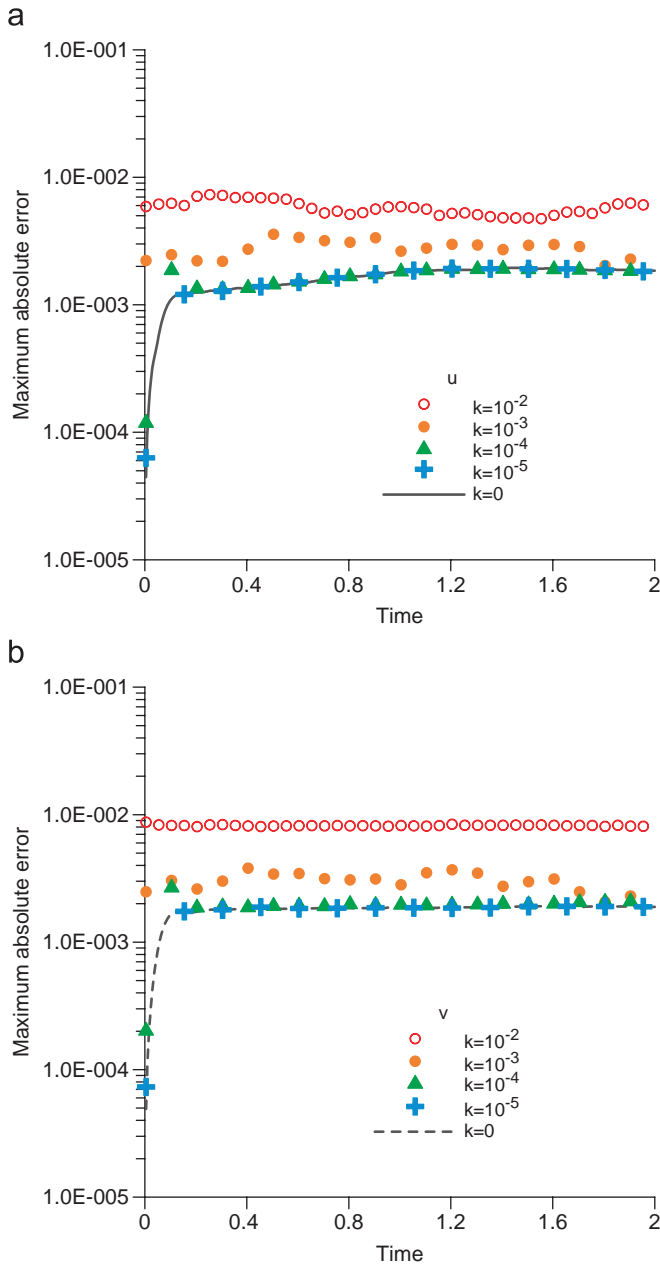


Fig. 10. Time history of maximum absolute errors of (a)  $u$  and (b)  $v$  on the problem 2 with noisy data at  $Re = 100$  ( $\Delta t = 0.005$ ,  $N = 441$ ).

uniform node distribution, with the number of nodes  $N = 121$  and  $441$ , respectively. The last columns in both Tables 3 and 4 show the numerical results by FDM [8] with a uniform mesh  $21 \times 21$ . By examining those results, the solution obtained by ELMFS is more accurate than FDM [8]. Even using only 121 coarse collocating points the ELMFS results have reached acceptable accuracy.

Furthermore, we consider the problem with noisy initial and boundary data as follows:

$$u(x, y, 0) = (1 + k\varepsilon) \left\{ \frac{3}{4} - \frac{1}{4[1 + \exp((-4x + 4y)(Re/32))]} \right\} \quad (x, y) \in \Omega, \quad (24)$$

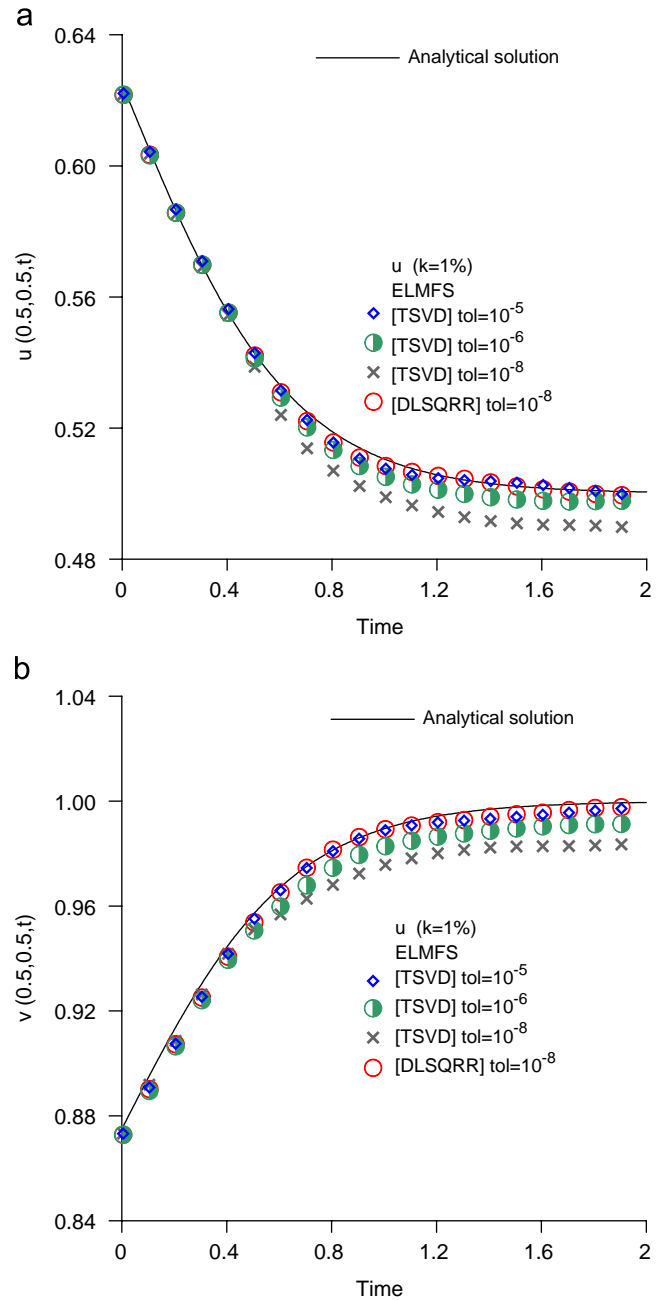


Fig. 11. Time history of (a)  $u$  and (b)  $v$  at  $(0.5, 0.5)$  on problem 2 with noisy data at  $Re = 100$  ( $\Delta t = 0.005$ ,  $N = 441$ ).

$$v(x, y, 0) = (1 + k\varepsilon) \left\{ \frac{3}{4} + \frac{1}{4[1 + \exp((-4x + 4y)(Re/32))]} \right\} \quad (x, y) \in \Omega, \quad (25)$$

$$u(x, y, t) = (1 + k\varepsilon) \left\{ \frac{3}{4} - \frac{1}{4[1 + \exp((-4x + 4y - t)/(Re/32))]} \right\} \quad (x, y) \in \partial\Omega, \quad (26)$$

$$v(x, y, t) = (1 + k\varepsilon) \left\{ \frac{3}{4} + \frac{1}{4[1 + \exp((-4x + 4y - t)/(Re/32))]} \right\} \quad (x, y) \in \partial\Omega, \quad (27)$$

where  $\varepsilon$  is a uniformly distributed random number and  $-1 \leq \varepsilon \leq 1$ . And  $k$  is the amplitude of noise level. These random numbers are generated by the FORTRAN subroutine RANDOM\_SEED. In our numerical experiment, we solve the problems with noise levels from  $k = 10^{-5}$  to  $10^{-2}$ . The maximum absolute errors of  $u$  and  $v$  are shown in Fig. 10 for different  $k$ . When the amplitude of  $k$  is smaller than  $10^{-2}$ , the results are accurate. For larger values of  $k$  (1%), the results are not as good as solutions with smaller  $k$  but still acceptable (within 1% error). In this test, the proposed ELMFS without regularization methods

can be used to successfully analyze problems with moderate noise level up to  $k = 10^{-2}$ . The same conjecture was also observed when the MFS is used to solve the Laplace equations with the moderate noise level [32]. This demonstrates that the present ELMFS is superior to other numerical methods as far as dealing with moderate noise level is concerned.

For larger noise disturbance we also consider the regularization methods to improve the accuracy of numerical results for  $k = 10^{-2}$ . Marin et al. [33] indicated that more accurate results could be obtained if the singular value decomposition (SVD) technique was used. Fig. 11 shows the time evolution of  $u$  and  $v$  at  $(0.5, 0.5)$  by the truncated SVD (TSVD) and QR decomposition with the regularization. The results of TSVD are obtained by the NUMERICAL RECIPES [34] subroutine SVDCMP; and the results of QR decomposition are found by the FORTRAN subroutine DLSQRR. In addition,  $tol$  is a parameter to be assigned. For TSVD, it means the singular value smaller than  $tol$  of matrix is allowed to be zero. For DLSQRR, it means the tolerance  $tol$  used to determine the

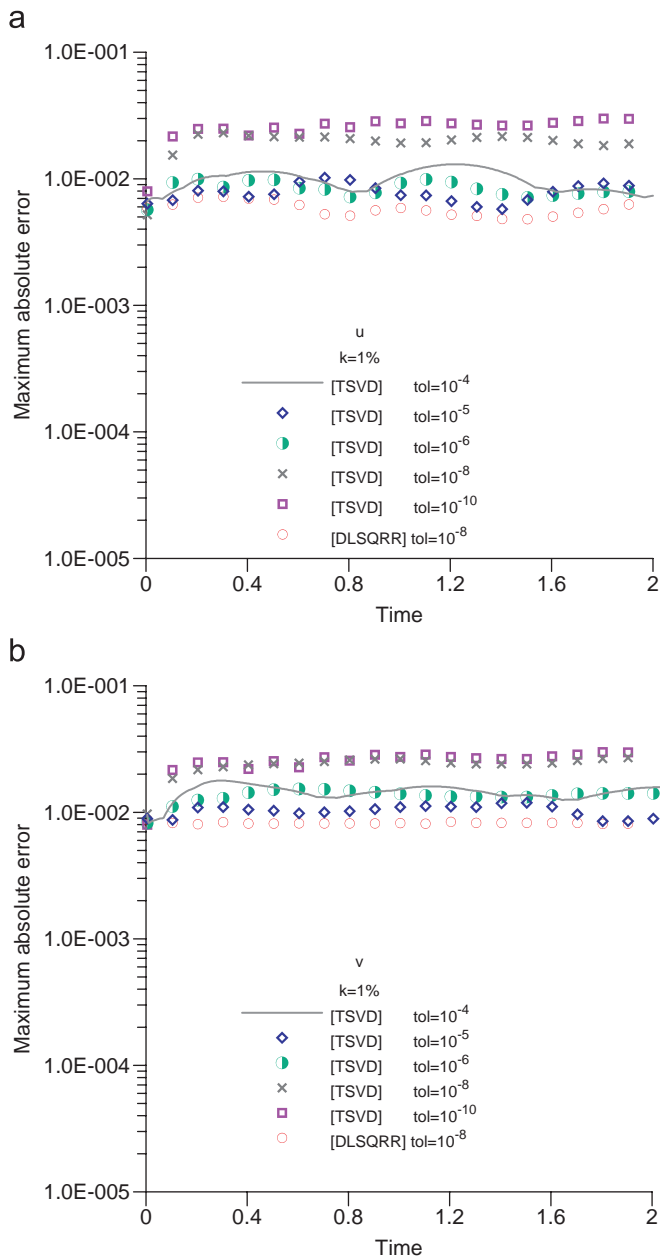


Fig. 12. Time history of maximum absolute errors of (a)  $u$  and (b)  $v$  on problem 2 for the amplitude of noise  $k = 1\%$  at  $Re = 100$  ( $\Delta t = 0.005$ ,  $N = 441$ ).

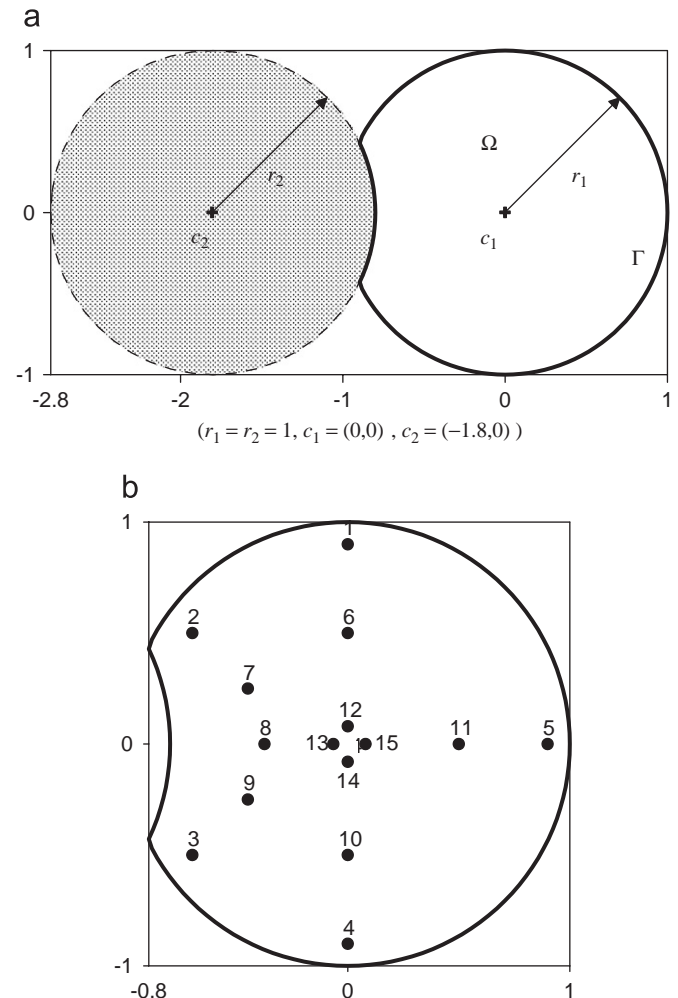


Fig. 13. (a) Computational domain of problem 3 (b) Distribution of some specific points of problem 3 for comparison.

subset of columns of matrix is included in the solution. Fig. 12 shows the maximum absolute errors of  $u$  and  $v$  by TSVD and QR decomposition (DLSQRR). Those figures indicate that the regularization by TSVD did not improve much numerical accuracy as DLSQRR did. Therefore, we conclude that the DLSQRR is a powerful algorithm to solve matrices in the regularization process. In summary, this ELMFS technique will produce accurate and stable solutions with or without regularization for the studied level of noise added into the data.

#### 4.3. Problem 3

After validating the above two problems by analytic solutions with and without noise consideration, it is found

that the ELMFS can handle the evolutionary process of the two-dimensional unsteady Burgers' equations in the regular domain. Even in the second problem, the ELMFS will give more accurate results than the FDM. In order to demonstrate the flexibility of the meshless method, the computational domain is chosen as an irregular one as shown in Fig. 13(a). The Burgers' equations in such an irregular domain are difficult to be handled by mesh-dependent methods, such as FDM or FEM. The analytical solution is the same as the one which is used in problem 2. The initial and boundary conditions are taken from the analytical solutions. The  $u, v$  results and absolute errors for  $Re = 100$  are present in Figs. 14 and 15, respectively. The fronts moved in the same direction as we expected and the absolute errors also moved with that front. To examine

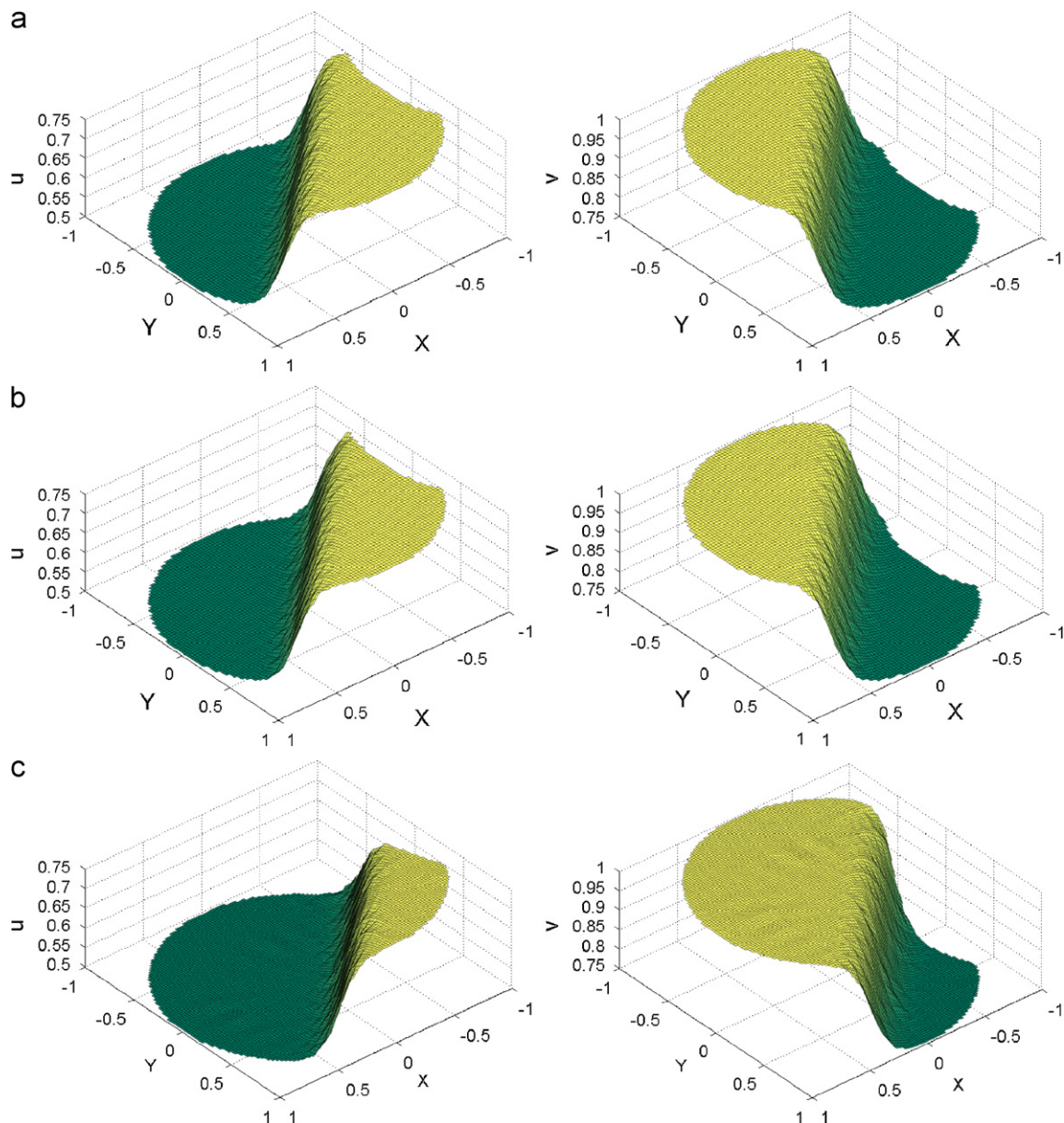


Fig. 14. Velocity profiles of problem 3 at different time levels ( $Re = 100$ ,  $\Delta t = 0.005$ ,  $N = 364$ ). (a)  $t = 0.01$ ; (b)  $t = 0.50$ ; (c)  $t = 2.00$ .

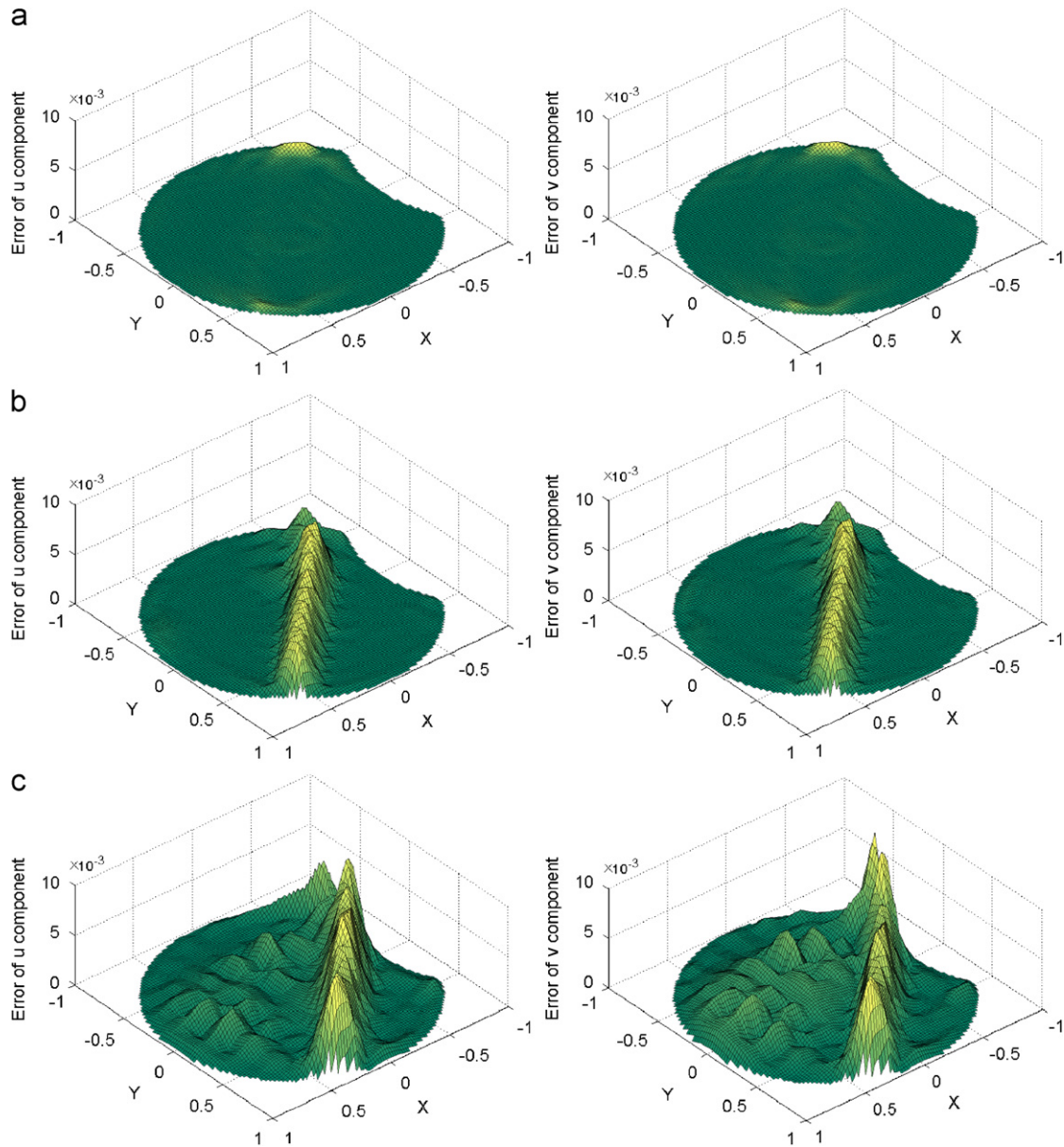


Fig. 15. Error profiles of problem 3 at different time levels ( $Re = 100$ ,  $\Delta t = 0.005$ ,  $N = 364$ ). (a)  $t = 0.01$ ; (b)  $t = 0.50$ ; (c)  $t = 2.00$ .

more seriously, the velocities and absolute errors at some specific points, which are drawn in Fig. 13(b), are recorded in Tables 5 and 6 for  $Re = 10$  and  $100$ , respectively. Those results are very accurate even in an irregular domain by inspecting these solutions in the tables. The proposed ELMFS can render the correct results in an irregular domain even using very coarse collocating points, and then it is proven that this method is a simple, stable and accurate scheme due to the features of meshless method.

## 5. Conclusions and discussions

The unsteady nonlinear two-dimensional Burgers' equations are analyzed by the ELMFS which is the combination

of the ELM and the MFS. The two-dimensional quasi-linear Burgers' equations are converted to the characteristic diffusion equations by the ELM, and then the MFS is applied to the diffusion equations. Finally, the solutions of the Burgers' equations can be obtained by performing the back-tracking scheme through the characteristics. The proposed numerical scheme, which is free from mesh generation and numerical integration, is a truly meshless method. Therefore, it is very easy to simulate the nonlinear Burgers' problem in irregular domain with or without the disturbances of noisy initial and boundary data. In addition the unsteady MFS is applied in time-space united system, so Laplace transform or difference discretization for time domain is not needed. Furthermore, through this

Table 5  
Numerical solutions of (a)  $u$  and (b)  $v$  at different time levels in some specific points of problem 3 ( $Re = 10$ ,  $\Delta t = 0.005$ ,  $N = 120$ )

$x$	$y$	$t = 0.01$			$t = 0.5$			$t = 2.0$		
		Analytical solution	ELMFS	ERROR	Analytical solution	ELMFS	ERROR	Analytical solution	ELMFS	ERROR
$(a)$										
0.00	0.90	0.68858	0.68863	4.88E−05	0.68122	0.68128	6.35E−05	0.65561	0.65584	2.23E−04
−0.70	0.50	0.70428	0.70430	1.81E−05	0.69828	0.69827	1.87E−06	0.67645	0.67648	3.41E−05
−0.70	−0.50	0.64035	0.64041	5.45E−05	0.63086	0.63114	2.83E−04	0.60183	0.60212	2.89E−04
0.00	−0.90	0.56113	0.56129	1.68E−04	0.55433	0.55475	4.15E−04	0.53701	0.53738	3.67E−04
0.90	0.00	0.56113	0.56130	1.70E−04	0.55433	0.55459	2.60E−04	0.53701	0.53736	3.53E−04
0.00	0.50	0.58698	0.58700	1.44E−05	0.57851	0.57859	8.22E−05	0.55568	0.55613	4.59E−04
−0.45	0.25	0.67628	0.67629	4.27E−06	0.66808	0.66819	1.04E−04	0.64054	0.64080	2.57E−04
−0.38	0.00	0.65359	0.65359	4.21E−06	0.64437	0.64453	1.56E−04	0.61525	0.61560	3.46E−04
−0.45	−0.25	0.64035	0.64037	2.02E−05	0.63086	0.63113	2.75E−04	0.60183	0.60221	3.80E−04
0.00	−0.50	0.58698	0.58699	7.03E−06	0.57851	0.57887	3.56E−04	0.55568	0.55616	4.83E−04
0.50	0.00	0.58698	0.58700	1.44E−05	0.57851	0.57859	8.22E−05	0.55568	0.55613	4.59E−04
0.00	0.08	0.63105	0.63107	1.82E−05	0.62149	0.62157	8.11E−05	0.59292	0.59339	4.66E−04
−0.07	0.00	0.62988	0.62989	1.28E−05	0.62031	0.62042	1.04E−04	0.59183	0.59228	4.55E−04
0.00	−0.08	0.61856	0.61858	1.65E−05	0.60907	0.60919	1.22E−04	0.58157	0.58205	4.78E−04
0.08	0.00	0.61856	0.61858	2.36E−05	0.60907	0.60917	9.40E−05	0.58157	0.58207	4.94E−04
$(b)$										
0.00	0.90	0.81142	0.81138	3.52E−05	0.81878	0.81873	5.47E−05	0.84439	0.84419	1.95E−04
−0.70	0.50	0.79572	0.79572	7.99E−06	0.80172	0.80175	2.86E−05	0.82355	0.82355	5.04E−06
−0.70	−0.50	0.85965	0.85961	4.21E−05	0.86914	0.86894	2.05E−04	0.89817	0.89796	2.09E−04
0.00	−0.90	0.93887	0.93872	1.50E−04	0.94567	0.94532	3.48E−04	0.96299	0.96269	2.98E−04
0.90	0.00	0.93887	0.93874	1.37E−04	0.94567	0.94546	2.07E−04	0.96299	0.96271	2.76E−04
0.00	0.50	0.91302	0.91301	8.04E−06	0.92149	0.92142	6.75E−05	0.94432	0.94394	3.82E−04
−0.45	0.25	0.82372	0.82372	8.14E−07	0.83192	0.83183	8.35E−05	0.85946	0.85924	2.16E−04
−0.38	0.00	0.84641	0.84641	2.98E−06	0.85563	0.85550	1.30E−04	0.88475	0.88446	2.88E−04
−0.45	−0.25	0.85965	0.85963	1.50E−05	0.86914	0.86893	2.15E−04	0.89817	0.89787	3.00E−04
0.00	−0.50	0.91302	0.91301	5.04E−06	0.92149	0.92117	3.19E−04	0.94432	0.94391	4.19E−04
0.50	0.00	0.91302	0.91301	8.04E−06	0.92149	0.92142	6.75E−05	0.94432	0.94394	3.82E−04
0.00	0.08	0.86895	0.86894	1.06E−05	0.87851	0.87845	6.80E−05	0.90708	0.90669	3.91E−04
−0.07	0.00	0.87012	0.87011	7.62E−06	0.87969	0.87959	9.19E−05	0.90817	0.90779	3.84E−04
0.00	−0.08	0.88144	0.88143	9.72E−06	0.89093	0.89082	1.08E−04	0.91843	0.91802	4.05E−04
0.08	0.00	0.88144	0.88143	1.35E−05	0.89093	0.89085	7.76E−05	0.91843	0.91801	4.13E−04

process we are able to extend the time-dependent MFS to solve nonlinear partial differential equations. In this article, the two-dimensional Burgers' equations in one and two variables are analyzed by the proposed meshless method and the ELMFS analysis compares very well with the analytical solutions and FDM results. Hence, it is convinced that the proposed method could provide a simple, robust and reliable numerical tool for Burgers' equations.

Although the proposed ELMFS can be easily used to deal with the nonlinear Burgers' equations, there are still some issues which have to be addressed at this stage. One of the issues is the stability of ELMFS which means the determinations of the time increment and the temporal location of the source points. Roughly speaking, the time increment of the ELMFS will be determined by a compromise of accurate schemes between the ELM (higher-order finite difference scheme will surely improve the accuracy) and the MFS (very accurate method). So there is no stability but only accuracy problem in the

ELMFS. On the other hand, the temporal location of the source points can be settled by the proposed empirical formula. More detailed numerical and theoretical study of the stability and accuracy will be performed in the near future.

Another relevant issue of ELMFS is the comparison of efficiency between the proposed method and conventional numerical methods. Though the proposed method outperforms conventional methods in the issue of mesh generation and numerical quadrature, and high powers to get accurate nonlinear solutions for dealing with the irregular domains and initial and boundary noise data by using very coarse collocating points, the full-populated matrices solvers are crucial for promoting efficiency of the ELMFS. It is too premature to draw a solid conclusion now to take into considerations of so many issues discussed above. Perhaps a thorough study to find an efficient matrices solver is of paramount importance to the popularity of the ELMFS and this investigation deserves more intensive research.

Table 6

Numerical solutions of (a)  $u$  and (b)  $v$  at different time levels in some specific points of problem 3 ( $Re = 100$ ,  $\Delta t = 0.005$ ,  $N = 364$ )

$x$	$y$	$t = 0.01$			$t = 0.5$			$t = 2.0$		
		Analytical solution	ELMFS	ERROR	Analytical solution	ELMFS	ERROR	Analytical solution	ELMFS	ERROR
$(a)$										
0.00	0.90	0.75000	0.74992	7.56E−05	0.74998	0.75011	1.29E−04	0.74833	0.74946	1.13E−03
−0.70	0.50	0.75000	0.75001	7.01E−06	0.75000	0.74979	2.12E−04	0.74996	0.75184	1.88E−03
−0.70	−0.50	0.73048	0.73155	1.07E−03	0.67965	0.67929	3.60E−04	0.50574	0.51385	8.10E−03
0.00	−0.90	0.50000	0.49995	5.45E−05	0.50000	0.50013	1.28E−04	0.50000	0.49996	3.74E−05
0.90	0.00	0.50000	0.49999	9.02E−06	0.50000	0.50004	3.73E−05	0.50000	0.50082	8.17E−04
0.00	0.50	0.74950	0.74951	6.85E−06	0.74772	0.74789	1.75E−04	0.62500	0.63329	8.29E−03
−0.45	0.25	0.74996	0.74995	5.36E−06	0.74981	0.74982	1.00E−05	0.73104	0.73304	2.00E−03
−0.38	0.00	0.74765	0.74765	7.59E−08	0.73948	0.73990	4.22E−04	0.54332	0.54915	5.82E−03
−0.45	−0.25	0.73048	0.73068	2.03E−04	0.67965	0.68394	4.29E−03	0.50574	0.50772	1.98E−03
0.00	−0.50	0.50047	0.50047	1.29E−06	0.50010	0.50014	4.32E−05	0.50000	0.49980	1.99E−04
0.50	0.00	0.50047	0.50048	1.74E−05	0.50010	0.50008	1.65E−05	0.50000	0.50087	8.67E−04
0.00	0.08	0.68122	0.68127	5.67E−05	0.59074	0.59524	4.49E−03	0.50131	0.50242	1.12E−03
−0.07	0.00	0.67149	0.67147	1.39E−05	0.58021	0.58433	4.13E−03	0.50108	0.50213	1.05E−03
0.00	−0.08	0.56571	0.56573	1.83E−05	0.51790	0.51827	3.77E−04	0.50018	0.50176	1.58E−03
0.08	0.00	0.56571	0.56567	3.90E−05	0.51790	0.51831	4.14E−04	0.50018	0.50070	5.22E−04
$(b)$										
0.00	0.90	0.75000	0.74993	7.63E−05	0.75002	0.74988	1.35E−04	0.75167	0.75059	1.08E−03
−0.70	0.50	0.75000	0.74992	7.61E−05	0.75000	0.75029	2.88E−04	0.75004	0.74792	2.12E−03
−0.70	−0.50	0.76952	0.76834	1.18E−03	0.82035	0.82075	4.00E−04	0.99426	0.98637	7.89E−03
0.00	−0.90	1.00000	0.99996	4.05E−05	1.00000	0.99999	4.49E−06	1.00000	1.00052	5.24E−04
0.90	0.00	1.00000	0.99985	1.42E−04	1.00000	0.99996	4.03E−05	1.00000	1.00213	2.13E−03
0.00	0.50	0.75050	0.75051	1.30E−05	0.75228	0.75214	1.44E−04	0.87500	0.86745	7.55E−03
−0.45	0.25	0.75004	0.75005	5.50E−06	0.75019	0.75018	8.44E−06	0.76896	0.76705	1.91E−03
−0.38	0.00	0.75235	0.75235	2.34E−08	0.76052	0.76012	4.01E−04	0.95668	0.95320	3.47E−03
−0.45	−0.25	0.76952	0.76932	2.03E−04	0.82035	0.81616	4.19E−03	0.99426	0.99471	4.59E−04
0.00	−0.50	0.99953	0.99955	1.24E−05	0.99990	0.99998	8.07E−05	1.00000	1.00276	2.76E−03
0.50	0.00	0.99953	0.99953	1.95E−06	0.99990	0.99993	3.34E−05	1.00000	1.00188	1.88E−03
0.00	0.08	0.81878	0.81873	5.63E−05	0.90926	0.90478	4.48E−03	0.99869	1.00030	1.61E−03
−0.07	0.00	0.82851	0.82853	1.28E−05	0.91979	0.91568	4.11E−03	0.99892	1.00062	1.71E−03
0.00	−0.08	0.93429	0.93427	2.03E−05	0.98210	0.98176	3.47E−04	0.99982	1.00096	1.14E−03
0.08	0.00	0.93429	0.93433	3.98E−05	0.98210	0.98169	4.15E−04	0.99982	1.00200	2.18E−03

## Acknowledgment

The National Science Council of Taiwan is greatly appreciated for providing financial support of this research under Grant no. NSC 94-2611-E-002-007. Prof. DL Young also likes to thank the support of the University of California at Irvine when he was a visiting scholar.

## References

- [1] Bateman H. Some recent researches on the motion of fluids. *Mon Weather Rev* 1915;43:163–70.
- [2] Burgers JM. A mathematical model illustrating the theory of turbulence. In: von Mises RV, von Karman TV, editors. *Advanced in applied mechanics*. New York: Academic Press; 1948.
- [3] Fletcher CAJ. Burgers' equation: a model for all reasons. In: Noye J, editor. *Numerical solutions of partial differential equations*. New York: North-Holland Pub Co; 1982.
- [4] Cole JD. On a quasi-linear parabolic equation occurring in aerodynamics. *Q Appl Math* 1951;19:225–36.
- [5] Hopf E. The partial differential equation  $u_t + uu_x = \mu_{xx}$ . *Commun Pure Appl Math* 1950;3:201–30.
- [6] Benton ER, Platzman GW. A table of solutions of the one-dimensional Burgers equation. *Q Appl Math* 1972;30:195–212.
- [7] Fletcher CAJ. Generating exact solutions of the two-dimensional Burgers' equation. *Int J Numer Methods Fluids* 1983;3:213–6.
- [8] Bahadir AR. A fully implicit finite-difference scheme for two-dimensional Burgers' equation. *Appl Math Comput* 2003;137:131–7.
- [9] Kutluay S, Bahadir AR, Ozdes A. Numerical solution of one-dimensional Burgers equation: explicit and exact-explicit finite difference methods. *J Comput Appl Math* 1999;103:251–61.
- [10] Radwan SF. Comparison of high-order accurate schemes for solving the two-dimensional unsteady Burgers' equation. *J Comput Appl Math* 2005;103:383–97.
- [11] Froncioni AM, Labbe P, Garon A, Camarero R. Interpolation-free space-time remeshing for the Burgers equation. *Commun Numer Methods Eng* 1997;13:875–84.
- [12] Kutluay S, Esen A, Dag I. Numerical solutions of the Burgers' equation by the least-squares quadratic B-spline finite element method. *J Comput Appl Math* 2004;167:21–33.
- [13] Chino E, Tosaka N. Dual reciprocity boundary element analysis of time-independent Burgers' equation. *Eng Anal Bound Elem* 1998;21:261–70.
- [14] Kakuda K, Tosaka N. The generalized boundary element approach to Burgers' equation. *Int J Numer Methods Eng* 1990;29:245–61.

- [15] Hon YC, Mao XZ. An efficient numerical scheme for Burgers' equation. *Appl Math Comput* 1998;95:37–50.
- [16] Li JC, Hon YC, Chen CS. Numerical comparisons of two meshless methods using radial basis functions. *Eng Anal Bound Elem* 2002;26:205–25.
- [17] Atluri SN. The meshless method (MLPG) for domain & b.e discretizations. Forsyth, GA, USA: Tech Science Press; 2004.
- [18] Atluri SN, Shen S. The meshless local Petrov-Galerkin (MLPG) method: a simple & less-costly alternative to the finite element and boundary element methods. *CMES* 2002;3:11–51.
- [19] Atluri SN, Zhu T. A new meshless local Petrov-Galerkin (MLPG) approach in computational mechanics. *Comput Mech* 1998;22: 117–27.
- [20] Lin H, Atluri SN. The meshless local Petrov-Galerkin (MLPG) method for solving incompressible Navier–Stokes equations. *CMES* 2001;2:117–42.
- [21] Golberg MA. The method of fundamental solutions for Poisson's equations. *Eng Anal Bound Elem* 1995;16:205–13.
- [22] Hu SP, Fan CM, Chen CW, Young DL. Method of fundamental solutions for Stokes' first and second problems. *J Mech* 2005;21:25–31.
- [23] Karageorghis A, Fairweather G. The method of fundamental solutions for the numerical solution of the biharmonic equation. *J Comput Phys* 1987;69:434–59.
- [24] Kupradze VD, Aleksidze MA. The method of functional equations for the approximate solution of certain boundary value problem. *Comput Math Math Phys* 1964;4(4):82–126.
- [25] Young DL, Fan CM, Tsai CC, Chen CW, Murugesan K. Eulerian–Lagrangian method of fundamental solutions for multi-dimensional advection–diffusion equation. *Int Math Forum* 2006;1(14):687–706.
- [26] Young DL, Ruan JW. Method of fundamental solutions for scattering problems of electromagnetic waves. *CMES* 2005;7:223–32.
- [27] Young DL, Chen CW, Fan CM, Murugesan K, Tsai CC. The method of fundamental solutions for Stokes flow in a rectangular cavity with cylinders. *Eur J Mech B-Fluids* 2005;24:703–16.
- [28] Young DL, Tsai CC, Murugesan K, Fan CM, Chen CW. Time-dependent fundamental solutions for homogeneous diffusion problems. *Eng Anal Bound Elem* 2004;29:1463–73.
- [29] Young DL, Tsai CC, Fan CM. Direct approach to solve non-homogeneous diffusion problems using fundamental solutions and dual reciprocity methods. *J Chin Inst Eng* 2004;27:597–609.
- [30] Young DL, Wang YF, Eldho TI. Solution of the advection–diffusion equation using the Eulerian–Lagrangian boundary element method. *Eng Anal Bound Elem* 2000;24:449–57.
- [31] Young DL. An Eulerian–Lagrangian method of fundamental solutions for Burger's equation. In: Sladek J, Sladek V, Atluri SN, editors. *Advances in the meshless method*. Forsyth, GA, USA: Tech Science Press; 2007.
- [32] Young DL, Tsai CC, Fan CM, Chen CW. The method of fundamental solutions and condition number analysis for inverse problem of Laplace equation. *Comput Math Appl*, 2007, in press, doi:10.1016/j.camwa.2007.05.015.
- [33] Marin L, Elliott L, Heggs PJ, Ingham DB, Lesnic D, Wen X. Comparison of regularization methods for solving the Cauchy problem associated with the Helmholtz equation. *Int J Numer Methods Eng* 2004;60:1933–47.
- [34] Press WH, Teukolsky SA, Vetterling WT, Flannery BP. *Numerical recipes in Fortran 77: the art of scientific computing*. Cambridge: Cambridge University Press; 1999.